Quaternary glaciation in Central Asia

Jigjidsurengiin Batbaatar

A dissertation

submitted in partial fulfillment of the

requirements for the degree of

Doctor of Philosophy

University of Washington

2018

Reading Committee:

Alan Gillespie, Chair

Summer Rupper

David Montgomery

Program Authorized to Offer Degree:

Department of Earth and Space Sciences

University of Washington

Abstract

Quaternary glaciations in Central Asia

Jigjidsurengiin Batbaatar

Chair of the Supervisory Committee:
Emeritus Research Professor Alan Gillespie
Department of Earth and Space Sciences

The mountain ranges in Central Asia were heavily glaciated during the Quaternary Period. The relative magnitudes of paleoglaciers varied spatially and temporally. The chronology of glacial standstills was established from 37 sites spread over nine ranges in Central Asia using cosmic-ray exposure, luminescence, and radiocarbon dating techniques, and the magnitudes of glacial standstills were estimated from equilibrium-line altitudes (ELA) of the paleoglaciers. The study sites were chosen in regions where the ELAs predicted from numerical modeling to exhibit different sensitivities to changes in air temperature and precipitation. The dating and the ELA depression from modern values (ΔELA) reveal that some paleoglaciers in humid regions advanced to their local maxima before the global Last Glacial Maximum (LGM), a period characterized by abrupt sea-level decrease and existence of large ice sheets on the continents. The glacier ELAs in these humid regions were modeled to be more sensitive to air temperatures than to precipitation.

Most of the paleoglaciers advanced to their maximum during the global LGM, suggesting a strong response to minima in insolation and air temperature at the time. In cold and arid regions, most of the paleoglaciers advanced to their maximum tens of thousands of years before the global LGM, and their extents during the global LGM were limited to their cirques. In one particular case, a paleoglacier in the Mongolian Gobi advanced to its maximum during early Holocene without evidence of earlier glaciation. This spatially and temporally asynchronous glaciations in cold and arid regions were probably driven more sensitively to changes in precipitation than in air temperatures, a consistent response per the numerical sensitivity models. The results highlight the importance of precipitation in controlling the advances of paleoglaciers in a continental setting.

TABLE OF CONTENTS

LIST OF FIGURES

LIST OF TABLES

Вашингтоны Их Сургууль

Хураангуй

Төв Ази дахь Дөрөвдөгчийн галвын мөстлөг

Жигжидсүрэнгийн Батбаатар

Удирдах комиссын ахлагч:
Профессор Алан Гиллеспи
Дэлхий ба Сансар Судлалын Салбар

Дөрөвдөгчийн галвын үед Төв Азийн уул нурууд их хэмжээний мөсөөр хучигдаж байсан бөгөөд эртний мөсөн голуудын хэмжээ орон зай болон цаг хугацааны хувьд харилцан адилгүй байсан. Энэхүү судалгаагаагаар Төв Азийн есөн уул нуруудаас 37 судалгааны талбай сонгон чулуу, хурдасны дээж авч, сансраас гаралтай изотоп, дотоод гэрлийн цацраг, мөн цацраг идэвхит нүүрстөрөгчийн агууламжийг хэмжсэнээр эртний мөстлөгийн насжилтыг тогтоов. Мөсөн голуудын түрэх эсвэл ухрах нь уур амьсгалын өөрчлөлтөөс шууд хамааралтай байдаг. Тоон загварчлалын үр дүнгээс харахад чийглэг, хур тунадас ихтэй нутгуудад мөсөн гол агаарын температурын өөрчлөлтөд мэдрэмтгий байдаг бол хуурай, хүйтэн нутгуудад мөсөн гол хур тунадасны өөрчлөлтөд илүү мэдрэмтгий байдаг. Дээж авах судалгааны талбайг сонгохдоо уур амьсгалын өөрчлөлтөд харилцан адилгүй мэдрэмжтэй мөсөн гол тархсан нутгуудыг багтаахыг зорьсон болно.

Энэхүү судалгааны үр дүнд харилцан адилгүй хэмжээ болон насжилттай мөсөн голуудын тархалтыг тогтоов. Хориод мянган жилийн өмнө явагдсан Сүүлчийн Дээд Мөстлөгийн (СДМ) үед чийглэг, хур тунадас ихтэй нутгуудын ихэнхи мөсөн голууд их хэмжээгээр түрж, томорч байсныг баримтжуулав. Эдгээр түрэлт нь нь уур амьсгал эрчимтэй хүйтэрсэнтэй холбоотой болно. Гэхдээ, тухайн үед хур тунадасны хэмжээ буурсны улмаас зарим мөсөн голуудын тэжээгдэл татарч харьцангуй бага түрэлттэй байсныг мөн баримтжуулан тогтоолоо. Түүнээс гадна, олон тооны мөсөн голуудын дээд хэмжээний түрэлт СДМ-өөс олон арван мянган жилийн өмнө явагдаж байсныг илрүүлэв. Тэр үед уур амьсгал харьцангуй дулаан байсан боловч хур тунадас ихсэж мөсөн голуудын тэжээгдэл нэмэгдсэн нь дээд хэмжээний түрэлт СДМ-өөс өмнө явагдах шалтгаан болжээ.

Хүйтэн, хуурай уур амьсгалтай нутгуудын ихэнхи мөсөн голууд СДМ-ийн үед маш бага хэмжээний түрэлт үзүүлж байсныг тогтоосон. Жишээ нь, Говь-Алтайн нурууны нэгэн мөсөн гол эртний Голоцений үед буюу СДМ дууссаны дараа түрж, томорч байсныг баримтжуулав. Төв Азийн мөсөн голууд орон зай болон цаг хугацааны хувьд харилцан адилгүй хэлбэлзэлтэй байсан нь магадгүй хур тунадасны өөрчлөлт газар нутгуудад харилцан адилгүй байсантай холбоотой болно. Харилцан адилгүй хэмжээ болон насжилттай эртний мөсөн голуудын тархалтыг тайлбарлахын тулд мөсөн голын уур амьсгалын өөрчлөлтөд үзүүлэх мэдрэмжийг тогтоох, ялангуяа хур тунадасны өөрчлөлтөд мөсөн голууд хэрхэн хариу үйлдэл үзүүлдэгийг цаашид нарийвчлан тогтоох шаардлагатай болно.

ACKNOWLEDGEMENTS

This dissertation was a culmination of support by many individuals to whom I am grateful. I am indebted to my advisor, Alan R. Gillespie, for his excellent mentorship. He showed me how to be a better scientist, a better colleague, and a better human. Thank you, Alan, for your unbelievable patience. The scientific works of my committee members were formative to my own work. I would like to thank James Feathers, David Montgomery, Gerard Roe, Summer Rupper, and John Stone for their ample inspiration and guidance.

Specific connections and opportunities built a strong foundation for my research. Amgalan Bayasgalan took me on a trip to Darhad basin, where I met Alan for the first time; and D. Sukhbaatar of "Damdin Da Foundation" provided logistical support in the collection of the early samples reported in my dissertation. I am grateful for the opportunity to contribute to great research by Matthew Smith and Rivka Amit.

I was not alone in carrying the intellectual (and physical) weight of my research; many people supported me with mentorship, expertise, equipment, and finances. As colleagues and mentors, B. Charlotte Schreiber, Ari Matmon, David Fink, Amit Mushkin, Michele Koppes, Yehouda Enzel, ZhongPing Lai, and Toshiyuki Fujioka were crucial to the success of my research. Ron Sletten, Howard Conway, Steve Warren, and Al Rasmussen lent their expertise and equipment for the weather measurements at Sutai mountain. Galhuu Bat-Ochir and Byambaa helped me in the field. Jody Bourgeois provided financial support for that trip through the department's graduate student awards. I am grateful to Carrie Garrison-Laney and Brian Sherrod, who analyzed the diatoms in my samples.

Without the support of the incredible staff at the Earth and Space Sciences department of UW, my life would have been much harder. Robert Winglee, Bruce Nelson, Harvey Greenberg, Eunice Yang, Kathy Gabriel, Noéll Bernard-Kingsley, Monick Keo, Ed Mulligan, and Dave McDougall all provided unwavering support. My fellow graduate students shared much-needed friendship and company during coffee breaks: Moon Young Choi, Zoë Harrold, Matthew Smith, Max Needle, Karl Lang, Mike Turzewski, and everybody else.

My parents, Tsetseg Damba and Jigjidsuren Gombojav, prodded me into a world of science and supported me all the way. With my love, adoration, and respect, thank you. My brothers, Bodisuren and Bodibaatar, have been good caretakers at home during my adventures abroad. My boys, Tsogt-Ochir and Munh-Orgil, were pure joy in my life except when they were asking for iPad passwords. Last, but certainly not the least, I cannot thank enough my wife, Bayarkhuu Bat-Ochir, who sacrificed her career and followed me along this journey.

DEDICATION

To my wife Bayaraa

Chapter 1

INTRODUCTION

1.1 MOTIVATION

The distinctive mountain landscapes carved by past glaciers and adorned by modern glaciers near high peaks fascinate every observer of nature. The almost-synchronous demise of modern glaciers around the globe, however, has become the self-evident 'pulse' on the current warming climate attributed to humans. This is because the glaciers directly respond to local climate conditions, and by aggregating the spatial and temporal patterns of glacier advances and retreats this response can be used to infer regional changes in climate (Roe et al., 2017). Furthermore, glacial deposits left from past glacial advances and retreats can be used to reconstruct paleoclimate variables in places where no other proxies are available. In general, an accurate reconstruction of paleoclimate from glacial deposits requires the following three steps: 1) Establish the chronology of glacial advances and/or standstills using radiometric dating; 2) Establish and quantify a consistent metric for the state of a glacier; 3) Establish the relationship between glacier state and climate parameters. Each of these steps has been addressed in the literature, which I will summarize in the following paragraphs and which will highlight the problems that need improvement. This dissertation is focused on glacial evidence in Central Asia because a large number of glacial deposits were left under various climatic or environmental conditions. The methods and approach used in this dissertation are summarized in Section 1.2 and the main results of the Chapters 2–4 are summarized in Section 1.3 of this Chapter.

The high mountain ranges of Central Asia were formed around 50 million years ago when the Eurasian and Indian continental plates collided (Molnar and Tapponier, 1975), and the cold peaks of these mountains have been modified by glaciers during the glacial cycles of the Pleistocene epoch (e.g., Koppes and Montgomery, 2009). Despite the vast expanse of glacial landscapes and deposits in Central Asia, the continent was not accessible to a broad scientific community from World War II to about 1990, due to the political divide between the countries in eastern and western hemispheres. The political thaw between the two camps around 1990's brought increased collaboration between researchers, which allowed, for example, a comparison of glaciations in the North and South Americas, Europe with those in Central Asia. One of the first such global observations by Gillespie and Molnar (1995; Figure 1.1) noted two general types of asynchronism between the glacial advances in different climate regions: 1) Asynchrony in the timing of maximum glacial extents; and 2) Asynchrony in the amplitude of glacial extents during the same climate stade. In other words, when the most continental ice sheets were gaining their maximum extents during the global Last Glacial Maximum (global LGM) around 21 ka many mountain glaciers were not at their maximum extents. Instead, many mountain glaciers extended to their maximum lengths tens of thousands of years before the global LGM, from which Gillespie and Molnar (1995) noted the importance of precipitation in regulating the glacier growth. However, the constraints on the ages of glacial advances were poor at that time and the high-resolution temporal comparison of different glacier advances was not possible. Since then, the development and widespread use of cosmogenic nuclides have allowed directly dating the boulders on moraines, which precisely mark the past positions of glaciers. A compilation of cosmic-ray exposure ages previously published in literature is now available in a global database

(http://expage.github.io) and comprises an invaluable tool for establishing temporal comparison of glacial advances.

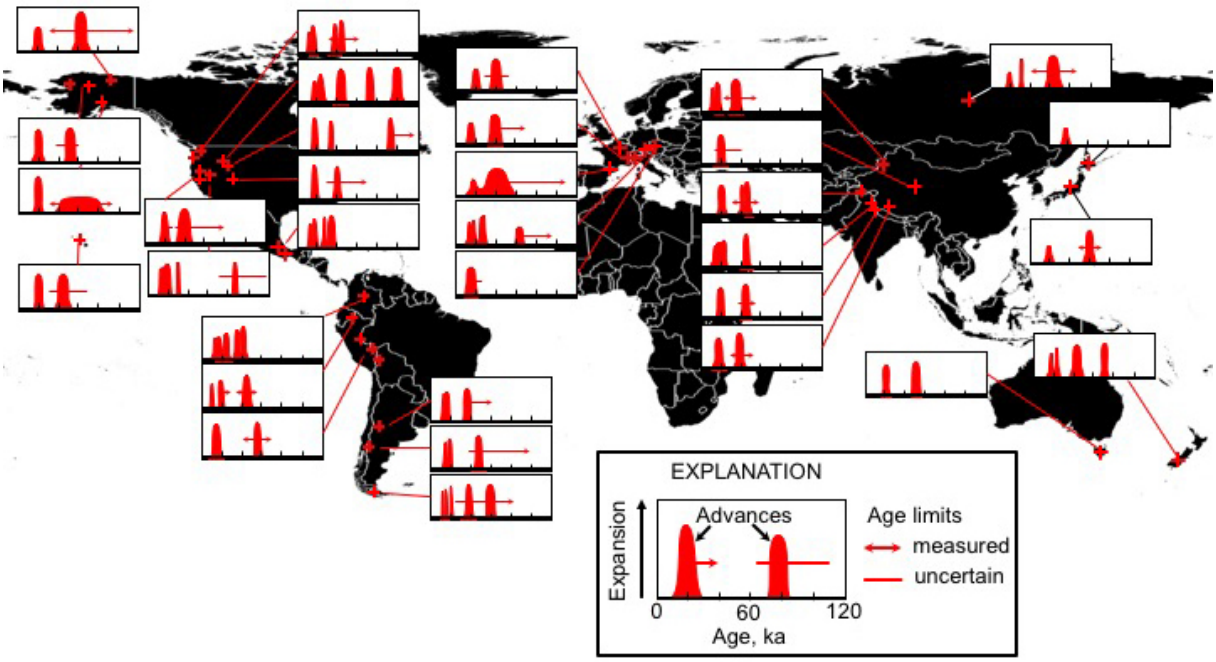

Figure 1.1 Glacial asynchrony around the globe (from Gillespie and Molnar, 1995). Schematic summary of the timing and relative extent of the of the late Pleistocene alpine glacial advances surveyed in Gillespie and Molnar (1995). The authors noted that the ages were poorly constrained, and this presentation was speculative. Locations of the study sites are shown by crosses, and the exact coordinates are available in the original article.

Although there are more than 2000 individual cosmogenic nuclide ages are available for approximately 500 glacial deposits in Central Asia, most of the ages are from the Pamir-Karakorum-Himalaya regions, in which the precipitation is derived mostly from Indian monsoon (Figure 1.2). In this dissertation, the study sites are chosen in the mountain ranges located in more continental climates, such as the Sayan, Hangai, Gobi-Altai, Tian Shan, Qilian Shan, and Kunlun ranges, to sample from the less represented regions. Chapter 2 covers the East Sayan ranges and Hangai ranges, establishing the glacial chronology (and the chronology of related giant glacial

outburst floods down the upper Yenisei River) in the northernmost parts of Central Asia. Chapter 3 focuses in the Gobi-Altai and Hangai ranges, documenting an extreme example of asynchronous glaciations within a short distance. Chapter 4 expands the glacial chronology to include the Tian Shan, Qilian Shan, and Kunlun ranges and evaluated the glacial history in the context of the glacial chronology in other regions.

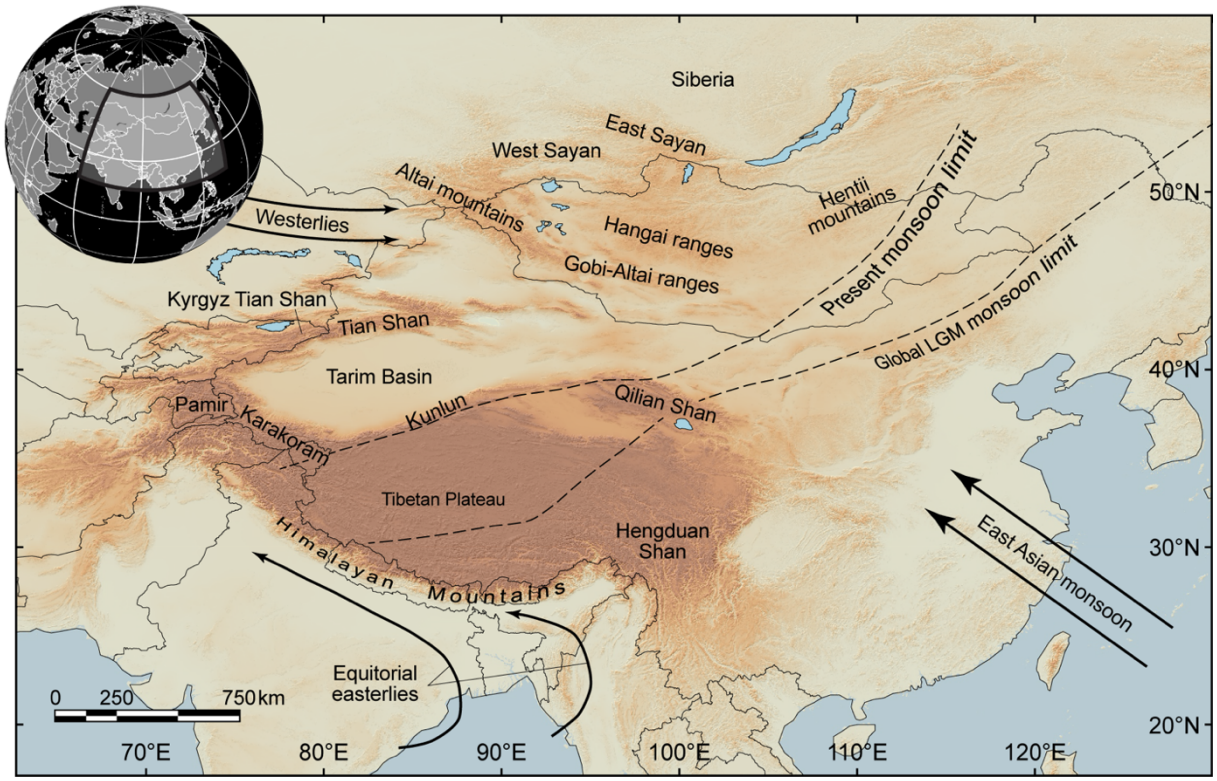

Figure 1.2. Geography of the mountain ranges in Central Asia. Dashed lines indicate the modern and global LGM limits of the East Asian monsoon (Shi, 2002). Solid lines indicate the general direction of major air flows (Benn and Owen, 1998).

The growth of a glacier is dictated by its mass balance, the difference between the annual accumulation and ablation. It is a straightforward metric of glacier growth: Precipitation fallen as snow accumulates in high altitudes and if it is greater than the mass lost to sublimation and seasonal melt then the glacierized ice flows downhill to a lower altitude until it is warm enough to melt the remaining ice. Relationships between the glacier mass balance and climate is addressed in the next paragraph, and here I discuss only the measuring of the glacier mass balance. In a geometric sense, mass of a glacier can be estimated at various altitudes by multiplying the glacier volume with measured or assumed density of ice. The volume can be measured in three quantities: length, width, and thickness. Among these three, the length is the most straightforward measure of glacier positions, past and present. Indeed, the longest records of historical measurements of glaciers were of their lengths (Roe et al., 2017). Glacier width varies from the accumulation zone to the ablation zone but is relatively easy to estimate for modern glaciers from aerial and satellite images. For example, Global Land Ice Measurements from Space project (GLIMS) uses satellite images to outline the glacier ice extents over the globe to compile a worldwide inventory of glaciers (Randolph Glacier Inventory: RGI, 2017). For paleoglaciers, however, it is not so easy to estimate the paleo-width because the glaciers are not there, and no automatic detection-algorithm has been developed to delineate the paleoglacier extents. Therefore, the mapping of paleoglacier extents require extensive field investigation and photo interpretative mapping, and these are labor-intensive efforts. As far as I know, there is no worldwide map of paleoglacial landscapes and deposits. A few regional-scale maps exist for Central Asia (Figure 1.3), covering NE Tibet (Heyman et al., 2008), Central Tibet (Morén et al., 2011), SE Tibet (Fu et al., 2012), the Tian Shan (Stroeven et al., 2013), and the Altai and Western Sayan (Blomdin et al., 2014) in addition to individual maps provided with the dating studies of glacial deposits.

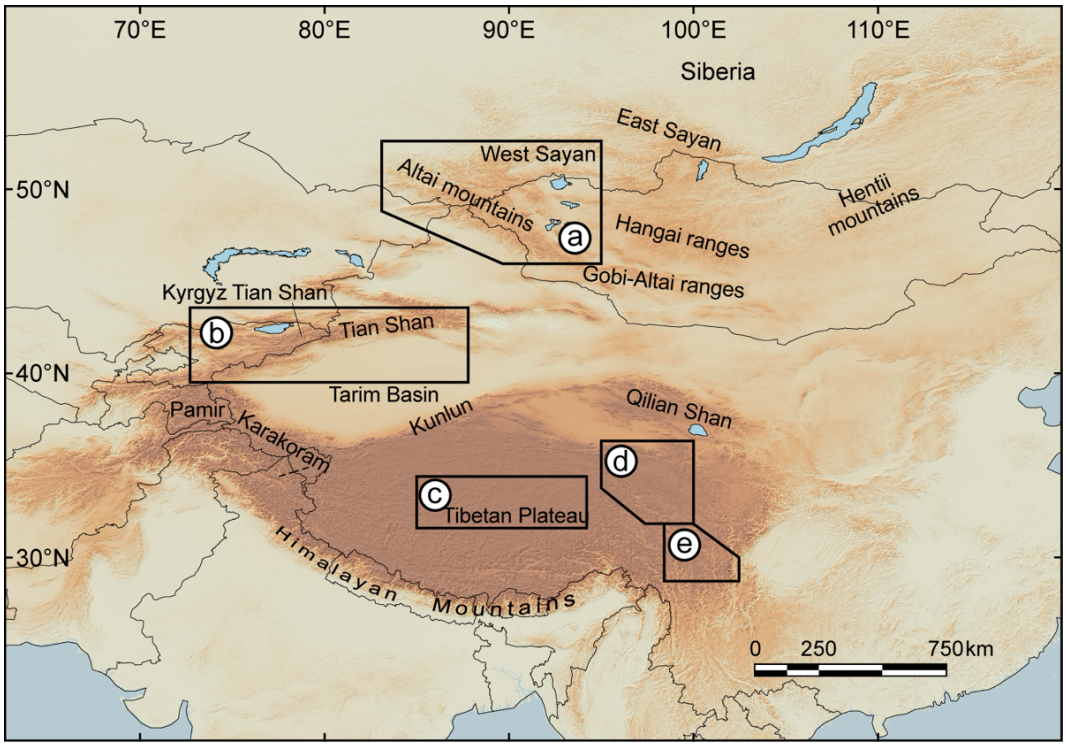

Figure 1.3. Areas with available glacial geomorphological maps in Central Asia (from Blomdin et al., 2014). The maps are for a) Altai and Western Sayan Mountains (Blomdin et al., 2014), b) Tian Shan (Stroeven et al., 2013), c) Tangula Shan (Morén et al., 2011), d) Bayan Har Shan (Heyman et al., 2008), and e) Shaluli Shan (Fu et al., 2012).

Thickness is the hardest of the three quantities to estimate. For a modern glacier, its bed topography can be estimated using a numerical model based on the empirical relationship between the bed slope and ice thickness (e.g., Frey et al., 2004, Kraaijenbrink et al., 2017). For paleoglaciers, Benn and Hulton (2010) developed a simple numerical model to reconstruct a surface topography of a glacier based on the basal stress caused by the weight of the ice. These labor-intensive mapping techniques of glacier volumes, however, do not directly relate to the amount of accumulation and ablation of a glacier. On the other hand, equilibrium-line altitude (ELA) of a glacier, an altitude of a zone on a glacier-surface in which the annual accumulation and ablation equals, provides a direct measure of glacial advance and retreat in response to the climate

forcing acting on the glacier. Among the many ways of estimating the ELA, the Toe-Headwall Altitude Ratio (THAR) and Accumulation-Area Ratio (AAR) methods are accepted to be the most reliable (e.g., Porter 1975; Meierding, 1982; Porter, 2001). The AAR method assumes that the accumulation area of the glacier covers a certain portion of the total area of the glacier (~65% for most temperate, debris-free glaciers, Porter, 2001) and it requires an accurate estimation of glacier outline and thickness of the paleoglacier, which is hard to acquire for the reasons mentioned above. The THAR method assumes a simple valley geometry for the glacier and estimates the ELA at the threshold value of the altitude difference between the toe and the headwall of a glacier (Eq. 1.1).

$$ELA = A_t + THAR(A_h - A_t) \quad (1.1)$$

where, A_t is toe altitude, A_h is headwall altitude, *THAR* is a threshold value. The value of *THAR* varies from glacier to glacier, but the recent compilation studies have shown that the median altitude of the glaciers were appropriate estimations of THAR ELAs (e.g., Heyman 2014; Nuimura et al., 2015). Maximum Elevation of Lateral Moraine (MELM) method assumes that the deposition of till occurs only below the ELA, where ablation exceeds accumulation (Meierding, 1975; Porter, 2001), and is a useful estimation of ELA where only lateral moraines exist and no end moraine is found. However, due to small chance of depositing lateral moraines on steep slopes or subsequent erosion the MELM considered to be the least reliable of the methods mentioned above (Meierding, 1982; Porter, 2001). Batbaatar and Gillespie (2012) used these three techniques to estimate the ELAs for well-defined mountain glaciers in the Eastern Sayan range and found that the disagreement between the ELAs estimated with the three methods was ~100 m (Figure 1.4), which was no more than the technique precision given by Meierding (1982) and Gillespie (1991). All ELAs for modern and paleoglaciers presented in the Chapter 2–4 were estimated using the THAR and MELM methods and the justification for the use of the methods is provided in each instance.

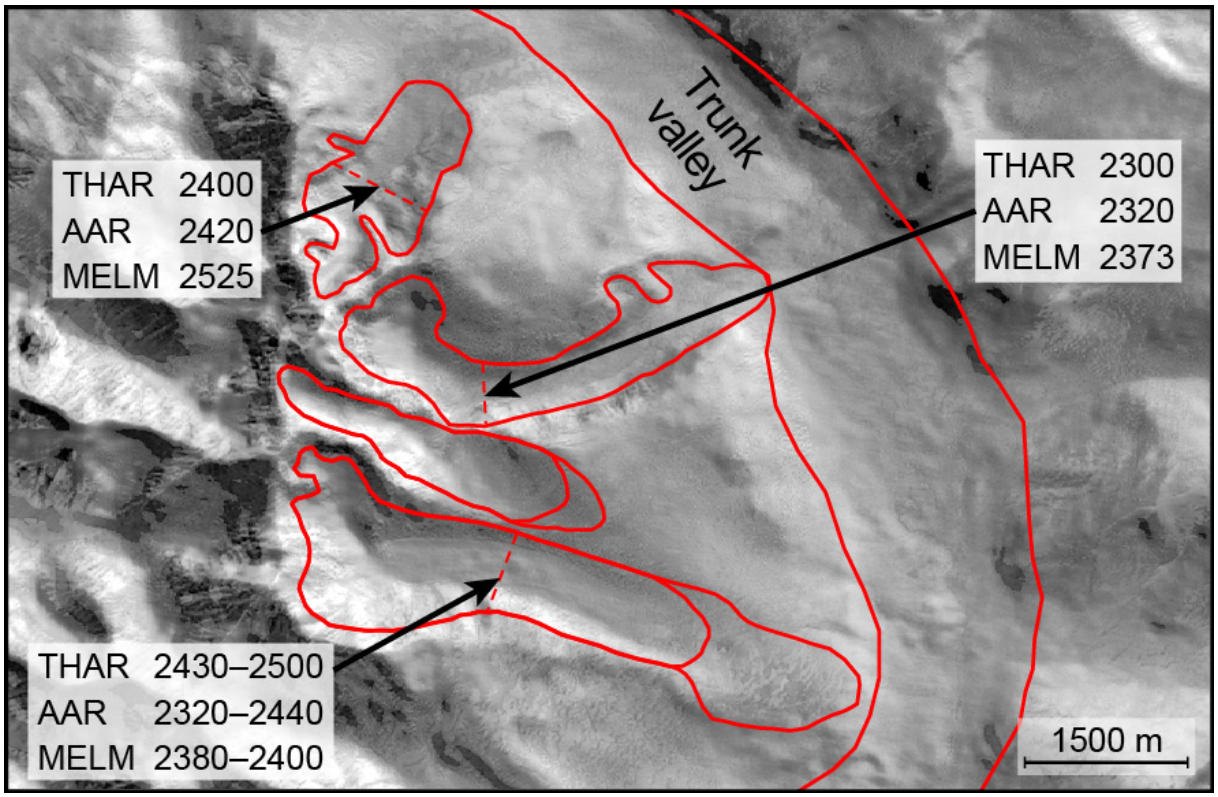

Figure 1.4. Paleo-ELA estimation at the Hoit Aguy mountain, southern Siberia (from Batbaatar and Gillespie, 2012). The ELA values (m asl) were estimated using THAR, AAR, and MELM methods. The location is near N 51.5.4° and E 98.7°.

The final step in the reconstruction of paleoclimate from glacial deposits depends on how reliable we understand the relationship between the ELA and the climate. In general, there are two models that establishes this relationship: 1) Empirical models based on the summer temperature and the annual precipitation at the ELA (e.g., Ohmura et al., 1992); and 2) Physically based numerical models that account for all the atmospheric variables and calculate the ablation for comparison to the accumulation (e.g., Kayastha et al., 1999; Mölg and Hardy, 2004; Rupper and Roe, 2008).

An empirical curve relating the summer mean air temperature and annual precipitation at the ELA was first established by Ohmura et al. (1992) by extrapolating the above-mentioned variables for 70 glaciers worldwide. Sakai et al. (2015; Figure 1.5) used a high-resolution gridded climate dataset to establish a similar empirical curve estimated for the modern glaciers in Central Asia.

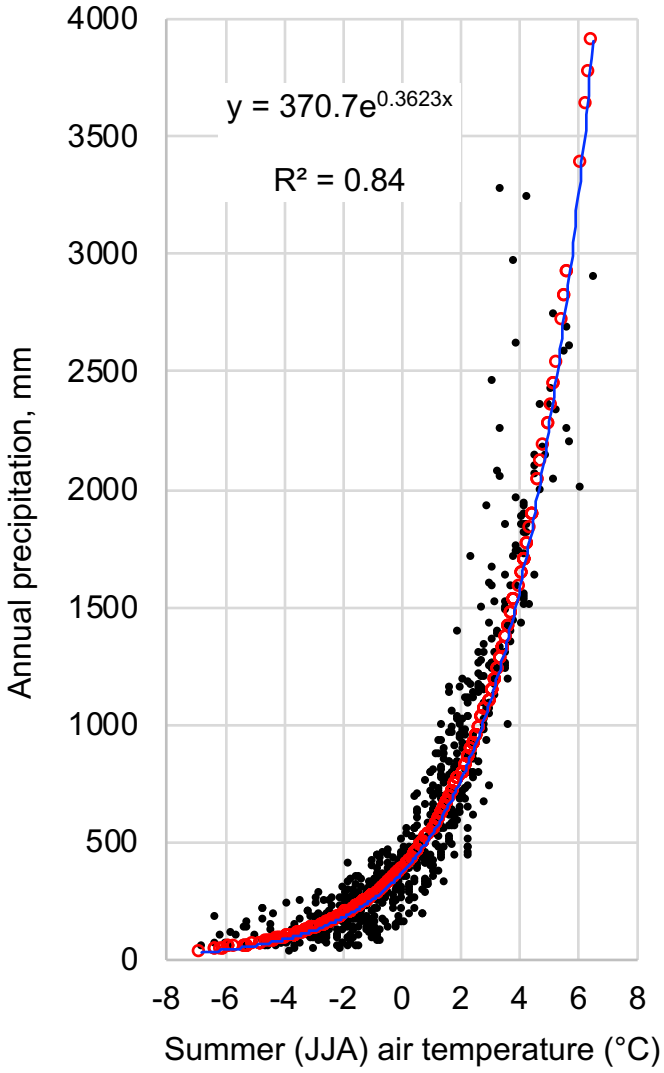

Figure 1.5. Annual precipitation and summer temperature at the modern ELAs for Central Asian glaciers. The black dots are the actual data from Sakai et al. (2015) and the red circles are calculated values from the equation derived from fitted exponential curve.

From this empirical curve two different regime of glaciers emerge: 1) In regions with summer temperature >0 °C the glaciers are sensitive to both temperature and precipitation, and the annual precipitation is always >150 mm; 2) In regions with summer temperature < −2 °C the glaciers are most sensitive to precipitation and the annual precipitation ranges from ~40–250 mm. This empirical relationship between summer air temperature and annual precipitation should also hold true for the paleoglaciers, and if one of the variables is known from an independent proxy, then the other could be estimated using the paleo-ELA. This is very appealing for its simplicity and establishes an important framework for reconstructing paleoclimate from glacial records.

Physically based numerical models calculate the ablation at various altitudes of a glacier using important atmospheric variables driving the glacier growth, such as air temperature, incoming and outgoing short and longwave radiations, and accounts for wind speed and cloud cover. The accumulation will exceed ablation at higher altitudes due to colder environment than in the lower altitudes. The decreased ablation with lowering altitude then must equal to accumulation at an altitude where the ELA is defined. Rupper and Roe (2008) developed such a model to predict the ELA sensitivities of Central Asian glaciers to climate variables and highlighted two modes of glacier ablation (Figure 1.6): 1) In regions with >500 mm annual precipitation, melt is responsible for most of the ablation and the ELA is more sensitive to air temperature than to precipitation; 2) In regions with <500 mm annual precipitation the sublimation plays larger role in ablation and the ELA becomes more sensitive to precipitation, especially since the temperature is already below freezing much of the time. The extreme example of this disparity in the ablation mechanism is more pronounced in arid regions (annual precipitation <150 mm).

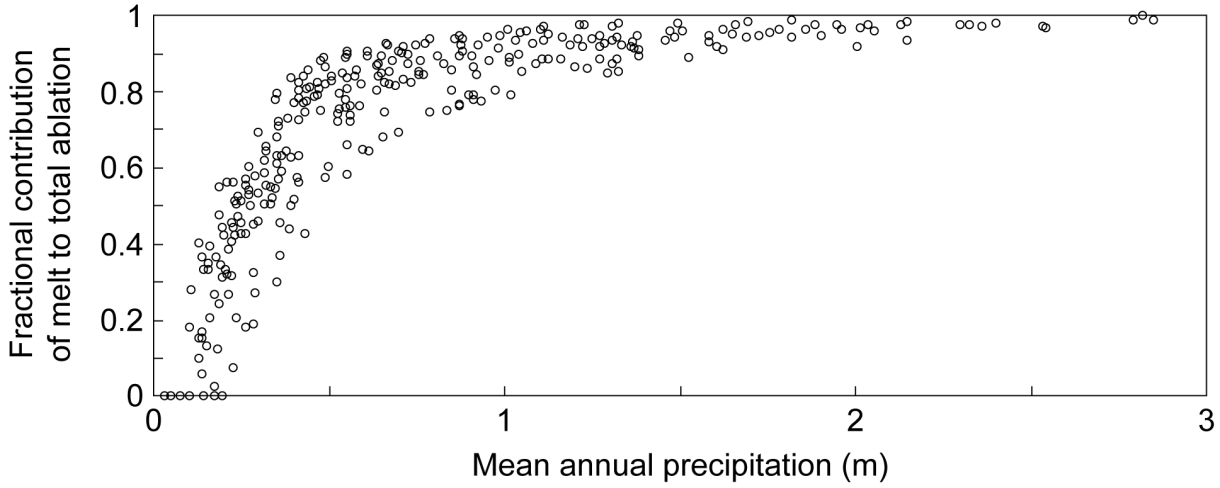

Figure 1.6. Mean annual precipitation vs. fractional contribution of melt to total ablation in Central Asia (from Rupper and Roe, 2008). Each data point represents NCEP-NCAR reanalysis grids (1.875°; Kalnay et al., 1996) used in the study.

I examined both of these approaches in my research to better understand the relationship between glacier mass balance and climate. In this dissertation modern summer temperature and annual precipitation were estimated at the modern ELAs from reanalysis climate data (e.g., Kalnay et al., 1996; Adler et al., 2003; Fan and van den Dool, 2008; Harris et al., 2014) and were presented in context of the studied paleoglaciers in Chapters 2–4. I adapted the surface-energy and mass-balance numerical model of Rupper and Roe (2008) to calculate the ablation rates at various altitudes in the Gobi-Altai range; the results are presented in Chapter 3. I used the data from Sakai et al. (2015) to fit an exponential curve and derived a linear equation to relate the summer temperature and annual precipitation at the ELA. Then I solved for the ELA sensitivity to temperature of glaciers in high-precipitation regions; the results are presented in Chapter 4.

1.2 METHODS AND APPROACH

The glacial deposits were mapped in the field. Photo-interpretative mapping was done using satellite images from ASTER (NASA, 2009–2018), Landsat (USGS, 2009–2018) using ENVI (https://www.harris.com/solution/envi), QGIS (https://qgis.org), ESRI ArcGIS (https://www.esri.com/arcgis/), and Google Earth with images supplied by DigitalGlobe and GeoEye (2008–2018). The particular scenes used in this dissertation are identified in the corresponding chapters. The final maps and figures presented in this dissertation were produced using Adobe Photoshop and Illustrator (https://www.adobe.com/products/). A total of 208 ^{10}Be, 52 ^{26}Al, ten ^{14}C, and nine luminescence ages (Figure 1.7) were collected over ten field seasons in Central Asia and are reported in Chapters 2–4. The samples for ^{10}Be analysis were prepared at the Cosmogenic Nuclide Laboratory at the University of Washington in Seattle, WA, USA, under the guidance of John Stone (http://depts.washington.edu/cosmolab/), the Cosmogenic Laboratory at the Hebrew University of Jerusalem (http://en.earth.huji.ac.il) in Jerusalem, Israel, under the guidance of Ari Matmon, and at the University of Vermont Cosmogenic Nuclide Extraction Laboratory (http://www.uvm.edu/cosmolab/) in Burlington, VT, USA, under the guidance of Paul Bierman. The samples for ^{26}Al analysis were prepared at the above-mentioned laboratories in the University of Washington and the University of Vermont. Some of the prepared ^{10}Be and ^{26}Al samples were then sent for AMS analysis to the Center for Accelerator Mass Spectroscopy at the Lawrence Livermore National Laboratory (CAMS, LLNL: https://cams.llnl.gov) in Livermore, CA, USA, and some of the ^{10}Be samples were sent to the Center for Accelerator Science at the Australian Nuclear Science and Technology Organisation's (http://www.ansto.gov.au) ANTARES facility in Sydney, Australia. The ^{14}C samples presented in Chapter 2 were sent to and analyzed at CAMS (LLNL). The luminescence samples presented in Chapter 2 were prepared and analyzed at

the Luminescence Laboratory at the University of Washington in Seattle, WA, USA (http://depts.washington.edu/lumlab/), under the guidance of James Feathers. The lab attributions are given where needed in Chapters 2–4. I personally prepared the samples and performed the analysis of the ^{10}Be and luminescence dating at the above-mentioned facilities, except the University of Vermont and the LLNL CAMS. The calculation of melt and sublimation rates for a glacier in the Gobi-Altai, presented in Chapter 3, was adapted from Rupper and Roe (2008).

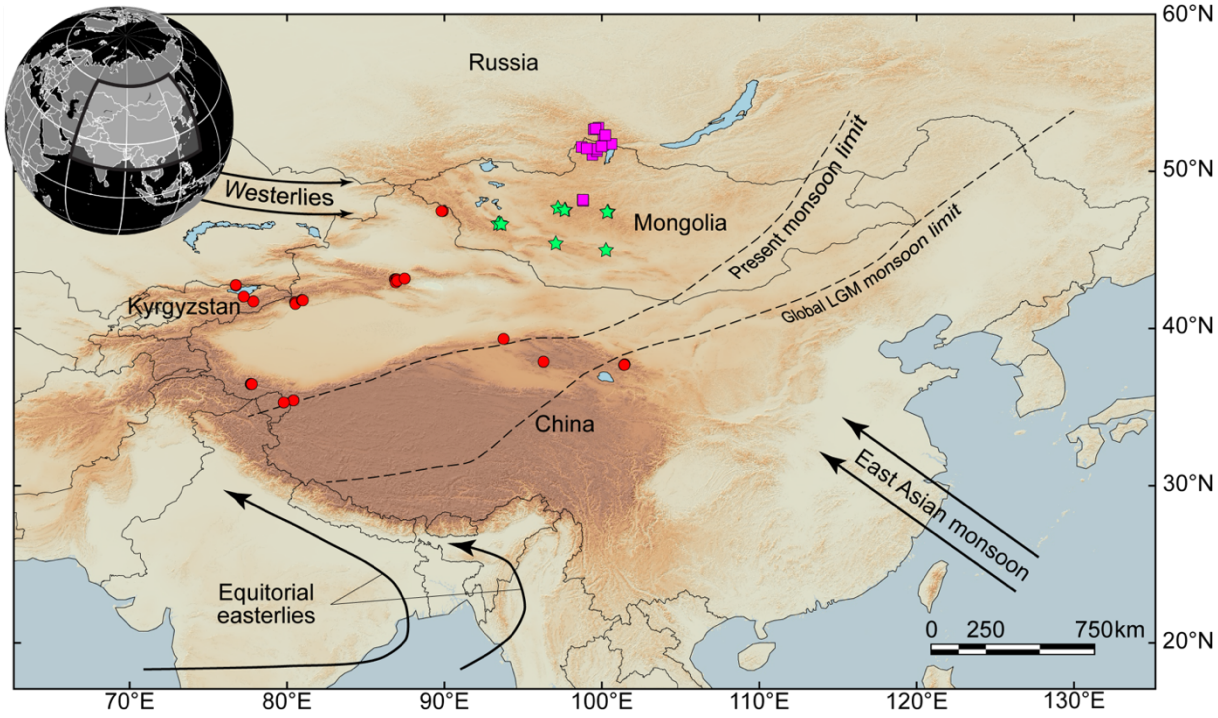

Figure 1.7. Sites with new radiometric ages reported in this dissertation. The purple squares show sites for samples presented in Chapter 2. The green stars show sites for samples presented in Chapter 3. The red circles show sites for samples presented in Chapter 4. A total of 208 ^{10}Be, 52 ^{26}Al, ten ^{14}C, and nine luminescence ages are reported in this dissertation.

1.3 ORGANIZATION OF THE DISSERTATION

As mentioned in the beginning of this chapter, the new results presented in Chapters 2–4 of this dissertation were used to reach three goals in order to reconstruct paleoclimate from glacial records in Central Asia:

1) Establish the glacial chronology in the study area

2) Estimate the ELA depression for the paleoglaciers in the study area

3) Establish the relationship between the ELA and climate parameters

The scope and the extent of the study areas covered in Chapters 2–4 differ, which I summarize below along with the main findings.

Chapter 2. This chapter is slightly unusual compared to the other chapters in two ways: a) It consists of two parts; b) A large portion of the content is focused on paleo megafloods along the Maly Yenisei river. This organization, however, is because the mountain ranges covered in Chapter 2 hosted large ice fields during the last glacial cycle, and some of their outlet glaciers impounded large lakes during their maximum extents. The late Pleistocene breach of one of these ice dams produced one of the largest paleofloods known on Earth. The large lakes themselves indicate the time of maximum advance, not just the transition from advance to retreat. Also, this extraordinary geologic phenomenon deserves study in its own right. The first part of the chapter reviews (and introduces new) evidence of the paleofloods along the Upper Yenisei river, and the second part provides new results from cosmic-ray exposure dating of glacial boulders and luminescence dating of sediments left by the glacially impounded lakes. The new ages presented in Chapter 2 constrain the chronology and the size of the maximum extents of the paleoglaciers in southern Siberia.

Chapter 3. I studied paleoglaciers in two mountain ranges in Mongolia, Hangai and Gobi-Altai, and present the results in Chapter 3. The study areas were chosen to sample from adjacent regions, in close proximity, where the ELA sensitivity to climate was starkly different according to Rupper and Roe (2008). The Hangai region represents the melt-dominated glaciers where ELA is predicted to be more sensitive to changes in temperature than in precipitation. The hyper-arid and cold regions of the Gobi-Altai represents the sublimation-dominated glaciers where the ELA is very sensitive to changes in precipitation. The results from cosmic-ray exposure dating, ELA analysis, and glacier surface-energy balance modeling are presented in Chapter 3.

Chapter 4. The content of Chapter 4 expands the scope and areal coverage to a continental scale—new results from cosmic-ray exposure dating in nine glaciated valleys over six mountain ranges in Central Asia. I also analyzed the compilation of cosmogenic dates available in Central Asia (Heyman, 2014; http://expage.github.io) and applied my new technique to identify outliers in the dataset. The modern and estimated ELA for the dated moraines were then compared. The ELA depressions were then used to infer paleo summer air temperature and precipitation using the empirical curve established by Ohmura et al. (1992) and Sakai et al. (2015).

Chapter 5 provides a synopsis of the content in Chapters 2–4 in addition to the discussion of the remaining questions to be investigated in the future.

1.4 REFERENCES IN CHAPTER 1

Adler, R.F., Huffman, G.J., Chang, A., Ferraro, R., Xie, P., Janowiak, J., Rudolf, B., Schneider, U., Curtis, S., Bolvin, D., Gruber, A., Susskind, J., Arkin, P., (2003), The Version 2 Global Precipitation Climatology Project (GPCP) Monthly Precipitation Analysis (1979-Present). Journal of Hydrometeorology 4, 1147–1167.

Batbaatar, J., and Gillespie, A.R., (2012), Equilibrium-line altitudes in cold hyperarid settings. Abstract C43E-06 presented at 2012 Fall Meeting, AGU, San Francisco, Calif., 3–7 Dec.

Benn, D.I., and Hulton, N.R.J., (2010), An Excel™ spreadsheet program for reconstructing the surface profile of former mountain glaciers and ice caps. Computers and Geosciences 36, 605–610.

Benn, D.I., and Owen, L.A., (1998), The role of the Indian summer monsoon and the mid- latitude westerlies in Himalayan glaciation: Review and speculative discussion. Journal of the Geological Society, London, 155, 353–363.

Blomdin, R., Heyman, J., Stroeven, A.P., Hättestrand, C., Harbor, J.M., Gribenski, N., Jansson, K.N., Petrakov, D.A., Ivanov, M.N., Alexander, O., Rudoy, A.N., Walther, M., (2014), Glacial geomorphology of the Altai and Western Sayan Mountains, Central Asia. Journal of Maps, 10.1080/17445647.2014.992177.

Fan, Y., and van den Dool, H., (2008), A global monthly land surface air temperature analysis for 1948–present. Journal of Geophysical Research 113, D01103, doi:10.1029/2007JD008470.

Frey, H., Machguth, H., Huss, M., Huggel, C., Bajracharya, S., Bolch, T., Kulkarni, A., Linsbauer, A., Salzmann, N., Stoffel, M., (2014), Estimating the volume of glaciers in the Himalayan–Karakoram region using different methods. The Cryosphere 8, 2313–2333, doi: 10.5194/tc-8-2313-2014.

Fu, P., Heyman, J., Hättestrand, C., Stroeven, A.P., Harbor, J.M., (2012), Glacial geomorphology of the Shaluli Shan area, southeastern Tibetan plateau. Journal of Maps 8, 48–55. http://dx.doi.org/10.1080/17445647.2012.668762.

Gillespie, A., and Molnar, P., (1995), Asynchronous maximum advances of mountain and continental glaciers. Reviews of Geophysics, 33, 311–364.

Gillespie, A.R., (1991), Testing a new climatic interpretation for the Tahoe glaciation. California, Proceedings of the White Mountain Research Station. Symposium. In: Hall Jr., C.A., Doyle-Jones, V., Widawski, B. (Eds.), I Natural History of eastern California and High-Altitude Research, vol. 3. University of California, Los Angeles, pp. 383–398.

GLIMS and NSIDC, (2018), Global Land Ice Measurements from Space glacier database. Compiled and made available by the international GLIMS community and the National Snow and Ice Data Center, Boulder CO, U.S.A. DOI:10.7265/N5V98602.

Harris, I., Jones, P.D., Osborn, T.J., Lister, D.H., (2013), Updated high-resolution grids of monthly climatic observations—The CRU TS3.10 dataset. International Journal of Climatology 34, 623–642, doi:10.1002/joc.3711.

Heyman, J., (2014), Paleoglaciation of the Tibetan Plateau and surrounding mountains based on exposure ages and ELA depression estimates. Quaternary Science Reviews 91, 30–41.

Heyman, J., (2018), Expage: A global compilation of glacial ^{10}Be and ^{26}Al data (expage-201803). Accessed at http://expage.github.io/index.html.

Heyman, J., Hättestrand, C.H., Stroeven, A.P., (2008), Glacial geomorphology of the Bayan Har sector of the NE Tibetan plateau. Journal of Maps 4, 42–62. http://dx.doi.org/ 10.4113/jom.2008.96.

Kalnay, E., Kanamitsu, M., Kistler, R., Collins, W., Deaven, D., Derber, J., Gandin, L., Saha, S., White, G., Woollen, J., Zhu, Y., Chelliah, M., Ebisuzaki, W., Higgins, W., Janowiak, J., Mo, K.C., Ropelewski, C., Wang, J., Leetma, A., Reynolds, R., Jenne, R., (1995), The NCEP/NCAR 40-year re-analysis project. Bulletin of the American Meteorological Society 77, 437–471.

Kayastha, R.B., Ohata, T., Ageta, Y., (1999), Application of a mass-balance model to a Himalayan glacier. Journal of Glaciology 45, 559–567.

Koppes, M.N., and Montgomery, D.R., (2009), The relative efficacy of fluvial and glacial erosion over modern to orogenic timescales. Nature Geoscience, 2 (9), 644–647.

Kraaijenbrink, P.D.A., Bierkens, M.F.P., Lutz, A.F., Immerzeel, W.W., (2017), Impact of a global temperature rise of 1.5 degrees Celsius on Asia's glaciers. Nature, 549 (7671), 257. doi: 10.1038/nature23878.

Meierding, T.C., (1982), Late Pleistocene glacial equilibrium-line in the Colorado Front Range: a comparison of methods. Quaternary Research 18, 289–310.

Mölg, T., and Hardy, D.R., (2004), Ablation and associated energy balance of a horizontal glacier surface on Kilimanjaro. Journal of Geophysical Research 109, D16104, doi:10.1029/2003JD004338.

Molnar, P., and Tapponnier, P., (1975), Cenozoic tectonics of Asia: Effects of a continental collision. Science 189, 419–26.

Morén, B., Heyman, J., Stroeven, A.P., (2011), Glacial geomorphology of the central Tibetan plateau. Journal of Maps 7, 115–125. http://dx.doi.org/10.4113/jom.2011.1161.

National Aeronautics and Space Administration LP DAAC, (2018), ASTER Level 1B Registered Radiance at the Sensor, Version 3. NASA EOSDIS Land Processes DAAC, USGS Earth Resources Observation and Science (EROS) Center, Sioux Falls, South Dakota (https://lpdaac.usgs.gov), accessed 2009–2018 at https://lpdaac.usgs.gov/dataset_discovery/aster/aster_products_table/ast_l1b.

Nuimura, T., Sakai, A., Taniguchi, K., Nagai, H., Lamsal, D., Tsutaki, S., Kozawa, A., Hoshina, Y., Takenaka, S., Omiya, S., Tsunematsu, K., Tshering, P., Fujita, K., (2015), The GAMDAM glacier inventory: A quality-controlled inventory of Asian glaciers. The Cryosphere 9, 849–864. https://doi.org/10.5194/tc-9-849-2015.

Ohmura, A., Kasser, P., Funk, M., (1992), Climate at the equilibrium line of glaciers. Journal of Glaciology. 38, 397–411.

Porter, S.C, (1975), Equilibrium-line altitudes of late Quaternary glaciers in the Southern Alps, New Zealand. Quaternary Research 5, 27–47.

Porter, S.C., (2001), Snowline depression in the tropics during the last glaciation. Quaternary Science Reviews 20, 1067–1091.

RGI Consortium, (2017), Randolph Glacier Inventory – A Dataset of Global Glacier Outlines: Version 6.0: Technical Report, Global Land Ice Measurements from Space, Colorado, USA. Digital Media. DOI: https://doi.org/10.7265/N5-RGI-60.

Roe, G.H., Baker, M.B., Herla, F., (2016), Centennial glacier retreat as categorical evidence of regional climate change. Nature Geoscience 10, 95–99.

Rupper, S., and Roe, G., (2008), Glacier changes and regional climate: A mass and energy balance approach. Journal of Climatology 21, 5384–5401.

Sakai, A., Nuimura, T., Fujita, K., Takenaka, S., Nagai, H., Lamsal, D., (2015), Climate regime of asian glaciers revealed by GAMDAM glacier inventory. The Cryosphere 9, 865–880. https://doi.org/10.5194/tc-9-865-2015.

Shi, Y., (2002), Characteristics of late quaternary monsoonal glaciation on the Tibetan plateau and in east Asia. Quaternary International, 97–98, 79–91.

Stroeven, A.P., Hättestrand, C., Heyman, J., Kleman, J., Morén, B.M., (2013), Glacial geomorphology of the Tian Shan. Journal of Maps 9, 505–512. http://dx.doi.org/10.1080/17445647.2013.820879.

U.S. Geological Survey, (2018), Landsat-7 image courtesy of the U.S. Geological Survey, accessed 2009–2018 at https://earthexplorer.usgs.gov.

Chapter 2

OUTBURST FLOODS OF THE MALY YENISEI

Chapter 2 consists of two parts: Part I – Review; and Part II – New age constraints from Darhad basin. Part I of this chapter was published in *International Geology Review*, Vol. 58, No 14, pp. 1723–1752, in 2016 with a title "Outburst floods of the Maly Yenisei: Part I" co-authored by Jigjidsurengiin Batbaatar and Alan R. Gillespie. Part II of this chapter was published in *International Geology Review*, Vol. 58, No 14, pp. 1753–1779, in 2016 with a title "Outburst floods of the Maly Yenisei: Part II – new age constraints from Darhad basin" co-authored by Jigjidsurengiin Batbaatar and Alan R. Gillespie. The content of this chapter is the author's version of the work and posted here with the permission from Taylor & Francis Group.

OUTBURST FLOODS OF THE MALY YENISEI
PART I – REVIEW

2.1 ABSTRACT FOR PART I

The Yenisei, the largest river flowing to the Arctic Ocean, repeatedly hosted cataclysmic floods during the Pleistocene. The largest of the known floods likely originated from paleolakes in northern Mongolia, at the headwaters of the Little, or Maly, Yenisei. These ancient floods are among the greatest known globally. They left giant current ripples along the Maly Yenisei, wide abandoned channels in the Kyzyl basin, and high terraces in the gorges upstream. However, few detailed field studies of the flood deposits and no measurements of their ages have been made thus far. The largest paleolakes were impounded during major glaciations by outlet glaciers from the East Sayan ice field in southern Siberia. The shorelines suggest four distinct paleolake depths of 290, 175, 145, and 65 m. The timing and location of the glacier impounding the deepest lakes are uncertain but at its maximum, the Tengis outlet glacier was likely capable of impounding the 175 m lake. The dating of glacial deposits in and around the basin reveals that the maximum was during Marine Oxygen Isotope Stage (MIS) 3. The ages for deep-lake sediments exposed in the basin behind the dam's location support this finding. During MIS 2 the Tengis glacier was large enough to impound at least the 145 m lake. However, the existence of a deep MIS 2 paleolake in the basin has been challenged because no evidence has been published of MIS 2 lake sediments from the cutbank outcrops and deep drilling cores. Additionally, the end moraines of the Tengis glacier, separated from the deeply eroded lateral moraines by the Maly Yenisei, remain undated; therefore it is uncertain exactly when this glacier crossed the river. This review is part I of a two-part article; Part II presents new age data to constrain the ages of the glacial dam.

2.2 INTRODUCTION TO PART I

Modern geology originated more than two centuries ago, partly in response to the desire to find signs of the singular Biblical flood on the modern landscape (e.g., Montgomery 2013). The absence of widespread evidence for such a global flood and the principle of uniformitarianism expounded by Charles Lyell (Lyell, 1830–3) put 'catastrophism' in disrepute, quelling the search for giant but infrequent floods for a century. This reaction ended only with J Harlen Bretz's (1923) recognition that huge, deep and fast-moving floods reshaped the landscape in the Pacific Northwest (USA). These Missoula floods are now thought to have breached their ice-age glacial dams multiple times (Baker 1973, Waitt 1980), ending around 13.5 ka (e.g., Benito and O′Connor 1993). The geologic significance, wide geographic distribution and number of large outburst floods modifying landscapes have become increasingly appreciated in recent decades (e.g., Malde 1968; Baker *et al.* 1993; Rudoy and Baker 1993; Komatsu *et al.* 1997; Grosswald 1999; Teller *et al.* 2002; Mangerud *et al.* 2004) and it is even suspected that they once coursed through Martian canyons (Baker and Milton 1974).

Outburst floods originate in many ways, for example by the overtopping of sills impounding lakes or seas (e.g., Lake Bonneville, USA: Malde 1968; Bosporus, western Asia: Ryan *et al.* 1997), collapse of glacial or moraine dams (e.g., Paleolake Missoula, USA: Pardee 1942; Yarlong Tsangpo, Tibet, Montgomery *et al.* 2004), or overtopping or erosion of landslide dams (e.g., Yigong Tsangpo, Tibet: Shang *et al.* 2003). Some, for example those from Lake Agassiz (Canada), arose multiple times from multiple causes over a period of a few thousand years during deglaciation of the Laurentide Ice Sheet (e.g., Fisher 2003 and references therein); others have occurred during modern times (e.g., Merzbacher Lake, Kyrgyz Tian Shan; Wortmann *et al.* 2014). Some of the greatest floods are summarized in Figure 2.1.

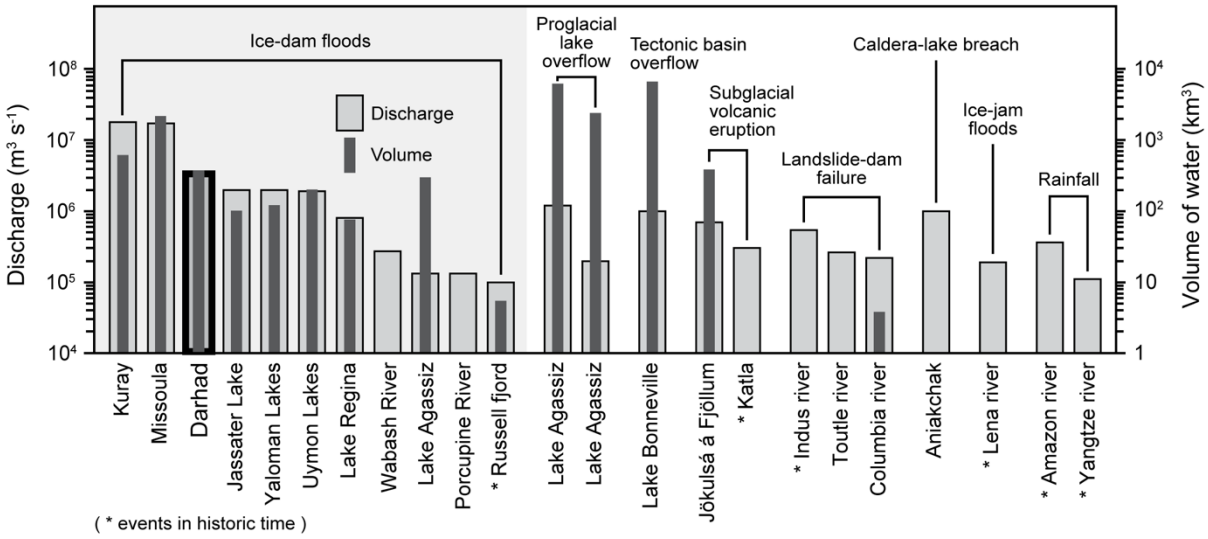

Figure 2.1. Peak discharge and volume of released water from major Quaternary floods (modified after O'Connor and Costa 2004). The most energetic floods are outbursts from failed glacier dams. The values for the Darhad flood are from the 172 m-deep paleolake impounded by the Tengis glacier. The outburst from the deepest paleolake Darhad was more energetic (see text for details).

The impact of outburst floods on the landscape depends on the total discharge, the depth of the flood, the flow speed and the sediment load entrained, as well as resistance of the landscape to erosion. The discharge rate depends on the speed with which the dam is breached, ice dams being eroded faster than bedrock sills. Floods with discharge rates exceeding 10^6 m^3 s^{-1} are termed "catastrophic" (Komatsu *et al.* 2016). A large flood from Paleolake Missoula had a total volume of 2184 km^3 (Clarke *et al.* 1984), a depth of 550 m or more, and flow speeds as high as 36 m s^{-1}, with discharge rates of 17×10^6 m^3 s^{-1} (O′Connor and Baker 1992). The initial outburst of the Missoula floods at the end of the Last Glacial Maximum (LGM) estimated to have transported at least 700 km^3 of eroded sediments to the ocean (Normark and Reid 2003), demonstrating its power as an agent of landscape evolution.

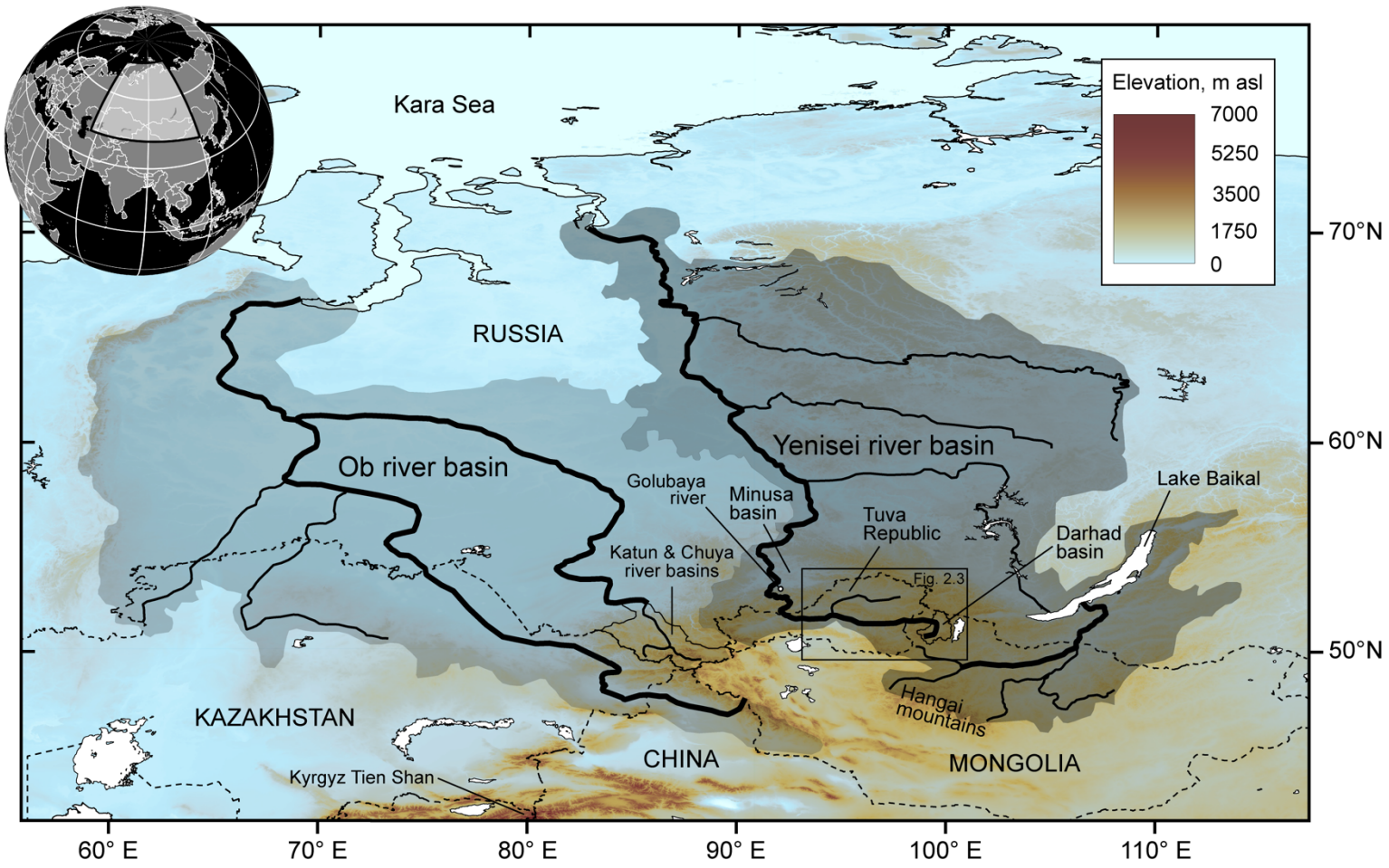

Figure 2.2. The largest Pleistocene floods in Siberia originated in the Kuray and Chuya basins and flowed into the Katun river (headwaters of the Ob river), and from Darhad basin (headwaters of the Yenisei river). The Kuray basin is included within the combined border for the Katun and Chuya rivers basins. Background: Shaded-relief image produced from 90-m Shuttle Radar Topographic Mission (SRTM) elevation data (Farr *et al.* 2007).

The major rivers of Siberia – among them the Ob, Yenisei, and Lena – all received outburst floods during the Pleistocene (Komatsu *et al.* 2016; Margold *et al.* 2011). The Yenisei (Figure 2.2) is one of the largest rivers in the world (annual discharge: 573 km^3; length ~3500 km long; basin area: 2.6×10^6 km^2: Yang et al. 2004), yet its outburst floods have received less attention than floods with comparable significance elsewhere, such as the Missoula Floods and those from the Kuray, Chuya, and Katun basins of the upper Ob river (Table 2.1). In this paper we consider some of the most catastrophic outburst floods yet studied, those of the upper reaches of the Yenisei river.

This paper consists of two parts, (I) a review of relevant previous studies and (II) a resolution with new data of important questions identified as unresolved by Krivonogov *et al.* (2012), who thoroughly summarized the literature on the history of a sequence of paleolakes in Darhad basin. These paleolakes were at the headwaters of the Maly Yenisei in northern Mongolia, one of the main tributaries of the Yenisei, and were the sources of the largest of the Yenisei floods (e.g., Komatsu *et al.* 2009). Here in part I we review the published evidence for the floods downstream of the paleolakes and the glacial and sediment dams that impounded the Darhad paleolakes, and the paleolakes themselves. We have performed new photointerpretation of satellite images (Google Earth) of the Maly Yenisei between the Kyzyl and Darhad basins, and the results are intercalated into the review (Sections 2.2.7.2 and 2.2.7.3).

Age control for the paleolakes has been provided by luminescence dating of lake sediments, ^{14}C dating of organic matter preserved in them, and ^{10}Be cosmic-ray exposure (CRE) dating of glacial deposits. The calibration curve for the ^{14}C dating has been revised recently with updated data sets. Therefore, we recalibrated the reported ^{14}C ages using the IntCal13 curve (Reimer *et al.* 2013) on Calib 7.1 online calculator (Stuiver and Reimer 1993). Hereafter we refer only to these recalibrated ages (cal yr BP). The ^{14}C dating studies are summarized in Section 2.3.1.

Table 2.1. Selected large outburst floods from glacier-dammed lakes

Name	Location	Peak discharge (10^6 m^3 s^{-1})	Depth (m)	Volume (km^3)	Reference
Kuray	Altai, Russia	18 10	- 400	- 607	Baker *et al.* 1993; Herget 2005
Missoula	NW USA	17	375	2184	O′Connor and Baker 1992; Clarke *et al.* 1984; Craig 1987
Darhad (1825 m[a])	Mongolia	>5.8[c]	287	809	Komatsu *et al.* 2009
Darhad (1710 m[b])	Mongolia	3.5	172	373	Komatsu *et al.* 2009
Yarlong Tsangpo	Tibet, China	1–5	680	832	Montgomery *et al.* 2004
Matanuska River	Alaska, USA	2.0–3.3[d]	<110	500–1400	Wiedmer *et al.* 2010

[a] Maximum highstand (Krivonogov *et al.* 2005; Gillespie *et al.* 2008), pre-LGM

[b] Local LGM maximum highstand (Gillespie *et al.* 2008; Komatsu *et al.* 2009)

[c] Estimate assuming velocity is no less than for the lower, modeled outburst (1710 m)

[d] Assuming dam-break origin; jökulhlaup origin would imply 0.15–0.27 × 10^6 m^3 s^{-1}

Recent developments in CRE dating techniques have suggested that the spallation production rate of ^{10}Be was lower than of the early estimations (e.g. Balco *et al.* 2009; Putnam *et al.* 2010; Young *et al.* 2013). Accordingly, we recalculated all the literature ages using globally calibrated ^{10}Be production rate of Heyman (2014). Hereafter we refer only to the recalculated ^{10}Be ages, and the summary of the CRE dating studies are provided in Section 2.3.2.

2.2.1 *Geographic names*

Many of the pioneer studies in Siberia and northern Central Asia were reported in Russian. Local geographic names in Evenki, Tuvan and Mongolian languages were approximated by Russian pronunciation and recorded in Cyrillic script. Names cited in scientific literature are a mixture of the Russian and local names and they were approximated from Cyrillic to Latin script. However, the Latin spellings of names and equivalents in the literature have been used inconsistently. In this

paper we have tried to use the most widely recognized, and we have summarized the local equivalents in Table 2.2a. We have translated generic geographic terms such as “river” or “lake” to English, and for clarity we added them in lower case where they are not part of the native name. Thus, the “Yenisei” (a stand-alone name for the river) becomes the “Yenisei river” if helpful. Common terms used in this paper are listed along with the translations in Table 2.2b.

Table 2.2. Geographic names used in this paper.

a. Spelling for common local names

This paper	Alternative spellings
Tuva	Tyva
Yenisei	Yenesei, Yenisey
Darhad	Darkhad, Darkhat, Darkhadyn
Baikal	Baigal
Hövsgöl	Kubsukul, Khovsgol
Todzha	Todza
Kaa	Ka
Shishhid	Shishged, Shishigt, Shishkit
Büsiin	Busein
Horidol	Khoridolyn
Högiin	Hogyin, Hogiin
Chuya	Chuja
Mönh Saridag	Monkh Saridag, Munku Saridag

b. Generic terms and their transliterations

Geographical terms	Tuvan	Russian	Mongolian
river	khem	reka	gol
lake	khöl	ozero	nuur
depression, basin	-	kotlovina	hotgor
mountains	uula	khrebty	uul, nuruu

2.2.2 *Geography of the Maly Yenisei river*

The Maly Yenisei (Figure 2.3) originates in the Ulaan Taiga mountains on the western margin of Darhad basin in Mongolia, where the river is known as the Shishhid. The Maly Yenisei exits Darhad basin through a narrow gorge between the Ulaan Taiga and the East Sayan mountains, both of which supported ice caps during the Pleistocene glaciations, (Figure 2.4), and flows west to the confluence with the north-flowing Büsiin and south-flowing Belin rivers, on the border between Mongolia and Tuva Republic of the Russian Federation. Downstream for ~80 km to a major confluence, the Maly Yenisei is known as the Kyzyl river (Figure 2.3). The north-flowing tributary is known as the Kaa river, and the combined flow retains this name downstream until the next major confluence, with the south-flowing Bolshoy Yenisei (or Bii river) at the city of Kyzyl, the Tuvan capital. The Bolshoy Yenisei drains the Todzha basin, itself the source of large outburst floods (Komatsu *et al.* 2009). Downstream from Kyzyl, the combined forks of the Yenisei are known as the Upper Yenisei, or Ulug river, until the river debouches from the West Sayan mountains into the Minusa basin (Figure 2.2), at elevation of 450 m above sea level (asl). Thereafter the Yenisei flows north ~2000 km to the Arctic Ocean. Local names for the tributaries of the Yenisei are summarized in Table 2.3 and shown in Figure 2.3.

Table 2.3. Names of geographic features, and their local variants

Geographic name	Local name	Headwaters and basin
Yenisei	-	Lower and Upper Yenisei
Lower Yenisei	-	Nizhnaya and Podkamennaya Tunguska, Angara
Upper Yenisei	Ulug river	Bolshoy and Maly Yenisei
Bolshoy Yenisei	Bii river	Systyg river (Todzha basin)
Maly Yenisei	Kaa river, Kyzyl river, Shishhid river	Darhad basin

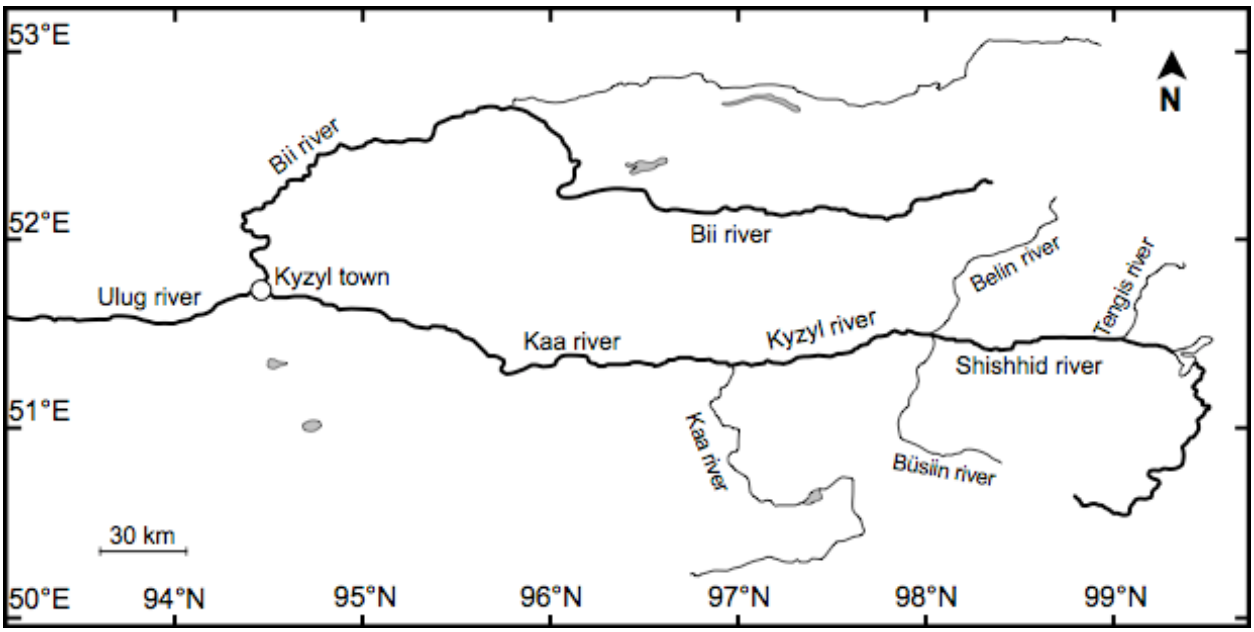

Figure 2.3. Major tributaries to the Yenisei river, and their local names.

2.2.3 *Flood evidence on the Upper Yenisei*

In this section we summarize the geomorphological and sedimentological features along the upper reaches of the Yenisei river that provide evidence for very large floods. Our review is primarily of the Maly Yenisei, but for context we also include the Ulug river and the Bolshoy Yenisei.

2.2.3.1 Evidence from the Minusa basin

After flowing through the narrow gorges of the West Sayan mountains the Yenisei river debouches onto the broad flood plains in the Minusa basin. In the western and central part of the basin at least two sets of braided and/or anastomosing paleochannels were identified from the satellite images by Komatsu *et al*. (2009). They proposed two alternatives for the origin of the paleochannels: either by migration of streams or by high-energy floods. However, no chronology has been determined for these paleochannels, they do not appear to have been studied in the field, and their origin could not be established decisively.

Komatsu *et al*. (2009) noted prominent high terraces in the mountains upstream from the Minusa basin. For example, there are ~10 m high terraces of cross-bedded fluvial sediments along the Golubaya river (52°57.155'N; 91°32.590'E), near the city of Sayanogorsk, where sand beds alternate with layers of coarser subangular pebbles. Yamskikh *et al.* (2001) considered these sediments to be alluvial and lacustrine, deposited behind a temporary glacial dam, but Carling *et al*. (2002) and Rudoy (2002) likened the terraces to the giant bars in the Katun and Chuya river valleys at the headwaters of the Ob river. These were deposited during catastrophic outburst floods when there was an abrupt decrease in stream energy, for example on the lee sides of the bends of the main valleys. Komatsu *et al*. (2009) interpreted the sediments of these high terraces to have been formed from the suspended load of an energetic flood, accumulated when the floodwaters stagnated in tributary canyons.

2.2.3.2 Evidence from the Ulug river

Upstream of the Minusa basin and the West Sayan, the Upper Yenisei (Ulug river) flows through the Kyzyl basin, a broad plain that preserves evidences of giant flood events. Along the banks of the Ulug river in the Kyzyl basin are several hanging valleys ending in cliffs ~200 m high and

flanking the main river. These indicate deep, erosive flow down Ulug river that the smaller tributaries could not match. Rudoy (2002) and Komatsu *et al*. (2009) both attributed the hanging valleys to intense erosion during giant floods, observing that high-energy floods would have completely or largely eroded pre-existing fans at the mouths of these hanging valleys and prevented the tributaries from adjusting to the lowered base level.

Downstream from and near the confluence of the Bolshoy and Maly Yenisei, the unstudied chronology of flooding may be complex because the sources of the floodwaters may be from the different basins and timing of dam disruption may not have been synchronized. On the Maly Yenisei upstream of the confluence, Komatsu *et al*. (2009) suspected that the largest floods originated from Darhad basin, and the chronology of flood deposits and other features above the modern floodplain may be accordingly simpler. However, smaller floods from tributary streams (e.g., Komatsu *et al.* 2009) may complicate the detailed geologic record of the Maly Yenisei as well. In the central part of the Kyzyl basin, south of the city of Kyzyl, two generations of northwest-trending linear features cover an area of ~1500 km^2, 45 km (NW-SE) × 33 km (NE-SW). Komatsu *et al.* (2009) suggested that these are aeolian dunes made of reworked flood sands from the Maly and Bolshoy Yenisei rivers.

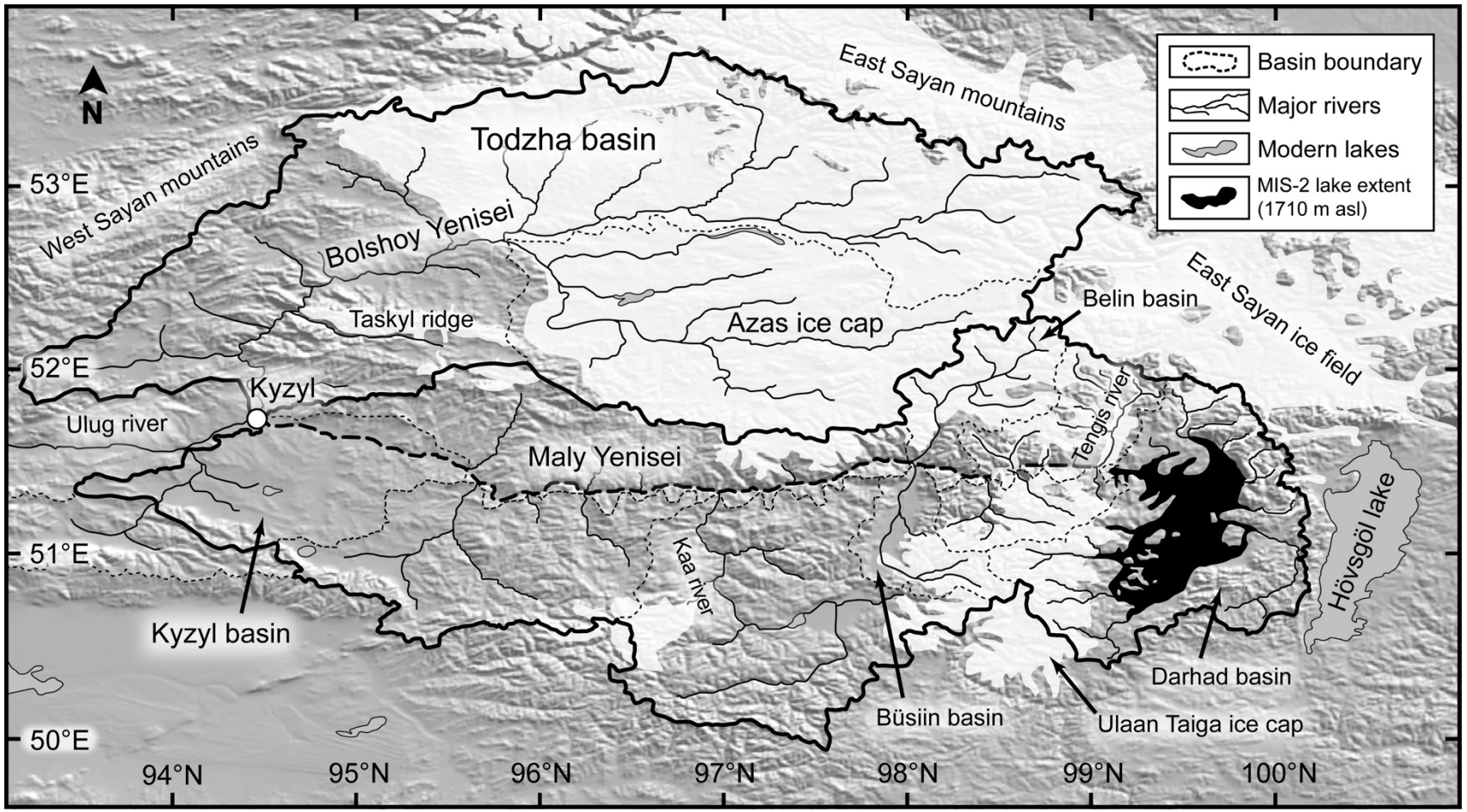

Figure 2.4. Basin map of the upper Yenisei river. Todzha basin collects water for the Bolshoy Yenisei river (blue polygon). The Maly Yenisei originates in Darhad basin and joins the Bolshoy Yenisei to form the Ulug river, the local name for the upper Yenisei. Outlet glaciers from the East Sayan ice field descended through the Tengis river valley and impounded large lakes in Darhad basin. The Pleistocene Azas ice cap occupied the Azas Plateau, which is also the location of the Azas Plateau volcanic field. Shaded-relief image produced from 90-m SRTM elevation data (Farr et al. 2007).

2.2.3.3 Evidence from Bolshoy Yenisei

The Todzha basin in Tuva (Figure 2.4) is drained by the Bolshoy Yenisei. Although Komatsu *et al.* (2009) regarded the basin as a source of outburst floods, field work there has not been completed and photo-reconnaissance has only been done at the resolution limits of available satellite remote-sensing data (75 m for Radarsat SCAN SAR: Raney *et al.* 1991); 30 m for Landsat TM: U.S. Geological Survey, 2012). Komatsu *et al.* (2009) admitted that as yet no clear cataclysmic flood indicators such as giant gravel dunes have been identified there, although there are some suggestive features near the Taskyl Ridge. These include truncated tributary terraces, ~40 m above the Bolshoy Yenisei (51°56'58.49"N; 94°24'28.70"E), and a possible high terrace on an inside bend ~50 m above the river (52°19'16.17"N; 94°35'4.69"E). Another possible high terrace 5 km downstream from the others is likely the remnant of a landslide.

Although definitive outburst flood evidence has not been discovered, the Todzha basin hosted giant lakes at different times in the Quaternary. During middle-late Pleistocene time lakes with depths up to 250 m covered areas of ~2000 km^2 (volume: 310 km^3), and during the late Pleistocene to Holocene there were smaller lakes with a maximum depth of 60 m (volume: 8 km^3) (Komatsu *et al.* 2009). Although these paleolakes drained down the Bolshoy Yenisei, the rate is unknown and dependent of the dams that impounded them. Possible dams include glaciers, debris/landslides, ice jams in the river, and tectonic scarps (Yamskikh and Yamskikh 1999; Arzhannikov *et al.* 2000; Komatsu *et al.* 2009).

Dam failures are not the only possible mechanism for floods from the Todzha basin. The Todzha basin and the Azas Plateau hosted an ice cap (Figure 2.4) at times during the Pleistocene, and Komatsu *et al.* (2007) showed that subglacial volcanic eruptions occurred from several middle-late Pleistocene (Litasov *et al.* 2001a) vents of the Azas Plateau volcanic field. These may

have been capable of producing meltwater floods as occur today from the subglacial Grímsvötn volcano in Iceland (Jóhannesson 2002).

Some of the mechanisms suggested for impounding the Todzha paleolakes appear to be improbable. For example, the continuous section of lacustrine sediments from the middle-late Pleistocene lake suggests continuous deposition over long period of time (Komatsu *et al.* 2009), inconsistent with ice jams or glacier dams from the Taskyl Ridge. In any case, the glaciers there appear to have terminated hundreds of meters above the river (Figure 2.4) and could not have impounded a 250 m deep lake (Grosswald 1965). Komatsu *et al*. (2009) concluded that these lakes developed behind a 1100 m high landslide block at the junction between the Bolshoy Yenisei and Krasnaya rivers (52°25.061′N, 94°46.351′E). If this is true, the release of water from the Todzha basin was unlikely to have been as sudden as for the floods down the Maly Yenisei, many of which were released from glacier dams. Therefore, the floodwater discharge rate along the Bolshoy Yenisei is likely to have been lower than for the Maly Yenisei floods, even if the released volume (Table 2.1) was of the same order of magnitude. Floodwaters in the Kyzyl basin and downstream could have originated from either the Todzha or Darhad basin, at the headwaters of the Maly Yenisei. Distinguishing flood sediments of Bolshoy and Maly Yenisei in the Kyzyl basin may require detailed study of the lithology and its chronology, and such studies have not yet been attempted.

2.2.4 *Evidence from the Maly Yenisei*

2.2.4.1 Giant current ripples in the Kyzyl basin

In the Kyzyl basin upriver from town of Kyzyl for ~100 km inset terraces are locally preserved above the modern flood plain and incised by the Maly Yenisei. There are at least three levels: ~10,

~30–40, and ~40–50 m above the modern river (Figure 2.5). Tributary streams have cut through the higher terraces and grade to the lowest terrace, on which they have deposited small fans.

At multiple locations (e.g., 51°40.997′N, 94°41.066′E, 670 m asl; 51°39.035′N, 94°55.103′E, 672 m asl) giant current ripples are preserved on the second-lowest terrace (Figure 2.5). The highest benches with smaller current ripples are found at 690–700 m asl (e.g., 51°40.069′N, 94°55.309′E). Grosswald (1987) was the first to attribute them to cataclysmic floods.

According to field observations by Komatsu *et al*. (2009) the giant current ripples are dune-shaped and asymmetrical, and the crests are nominally perpendicular to the river. The crest spacing is typically 50–80 m, and the amplitudes are a few meters. The dunes are rich in gravel, containing occasional boulders up to a meter in diameter. A top layer of loess overlies the cryoturbated gravels. Many of the gravel dunes occur in the lee of structural obstructions, such as bedrock knobs that would have slowed the floodwaters and reduced their carrying capacity for suspended sediment.

The Yenisei giant current ripples or dunes have smaller amplitudes than that of the ones accumulated by the Altai floods down the Ob from the Kuray–Chuya basins, some of which are 10 m or more in height. Komatsu *et al*. (2009) suggested that the lower height of the Yenisei dunes might be due to three possible reasons: 1) erosion of dune crests after the flood events; 2) limited supply of sediments to grow the dunes; 3) scouring of the dunes by relatively calm floodwaters after the initially powerful floods. However, it is also possible that the depths of the Yenisei floods were less than those of the Ob (cf. Wiedmer *et al.* 2010).

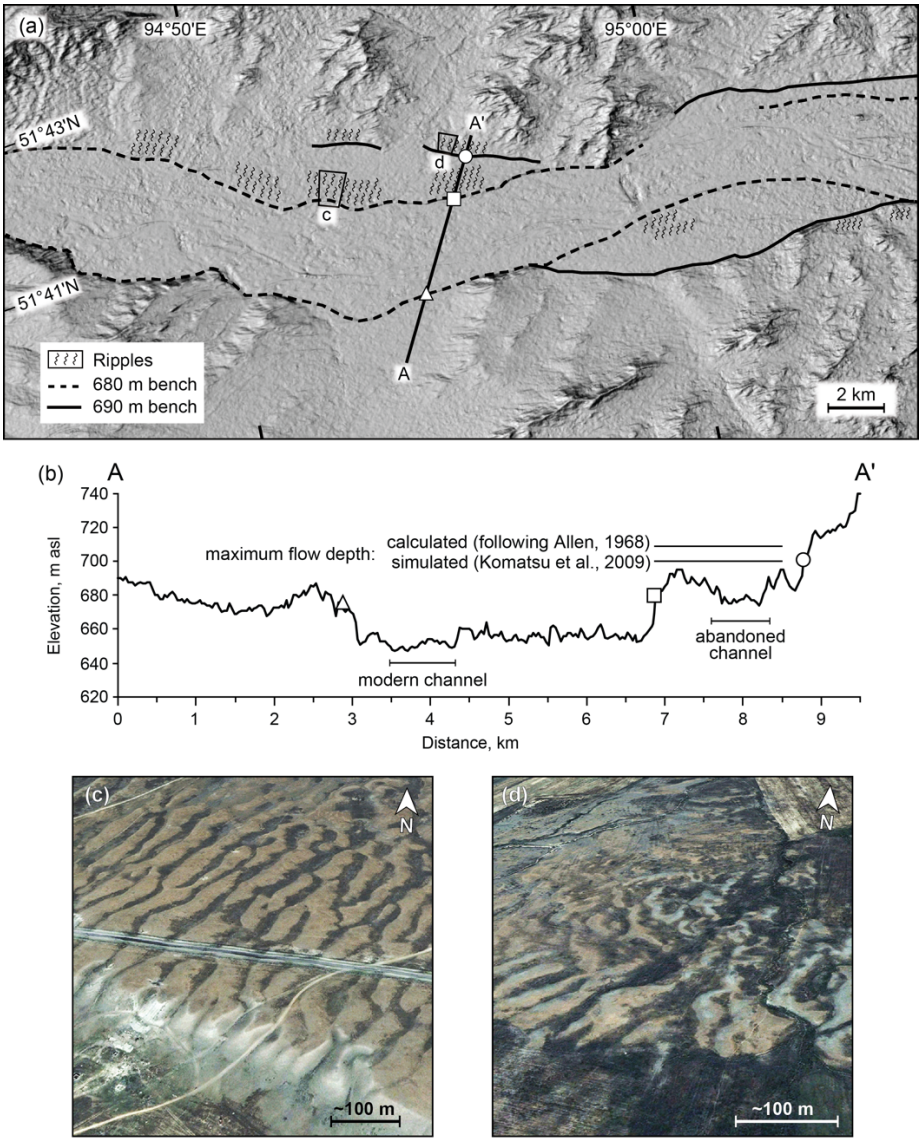

Figure 2.5. Giant current ripples in the Kyzyl basin. a) Shaded-relief image from 15-m ASTER elevation data. Highest benches with current ripples are found at up to 700 m asl. Lower but better preserved ripple marks are found at ~680 m asl. b) Elevation profile along transect A–A'. Abandoned channels are present on the 680 m bench on both sides of the Maly Yenisei. The maximum depth of floodwater over the 680 m bench (~20 m) was estimated by Komatsu *et al.* (2009), using a numerical model. The 690 m bench continues up to 700 m asl, and the ripple height of ~2 m is related to a flow depth of ~14 m using an equation of Allen (1968). The modern channel is at ~650 m asl. c) Google-Earth perspective view of the current ripples on the 680 m bench. d) Google-Earth perspective view of the current ripples on the 690 m bench. (Image data: DigitalGlobe).

Komatsu *et al*. (2009) estimated the stream power required for the dune formation to be 9–27 $\times 10^3$ W m^{-2}, based on the empirical relationship between the stream power and cord length in the Channeled Scabland of Washington State, USA (Baker 1982). Because the dunes formed in the lee of obstructions, the stream power for the unimpeded floodwaters may have been greater than this estimated range; however, the estimated range is much lower than the values of 2×10^5 W m^{-2} that O′Connor and Baker (1992) estimated for the Missoula floods and 1×10^6 W m^{-2} that Baker *et al*. (1993) estimated for the Altai floods.

The stream gradient of the Maly Yenisei near the dunes in the eastern Kyzyl basin is only ~1.5 m km^{-1}, similar to the 2 m km^{-1} gradient of the Katun river, downstream from its steeper Chuya tributary, the initial pathway of the Kuray floods (≤6 m km^{-1}: Herget 2005). However, the Maly Yenisei steepens upstream of the Kyzyl basin and its average gradient between the Kaa-Kyzyl confluence and the Tengis river in Mongolia is ~2.6–3.5 m km^{-1}. The estimated stream power and the associated gradients suggest that the floods along the Maly Yenisei were capable of transporting and depositing large amount of debris, like the Kuray floods.

Computer simulation of a flood from 172 m deep lake originating from Darhad basin (Komatsu *et al.* 2009) showed that the flow depth was ~20 m above the second-lowest terrace (water surface at 700 m asl). Using the empirical equation relating ripple height and water depth by Allen (1968)[1] suggests that there was ~14 m of water above the highest current ripples at 700 m asl, consistent with numerical simulations by Komatsu *et al*. (2009). We think that these current ripples were left by a single flood along the Maly Yenisei, in which the suspended loads were deposited at the highest level first and then at lower levels as the water flux decreased. A similar

[1] $H = 0.086D^{1.19}$. H – Ripple height, in m; D – Water depth, in m.

sequence of sedimentation at various levels from a single flood was observed in Kuray and Chuya basins (Herget 2012).

2.2.4.2 The gorge of the Maly Yenisei in the East Sayan

Upstream of the Kyzyl basin, the Maly Yenisei flows for ~175 km through a deep (~0.5 km), narrow (~1.5 km) and roughly linear gorge that opens at its confluence with the Belin and Büsiin rivers (Figure 2.4). This triple confluence is at the Mongolian border. The gorge continues east for another ~70 km to the confluence with the Tengis river, where it broadens again at the entrance to Darhad basin. The river is typically 150 m wide near the Kyzyl basin, narrowing upstream to ~50 m. The underfit river meanders within the gorge.

Photointerpretation of satellite images shows that most of the tributaries to the Maly Yenisei in this reach lack large alluvial fans at their junctions, suggesting to Komatsu *et al*. (2009) that high-energy floods removed the pre-existing fans as well as incising the valley, as they also claimed for the hanging valleys of the Ulug river.

Not all the flood deposits were eroded, however. On a big bend of the river, near (~18 km) the downstream end of the gorge (51°17.985′N; 95°45.165′E; 760 m asl), photointerpretation indicates multiple bars as much as 80 m above and on an inside bend of the river, a favorable location for deposition and preservation. Their large size reinforces the interpretation that the apparent scarcity of similar massive flood deposits upstream is due to poor preservation. In addition, other bar sequences are encountered ~15 km (95° 57′ E) and ~35 km (96° 16′ E) farther east, but still downriver from the confluence of the Kyzyl and Kaa rivers. At the first site, bars are found on the north side of the gorge 16, 40 and 80 km above the modern Maly Yenisei. Across the river appears to be a barrier or cut-off bar, 90 m above the river and blocking a tributary canyon.

At the second site bars are found 20, 40, 75 and 140 m above the river, again above its north. At 96° 52′ E an eroded veneer of sediment is found on the north side of the gorge up to 130 m above the river. All these bars are strong evidence for deep floods down the Maly Yenisei.

Near the confluence of the Kaa and Maly Yenisei rivers, basalt flows once filled the lower elevations of the gorge. The flows have been incised by the Maly Yenisei and today basalt flows (~100 m thick) cap terraces as much as ~250 m above the river. Although the gorge at the terrace elevation remains ~2 km wide, the steep-sided inner gorge through the flows here is only 0.9 km wide. Major tributaries have incised the flows, but lesser ones have not yet done so. Grosswald (1965) and Litasov *et al*. (2001b) regarded the basalt flows as Pleistocene in age. In the Channeled Scabland, high-energy floods have deeply eroded hard basaltic rocks, both by abrasion and by plucking. Thus, Komatsu *et al*. (2009) suggested that the Maly Yenisei floods similarly contributed to the incision of the basalt terraces near Kyzyl.

Grosswald and Rudoy (1996a, b) went further and attributed the origin of the gorge itself to catastrophic floods. However, direct evidence for this has not been shown, and it seems likely that its early history – long before its flooding by the basalts – involved fluvial processes by the antecedent stream. Nevertheless, by analogy with the Channeled Scabland, it seems possible that the incision of the inner gorge, cutting through the lava flows, could be due to catastrophic flooding.

Upstream from the basalt terraces and 8 km downstream from the confluence with the Belin (97° 55′ E) there appears, on satellite images, to be at least one and possible two steeply dipping strandlines (55 m km^{-1}) on the south side of the entrance to the ~1.5 km wide gorge, 120 m above the river. Conceivably these resulted from the spillover from the hydraulic dam impounding

Darhad floodwaters in the Büsiin–Belin valleys. Additionally, a possible run-up ramp is found immediately downstream in a steep tributary valley, also on the south side of the Maly Yenisei. Immediately upstream, Komatsu *et al*. (2009) calculated that 20 hours after the inception of a giant outburst flood from Darhad basin to the east, the water level behind the hydraulic dam would have reached a depth of ~247 m, although the calculated depths are uncertain because of the low resolution of the DEM available when the model was run (G. Komatsu, pers. comm., 2015). If the floodwaters were impounded even to a depth of ~100 m, however, they would have reached ~30 km south along the Büsiin river and ~20 km north along the steeper Belin river. This temporary hydraulically dammed lake is shown in the modeled hydrographs of Komatsu *et al*. (2009), who calculated that it persisted for more than 3 days.

2.2.4.3 The Maly Yenisei from the Tuva border to Darhad basin

East of the border with Mongolia, the Maly Yenisei flows through a deep (1100 m), steep-sided (~30°) gorge in which few deposits appear to have been preserved. Here the glaciated peaks and ridges crowd closer to the river on both sides, and some moraines appear to lie only 80–90 m above the river (98°15′ E). The close approach of the paleoglaciers may have been assisted by the steep slope, averaging 36° for the last 400 m above the Maly Yenisei; across the river to the north and in general, the end moraines appear to be ~350 m higher. The lowest termini of the glaciers may have been under water during the largest floods from Darhad basin: Komatsu *et al*. (2009) calculated that the flood depth 20 hours after the dam breached would have been ~130 m, such that the glaciers must have re-advanced after the last of the giant floods, as the moraines do not appear to have been eroded.

The broad (~ 15 km) Büsiin basin that straddles the border is a tectonic depression that was not filled with glacial ice during the late Pleistocene, although it hosted a few large piedmont

glaciers that were fed from the east (Ulaan Taiga). The tectonic basin continues north across the Maly Yenisei, where it is occupied by the Belin river. Although the upper Belin valley, above ~1200 m asl, hosted an outlet glacier from the East Sayan ice field (Arzhannikov *et al.* 2012; Grosswald 1965; Olyunin 1965), the lower valley was unglaciated. Nevertheless, its steep eastern wall – possibly a fault-line scarp – is marked by hanging valleys 250–300 m above the Belin river that resemble the hanging valleys along the Ulug river. The wall was possibly eroded by outburst floods from the East Sayan ice field; these floods would have added further to the complexity of the flood record west of the border.

Between the international border and the Tengis river, near Darhad basin, the Maly Yenisei is flanked by sequences of terraces and bars (Komatsu *et al.* 2009; Figure 2.6a). The Tengis river was the site of the outlet glacier from the East Sayan ice field thought to have dammed paleolake Darhad (e.g., Krivonogov *et al.* 2005). Near the western end of this reach, at 98°35′E, the floor of the river valley is covered with kettle-pocked fill, 20 m above the modern river, probably due to a resurgent glacier entering the valley from the north. This till (?) is found at the same elevation both upstream 1 km and downstream 5 km. A glacier blocking the Maly Yenisei ("ice dam #4" in Komatsu *et al.* 2009) would impound the trunk river, but from the elevation of the uneroded moraine remnants it appears that the lake would back up only to about the confluence with the Tengis river and consequent flooding downstream would have been relatively minor.

At the downstream end of the putative till, photointerpretation suggests that a remarkable series of four arcuate bars fill a canyon mouth. The elevation of the bars rises into the side canyon, from ~1465 to 1520 m asl; the convex sides point into the canyon also. The tributary valley is filled (~1510 m asl) with a flat deposit ~10 m lower than the impounding bars. Because they rise

and point into the tributary, it seems unlikely that they could be glacial, and may therefore represent a standing back-wave of one of the megafloods, up to 140 m above the modern channel.

For ~7 km upriver from the location of "ice dam #4" the Maly Yenisei flows through a V-shaped gorge that is straight, narrow (~ 2500 m) and deep (~800 m or more). The floor contains neither terraces nor large gravel bars. This gorge separates the Hoit Aguy massif from the Ulaan Taiga mountains.

Gillespie *et al.* (2008) suggested that the tributary Hadar Üüs valley on the eastern side of the Hoit Aguy massif hosted an outlet glacier from the East Sayan ice field that likely dammed the Maly Yenisei ("ice dam #2": Figure 2.7). Here the lateral moraines and trimlines of the Hadar Üüs approach the Maly Yenisei closely. Ice dam #2 probably formed more than once. One possible moraine is at an elevation of ~1750 m asl, and in the absence of other dams upstream would have backed up a deep lake into Darhad basin. However, photointerpretation hints at an even higher, eroded moraine preserved at 1859 m asl ~1.6 km north of the Maly Yenisei. The glacier that built this moraine could in principle have impounded an even deeper lake. The interpretations are photointerpretive only (Google Earth), and no geological studies appear to have been made of this drainage and its ancient glaciers.

The Hoit Aguy massif itself was heavily glaciated, evident from the well-developed cirques, and wide, long side canyons with paternoster lakes. The end moraines limiting the paternoster lakes of the Hoit Aguy massif are found at 2050–2220 m asl, higher than the trimlines of the East Sayan outlet glaciers, suggesting that the local alpine glaciers did not dam the Maly Yenisei.

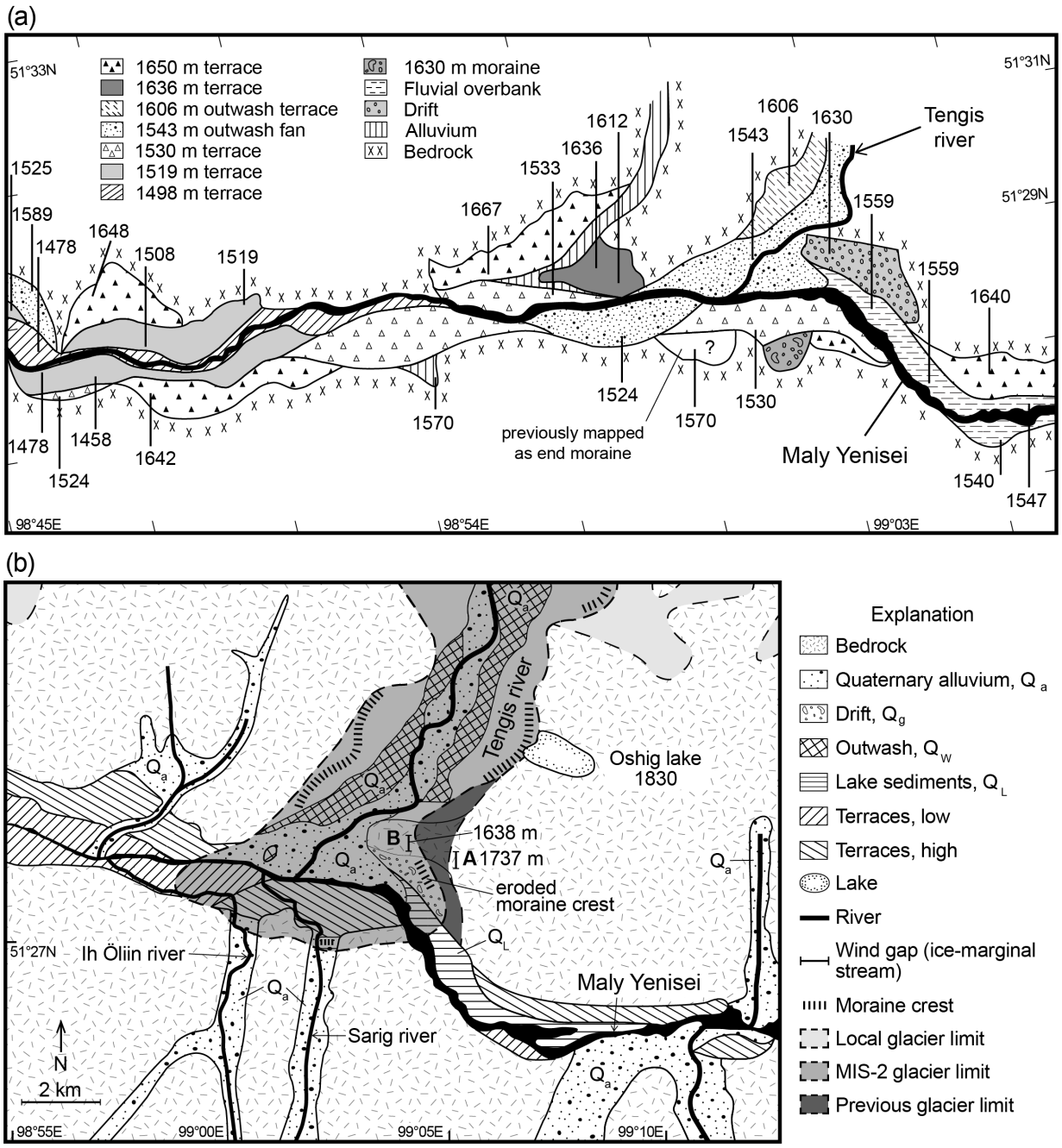

Figure 2.6. Maps of the lower Tengis river and the Maly Yenisei below the confluence showing: a) terraces with spot elevations from the SRTM. The sediments at the mouth of the Ih Öliin river valley at 1570 m asl do not appear to be a moraine. We corrected the elevation of the end moraine at the Sarig river valley. The map adapted after Komatsu *et al.* (2009); b) extent of the late Pleistocene glaciers and deposits, adapted after Gillespie *et al.* (2008).

Upstream from the Hoit Aguy massif, the valley widens to ~3000 m and becomes flat-floored, with sets of terraces at 1498–1650 m asl, no higher than ~150 m above the river level (Figure 2.6a). The terraced floor extends ~22 km to the confluence with the Tengis river. Komatsu *et al*. (2009) described some of these terraces as having river-parallel (east-west) channels and levees, an indication of large floods. The highest are eroded intracanyon basalt flows (e.g. Krivonogov *et al.* 2005), as was also the case in Tuva. At least some of these are capped by fluvial gravels (Komatsu *et al.* 2009).

Six km west of the Tengis confluence, a pre-LGM ice cap in the Ulaan Taiga may temporarily have sent ice tumbling into the gorge of the Maly Yenisei to block the river (Komatsu *et al.* 2009). However, any direct evidence of such a putative dam, if ever present, has been eroded by subsequent floods. This ice dam, located somewhere between ice dam #2 and the Tengis glacier dam, would have been yet another candidate for impounding deep lakes in Darhad basin. The evidence for the Ulaan Taiga ice cap is a series of deeply eroded stepped terraces that once rose above the ice cap as nunataks. Fresh-appearing stepped terraces are more obviously related to the ice cap (likely the pre-LGM ice cap), but are higher in the mountains and are farther from the river. Therefore, it appears that the Ulaan Taiga ice cap did not dam the Maly Yenisei during the LGM. Komatsu *et al.* (2009) speculatively suggested that the pre-LGM Ulaan Taiga dam might have been responsible for the deepest paleolake Darhad (1825 m asl), whereas the outlet valley glaciers impounded paleolake Darhad during the LGM and at other times. Grosswald (1987, 1999) and Grosswald and Rudoy (1996b) earlier proposed an ice field spanning the Maly Yenisei and flowing together from both north (Sayan) and south (Ulaan Taiga). However, there is no direct evidence that the East Sayan ice field ever approached the Maly Yenisei closely and their suggestion does not seem to have been widely accepted.

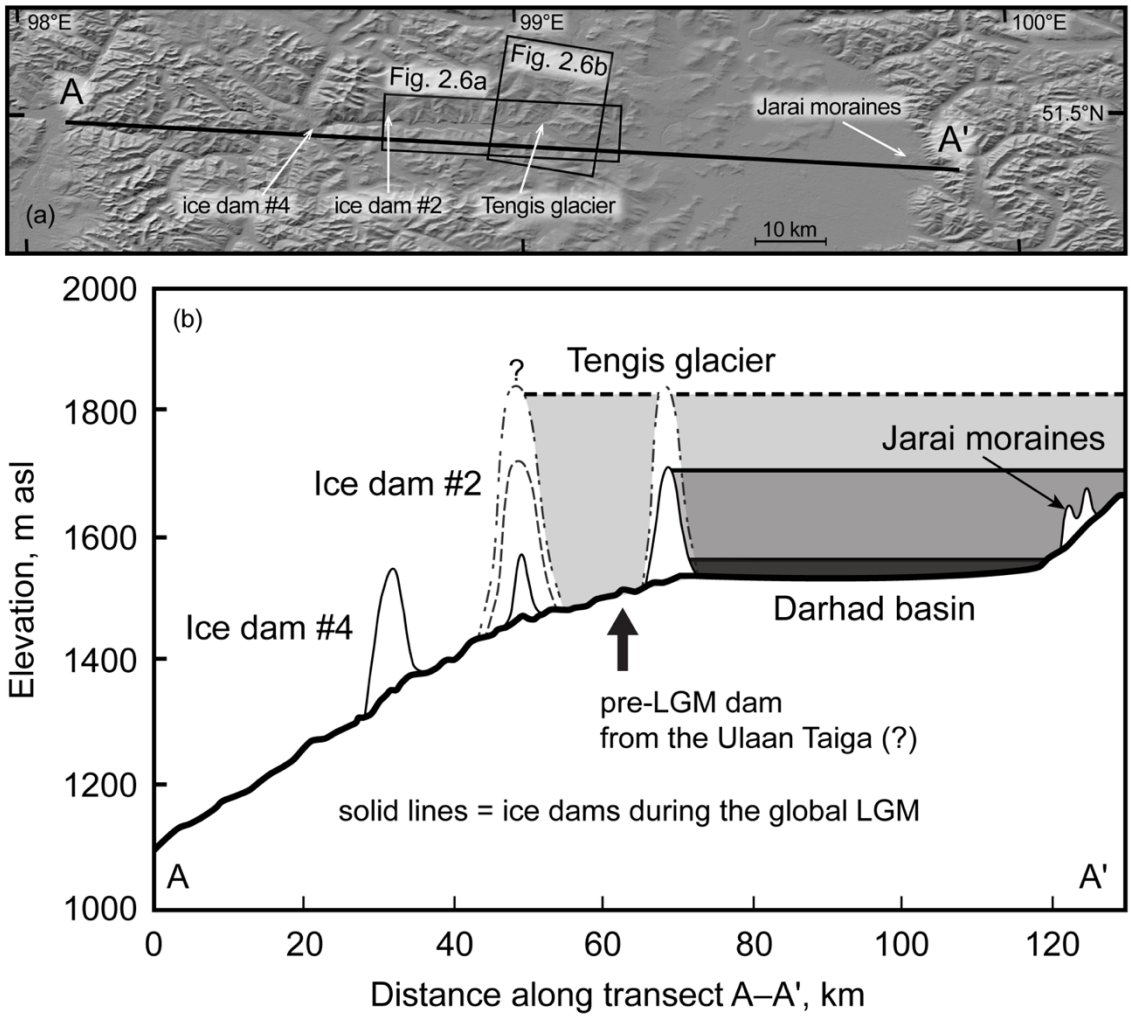

Figure 2.7. Topographic profile along the Maly Yenisei and across Darhad basin. a) Locations indicated on the shaded-relief image from ASTER DEM. b) Profile up the Maly Yenisei showing paleo highstands of Darhad basin and other glacier dams downriver. The 1825 m highstand (dashed line) exceeded the height of the Tengis moraines by ~100 m and likely predated MIS 2. Komatsu *et al.* (2009) hypothesized that an ice cap from the Ulaan Taiga mountains impounded that deepest paleolake. We propose yet another blocking mechanism from the outlet glaciers of the East Sayan ice field, damming the Maly Yenisei near the Hoit Aguy massif.

Krivonogov *et al.* (2005) and Komatsu *et al.* (2009) both identified what Krivonogov *et al.* called a "fan terrace" about 50 m above the Tengis river. Komatsu *et al.* (2009) mapped this outwash surface west of the Tengis river at an elevation of 1606 m asl (Figure 2.6). This surface slopes down to the south at ~9 m km^{-1}. The outwash consists of sandy silts mixed with angular gravels underlying ~20 cm thick dark soil. The modern Tengis river incises a lower outwash or alluvial fan (gravel and boulder "cone" of Krivonogov *et al.* 2005) having a lower gradient (~7 m km^{-1}). Krivonogov *et al.* (2005) inferred that the upper terrace could have formed a dam reaching a minimum elevation of ~1580 m asl, and impounding a lake in Darhad basin to similar level. The incised lower fan terminates at two levels, 6 and 2 m above the modern Maly Yenisei according to Krivonogov *et al.* (2005). They suggested that these alluvial deposits may have impounded shallow lakes in Darhad basin. The fan must have originated after the Tengis had incised the 1606 m asl outwash plain, and its base level was 10 m or less above the modern Maly Yenisei. Furthermore, within ~0.5 km of the Maly Yenisei, the fan is topographically ~flat: it does not grade up-river with the Tengis, although farther from the Maly Yenisei it does. The ~flat lower part of the fan may have been the spillway for the Maly Yenisei exiting the low paleolake.

We observed in the field that for ~2 km east of the Tengis confluence the lower part of the fan, below ~1555 m asl, is covered with ripples, ~1 m high and ~50 m crest-to-crest. They are perpendicular to the Maly Yenisei but oblique to the Tengis. These ripples likely formed due to currents of water draining the sediment-dammed lake and the flow was likely no deeper than 20–25 m, as calculated by the equation of Allen (1968). We interpret that the ripples were formed during the last flood from a paleolake with a surface level at ~1565 m asl, or the earlier and higher floods formed the ripples but the subsequent smaller floods failed to erode the ripples.

Upriver from the Tengis confluence, terraces still flank the Maly Yenisei, although their character is different. South of the river, one level is about 1580 m asl. From photointerpretation, this terrace appears to be composed of light-toned lake sediments, such as are not observed downriver from the Tengis. On the north side of the river is a prominent terrace composed or covered by lake sediments, at about 1640 m asl (Figure 2.6). The cap sediments on the terrace include gravels and rounded basalt boulders up to a meter in diameter. These exotic boulders must have been transported a kilometer or so from their source (Komatsu *et al.* 2009). They are found in a region that is well above the modern river but would have been under the Pleistocene highstands. The most likely mechanism for their transport would have been rapid discharge through Tengis dam ~9 km downstream.

2.2.4.4 Evidence of a glacier dam at the Tengis river confluence

The early history of ideas concerning the impounding of paleolakes in Darhad basin was well summarized by Krivonogov *et al.* (2005). The basalt flows must have blocked the Maly Yenisei at times but the ages are unknown and geomorphic evidence such as the deep incision of side canyons through the lava terraces suggests that they are not recent. In this tectonically active region, it would be hard to reconstruct the highstand of any lakes dammed by ancient flows. It is also possible that landslides occasionally have blocked the Maly Yenisei (e.g., Komatsu *et al.* 2009) but there is no direct evidence of this near the Tengis confluence in late Quaternary time. It appears that the Tengis glacier (Figure 2.4) is the main candidate for damming the late Pleistocene paleolakes that left most of the geomorphic evidence in the basin and the gorges of the Maly Yenisei although, as mentioned in the previous section, glacier dams farther downstream may have contributed also.

Evidence of the glacier dams themselves is sparse. Due to their location, they were eroded during large outburst floods. Furthermore, it is unclear how much debris was transported by the Tengis glacier to its terminus. If the glaciers were largely cold-based during the time leading up to the flood, they may well have transported little debris then, even if they became warm-based and relatively debris rich at the end of the glaciation as the climate warmed. We are thus left to look for moraine remnants away from the spillway floods.

Lateral moraines are preserved on the slopes of the Tengis river valley and are indirect evidence of the presence of a glacier dam across the Maly Yenisei. The right-lateral moraine 170 m above the modern Tengis river approaches the Maly Yenisei to within ~2 km. A glacier left this moraine would have impounded a paleolake in Darhad basin to a level of ~1710 m asl.

A higher left-lateral Tengis moraines is found at ~1840 m asl, impounding the Oshig lake (Figure 2.6b). It is matched by "ice-push scarps" across the valley mapped at similar elevations by Krivonogov *et al.* (2005). The glacier that left this moraine must have been >270 m deep. Although the moraines at Oshig lake are preserved no closer than ~5 km from the Maly Yenisei, both Krivogonov *et al.* (2005) and Gillespie *et al*. (2008) observed exotic clasts on the ridge between the Tengis and Maly Yenisei valleys at 1831 and ~1825 m asl, respectively, and considered them to have been glacially transported. The glacier may have impounded a paleolake in Darhad basin to a level of ~1825 m asl.

Merle (2001), Krivonogov *et al.* (2005) and Gillespie *et al.* (2008) all reported remnants of end moraines blocking the mouths of two neighboring valleys across the Maly Yenisei from the Tengis river (Figure 2.6b). We have now visited the eastern of these valleys (Sarig river) and confirm that the ridge there is indeed a moraine, with its crest at ~1630 m asl. It is covered with

exotic porphyritic granite boulders up to 3 m in diameter. The other sediment ridge near the mouth of the Ih Öliin river (Figure 2.6b) is much lower (1570 m asl) than the end moraine in the Sarig valley. If this mound was an end moraine, the floodwater must have eroded its top. We propose two alternative hypotheses for its formation: it could be a barrier bar that was deposited by an energetic flood, or it could be the runout from a landslide from the western wall of the valley. A second fresh landslide scar is found adjacent to the first, but on the southern wall of the Maly Yenisei valley. The runout from this second landslide is nowhere to be found; perhaps it was eroded by the outburst floods. In their Figure 3a, Krivonogov *et al.* (2005) mapped their "end moraine" as a low (~10 m according to Google Earth) ~circular feature ~0.5 m in diameter and 1 km south of the "barrier bar." This putative moraine remnant lacks an associated headwall scarp and therefore lacks critical evidence that would identify it as a landslide, too. There appears to have been no detailed field study of these important geomorphic features.

There are two north-south oriented bedrock wind gaps on the mountain ridge separating the Tengis and Maly Yenisei rivers today. The eastern, higher wind gap (A: Figure 2.6b) is ~10 m deep where it crosses the ridge at ~1737 m asl; the incision terminates on the north side of the ridge only a few meters lower, but on the south side the deeper part of the incision terminates at ~1695 m asl, suggesting flow out of Tengis valley into a paleolake ~45 m or more below the spillway. The western, lower wind gap (B: Figure 2.6b) is eroded into basalt at ~1638 m asl. Gillespie *et al*. (2008) found 2-m granodiorite boulders, originating from the Tengis headwaters, sitting atop the water-eroded basalt in the spillway, supporting the interpretation that the wind gaps provided passage for water from ice-marginal streams into the Darhad paleolakes. These boulders yielded ^{10}Be ages of 21 and 24 ka (Gillespie *et al.*, 2008).

Above we mentioned the suggestion of Krivonogov *et al.* (2005) that post-glacial sediments may have dammed the Maly Yenisei. Kettle topography and the large volume of the sediments flanking the Tengis river (~8 km^3) suggested to Gillespie *et al*. (2008) that a debris-rich glacier in the Tengis valley persisted for some time after its initial retreat. This could have been the case even if the glacier at its maximum advance was cold-based and debris-poor.

2.2.4.5 Evidence of a paleolake in Darhad basin

Darhad basin is ~100 km long (north-south) and 20–40 km wide. The clearest evidence of deep paleolakes in Darhad basin is the presence of shorelines (Selivanov 1967) on the walls east of the Tengis river at 1593 to 1713 m asl, the latter equivalent to a paleolake with a surface 172 m above the modern level of lake Dood Tsagaan (Figures 2.7, 2.8). Gillespie *et al.* (2008) observed higher shorelines indicated by degraded horizontal terraces on the basin walls near Zayadai lake as high as 1825 m asl. Krivonogov *et al.* (2005) considered the shorelines up to 1713 m asl to represent temporary stillstands of the rising lake that were not eroded during the subsequent rapid drawdown. The higher shoreline must have been left by an older, deeper lake.

Not all the lake-shore features are horizontal. A notch in the northern wall of the pass connecting Zayadai lake (Figure 2.8) to the main Darhad basin slopes to the east, at 3–4 degrees, suggesting strong outflow through the narrow pass to a lower lake in the main basin. The gradient could have resulted from either an outburst flood from the headwaters of the Shishhid river in the Ulaan Taiga, or from rapid lowering of the lake in the main basin during an outburst flood down the Maly Yenisei. Prominent highstands of paleolake Darhad and their corresponding parameters are summarized in Table 2.4.

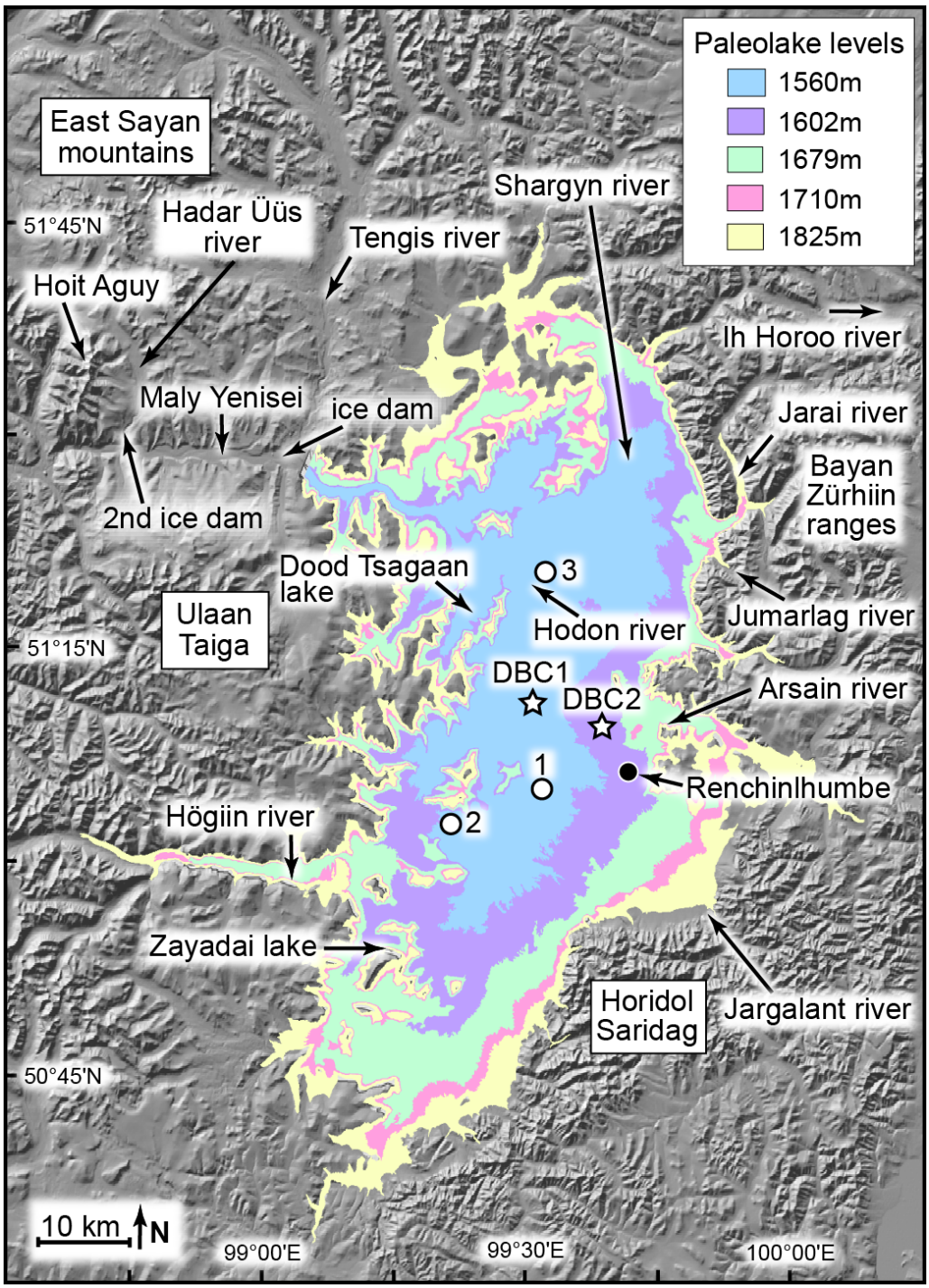

Figure 2.8. Geographic names and the extent of the paleolake when Darhad basin filled to 1560, 1602, 1679, 1710, and 1825 m asl (successive shades of gray; colored version is available online). Circles numbered 1, 2 indicate wells of Ufland *et al.* (1971), and 3 indicates DDB10-3 core (Krivonogov *et al.* 2012). Star symbols indicate two wells of Gillespie *et al.* (2005). Shaded-relief image from SRTM data. The map is from Gillespie *et al.* (2008).

There are some aeolian dunes on the floor of the basin, but also ripple fields. At Högiin river, the ripples may be left by outburst floods when an impounded lake breached its moraine dam there (Carson *et al.* 2003). Near the town of Renchinlhumbe, aeolian sand streaks up to ~1.5 km long point southeast, probably reworked from lacustrine and fluvial sands. South of Renchinlhumbe 4-5 m of gravels up to 15 cm in diameter overlie the lake sediments. They are shallowly buried below 1578 m asl and must have been deposited as a fan or delta of the Jargalant river after the last of the deep paleolakes drained.

Table 2.4. Highstands and volumes of the paleolake Darhad

Highstand elevation (m asl)	Lake volume (km^3)	Location of the highstand
1825	809	Degraded shorelines near Zayadai lake[a] Exotic clasts transported by the Tengis glacier[a, b] Trimlines of outlet glaciers from the East Sayan ice field (Hoit Aguy) Left-lateral moraine of the Tengis impounding Oshig lake[a]
1710	373	Beach sands 2 km south of Jarai river, near the Jumarlag river[a] Wind gap (1732 m asl) east of the Tengis river[a]
1679	276	Highest shoreline cut on the MIS 2 Jarai moraines[a]
1602	85	Outwash plain west of the Tengis river, measured near erosional scarp ~11 cal ka BP clam shells from a shoreline near Zayadai lake[a] 10-11 cal ka BP larch twigs in lake sediments near Jarai river[a]
1560	16	Outwash from the Jargalant river terminating ~15 km south of Jarai river[a]

[a] The evidence and data from Gillespie *et al*. (2008)

[b] Krivonogov *et al.* (2005) measured the elevation up to 1831 m asl.

Lake sediments in Darhad basin are rich in fossils of comparatively deep-water biota, such as clam and ostracod shells, fish scales, and aquatic plants. The dated fossils from the cutbanks of the Shargyn river indicate an MIS 3 lake (Gillespie *et al.* 2008) of long-enough duration to establish large populations (Gravis 1974). In addition to aquatic biota there are many subaerial plant fossils, e.g. larch twigs, moss, and other terrestrial plants, found in the lake sediments

indicating that the Darhad paleolake level fluctuated, and sometimes the basin was mostly dry (Gillespie *et al.* 2008).

2.2.4.6 Permafrost in Darhad basin

The floor of Darhad basin is heavily modified by active periglacial processes, as shown by polygonal patterned ground, thermokarst sinks, ice wedges, and earth hummocks. Sharkhuu *et al.* (2007) estimated that the active layer near Dood Tsagaan lake reaches 1.5 m, and attributed its shallow depth to the low thermal conductivity of ice-rich fine-grained sediments.

Gravis (1974) considered the permafrost in Darhad basin to have formed at the end of the Sartan glaciation, an equivalent to Marine Oxygen Isotope Stage (MIS) 2, after the deep Darhad paleolakes drained. Krivonogov *et al.* (2012) estimated that the permafrost in Darhad basin was thicker in the south (>127 m) than in the north (~47 m), based on the maximum depth of ground ice encountered in the deep boreholes of Ufland *et al.* (1971), Gillespie *et al.* (2005), and Krivonogov *et al.* (2012) (Figure 2.8). Equating the depth of the ground ice to its age, Krivonogov *et al.* (2012) inferred that Darhad basin started drying from the south. The disseminated plant material in the fill sediments of a thermokarst depression near Shargyn river gave an age of ~8.1 cal ka BP, suggesting to them that the modern permafrost in Darhad basin formed since then.

2.2.4.7 Summary of the flood and paleolake evidence

The past existence of a large lake in Darhad basin is evident from shoreline features and abundant lacustrine sediments. Lithology and unconformity of layers exposed in the Shargyn cutbanks suggest rapid erosion of sediments during the outburst floods, slumping, and fluctuating lake levels. A glacial dam is the most viable mechanism to create such deep and ephemeral lakes. However, sediment dams at Tengis river, such as from the alluvial fans or outwash terraces, likely

formed shallower lakes following the major glacial retreats. Hanging valleys and strath terraces in the valley of the Maly Yenisei are attributed to the outburst floods of the paleolake Darhad (Section 2.2 above). Floodwaters deposited large amount of sediment downstream as giant current ripples and fluvial terraces in the Kyzyl basin. However, none of these flood deposits downstream from Darhad basin have been directly dated so far and the only constraint on timing of these flood events themselves is indirect, from the dating of glacial deposits around Darhad basin and adjacent areas, but not from the putative glacial dam itself.

Although long sediment cores (~140 m) have been extracted from the center of Darhad basin (Ufland *et al.* 1971), these have no associated age control. Recent shallow-water sediments have been dated near the depocenter of Darhad basin, but deep-lake sediments have only been dated near the shores, where erosion, slumping, and the potential for an incomplete record is greatest (e.g. Shargyn cutbank section of Gillespie *et al.* 2008, maximum water depth ~155 m). An age model for the deep-water sediments from the largest paleolakes that generated the biggest floods down the Maly Yenisei has not been generated.

2.3 TIMING OF THE FLOODS

Without direct dating of the flood sediments the size and timing of the Maly Yenisei flood events has been constrained only indirectly, by dating lake sediments and glacial deposits in and around Darhad basin. In this section we review previous dating efforts for such purposes.

2.3.1 *Quantitative dating of lake sediments in Darhad basin*

A pair of ^{14}C ages for bulk sediments and a wood sample retrieved from below the modern floor of the Dood Tsagaan lake showed an extreme age offset of ~3500 ^{14}C yr (Peck *et al.* 2001). The discrepancy was attributed either to hard-water effects or to the influx of older detrital sediments

to the lake bottom. Gillespie *et al.* (2008) recommended correcting the ^{14}C ages by 2500 ^{14}C yr, based on the age discrepancy between a pair of larch twigs and snail shells sampled from the same depth in the lake sediments overlying the Jarai outwash. Similar experiment was done at the Hodon river cutbank by Krivonogov *et al.* (2012), and their ^{14}C ages for shells consistently overestimated the ages for wood materials by ~2500 ^{14}C yr. We applied the correction of 2500 ^{14}C yr to the published ages for shells and bulk sediments. Gillespie *et al.* (2008) treated the peat samples as bulk organics and we applied a 2500 ^{14}C yr correction to the recalibrated ages. We did not apply corrections to the macrofossil ages for individual fragments of plants, including larch twigs, roots, and grasses extracted from the peat or bulk sediments. Hereafter, only the recalibrated and corrected published ^{14}C ages, summarized in Table 2.5, are referred to in this review.

^{14}C dating was first used on sediments extracted from the modern Dood Tsagaan lake (Figure 2.8) by Dorofeyuk and Tarasov (1998). Their gyttja samples at depths of 1.2 and 2.4 m below the lake floor yielded corrected ages of ~6.6 and ~10.8 cal ka BP., respectively. The deepest part of Dood Tsagaan lake was cored by Peck *et al*. (2001), and the surface bulk sediments yielded corrected ^{14}C ages of ~0.4 cal ka BP. At a depth of ~4 m in the core the ages for bulk sediments and wood samples were ~6.4 cal ka BP, corrected to ~2.9 cal ka BP, and ~2.1 cal ka BP, respectively. Krivonogov *et al*. (2012) augmented the earlier studies in Darhad basin, extracting three short cores from the modern lake Dood Tsagaan. Eleven organic samples taken at various depths from the 6.4 m core (DN-1) gave ^{14}C ages ranging from ~9.5 to 12.7 cal ka BP. A second core from Dood Tsagaan lake (DN-2: 4.3 m long) was studied by Narantsetseg *et al*. (2013), who reported two ^{14}C age of ~4.8 and ~5.1 cal ka BP for bulk organics from depths of 0.5 and 2.6 m, respectively; Krivonogov *et al.* (2012) reported a ^{14}C age of ~14 cal ka BP for wood found at a depth of ~4 m in the same core.

Gillespie *et al*. (2008) provided a more complete chronology of lake evolution and glacial advances in Darhad basin, using ^{14}C dating of organics, including twigs, incorporated in the lake sediments. They also used luminescence techniques (IRSL) for directly dating the lake sediments, and CRE dating for the glacially abraded and transported boulders found on moraines. These are summarized below.

There are lake silts, at 1581 m asl, overlying the outwash plain deposited by the paleoglaciers of Jarai river valley. Peat, shells, charcoal, and wood materials were sampled from the same depth of ~1 m, and the consistent ^{14}C ages for the six samples gave an average age of ~10.1 cal ka BP. Two shell samples from ancient beach sands at 1602 m asl near Zayadai lake (Figure 2.8) dated to 10.3 and 11.2 cal ka BP. These ages suggest that Darhad paleolake was at least 65 m deep in the early Holocene, consistent with presence of a lower sediment (outwash) dam but not the higher ice dams at the Tengis confluence.

An outcrop at the Hodon river cutbank (Figure 2.8) exposes a ~13 m thick section of lake sediments at 1552 m asl. Krivonogov *et al*. (2012) dated 16 samples taken from this cutbank, including four pairs of wood and shell from the same depth (3.6, 5.2, 5.6, and 7.0 m). The uppermost layer was dated to ~4.8 cal ka BP. The ages increased with depth, and the layer at ~10 m depth was dated to ~9 cal ka BP. Based on the sandy composition and abundance of wood materials at lower sections of the Hodon outcrop, Krivonogov *et al.* (2012) argued that Darhad basin was largely dry by ~9 ka. Narantsetseg *et al.* (2013) extracted diatom remnants in the sediments from the DN-1 and DN-2 cores but did not find any diatom fossils in the sediments from ~10–14 ka. The minimal concentration of organic carbon coincided with the absence of diatoms in the paleolake Dood Tsagaan, suggesting to Narantsetseg *et al.* (2013) that Darhad basin was largely dry then. They correlated the stratigraphy of the DN-1 and DN-2 cores with the records

from the Hodon cutbank and the DDP10-3 core (Figure 2.9) and subdivided the sediments younger than 10 ka into four units with approximate boundaries at 8.5, 7.8, and 5.8 ka. However, all of the corrected ^{14}C ages for the DN-1 were not distinguishable for the entire ~6 m of the core, and the boundaries of the subdivision of Dood Tsagaan lake sediments largely relied on the ages from the Hodon cutbank. Therefore, the ages for the boundaries of sediment units in the DN-1 core are not precise.

The suggestion of dry Darhad basin at ~9 ka by Krivonogov *et al.* (2012) and Narantsetseg *et al.* (2013) appears to conflict with the establishment by Gillespie *et al.* (2008) of a deep lake up to ~1600 m asl at about the same time. There are two ways to resolve this dilemma: first, the uncertainties in dating allows for the rapid drainage of the 1600 m asl lake, followed by lengthy subaerial exposure; or second, some of the Hodon ages may be greater than the age of deposition such that the dilemma is only apparent. The Hodon cutbank is located at the junction of Shargyn, Jarai, and Hodon rivers due to reworking, a place susceptible to the deposition of eroded sediments from upstream. Therefore, it is possible that Darhad basin was filled to 1600 m asl in the early Holocene, consistent with the post-glacial outwash plains of the Tengis river at 1606 m asl impounding the lake.

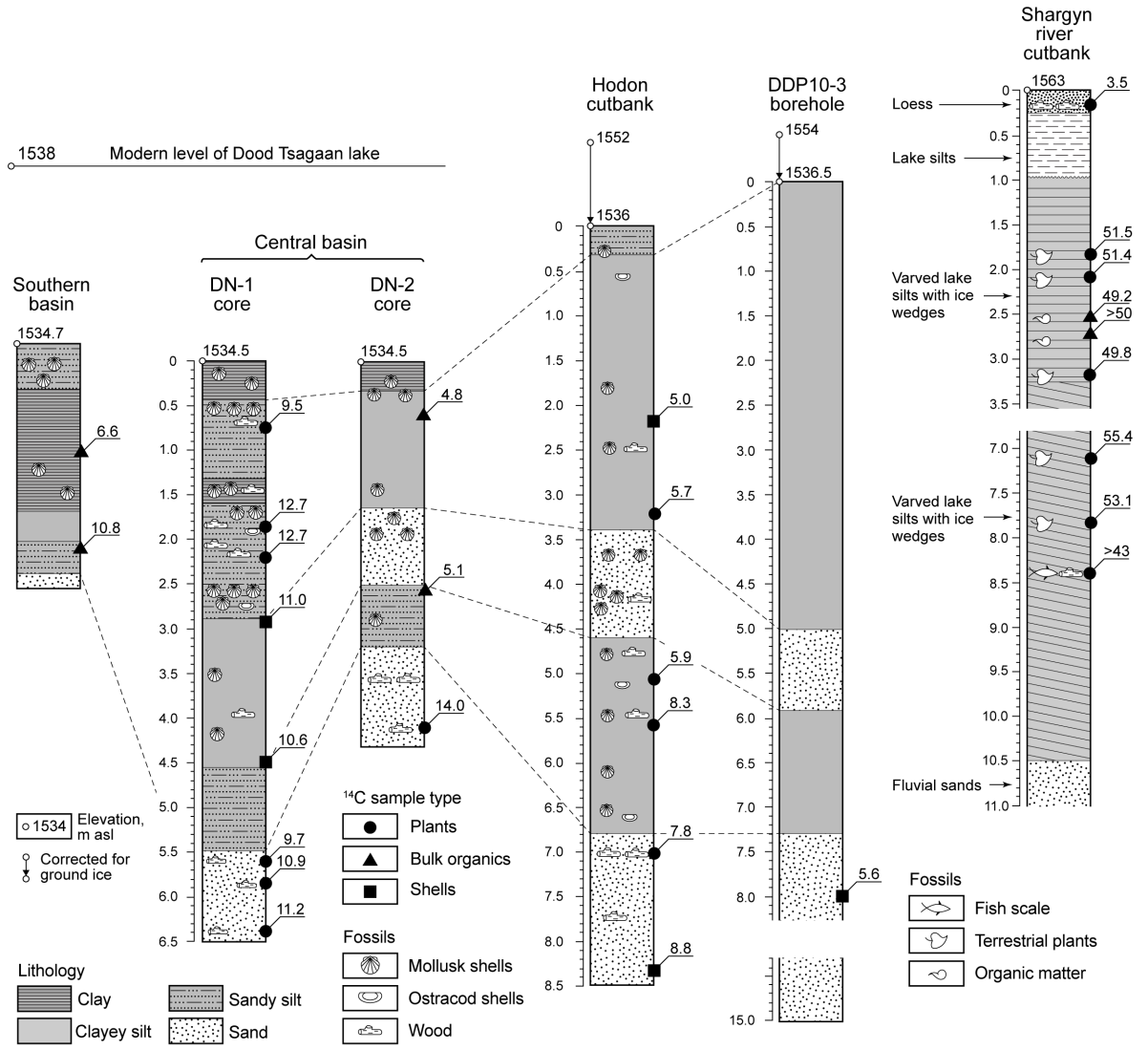

Figure 2.9. Stratigraphic relationship of post-LGM sediments between the studied outcrops and the boreholes. All the ^{14}C ages (cal ka BP) are recalibrated and corrected for hard-water effects. The ages from the southern basin of Dood Tsagaan lake are from Dorofeyuk and Tarasov (1998). The sediments in the Hodon river cutbank, the boreholes DN-1, DN-2, and DDP10-3 were dated by Krivonogov *et al.* (2012). Narantsetseg *et al.* (2013) provided two ages for the DN-2 and constructed the stratigraphic correlations. Note that the Shargyn river cutbank is located at a higher elevation and not aligned to the other records (data from Gillespie *et al.* 2008).

Table 2.5. ^{14}C samples collected in Darhad basin

Sample ID	Lab number	Material	Depth (m)	^{14}C age (yr ± 1σ)	Calibrated age[a] (cal yr BP ± 2σ)	Corrected ages for hard-water effect[b] (cal yr BP ± 2σ)	References
Jarai river, lake silts overlying outwash below the end moraines: N 51.400067°, E 99.751650°, 1581 m asl							
100800 rmb-03	76360	Peat	1.12	11090 ± 60	12940 ± 140	10440 ± 140	Gillespie *et al*. 2008[a]
100800 rmb-03	76361	Wood from peat	1.12	5700 ± 50	6520 ± 120	6520 ± 120	
100800 arg-03	76694	Charcoal	1.00	9200 ± 40	10345 ± 95	10345 ± 95	
072301 arg-001a	79695	Wood	1.00	9480 ± 40	10695 ± 105	10695 ± 105	
072301 arg-001a	79696	Snail shells	1.00	11930 ± 40	13710 ± 140	11210 ± 140	
260701 rmb-10 #5	79698	Clam shells	1.00	11900 ± 40	13680 ± 110	11180 ± 110	
Zayadai lake, lacustrine silts underlying reworked beach sands: N 50.900050°, E 99.229217°, 1602 m asl							
071901 arg-002	79697	Clam shells	1.20	10960 ± 50	12845 ± 125	10345 ± 125	Gillespie *et al*. 2008
071901 arg-003	79698	Snail shells	1.20	11810 ± 50	13650 ± 110	11150 ± 110	
Shargyn river cutbank in Jarai delta, lake silts: N 51.401550°, E 99.750183°, 1563 m asl							
062002 arg JG-04	97489	Charred wood	0.25	3285 ± 40	3525 ± 85	3525 ± 85	Gillespie *et al*. 2008
062002 arg JG-04	97490	Wood charcoal	0.25	3210 ± 40	3435 ± 75	3435 ± 75	
062002 arg SG-n1	97491	Vegetation stems	1.85	47500 ± 1900	51495 ± 3025	51495 ± 3025	
062002 arg SG-n2	97492	Grass	2.10	47400 ± 1900	51355 ± 3015	51355 ± 3015	
062002 arg SG-n5	97493	Organic matter	2.54	45700 ± 1500	49230 ± 2330	49230 ± 2330	
062002 arg SG-n9	97494	Vegetation remains	3.23	46200 ± 1600	49810 ± 2540	49810 ± 2540	
062002 arg SG-n19	97495	Grass blades	7.13	49500 ± 2400	55350 ± 4700	55350 ± 4700	
062102 arg SG-n2-1	97496	Organic matter	2.72	51700 ± 3200	>50000	>50000	
062102 arg SG-n2-2	97497	Mat fibers	3.89	52800 ± 3600	>50000	>50000	
062102 arg SG-n2-7	97498	Moss fragments	7.84	48500 ± 2100	53075 ± 3395	53075 ± 3395	
260701 rmb-10 #7	79699	Fish scale	~8.40	39300 ± 2600	43280 ± 4970	43280 ± 4970	
260701 rmb-10 #3	79700	Wood twigs	~8.40	> modern	>modern	>modern	
260701 rmb-10 #1	79701	Wood fragments	~8.40	> 35700	>41000	>41000	
260701 rmb-10	80308	Aquatic plants	~8.40	33600 ± 1500	37905 ± 3155	37905 ± 3155	
Tengis river confluence with Maly Yenisei river, lake silts: N 51.440483°, E 99.061283°, 1540 m asl							
180800 rjc	71885	Clam shells	1.00	10530 ± 40	12510 ± 110	10010 ± 110	Gillespie *et al*. 2008
Tengis river outwash, interbedded silt: N 51.650383°, E 99.118083°, 1729 m asl							
150800 rmb-02	76362	Wood	0.90	7750 ± 40	8515 ± 85	8515 ± 85	Gillespie *et al*. 2008
Högiin river moraine: N 51.005767°, E 99.141450°, 1716 m asl							
200800 rmb-02	76363	Wood	0.38	1060 ± 50	990 ± 90	990 ± 90	Gillespie *et al*. 2008
DDP10-3 borehole: N 51.336330°, E 99.501639°, 1554 m asl							
-	ICa100044	Shells	8.02	7280 ± 60	8085 ± 115	5585 ± 115	Krivonogov *et al.* 2012

Table 2.5 (continued)

Sample ID	Lab number	Material	Depth (m)	^{14}C age (yr ± 1σ)	Calibrated age[a] (cal yr BP ± 2σ)	Corrected ages for hard-water effect[b] (cal yr BP ± 2σ)	References
Dood Tsagaan lake (central basin) DN-1 borehole: N 51.407200°, E 99.325194°, 1538 m asl, water depth 3.5 m							
-	AA79206	Roots of herbs	0.74	8500 ± 40	9500 ± 40	9500 ± 40	Krivonogov *et al.* 2012
-	AA79207	Roots of herbs	1.87	10780 ± 60	12685 ± 85	12685 ± 85	
-	AA79208	Piece of stem	1.98	10730 ± 45	12665 ± 65	12665 ± 65	
-	AA79209	Shell	2.09	10870 ± 45	12750 ± 60	10250 ± 60	
-	AA79210	Plant fragment	2.21	10720 ± 45	12660 ± 70	12660 ± 70	
-	AA79212	Shell of pelecipod	2.95	11690 ± 60	13520 ± 120	11020 ± 120	
-	AA79213	Shells of Lymnaea	4.49	11270 ± 110	13095 ± 245	10595 ± 245	
-	AA79214	Charcoal	5.64	8690 ± 45	9660 ± 120	9660 ± 120	
-	AA79215	Pieces of wood	5.85	9590 ± 55	10945 ± 205	10945 ± 205	
-	AA79216	Pieces of wood	6.44	9810 ± 45	11230 ± 60	11230 ± 60	
Dood Tsagaan lake (central basin) DN-2 borehole: N 51.395389°, E 99.359361°, 1538 m asl, water depth 3.5 m							
-	AA94382	Bulk organics	0.56–0.58	6410 ± 50	7345 ± 75	4845 ± 75	Narantsetseg *et al.* 2013
-	AA94383	Bulk organics	2.60–2.62	6780 ± 45	7630 ± 60	5130 ± 60	Narantsetseg *et al.* 2013
-	AA79217	Pieces of wood	4.13	12130 ± 50	13980 ± 170	13980 ± 170	Krivonogov *et al.* 2012
Hodon river cutbank: N 51.335833°, E 99.500778°, 1552 m asl							
-	ICa100033	Shells	0.55-0.6	6380 ± 50	7330 ± 90	4830 ± 90	Krivonogov *et al.* 2012
-	ICa100034	Shells	2.20	6540 ± 60	7490 ± 80	4990 ± 80	
-	IWd100391	Wood	3.25	4920 ± 50	5670 ± 80	5670 ± 80	
-	ICa100035	Shells	3.25	6650 ± 50	7515 ± 75	5015 ± 75	
-	ICa100036	Shells	4.18	8350 ± 60	9360 ± 130	6860 ± 130	
-	ICa100037	Shells	4.85	8630 ± 60	9615 ± 125	7115 ± 125	
-	IWd100392	Wood	5.15	5180 ± 50	5940 ± 80	5940 ± 80	
-	ICa100038	Shells	5.15	8590 ± 60	9585 ± 105	7085 ± 105	
-	IWd100393	Wood	5.63	7420 ± 60	8270 ± 110	8270 ± 110	
-	ICa100039	Shells	5.63	9280 ± 60	10425 ± 165	7925 ± 165	
-	IWd100394	Wood	7.01	6970 ± 60	7785 ± 95	7785 ± 95	
-	ICa100040	Shells	7.01	9760 ± 70	11195 ± 125	8695 ± 125	
-	ICa100041	Shells	8.31	9870 ± 70	11300 ± 120	8800 ± 120	
-	ICa100042	Shells	8.91	10040 ± 70	11550 ± 280	9050 ± 280	
-	ICa100043	Shells	10.08	10130 ± 70	11715 ± 315	9215 ± 315	
-	IWd100395	Wood	10.80	7690 ± 60	8495 ± 95	8495 ± 95	

Table 2.5 (continued)

Sample ID	Lab number	Material	Depth (m)	^{14}C age (yr ± 1σ)	Calibrated age[a] (cal yr BP ± 2σ)	Corrected ages for hard-water effect[b] (cal yr BP ± 2σ)	References
Talyn lake, paleolake sediments: N 51.4333°, E 99.6168°, 1554 m asl							
-	IWd100396	Wood	2.50	55260 ± 2080	>55000	>55000	Krivonogov *et al.* 2012
Shargyn river, filling of a thermokarst basin: N 51.4167°, E 99.6167°, 1543 m asl							
-	SOAN-5080	Plant fragments	3.85	7075 ± 75	7875 ± 145	7875 ± 145	Krivonogov *et al.* 2012
-	SOAN-5081	Plant fragments	7.00	7255 ± 85	8075 ± 145	8075 ± 145	
Jumarlag river, filling of a thermokarst basin: N 51.4000°, E 99.6667°, ~1550 m asl							
-	Beta-174246	Wood	3.00	5140 ± 40	5905 ± 45	5905 ± 45	Krivonogov *et al.* 2012
Jumarlag river, filling of a thermokarst basin: N 51.3833°, E 99.6667°, ~1550 m asl							
-	SOAN-5079	Wood	4.00	3180 ± 50	3415 ± 95	3415 ± 95	Krivonogov *et al.* 2012
Tsagaan lake, thermokarst lake sediments: N 51.3339°, E 99.5000°, 1540 m asl							
-	SOAN-5532	Humic soil	1.20	3515 ± 75	3795 ± 185	3795 ± 185	Krivonogov *et al.* 2012
Jarain river, sand cover above periglacial fan: N 51.4000°, E 99.7500°, 1579 m asl							
-	SOAN-5531	Wood	1.00	2460 ± 25	2465 ± 85	2465 ± 85	Krivonogov *et al.* 2012
DBC1 borehole: N 51.187222°, E 99.497556°, 1547 m asl							
-	AA-79019	Roots of herbs	16.27	15530 ± 140	18790 ± 300	18790 ± 300	Krivonogov *et al.* 2008
Dood Tsagaan lake (southern basin): N 51.3333°, E 99.3833°, 1538 m asl, water depth ~14 m							
-	-	Bulk sediments	surface	3570 ± 36[c]	3900 ± 80	400 ± 80	Peck *et al.* 2001
-	-	Bulk sediments	4.09	5530 ± 55[c]	6350 ± 90	2850 ± 90	
-	-	Wood	4.09	2080 ± 21[c]	2060 ± 60	2060 ± 60	
Dood Tsagaan lake (southern basin): 200 m from its eastern shore, N 51.3333°, E 99.3833°, 1538 m asl, water depth 3.3 m							
-	Vib-112	Gyttja	1.23	8150 ± 60	9140 ± 150	6640 ± 150	Dorofeyuk and Tarasov 1998
-	Vib-113	Gyttja	2.38	11470 ± 100	13290 ± 190	10790 ± 190	

a 2σ range calculated using CALIB version 7.1 (Stuiver and Reimer 1993) and IntCal13 calibration curve (Reimer *et al.* 2013), and rounded to nearest decade.
b Hard-water corrections to the ages for bulk sediments, peat, and gyttja were taken from the recommendations of the corresponding articles. Gillespie *et al.* (2008): 2500 ^{14}C yr; Krivonogov *et al.* (2012): 2500 ^{14}C yr; Peck *et al.* (2001): 3500 ^{14}C yr; We used 2500 ^{14}C yr for ages of Krivonogov *et al.* (2005, 2008) and Dorofeyuk and Tarasov (1998).
c Peck *et al.* (2001) did not provide the uncertainty, and we assumed 1% error, rounded to the nearest decade.

The Shargyn river cutbank (Figure 2.8; 1563 m asl) exposes another deep section (~13 m) of lake sediments in Darhad basin. Two charcoal samples from its uppermost 25 cm aeolian layer were dated to ~3.5 cal ka BP (Gillespie *et al.* 2008). A prominent unconformity separates this top layer from the underlying varved lake sediments, which Gillespie *et al.* (2008) correlated to the ~10–11 ka lake sediments on Jarai moraines. These early Holocene sediments unconformably sit on dark rhythmite, probably varved, lake sediments. Eleven organic samples taken from this lake sediments at depths of ~2–8 m gave ages from ~38 cal ka BP to more than 50 cal ka BP (MIS 3 or older). A direct infrared-stimulated luminescence (IRSL) dating of lake sediments in the Shargyn cutbank at 9 m depth gave ages of 40.9 ± 10.8 ka, consistent with the ^{14}C ages. Because most of the likely varves at the Shargyn river are ~0.6 cm thick, the whole 10-m sequence exposed in the cutbank may represent <2000 yr, much less than the scatter of the ages, and Gillespie *et al* (2008) attributed to residual reservoir effects, carbon exchange, and contamination. No MIS 2 lake sediments were found at the Shargyn river cutbank.

In 2004, a new 92.6 m deep core (DBC1) was drilled in the depocenter of Darhad basin, and Gillespie *et al.* (2005) provided its first description. Preliminary results of luminescence dating of the core revealed MIS 2 lake sediments from a depth of ~9 m (Batbaatar *et al.* 2008, 2009), but they admitted that the large uncertainty of the age required further analysis. Krivonogov *et al.* (2008) took eleven samples from this same core at an interval of 3–17 m depth. One sample of plant remains at the depth of ~16 m yielded the age of ~18.8 cal ka BP. The remaining ten seemed too old or too young to Krivonogov *et al.* (2008), which they blamed on sample contamination after the extraction; those ages were not reported. The DBC1 core was later described by Krivonogov *et al.* (2012) who proposed another age model for the upper 50 m of the core, based on the paleomagnetic reversals identified by visually matching the magnetic inclination curve for

the DBC1 core and the magnetic field paleointensity record from marine sediments (Channell *et al.* 2009). The paleomagnetic age model of Krivonogov *et al.* (2012) gives a sedimentation rate of ~0.34 m ka^{-1} and ages that agree with a last deep lake during MIS 3. The model, however, assumes a constant rate of sedimentation, which is not supported by the evidence from the core itself due to the existence of many breaks in sedimentation (Batbaatar *et al.* 2012) as was acknowledged by Krivonogov *et al.* (2012).

The latest drilling in Darhad basin, ~10 km west of the town of Renchinlhumbe, reached a depth of 163.8 m (DDP10-3: Figure 2.8) and Krivonogov *et al*. (2012) reported an age of ~5.6 cal ka BP for gastropod shells found at a depth of ~8 m. The full results of the DDP10-3 core are not published yet.

2.3.2 *Chronology of glacial advances in and around Darhad basin*

Gillespie *et al.* (2008) radiometrically dated (^{10}Be) glacial deposits around Darhad basin in order to establish the glacial chronology there and in order to estimate the age of the Tengis glaciers thought to have impounded the deep paleolakes. Other studies have reported glacial ages for the surrounding mountains. In this section we examine those published ages, recalibrated for current estimates of ^{10}Be production rates. We also report of estimate equilibrium-line altitudes (ELA) for the dated advances to help in regional correlation.

In this review we consider glaciers related to the East Sayan ice field and other mountains surrounding Darhad basin, and Otgontenger peak in the central massif of Mongolia, 300 km south of Darhad. The summary of the recalculated ^{10}Be ages previously published is given in Table 2.6 and Figure 2.10. To constrain the chronology of glacial advances in the mountains bordering Darhad basin, Gillespie *et al.* (2008) sampled 22 granitic boulders sitting on moraines and outwash

in the Tengis, Jarai, and Högiin river valleys (Figure 2.8) and measured CRE ages from their ^{10}Be. The bedrock wind gap east of the Tengis river at 1638 m asl was once a spillway of an ice-marginal stream into a Darhad paleolake, and two exotic boulders there were dated to ~21 and 24 ka. These ages may have been younger than the 1710 m asl highstand, but showed that an MIS 2 glacier was at least within ~3 km of blocking the outlet from Darhad basin.

There was considerable variability in the ages of boulders from the moraines. In Tengis valley, upstream from the Yenisei/Tengis confluence, the ages for three of the four dated boulders were ~28–35 ka; the fourth was younger at ~17 ka. Only one of the four postdated MIS 3. Taken together, the six samples from the Tengis valley suggest that the outlet glaciers in the Tengis valley likely dammed the Maly Yenisei during MIS 3, and MIS 2 glaciers may have done so too.

A different outlet glacier from the East Sayan ice field advanced down the Jarai river valley and left two sets of piedmont moraines on the eastern side of Darhad basin. Seven of the ten ^{10}Be ages for these moraines scattered from ~19–25 ka (MIS 2); the other three (30–45 ka) predated MIS 2. Gillespie *et al.* (2008) attributed the scatter to inherited ^{10}Be. These moraines postdated the 1710 m asl highstand of the paleolake but were themselves inundated to 1679 m asl, and on the strength of these ages Gillespie *et al.* (2008) argued that the latest deep paleolakes dated from MIS 2, provided that the Jarai glaciers advanced synchronously with the damming Tengis glaciers.

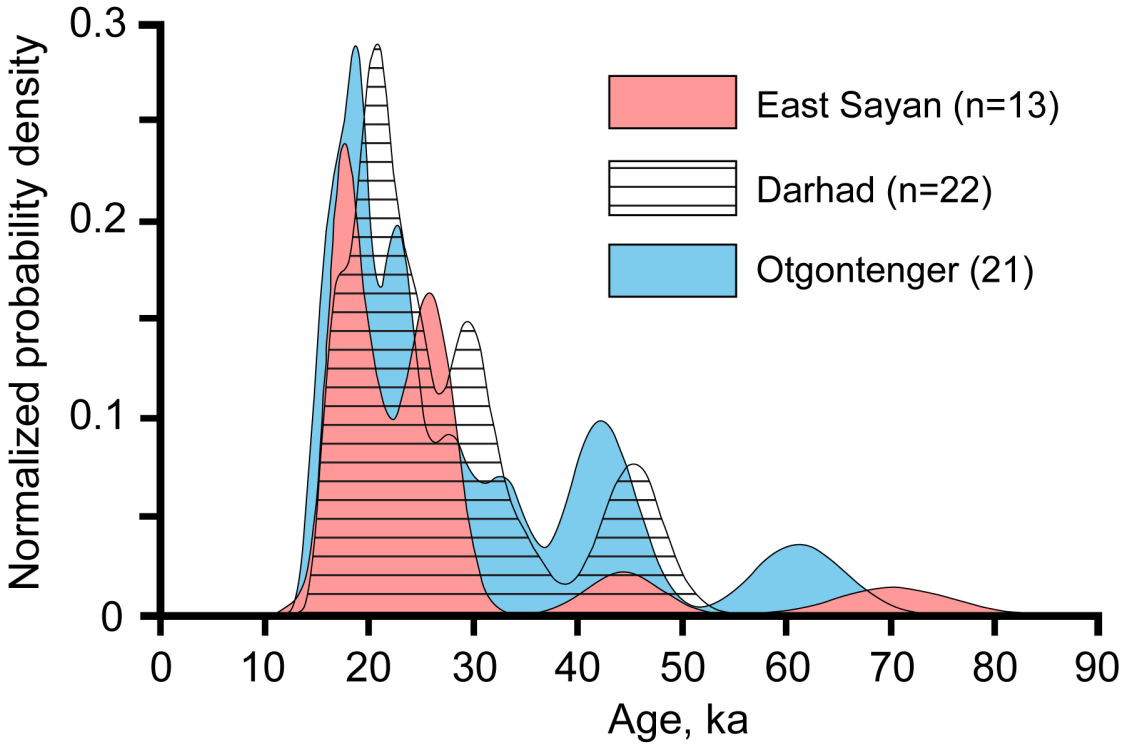

Figure 2.10. Summed normal distribution density of 10Be cosmic-ray exposure ages discussed in this paper. The East Sayan mountain group includes the 13 ages from Jombolok, Sentsa, and Sailag river valleys (Arzhannikov *et al.* 2012). Darhad basin group includes the 22 ages from Gillespie *et al.* (2008). The 21 ages for the Otgontenger mountain are from Rother *et al.* (2014).

Table 2.6. Published and recalculated ^{10}Be ages for glacial deposits in and around Darhad basin

Sample identification	Latitude / Longitude (decimal degrees)	Elevation (m asl)	Sample description	Published ages (ka ± 2σ)	Recalculated ages (ka ± 2σ)	Increase in the published ages (%)	References
Tengis river, bedrock (basalt) overflow channel, the Maly Yenisei exit from Darhad basin							Gillespie *et al.* 2008
081400-arg-Tin-01	51.479217 / 99.055533	1638	Quartzite boulder	19.2 ± 1.3	21.3 ± 1.3	10	
081400-arg-Tin-01b	51.479217 / 99.055533	1638	Granite boulder	21.6 ± 1.5	23.9 ± 1.5	10	
Tengis river, ground till and recessional outwash, the Maly Yenisei exit from Darhad basin							Gillespie *et al.* 2008
081700-rmb-Tin-01a	51.650383 / 99.118083	1729	Granite boulder	31.2 ± 2.2	34.5 ± 2.2	10	
081700-rmb-Tin-01c	51.650383 / 99.118083	1729	Quartzite boulder	25.3 ± 1.7	28.0 ± 1.7	10	
Tengis river, ground till & recessional outwash at Uzgen lake, the Maly Yenisei exit from Darhad basin							Gillespie *et al.* 2008
081700-arg-Uzg-002d	51.624200 / 99.189100	1932	Dacite boulder	15.6 ± 1.1	16.8 ± 1.1	7	
081700-arg-Uzg-003	51.624200 / 99.189100	1932	Granitic boulder	27.7 ± 2.0	30.5 ± 2.0	9	
Jarai river, older right-lateral piedmont moraines, Darhad basin							Gillespie *et al.* 2008
080900-arg-Gar-Ia-001	51.399567 / 99.772200	1633	Granitic boulder	21.4 ± 1.5	23.7 ± 1.5	10	
080900-arg-Gar-Ia-002	51.399567 / 99.772200	1633	Granitic boulder	19.0 ± 1.3	21.1 ± 1.3	10	
081000-arg-Gar-Ia-003	51.399567 / 99.772200	1633	Granitic boulder	21.7 ± 1.5	25.1 ± 1.5	13	
081000-arg-Gar-Ia-010	51.399567 / 99.772200	1633	Granitic boulder	40.9 ± 2.7	45.4 ± 2.7	10	
081000-arg-Gar-Ia-011	51.399567 / 99.772200	1633	Granitic boulder	40.3 ± 4.1	44.7 ± 4.1	10	
081000-arg-Gar-Ia-012	51.399567 / 99.772200	1633	Granitic boulder	17.6 ± 1.2	19.5 ± 1.2	10	
081000-arg-Gar-Ia-013	51.399567 / 99.772200	1633	Granitic boulder	18.3 ± 1.3	20.3 ± 1.3	10	
Jarai river, younger right-lateral piedmont moraines, Darhad basin							Gillespie *et al.* 2008
081000-arg-Gar-IIa-005	51.399350 / 99.799900	1676	Granitic boulder	27.4 ± 1.9	30.4 ± 1.9	10	
081000-arg-Gar-IIa-007	51.399350 / 99.799900	1676	Granitic boulder	16.8 ± 1.1	18.6 ± 1.1	10	
081000-arg-Gar-IIa-008	51.399350 / 99.799900	1676	Granitic boulder	19.3 ± 1.3	21.4 ± 1.3	10	
Högiin river pre-MIS 2 left-lateral kame(?), Darhad basin							Gillespie *et al.* 2008
082100-arg-Huj-01a	51.005767 / 99.141450	1716	Granitic boulder	221.4 ± 19.2	246.9 ± 19.2	10	
082100-arg-Huj-01b	51.005767 / 99.141450	1716	Granitic boulder	100.8 ± 6.7	111.9 ± 6.7	10	
082100-arg-Huj-01c	51.005767 / 99.141450	1716	Granitic boulder	128.5 ± 8.6	142.8 ± 8.6	10	

Table 2.6 (continued)

Sample identification	Latitude / Longitude (decimal degrees)	Elevation (m asl)	Sample description	Published ages (ka ± 2σ)	Recalculated ages (ka ± 2σ)	Increase in the published ages (%)	References
Högiin river end moraine, Darhad basin							Gillespie *et al.* 2008
082100-arg-Huj-02c	51.323000 / 99.160000	1679	Granitic boulder	14.9 ± 1.1	16.5 ± 1.1	10	
082100-arg-Huj-02d	51.323000 / 99.160000	1679	Granitic boulder	40.9 ± 2.8	45.3 ± 2.8	10	
082100-arg-Huj-02e	51.323000 / 99.160000	1679	Granitic boulder	26.3 ± 1.9	29.1 ± 1.9	10	
Sentsa river valley terminal moraine, East Sayan mountains							Arzhannikov *et al.* 2012
S07BE6	52.680400 / 99.506750	1443	Granitic boulder	16.1 ± 3.2	18.1 ± 3.2	11	
S07BE7	52.682430 / 99.509000	1445	Granitic boulder	18.2 ± 1.4	20.6 ± 1.4	11	
S07BE8	52.682460 / 99.508750	1453	Granitic boulder	16.0 ± 1.5	18.1 ± 1.5	11	
S07BE9	52.682730 / 99.509050	1453	Granitic boulder	15.4 ± 1.3	17.4 ± 1.3	11	
Jombolok river terminal moraine front, East Sayan mountains							Arzhannikov *et al.* 2012
S07BE10	52.752210 / 99.708550	1293	Granitic boulder	23.2 ± 1.9	26.4 ± 1.9	12	
S07BE11	52.752130 / 99.707250	1294	Granitic boulder	21.4 ± 1.8	24.3 ± 1.8	12	
S07BE12	52.752500 / 99.705080	1294	Granitic boulder	22.1 ± 2.8	25.0 ± 2.8	12	
Jombolok river valley terminal moraine, East Sayan mountains							Arzhannikov *et al.* 2012
S07BE13	52.740030 / 99.633030	1420	Granitic boulder	23.9 ± 1.9	27.0 ± 1.9	11	
S07BE14	52.739800 / 99.633183	1420	Granitic boulder	23.0 ± 2.5	26.0 ± 2.5	11	
S07BE15	52.739700 / 99.633370	1413	Granitic boulder	39.3 ± 3.6	44.4 ± 3.6	12	
Sailag river terminal moraine, East Sayan mountains							Arzhannikov *et al.* 2012
S07BE16	52.777116 / 99.718416	1383	Granitic boulder	62.1 ± 5.7	70.2 ± 5.7	12	
S07BE17	52.777683 / 99.718616	1385	Granitic boulder	15.0 ± 1.4	17.0 ± 1.4	12	
S07BE18	52.778333 / 99.721216	1385	Granitic boulder	16.0 ± 1.6	18.1 ± 1.6	11	
Recessional moraines of the southern outlet glacier, Otgontenger, Hangai mountains							Rother *et al.* 2014
MON-D-II-I	47.6789 / 97.2083	2084	Granite boulder	15.3 ± 1.8	16.6 ± 1.0	8	
MON-D-II-II	47.6791 / 97.2084	2082	Granite boulder	15.2 ± 1.3	16.5 ± 1.0	8	
MON-D-II-III	47.6780 / 97.2097	2094	Granite boulder	29.9 ± 3.6	33.5 ± 2.0	11	
MON-D-IV-I	47.6883 / 97.2496	2150	Granite boulder	19.6 ± 2.4	21.6 ± 1.3	9	
MON-D-IV-II	47.6881 / 97.2505	2150	Granite boulder	17.0 ± 1.5	18.7 ± 1.1	9	
MON-D-IV-III	47.6881 / 97.2505	2151	Granite boulder	13.8 ± 1.7	15.0 ± 0.9	8	

Table 2.6 (continued)

Sample identification	Latitude / Longitude (decimal degrees)	Elevation (m asl)	Sample description	Published ages (ka ± 2σ)	Recalculated ages (ka ± 2σ)	Increase in the published ages (%)	References
Left lateral moraines of the southern outlet glacier, Otgontenger, Hangai mountains							Rother *et al.* 2014
MON-F-I-I	47.6699 / 97.2618	2243	Granite boulder	23.9 ± 2.9	26.8 ± 1.7	11	
MON-F-I-II	47.6698 / 97.2618	2272	Granite boulder	25.3 ± 3.1	28.5 ± 1.7	11	
MON-F-I-IV	47.6734 / 97.2723	2300	Granite boulder	20.9 ± 2.5	23.4 ± 1.4	11	
Right lateral moraines of the southern outlet glacier, Otgontenger, Hangai mountains							
MON-E-III-I	47.7147 / 97.2808	2269	Bedrock	17.3 ± 2.1	19.2 ± 1.2	10	
MON-E-III-II	47.7153 / 97.2815	2274	Granite boulder	17.1 ± 2.1	18.9 ± 1.2	10	
MON-E-III-III	47.7164 / 97.2824	2277	Granite boulder	16.8 ± 2.0	18.6 ± 1.1	10	
Terminal moraines of the southern outlet glacier, Otgontenger, Hangai mountains							Rother *et al.* 2014
MON-D-I-I	47.6835 / 97.2098	2140	Granite boulder	39.8 ± 4.8	45.1 ± 2.7	12	
MON-D-I-II	47.6837 / 97.2099	2133	Granite boulder	20.3 ± 2.5	22.4 ± 1.4	9	
MON-D-I-III	47.6836 / 97.2098	2137	Granite boulder	37.1 ± 4.5	41.9 ± 2.6	12	
Terminal moraines pushed up the side valley from the northern outlet glacier, Otgontenger, Hangai mountains							Rother *et al.* 2014
MON-E-I-I	47.8498 / 97.3333	2568	Granite boulder	36.9 ± 4.5	42.9 ± 2.6	14	
MON-E-I-II	47.8598 / 97.3334	2563	Granite boulder	50.7 ± 6.2	59.5 ± 3.6	15	
MON-E-I-III	47.8597 / 97.3336	2560	Granite boulder	27.7 ± 3.6	31.9 ± 2.4	13	
MON-E-II-I	47.8595 / 97.3159	2580	Granite boulder	54.2 ± 6.6	63.5 ± 4.0	15	
MON-E-II-II	47.8587 / 97.3199	2596	Granite boulder	20.8 ± 2.5	23.6 ± 1.5	12	
MON-E-II-III	47.8584 / 97.3217	2600	Granite boulder	34.5 ± 4.2	40.1 ± 2.5	14	

The ^{10}Be ages were recalculated using CRONUS-Earth version 2.2 (Balco *et al.* 2008) with the calibrated ^{10}Be production rate of 3.99 ± 0.22 atoms g^{-1} yr^{-1} (Heyman 2014) when referenced to the scaling of Stone (2000). Gillespie *et al.* (2008) used CRONUS-Earth version 1.2 with a production rate of 5.2 atoms g^{-1} yr^{-1} and adopted the scaling of Lal (1991) corrected for paleomagnetic variation, which is called Lm scheme of Lal (1991)/Stone (2000). Arzhannikov *et al.* (2012) reported using the production rate of 4.49 ± 0.29 atoms g^{-1} yr^{-1}; Rother *et al.* (2014) used 4.43 ± 0.52 atoms g^{-1} yr^{-1} referenced to Dunai scaling (Dunai 2001). For consistency we accepted only the ages with the scaling of Stone (2000) without paleomagnetic correction because the uncertainty of the ages from the other scaling schemes did not exceed the margin of analytical error (see supplementary for calculations with alternative scaling schemes). We used 2.7 g cm^{-3} for sample density (same value used in Gillespie *et al.* 2008), instead of 2.5 g cm^{-3} in Arzhannikov *et al.* (2012) and 2.6 g cm^{-3} in Rother *et al.* (2014). Using 2.6 g cm^{-3} would make less than 0.3% difference in the apparent age for samples <10 cm thick. No burial history and erosion was assumed in the recalculation of the ^{10}Be ages.

South of the Maly Yenisei and on the western side of Darhad basin, the Ulaan Taiga ice cap fed glaciers in the Högiin valley. Three samples from an older left-lateral moraine significantly predated MIS 2, ranging from ~112 to 247 ka. A younger glacier terminated on a paleolake shore at ~1670 m asl; it yielded three ages of 17, 29 and 45 ka.

Mountains around Hövsgöl basin, another extensional basin in the Baikal rift east of Darhad, also hosted Pleistocene glaciers. An outlet glacier from the East Sayan ice field advanced to Hövsgöl basin through the Bayan Zürhiin ranges along the Ih Horoo river valley, where Wegmann *et al.* (2011) dated granite boulders from two end moraines. Two of six ^{10}Be samples from the lower piedmont moraine postdated MIS 2 at ~9 and 12 ka and one predated MIS 2 at ~32 ka. The remaining three clustered from 20 to 25 ka. Five km upvalley Wegmann *et al.* (2011) dated six boulders from the other end moraine. Two of the ^{10}Be ages were 28 and 23 ka; The remaining four were from 14 to 16 ka. These ages were calculated using the out-of-date "default" ^{10}Be production rate of the CRONUS calculator, and in their abstract Wegmann *et al.* (2011) did not provide the analytical data necessary to recalculate new ages using the revised rate. Recalculation with the new production rate of Heyman (2014) increased the published ages of Gillespie *et al.* (2008) in Darhad basin by no more than 15%. Recalculation of the ages of Wegmann *et al.* (2011) should lead to a similar increase, but it is not enough to change their interpretation here.

North of Darhad basin, Arzhannikov *et al.* (2012) dated sequences of moraines left by outlet glaciers advancing to the northeast from the East Sayan ice field (Figure 2.4). At the Jombolok river valley a total of five ^{10}Be samples from the two sets of terminal moraines yielded an average MIS 2 age of ~24 ka, excluding an additional older sample at ~45 ka. They also dated four boulders from moraines of the neighboring Sentsa river valley, ~8 km southwest of the

Jombolok moraines. These had an average age of ~18 ka. Arzhannikov *et al.* (2012) also dated three boulders from the terminal moraines of the Sailag river valley, also neighboring the Jombolok valley. Two of the three ^{10}Be ages averaged ~18 ka; the third was significantly older at ~74 ka and may have been reworked from an older exposure. Arzhannikov *et al.* (2012) interpreted their findings to show that the local LGM advances in the East Sayan occurred during MIS 2. This is consistent with the timing of the Jarai moraines in Darhad basin, as documented by Gillespie *et al.* (2008).

About 320 km southwest of Darhad basin, the Hangai mountains (Figure 2.2), were also extensively glaciated during the Pleistocene, with multiple ice fields. One was centered north of Otgontenger peak, which is still capped by a firn field today. Rother *et al.* (2014) dated six samples from end moraines at ~2590 m asl to ~38 ka (MIS 3) where an outlet glacier pushed up a side valley. A younger terminal moraine, at a lower elevation of ~2500 m asl, did not reach as far (~1.5 km) up the side valley as the MIS 3 moraines. Rother *et al.* (2014) regarded it as MIS 2 based on its minimal erosion. In the nearby valley of a different outlet glacier, three boulders from the lateral moraines were dated to ~26 ka. In the valley floor, five of six boulders from recessional moraines were dated to ~18 ka and the sixth, probably anomalous, to ~34 ka.

2.3.3 *Equilibrium line altitudes*

In this review, the main use of dating is to establish the timing of the glacier dams that impounded the paleolake sources of the giant outburst floods down the Maly Yenisei. The available dating provides an imperfect chronology, because despite the effort invested the area is large and because natural geologic disturbances such as reworking, cryoturbation and exhumation of dated boulders have led to variability of measured CRE ages, even from boulder to boulder on the same moraine.

In establishing a regional chronology, it is necessary to know which moraines belong to the same advance, so that the ages can be grouped. If the regional ELA depression is similar for the different advances, that is an aide in the correlation.

Together, the studies cited above give a preliminary glacial chronology, but it is necessary to ask what degree of spatial coherence may be expected for glacial advances and retreats over the region, such as would be necessary if the chronology were used to determine the ages of impounded paleolakes in Darhad basin. This is because the temporal patterns of glacier expansion/retreat and ELA depression in Central Asia have been shown to differ from place to place (Gillespie and Molnar 1995). For example, Koppes *et al*. (2008) reported that the global LGM glaciers in Kyrgyz Tian Shan were limited to the cirques when mountain glaciers in Europe and North America advanced to their maximum extents. A similar pattern was observed in northeastern Tibet where the last maximum glacial advances occurred during MIS 3 (Heyman *et al.* 2011). Modeling experiments by Rupper *et al*. (2009) suggested that the ELA differences in Central Asia are largely due to spatially and temporally variable snowfall amounts in the arid, cold setting, although in warmer areas melting may be the limiting factor.

If the ELAs as well as the ages show a consistency across the region including Darhad basin, it increases confidence in the application of the grouped chronology to estimate the extent of the Tengis glaciers and the timing of the dams, not yet dated directly. To do this, it is necessary to determine local values for the empirical coefficients in the ELA calculations.

Gillespie *et al.* (2008) calculated by comparison to the maximum elevation of well-preserved lateral moraines a local toe-to-headwall altitude ratio (THAR) of 0.58 for the Hoit Aguy massif to estimate the ELA of the glaciers of Darhad basin. Although the MIS 3 glaciers were

larger than the MIS 2 glaciers around Darhad basin, their corresponding ELAs were no more than ~75 m lower than for the MIS 2 glaciers (ELA ~2300 m asl). Gillespie *et al.* (2008) interpreted these ages and ELAs around Darhad basin to indicate that the Tengis glaciers during both MIS 2 and MIS 3 were large enough to dam Darhad basin; however, Krivonogov *et al.* (2012) regarded this conclusion regarding MIS 2 as an open question.

For the Ih Horoo advances, we estimated the ELAs to be ~2320 and ~2300 m asl, consistent with the ELAs in Darhad basin. We calculated the ELAs for Jombolok and Sailag glaciers at 2030 –2230 m asl, also consistent with the Darhad values. The highest lateral moraines detectable from Google Earth are at ~2760 m asl for the dated Hangai paleoglaciers, consistent with their more southerly latitudes. However, the highest MIS 2 lateral moraines are found ~90 m below the highest MIS 3 moraines, and the relative differences are about the same as in Darhad basin. Thus, direct dating of glacial deposits in the East Sayan and central Mongolia shows that in both areas the local LGM occurred during the MIS 3, but the MIS 2 glaciers were similar in extent. Furthermore, the ELAs of the same age appear to change over this entire region only with latitude, such that the composite chronology is likely applicable to the Tengis glaciers.

2.4 Discussion in Part I

Giant current ripples in the Kyzyl basin, high flood terraces in Tuva, and the evidence of deep lakes in Darhad basin are all evidence of cataclysmic floods down the Maly Yenisei river. The largest of the floods on Earth as measured by estimated peak discharge, the Missoula floods of the Washington State, USA and the floods from the Kurya-Chuya basin in the Russian Altai, were both initiated after the breaching of glacier dams at the end of the global LGM (e.g., Bretz 1969; Reuther *et al.* 2006). The size of the Darhad floods also implies a deep dam that was suddenly

breached, and glacial ice is the most likely candidate, especially considering the apparent absence of landslide headwall scarps of sufficient size to block the Maly Yenisei to the necessary depth. However, the existence of a higher glacier dam does not preclude lower outwash or alluvium dams created during glacier retreat, and such appear to have existed at the mouth of the Tengis river.

Komatsu *et al*. (2009) used numerical modeling to simulate a flood from paleolake Darhad assuming a surface level at 1710 m asl, which equates to a 172 m deep lake with the volume of ~373 km^3. This is not the deepest paleolake in Darhad basin (~1825 m asl), but it is the best documented, and the most likely to correspond to preserved landforms downstream. The dam was assumed to have been glacial ice that failed instantaneously. In the modeled hydrograph, the discharge peaked at ~3.5×10^6 m^3 s^{-1} within 10 minutes of the initial breach. Water depth remained high (50–100 m) in the gorges north of Ulaan Taiga long after the initial surge (Figure 2.11). The floodwaters would have traveled more than 100 km in 20 hours and past the Kyzyl basin within 80 hours.

The Darhad paleolake with a surface level at 1710 m asl requires impounding by glacier ice, likely the Tengis glacier. The age of this paleolake was MIS 3 given the fossil evidence and dating from the Shargyn river cutbank. It may have refilled to the roughly same level during MIS 2, but this cannot be confirmed definitely by the available ages. Grosswald (1987) used the evaporation rate of the Volga river basin and modern annual precipitation in Darhad basin to estimate that the basin could be refilled within 100–130 years to 1720 m asl. Krivonogov *et al.* (2005) roughly estimated that it would take 285 years to fill Darhad basin to a level of 1700 m asl, at a rate of ~0.35 m $year^{-1}$ adjusted from the modern value for the runoff in Hövsgöl basin. From the shorelines on the dated Jarai moraines, it does appear that a deep MIS 2 paleolake did occupy Darhad basin at least to 1679 m asl.

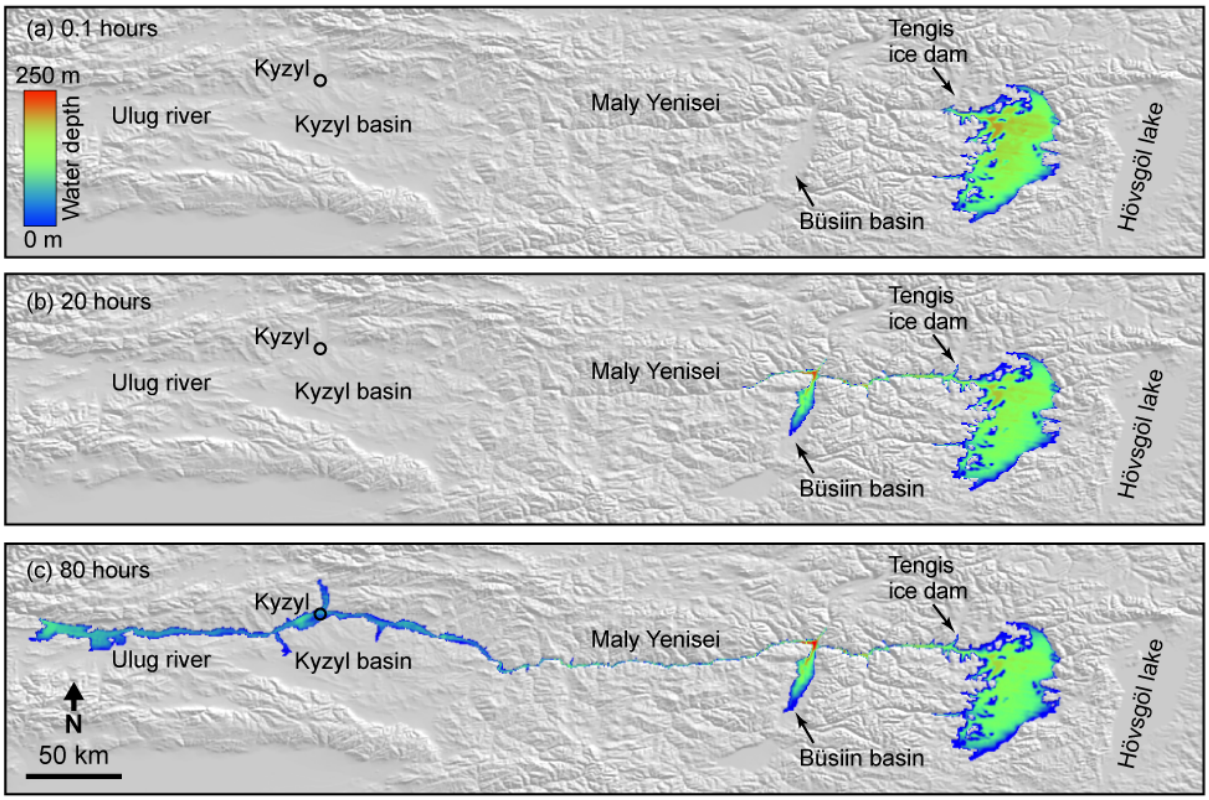

Figure 2.11. Inundation map of a flood from the Darhad paleolake with surface level at 1710 m asl, adapted from Komatsu *et al.* (2009). The background is the shaded-relief image from the SRTM DEM. Due to limited computing power they used low-resolution DEM from the US Geological Survey (927 × 598 m grids) in which the elevation of the Büsiin basin was underestimated. The DEM also had other artifacts, such as striping in Darhad basin, and their numerical model may have overestimated the water depth at some locations (G. Komatsu, pers. comm., 2015).

The dated boulders on the wind gaps east of the Tengis river suggest the MIS 2 glacier approached the Maly Yenisei within 2 km. The dating of the flood-eroded end moraines in the Sarig valley should determine if the Tengis glacier actually crossed the Maly Yenisei during MIS 2, but will not indicate the depth of the paleolake. Beach sands exist at high elevations in Darhad basin, for example at ~1670 m asl near Arsain river, and direct dating of these deposits should constrain the timing of the deeper lake.

Direct dating of lake sediments in Darhad basin is, so far, restricted to outcrops within the basin and short cores extracted from the modern lake floors. The controversy identified by Krivonogov *et al.* (2012) regarding the existence of a deep MIS 2 lake was raised mostly because no lake sediments from the time period were found in the incomplete sections from the cutbanks. More complete records of lake sediments are buried under the basin floor, and only deep drilling in the basin will likely retrieve the MIS 2 and older lake sediments.

There may have been smaller floods along the Maly Yenisei river from other sources than Darhad basin. For example, retreating glaciers may have sent outburst floods through the narrow gorges of the Kaa river and to the Maly Yenisei. The glaciers from the Ulaan Taiga ice cap may have provided small outburst floods from ice-marginal lakes in the mountain highlands that drained through the Büsiin basin.

Smaller floods from Darhad itself were also possible even when a glacial dam was present. Partial draining of the paleolakes through the Tengis glacier dam may have occurred via subglacial tunneling, floatation, partial collapse of the glacier front, or overtopping, especially when the glacier dam was low during advance or retreat. High amounts of debris in the Tengis glacier (Gillespie *et al.* 2008) would also suppress the ice floatation and possibly allow overtopping and downward erosion at a lower pace than sudden disruption of the dam via tunneling.

To our best knowledge, direct dating of flood deposits along the Maly Yenisei has not been conducted. Luminescence or radiocarbon dating of giant current ripples in the Kyzyl basin, and the sediments capping the basalt terraces near Darhad basin should help determine the timing and the corresponding floodwater level. Any smaller floods must also have left the flood deposits along the Maly Yenisei, and careful dating of these flood deposits would be useful for validating future

hydraulic modeling of the Maly Yenisei floods. Higher-resolution DEM's (e.g., from NASA's stereo ASTER sensor: Tachikawa *et al.* 2011) are available now, compared to those used by Komatsu et al. (2009).

2.5 SUMMARY

The banks of the Maly Yenisei preserve sediments transported by many floods with various origins. The largest of them were from outburst floods that originated from Darhad basin. The timing of the highstands of the Darhad paleolakes is derived from either the dating of beach sands having measured elevations, from dating of moraines upon which shorelines have been eroded, or from dating of glacial deposits near the spillway for which ice thicknesses have been estimated. The shoreline elevations and available ages are summarized in Figure 2.12.

The outlet glaciers from the East Sayan ice field blocked Darhad basin at least twice during the late Pleistocene (19–22 ka, MIS 2, and ~35–53 ka, MIS 3). Direct dating of moraines suggests that Darhad basin hosted a 180-m deep lake during the local LGM, which was likely during MIS 3. Shoreline features and glacial deposits found in Darhad basin at even higher elevation of 1825 m asl suggest greater floods may have occurred. This event may have happened during MIS 6, but no detailed study confirms this possibility.

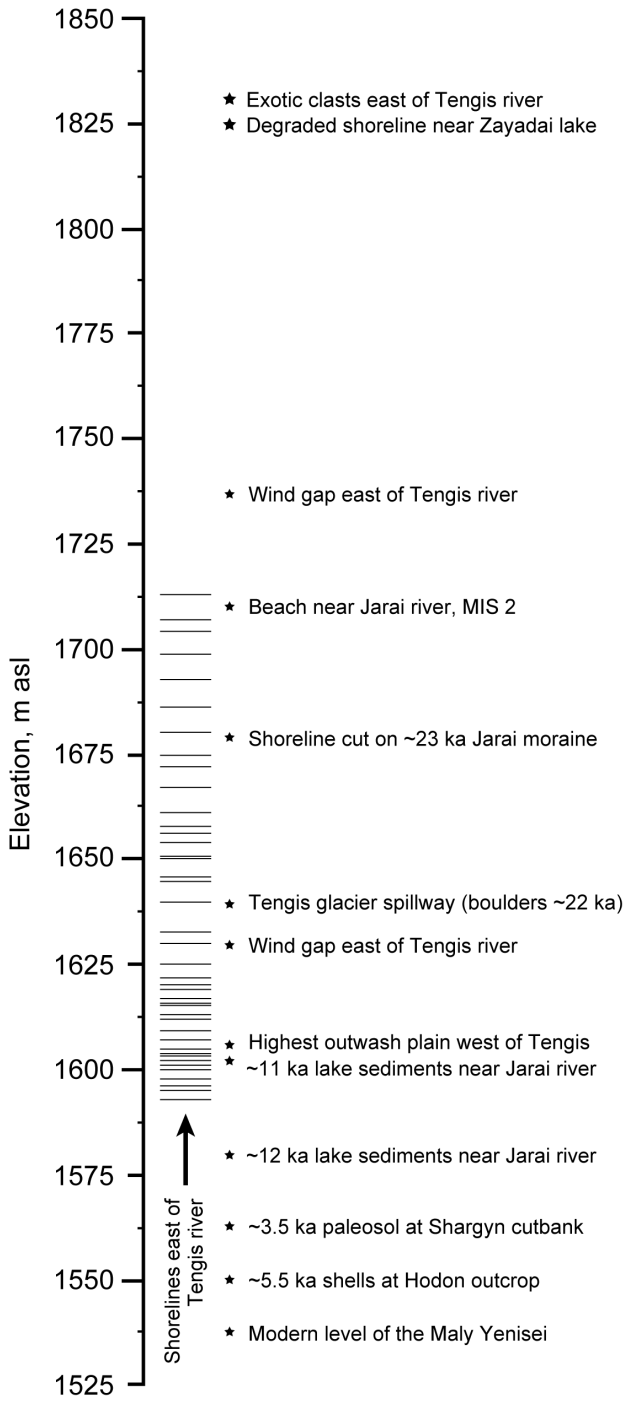

Figure 2.12. Shorelines and highstands of Darhad paleolakes. Elevation of shorelines east of the Tengis river was measured by Krivonogov *et al.* (2005). The shells at Hodon outcrop was analyzed by Krivonogov *et al.* (2012). The ages from Jarai, Tengis, and Shargyn rivers are from Gillespie *et al.* (2008).

Despite the widespread evidence of cataclysmic floods along the Maly Yenisei and recent advancements in the CRE and luminescence dating methods, there have been little or no detailed studies of the flood sediments and their ages over the broad geographic region affected by the floods. Such future studies might allow us to improve our understanding of the temporal relationships between paleolakes, dams, and flood deposits in the Maly Yenisei.

Acknowledgments

Support for this review was from the Quaternary Research Center, Department of Earth and Space Sciences at the University of Washington.

2.6 REFERENCES IN CHAPTER 2: PART I

Allen, J.R.L., (1968), Current ripples: their relation to patterns of water and sediment motion: North-Holland Pub. Co., 433 p.

Arzhannikov, S.G., Alexeev, S.V., Glyzin, A.V., Razmakhnina, T.B., Orlova, L.A., (2000), Prirodnaya obstanovka v golotsene zapadnoi chasti Todzhinskoi vpadiny (na primere razreza Merzly Yar) (Natural conditions in the western part of the Todzhinsky basin in the Holocene (by the example of "Merzly Yar" section)): The Problems of Climatic and Environmental Reconstruction in the Holocene and Pleistocene, Novosibirsk, p. 18–29 (in Russian).

Arzhannikov, S.G., Braucher, R., Jolivet, M., Arzhannikova, A.V., Vassallo, R., Chauvet, A., Bourlès, D., Chauvet, F., (2012), History of late Pleistocene glaciations in the central Sayan-Tuva Upland (southern Siberia): Quaternary Science Reviews, v. 49, p. 16-32.

Baker, V.R., (1973), Paleohydrology and sedimentology of Lake Missoula flooding in Eastern Washington: Geological Society of America Special Paper, v. 144, p. 1–79.

Baker, V.R., (1982), The channels of Mars: University of Texas Press, Austin, Texas, 198 p.

Baker, V.R., and Milton, D.J., (1974), Erosion by catastrophic floods on Mars and Earth: Icarus, v. 23, p. 27–41.

Baker, V.R., Benito, G., Rudoy, A.N., (1993), Paleohydrology of late Pleistocene superflooding, Altai Mountains, Siberia: Science, v. 259, p. 348–350.

Balco, G., Stone, J.O., Lifton, N.A., Dunai, T.J., (2008), A complete and easily accessible means of calculating surface exposure ages or erosion rates from Be-10 and Al- 26 measurements: Quaternary Geochronology, v. 3, p. 174–195.

Balco, G., Briner, J., Finkel, R.C., Rayburn, J.A., Ridge, J.C., Schaefer, J.M., (2009), Regional beryllium-10 production rate calibration for northeastern North America: Quaternary Geochronology, v. 4, p. 93-107.

Batbaatar, J., Gillespie, A.R., Fedotov, A., Bayasgalan, A., (2008), The 92-m sediment core from paleolake Darhad, Mongolia: Proceedings, 7th International Symposium "Environmental Changes in East Eurasia and Adjacent Areas – High Resolution Environmental Records of Terrestrial Sediments", Ulaanbaatar–Hatgal, Mongolia, August 23-29, p. 66–74.

Batbaatar, J., Feathers, J.K., Gillespie, A.R., (2009), IRSL feldspar dates for paleolake sediments from Darhad Basin, Mongolia: Geological Society of America, Abstracts with Programs, v. 41, no. 7, p. 382.

Batbaatar, J., Gillespie, A.R., Schreiber, B C., (2012), Tectonics and environment at the western end of the Baikal rift: Paleolake sediment record from Darhad Basin, northern Mongolia: Geological Society of America Abstracts with Programs, v. 44, no. 3, p. 56.

Benito, G., and O'Connor, J.E., (2003), Number and size of last-glacial Missoula floods in the Columbia River valley between the Pasco Basin, Washington, and Portland, Oregon: Geological Society of America Bulletin, v. 115, no. 5, p. 624–638.

Bretz, J H., (1923), The Channeled Scablands of the Columbia Plateau: Journal of Geology, v. 31, p. 617–649.

Bretz, J H., (1969), The Lake Missoula floods and the Channeled Scabland: The Journal of Geology, v. 77, no. 5, p. 505–543.

Carling, P.A., Kirkbride, A.D., Parnachov, S., Borodavko, P.S., Berger, G.W., (2002), Late Quaternary catastrophic flooding in the Altai Mountains of south-central Siberia: a synoptic overview and introduction to flood deposit sedimentology, *in* Martini, I.P., Baker, and V.R., Garzon, G., eds., Flood and Megaflood Processes and Deposits: Recent and Ancient Examples: International Association of Sedimentologists Special Publication, v. 32, Blackwell Science, London, p. 17–35.

Carson, R.J., Gillespie, A.R., Bayasgalan, A., (2003), Late Quaternary geology along the Högiin Gol, northern Mongolia: Proceedings of the Oregon Academy of Science, v. 39, p. 20–21.

Channell, J.E.T., Xuan, C., Hodell, D.A., (2009), Stacking paleointensity and oxygen isotope data for the last 1.5 Myr (PISO-1500): Earth and Planetary Sciences Letters, v. 283, p. 14–23.

Clarke, G.K.C., Mathews, W.H., Pack, R.T., (1984), Outburst floods from glacial Lake Missoula: Quaternary Research, v. 22, p. 289–299.

Craig, R.G., (1987), Dynamics of a Missoula flood, *in* Mayer, L., and Nash, D., eds., Catastrophic flooding, Winchester, Allen and Unwin, p. 305–332.

Dorofeyuk, N.I., and Tarasov, P.E., (1998), Vegetation and levels of the lakes in the north of Mongolia during the last 12500 years, by the data of palynologic and diatom analyses: Stratigraphy and Geological Correlation, v. 6, p. 73–87.

Dunai, T., (2001), Influence of secular variation of the geomagnetic field on production rates of in situ produced cosmogenic nuclides: Earth and Planetary Science Letters, v. 193, p. 197–212.

Farr, T.G., Rosen, P.A., Caro, E., Crippen, R., Duren, R., Hensley, S., Kobrick, M., Paller, M., Rodriguez, E., Roth, L., Seal, D., Shaffer, S., Shimada, J., Umland, J., Werner, M., Oskin, M., Burbank, D., Alsdorf, D., (2007), The Shuttle Radar Topography Mission: Reviews of Geophysics, v. 45, RG2004, p. 1–33.

Fisher, T. G., (2003), Chronology of glacial Lake Agassiz meltwater routed to the Gulf of Mexico: Quaternary Research, v. 59 no. 2, p. 271–76.

Gillespie, A.R., and Molnar, P., (1995), Asynchronism of maximum advances of mountain and continental glaciations: Reviews of Geophysics v. 33, p. 311–364.

Gillespie, A.R., Bayasgalan, A., Kuharic, M.V., (2005), Sediment core from ice-dammed paleolake Darhad, Mongolia: Geological Society of America Abstracts with Programs, v. 37, no. 7, p. 543.

Gillespie, A.R., Burke, R.M., Komatsu, G., Bayasgalan, A., (2008), Late Pleistocene glaciers in Darhad Basin, northern Mongolia: Quaternary Research v. 69, p. 169–187.

Gravis, G.F., (1974), Geocryological conditions of Mongolian People's Republic, *in* Melnikov, P.I., ed., Transactions of the Joint Soviet-Mongolian Scientific-Research Geological Expedition, v. 10, Nauka, Moscow, p. 117–132 (in Russian)

Grosswald, M.G., (1965), Razvitie relyefa Sayano-Tuvinskogo nagorya (Geomorphological development of the Sayan-Tuva upland): Nauka, Moscow, 166 p. (in Russian).

Grosswald, M.G., (1987), Poslednee oledenenie Sayano-Tuvinskogo nagorya: morfologiya, intensivnost pitaniya, podprudnye ozera (The last glaciation of the Sayany-Tuva highland: morphology and the rate of filling of ice-dammed lakes), *in* Kotikov, V.M., and Grosswald, M.G., eds., Interaction of Glaciations with the Atmosphere and Ocean, Nauka, Moscow, p. 152–170 (in Russian).

Grosswald, M.G., (1999), Evraziiskie gidrosfernye katastrofy i oledenenie Arktiki (Cataclysmic Megafloods in Eurasia and the Polar Ice Sheets): Nauchny Mir, Moscow, 117 p. (in Russian).

Grosswald, M.G., and Rudoy, A.N., (1996a), Chetvertichnye lednikovo-podprudnye ozera v gorakh Sibiri (Quaternary ice-dammed lakes in the South Siberia mountains): Izvestiya Akademii Nauk SSSR, Seriya geograficheskaya, v. 6, p. 112–126 (in Russian).

Grosswald, M.G., and Rudoy, A.N., (1996b), Quaternary glacier-dammed lakes in the mountains of Siberia: Polar Geography, v. 20, p. 180–198.

Herget, J., (2005), Reconstruction of Pleistocene Ice-dammed Lake Outburst floods in the Altai Mountains, Siberia: Geological Society of America Special Paper, v. 386, 118 p.

Herget, J., (2012), Ice-dammed lake outburst floods in the Altai Mountains, Siberia – A review with links for further readings: Tomsk State University Journal of Biology, v. 1 no. 17, p. 148–168.

Heyman, J., (2014), Paleoglaciation of the Tibetan Plateau and surrounding mountains based on exposure ages and ELA depression estimates: Quaternary Science Reviews, v. 91, p. 30–41.

Heyman, J., Stroeven A.P., Caffee, M.W., Hättestrand, C., Harbor, J.M., Li, Y., Alexanderson, H., Zhou, L., Hubbard, A., (2011), Palaeoglaciology of Bayan Har Shan, NE Tibetan Plateau: exposure ages reveal a missing LGM expansion: Quaternary Science Reviews, v. 30, p. 1988–2001.

Jóhannesson, T., (2002), The initiation of the 1996 jökulhlaup from Lake Grímsvötn, Vatnajökull, Iceland, *in* Snorrason, Á., Finnsdóttir, H.P., and Moss, M., eds., The extremes of the extremes—Extraordinary floods: Wallingford, Oxfordshire, England, IAHS Press, International Association of Hydrological Sciences Publication No. 271, p. 57–64.

Komatsu, G., Clute, S.K., Baker, V.R., (1997), Preliminary remote sensing assessment of Pleistocene cataclysmic floods in Central Asia, *in* Proceedings, Lunar and Planetary Science Conference, 28th, p. 747–748.

Komatsu, G., Arzhannikov, S.G., Arzhannikova, A.V., Ori, G.G., (2007), Origin of glacial-fluvial landforms in the Azas Plateau volcanic field, the Tuva Republic, Russia: Role of ice-magma interaction: Geomorphology, v. 88, p. 352–366.

Komatsu, G., Arzhannikov, S.G., Gillespie, A.R., Burke, R.M., Miyamoto, H., Baker, V.R., (2009), Quaternary paleolake formation and cataclysmic flooding along the upper Yenisei River: Geomorphology, v. 104, p. 143–164.

Komatsu, G., Baker, V.R., Arzhannikov, S.G., Gallagher, R., Arzhannikova, A.V., Murana, A., Oguchi, T., (2016), Late Quaternary catastrophic flooding related to paleodrainage reorganization and paleolake formation in northern Eurasia: A history of alternative hypotheses and indications for future research: International Geology Review, v. (in press).

Koppes, M., Gillespie, A.R., Burke, R.M., Thompson, S.C., Stone, J., (2008), Late Quaternary glaciation in the Kyrgyz Tien Shan: Quaternary Science Reviews, v. 27, p. 846–866.

Krivonogov, S.K., Sheinkman, V.S., Mistryukov, A.A., 2005, Ice damming of the Darhad paleolake (northern Mongolia) during the Late Pleistocene: Quaternary International, v. 136, p. 83–94.

Krivonogov, S.K., Kazansky, A.Y., Oyunchimeg, Ts., Narantsetseg, Ts., Tomurhuu, D., Dolgorsuren, Kh., (2008), New in studies of the Darhad basin, Mongolia: Proceedings, 7th International Symposium "Environmental Changes in East Eurasia and Adjacent Areas – High Resolution Environmental Records of Terrestrial Sediments", Ulaanbaatar–Hatgal, Mongolia, August 23-29, p. 66–74.

Krivonogov, S.K., Yi, S., Kashiwaya, K., Kim, J.C., Narantsetseg, T., Oyunchimeg, T., Safonova, I.Y., Kazansky, A.Y., Sitnikova, T., Kim, J.Y., Hasebe, N., (2012), Solved and unsolved problems of sedimentation, glaciation and paleolakes of the Darhad Basin, Northern Mongolia: Quaternary Science Reviews, v. 56, p. 142–163.

Lal, D., (1991), Cosmic ray labeling of erosion surfaces: in situ nuclide production rates and erosion models: Earth and Planetary Science Letters, v. 104, p. 424–439.

Litasov, Yu., Hasenaka, T., Litasov, K., Yarmolyuk, V., Sugorakova, A., Lebedev, V., Sasaki, M., Taniguchi, H., (2001a), Petrologic characteristics of Cenozoic alkaline basalts from the Azas Plateau, northeast Tuva (Russia): Northeast Asian Studies 6, Center for Northeast Asian studies, Tohoku University, p. 201–226.

Litasov, K., Ito, Y., Litasov, Yu., Kitakaze, A., Taniguchi, H., (2001b), Lithosphere structure and thermal regime of the upper mantle along Baikal rift axis: Evidences from deep-seated xenoliths: Northeast Asian Studies, v. 6, p. 227–252.

Lyell, C., (1830–3), Principles of Geology, being an attempt to explain the former changes of the Earth's surface, by reference to causes now in operation, vols. 1–3: John Murray, London.

Malde, H.E., (1968), The catastrophic late Pleistocene Bonneville flood in the Snake River Plain, Idaho, *in* U.S. Geological Survey Professional Paper, v. 596: United States Government Printing Office, Washington, 52 p.

Mangerud, J., Jakobsson, M., Alexanderson, H., Astakhov, V., Clarke, G., Henriksen, M., Hjort, C., Krinner, G., Lunkka, J.P., Möller, P., Murray, A., Nikolskaya, O., Saarnisto, M., Svendsen, J.I., (2004), Ice-dammed lakes and rerouting of the drainage of Northern Eurasia during the last glaciation: Quaternary Science Reviews, v. 23, p. 1313–1332.

Margold, M., Jansson, K. N., Stroeven, A. P., Jansen, J.D., (2011), Glacial Lake Vitim, a 3000-km^3 outburst flood from Siberia to the Arctic Ocean: Quaternary Research, v. 76, p. 393–396.

Merle, J.R., (2001), Quaternary geology of the Tengis-Shishid Gol region, Khovsgol, Mongolia [Senior thesis]: Whitman College, 56 p.

Montgomery, D. R., (2013), The Rocks Don't Lie: A Geologist Investigates Noah's Flood: W. W. Norton & Company, 320 p.

Montgomery, D. R., Hallet, B., Yuping, L., Finnegan, N., Anders, A., Gillespie, A., Greenberg, H. M., (2004), Evidence for Holocene megafloods down the Tsangpo River gorge, southeastern Tibet: Quaternary Research, v. 62, p. 201-207.

Narantsetseg, Ts., Krivonogov, S.K., Oyunchimeg, Ts., Uugantsetseg, B., Burr, G.S., Tomurhuu, D., Dolgorsuren, Kh., (2013), Late Glacial to Middle Holocene climate and environmental changes as recorded in Lake Dood sediments, Darhad Basin, northern Mongolia: Quaternary International, v. 311, p. 12–24.

Normark, W.R., and Reid, J.A., (2003), Extensive deposits on the Pacific Plate from Late Pleistocene North American glacial lake outbursts: The Journal of Geology, v. 111, p. 617–637.

O'Connor, J.E., and Baker, V.R., (1992), Magnitudes and implications of peak discharges from Glacial Lake Missoula: Geological Society of America Bulletin, v. 104, p. 267–279.

O'Connor, J.E., and Costa, J.E., (2004), The world's largest floods: Their causes and magnitudes: U.S. Geological Survey Circular 1254, 13 p.

Olyunin, V.N., (1965), Neotectonics and Glaciation of East Sayan: Nauka, Moscow, 128 p. (in Russian).

Pardee, J.T., (1942), Unusual currents in Lake Missoula, Montana: Geological Society of America Bulletin, v. 53, p. 1569-1599.

Peck, J.A., Khosbayar, P., King, J., Fowell, S.J., Aurienbyleg, K., Soninkhishig, N., (2001), The Latest Holocene sedimentary environmental magnetic record from Lake Dood, Mongolia: EOS, v. 82, F337.

Putnam, A.E., Denton, G.H., Schaefer, J.M., Barrell, D.J.A., Andersen, B.G., Finkel, R.C., Schwartz, R., Doughty, A.M., Kaplan, M.R., Schlüchter, C., (2010), Glacier advance in southern middle-latitudes during the Antarctic Cold Reversal: Nature Geoscience, v. 3, p. 700–704.

Raney, R.K., Luscombe, A.P., Langham, E.J., Ahmed, S., (1991), RADARSAT: Proceedings of the IEEE, v. 79, no. 6, p. 839–849.

Reimer, P.J., Bard, E., Bayliss, A., Beck, J.W., Blackwell, P.G., Ramsey, C.B., Buck, C.E., Cheng, H., Edwards, R.L., Friedrich, M., Grootes, P.M., Guilderson, T.P., Haflidason, H., Hajdas, I., Hatté, C., Heaton, T.J., Hoffmann, D.L., Hogg, A.G., Hughen, K.A., Kaiser, K.F., Kromer, B., Manning, S.W., Niu, M., Reimer, R.W., Richards, D.A., Scott, E.M., Southon, J.R., Staff, R.A., Turney, C.S.M., Plicht, J., (2013), IntCal13 and MARINE13 radiocarbon age calibration curves 0–50,000 years cal BP: Radiocarbon, v. 55, no. 4, p.1869–1887.

Reuther, A.U., Herget, J., Ivy-Ochs, S., Borodavko, P., Kubik, P.W., Heine, K., (2006), Constraining the timing of the most recent cataclysmic flood event from ice-dammed lakes in the Russian Altai Mountains, Siberia, using cosmogenic in situ ^{10}Be: Geology, v. 34, no. 11, p. 913–916.

Rother, H., Lehmkuhl, F., Fink, D., Nottebaum, V., (2014), Surface exposure dating reveals MIS-3 glacial maximum in the Khangai Mountains of Mongolia: Quaternary Research, v. 82, p. 297–308.

Rudoy, A.N., (2002), Glacier-dammed lakes and geological work of glacial superfloods in the Late Pleistocene, Southern Siberia, Altai Mountains: Quaternary International, v. 87, p. 119–140.

Rudoy, A.N., and Baker, V.R., (1993), Sedimentary effects of cataclysmic late Pleistocene glacial outburst flooding, Altai Mountains, Siberia: Sedimentary Geology, v. 85, p. 53–62.

Rupper, S., Roe, G., Gillespie, A., (2009), Spatial patterns of Holocene glacier advance and retreat in Central Asia: Quaternary Research, v. 72, p. 337–346.

Ryan, W. B. F., Pitman III, W. C., Major, C. O., Shimkus, K., Moskalenko, V., Jones, G. A., Dimitrov, P., Goriir, N., Saking, M., Yiice, H., (1997), An abrupt drowning of the Black Sea shelf: Marine Geology, v. 138, p. 119–126.

Selivanov, E.I., (1967), Neogene-Quaternary giant lakes in Transbaikalia and North Mongolia: Reports of the Academy of Sciences of the USSR, v. 177, p. 175–178 (in Russian).

Shang, Y., Yang, Z., Li, L., Liu, D., Liao, Q., Wang, Y., (2003), A super-large landslide in Tibet in 2000: background, occurrence, disaster, and origin: Geomorphology, v. 54, no. 3–4, p. 225-243.

Sharkhuu, A., Sharkhuu, N., Etzelmüller, B., Heggem, E.S.F., Nelson, F.E., Shiklomanov, N.I., Goulden, C.E., Brown, J., (2007), Permafrost monitoring in the Hovsgol mountain region, Mongolia: Journal of Geophysical Research, v. 112, F02S06, doi:10.1029/2006JF000543.

Stone, J., (2000), Air pressure and cosmogenic isotope production: Journal of Geophysical Research, v. 105, no. 23, p. 753–23,759.

Stuiver, M., and Reimer, P.J., (1993), Extended ^{14}C database and revised CALIB radiocarbon calibration program: Radiocarbon, v. 35, p. 215–230.

Tachikawa, T., Kaku, M., Iwasaki, A., Gesch, D., Oimoen, M., Zhang, Zh., Danielson, J., Krieger, T., Curtis, B., Haase, J., Abrams, M., Crippen, R., Carabajal, C., (2011), ASTER Global Digital Elevation Model Version 2 – Summary of Validation Results. Online: http://asterweb.jpl.nasa.gov/gdem.asp.

Teller, J.T., Leverington, D.W., Mann, J.D., (2002), Freshwater outbursts to the oceans from glacial Lake Agassiz and their role in climate change during the last deglaciation: Quaternary Science Reviews, v. 21, p. 879–887.

U.S. Geological Survey, (2012), Landsat – A global land-imaging mission: U.S. Geological Survey Fact Sheet 2012, 3072, p. 3.

Ufland, A.K., Iljin, A.V., Spirkin, A.I., Shilova, G.N., (1971), Main features of stratigraphy and formation of Cenozoic deposits in Prekosogol (MPR): Bulletin of the Moscow Society of Naturalists (MOIP). Geology Series, v. 46, p. 54–69 (in Russian).

Waitt, R.B., Jr., (1980), About 40 last-glacial Lake Missoula jökulhlaups through southern Washington: Journal of Geology, v. 88, p. 653–679.

Wegmann, K.W., Amgaa, Ts., Frankel, K.L., Dewett, A.P., Bayasgalan, A., (2011), Geologic, geomorphic, and environmental change at the northern termination of the Lake Hövsgöl rift, Mongolia: Proceedings of the Twenty-Fourth Annual Keck Research Symposium in Geology, Union College, Schenectady, NY, April, 2011, p. 220–229.

Wiedmer, M., Montgomery, D. R., Gillespie, A. R., Greenberg, H., (2010), Late Quaternary megafloods from Glacial Lake Atna, Southcentral Alaska, U.S.A.: Quaternary *Research, v.* 73, p. 413–424. doi: 10.1016/j.yqres.2010.02.005.

Wortmann, M., Krysanova, V., Kundzewicz, Z. W., Su, B., Li, X., (2014), Assessing the influence of the Merzbacher Lake outburst floods on discharge using the hydrological model SWIM in the Aksu headwaters, Kyrgyzstan/NW China: Hydrological Processes, v. 28, p. 6337–6350.

Yamskikh, A.F., and Yamskikh, A.A., (1999), Dynamics of the Todza ice-dammed lake (upper Yenisei River, southern Siberia) during the late Pleistocene and Holocene: Science Reports of Tohoku University, 7th Series (Geography) 49, (Special Issue on GLOCOPH 98), p. 143–159.

Yamskikh, A.F., Yamskikh, G.Y., Vasiliev, S.A., Ermolova, N.M., (2001), Paleoecology of the Maina group of multiplayer Paleolithic sites in the Yenisei River valley (at the boundary between West Sayan Mountains and Minusa Depression): Field Guidebook for the Global Continental Paleohydrology Meeting, Krasnoyarsk-Khakassia Tuva Region, Russia, pp. 146–156.

Yang, D., Ye, B., and Kane, D.L., (2004), Streamflow changes over Siberian Yenisei River Basin: Journal of Hydrology, v. 296, p. 59–80.

Young, N.E., Schaefer, J.M., Briner J.P., Goehring, B.M., (2013), A Be-10 production rate calibration for the Arctic: Journal of Quaternary Science, v. 28, p. 515–526.

OUTBURST FLOODS OF THE MALY YENISEI
PART II – NEW AGE CONSTRAINTS FROM DARHAD BASIN

2.7 ABSTRACT FOR PART II

Some of the largest cataclysmic floods of the Quaternary followed multiple breaches of glaciers damming the headwaters of the Maly Yenisei river in southern Siberia. The shorelines of the impounded lake in Darhad basin suggest at least four depths of 290, 175, 145, and 65 m. Fossil evidence, together with previous ^{14}C and luminescence dating, indicates the existence of a deep lake during MIS 3; the eroded character of the highest shoreline suggests that the deepest lake was older. ^{10}Be dating of moraines in the surrounding mountains has documented major glacial advances during MIS 2, although no published direct dating has confirmed a highstand of the lake then. To address this problem, we extracted lake sediments from a 92.6 m-deep borehole, sampled beach sands from the nearby basin edge, and dated them both using luminescence methods. We also dated, with ^{10}Be, the eroded remnants of the end moraine deposited by the last glacier that dammed Darhad basin, as well as other moraines in the mountains surrounding the basin. These numerical ages confirm that a deep lake existed in Darhad basin at ~20 ka and that a large glacier crossed the Maly Yenisei and dammed Darhad basin at ~21 ka. The deep lake persisted episodically until ~14 ka. The ^{10}Be dating in the surrounding mountains shows that the MIS 2 glaciers subsequently retreated but stalled or readvanced at ~12, 10, and 1.5 ka. ^{10}Be dating from the central massif of Mongolia is consistent with this chronology and confirms that MIS 3 equilibrium-line altitudes were slightly (~75 m) lower or approximately the same as those of the MIS 2. The temporal and spatial patterns of glacial advances in southern Siberia and central Mongolia coincided with those of glacial advances in similar climate conditions of the Altai mountains.

2.8 INTRODUCTION TO PART II

The cataclysmic floods down the Yenisei river in Siberia (Figure 2.2) were among the largest on Earth according to their estimated discharge rates (O'Connor and Costa 2004). The high abandoned terraces and giant gravel dunes in the Kyzyl basin (Figure 2.2; Batbaatar and Gillespie 2016) provide evidence for the large floods of the Yenisei. However, no flood deposits have yet been directly dated. The largest of the floods on the Maly Yenisei came from Darhad basin in northern Mongolia, which during the Pleistocene held lakes up to 290 m-deep and with a volume of up to 809 km^3 (Komatsu *et al.* 2009). At the end of the Pleistocene Epoch, the lakes were impounded by glaciers, especially the Tengis glacier, an outlet glacier from the East Sayan ice field (Figure 2.13) (Merle 2001; Krivonogov *et al.* 2005; Gillespie *et al.* 2008). At its maximum extent, the Tengis glaciers created a series of high ice dams. The outwash gravels from the retreating Tengis glacier subsequently created lower gravel dams at the same location (Krivonogov *et al.* 2005; Batbaatar and Gillespie 2016).

The ages of the heretofore undated dams are controversial. Krivonogov *et al.* (2005) proposed that the Tengis glacier grew large enough to dam Darhad basin during or before Marine Oxygen Isotope Stage (MIS) 3[2]. He based this deduction on (1) two observations from Darhad basin itself, and (2) two telecorrelations. In regard to (1), Gravis and Lisun (1974) reported a high abundance of tree pollen in lake sediments in Darhad basin, which suggested to them a warmer climate of the MIS 3 Karginian Interstade, and Krivonogov *et al.* (2005) reported wood remains in deltaic sediments near Talyn lake, on the floor of the basin, that yielded three ages near the limit of the ^{14}C method, >46090, >46080, and ≥44900 ± 1200 ^{14}C year. In regard to (2), telecorrelations

[2] Lisiecki and Raymo (2005) defined MIS 2 as 29–14 ka, and MIS 3 as 57–29 ka. We used the term "MIS" in this article as stratigraphic nomenclature.

with moraines of the local Last Glacial Maximum (LGM_L: e.g. Gillespie and Molnar 1995) ~130 km NE of Darhad basin (Figure 2.2) that have two thermoluminescence ages of ~70 ka (Shchetnikov 2001), may indicate that the LGM_L in Darhad basin was similarly early, such that the glacial lakes there most likely predate MIS 3. Krivonogov *et al.* (2005) reasoned that because the favorable conditions for a development of Siberian glaciation occurred during the MIS 5d interstade, as inferred from the glacial sediments identified in the Lake Baikal cores (e.g. Prokopenko *et al.* 2001), large MIS 2 glaciers in Darhad were unlikely.

In short, Krivonogov *et al.* (2005) contended that no large lakes existed in Darhad basin after MIS 3, that only the Tengis sediment dams could have impounded lakes during MIS 2, and that those lakes must therefore have been shallow. But Krivonogov *et al.* (2005) offered no direct evidence of the timing of the deepest lakes.

Gillespie *et al.* (2008) dated glacial deposits using cosmic-ray exposure (CRE) (^{10}Be) analysis and dated the lake sediments using radiocarbon and luminescence analysis in and around Darhad basin. They found that the glaciers around the basin advanced to their maxima during MIS 3, and that the MIS 2 glaciers were likely slightly smaller but big enough to impound at least the 145-m-deep lake. These findings appeared to rule out the two telecorrelation arguments of Krivonogov *et al.* (2005), but not those from the observations in Darhad basin. Indeed, Gillespie *et al.* (2008) confirmed with ^{14}C and luminescence dating the conclusions of Gravis and Lisun (1974) that the lake sediments at the Shargyn river cutbank (Figure 2.13) were from MIS 3. Gravis and Lisun (1974) also reported younger lake sediments in this area with high content of moss pollen that they assigned to the cold climate of MIS 2 Sartan Stade. However, Gillespie *et al.* (2008) could not find MIS 2 sediments in the cutbank of the Shargyn river, and they suspected that Shargyn vicinity was prone to erosion during the sudden draining of the paleolakes, and that

possibly any MIS 2 lake sediments were eroded then. Lastly, Krivonogov *et al.* (2005) evidently did not consider the possibility that the ≥45 ka wood from the Talyn delta could have been reworked from older deposits.

The above outlines the current state of the "controversy" concerning the timing of the last deep paleolake. In this article, we present new chronological data for the long drill cores we extracted from the Darhad basin, intended to determine the timing of the most recent Pleistocene lakes there. These data by themselves cannot establish the depth of those lakes, so we also dated associated shoreline deposits with measured elevations. The lake sediments do not directly link the paleolake to the hypothesized but eroded glacier dam. The end moraine left by the Tengis outlet glacier (Figure 2.13) – evidence that the glacier indeed crossed the Maly Yenisei to impound a large lake behind it – has not been definitely dated until now. If ^{10}Be ages for the end moraine show that the latest dams indeed occurred during MIS 2, the existence of the paleolake then and its depth, plus the linkage to the glacier dam, would all be established and the controversy would be resolved.

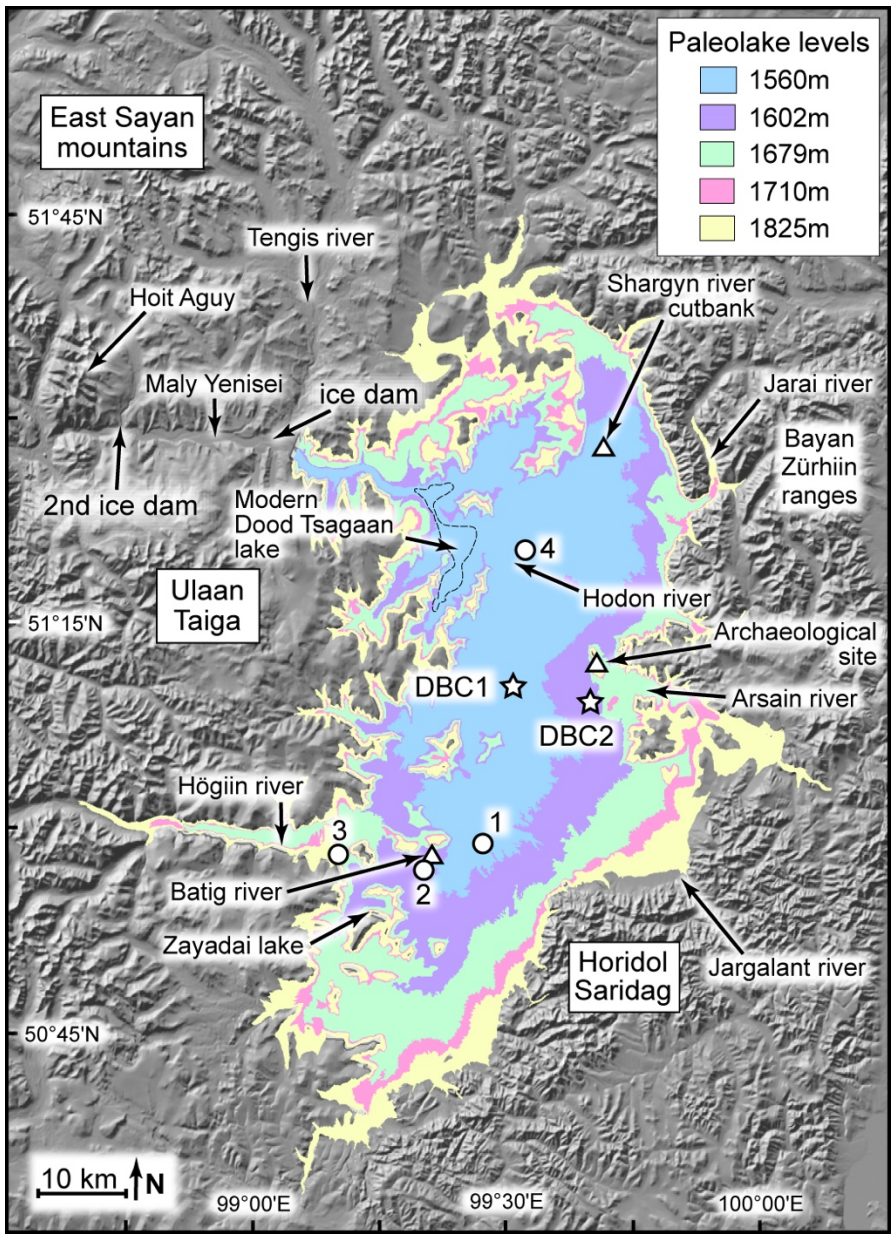

Figure 2.13. Darhad basin map (with lake levels): Geographic names and the extent of the paleolake when Darhad basin filled to 1560, 1602, 1679, 1710, and 1825 m asl. Circles numbered 1, 2, 3 indicate wells of Ufland *et al.* (1971), and 4 indicates the DDB10-3 core (Krivonogov *et al.* 2012). Star symbols indicate two cores presented in this article. Triangles are ^{14}C-sampling sites. Shaded-relief image from SRTM data. The map is from Gillespie *et al.* (2008).

2.9 METHODS IN PART II

In this section we describe the methods used for drilling the boreholes in Darhad basin, the physical investigation and analysis of the sediments, and the methods for dating the sediments from the core as well as from the beach and moraines. We also describe the methods we used to estimate the ELAs in order to provide a regional spatial pattern against which to validate the local dated palaeoglacier sequences.

2.9.1 *Drilling and sediment-extraction methods*

In November 2004, three boreholes, DBC1A and B at 1547 m asl, and DBC2 at 1583 m asl, were drilled in Darhad basin to study the sediments of paleolake Darhad and to date them with luminescence methods. DBC1A was 92.6 m long, but from depths of 2 to 4 m segregation ice was encountered and the core was not recovered intact. Longer sections of lake sediments proved to be difficult to extract from the steel tubes, and below 4 m the core was recovered in short ~40–80 cm segments. Therefore, a second borehole, DBC1B (10.6 m deep), was drilled ~20 m from DBC1A specifically to sample the uppermost lake sediments and complete top of core DBC1A. The stratigraphies for cores DBC1A and B are combined and treated as though taken from a single core, 'DBC1', as located in Figure 2.13.

Another shallow core, DBC2 (14.1 m), was located closer to the eastern edge of the paleolake (Figure 2.13). It was drilled through a gravel dune field, likely of outwash, from either the Arsain or Jargalant river. The core was extracted to find and examine the base of the outwash and to look for datable material, but none was found, and the core was not described fully.

In the field, we visually inspected the cores DBC1A and DBC1B, measured magnetic susceptibility, and examined the lithology of sediments to determine the suitability of sands for

luminescence dating. The cores were then split into halves for photography and subsampling of sediments and organic materials. Half of each core was stored in boxes and later sent to the Institute of Geology and Mineral Resources (Mongolian Academy of Sciences) in Ulaanbaatar for storage. Sergey Krivonogov (Institute of Geology and Mineralogy, Siberian Branch of the Russian Academy of Sciences) took detailed photos of the archived core in 2007. The archived core was later cut into small pieces and moved to the Siberian Branch of the Russian Academy of Sciences, Irkutsk, for grain-size analysis and magnetic inclination measurements. Labeled pieces of DBC1 in ~5 or 10-cm increments are now stored at the University of Washington and the Mongolian Academy of Sciences.

2.9.1.1 Grain-size analysis

Grain sizes of the sediments in the DBC1 were measured at the Institute of Petroleum Geology of the Siberian Branch of RAS, using the equipment Microtrac X100 and Microtrac ASVR. The samples were prepared from the core at intervals of 5 or 10 cm.

2.9.1.2 Magnetic susceptibility

Sediment influx to a basin increases due to greater erosion during the glacial advances, which tend to correlate with higher concentrations of magnetic minerals in high-latitude and high-altitude environments (Verosub and Roberts 1995). To document the temporal variation in the sediment influx to Darhad basin, we measured the magnetic susceptibility in the field as cores DBC1A and B was extracted, but for only the top 35 m. The Bartington MS2 meter with a MS2E sensor then froze and could not be operated in ambient temperatures that ranged down to -30°C. We measured the magnetic susceptibility on the archived core later in Ulaanbaatar. Repeat measurements on the top segment of the core agreed with the existing field measurements.

2.9.1.3 Borehole temperature

We used a conventional mercury thermometer to measure the temperatures in the borehole DBC1B. The thermometer was lowered and left in the well at a particular depth for ~10 min to equilibrate with the borehole temperature. The uncertainty of the thermometer is <0.5°C.

2.9.1.4 Diatom counting

We subsampled the archive core in 2013 to examine the diatom assemblages in the DBC1 core at the depth of 78.9–79.8 m. The subsamples were 2 cm long taken at every 10 cm depth interval of the 1-m segment. Brian L. Sherrod (U.S. Geological Survey) prepared the samples and performed the species identification and counting of the diatom fossils. The sediments were disaggregated in HCl and then treated with 30% H_2O_2. The resulting diatom-rich material was dripped onto a cover slip and allowed to evaporate over gentle heat. Then the slides were prepared using the Cargille Meltmount™ media and the counts consisted of ~200 valves of diatoms per slide. General environment of the diatom species is taken from AlgaeBase (Guiry and Guiry 2015).

2.9.2 *Dating*

For this study we dated sediments with luminescence and ^{14}C techniques, and boulders from moraines by their cosmic-ray exposure (^{10}Be).

2.9.2.1 Luminescence dating

We used different luminescence dating methods as required by the nature of the samples collected. These included both Optically Stimulated Luminescence (OSL) and Infrared-Stimulated Luminescence (IRSL) techniques to measure luminescence signals using continuous wave and pulsed stimulations. We followed Single-Aliquot Regenerative (SAR), the double SAR protocols in these measurements. The details of the measurements and analyses are described below.

Sites and sampling procedures: For luminescence dating, we sampled lake sediments from the DBC1 core, beach sands on the range front near the Arsain river, and the terminal moraine in the Sarig valley. If the core segment appeared to contain datable sand, it was not split until night, so that it could be sampled in the dark. The samples were wrapped in aluminum foil and placed in light-proof bags for shipment to the laboratory at the University of Washington. When this approach was not feasible, samples were wrapped in aluminum foil immediately upon extraction (exposure: ~5 s) and transported to the laboratory in light-tight containers. The exposed exterior was shaved off in the dark laboratory and saved for radioactivity measurements. The inner core was re-packaged into lightproof plastic tubes. The sediments to be dated were extracted from the unexposed interior of the archived core.

Sample DB-AG-2007-02, from the end moraine of the Tengis glacier, was extracted using hand-augers and was wrapped in aluminum foil immediately after extraction. The inner parts were sub-sampled later in the darkroom. The beach sands near the Arsain river, sample DB-AG-2004-03A, were sampled directly by driving light-proof tubes into the deposit. Later in the dark laboratory, the exposed sediments at both ends of the tube were removed for radioactivity measurements, and only the inner parts of the sample were used for luminescence measurements.

Sample preparation for luminescence analysis. Coarse-grain extractions included wet sieving to separate the 150–212 μm grains, then treating with HCl to remove carbonates and with H2O2 to reduce organics. Quartz extraction involved treatment with 48% HF for 40 min followed by density separation of grains less than 2.67 specific gravity using a solution of lithium metatungstate. No HF etch was employed for feldspar extraction, which just involved density separation of grains <2.58 specific gravity. Individual grains were transferred onto specially milled disks by hand. We also prepared multi-mineral aliquots from the core sections where sand

fraction was not available, extracting 1–8 μm fine sediments from the unexposed interior of the archive core. This was done by suspending the sediments in acetone for 2 min before retaining the suspended loads, and the sediments at the bottom after 20 min settling. The 20-min settling was done at least twice to insure the removal of all grains <1 μm. The samples were then transferred onto 1 cm stainless still disks by evaporating the acetone at 50°C.

Measurement and analysis of the luminescence data. The sediments were prepared and analyzed in the Luminescence Laboratory, University of Washington, under the guidance of James Feathers. Luminescence measurements were made on both quartz and feldspar. Coarse (150–212 μm) grains of quartz and feldspar and fine (1–8 μm) grains of multi minerals were separated from each of the bulk samples following the chemical procedures of Feathers *et al.* (2012). We measured the luminescence in the coarse grains following the single-aliquot regenerative (SAR) protocol for quartz (Wintle and Murray 2006) and the modified SAR protocol for feldspars (Auclair *et al.* 2003). Multi-mineral aliquots of fine grains were analyzed using the double SAR method (Banerjee *et al.* 2001) and pulsed measurements (Feathers *et al.* 2012). Feldspar measurements were corrected after the fading assessments (Auclair *et al.* 2003; Huntley and Lamothe 2001). We evaluated the equivalent dose (D_e) values for the same sample using minimum-age and central-age models (Galbraith and Roberts 2012).

The luminescence was measured on a Risø DA-20 reader. For quartz preheating of 240°C for 10 s after the regeneration doses and 200°C cut after the test doses was used; for feldspar preheating of 250°C for 1 min following both regeneration and test doses was used. Stimulation for single grains of quartz was with a 532 nm laser; for single grains of feldspar stimulation was with a 830 nm laser. Stimulation for multi-mineral aliquots used successive exposure to 470 nm

and 870 nm LEDs. Emission for both quartz and multi-mineral aliquots was through 7.5 mm Hoya U-340 filters (UV). Emission for feldspar was through a blue filter pack (350–450 nm).

Pulsed measurements (Feathers *et al.* 2012) were done on fine grains from samples DBC1-79.6 and DBC1-9.15 to isolate the quartz signals from feldspar in the multi-mineral aliquots better. In pulsed OSL measurements the light stimulation is turned on and off, and luminescence is obtained during the off time, rather than during the stimulation as in the SAR protocol. The details on the procedure can be found in Feathers *et al.* (2012).

Fading assessment for the coarse-grained feldspars was conducted on single grains following Auclair *et al.* (2003) using the correction procedure of Huntley and Lamothe (2001). The multi-mineral analysis employed the double SAR method where the IR stimulation precedes the OSL stimulation (Banerjee *et al.* 2001). While the purpose of the IR stimulation is to reduce the feldspar signal, and therefore the fading signal, it may not remove this signal altogether. However, alpha efficiency factors, using the b-value system (0.6–0.7 Gy μm^2), were in the range of quartz for the OSL stimulation, so the OSL signal likely lacked a significant fading component (Janz *et al.* 2015).

The dose rates were assessed by thick source alpha counting, beta counting, and flame photometry. We measured the moisture contents for the analysis. Dose rate conversions followed Adamiec and Aitken (1998). Cosmic dose determinations followed Prescott and Hutton (1994).

2.9.2.2 ^{14}C dating

We used ^{14}C analysis opportunistically to date samples of charcoal, wood, and peat from lacustrine and paludal sediments of Darhad basin and paludal and fluvial sediments related to the outlet

glaciers of the East Sayan ice field in Siberia. The thin peaty layers in the lacustrine sediments developed during lake regressions.

East Sayan, the profile samples: Paludal sediments accumulated against a left-lateral moraine of the outlet glaciers in the Sentsa river valley after the LGM_L, ~6 km upriver from the terminal position of the glacier (Vasil'chuk *et al.* 2015). A ~2.5 m section is exposed in the bank of a thermokarst lake, and this was sampled for ^{14}C analysis. The uppermost 12 cm consist of loess. From 12 to 20 cm is a charcoal-bearing buried A horizon. Below is fine sand, and a lens of segregation ice at 200 cm. One charcoal sample was taken from the buried horizon and four samples of reeds and grass were taken from depths of 60, 73, 172, and 195 cm. The sediments were dated to help establish the post-glacial evolution of the valley as well as to possibly obtain a limiting minimum age for the Sentsa glacier.

Against a right-lateral moraine of the Oka river valley is a sand quarry whose base is in fluvial cobbles ~10 m above river level. Above the likely outwash are ~4.5 m of cross-bedded sand. The sands may be from an ice marginal lake, in which case the outcrop provides the opportunity for a close minimum limiting age for the Oka glacier. We collected two samples of wood fragments from 315 and 432 cm depth to test this possibility.

Darhad basin sediments: We collected two near-surface (depth ~10 cm) samples, of peat and woody roots, from near the Batig river, on the western edge of the depocenter of the basin and in an area of active thermokarst. We collected these samples to see if the topmost sediments here and at Shargyn river cutbank (Gillespie *et al.* 2008; Batbaatar and Gillespie 2016) have the same age.

We also collected a sample of charred larch wood from a palaeosol in sand dunes NE of the Arsain river, near the eastern edge of Darhad basin. The site was on the rim of a half-circular ridge that Gillespie *et al.* (2008) proposed to be a possible end moraine that formed underwater, although no glacial deposits have been identified in the valley upstream (this is also the case for the clearly glaciated Jarai valley). There are large (~10 m high) mounds in this hummocky terrain, which Ishikawa and Yamkhin (2015) interpreted as permafrost pingos. It is possible that the pingos were formed inside the wide (~1.5 km) end moraine (?) of the Arsain glacier, just as permafrost features occur behind the end moraines at the nearby Jarai river. We dated the charcoal at Arsain river to establish a confident minimum age for the putative Arsain moraine.

Lastly, we collected two more samples from the Shargyn river cutbank. They were peat from ~8 m depth and were taken from unconformities near the southern end of the cutbank where the stratigraphy has been affected by slumping, but where nearby sediments dated by Gillespie *et al.* (2008) suggested an age near the ^{14}C limit of 45 ka. This is an important outcrop for understanding the chronology of the Darhad paleolake, and we collected these samples to confirm the MIS 3 ages of this southern section.

^{14}C sample treatment and data analysis: In the field, the collected samples were brushed to remove adhered sand and silt, placed in small plastic bags or photographic film canisters, and air-dried as soon as feasible. They were transported to the laboratory at UW in dark containers. In the lab, coarse samples were cleaned again with a brush. Coarse stems were hand selected from peat samples and grass samples. About 0.5 g of each sample was transferred to glass vials for mailing to a laboratory for measurement. ^{14}C was measured at the Center for Acceleration Mass Spectrometry (CAMS) of the Lawrence Livermore National Laboratory in California. No correction for hard-water effects was necessary because no shells were dated, only land plants.

2.9.2.3 Cosmic-ray exposure dating (^{10}Be)

CRE analysis was used to date till boulders exposed on moraine crests. The number of suitable boulders on our key site, the end moraine of the Tengis glacier, was limited. We also dated other moraines from the region in order to establish a regional chronology of late Quaternary glaciation near Darhad basin.

Sampling sites: We collected CRE samples from three general areas: Darhad basin and along the Maly Yenisei; the East Sayan mountains; and the central massif of Mongolia. Samples from the first group were intended to determine when glaciers dammed the Maly Yenisei; the second group was to improve the glacial chronology for the Darhad region; and the third group was intended to test how reliably glacial chronologies could be extended geographically – i.e. did East Sayan ages also apply to the Darhad basin ~150 km to the south? Sample sites are shown in Figure 2.14.

Group 1: Group 1 contained sites at the mouth of the Tengis river, the Hoit Aguy massif, and the headwaters of the Jarai river. We sampled the undated terminal moraines of the late Pleistocene Tengis glacier, thought to have crossed the Maly Yenisei and dammed the Darhad paleolakes. Its terminal moraines blocked the mouth of the north-flowing Sarig river, south of the Maly Yenisei. Therefore, dating the Tengis terminals directly dates the impounding of the paleolakes and, approximately, at least one of the catastrophic outburst floods.

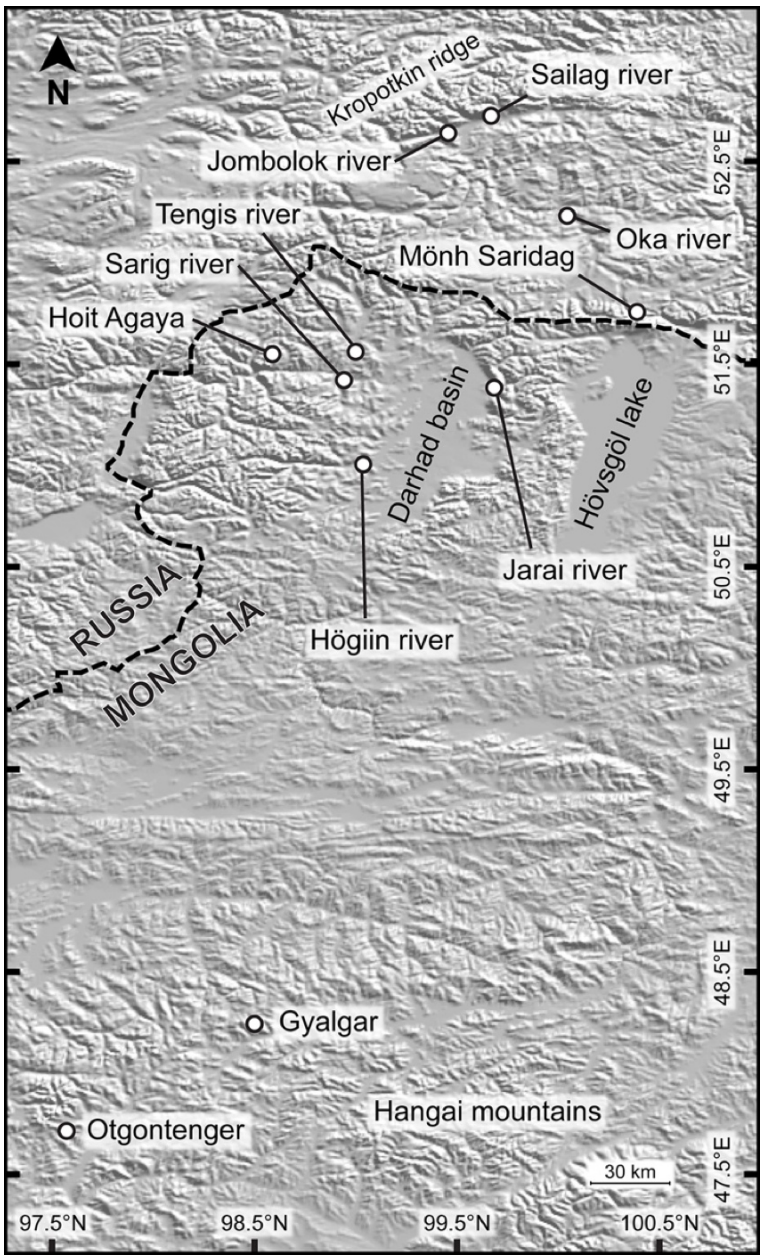

Figure 2.14. CRE dating sites: Index map showing Sayan, Hoit Aguy, Darhad, Hangai sites: SRTM shaded-relief image showing the locations of the 99 ^{10}Be sampling sites referred to in this study. Gillespie *et al.* (2008) sampled 22 boulders in Darhad basin. Rother *et al.* (2014) sampled 21 boulders in the Otgontenger mountain. Arzhannikov *et al.* (2012) dated moraines at the Jombolok and Sailag rivers (13 samples).

We also mapped and sampled moraines of the eastern side of the Hoit Aguy massif, a high ridge near the Tuvan-Mongolian border that rose above the south-flowing outlet glaciers of the East Sayan ice field. One goal in doing so was to date another possible glacier dam across the Maly Yenisei ("2nd ice dam" on Figure 2.13; Komatsu *et al.* 2009); another goal was to establish a dated palaeo ELA.

The final site from Group 1 was in the headwaters of the Jarai river, for which LGM_G piedmont moraines were dated by Gillespie *et al.* (2008). The site was on a pass that separated the Jarai drainage from a local ice cap to the north that at its maximum extent fed ice south across the pass and into Darhad basin. During deglaciation, the sampled granitic boulders were left on the pass as erratics; their only possible source was north of the pass. Dating these erratics intended to provide an age for the end of the LGM_L in the Darhad area, and thus a minimum age for the ice-dammed paleolakes and the catastrophic outburst floods from them.

Group 2: We also sampled in 2002, with Sergei Arzhannikov, Anastasia Arzhannikova, Vladimir Sheinkman (all: Russian Academy of Sciences, Siberian Branch), and Paul Gillespie, and dated boulders from different moraines on the northern margin of the East Sayan ice field. Arzhannikov *et al*. (2012) later resampled and ^{10}Be-dated boulders from Pleistocene moraines in the same area. Our new ages, from the original sampling, augment this chronology and add to its scope significantly by including late Pleistocene retreat moraines and Holocene moraines from the only remaining glaciated peak in the East Sayan, Mönh Saridag, north of Hövsgöl lake.

Group 3: To test the heterogeneity of late Pleistocene glacier variations in the vicinity of Darhad basin, we also sampled and ^{10}Be-dated moraine boulders near Gyalgar peak, the closest (~340 km) massif to the south that was glaciated during the Pleistocene. These new ages augment

the dating efforts by Rother *et al*. (2014) at Otgontenger peak, ~130 km further southwest in the Hangai mountains.

Sampling protocol: Where possible we sampled large granitic boulders (> 1 m in diameter) sitting within 2 m of moraine crests to minimize post-depositional disturbances of boulders. In contrast, Hallet and Putkonen (1994) and Putkonen and Swanson (2003) recommended that the preferred location for sampling was the intersection point between erosion (crest) and aggradation (toe slope) because boulders there were neither exposed by erosion nor shielded by burial, but in permafrost regions such as northern Mongolia solifluction removes material from the flanks of moraines, eliminating this advantage. The boulders were selected to meet the criteria of having minimal erosion: a "fresh" appearance with few surface irregularities (pits, pans), and no apparent burial or exhumation history. Surfaces with indications of erosion, such as spalling, eroded fractures, or rainwater pits, were not sampled. We collected the rock samples by chisel from the top of the boulders, at least 50 cm above the ground, to minimize burial history. The locations of the samples were recorded in the field using hand-held GPS, or 1:50000 topographic maps. Topographic shielding from the horizon was measured by clinometer.

Analysis: We sent the rock samples to the chemical laboratories at the University of Washington and the Hebrew University of Jerusalem, where the quartz was separated by the chemical processing methods of Stone (2000) following Ditchburn and Whitehead (1994). $^{10}Be/^{9}Be$ ratios were measured at the Lawrence Livermore National Laboratory, and at the Australian Nuclear Science and Technology Organisation. The data were converted to ^{10}Be concentrations using the sample weights, following Balco (2006).

^{10}Be ages were calculated using CRONUS-Earth version 2.2 (Balco *et al.* 2008). We used the globally calibrated ^{10}Be production rate of Heyman (2014), which is 3.99 ± 0.22 atoms g^{-1} $year^{-1}$ when referenced to the scaling of Stone (2000). All calculations of ^{10}Be ages assumed zero erosion and burial, and we did not account for neutron shielding by snow. The sensitivity analysis of the CRE age estimations to erosion, scaling scheme, and snow cover is given in detail in the Results section (2.10).

2.9.3 *Equilibrium-line altitude (ELA) estimation*

Glacier growth responds primarily to precipitation as snow and summer temperatures, with ice accumulating at higher elevations and then flowing downhill. ELAs are the altitude at which balance between accumulation and ablation is achieved. Where modern glaciers are found and the current ELAs can be determined, the relative lowering of ELA in the past glaciations (**Δ**ELA) is routinely used as a climate proxy. If the climatic drivers of glacier growth are constant or vary smoothly, ELAs offer a method of telecorrelation for palaeoglaciers. This is helpful in validating CRE ages estimated from small number of samples. In this study, we use ELAs as such a "reasonableness" test for CRE ages for moraines, comparing Darhad ages with those of nearby palaeoglaciers with similar ELAs. Some ELAs have already been published, and we added to this database our own new data for this study. See details in the Results section (2.10).

2.9.3.1 Alpine palaeoglaciers

Palaeo ELAs must be determined from the distribution of glacial deposits since the ancient glaciers no longer exist. The techniques of ELA estimation mentioned below are applicable on modern glaciers as well as on these deposits. Where possible, we used GPS measurements of elevation; elsewhere we used elevations from Google Earth. Our favored method was the MELM (maximum elevation of the lateral moraine) approach, which equates the ELA with the elevation of the highest

lateral moraine (Andrews 1975; Meierding 1982; Porter 2001). The MELM approach is valid only if the lateral moraine has not been covered by talus or eroded. If that was the case we estimated the ELA from the toe-to-headwall ratio (THAR: Charlesworth 1957; Manley 1959), using the threshold value of 0.58 determined for the Darhad region by Gillespie *et al.* (2008). We also estimated ELAs by comparing the areas of accumulation and ablation from the surface topography of palaeoglaciers as reconstructed from ASTER (Advanced Spaceborne Thermal Emission and Reflection Radiometer) digital elevation models (GDEM version 2) (National Aeronautics and Space Administration 2015). Then the ratio of accumulation area to the total area of the palaeoglacier (AAR: Meier and Post 1962; Porter 1975; Gross *et al.* 1976; Torsnes *et al.* 1993) was calculated to find the palaeo ELAs, using a threshold value of 0.6 ± 0.05 determined locally by comparison to MELM ELAs. According to Meierding's (1982) comparison of different methods for the Front Range in Colorado (USA), the most reliable ELA estimations for the front ranges of Colorado were by the THAR and AAR methods, whereas the MELM was less reliable. On the other hand, in a different setting in the Sierra Nevada of California (USA) Gillespie (1991) and in the tropical Andes (central Peru) Ramage *et al.* (2005) considered the MELM technique to be the simplest and most reliable. Comparisons with ELAs calculated by the THAR and AAR methods there indicated agreement within ~100 m.

2.9.3.2 Ice caps and outlet palaeoglaciers

Estimating the ELA for ice caps and outlet glaciers from ice fields is more complicated and less reliable than for alpine valley glaciers. For modern ice caps the ELA lies between the crest and the perimeter, but for palaeo ice caps the highest elevation is unknown, so the THAR approach is difficult to use. In addition, the accumulation area usually covers multiple cirques and high plateaus, and the ice-flow patterns are hard to estimate from the bedrock topography alone.

Drainage basins within the palaeo ice cap are accordingly hard to define (AAR; cf. Torsnes *et al.* 1993). The MELM approach applied to moraines of outlet glaciers may provide at least a lower limit to the ELA. Therefore, we used the MELM and THAR approaches, using the highest point in the bedrock topography within the estimated watershed of the outlet glacier for the headwall altitude.

2.10 RESULTS

In this section, we first present the physical characteristics of the lake sediments in DBC1 core. Then we present age constraints for the Darhad paleolakes from luminescence and ^{14}C dating of lake sediments, and from ^{10}Be dating of the Tengis end moraine. Finally, we provide new results on chronology and extent of the palaeoglaciers in the vicinity of Darhad basin.

2.10.1 *Physical characteristics of lake sediments in DBC1 core*

2.10.1.1 Grain-size analysis

The stratigraphy of the sediments in the DBC1 core is summarized in Figure 2.15. The upper 1.5 m of the DBC1 core consists of reworked sandy lacustrine silt. It is equivalent to the surface layer at the Shargyn river cutbank described by Gillespie *et al.* (2008), which was ^{14}C dated to ~3.5 cal ka BP. This upper section was lighter-toned than the lower section, probably because carbonates have coated the fine sands. Below 1.5 m the core is dominated by darker-colored clayey lacustrine silt, rhythmically bedded at a scale of ~1 mm. Sparse shells of pelecypods (*Sphaerium simile*?) and gastropods (*Lioplax subcarinata*, and *Gyraulus deflectus*?) were scattered throughout this lower section. The upper section of 0–11 m is generally sandier than the lower part of the core, with thin layers of (~10 cm) fine sands at depths of ~9 and ~10 m. Other thin sandy layers were encountered at 13.4 m and 16.10. From 16.1 m to 39 m, the core is clayey to sandy silt, coarsening

below ~31 m depth. A series of fine sandy layers occur between 39 m and 49.5 m, with the thickest layer occurring at 41.2 to 44.0 m depth. Well-preserved gastropod and disarticulated bivalve shells were found occasionally. From 49.5 to 70 m the sediments are approximately uniform clayey silt, layered at scales of 1 mm to 1 cm. Below 70 m, to the bottom of the core, are scattered sandy silt layers. The most prominent of these sandy layers were at 77.0 to 77.5 m depth. From 79 to 80 m there is a distinctive carbonate layer, unique in that it is largely free of clastic material. This layer is fissile, and contains abundant plant remnants, amorphous cyanobacterial and algal material, fresh-water sponge spicules, sparse fresh-water diatoms, and numerous opaline phytoliths (from grass). There are also shells of shallow water gastropod limpets (*Ferrisia sp.*). These air-breathing limpets feed on diatoms and other algae scraped from the surface, and are highly tolerant of desiccated environments, suggesting a largely dry lake. Below the carbonate layer, to the bottom of the core at 92.6 m depth the sediments are again dominated by clayey silt.

In contrast to the cores of Ufland *et al.* (1969), extracted from nearer to the basin depocentre, fewer lenses of segregation ice were encountered in DBC1. The length of drilling tubes dictated the lengths of the core segments, and sedimentary structures such as ice lenses or the stratigraphic boundaries were recovered intact within the segments.

2.10.1.2 Magnetic susceptibility

The volume magnetic susceptibility values for the core DBC1 are shown in Figure 2.15. The magnetic susceptibility values were higher and varied significantly in the upper 60 m of the core, averaging at 47.7 ± 30.6 (10^{-6} cm^3 g^{-1} CGS ± 1σ). We interpret the high values as corresponding to increased erosion in the mountains around Darhad basin, probably due to glacial advances. High concentrations of magnetic minerals in the Lake Baikal sediments were also correlated with glacial intervals (Peck *et al.* 1994). In contrast, the sediments at lower depths of 60–92 m exhibit low

magnetic susceptibility, averaging 13.6 ± 5.8 (10^{-6} cm^3 g^{-1} CGS ± 1σ), indicating that the influx of magnetic minerals to the basin were low and did not vary much during this time. In addition, the fewer number of sedimentation breaks below 60 m implies a stable glacier and continuous dam during this period.

In general, coarser grain size due to rapid erosion and high runoff correlates well with an increase in the magnetic susceptibility (Verosub and Roberts 1995). However, the 0.65 m thick massive fine sand layer at the depth of 76.9 m had a very low magnetic susceptibility similar to silts above and below this layer, suggesting that the increased grain size there is not related to increased runoff. Above these massive sands, a thin layer of cross-bedded sands is sandwiched between silt layers at 76.7 m (Figure 2.15; Table 2.7), suggesting a rapidly fluctuating lake. This layer is very close to the massive sands at 76.9 m, which could have been locally reworked in the paleolake, probably due to wave action of a shallow lake or slumping in a deep lake.

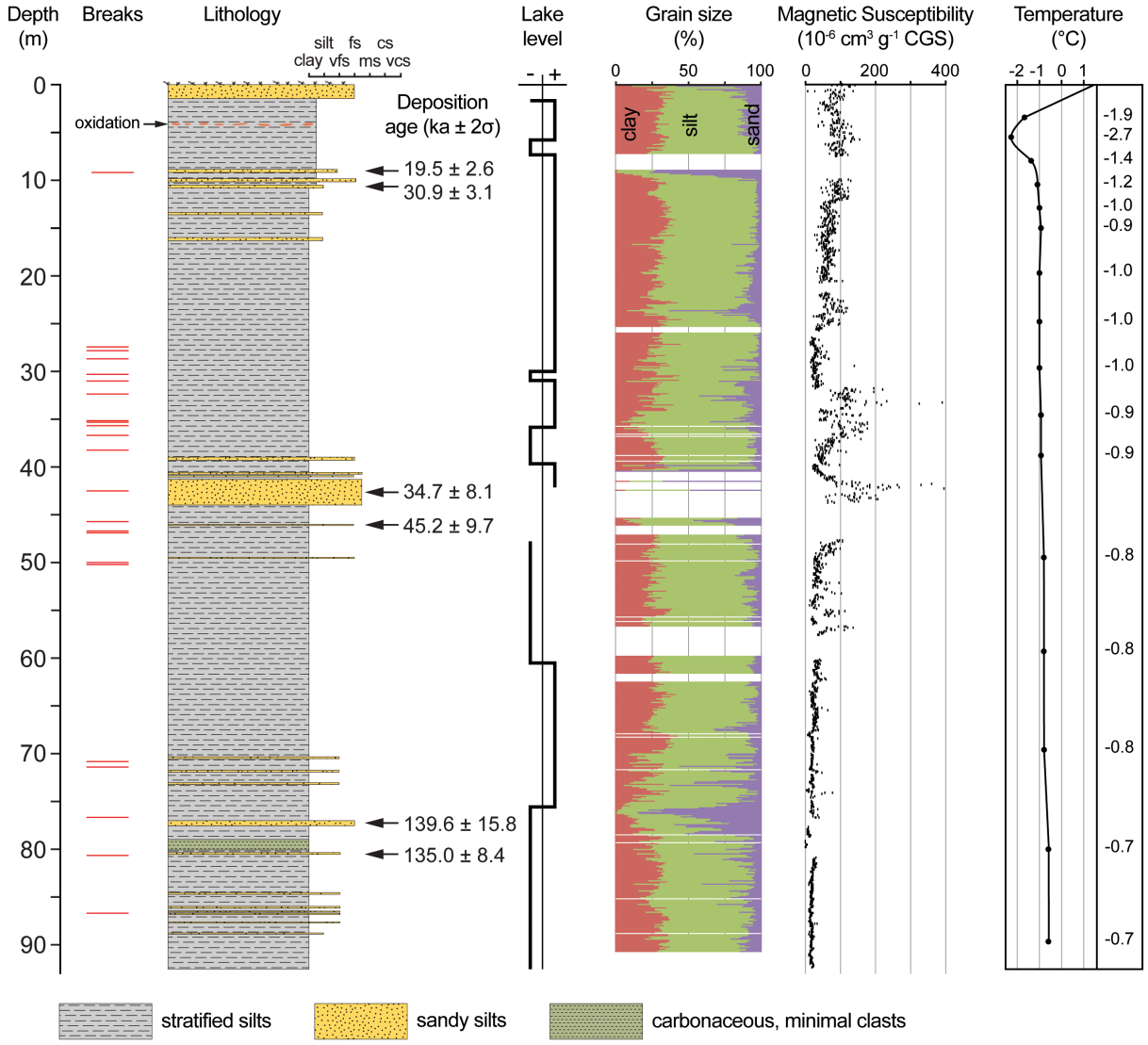

Figure 2.15. Stratigraphic column of the DBC1 core. Sand and silts from the core used for luminescence dating. Lake level was inferred from the facies by Andrei Fedotov, Limnological Institute, Siberian Branch, Russian Academy of Sciences (2008 personal communication). Magnetic susceptibility was measured in the field, and re-measured in the laboratory using Bartington reader MS2B. Grain size was measured at the Institute of Petroleum Geology and Geophysics, SB RAS, using Microtrac X100 and Microtrac ASVR. Temperature of the borehole was measured by conventional thermometry.

Table 2.7. Sedimentation breaks in the DBC1 core. The scale is in cm.

Depth, m	Type of sedimentation break	Photograph
9.1	Slumping	
27.5	Tilted bed	
27.7	Tilted bed	
30.4	Cross bedding	
31.0	Cross bedding	
32.3	Large clast (drop stone?)	
35.1	Slumping	
35.3	Slumping	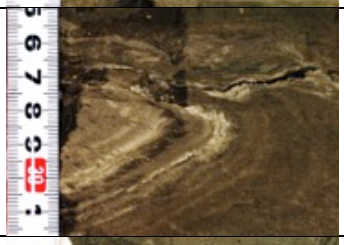
35.6	Slumping	

Table 2.7 (continued)

Depth, m	Type of sedimentation break	Photograph
36.7	Slumping	
38.1	Slumping	
41.6	Cross bedding	
43.6	Abrupt end of lamination	
45.7	Turbidity flow	
46.9	Erosion	
50.0	Slumping (deformation)	

Table 2.7 (continued)

Depth, m	Type of sedimentation break	Photograph
50.1	Erosion	
70.9	Erosion	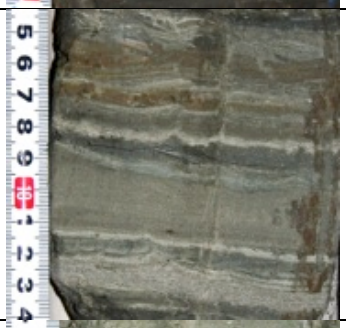
71.3	Cross bedding	
76.7	Cross bedding	
80.6	Deformation	
81.7	Micro fault	
81.8	Erosion	

2.10.1.3 Temperatures in the borehole

The temperature in the well averaged around −1 °C but ranged between +1°C near the surface and −2.7 °C at ~6 m depth (Figure 2.15). The depth of the modern active layer near Shargyn river is ~3 m (Sharkhuu *et al.* 2007). The ice content in the sediments decreased below 40 m depth in the core DBC1. Between the depths of ~6 and 12 m the temperature decreased rapidly to −1°C, then it increased gradually until the bottom of the borehole when it was −0.7°C. The thermal gradient in the lower portion of the borehole is much lower than the geothermal gradient for crust (global average 25–30°C km^{-1}; Fridleifsson *et al.* 2008), which could be explained by low thermal conductivity of ice-poor lake sediments (Clauser and Huenges 1995; Cortes *et al.* 2009 and references therein) that cover Darhad basin to a depth of at least 200 m (Ufland *et al.* 1971).

2.10.1.4 Sedimentation breaks in the DBC1 core

Most of the silt-dominated sections show horizontal laminations of sediments having repeated alternation in color and composition (rhythmites). The changes in sediment are likely seasonal and the sediments are likely varves, but in absence of a densely dated section this is hard to establish with certainty, especially for a lake with episodically fluctuating depth. However, these rhythmic sediments were disturbed, or partially removed many times due to different processes, showing that the sediment record in the DBC1 core is not continuous (Batbaatar *et al.* 2012). Although many of the breaks are disconformities of uncertain depositional significance, we identified 25 unconformities in the DBC1 core, including disturbance due to turbidity currents, cross beds, deformed layers, erosion surfaces, and a micro-fault. These are summarized in Table 2.7. We note that the number of identified unconformities is likely a minimum; probably there are more disturbances throughout the core.

The discontinuous records of lake sediments in the DBC1 core are consistent with the idea of Grosswald and Rudoy (1996) that the paleolakes in Darhad basin repeatedly drained and filled. They also show that a linearly interpolated deposition age between any two independently dated sections is unreliable unless continuous deposition between them can be demonstrated. Therefore, a dating method that relies on the assumption of a constant sedimentation rate, such as correlation of magnetic inclinations (e.g. Krivonogov *et al.* 2012), should only be used with care on the records from the DBC1 core. Furthermore, as other sections such as the cutbank of the Shargyn river (e.g. Gillespie *et al.* 2008) likewise contain angular unconformities suggesting episodes of coarse-scale slumping or erosion, and as such features may be widespread in the basin, age models for any sections or cores from Darhad basin must be used cautiously.

2.10.1.5 Diatom assemblages at 79–80 m depth

The 1-m layer below 79 m depth was distinct from the other lake sediments in the DBC1 due its clast-free and carbonate-rich composition. Within it, the diatom assemblages were largely restricted to two or three species, especially in the lower 50 cm of the layer. The low diversity of diatoms suggests (Table 2.8) that at the time the Darhad paleolake existed under stable conditions. However, the number of fossils varied considerably over the section, and the top of the section contained virtually no diatom fossils. The most dominant species of diatom was *Planothidium delicatulum*, which occurred in large numbers (maximum: ~100% of 200) in all the 10-cm subsamples. *Planothidium delicatulum* occur in alkaline or fresh waters (Round and Bukhtiyarova 1996). The second most common species (maximum: ~190 out of 200) was *Fragilaria construens*, especially at the depths of 79.20–79.30, 79.40–79.50, and 79.90–80.00 m. The colonies of this species are not attached to the substrate and prefer slightly alkaline water (Cejudo-Figueiras *et al.* 2011). The third most common diatom, *Cyclotella ocellata*, was found in the order of tens at depths

of 79.10–79.20 m. This planktonic diatom species is commonly found in oligotrophic lakes (Edlund *et al.* 2003).

Table 2.8. Diatom species in the lake sediments from the DBC1 core.

Diatom species	Number of diatoms per slide at each 10-cm depth interval (m)[a,b]							
	78.95	79.05	79.15	79.25	79.35	79.45	79.55	79.75
Achnanthes lanceolata	10	-	-	-	-	-	-	-
Amphora ovalis	-	5	4	4	-	-	-	-
Cocconeis placentula	-	-	1	-	2	-	-	-
Cocconeis sp.	-	-	-	-	-	1	-	-
Cyclotella ocellata[c]	-	19	55	14	-	-	-	-
Cymbella cf. aspera	-	-	-	-	-	1	-	-
Cymbella inaequalis	-	-	-	-	-	2	-	-
Cymbella minuta	1	18	16	5	9	6	-	2
Cymbella sp.	-	-	-	-	-	3	-	-
Diploneis ovalis	-	1	4	1	-	-	-	-
Epithemia sp.	-	-	1	-	-	-	-	-
Epithemia turgida	-	-	-	1	-	-	-	-
Fragilaria constricta	13	1	2	-	-	-	-	-
Fragilaria construens[c]	192	8	25	122	43	190	-	9
Fragilaria pinnata	-	-	-	1	-	3	-	-
Gomphonema acuminatum	-	-	-	-	-	2	-	-
Gomphonema sp.	-	1	1	1	-	-	-	-
Gomphonema subtile	-	-	16	5	-	-	-	-
Luticola mutica	-	3	-	-	-	1	-	-
Navicula digitoradiata	-	7	5	2	-	1	-	-
Navicula mutica	-	-	-	-	-	1	-	-
Navicula radiosa	-	3	-	4	-	-	-	-
Navicula sp.	-	-	-	3	-	-	-	-
Nitzschia sp.	-	-	1	1	-	-	-	1
Planothidium delicatulum[c]	7	155	70	56	171	23	200+	200+
Parlibellus sp.	-	4	3	-	-	-	-	-
Pinnularia cf. viridis	-	-	1	-	-	-	-	-
Sellaphora pupula var. rectangularis	-	4	-	2	-	-	-	-
Stephanodiscus sp.	-	1	-	-	-	1	-	-
Synedra sp.	-	-	1	-	-	-	-	-
Tabellaria cf. lacustris	-	-	-	4	-	-	-	-
Tabellaria cf. ventricosa	-	-	4	-	-	-	-	-
Tetracyclus cf. lacustris	2	6	-	-	-	4	-	-
Unknown	-	4	10	2	2	2	-	-
Cysts[d]	-	-	-	-	2	-	3	-

[a] Depths of the beginning of each 10-cm increment are shown.
[b] No diatoms were found at the depth of 79.00 m.
[c] Species names in bold are discussed in the main text.
[d] The cysts are not specific to particular species.

2.10.2 *Chronology of Darhad paleolakes*

2.10.2.1 Lake and beach sediments in Darhad basin

Insufficient sunlight under water makes it hard to fully reset the luminescence in lacustrine and fluvial sediments (e.g. Thomas *et al.* 2003; Arnold *et al.* 2007; Lüthgens *et al.* 2010) and partial bleaching was apparent in the sediments from DBC1, as shown by the large discrepancy between the ages for quartz and feldspar (Tables 2.9, 2.10, and 2.11) estimated by the "central-age" model (Galbraith and Roberts 2012). Quartz minerals bleach more efficiently than feldspars (Wallinga *et al.* 2001), which make them ideal for OSL dating, but the coarse quartz grains in our samples had low sensitivity to radiation, yielding too few photons to date the samples reliably. Low sensitivity of quartz has also been observed in samples from the Gobi (Hülle *et al.* 2010) and central Mongolia (Lehmkuhl *et al.* 2011). We therefore used the minimum-age modeling (Galbraith and Roberts 2012) to estimate the D_e of feldspar grains. These gave age estimates consistent with those from quartz.

Sample DB-AG-2004-03A consisted of sand from a beach at an elevation of 1668 m asl near the Arsain river (Figure 2.13). Beach environments have greater sunlight exposure than lakes themselves and bleaching there is likely to be more complete. The ages estimated using the minimum and central age models were statistically the same for this sample. This was not true for the deep-water or moraine samples, supporting our interpretation that the partial bleaching is common in deep-water sediments from DBC1. The sands gave a luminescence age of ~14 ka, suggesting that at least a 120 m deep paleolake existed at that time. The elevation of this beach is only ~10 m lower than the wave-cut benches on the MIS 2 moraines at the Jarai river (Gillespie *et al.* 2008), but ~70 m above the deeply incised outwash plains at Tengis river.

Table 2.9. Radioactivity data for the luminescence samples. Internal K was assumed to be 12 ± 2% for all samples.

Sample identification[a]	Total dose rate (Gy ka^{-1} ± 2σ)	K (% ± 1σ)	^{232}Th (ppm ± 1σ)	^{238}U (ppm ± 1σ)
DBC1B-9.15 (UW1264)	1.53 ± 0.09	1.0 ± 0.1[b]	3.7 ± 0.4	1.3 ± 0.2
DBC1B-9.50 (UW1867)	1.29 ± 0.06	0.92 ± 0.03	2.3 ± 0.5	1.2 ± 0.1
DBC1A-43.7 (UW1265)	1.46 ± 0.07	1.03 ± 0.03	4.0 ± 0.8	1.5 ± 0.1
DBC1A-46.8 (UW1292)	1.38 ± 0.07	0.95 ± 0.02	5.4 ± 0.9	1.0 ± 0.1
DBC1A-76.9 (UW1293)	2.13 ± 0.12	1.0 ± 0.11	4.3 ± 0.8	1.8 ± 0.1
DBC1A-80.1 (UW2702)	3.30 ± 0.16	1.64 ± 0.11	9.8 ± 1.3	1.9 ± 0.2
DB-AG-2004-03A (UW1868)	1.63 ± 0.08	1.02 ± 0.02	5.6 ± 0.8	0.8 ± 0.1
DB-AG-2007-002 (UW1872)	1.79 ± 0.11	1.28 ± 0.09	3.3 ± 0.7	0.9 ± 0.1

[a] University of Washington laboratory numbers are given in the parentheses.

[b] Assumed concentration. The measured concentration of K in sample DBC1-9.15 was too high, probably due to machine error, and we assumed a value of 1.0 ± 0.1, similar to the other samples.

Table 2.10. Luminescence ages (ka ± 2σ) for the Darhad basin samples, estimated from single-grain coarse quartz and feldspar, and from multi-mineral aliquots. Ages estimated using a finite mixture model (Galbraith and Roberts 2012) are given with the component and its percentage in parentheses. Ages from the coarse feldspar and multi-mineral aliquots are all corrected for anomalous fading (Huntley and Lamothe 2001). Reasoning for the assigned deposition ages is discussed in detail in section 2.10.2.

Sample identification[a]	Coarse single-grain SAR ages (ka)				Fine multi-mineral aliquot ages (ka)		Assigned deposition age (ka, as in Table 1)
	Quartz	n	Feldspar	n	OSL	IRSL	
DBC1B 9.15 (UW1264) (deep-water lake sediment)	18.3 ± 4.0 (central)	2	19.5 ± 2.6 (minimum) 46.2 ± 2.0 (2nd: 94%)	83	28.0 ± 2.1	48.9 ± 5.9	19.5 ± 2.6
DBC1B 9.50 (UW1867) (deep-water lake sediment)	28.2 ± 4.0 (central)	5	30.9 ± 3.1 (minimum) 46.5 ± 1.9 (2nd: 93%)	114	-	-	30.9 ± 3.1
DBC1A 43.7 (UW1265) (deep-water lake sediment)	34.7 ± 8.1 (minimum) 100.9 ± 18.3 (central) 34.5 ± 6.8 (1st: 18.4%) 104.7 ± 11.5 (2nd: 66%)	21	70.3 ± 16.0 (1st: 100%)	5	-	-	34.7 ± 8.1
DBC1A 46.8 (UW1292) (deep-water lake sediment)	45.2 ± 10.1 (minimum) 103.6 ± 24.4 (central) 79.7 ± 9.5 (1st: 83%)	13	45.2 ± 9.7 (minimum) 101.6 ± 8.2 (1st: 100%)	59	-	-	45.2 ± 9.7
DBC1A 76.9 (UW1293) (shallow (?) lake sediment)	-	-	-	-	126.5 ± 19.8	162.8 ± 26.4	139.6 ± 15.8 (weighted average)
DBC1A 80.1 (UW2702) (deep-water lake sediment)	-	-	-	-	56.5 ± 4.2	135.0 ± 8.4	135.0 ± 8.4
DB-AG-2004-03A (UW1868) (beach sand)	14.7 ± 4.5 (central)	2	14.3 ± 1.7 (minimum) 16.0 ± 1.1 (1st: 100%)	138	-	-	14.3 ± 1.7
DB-AG-2007-002 (UW1872) (moraine till)	11.9 ± 7.5 (minimum) 57.5 ± 27.2 (central) 8.3 ± 4.5 (1st: 20%) 81.7 ± 21.0 (2nd: 52%)	6	12.0 ± 7.5 (minimum) 72.8 ± 3.5 (1st: 100%)	25	-	-	12.0 ± 7.5 (age is minimum)

[a] University of Washington laboratory numbers and the depositional environments are given in the parentheses.

Table 2.11. Luminescence ages for lacustrine and glacial sediments from Darhad basin.

Sample identification	Lithology	Depth (m)	Analysis type	Deposition age (ka ± 2σ)
Lake sediments from the DBC1 core, N 51.187472°, E 99.497556°, 1547m asl				
DBC1B-9.15	fine sand	9.15	Feldspar MAM[a]	19.5 ± 2.6
DBC1B-9.50	fine sand	9.50	Feldspar MAM[a]	30.9 ± 3.1
DBC1A-43.7	fine sand	43.7	Quartz MAM[a]	34.7 ± 8.1
DBC1A-46.8	fine sand	46.8	Feldspar MAM[a]	45.2 ± 9.7
DBC1A-76.9	fine sand	76.9	Multi-mineral aliquot: OSL[b]	139.6 ± 15.8
DBC1A-80.1	silt	80.1	Multi-mineral aliquot: IRSL[c]	135.0 ± 8.4
Beach deposit near Arsain river, N 51.201611º, E 99.648556º, 1668 m asl				
DB-AG-102504-03A	fine sand	1.5	Feldspar MAM[a]	14.3 ± 1.7
Till from the end moraine at the Sarig valley: N 51.449861º, E 99.034278º, 1611 m asl				
DB-AG-2007-002	fine sand	~0.5	Feldspar MAM[a]	12.0 ± 7.5

[a] MAM: Minimum-age model (Galbraith and Roberts 2012)
[b] OSL: Optically stimulated luminescence (protocols of Feathers *et al.* 2012)
[c] IRSL: Infrared stimulated luminescence (protocols of Feathers *et al.* 2012)

Laminated grey sandy silts at 9.15 m in DBC1 yielded a deposition age of ~20 ka, consistent with the timing of last glacial advances at Jarai river 23 km to the northeast (Gillespie *et al.* 2008). Krivonogov *et al.* (2012) related the high concentration of sands in this layer to shoreline deposition and/or fluvial conditions and suggested that only a shallow lake existed during this time. However, we observed that this sandy layer is not massive, but rather finely laminated suggesting calm conditions during its deposition and a deeper lake. Also, these sands were angular to subangular with low sphericity, indicating minimal transport from the source and deposition with little reworking. We infer that these sands were derived from glaciofluvial sediments when glaciers had advanced close to the range front. The relatively high magnetic susceptibility of these sediments supports our interpretation. The sandy lamina in the layer at 9.15 m alternate with silty

lamina, which may indicate frequent fluctuations in lake depth, sediment supply or lake currents. The sands at 9.50 m were deposited at ~31 ka. The sediments at this depth are similar to that from the 9.15 m level, suggesting a similar glaciofluvial source. Overall, we interpret this 1 m-thick sandy layer at depths of 9–10 m in the DBC1 core as evidence that a fluctuating deep paleolake existed in Darhad basin during MIS 2. The sandy layer abruptly terminates at the depth of ~10.1 m, below which only the grey silty laminae are found, an indication to us of less energetic runoff probably because the glaciers were farther from the lake at that time.

For this study, we rejected central feldspar ages due to partial bleaching, and accepted minimum feldspar ages as reliable. Feldspar measurements had better statistics than for quartz, and the minimum feldspar ages were consistent with quartz central ages within the 2σ error. However, luminescence measurements of the sample DBC1A-43.7 (43.7 m depth) yielded only five readings from feldspar, so we accepted its minimum quartz age of 34.7 ± 8.1 ka (n=21) as the sample age. Fine sands from 46.8 m in the DBC1 core yielded a deposition age of 45.2 ± 9.7 ka. A significant increase in the magnetic susceptibility suggests that these sands were derived mostly from runoff sediments. We note that the error for these MIS 3 samples is relatively high (>20%) relative to the younger samples, which prevents estimating the sedimentation rates accurately for this time period. The two new peat samples from the Shargyn river cutbank (Figure 2.13) yielded ^{14}C ages of ~46 and 48 ^{14}C ka BP (Table 2.12), which were beyond the limit of the IntCal13 calibration curve (Reimer *et al.* 2013). Nonetheless, these ages for the lake sediments recovered from the DBC1 and Shargyn river cutbank support the findings of Gillespie *et al.* (2008) that Darhad basin hosted a deep lake at least intermittently (53–35 ka) during MIS 3.

Table 2.12. ^{14}C samples and data

Sample ID	Lab number	Material	Depth (cm)	Fraction modern	*D*14	^{14}C age (^{14}C year BP ± 1σ)	Corrected ^{14}C ages (^{14}C year BP ± 1σ)	Calibrated age (cal year BP ± 2σ)
Sentsa river, eroded cliff of thermokarst lake, N 52.665850°, E 99.489833°, E, 1326 m asl								
071002-Rsna-01	97499	Charcoal	12-20	0.9377 ± 0.0043	-62.3 ± 4.3	515 ± 40	515 ± 40	500–560
071002-Rsna-02	97500	Sedge blade	60	0.4442 ± 0.0021	-555.8 ± 2.1	6520 ± 40	6520 ± 40	7410–7510
071002-Rsna-03	97501	Plant remains	73	0.8117 ± 0.0036	-188.3 ± 3.6	1675 ± 40	1675 ± 40	1520–1700
071002-Rsna-04	97502	Plant remains	195	0.4630 ± 0.0025	-537 ± 2.5	6185 ± 45	6185 ± 45	6950–7180
071002-Rsna-05	97503	Wood	172	0.7767 ± 0.0034	-223.3 ± 3.4	2030 ± 40	2030 ± 40	1890–2070
Oka river, cross-bedded sand from ice marginal lake, N 52.315567°, E 100.113133°, 1469 m asl								
071202-Roka-04	97504	Wood	3.2	0.2212 ± 0.0011	-778.8 ± 1.1	12120 ± 40	12120 ± 40	13820–14130
071202-Roka-05	97505	Wood	4.3	0.2141 ± 0.0011	-785.9 ± 1.1	12380 ± 45	12380 ± 45	14140–14740
Batig river, aeolian sands capping the Darhad paleolake sediments, N 51.039633°, E 99.400283°, 1559 m asl								
061802-ag-DB-02	97357	Woody roots	0.1	0.6378 ± 0.0029	-366.3 ± 2.9	3615 ± 40	3615 ± 40	3830–4000
061802-ag-DB-01	97358	Peat	0.1	0.5847 ± 0.0026	-419.1 ± 2.6	4310 ± 40	3810 ± 40	4090–4300
Arsain river, archaeological site formed after the Darhad paleolake dried, N 51.281650°, E 99.690733°, 1559 m asl								
061902-ag-AG-11	97359	Charcoal	~0.5	0.7486 ± 0.0034	-256.2 ± 3.4	2325 ± 40	2325 ± 40	2300–2460
Shargyn river, cutbank exposing the Darhad paleolake sediments, N 51.428433°, E 99.702400°, 1558 m asl								
062002-ag-JG-02	97360	Peat	~8.1	0.0023 ± 0.0006	-997.7 ± 0.6	48890 ± 2230	48390 ± 2230	>47500
062002-ag-JG-03	97361	Peat	~7.8	0.0028 ± 0.0006	-997.3 ± 0.6	47340 ± 1840	46840 ± 1840	>47500

Analyses performed at Center for Acceleration Mass Spectrometry (CAMS), Lawrence Livermore National Laboratory. $\delta^{13}C$ values of –25‰ were assumed according to Stuiver and Polach (1977) when given without decimal places. Values measured for the material itself are given with a single decimal place. Radiocarbon concentrations are given as fraction modern and $D^{14}C$. Ages are calculated using the Libby half life of 5568 year and following the conventions of Stuiver and Polach (1977). Sample preparation backgrounds have been subtracted, based on measurements of samples of ^{14}C-free coal or calcite. Backgrounds were scaled relative to sample size. ^{14}C ages for peat were corrected for reservoir effect of 500 ^{14}C year, a value observed in disseminated organic carbon in the Hövsgöl lake (Gillespie *et al.* 2008). 2σ range calculated using CALIB version 7.1 (Stuiver and Reimer 1993) and IntCal13 calibration curve (Reimer *et al.* 2013) and rounded to nearest decade.

There is a massive sandy layer at a depth of 76.9 m. The low magnetic susceptibility of the sands in this 0.65-m thick layer and their unconformable contact with the deep-water lake sediments suggest that these were reworked sands deposited in a shallow lake. The sand fractions in the sample DBC1A-76.9 was insensitive to green-laser stimulation, but fine grained multi-mineral aliquots prepared from the same sample gave an OSL age of 126.5 ± 19.8 ka and an IRSL age of 162.8 ± 26.4 ka, which overlap each other at the 2σ level. In this case, we calculated the weighted average for the estimated age at 139.6 ± 15.8 ka for DBC1A-76.9. A silt-dominated layer abruptly interrupts the sands at 77.6 m and continues until ~79 m depth.

Below the silt there is the unique 1-m carbonate layer. Mollusk shells are abundant and embedded within the thin laminations of this section, suggesting a very shallow lake, probably in an interglacial climate. Batbaatar *et al.* (2012) found sponge spicules and stratospores in the carbonate layer, probably an indication of a paleolake with restricted environment and summer desiccation from a seasonally dry climate.

There were no clastics in the carbonate layer suitable for dating; therefore, we subsampled and dated the underlying silts from 80.1 m depth. The OSL measurements of the sample DBC1A-80.1 underestimated the age, possibly due to saturation effects in the quartz grains (Feathers and Pagonis 2015). We accepted the IRSL age of 135.0 ± 8.4 ka for DBC1A-80.1. However, we note that the accepted ages for the samples DBC1A-76.9 and DBC1A-80.1 are not precise, overlapping within the 2σ error, and we could not definitely constrain the maximum ages for both samples.

2.10.2.2 End moraine of the Tengis glacier

The end moraines in the Sarig valley, 1 km south of the Maly Yenisei river, are perhaps the most convincing evidence to support that the Tengis glacier crossed the river and impounded a lake in Darhad basin (Figures 2.13 and 2.16). We dated two granitic boulders there (Tables 2.13 and 2.14), yielding exposure ages of ~21 and ~24 ka that overlap within 2σ uncertainty. The MIS 2 age for the terminal moraines of the Tengis glacier is consistent with the results of Gillespie *et al.* (2008) that the glaciers around Darhad basin were large and extended to the basin floor during MIS 2. The luminescence ages for the sandy layers at ~9 m depth in the DBC1 core suggest the existence of a deep MIS 2 lake in Darhad basin, which further support the conclusion of Gillespie *et al.* (2008) that the latest Tengis glacier to impound the Maly Yenisei was during the global LGM.

Table 2.13. ^{10}Be data for new samples reported in Chapter 2.

Sample identification	Latitude N / Longitude E (decimal degrees)	Altitude (m asl)	Lithology	Sample thickness (cm)	Shielding correction factor	Quartz (g)	Be carrier (mg)	$^{10}Be/^{9}Be \times 10^{-15}$	Be standard	$[^{10}Be] \pm 1\sigma$ (10^3 atoms g^{-1})
070402-ag-RMS-1	51.736086 / 100.599854	2640	granodiorite	2.5	0.99	30.009	0.2960	629.10 ± 28.00	NIST_27900	414.6 ± 20.7
070402-ag-RMS-2	51.736086 / 100.599854	2640	granodiorite	2.5	0.99	30.003	0.2950	629.90 ± 14.20	NIST_27900	413.9 ± 13.1
070402-ag-RMS-3	51.730918 / 100.600732	2800	granodiorite	2.5	0.99	30.071	0.2950	611.50 ± 18.60	NIST_27900	400.9 ± 15.1
070402-ag-RMS-4	51.730918 / 100.600732	2800	granodiorite	2.5	0.99	22.481	0.2950	444.70 ± 21.70	NIST_27900	389.9 ± 20.9
070402-ag-RMS-5	51.730918 / 100.600732	2800	granodiorite	2.5	0.99	13.931	0.2940	258.40 ± 11.60	NIST_27900	364.4 ± 18.3
070402-ag-RMS-6	51.728600 / 100.598324	2900	granodiorite	2.5	0.99	22.533	0.2950	67.50 ± 5.50	NIST_27900	59.1 ± 5.0
070402-ag-RMS-7	51.728600 / 100.598324	2900	quartz vein	2.5	0.99	20.013	0.2902	51.03 ± 3.54	NIST_27900	49.4 ± 3.6
070402-ag-RMS-8A	51.738667 / 100.600855	2640	quartz vein	2.5	0.99	30.065	0.2930	1355.20 ± 26.30	NIST_27900	882.5 ± 26.1
070402-ag-RMS-8B	51.738667 / 100.600855	2640	quartz vein	2.5	0.99	20.008	0.2911	693.32 ± 13.71	NIST_27900	674.1 ± 20.1
070402-ag-RMS-9	51.738667 / 100.600855	2640	quartz vein	2.5	0.99	18.781	0.2890	925.50 ± 13.30	NIST_27900	951.6 ± 25.3
070802-ag-RSLK-1	52.788700 / 99.736472	1454	granite	1.0	0.99	16.410	0.2310	316.00 ± 11.30	NIST_27900	297.2 ± 12.5
070802-ag-RSLK-2	52.788700 / 99.736472	1454	red granite	2.5	0.99	15.597	0.2330	320.00 ± 11.80	NIST_27900	319.4 ± 13.8
070802-ag-RSLK-3	52.788700 / 99.736472	1464	red granite	7.5	1.00	19.559	0.2320	357.50 ± 12.30	NIST_27900	283.4 ± 11.6
070802-ag-RSLK-4	52.788700 / 99.736472	1454	red granite	2.0	1.00	14.580	0.2310	857.20 ± 22.80	NIST_27900	907.5 ± 31.5
070802-ag-RSLK-5	52.788700 / 99.736472	1454	red granite	10	1.00	18.654	0.2330	319.60 ± 11.60	NIST_27900	266.8 ± 11.4
070802-ag-RSLK-6	52.784657 / 99.732189	1454	red granite	5.0	1.00	14.937	0.2310	190.30 ± 7.30	NIST_27900	196.7 ± 8.7
070802-ag-RSLK-7	52.784657 / 99.732189	1454	red granite	5.0	1.00	22.119	0.2290	331.10 ± 9.80	NIST_27900	229.1 ± 8.5
070802-ag-RSLK-8	52.784657 / 99.732189	1454	diorite	2.5	1.00	10.004	0.1470	180.00 ± 15.70	NIST_27900	176.7 ± 15.9
070802-ag-RSLK-10	52.784657 / 99.732189	1454	granodiorite	2.5	1.00	18.479	0.2340	314.30 ± 12.00	NIST_27900	266.0 ± 11.8
071002-ag-RDJO-1	52.731073 / 99.615047	1410	granodiorite	1.0	1.00	25.084	0.2890	356.60 ± 14.00	NIST_27900	274.5 ± 12.4
071002-ag-RDJO-2	52.731073 / 99.615047	1410	granodiorite	1.0	1.00	25.092	0.2950	366.20 ± 14.10	NIST_27900	287.7 ± 12.8
071002-ag-RDJO-3	52.731073 / 99.615047	1410	granite	3.0	1.00	25.044	0.2930	599.00 ± 36.40	NIST_27900	468.3 ± 30.3
071002-ag-RDJO-5	52.731073 / 99.615047	1410	granodiorite	1.0	1.00	6.176	0.1460	201.40 ± 13.50	NIST_27900	318.1 ± 22.5
071002-ag-RDJO-6	52.717833 / 99.599533	1392	granodiorite	8.0	1.00	12.667	0.2350	204.60 ± 6.60	NIST_27900	253.6 ± 10.0
071202-ag-ROKA-06	52.298633 / 100.224617	1518	gneiss	5.0	0.99	20.880	0.2873	258.90 ± 11.14	NIST_27900	238.0 ± 11.5
080709-HA-JB-02	51.552057 / 98.714686	2332	granite	2.5	1.00	17.572	0.2135	1206.80 ± 23.40	07KNSTD	979.9 ± 29.0
080709-HA-JB-03	51.552057 / 98.714686	2335	granite	2.5	1.00	5.924	0.2121	387.31 ± 16.54	07KNSTD	926.6 ± 44.7
150707-DB-ag-003A	51.453579 / 99.038698	1631	granite	5.0	0.99	10.630	0.2509	237.10 ± 3.89	07KNSTD	374.0 ± 10.4
150707-DB-ag-003C	51.453579 / 99.038698	1631	granite	5.0	0.99	10.166	0.2511	196.40 ± 5.15	07KNSTD	324.2 ± 11.2
6-25-02-ag-JG01a	51.595383 / 99.986200	2459	granitic	1.0	1.00	10.619	0.2544	820.7 ± 124.8	07KNSTD	1313.7 ± 283.1
6-25-02-ag-JG01b	51.595383 / 99.986200	2459	granitic	2.5	1.00	11.843	0.2724	354.2 ± 10.0	07KNSTD	544.5 ± 23.1
6-25-02-ag-JG01c	51.595383 / 99.986200	2459	quartz vein	1.0	1.00	11.129	0.2585	290.9 ± 9.7	07KNSTD	451.6 ± 22.2
ZAG-ARG-01A	48.183767 / 98.781450	2472	granite	4.0	0.99	14.075	0.2479	643.09 ± 16.12	KNSTD	756.9 ± 28.9
ZAG-ARG-01B	48.183767 / 98.781450	2472	granite	4.0	0.99	14.962	0.2502	562.76 ± 10.65	KNSTD	628.7 ± 19.0
ZAG-ARG-02B	48.120000 / 98.813417	2285	granite	4.0	0.99	13.272	0.2495	375.38 ± 9.82	KNSTD	471.5 ± 18.7
ZAG-ARG-03A	48.118050 / 98.815833	2253	pink granite	4.0	0.99	12.835	0.2507	462.511 ± 8.49	KNSTD	603.6 ± 35.2
ZAG-ARG-03B	48.118050 / 98.815833	2253	granite	4.0	0.99	14.361	0.2501	3513.60 ± 98.96	KNSTD	4088.2 ± 172.8
ZAG-ARG-04B	48.129017 / 98.798217	2332	granite	4.0	0.99	14.293	0.2500	674.44 ± 15.70	KNSTD	788.3 ± 28.2
ZAG-SB-04A	48.182884 / 98.804676	2585	granite	4.0	0.99	13.275	0.2506	680.47 ± 11.80	KNSTD	858.4 ± 24.3
ZAG-SB-04B	48.182884 / 98.804676	2585	granite	4.0	0.99	14.583	0.2507	1445.15 ± 17.11	KNSTD	1660.1 ± 36.4
ZAG-SB-04C	48.182884 / 98.804676	2585	granite	4.0	0.99	15.082	0.2502	632.23 ± 10.98	KNSTD	700.7 ± 19.9
ZAG-SB-05	48.195113 / 98.792166	2815	granite	4.0	0.99	14.810	0.2504	3872.7 ± 145.43	KNSTD	4374.8 ± 95.4

We used 2.7 g cm^{-3} for sample density. Using 2.6 g cm^{-3} would make less than 0.3% difference in the apparent age for samples <10 cm thick.

Table 2.14. ^{10}Be ages for samples from Mönh Saridag peak, East Sayan and Hangai mountains, Hoit Aguy massif, and the Tengis end moraine at the Sarig river valley.

Sample identification	Sample description	Maximum diameter (m)	Exposure age[a] (ka ± 1σ)	Internal uncertainty (1σ)
Mönh Saridag, left-lateral moraine, N 51.736086°, E 100.599854°, 2640 m asl				
070402-AG-RMS-1	quartz vein boulder	1.0	12.3 ± 0.9	0.6
070402-AG-RMS-2	red granite boulder	1.5	12.3 ± 0.8	0.4
Mönh Saridag, medial moraine, N 51.730918°, E 100.600732°, 2800 m asl				
070402-AG-RMS-3	granodiorite boulder	1.5	10.7 ± 0.7	0.4
070402-AG-RMS-4	granodiorite boulder	4.0	10.4 ± 0.8	0.4
070402-AG-RMS-5	quartz vein in pegmatite	2.0	9.7 ± 0.7	0.6
Mönh Saridag, left-lateral moraine, N 51.728600°, E 100.598324°, 2900 m asl				
070402-AG-RMS-6	granodiorite boulder	2.0	1.5 ± 0.1	0.1
070402-AG-RMS-7	quartz boulder	1.5	1.2 ± 0.1	0.1
Mönh Saridag, end moraine, N 51.738667°, E 100.600855°, 2640 m asl				
070402-AG-RMS-8A	quartz vein	1.0	26.4 ± 1.7	0.8
070402-AG-RMS-8B	quartz vein	1.0	20.1 ± 1.3	0.6
070402-AG-RMS-9	quartz vein in granodiorite	2.0	28.4 ± 1.8	0.8
Sailag river, broad left lateral–end moraine, N 52.788700°, E 99.736472°, 1454 m asl				
070802-AG-RSLK-1	granite boulder	4.0	20.9 ± 1.5	0.9
070802-AG-RSLK-2	red granite boulder	1.5	22.7 ± 1.6	1.0
070802-AG-RSLK-3	red granite boulder	1.2	20.6 ± 1.4	0.9
070802-AG-RSLK-4	red granite boulder	2.0	64.4 ± 4.3	2.3
070802-AG-RSLK-5	red granite boulder	2.0	20.0 ± 1.4	0.9
Sailag river, stagnant ice terrain on the fan, N 52.784657°, E 99.732189°, 1410 m asl				
070802-AG-RSLK-6	red granite boulder	1.0	14.1 ± 1.0	0.6
070802-AG-RSLK-7	diorite boulder	1.0	16.5 ± 1.1	0.6
070802-AG-RSLK-8	granodiorite boulder	1.5	12.4 ± 1.3	1.1
070802-AG-RSLK-10	red granite boulder	1.5	18.7 ± 1.3	0.8
Jombolok river, end moraine, N 52.731073°, E 99.615047°, 1410 m asl				
071002-AG-RDJO-1	granodiorite boulder	1.5	19.8 ± 1.4	0.9
071002-AG-RDJO-2	granodiorite boulder	1.0	20.8 ± 1.5	0.9
071002-AG-RDJO-3	granite boulder	1.0	34.5 ± 3.0	2.3
071002-AG-RDJO-5	granodiorite boulder	0.8	23.0 ± 2.1	1.6
Jombolok river, right-lateral moraine, N 52.717833°, E 99.599533°, 1392 m asl				
071002-AG-RDJO-6	granodiorite boulder	6.0	18.8 ± 1.3	0.7
Oka river, broad end moraine, N 52.298633°, E 100.224617°, 1518 m asl				
071202-AG-ROKA-6	meta-granodiorite / gneiss	0.6	16.1 ± 1.2	0.8

[a]Exposure age includes total uncertainty, compounded from random errors in measuring the Be concentration (internal uncertainty), and from systematic errors arising from modeling the production rate of Be rate due to nuclear spallation and due to muons.

Table 2.14 (continued)

Sample identification	Sample description	Maximum diameter (m)	Exposure age* (ka ± 1σ)	Internal uncertainty (1σ)
Gyalgar peak, left-lateral moraine in the trunk valley, N 48.183767°, E 98.781450°, 2472 m asl				
ZAG-ARG-01A	granitic boulder	6.0	24.4 ± 1.6	0.7
ZAG-ARG-01B	granitic boulder	-	20.2 ± 1.3	0.5
Gyalgar peak, end moraine in the trunk valley, N 48.1200°, E 98.813417°, 2285 m asl				
ZAG-ARG-02B	granitic boulder	1.5	17.2 ± 1.2	0.5
Gyalgar peak, end moraine in the trunk valley, N 48.118050°, E 98.815833°, 2253 m asl				
ZAG-ARG-03A	pink granitic boulder	1.0	22.6 ± 1.8	1.0
ZAG-ARG-03B	granitic boulder	1.2	158.3 ± 11.4	5.2
Gyalgar peak, right-lateral moraine in the trunk valley, N 48.129017°, E 98.798217°, 2352 m asl				
ZAG-ARG-04B	granitic boulder	0.3	27.6 ± 1.8	0.7
Gyalgar peak, left-lateral moraine in the side valley, N 48.182884°, E 98.804676°, 2585 m asl				
ZAG-SB-04A	granitic boulder	-	30.0 ± 1.9	0.6
ZAG-SB-04B	granitic boulder	-	58.5 ± 3.5	0.8
ZAG-SB-04C	granitic boulder	-	24.5 ± 1.5	0.5
Gyalgar peak, bedrock above the side valley, N 48.195113°, E 98.792166°, 2815 m asl				
ZAG-SB-05	granitic boulder	-	158.1 ± 9.8	2.1
Hoit Aguy massif, right-lateral moraine, N 51.552057°, E 98.714686°, 2335 m asl				
080709-HA-JB-02	granitic boulder	0.3	36.1 ± 2.3	1.1
080709-HA-JB-03	granitic boulder	0.8	34.0 ± 2.5	1.7
Sarig valley, end moraine of the Tengis glacier, N 51.453579°, E 99.038698°, 1631 m asl				
150707-DB-AG-003A	pink granitic boulder	1.5	23.8 ± 1.5	0.7
150707-DB-AG-003C	red granitic boulder	1.5	20.7 ± 1.4	0.7
Jarai pass, boulders on the N 51.595383°, E 99.986200°, 2459 m asl				
6-25-02-ag-JG01a	red granitic boulder	1.5	43.8 ± 9.9	9.5
6-25-02-ag-JG01b	granitic boulder	1.5	18.3 ± 1.3	0.8
Jarai pass, bedrock, N 51.595383°, E 99.986200°, 2459 m asl				
6-25-02-ag-JG01c	quartz vein in schist	1.0[b]	15.0 ± 1.1	0.7

[b] 1-cm quartz vein on upper surface of a 1-m schist erratic boulder on bedrock.

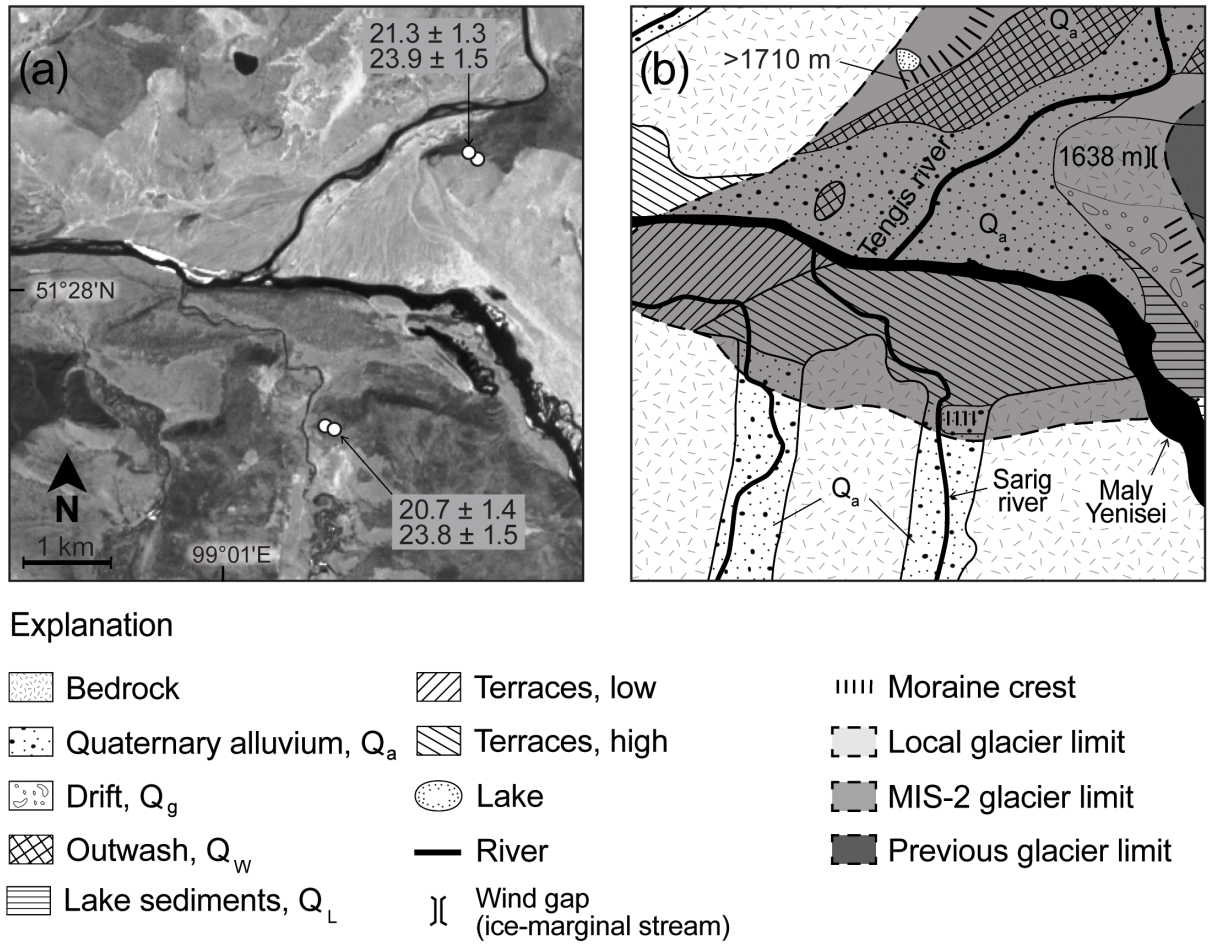

Figure 2.16. CRE sampling site of the end moraine of the Tengis glacier. a) ASTER band 3N showing the end moraine in the Sarig river valley and the confluence of Tengis river to the Maly Yenisei. The ages for the boulders on the wind gap are from Gillespie *et al.* (2008). Ages are in ka ± 1σ; b) Generalized map of the same area as in (a), from Gillespie *et al.* (2008).

We attempted to date the moraine tills in the Sarig valley directly, using luminescence dating. The quartz grains were insensitive to the light stimulation and yielded very few signals. The feldspars were much better in yielding signals, but the equivalent doses varied significantly, probably because the existing luminescence signals were not properly reset due to incomplete exposure to sunlight. Therefore, we used the minimum-age model of Galbraith and Roberts (2012), which estimated the minimum age at ~12 ka with a large error of ±7.5 ka (2σ).

2.10.2.3 Surface sediments from Darhad basin

We sampled the surface sediments overlying the lake sediments in Darhad basin to constrain the time when the basin was completely drained and started to resemble its modern condition. The Batig river (Figure 2.13) flows through a nearly flat plain near the center of the basin and exposes an outcrop of aeolian sands capping the lake sediments. Two samples of wood and peat there yielded calibrated ^{14}C ages of ~3.9 and 4.1 cal ka BP. We also found an archeological site near the Arsain river that was littered with broken pieces of animal bones and the remains from a fireplace. The charcoal sample from this site yielded a ^{14}C age of ~2.3 cal ka BP. These ages suggest that the last of the shallow Darhad paleolakes were drained by ~4 ka, and probably the basin has remained largely dry since then. Consistent with this interpretation, Ishikawa and Yamkhin (2015) found that the permafrost pingo near the Arsain river started forming after ~4.5 ka.

2.10.3 *3.3. Glacial chronology in the vicinity of Darhad basin*

2.10.3.1 East Sayan ice field

The Jombolok river valley was occupied by an outlet glacier from Kropotkin ridge in the East Sayan ice field. Its end moraine is located ~2 km upvalley from an MIS 3 buried soil dated to 38380–43860 cal yr BP by Arzhannikov *et al*. (2012). We sampled four boulders sitting on the end moraine (Figure 2.17d). One sample was older and appeared to have inherited ^{10}Be, but the average age for the other three was ~21 ka. Downvalley from this moraine ~2 and 6 km are two sets of end moraines that Arzhannikov *et al.* (2012) dated to ~26 and 25 ka, respectively (recalculated ages: Batbaatar and Gillespie 2016). The ^{10}Be ages for these two end moraines correspond to standstills or minor readvances of the Jombolok outlet glacier during MIS 2. We also dated a boulder from a right-lateral moraine of the same outlet glacier at ~19 ka.

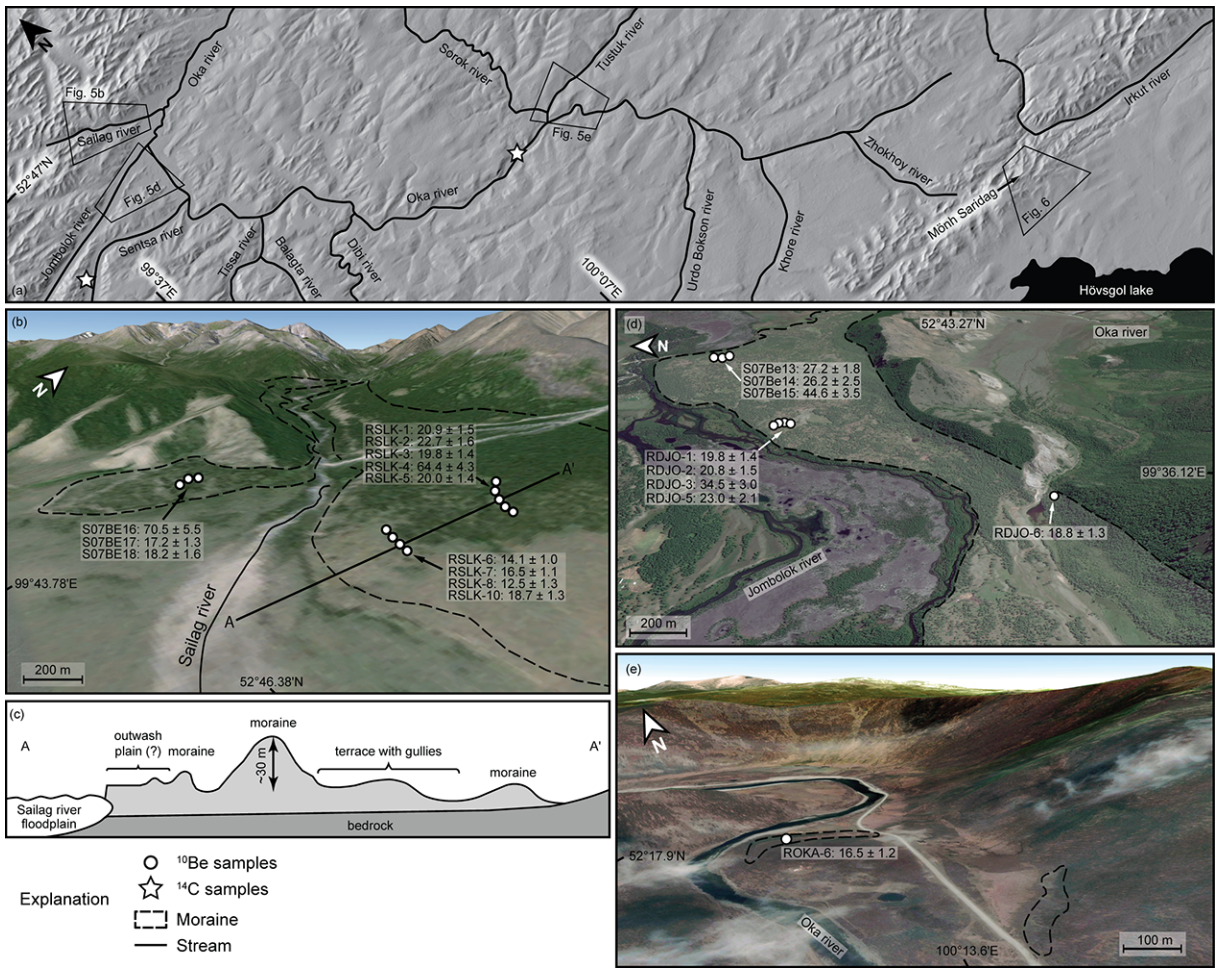

Figure 2.17. East Sayan sampling sites: a) Shaded-relief image showing major tributaries to the Oka river. Stars indicate ^{14}C sampling sites at the Sentsa and Oka rivers; b) Google Earth perspective view of the Sailag river valley (overlay image: Landsat TM); c) Sketch profile across the sampled moraine. Distance not to scale; d) Google Earth perspective view of the Jombolok river valley and the CRE sample locations (overlay image: DigitalGlobe); e) Google Earth perspective view of the Oka river valley and the CRE sample location (overlay image: DigitalGlobe). Samples labeled S07Be are from Arzhannikov *et al.* 2012. Ages are in ka ± 1σ.

Another outlet glacier from the East Sayan ice field descended the Sentsa river valley before ultimately merging with the Jombolok river valley. Arzhannikov *et al.* (2012) sampled boulders on the left-lateral moraines and dated them to ~19 ka. At the bank of a thermokarst lake Vasil'chuk *et al.* (2015) dated the oldest sediments at ~7 cal ka BP. We examined the eroded cliff of another thermokarst lake in the valley, 500 m west of this site, to determine the minimum ages for the glacial retreat, sampling organic materials stratigraphically overlying the glacial deposits. The oldest plant remains from the ~2 m depth dated to ~7 cal ka BP. Two of the ^{14}C ages don't agree stratigraphically, probably due to carbon contamination from other sources. The charcoal sample at the top underlies the loess sediments capping the stratigraphy and was dated to ~0.5 cal ka BP. The ^{14}C Sentsa ages therefore provide only loose constraints for the end of the last glaciation there.

The Sailag river merges with the Jombolok river from the northwest, and the glaciers there originated from the local peaks, rather than from a distant ice field. This simplicity makes the estimation of local ELA easier and more reliable, and therefore is important to establish a robust chronology of glacial advances there. The average age for the four boulders (Figure 2.17: b, c) collected from the stagnant-ice terrain at elevation 1454 m asl was ~15 ka. A few metres higher in this terrain, the left-lateral moraine yielded an age of ~21 ka averaged from four samples (excluding RSLK-4: ~64 ka). The ages are consistent with the ~18 ka age that Arzhannikov *et al.* (2012) measured for two boulders from the right-lateral moraine in the same valley. The estimated ELA for this MIS 2 advance is ~2020–2100 m asl (THAR=0.58, Gillespie *et al.* 2008).

The Oka river hosted outlet glaciers from the East Sayan ice field, as shown by lateral and recessional moraines found along the river. We dated a single boulder, ~16 ka, sitting on a recessional moraine at ~1510 m asl (Figure 2.17e). Numerous lakes, reversed and crossing

drainages, and nunataks in the surrounding Sayan mountains suggest that a vast ice field covered the uplands down to ~2050 m asl there (Figure 2.4). Our sample represents a time when the outlet glaciers from the East Sayan ice field had retreated from their maximum extents of MIS 2.

Mönh Saridag (3491 m asl) is the highest peak of the East Sayan mountains. In a cirque on its northern side is a series of moraines leading up to the modern Peretolchin glacier at ~2930–3270 m asl. We sampled ten boulders from the moraine crests there (Figure 2.18a). Three boulders from the lowest moraine of the series, on a bedrock ridge impounding a tarn at ~2620 m asl, gave an average age of ~25 ka, consistent with the MIS 2 glacier advance recorded elsewhere in the East Sayan mountains. These three ages suggest that by 25 ka the MIS 2 glaciers had already retreated to the lip of the cirque. Upvalley ~400 m, a higher moraine dated to ~12 ka (n=2) suggests further gradual episodic retreat or retreat and readvance. Three boulders from a recessional moraine even further upvalley at ~2800 m asl were dated at ~10 ka, consistent with continued gradual retreat. The highest of the dated end moraines is at ~2900 m asl, ~300 m from the modern ice tongue. Two boulders from this moraine dated at ~1.3 ka. The Peretolchin glacier in 1898 (Peretolchin 1908) was very close to this late neoglacial moraine. Our visual matching of the 1898 photo and Google Earth (Figure 2.18b) suggests that the 1898 glacier advance did not overrun the older moraines we dated.

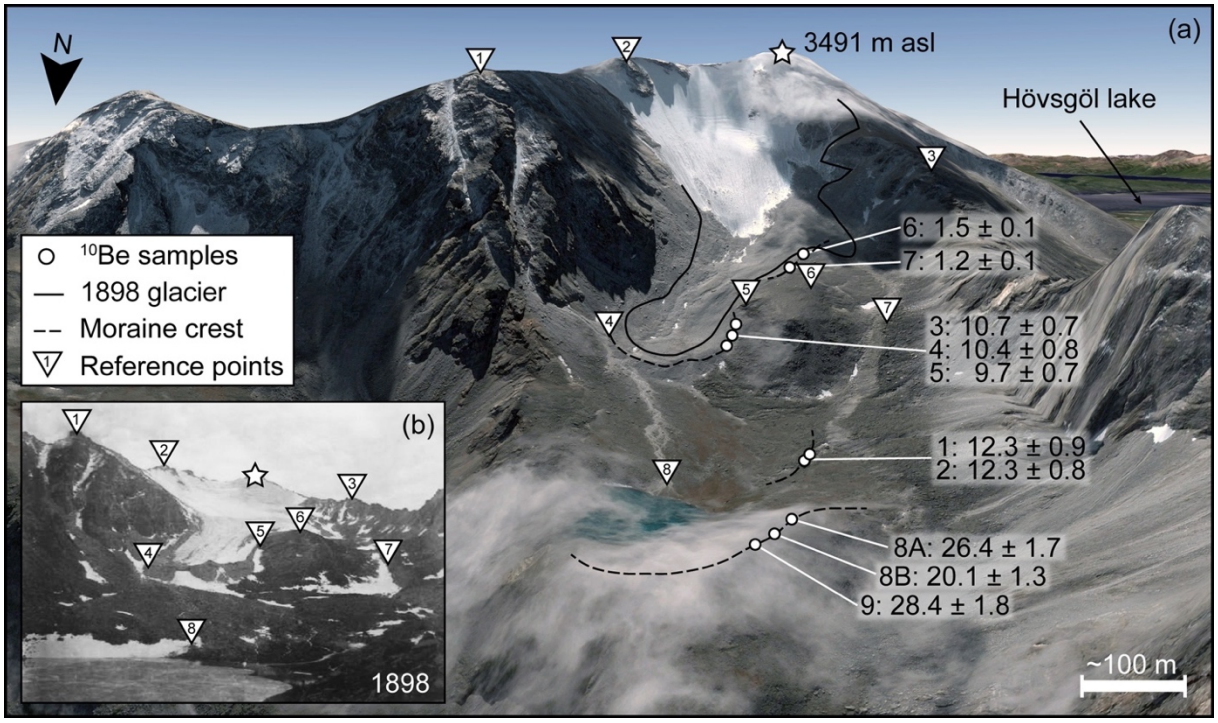

Figure 2.18. CRE sampling site at the Mönh Saridag mountain. a) Google Earth perspective view showing the modern glacier Peretolchin, and CRE sample locations on moraine crests (overlay image: DigitalGlobe); b) Photo taken in 1898 of the Peretolchin glacier (Peretolchin 1908). We used more reference points than shown in the figure to visually match the landscape features in Google Earth image and the photograph. All sample numbers refer to 070402-AG-RMS- as listed in Tables 2.13 and 2.14. Ages are given in ka ± 1σ.

2.10.3.2 Bayan Zürhiin ranges

To the east of Darhad basin, the Bayan Zürhiin ranges were another centre of glaciation. The wide U-shaped valleys of the Utragiin, Jarai, Jumarlag, and Hodon river valleys (Figure 2.13) contain end moraines and hummocky terrain at the edge of Darhad basin. Gillespie *et al.* (2008) dated the sequence of end moraines at the mouth of the Jarai river valley to ~40 ka and ~22 ka, establishing the chronology for the largest extents of glaciers there. However, the timing of the glacial retreat is unknown. To address this problem, we sampled two glacial boulders and one glacially eroded bedrock at the head of the Jarai river (Figure 2.19). The site marks a pass between Darhad and

Hövsgöl basins. There are red granitic erratics resting on the local schist bedrock of the pass. Numerous tarns on the flat, glaciated upland between Jarai pass and the Ih Horoo valley to its north indicate the presence of a local ice cap between the drainages (Batbaatar and Gillespie 2016). The Ih Horoo valley was last glaciated during MIS 2 (Wegmann *et al.* 2011), and that is likely the age of the ice cap also. The erratics on the pass were likely deposited when the flux of ice south of the pass ended.

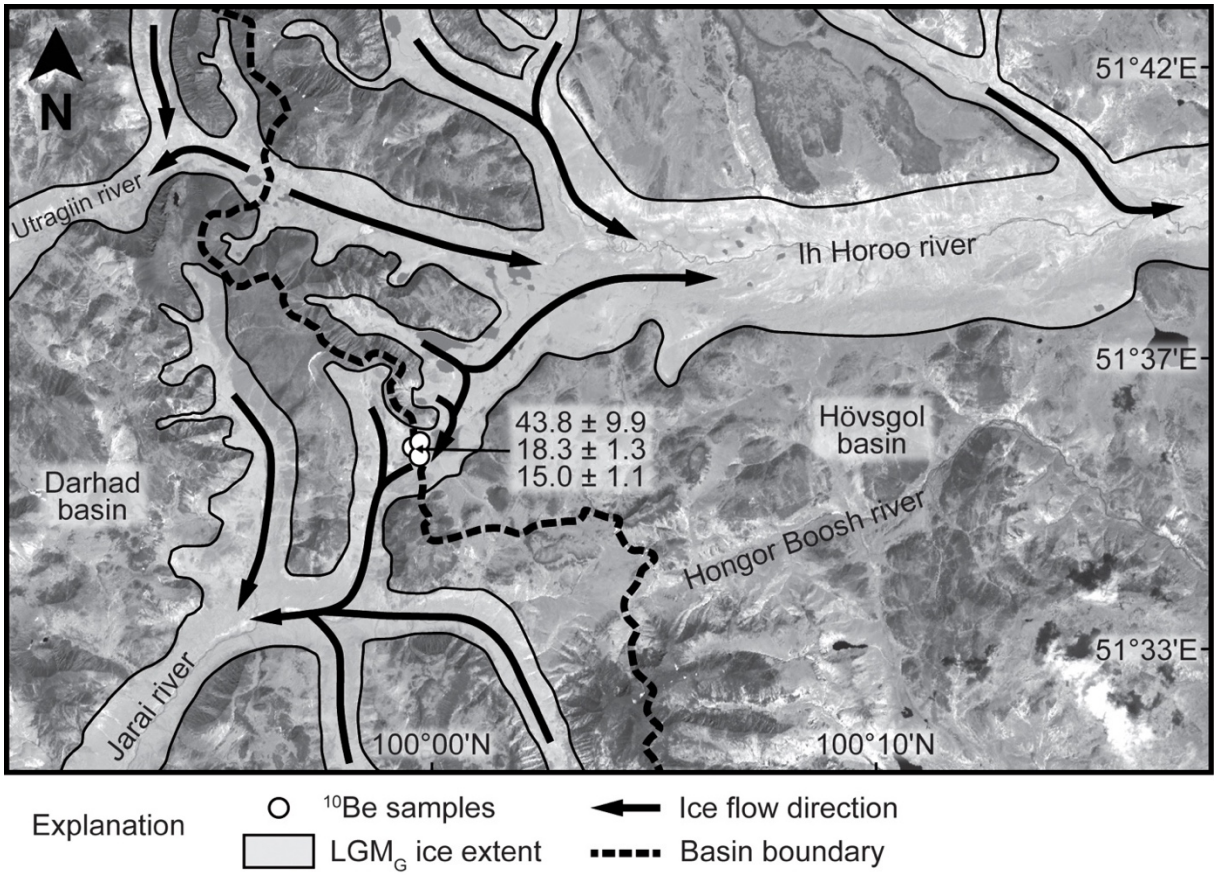

Figure 2.19. CRE sampling site at the pass between Darhad and Hövsgöl basins. The background image is ASTER band 3N. The ice extent is adapted from Figure 2.4. Ages are in ka ± 1σ.

Two granitic boulders on Jarai pass dated to ~44 and 18 ka, and quartz from a lens in the schist bedrock dated to ~15 ka. Assuming that the oldest sample was exposed before the glacial transport and thus contained inherited ^{10}Be, we conclude that the Jarai glacier had retreated all the way to the cirques by ~15 ka and the Bayan Zürhiin ranges became largely ice-free by then. This is a few thousand years after the MIS 2 glacier at Mönh Saridag retreated to its cirque. The timeframe for the glacier retreat from the Bayan Zürhiin ranges, 15–18 ka, coincides with the timing of the retreat of outlet glaciers in the Jombolok, Oka, and Sailag river valleys.

2.10.3.3 Hoit Aguy massif

At their maximum extents, some of the valley glaciers in the Hoit Aguy massif joined the outlet glaciers descending from the East Sayan ice field. The terminal moraines in other valleys of the Hoit Aguy sit above the main outlet glacier. We sampled two boulders from a right-lateral moraine extending into a terminal moraine that lies ~50 m above the trunk outlet trimlines at ~2030 m asl there (Figure 2.20). The lateral moraine was dated to ~35 ka, suggesting an MIS 3 advance at the Hoit Aguy massif with an ELA of ~2330 m asl (MELM). Elevated hummocky terrain between the valleys suggests that the valley glaciers of the Hoit Aguy massif were not always individually separated and constrained within their valleys. This means that larger glaciers existed there once and must have been part of the East Sayan ice field. The terminal moraines impounding the modern paternoster lakes of Hoit Aguy massif sit very close and are interior to the MIS 3 moraines. The ELA for these smaller moraines is only 50 m above the MIS 3 advance. This is consistent with the pattern of ELA for the MIS 2 and 3 moraines dated in Darhad basin (Gillespie *et al.* 2008).

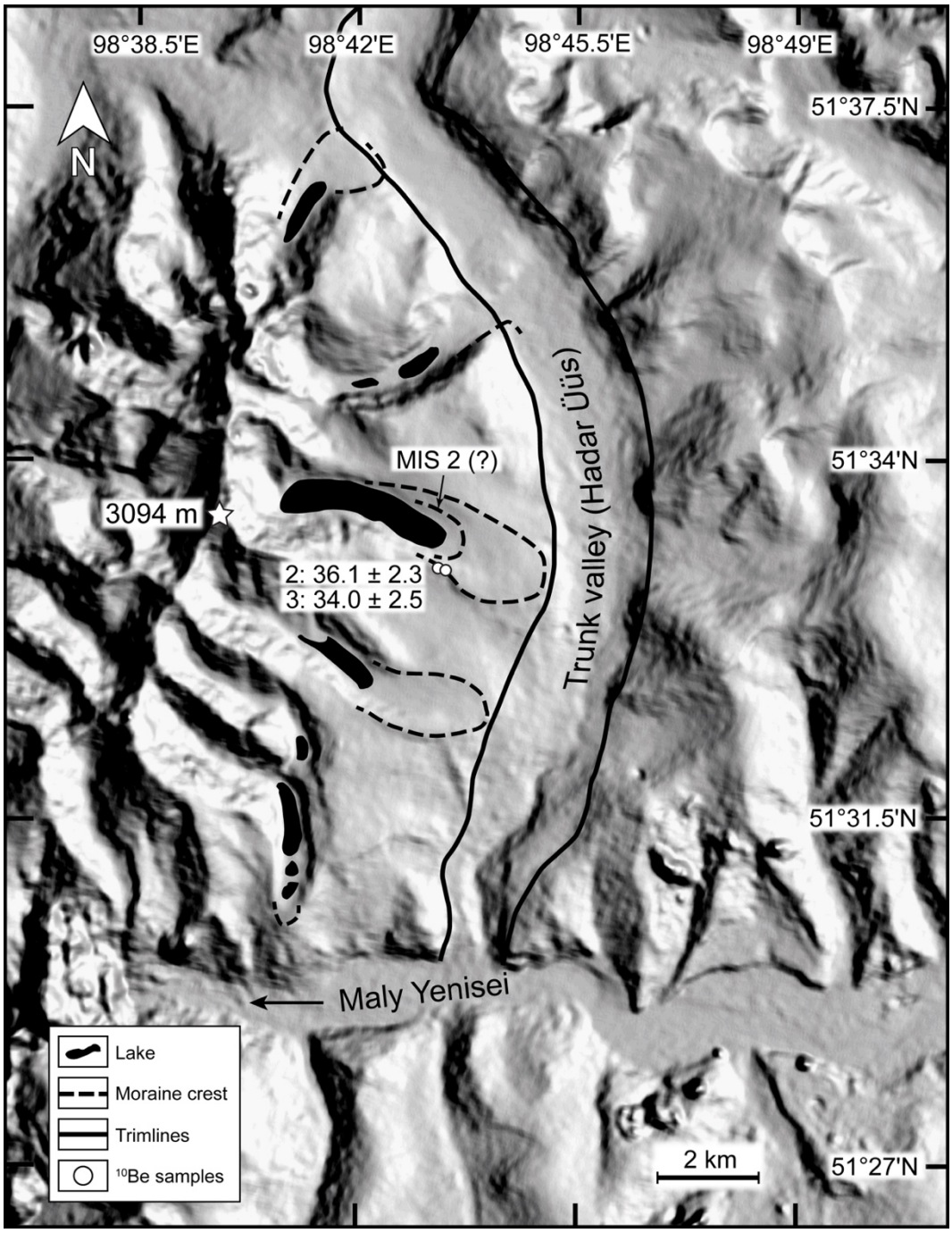

Figure 2.20. Hoit Aguy moraine map: Shaded-relief image of the Hoit Aguy massif and ^{10}Be sample location. Sample numbers refer to 080709-HA-JB- in Tables 2.13 and 2.14. Ages are in ka ± 1σ. Palaeoglaciers in the main trunk valley (Hadar Üüs river) originated from the East Sayan ice cap. The MIS 3, and LGM_G moraines in the Hoit Aguy hang above the trimlines of the larger glacier in the trunk valley.

2.10.3.4 Hangai massif in central Mongolia

The Hangai mountains of central Mongolia, a center of extensive glaciations separate from the Siberian glaciers, provide an excellent location at which to understand the regional pattern of glacial extents better. We analyzed ten samples from a formerly glaciated valley near Gyalgar peak (Figures 2.14 and 2.21), nine of which were from the moraines and one of which was from a bedrock outcrop above the highest lateral moraines there. Two of the ages significantly disagreed with the other ^{10}Be ages, at ~158 and ~59 ka, probably due to inherited ^{10}Be. The remaining seven ages scattered from 17.2 to 30 ka, and the average age for these moraines at ~24 ka suggests that the maximum glaciation there coincided with the MIS 2 glaciers of Darhad basin and the East Sayan mountains.

The outlet glaciers near Otgontenger peak, another glaciated center in the Hangai mountains, showed a similar timing of the maximum glaciations – the local LGM occurred during MIS 3 but the MIS 2 glaciers were nearly as large (Rother *et al.* 2014) as also occurred in Darhad basin.

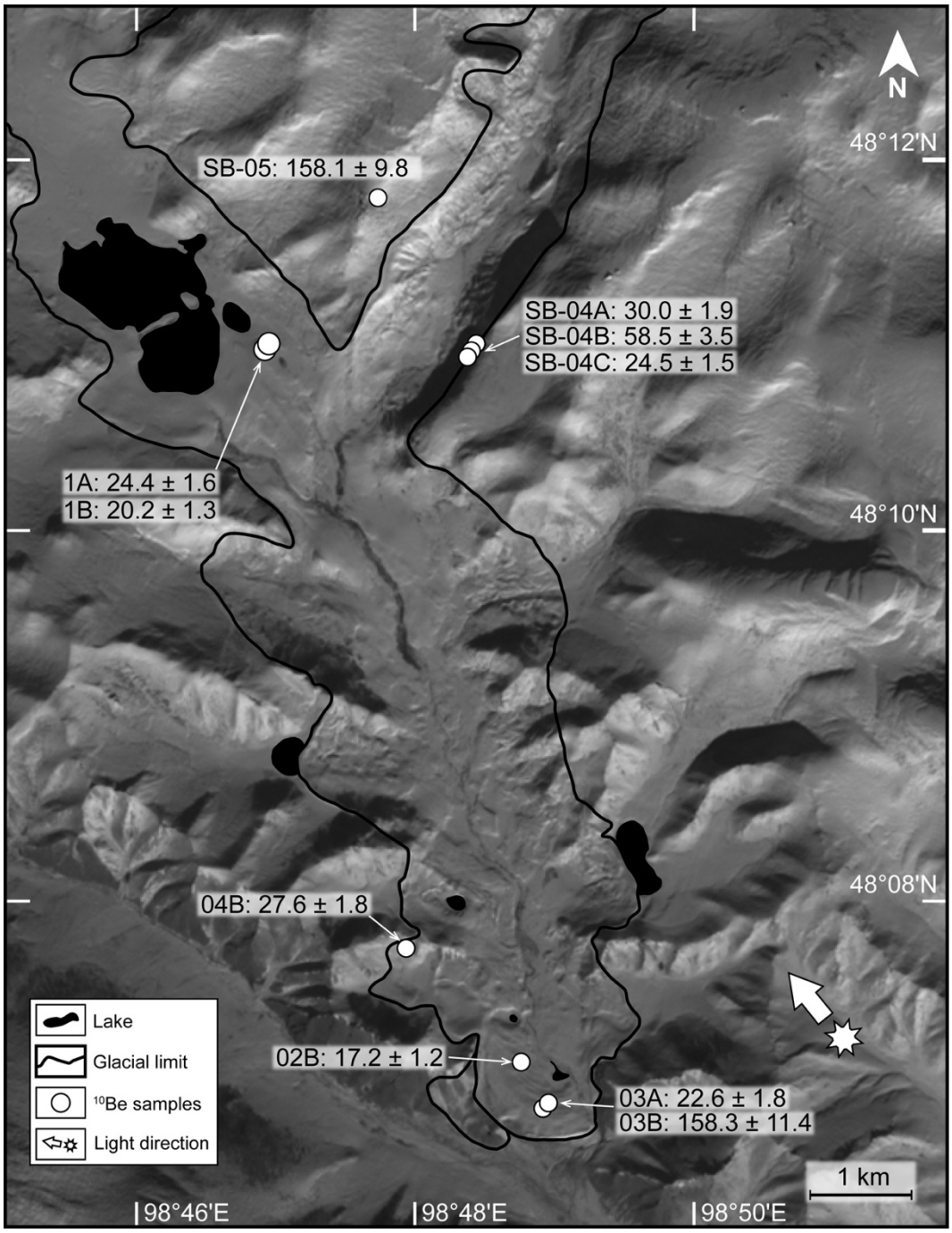

Figure 2.21. ASTER 3N image (acquisition: January 7, 2007) showing the Gyalgar mountain area and the CRE sample locations. All the sample numbers refer to ZAG-ARG- as listed in Tables 2.13 and 2.14, except SB- is for ZAG-SB- in the table. Ages are in ka ± 1σ.

2.10.4 *Equilibrium-line altitude estimations*

According to Gillespie *et al.* (2003, 2008) Darhad basin and the adjacent area belongs in a region where MIS 2 and earlier MIS 3 glaciers were similar in size and ELA. Modeling by Rupper *et al.* (2009) suggested that the glaciers in this region respond strongly to changes in temperature, which varies spatially much less than precipitation in Central Asia. Accordingly, we expect MIS 3 – MIS 2 ELA changes to be consistent across the region. In this section, we first describe the modern ELA pattern in the regions adjacent to Darhad basin within ~1000 km, an arbitrarily chosen radius, where more than 60% of the annual precipitation falls in summer and the glaciers have a similar accumulation regime (Sakai *et al.* 2015). Then, we present the palaeo-ELA estimations for the dated moraines to compare with the modern values. In order to explain the climate conditions in the region we compared the regional temperature and precipitation from 1901 to 1931, compiled from the interpolated climate dataset CRU TS3.10 (Harris *et al.* 2014).

2.10.4.1 Modern glaciers and ice caps

Today only a few peaks within 500 km from Darhad basin host small cirque glaciers and ice caps: Mönh Saridag, Topografov, and Grandiozny in the East Sayan, and Otgontenger in the Hangai mountains (Figure 2.2). The ELA of a small cirque glacier at the Grandiozny peak is ~2250 m asl, a low elevation consistent with colder climate of the high latitude. The ELA increases to the south, to ~2520–2680 m asl at Topografov peak and ~3190 m asl at Mönh Saridag. Approximately 500 km farther south, the ice cap on the Otgontenger peak has an ELA of ~3840 m asl, which reflects an increased ELA due to warmer climate at its lower latitude.

The correlation between the increasing ELA and the decreasing latitude is more pronounced when we include modern glaciers located within ~1000 km radius from Darhad basin. These are the glaciers in the Altai mountains in the west, the eastern Tian Shan in the southeast,

and the Transbaikalian mountains in the northeast. The mountain ranges in this region receives at least at least 50% of the precipitation in summer and, in general, the annual precipitation increases from ~100 mm at 45° N to ~600 m at 55° N. The long-term (1901–1931) summer (JJAS) temperature decreases from ~10°C to ~5°C from latitude 40° N to 55° N, which corresponds to the increased ELA in the colder climates. The modern ELA of glaciers within ~1000 km from Darhad basin is lowered by ~150 m per degree of increase in latitude (see details in supplementary material).

2.10.4.2 Palaeoglaciers in the vicinity of Darhad basin

The THAR ELA for the Tengis end moraine that dated to MIS 2 was ~2100 m asl, and that for the highest lateral moraine was ~2200 m asl (Gillespie *et al.* 2008). Similarly, the end moraine (?) of the MIS 2 glaciers in the Arsain river valley implied an ELA of ~2160 m asl, and the adjacent Jarai valley had a THAR ELA of 2065 m asl (MIS 2), but also received ice from the ice cap between the Jarai and Ih Horoo glaciers (Gillespie *et al.* 2008). The glaciers from the Kropotkin ridge (Figure 2.14) that filled the Jombolok river valley during MIS 2 had a THAR ELA was ~2120 m asl. The simple geometry of the Sailag river valley allowed a more confidant THAR ELA determination for the MIS 2 moraines there of ~2050 m asl. The exception among the dated moraines in the East Sayan mountains was the MIS 2 glacier of Mönh Saridag with an ELA of ~3000 m asl, but this glacier was in retreat.

The ELA for the dated Hoit Aguy MIS 3 moraine was ~2240 m asl (THAR) or ~2330 m asl (MELM), roughly 150 m higher than for glaciers from the main part of the East Sayan. The Hoit Aguy massif is oriented roughly N-S, and we speculate that the ridge blocks the westerlies and places the east-side drainages in a rain shadow, raising the ELAs there. The lowest end moraines on the western valleys give the THAR ELAs of 2110–2190 m asl, which was ~100 m

lower than for the lowest end moraines on the eastern valleys. In addition, we found that the THAR ELA we estimated for valleys with multiple cirques was consistently lower (by ~100 m) than for valleys with a single cirque, likely because the accumulation area in the former was greater. An inset moraine (MIS 2?) is ~700 m upvalley from the dated MIS 3 moraine, giving an estimated THAR ELA of ~2290 m asl there. After adjusting for the rain-shadow effect (2190 m asl) and variation in accumulation area differences (2090 m asl), it appears that the ELAs for the Hoit Aguy and East Sayan are about the same.

We may also compare the MELM ELAs: In the dated valley in the Hoit Aguy, the MELM ELA corrected for the rain-shadow effect is ~2230 m asl (MIS 3) or ~2280 m asl (MIS 2), ~80 m higher than the MELM ELA of ~2200 m asl for the MIS 2 Tengis glacier. This is within the ELA estimation error of 100 m.

The end moraines of the MIS 2 Gyalgar glacier in the Hangai massif implied a THAR ELA of ~2650 m asl. This is similar to the THAR ELA for the MIS 2 end moraines of the Otgontenger glacier reported by Rother *et al.* (2014). The elevation of the highest lateral moraine there was ~2750 m asl, only ~100 m above the THAR ELA. Similar to the modern ELA pattern in the vicinity of Darhad basin, the ELAs for the MIS 2 glaciers were also lower in the East Sayan than in the Hangai. The difference of ~500 m between the MIS 2 ELAs of the East Sayan and the Hangai suggest that the MIS 2 ELA varied by ~130 m per degree of latitude. The ELA estimations are summarized in Table 2.15.

Table 2.15. The equilibrium-line altitude for modern glaciers and the mean (1901–1931) climate parameters in the vicinity of Darhad basin

Assigned name	Latitude, degrees N	Longitude, degrees E	ELA (THAR=0.58), m asl	Mean annual PPT, mm	Mean summer (JJAS) temperature, °C	Portion of summer (JJAS) PPT, %
Aktru glacier	50.122308	87.714013	2955	400	7.7	57
Barkol Shan	43.396359	93.421594	3742	89	13.9	67
Barkol Shan	43.391621	93.360286	3938	89	13.9	67
Belukha peak	49.861533	86.659125	2980	482	5.2	56
Belukha peak	49.842899	86.498465	2990	482	5.2	56
Belukha peak	49.851076	86.580478	3078	482	5.2	56
Belukha peak	49.851076	86.580478	3012	482	5.2	56
Bogd peak	43.825056	88.496799	3940	215	10.5	53
Bogd peak	43.813125	88.501683	3808	215	10.5	53
Bogd peak	43.817914	88.372126	3885	215	10.5	53
Bogd peak	43.770951	88.356579	4041	215	10.5	53
Bolshoy Aktru	50.063454	87.689233	3159	400	7.7	57
Border area	49.057638	87.793280	3221	387	4.8	57
Dayan nuur	48.351140	88.629313	3355	250	7.8	60
Dayan nuur	48.356373	88.569547	3422	250	7.8	60
East Bogd	43.469190	89.385254	3773	144	15.8	51
East Bogd	43.460639	89.406934	3785	144	15.8	51
East Bogd	43.460635	89.406951	3748	144	15.8	51
East Bogd	43.463022	89.435862	3728	144	15.8	51
East Bogd	43.367011	89.565573	3887	144	15.8	51
East Bogd	43.384498	89.627163	3701	144	15.8	51
East Bogd	43.378960	89.614013	3671	144	15.8	51
Grandiozniy	53.856739	96.178077	2253	664	8.4	61
Harhiraa	49.589676	91.251310	3602	356	5.8	60
Harhiraa	49.531142	91.439718	3493	356	5.8	60
Harhiraa	49.587889	91.392292	3309	356	5.8	60
Harhiraa	49.589676	91.251310	3379	356	5.8	60
Harhiraa	49.524000	91.396645	3472	356	5.8	60
Harhiraa	49.575957	91.398259	3487	356	5.8	60
Kanas river	49.083478	87.468999	3088	400	6.0	56
Kanas river	49.083478	87.468999	3026	400	6.0	56
Kanas river	49.083478	87.468999	2848	400	6.0	56
Kanas river	49.100891	87.339603	2982	400	6.0	56
Kara oyuk river	49.796303	87.909607	3148	412	4.9	56
Möngön Taiga	50.278836	90.066643	3199	355	7.1	58
Möngön Taiga	50.285085	90.135820	3536	355	7.1	58
Möngön Taiga	50.269810	90.146286	3390	355	7.1	58
Mönh Hairhan	46.837444	91.698230	3584	205	7.8	67
Mönh Hairhan	46.961590	91.447763	3687	205	7.8	67
Mönh Hairhan	46.902992	91.526653	3565	205	7.8	67
Mönh Saridag	51.722757	100.600457	3194	430	6.4	74

Table 2.15 (continued)

Assigned name	Latitude, degrees N	Longitude, degrees E	ELA (THAR=0.58), m asl	Mean annual PPT, mm	Mean summer (JJAS) temperature, °C	Portion of summer (JJAS) PPT, %
Otgontenger	47.620185	97.535583	3843	308	5.4	73
Sutai	46.663988	93.552129	3783	181	10.2	72
Sutai	46.625774	93.600142	3795	181	10.2	72
Sutai	46.628266	93.597447	3752	181	10.2	72
Sutai	46.652719	93.553588	3723	181	10.2	72
Sutai	46.612811	93.564922	3623	181	10.2	72
Sutai	46.605113	93.651510	3886	181	10.2	72
Sutai	46.643772	93.600827	3836	181	10.2	72
Taldur glacier	49.817514	87.716003	2968	412	4.9	56
Potanin glacier	49.154196	87.874787	3459	387	4.8	57
Tomort peak	43.214871	94.239697	3972	111	10.0	68
Tomort peak	43.214871	94.239697	3983	111	10.0	68
Tomort peak	43.021123	94.304215	4034	111	10.0	68
Topografov peak-North	52.517122	98.773056	2684	488	6.7	70
Topografov peak-North	52.516565	98.809538	2550	488	6.7	70
Topografov peak-North	52.507467	98.808292	2543	488	6.7	70
Topografov peak-South	52.499411	98.839464	2602	483	6.2	71
Topografov peak-South	52.466862	98.795974	2534	483	6.2	71
Transbaikalia	56.880323	117.520653	2576	402	7.6	73
Transbaikalia	56.877943	117.540413	2357	402	7.6	73
Transbaikalia	56.887536	117.577484	2275	402	7.6	73
Tsengel Hairhan	48.625752	89.112385	3182	260	6.9	61
Turgen peak	49.664062	91.368397	3341	356	5.8	60
Turgen peak	49.654316	91.484847	3355	356	5.8	60
Turgen peak	49.716592	91.342580	3310	356	5.8	60

2.11 DISCUSSION IN PART II

We expect that the ^{10}Be ages from Darhad basin and the corresponding ELAs for the local maximum glacial (LGM_L) advances should correlate well with the glaciations in the adjacent areas based on four reasons: 1) The seasonality of precipitation is similar, hence the glacier accumulation regime is likely similar also (e.g. Sakai *et al.* 2015; supplementary material); 2) The modern ELAs show a consistent pattern of smooth variation, changing only with latitude; 3) The sensitivity of glaciers in the region is expected to be similar (e.g. Rupper and Roe, 2008) because they are mostly controlled by changes in temperature, which is less spatially heterogeneous than precipitation; 4) General circulation models show that both precipitation and temperature exhibited low variability during MIS 2 in northern Mongolia (e.g. Rupper and Koppes 2010), suggesting that the amplitude of climate forcing was similar from place to place.

A large number (67) of ^{10}Be ages for glacial deposits, at least 2–5 per moraine, has now been determined for the southern and northern limits of the East Sayan ice field (Gillespie *et al.* 2008; Arzhannikov *et al.* 2012; this study). This dataset not only constructs a regional chronology of glacial advances around Darhad basin, but also allows detailed comparison of glacial extents during various times, for example the small difference in the ELA during MIS 3 and MIS 2. These temporal and spatial patterns of glaciations in the Darhad region is similar to those in the Hangai (Rother *et al.* 2014; this study; summarized in Figure 2.22) suggesting that climate variations and the response of glaciers to them over all of north-central Mongolia have been similar, or smoothly varying. Palynological analysis of ^{14}C-dated lake sediments from Kotokel lake, east of Lake Baikal (Bezrukova *et al.* 2010), suggests that a cold and harsh climate dominated much of MIS 3, between ~45 and 35 ka, followed by drier conditions during MIS 2, at ~30–17 ka. This climate pattern of

cold intervals both in MIS 3 and 2 is consistent with the glacial records from the Darhad and Hangai regions.

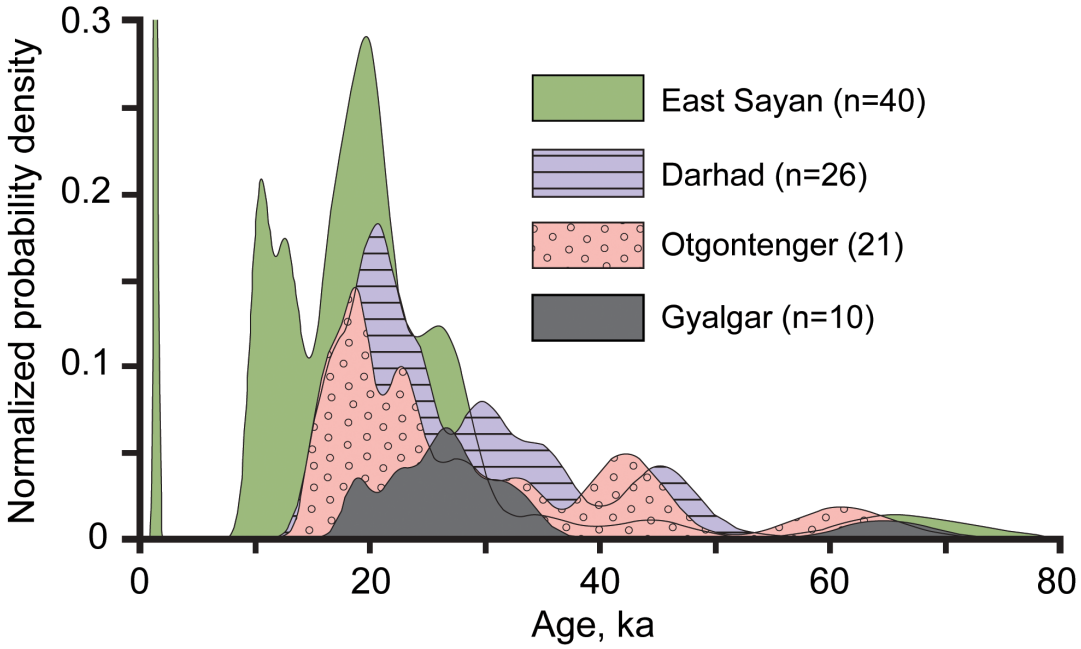

Figure 2.22. Summed normal distribution density of the 97 ^{10}Be cosmic-ray exposure ages discussed in this article. The Sayan mountain group includes the ages from Jombolok, Sailag (of 13 samples from Arzhannikov *et al.* 2012), Oka rivers, and Mönh Saridag peak. Darhad basin group includes the ages from Gillespie *et al.* (2008) and new ages from the Hoit Aguy massif and the Tengis terminal moraine. Otgontenger mountain ages are all from Rother *et al.* (2014). Gyalgar mountain ages are first reported in this article.

The two ^{10}Be ages for the eroded end moraine in the Sarig valley overlap within 2σ error and are direct evidence that the Tengis glacier crossed the Maly Yenisei during the LGM_G. On the east of the Maly Yenisei Gillespie *et al.* (2008) dated two boulders sitting on a wind gap at 1638 m asl to ~22 ka, supporting the two ^{10}Be ages from the Tengis end moraine. However, the two ^{10}Be ages from the wind gap barely overlap with each other within 2σ error, and the CRE dating

of moraine boulders around Darhad basin (Gillespie *et al.* 2008) showed that there is a considerable variability of CRE ages from boulder to boulder. The high variability of CRE ages for moraine boulders around Darhad basin may suggest that the MIS 2 glaciers were stable for a long time that the boulders were deposited at different times over the span of a few thousand years.

There are beach sands at 1711 m asl on the basin wall 2.7 km south of the left-lateral Jarai moraines (Gillespie *et al.* 2008) suggesting a 175-m deep lake. This lake would have overtopped both of the Jarai piedmont moraines, for which there is no direct evidence (Gillespie *et al.* 2008). However, a lakeshore was eroded into the younger moraine at 1679 m. Therefore, it appears that the 1711-m beach dated from early in MIS 2 and the MIS 2 lake had begun to lower by ~18 ka, or that 1679 m asl was the maximum MIS 2 highstand and the 1711-m highstand dated from MIS 3 or earlier. The luminescence-dated beach sands at ~1670 m asl near the Arsain river suggests that the lake was at least 145 m deep at ~14 ka. This was likely the same highstand that left the 1679 m shoreline on the Jarai moraine, and together these sites and shorelines suggest the MIS 2 lake was high, perhaps episodically, from 18 to 14 ka. It is unlikely that a continuous deep lake preceded the first Jarai moraine, since it would then likely have terminated in a calving front, and the presence of the moraine suggests that it did not.

Because the piedmont moraines at Jarai river and the Tengis end moraine at Sarig valley all date from the LGM_G, but the lake core and Shargyn cutbank evidence show older lake sediments from MIS 3, the question as to the presence of a MIS 3 moraine arises. At Hoit Aguy, the dated MIS 3 glacier was bigger than the putative MIS 2 glacier, and this suggests that the Jarai and Tengis glaciers then must have left moraine complexes roughly as large as the one from MIS 2, but if so they have not been found, and we did not see any evidence of other moraines on 15-m ASTER images. If the MIS 3 moraines were deposited close to the position of the future MIS 2

end moraines, they could have been buried. Alternatively, the MIS 3 end moraine in Sarig valley could have been placed further up valley, beyond where we traveled, or the MIS 3 glacier may have extended farther down the Maly Yenisei, its moraines having been eroded in subsequent outburst floods. However, the luminescence ages for the lake sediments in the DBC1 core do confirm the presence of a lake in Darhad during both MIS 3 and MIS 2.

Darhad basin is located at the western end of the Baikal rift, and on the eastern side of the basin an active normal fault offsets the 23.7 ± 1.5 ka Jarai moraine by 7–7.7 m (Bacon *et al.* 2003), which equates to an average slip rate of 0.31 ± 0.02 m ka^{-1}. The lake sediments at 76.9 m depth in the DBC1 core was dated to 139.6 ± 15.8 ka, a sedimentation rate of at least 0.56 ± 0.05 m ka^{-1}, not accounting for compression and erosion of the lake sediments. The subsidence of the basin floor should be more than the sedimentation in order to accommodate >200 m thick sediments. We propose that the subsidence of Darhad basin is not uniform, and the inconsistent subsidence and uplift rates are due to "hinging" of the basin on its western margin, where surficial evidence of faulting is less pronounced than on the east side. This mechanism requires that the Ulaan Taiga in the east must be subsiding slower than the Bayan Zürhiin ranges in the west (Figure 2.23).

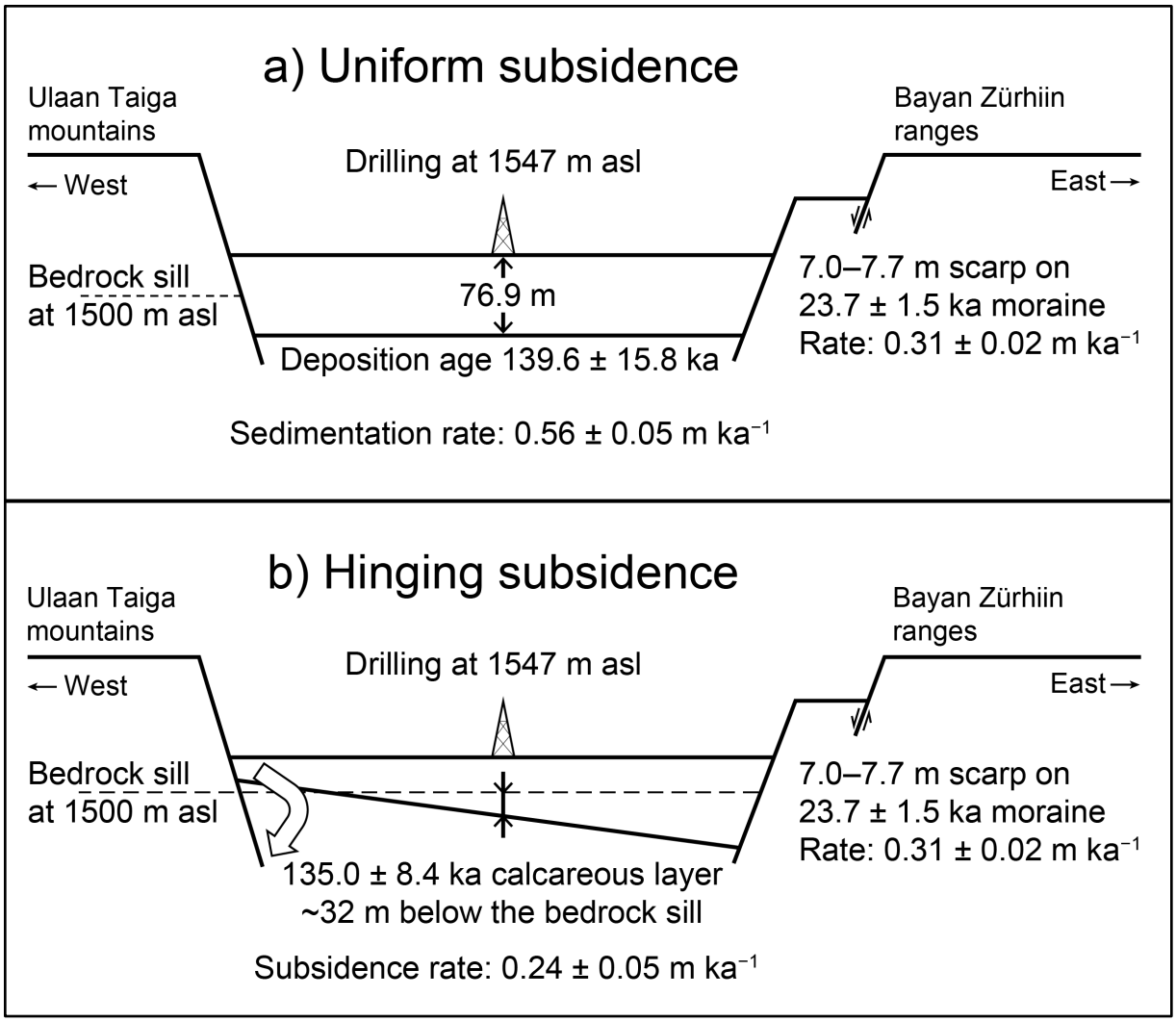

Figure 2.23. Two alternative models for subsidence of the Darhad basin floor. a) Uniform subsidence assumes the same rate applies everywhere; b) Hinging subsidence assumes faster rates on the east than in the west. The subsidence rate would be intermediate in the middle of the basin. The fault scarps on the east side are more distinct and/or larger than on the west.

There is a unique ~1 m thick layer in the DBC1 core at ~79 m depth. The layer consists of finely laminated biogenic carbonates with abundant bivalve clam fossils. The layer is almost devoid of clastic material, which suggests that the thick calcareous layer must have been bio-chemically precipitated in quiet and relatively warm water. The high concentration of the mollusk shells suggests that the lake was shallow at that time. It is a distinct change of depositional

environment from a deep cold lake to a shallow warm lake. The lake silts below the calcareous layer, at 80.1 m depth, was dated to 135.0 ± 8.4 ka. We propose two explanations for the formation of this shallow lake: (1) It was an isolated small lake, similar to the ones found today; (2) It was a basin-wide shallow lake in a tectonically closed basin. The first hypothesis doesn't require any subsidence. However, if the second hypothesis was correct the floor of the basin-wide shallow lake must have been subsiding faster than the sedimentation of the calcareous layer. Another long core from the margins of the basin should reveal whether it was a basin-wide lake or an isolated lake. According to the second hypothesis, a subsidence rate can be estimated from the absolute elevation of the calcareous layer at ~1468 m asl (79 m below the modern ground elevation 1547 m asl). Accounting for the GPS measurement error, the calcareous layer now sits ~32 ± 5 m below the modern sill at ~1500 m asl. In other words, the ground must have subsided 32 m or more since ~135 ka to accommodate the deposition of lake sediments. We estimate the subsidence rate in the centre of Darhad basin as ~0.24 ± 0.05 m ka^{-1} for 10^5-year scale, a consistent value with the "hinged" subsidence model, considering the faster uplift rate in the east of the basin at 0.31 ± 0.02 m ka^{-1} for 10^3-year scale.

2.12 Conclusions to Part II

The East Sayan mountains were glaciated extensively during MIS 2 (19–21 ka), the LGM_L, and outlet glaciers descended through the Tengis river valley and blocked the Maly Yenisei river. Ages for the end moraine in the Sarig valley and lake sediments from Darhad basin floor constrain the timing of the impounding and existence of a deep lake. The beach sands near the Arsain and Jarai rivers constrain the depth of MIS 2 lake to at least 145 m deeper than the spillway of the modern Maly Yenisei river at 1535 m asl (Figure 2.24). This resolves the controversy identified by Krivonogov *et al*. (2005, 2012) that is the main factor behind this paper.

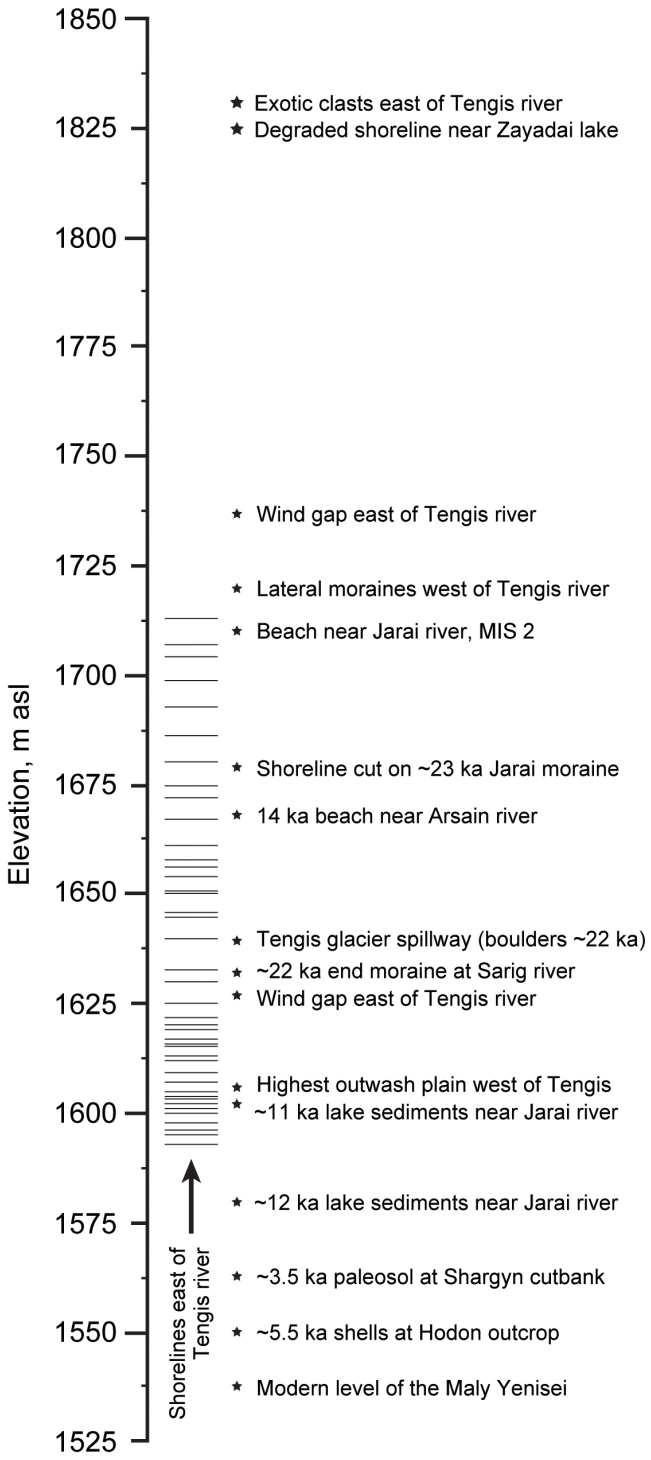

Figure 2.24. Shorelines and highstands of Darhad paleolakes. Elevation of shorelines east of the Tengis river was measured by Krivonogov *et al.* (2005). The shells at Hodon outcrop was analyzed by Krivonogov *et al.* (2012), and we calibrated the radiocarbon ages for comparison with the other ages. The ages from Jarai, Tengis, Shargyn rivers are from Gillespie *et al.* (2008).

The mountains around Darhad basin were also heavily glaciated during MIS 3 (~35–57 ka) and blocked the Maly Yenisei then. At Hoit Aguy, the ELA difference between the dated MIS 3 and nearby MIS 2 (?) moraine was only ~50 m (2290–2240 m asl). It remains possible that the 1710-m paleolake highstand predated the MIS 2 Jarai moraines, in which case it probably dates from MIS 3. Many unconformities and disturbances in the lake sediment record suggest the depth of the Darhad paleolakes fluctuated frequently. The lake drained significantly after ~14 ka, and by ~4 ka Darhad basin was largely dry.

Comparison of palaeo ELAs for glaciers in central Mongolia, East Sayan mountains, and Altai mountains shows that the pattern of strong latitudinal variation of glacier extents persisted both during MIS 3 and MIS 2. Glaciers in central and northern Mongolia appear to have been more sensitive to changes in temperature than in precipitation.

Acknowledgements

We are grateful to the following persons for discussions and assistance with this research: Anastasia Arzhannikova (Siberian Branch, Russian Academy of Sciences), Sergei Arzhannikov (Siberian Branch, Russian Academy of Sciences), A. Bayasgalan (Mongolian University of Science and Technology), Beejinkhuu and his drilling crew (Ulaanbaatar), Raymond (Bud) Burke (Humboldt State University), James Feathers (University of Washington), Andrei Fedotov (Siberian Branch, Russian Academy of Sciences), David Fink (Australian Nuclear Science and Technology Organisation), Carrie Garrison-Laney (University of Washington), Goro Komatsu (Università d'Annunzio, Pescara, Italy), Sergey Krivonogov (Siberian Branch, Russian Academy of Sciences), Ari Matmon (The Hebrew University of Jerusalem), B. Charlotte Schreiber (University of Washington), Vladimir Sheinkman (Siberian Branch, Russian Academy of Sciences), Brian Sherrod (U.S. Geological Survey), and John Stone (University of Washington). We are especially grateful to D. Sukhbaatar and the Damdin Da Fund for the Development of Intellectual Potential (Ulaanbaatar) for continuing logistical support. We thank Victor Baker and Sergei Arzhannikov for insightful and helpful formal reviews.

Funding

Funding for drilling was provided by the Royalty Research Fund of the University of Washington and for CRE analysis by a grant from the Quaternary Research Center (UW). Aspects of the research were also supported by the Terra/ASTER program operated by the Jet Propulsion Laboratory of NASA.

2.13 SUPPLEMENTARY MATERIAL TO CHAPTER 2

2.13.1 *Calculation of ^{10}Be ages*

We calculated ^{10}Be ages with CRONUS (version 2.2, Balco *et al.* 2008) using Heyman's (2014) globally calibrated ^{10}Be production rate of 3.99 ± 0.22 atoms g^{-1} yr^{-1} when referenced to the scaling of Stone (2000). For interpretation of the ages, we accepted the ages calculated with magnetic field-constant scaling scheme of Stone (2000), because the differences between ages calculated with various scaling schemes were less than the average 1σ measurement errors for individual sample (<10%; Table 2.16). In Part 1 (Batbaatar and Gillespie 2016) we also updated the published ^{10}Be ages using the same calculation scheme. Gillespie *et al.* (2008) used a production rate of 5.9 atoms g^{-1} yr^{-1}; Arzhannikov *et al.* (2012) reported using 4.49 ± 0.29 atoms $g^{-1}yr^{-1}$; and Rother *et al.* (2014) used 4.43 ± 0.52 atoms g^{-1} yr^{-1} referenced to Dunai scaling (Dunai 2001). The sea-level production rates were scaled to the latitude and altitude of the sampling sites, with corrections for the sample thickness and topographic shielding in the CRONUS calculator.

2.13.2 *Sensitivity of ^{10}Be ages to erosion*

In calculating apparent ^{10}Be ages, we assumed that boulder erosion had been negligible. Although we sampled apparently uneroded rocks, mainly deposited on the most recent (local last glacial maximum (LGM), or LGM_L) moraines, evidence of boulder erosion on pre-LGM_L moraines in northern Mongolia (e.g. at the Högiin and Jombolok rivers) suggests that slow erosion does occur

there, and our calculated ages are therefore minima. To test the sensitivity of the CRE ages to erosion, we recalculated the ages assuming that the boulder erosion rate was up to 0.5 cm ka^{-1} (e.g. Nichols *et al*. 2006).

The calculated exposure ages of Table 2.14 corrected for erosion are shown in Table 2.17 and summarized graphically in Figure 2.25. Exposure ages of 30 ka that we report in Table 2.14 are as much as 4.5 ka too young, if erosion was at 0.5 cm ka^{-1}. The erosion of ≥0.4 cm ka^{-1} in some of the old samples would have been enough to balance the fresh production of ^{10}Be, so that the concentration does not increase with age. Therefore, the concentration of ^{10}Be "saturates" and it becomes impossible to calculate an apparent age greater than those for surfaces with lower erosion rates, regardless of the actual age.

2.13.3 *Sensitivity of ^{10}Be ages to neutron shielding by snow*

The ^{10}Be ages reported in Table 2.14 have not been corrected for shielding by persistent snow cover. Although the studied moraines were between latitudes 45°N and 53°N, Mongolia is in the arid interior of Asia. Modern annual precipitation in northern Mongolia at the elevations of the glacier termini (~1550 m asl) is 430 mm, ~65% of which is ephemeral summertime snow or rain (CRU 2.0 data: Mitchell and Philip 2005). Conditions were drier and colder there during the LGM, with ~10–50% less precipitation based on the lake-level depression for Hövsgöl lake (Prokopenko *et al*. 2005), and a ~5 K decrease in temperature based on the equilibrium-line altitude depression of ~900 m around Darhad basin (Gillespie *et al*. 2008). A 4-month per year snowpack of 250 mm depth (density 0.3 g cm^{-3}) would increase the exposure age by 2% (Gosse and Phillips 2001), accounting for an increase of ~0.4 ka in apparent age for global LGM (MIS 2) landforms.

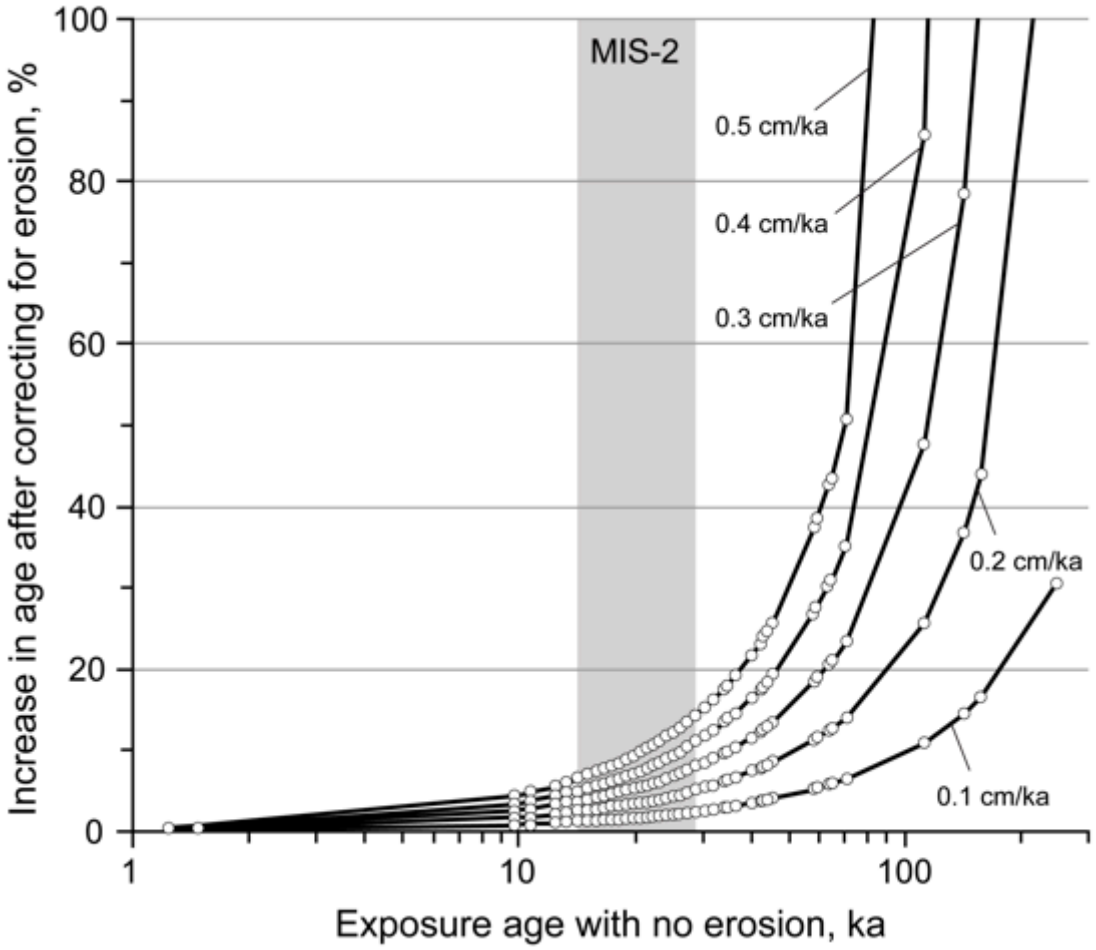

Figure 2.25. Potential increase in the apparent exposure ages (circles) after correcting for various erosion rates. The population includes the new and literature dates from Gillespie *et al*. (2008), Arzhannikov *et al*. (2012), and Rother *et al*. (2014). The increase of the ages by more than 100% is excluded in the plot. The percent increases of the ^{10}Be ages after correction are given in Table 2.17.

Table 2.16. ^{10}Be exposure ages (in ka ± 1σ) for the new samples summarized in Figure 2.22 in the main text calculated using various scaling schemes for spallation. St: Lal (1991)/Stone (2000); De: Desilets and Zreda (2003) and Desilets *et al*. (2006); Du: Dunai (2001); Li: Lifton *et al*. (2005); Lm: Time-dependent Lal (1991)/Stone (2000). The ages shown in bold (St) are discussed in the text. The maximum difference for MIS 2 samples is ~0.8 ka.

Sample ID	**St**	De	Du	Li	Lm
070402-AG-RMS-1	**12.3 ± 0.9**	12.0 ± 1.1	12.1 ± 1.0	11.7 ± 1.0	12.5 ± 0.9
070402-AG-RMS-2-47	**12.3 ± 0.8**	12.0 ± 1.0	12.1 ± 0.9	11.7 ± 0.9	12.5 ± 0.8
070402-AG-RMS-2-64	**13.0 ± 0.9**	12.6 ± 1.0	12.7 ± 1.0	12.3 ± 0.9	13.1 ± 0.8
070402-AG-RMS-3-47	**10.7 ± 0.7**	10.3 ± 0.8	10.4 ± 0.8	10.1 ± 0.8	10.9 ± 0.7
070402-AG-RMS-3-64	**10.5 ± 0.7**	10.2 ± 0.9	10.2 ± 0.8	9.9 ± 0.8	10.7 ± 0.7
070402-AG-RMS-4	**10.4 ± 0.8**	10.1 ± 0.9	10.1 ± 0.9	9.8 ± 0.8	10.6 ± 0.8
070402-AG-RMS-5	**9.7 ± 0.7**	9.4 ± 0.8	9.5 ± 0.8	9.2 ± 0.8	9.9 ± 0.7
070402-AG-RMS-6	**1.5 ± 0.1**	1.5 ± 0.2	1.5 ± 0.2	1.4 ± 0.2	1.5 ± 0.2
070402-AG-RMS-7	**1.2 ± 0.1**	1.2 ± 0.1	1.2 ± 0.1	1.2 ± 0.1	1.3 ± 0.1
070402-AG-RMS-8A	**26.4 ± 1.7**	25.3 ± 2.0	25.4 ± 1.9	24.4 ± 1.8	26.5 ± 1.6
070402-AG-RMS-8B	**20.1 ± 1.3**	19.4 ± 1.5	19.5 ± 1.5	18.8 ± 1.4	20.3 ± 1.2
070402-AG-RMS-9	**28.4 ± 1.8**	27.3 ± 2.1	27.4 ± 2.1	26.3 ± 1.9	28.6 ± 1.7
070802-AG-RSLK-1	**20.9 ± 1.5**	21.3 ± 1.8	21.5 ± 1.8	20.8 ± 1.6	21.1 ± 1.4
070802-AG-RSLK-2	**22.7 ± 1.6**	23.2 ± 2.0	23.4 ± 1.9	22.6 ± 1.8	22.9 ± 1.5
070802-AG-RSLK-3	**20.6 ± 1.4**	21.1 ± 1.8	21.2 ± 1.7	20.6 ± 1.6	20.8 ± 1.4
070802-AG-RSLK-4	**64.4 ± 4.3**	65.5 ± 5.3	65.5 ± 5.2	63.3 ± 4.7	64.5 ± 4.0
070802-AG-RSLK-5	**20.0 ± 1.4**	20.4 ± 1.7	20.6 ± 1.7	19.9 ± 1.6	20.1 ± 1.3
070802-AG-RSLK-6	**14.1 ± 1.0**	14.5 ± 1.2	14.6 ± 1.2	14.2 ± 1.1	14.3 ± 1.0
070802-AG-RSLK-7	**16.5 ± 1.1**	16.8 ± 1.4	17.0 ± 1.3	16.5 ± 1.2	16.6 ± 1.0
070802-AG-RSLK-8	**12.4 ± 1.3**	12.8 ± 1.5	12.9 ± 1.5	12.6 ± 1.4	12.6 ± 1.3
070802-AG-RSLK-10	**18.7 ± 1.3**	19.2 ± 1.6	19.3 ± 1.6	18.7 ± 1.5	18.9 ± 1.3
071002-AG-RDJO-1	**19.8 ± 1.4**	20.3 ± 1.7	20.4 ± 1.7	19.8 ± 1.6	20.0 ± 1.4
071002-AG-RDJO-2	**20.8 ± 1.5**	21.2 ± 1.8	21.4 ± 1.8	20.7 ± 1.6	20.9 ± 1.4
071002-AG-RDJO-3	**34.5 ± 3.0**	35.2 ± 3.4	35.3 ± 3.4	34.1 ± 3.2	34.6 ± 2.9
071002-AG-RDJO-5	**23.0 ± 2.1**	23.5 ± 2.4	23.6 ± 2.4	22.9 ± 2.2	23.1 ± 2.0
071002-AG-RDJO-6	**18.8 ± 1.3**	19.3 ± 1.6	19.4 ± 1.6	18.8 ± 1.4	19.0 ± 1.2
071202-AG-ROKA-6	**16.5 ± 1.2**	16.8 ± 1.5	17.0 ± 1.4	16.5 ± 1.3	16.6 ± 1.2
080709-HA-JB-02	**36.1 ± 2.3**	35.3 ± 2.3	35.3 ± 2.7	33.9 ± 2.4	36.1 ± 2.1
080709-HA-JB-03	**34.0 ± 2.5**	33.3 ± 2.9	33.3 ± 2.8	32.0 ± 2.6	34.1 ± 2.4
150707-DB-AG-003A	**23.8 ± 1.5**	24.2 ± 1.9	24.4 ± 1.8	23.6 ± 1.7	24.0 ± 1.4
150707-DB-AG-003C	**20.7 ± 1.4**	21.0 ± 1.7	21.2 ± 1.7	20.6 ± 1.5	20.8 ± 1.3
ZAG-ARG-01A	**24.4 ± 1.6**	23.5 ± 1.9	23.6 ± 1.9	23.1 ± 1.7	24.2 ± 1.5
ZAG-ARG-01B	**20.2 ± 1.3**	19.6 ± 1.5	19.7 ± 1.5	19.3 ± 1.4	20.1 ± 1.2
ZAG-ARG-02B	**17.2 ± 1.2**	17.0 ± 1.4	17.1 ± 1.4	16.8 ± 1.3	17.2 ± 1.1
ZAG-ARG-03A	**22.6 ± 1.8**	22. ± 12.1	22.3 ± 2.0	21.8 ± 1.9	22.5 ± 1.7
ZAG-ARG-03B	**158.3 ± 11.4**	150.4 ± 13.1	150.6 ± 12.7	145.2 ± 11.7	154.1 ± 10.6
ZAG-ARG-04B	**27.6 ± 1.8**	26.7 ± 2.2	26.8 ± 2.1	26.2 ± 2.0	27.3 ± 1.7
ZAG-SB-04A	**30.0 ± 1.9**	29.0 ± 2.3	29.1 ± 2.2	28.4 ± 2.0	29.7 ± 1.7
ZAG-SB-04B	**58.5 ± 3.5**	55.9 ± 4.3	56.0 ± 4.1	54.2 ± 3.8	57.5 ± 3.2
ZAG-SB-04C	**24.5 ± 1.5**	23.8 ± 1.9	23.9 ± 1.8	23.4 ± 1.7	24.3 ± 1.4
ZAG-SB-05	**158.1 ± 9.8**	149.4 ± 11.7	149.61 ± 1.3	144.1 ± 10.2	154.0 ± 8.8

Table 2.17. Increase in the calculated exposure ages after correcting for various erosion rates. Tabulated samples are those newly dated for this paper. Exposure ages are calculated using the time-constant spallation scaling scheme of Stone (2000). The highest erosion rate of 0.5 cm ka^{-1} will decrease an uncorrected MIS 2 ages by 4 ka at most.

Sample ID	Exposure age with no erosion (ka ± 1σ)	% Increase in age for various erosion rates				
		0.1 cm ka^{-1}	0.2 cm ka^{-1}	0.3 cm ka^{-1}	0.4 cm ka^{-1}	0.5 cm ka^{-1}
070402-AG-RMS-1	12.3 ± 0.9	1.1	2.1	3.2	4.4	5.5
070402-AG-RMS-2-47	12.3 ± 0.8	1.0	2.1	3.2	4.4	5.5
070402-AG-RMS-2-64	13.0 ± 0.9	1.1	2.3	3.5	4.7	6.0
070402-AG-RMS-3-47	10.7 ± 0.7	0.9	1.8	2.8	3.8	4.8
070402-AG-RMS-3-64	10.5 ± 0.7	0.9	1.8	2.8	3.7	4.7
070402-AG-RMS-4	10.4 ± 0.8	0.9	1.8	2.7	3.7	4.6
070402-AG-RMS-5	9.7 ± 0.7	0.8	1.7	2.5	3.4	4.3
070402-AG-RMS-6	1.5 ± 0.1	0.1	0.3	0.4	0.5	0.7
070402-AG-RMS-7	1.2 ± 0.1	0.1	0.2	0.3	0.4	0.5
070402-AG-RMS-8A	26.4 ± 1.7	2.3	4.7	7.3	10.0	13.0
070402-AG-RMS-8B	20.1 ± 1.3	1.7	3.5	5.4	7.4	9.5
070402-AG-RMS-9	28.4 ± 1.8	2.5	5.1	7.9	11.0	14.2
070802-AG-RSLK-1	20.9 ± 1.5	1.8	3.6	5.6	7.7	9.8
070802-AG-RSLK-2	22.7 ± 1.6	1.9	4.0	6.1	8.4	10.8
070802-AG-RSLK-3	19.8 ± 1.4	1.8	3.6	5.5	7.5	9.7
070802-AG-RSLK-4	64.4 ± 4.3	5.8	12.6	20.8	30.7	43.4
070802-AG-RSLK-5	20.0 ± 1.4	1.7	3.5	5.3	7.3	9.3
070802-AG-RSLK-6	14.1 ± 1.0	1.2	2.4	3.7	5.0	6.4
070802-AG-RSLK-7	16.5 ± 1.1	1.4	2.8	4.3	5.9	7.5
070802-AG-RSLK-8	12.4 ± 1.3	1.0	2.1	3.2	4.4	5.5
070802-AG-RSLK-10	18.7 ± 1.3	1.6	3.3	5.0	6.8	8.7
071002-AG-RDJO-1	19.8 ± 1.4	1.7	3.4	5.3	7.2	9.3
071002-AG-RDJO-2	20.8 ± 1.5	1.8	3.6	5.6	7.6	9.8
071002-AG-RDJO-3	34.5 ± 3.0	3.0	6.2	9.7	13.6	17.8
071002-AG-RDJO-5	23.0 ± 2.1	2.0	4.0	6.2	8.5	11.0
071002-AG-RDJO-6	18.8 ± 1.3	1.6	3.3	5.0	6.8	8.7
071202-AG-ROKA-6	16.1 ± 1.2	1.4	2.8	4.3	5.9	7.5
080709-HA-JB-02	36.1 ± 2.3	3.1	6.6	10.3	14.5	19.1
080709-HA-JB-03	34.0 ± 2.5	3.0	6.2	9.7	13.5	17.7
150707-DB-AG-003A	23.8 ± 1.5	2.0	4.2	6.5	8.9	11.5
150707-DB-AG-003C	20.7 ± 1.4	1.8	3.6	5.5	7.6	9.7
ZAG-ARG-01A	24.4 ± 1.6	2.1	4.3	6.7	9.2	11.8
ZAG-ARG-01B	20.2 ± 1.3	1.7	3.5	5.4	7.4	9.5
ZAG-ARG-02B	17.2 ± 1.2	1.5	3.0	4.6	6.2	8.0
ZAG-ARG-03A	22.6 ± 1.8	1.9	4.0	6.1	8.4	10.8
ZAG-ARG-03B	158.3 ± 11.4	16.6	43.9	105.1	saturated	saturated
ZAG-ARG-04B	27.6 ± 1.8	2.4	4.9	7.6	10.5	13.7
ZAG-SB-04A	30.0 ± 1.9	2.6	5.4	8.4	11.6	15.1
ZAG-SB-04B	58.5 ± 3.5	5.3	11.4	18.5	27.1	37.6
ZAG-SB-04C	24.5 ± 1.5	2.1	4.3	6.7	9.2	11.9
ZAG-SB-05	158.1 ± 9.8	16.6	43.9	105.1	saturated	saturated

2.13.4 *Modern ELA and climate in the vicinity of Darhad basin*

The dating of some of the moraines from Darhad basin so far has been problematical (cf. Gillespie et al., 2008). Only a handful of ^{10}Be ages have been determined for each moraine, and for some moraines the ages have scattered greatly relative to their precisions, likely due to geological complications such as inheritance and/or solifluction that were not recognized during sampling. Telecorrelation with nearby dated moraines from the same glaciation could improve our confidence in the ages, except that relative dating and soil development may not be trustworthy indicators of surface age in areas of permafrost, such as northern Mongolia, and the age of the LGM_L itself appears to vary significantly from place to place in Central Asia on a scale of 500 km or more (Koppes *et al*. 2008; Rupper *et al.* 2009). Therefore, the best approach for telecorrelating the moraine ages is to limit the telecorrelation between moraines to separations less than 500 km, and to limit comparisons to moraines having the same equilibrium-line altitude (ELAs), assuming that ELAs that differ by no more than the technique precision (~100 m: e.g., Meierding 1982; Gillespie 1991) probably refer to the same climatic episode, and that the numerical ages for the different moraines can be grouped to improve their reliability.

However, before correlating moraines in northern Mongolia it is necessary first to establish the scale of climatic variability there, since the ~500 km scale from Rupper *et al.* (2009) was imposed by the resolution of the climate models they had access to. To do this, we first estimated ELAs for moraine sequences for a few hundred km around Darhad basin, and then fit trend lines to them. We argue that if the trend lines show no erratic fluctuations such as observed by Rupper *et al*. (2009) it is helpful to assess timing of maximum glacial extents for Darhad in the context of chronosequences for the surrounding mountain ranges.

For this purpose, we dated moraine sequences near the highest peak of the East Sayan ice field, Mönh Saridag, which hosts a small active cirque glacier. We also dated moraine sequences in the Jombolok, Sailag, and Oka river valleys to determine a chronosequence for the East Sayan ice field independent of the Tengis glaciers. Komatsu *et al.* (2009) proposed another location for an ice dam on the Maly Yenisei – the outlet glacier that descended the Hadar Üüs river valley, west of the Hoit Aguy massif (Figure 2.7). We present a new ^{10}Be age for a moraine in Hoit Aguy, which was not covered by the East Sayan ice field, in order to provide local control on the ELA for the glacier, and to estimate the local ELA independent of complicating factors due to the ice field itself. To the south, ~300 km from Darhad basin, we dated moraine sequences near Gyalgar peak to help provide the regional pattern of glacial extents during MIS 2.

The modern climate in the vicinity (~1000 km) of Darhad basin is described from the reanalysis climate data (CRU TS version 3.23; Harris *et al.* 2014) and shown in Figures 2.26 and 2.27. The annual precipitation decreases with latitude in the vicinity of Darhad basin. There is no apparent correlation between the precipitation and longitude. In the region, 50–70% of the annual precipitation falls in summer, suggesting a similar accumulation regime of the glaciers there (Figure 2.26 c, d; Sakai *et al.* 2015).

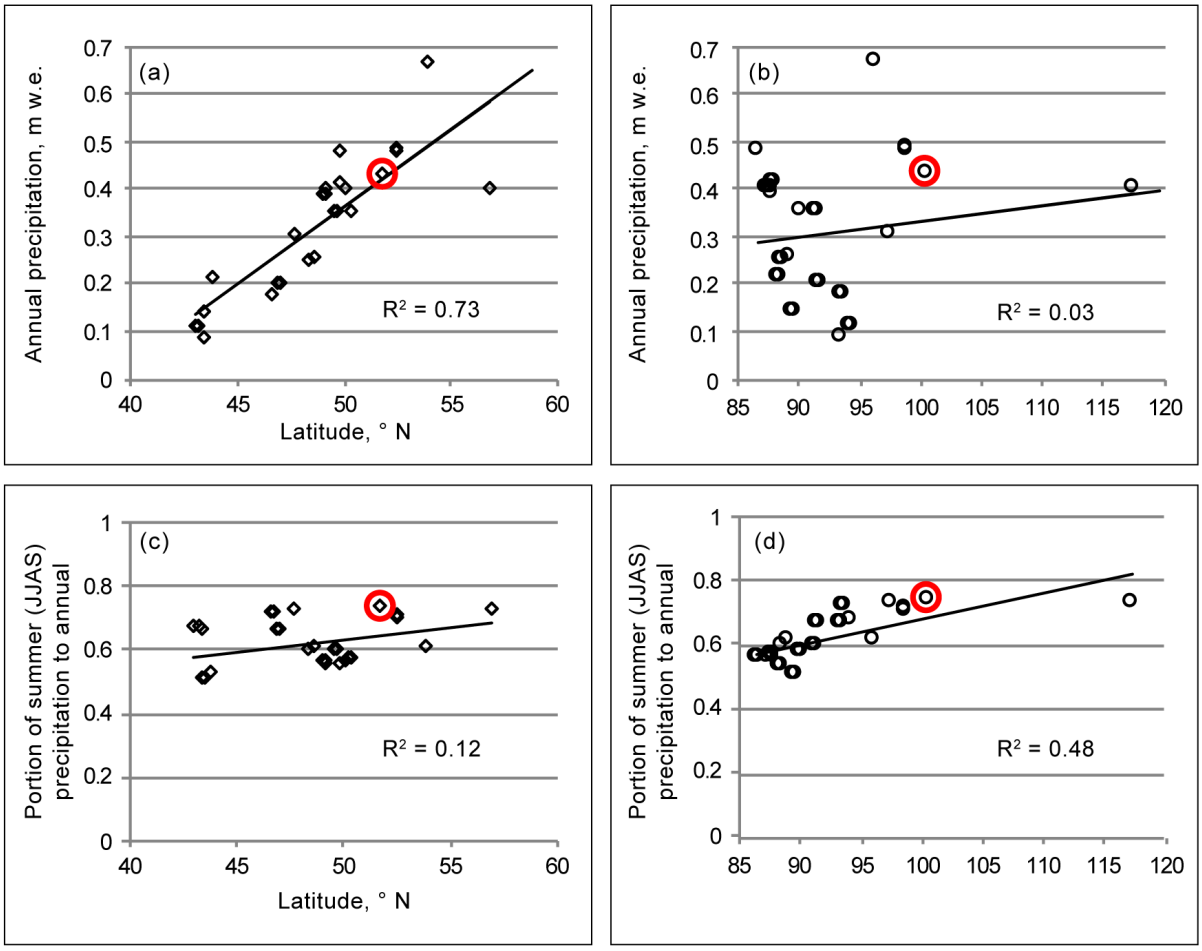

Figure 2.26. The relationship between the latitude and longitude and the precipitation in the vicinity of Darhad basin, showing the annual precipitation rate (w.e. = water equivalent) in relation to (a) latitude and (b) longitude. The portion of summer (JJAS) precipitation is shown in relation to (c) latitude and (d) longitude. The precipitation data are for the 0.5° grid of the CRU data (Harris *et al*. 2014) that includes the mountain range with the calculated ELA. R^2 refers to the correlation coefficient for the linear regression line. The red circle shows the data for the modern glacier on Mönh Saridag, the peak closest to Darhad basin.

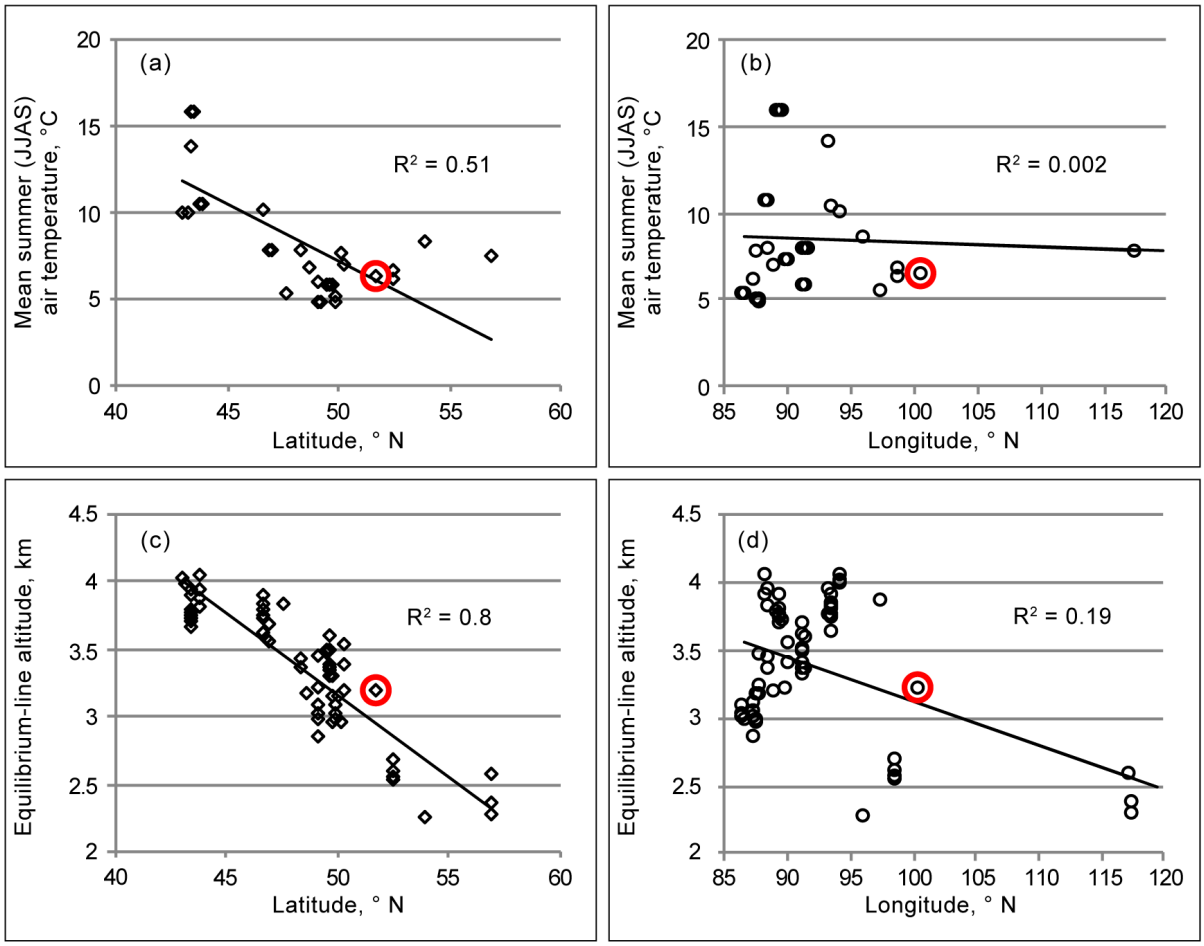

Figure 2.27. Summer (JJAS) temperature and the ELA in the vicinity of Darhad basin. The summer temperature is shown in relation to (a) latitude and (b) longitude. ELA is shown in relation to (c) latitude and (d) longitude. The precipitation data are for the 0.5° grid of the CRU data (Harris *et al*. 2014) that includes the mountain range with the calculated ELA. R^2 refers to the correlation coefficient for the linear regression line. The red circle shows the data for the modern glacier on Mönh Saridag, the peak closest to Darhad basin.

Summer temperature increases with the lowering of latitude (Figure 2.27a). The ELA corresponds strongly to this trend, lowering at a rate ~150 m per degree of decrease in latitude (Figure 2.27c). There is no apparent correlation between the summer air temperature and longitude (Figure 2.27b), which results the similar low variability of ELA with longitude (Figure 2.27d). The air temperature is regulated by solar insolation as a function of latitude and the strong correlation between summer temperature and the ELA suggests that the glaciers in the mountain ranges within ~1000 km of Darhad basin respond mostly to changes in temperature. The ELA and the precipitation for the same showed no correlation ($R^2 = 0.06$), suggesting that the glaciers in the region do not vary much due to changes in precipitation.

2.14 REFERENCES IN CHAPTER 2: PART II

Adamiec, G., and Aitken, M., (1998), Dose-rate conversion factors: update: Ancient TL, v. 16, no. 2, p. 37–50.

Andrews, J.T., (1975), Glacial Systems. An Approach to Glaciers and their Environments: North Scituate, MA, Duxbury Press.

Arnold, L.J., Bailey, R.M., Tucker, G.E., (2007), Statistical treatment of fluvial dose distributions from southern Colorado arroyo deposits: Quaternary Chronology, v. 2, p. 162–167.

Arzhannikov, S.G., Braucher, R., Jolivet, M., Arzhannikova, A.V., Vassallo, R., Chauvet, A., Bourlès, D., Chauvet, F., (2012), History of late Pleistocene glaciations in the central Sayan-Tuva Upland (southern Siberia): Quaternary Science Reviews, v. 49, p. 16-32.

Auclair, M., Lamothe, M., Huot, S., (2003), Measurement of anomalous fading for feldspar IRSL using SAR: Radiation Measurements, v. 37, p. 487–492.

Bacon, S.N., Bayasgalan, A., Gillespie, A., Raymond, B., (2003), Paleoseismic displacement from landform subjected to periglacial processes: Observations along the Jarai Gol fault near the Tamyn Am Hills, Darhad Depression, northern Mongolia: XVI INQUA Congress, Geological Society of America Abstracts with Programs, p. 103.

Balco, G., (2006), Converting Al and Be isotope ratio measurements to nuclide concentrations in quartz: Documentation for CRONUS-Earth Calculator, version 2.2. Online: http://hess.ess.washington.edu/math/docs/al_be_v22/al_be_docs.html.

Balco, G., Stone, J.O., Lifton, N.A., Dunai, T.J., (2008), A complete and easily accessible means of calculating surface exposure ages or erosion rates from ^{10}Be and ^{26}Al measurements: Quaternary Geochronology, v. 3, p. 174–195.

Banerjee, D., Murray, A.S., Bøtter-Jensen, L., Lang, A., (2001), Equivalent dose estimation using a single aliquot of polymineral fine grains: Radiation Measurements, v. 33(1), p. 73–94.

Batbaatar, J., and Gillespie, A.R., (2016), Outburst floods of the Maly Yenisei. Part I – review: International Geology Review. doi:10.1080/00206814.2015.1114908

Batbaatar, J., Gillespie, A.R., Schreiber, B C., (2012), Tectonics and environment at the western end of the Baikal rift: Paleolake sediment record from Darhad Basin, northern Mongolia: Geological Society of America Abstracts with Programs, v. 44, no. 3, p. 56.

Bezrukova, E.V., Tarasov, P.E., Solovieva, N., Krivonogov, S.K., Riedel, F., (2010), Last glacial-interglacial vegetation and environmental dynamics in southern Siberia: chronology, forcing and feedbacks: Palaeogeography, Palaeoclimatology, Palaeoecology, v. 296, p. 185–198.

Cejudo-Figueiras, C., Morales, E.A., Wetzel, C.E., Blanco, S., Hoffmann, L., Ector, L., (2011), Analysis of the type of Fragilaria construens var. subsalina (Bacillariophyceae) and description of two morphologically related taxa from Europe and the United States: Phycologia, v. 50 (1), p. 67–77.

Charlesworth, J.K., (1957), The Quaternary Era: London, Edward Arnold, 2 vols, 591 pp. and 1700 pp.

Clauser, C., and Huenges, E., (1995), Thermal conductivity of rocks and minerals, *in* Ahrens, T.J., ed., Rock physics and phase relations: A handbook of physical constants: Washington DC, American Geophysical Union Reference Shelf, v. 3, p. 105–126.

Cortes, D.D., Martin, A.I., Yun, T.S., Francisca, F.M., Santamarina, J.C., Ruppel, C., (2009), Thermal conductivity of hydrate-bearing sediments: Journal of Geophysical Research, v. 114, B11103, p. 1–10.

Desilets, D., and Zreda, M., (2003), Spatial and temporal distribution of secondary cosmic-ray nucleon intensities and applications to in-situ cosmogenic dating: Earth and Planetary Science Letters, v. 206, p. 21–42.

Desilets, D., Zreda, M., Prabu, T., 2006, Extended scaling factors for in situ cosmogenic nuclides: new measurements at low latitude: Earth and Planetary Science Letters, v. 246, p. 265–276.

Ditchburn, R.G. and Whitehead, N.E., (1994), The separation of ^{10}Be from silicates: 3d Workshop of the South Pacific Environmental Radioactivity Association, p. 4-7.

Dunai, T., (2001), Influence of secular variation of the geomagnetic field on production rates of in situ produced cosmogenic nuclides: Earth and Planetary Science Letters, v. 193, p. 197–212.

Edlund, M.B., Williams, R.M., Soninkhishig, N., (2003), The planktonic diatom diversity of ancient Lake Hovsgol, Mongolia: Phycologia, v. 42, p. 232–260.

Farr, T.G., Rosen, P.A., Caro, E., Crippen, R., Duren, R., Hensley, S., Kobrick, M., Paller, M., Rodriguez, E., Roth, L., Seal, D., Shaffer, S., Shimada, J., Umland, J., Werner, M., Oskin, M., Burbank, D., Alsdorf, D., (2007), The Shuttle Radar Topography Mission: Reviews of Geophysics, v. 45, RG2004, p. 1–33.

Feathers, J.K., Casson, M.A., Henck, A.S., Chithambo, M.L., (2012), Application of pulsed OSL to polymineral fine-grained samples: Radiation Measurements, v. 47, p. 201–209.

Feathers, J.K., and Pagonis, V., (2015), Dating quartz near saturation – Simulations and application at archaeological sites in South Africa and South Carolina: Quaternary Geochronology, v. 30, p. 416–421.

Fridleifsson, I.B., Bertani, R., Huenges, E., Lund, J.W., Rybach, L., (2008), The possible role and contribution of geothermal energy to the mitigation of climate change, *in* Hohmeyer, O., and Trittin, T., eds., Proceedings of IPCC Scoping meetings on renewable energy sources, Lübeck, Germany, p. 59–80.

Galbraith, R.F., and Roberts, R.G., (2012), Statistical aspects of equivalent dose and error calculation and display in OSL dating: an overview and some recommendations: Quaternary Geochronology, v. 11, p. 1–27.

Gillespie, A.R., (1991), Testing a new climatic interpretation for the Tahoe glaciation, *in* Hall Jr., C.A., Doyle-Jones, V., and Widawski, B., eds, Natural History of Eastern California and High-Altitude Research, White Mountain Research Station Symposium Volume 3: Los Angeles, CA, University of California, p. 383–398.

Gillespie, A.R., and Molnar, P., (1995), Asynchronous maximum advances of mountain and continental glaciers: Reviews of Geophysics, v. 33, p. 311–364. doi:10.1029/95RG00995

Gillespie, A.R., Rupper, S., Roe, G., (2003), Climatic interpretation from mountain glaciations in Central Asia: Geological Society of America Abstracts with Programs, v. 35, p. 414.

Gillespie, A.R., Burke, R.M., Komatsu, G., Bayasgalan, A., (2008), Late Pleistocene glaciers in Darhad Basin, northern Mongolia: Quaternary Research v. 69, p. 169–187.

Gravis, G.F., and Lisun, A.M., (1974), Ritmostratigrafiya chetvertichnykh otlozheniy Mongoliy po palinologicheskim dannym i istoriya razvitiya mnogoletnemerzlykh gornykh porod (Rhythmic-stratigraphy of Quaternary sediments in Mongolia according to palynological

evidence and evolution history of permafrost), *in* Melnikov, P.I., ed., Geocryological conditions of Mongolian People's Republic, Transactions of the Joint Soviet-Mongolian Scientific-Research Geological Expedition, v. 10: Moscow, Nauka, p. 148–186. (in Russian)

Gross, G., Kerschner, H., Patzelt, G., (1976), Methodische Untersuchungen über die Schneegrenze in alpinen Gletschergebieten: Zeitschrift für Gletscherkunde und Glazialgeologie, v. 12, p. 223–251.

Gosse, J.C., and Phillips, F.M., (2001), Terrestrial in situ cosmogenic nuclides: theory and application: Quaternary Science Reviews, v. 20, p. 1475–1560.

Grosswald, M.G., and Rudoy, A.N., (1996), Quaternary glacier-dammed lakes in the mountains of Siberia: Polar Geography, v. 20, p. 180–198.

Guiry, M.D., and Guiry, G.M., (2015), AlgaeBase. World-wide electronic publication, National University of Ireland, Galway: http://www.algaebase.org; searched in September, 2015.

Hallet, B., and Putkonen, J., (1994), Surface dating of dynamic landforms: Young boulders and aging moraines: Science, v. 265, p. 937–940.

Harris, I., Jones, P.D., Osborn, T.J., Lister, D.H., (2014), Updated high-resolution grids of monthly climatic observations – the CRU TS3.10 Dataset: International Journal of Climatology, v. 34, p. 623–642.

Heyman, J., (2014), Paleoglaciation of the Tibetan Plateau and surrounding mountains based on exposure ages and ELA depression estimates: Quaternary Science Reviews, v. 91, p. 30–41.

Hülle, D., Hilgers, A., Radtke, U., Stolz, C., Hempelmann, N., Grunert, J., Felauer, T., Lehmkuhl, F., (2010), OSL dating of sediments from the Gobi Desert, Southern Mongolia: Quaternary Geochronology, v. 5, p. 107–113.

Huntley, D.J., and Lamothe, M., (2001), Ubiquity of anomalous fading in K-feldspars and the measurement and correction for it in optical dating: Canadian Journal of Earth Sciences, v. 38, p. 1093–1106.

Ishikawa, M., and Yamkhin, J., (2015), Formation chronology of Arsain pingo, Darhad basin, northern Mongolia: Permafrost and Periglacial Processes, doi: 10.1002/ppp.1877.

Janz, L., Feathers, J.K., Burr, G.S., (2015), Dating surface assemblages using pottery and eggshell: assessing radiocarbon and luminescence techniques in Northeast Asia: Journal of Archaeological Science, v. 57, p. 119–129.

Komatsu, G., Arzhannikov, S. G., Gillespie, A. R., Burke, R. M., Miyamoto, H., Baker, V. R., (2009), Quaternary paleolake formation and cataclysmic flooding along the upper Yenisei River: Geomorphology, v. 104, p. 143–164.

Koppes, M., Gillespie, A.R., Burke, R.M., Thompson, S.C., Stone, J., (2008), Late Quaternary glaciation in the Kyrgyz Tien Shan: Quaternary Science Reviews, v. 27, p. 846–866. doi:10.1016/j.quascirev.2008.01.009

Krivonogov, S.K., Sheinkman, V.S., Mistryukov, A.A., (2005), Ice damming of the Darhad paleolake (northern Mongolia) during the Late Pleistocene: Quaternary International, v. 136, p. 83–94.

Krivonogov, S.K., Yi, S., Kashiwaya, K., Kim, J.C., Narantsetseg, T., Oyunchimeg, T., Safonova, I.Y., Kazansky, A.Y., Sitnikova, T., Kim, J.Y., Hasebe, N., (2012), Solved and unsolved problems of sedimentation, glaciation and paleolakes of the Darhad Basin, Northern Mongolia: Quaternary Science Reviews, v. 56, p. 142–163.

Lal, D., (1991), Cosmic ray labeling of erosion surfaces: in situ nuclide production rates and erosion models: Earth and Planetary Science Letters, v. 104, p. 424–439.

Lehmkuhl F., Hilgers, A., Fries, S., Hülle, D., Schlütz, F., Shumilovskikh, L., Felauer, T., Protze, J., (2011), Holocene geomorphological processes and soil development as indicators for environmental change around Karakorum, Upper Orkhon Valley (Central Mongolia): Catena, v. 87, p. 31–44.

Lifton, N.A., Bieber, J.W., Clem, J.M., Duldig, M.L., Evenson, P., Humble, J.E., Pyle, R., (2005), Addressing solar modulation and long-term uncertainties in scaling in situ cosmogenic nuclide production rates: Earth and Planetary Science Letters, v. 239, p. 140–161.

Lisiecki, L.E., and Raymo, M.E., (2005), A Pliocene-Pleistocene stack of 57 globally distributed benthic $\delta^{18}O$ records: Paleoceanography, v. 20, PA1003, doi:10.1029/2004PA001071.

Lüthgens, C., Krbetschek, M., Böse, M., Fuchs, M.C., (2010), Optically simulated luminescence dating of fluvioglacial (sandur) sediments from north-eastern Germany: Quaternary Geochronology, v. 5, p. 237–243.

Manley, G., (1959), The late-glacial climate of north-west England: Liverpool and Manchester Geological Journal, v. 2, p. 188–215.

Meier, M.F., and Post, A.S., (1962), Recent variations in mass net budgets of glaciers in western North America: International Association of Hydrological Sciences Publication, v. 58, p. 63–77.

Meierding, T.C., (1982), Late Pleistocene glacial equilibrium-line in the Colorado Front Range: a comparison of methods: Quaternary Research, v. 18, 289–310.

Merle, J.R., (2001), Quaternary geology of the Tengis-Shishid Gol region, Khovsgol, Mongolia [Senior thesis]: Whitman College, 56 p.

Mitchell, T. D., and Philip, D. J., (2005), An improved method of constructing a database of monthly climate observations and associated high resolution grids: International Journal of Climatology, v. 25, p. 693–712.

National Aeronautics and Space Administration (2015), The ASTER L1B data product was retrieved from the online Data Pool, courtesy of the NASA Land Processes Distributed Active Archive Center (LP DAAC), USGS/Earth Resources Observation and Science (EROS) Center, Sioux Falls, South Dakota, https://lpdaac.usgs.gov/data_access/data_pool. ASTER GDEM is a product of METI, Japan and NASA, USA.

Nichols, K.K., Bierman, P.R., Foniri, W.R., Gillespie, A.R., Caffee, M., Finkel, R., (2006), Dates and rates of arid region geomorphic processes: GSA Today, v. 16, no. 8, p. 4–11. doi: 10.1130/GSAT01608.1.

O'Connor, J.E., and Costa, J.E., (2004), The world's largest floods – Their causes and magnitudes: U.S. Geological Survey Circular 1254, Reston, VA, U.S. Geological Survey, 13 p.

Peck, J.A., King, J.W., Colman, S.M., Kravchinsky, V.A., (1994), A rock-magnetic record from Lake Baikal, Siberia: Evidence for Late Quaternary climate change: Earth and Planetary Science Letters, v. 122, p. 221–238.

Peretolchin, S.P., (1908), Ledniki hrebta Munku-Sardyk (Glaciers of the Munku-Sardyk ridge): Tomsk, Izvestiya Tomskogo Teknologicheskogo Instituta (Proceedings of the Tomsk Technological Institute), v. 9, no. 1, p. 47. (in Russian).

Porter, S.C., (1975), Equilibrium line altitudes of late Quaternary glaciers in the Southern Alps, New Zealand: Quaternary Research, v. 5, p. 27–47.

Porter, S.C., (2001), Snowline depression in the tropics during the Last Glaciation: Quaternary Research, v. 20, p. 1067–1091.

Prescott, J.R., and Hutton, J.T., (1994), Cosmic ray contributions to dose rates for luminescence and ESR dating: Large depths and long-term time variations: Radiation Measurements, v. 23, p. 497–500.

Prokopenko, A.A., Kuzmin, M.I., Williams, D.F., Gelety, V.F., Kalmychkov, G.V., Gvozdkov, A.N., Solotchin, P.A., (2005), Basin-wide sedimentation changes and deglacial lake-level rise in the Hovsgol basin, NW Mongolia: Quaternary International, v. 136, p. 59–69.

Prokopenko, A.A., Karabanov, E.B., Kuz'min, M.I., Williams, D.F., (2001), The mechanism of early glaciation during the transition from Kazantsevo climatic optimum to Zyrjanka glacial period (Evidence from bottom sediments of Lake Baikal): Geologiya i Geofizika (Russian Geology and Geophysics), v. 42 (1–2), p. 64–75 (55–65).

Putkonen, J., and Swanson, T., (2003), Accuracy of cosmogenic ages for moraines: Quaternary Research, v. 59, p. 255–261.

Ramage, J.M., Smith, J.A., Rodbell, D.T., Seltzer, G.O., (2005), Comparing reconstructed Pleistocene equilibrium-line altitudes in the tropical Andes of central Peru: Journal of Quaternary Science, v. 20, p. 777–788.

Reimer, P.J., Bard, E., Bayliss, A., Beck, J.W., Blackwell, P.G., Ramsey, C.B., Buck, C.E., Cheng, H., Edwards, R.L., Friedrich, M., Grootes, P.M., Guilderson, T.P., Haflidason, H., Hajdas, I., Hatté, C., Heaton, T.J., Hoffmann, D.L., Hogg, A.G., Hughen, K.A., Kaiser, K.F., Kromer, B., Manning, S.W., Niu, M., Reimer, R.W., Richards, D.A., Scott, E.M., Southon, J.R., Staff, R.A., Turney, C.S.M., Plicht, J., (2013), IntCal13 and MARINE13 radiocarbon age calibration curves 0–50,000 years cal BP: Radiocarbon, v. 55, no. 4, p. 1869–1887. doi:10.2458/ azu_js_rc.55.16947

Rother, H., Lehmkuhl, F., Fink, D., Nottebaum, V., (2014), Surface exposure dating reveals MIS-3 glacial maximum in the Khangai Mountains of Mongolia: Quaternary Research, v. 82, p. 297–308.

Round, F.E., and Bukhtiyarova, L., (1996), Four new genera based on Achnanthes (Achnanthidium) together with a re-definition of Achnanthidium: Diatom Research, v. 11, p. 345–361.

Rupper, S., and Roe, G., (2008), Glacier changes and regional climate: A mass and energy balance approach: Journal of Climate, v. 21, p. 5384–5401.

Rupper, S., Roe, G., Gillespie, A., (2009), Spatial patterns of Holocene glacier advance and retreat in Central Asia: Quaternary Research, v. 72, p. 337–346.

Rupper, S., and Koppes, M., (2010), Spatial patterns in Central Asian climate and equilibrium line altitudes: IOP Conference Series: Earth and Environmental Science, v. 9, no. 012009. doi:10.1088/1755-1315/9/1/012009

Sakai, A., Nuimura, T., Fujita, K., Takenaka, S., Nagai, H., Lamsal, D., (2015), Climate regime of Asian glaciers revealed by GAMDAM glacier inventory: The Cryosphere, v. 9, p. 868–880.

Sharkhuu, A., Sharkhuu, N., Etzelmüller, B., Heggem, E.S.F., Nelson, F.E., Shiklomanov, N.I., Goulden, C.E., Brown, J., (2007), Permafrost monitoring in the Hovsgol mountain region, Mongolia: Journal of Geophysical Research, v. 112, F02S06. doi:10.1029/2006JF000543

Shchetnikov, A.A., (2001), Struktura reliefa i noveyshaya tektonika Tunkinskogo rifta (Structure of Relief and Neotectonics of the Tunka Rift) [Abstract of PhD Thesis]: Irkutsk, Institute of Earth's Crust, Siberian Branch, Russian Academy of Sciences, 19 p. (in Russian).

Stone, J., (2000), Air pressure and cosmogenic isotope production: Journal of Geophysical Research, v. 105, no. 23, p. 753–23,759.

Stuiver, M., and Polach, H.A., (1977), Discussion: reporting of ^{14}C data: Radiocarbon, v. 19, p. 355.

Stuiver, M., and Reimer, P.J., (1993), Extended ^{14}C database and revised CALIB radiocarbon calibration program: Radiocarbon, v. 35, p. 215–230.

Thomas, P.J., Murray, A.S., Sandgren, P., (2003), Age limit and age underestimation using different OSL signals from lacustrine quartz and polymineral fine grains: Quaternary Science Reviews, v. 22, p. 1139–1143.

Torsnes, I., Rye, N., Nesje, A., (1993), Modern and Little Ice Age equilibrium-line altitudes on outlet valley glaciers from Jostedalsbreen, western Norway: an evaluation of different approaches to their calculation: Arctic and Alpine Research, v. 25, p. 106–116.

Ufland, A.K., Ilyin, A.V., Spirkin, A.I., (1969), Vpadiny baikal'skogo tipa severnoi Mongolii (Baikal-type basins of northern Mongolia): Bulletin of the Moscow Society of Naturalists (MOIP), Geology series, Moscow, Moscow University Publ., v. 44, no. 6, p. 5–22. (in Russian).

Ufland, A.K., Ilyin, A.V., Spirkin, A.I., Shilova, G.N., (1971), Osnovniye cherty stratigrafii i usloviya formirovanya Kainozoiskikh obrazovanii Prikosogolya (MNR) (Main features of stratigraphy and formation of Cenozoic deposits in Prekosogol) (MPR): Bulletin of the Moscow Society of Naturalists (MOIP), Geology Series, Moscow, Moscow University Publ., v. 46, p. 54–69. (in Russian).

Vasil'chuk, Yu.K., Alekseev, S.V., Arzhannikov, S.G., Alekseeva, L.P., Budantseva, N.A., Chizhova, Ju.N., Arzhannikova, A.V., Vasil'chuk, A.C., Kozyreva, E.A., Rybchenko, A.A., Svetlakov, A.A., (2015), Oxygen and hydrogen isotope compositions of lithalsa frozen core: A case study from the Sentsa River valley, East Sayan: Kriosfera Zemli (Earth's Cryosphere), v. 19, no. 2, p. 46–58. http://www.izdatgeo.ru/pdf/earth_cryo/2015-2/46_eng.pdf

Verosub, K.L., and Roberts, A.P., (1995), Environmental magnetism: Past, present, and future: Journal of Geophysical Research, v. 100, no. B2, p. 2175–2192.

Wallinga, J., Murray, A.S., Duller, G.A.T., Törnqvist, T.E., (2001), Testing optically simulated luminescence dating of sand-sized quartz and feldspar from fluvial deposits: Earth and Planetary Science Letters, v. 193, p. 617–630.

Wegmann, K.W., Amgaa, Ts., Frankel, K.L., Dewett, A.P., Bayasgalan, A., (2011), Geologic, geomorphic, and environmental change at the northern termination of the Lake Hövsgöl rift, Mongolia: Proceedings of the Twenty-Fourth Annual Keck Research Symposium in Geology, Union College, Schenectady, NY, April, 2011, p. 220–229.

Wintle, A.G., and Murray, A.S., (2006), A review of quartz optically stimulated luminescence characteristics and their relevance in single- aliquot regeneration dating protocols: Radiation Measurements, v. 41, p. 369–391.

Chapter 3

ASYNCHRONOUS GLACIATIONS IN ARID CONTINENTAL CLIMATE

The content in Chapter 3 was published in *Quaternary Science Reviews*, Vol. 182, pp. 1–19, in 2018 with a title "Asynchronous glaciations in arid continental climate" co-authored by Jigjidsurengiin Batbaatar, Alan R. Gillespie, David Fink, Ari Matmon, and Toshiyuki Fujioka. The contents in chapter are the author's version of the work and posted here with the permission from Elsevier.

3.1 ABSTRACT

Mountain glaciers at ~26–19 ka, during the global Last Glacial Maximum near the end of the last 100,000 yr glacial cycle, are commonly considered on the basis of dating and field mapping in several well-studied areas to have been the largest of the late Quaternary and to have advanced synchronously from region to region. However, a numerical sensitivity model (Rupper and Roe, 2008) predicts that the fraction of ablation due to melting varies across Central Asia in proportion to the annual precipitation. The equilibrium-line altitude of glaciers across this region likely varies accordingly: in high altitude, cold and arid regions sublimation can ablate most of the ice, whereas glaciers fed by high precipitation cannot ablate completely due to sublimation alone but extend downhill until higher temperatures there cause them to melt. We have conducted field studies and ^{10}Be dating at five glaciated sites along a precipitation gradient in Mongolia to test the Rupper/Roe model. The sites are located in nearby 1.875×1.875° cells of the Rupper/Roe model, each with a different melt fraction, in this little-studied region. The modern environment of the sites ranges from dry subhumid in the north (47.7° N) to arid in the south (45° N). Our findings show that the maximum local advances in the dry subhumid conditions predated the global Last Glacial Maximum and were likely from MIS 3. However, we also found that at ~8–7 ka a cirque glacier in one mountain range of the arid Gobi desert grew to a magnitude comparable to that of the local maximum extent. This Holocene maximum occurred during a regional pluvial period thousands of years after the retreat of the Pleistocene glaciers globally. This asynchronous behavior is not predicted by the prevailing and generally correct presumption that glacier advances are dominantly driven by temperature, although precipitation also plays a role. Our findings are consistent with and support the Rupper/Roe model, which calls for glaciation in arid conditions only at high altitudes of sub-freezing temperatures, where the melt fraction in ablation is low. We expect a heterogeneous pattern of glacial responses to a changing modern climate in cold arid regions; an individual glacier advance should not be necessarily interpreted as evidence of cooling climate.

3.2 INTRODUCTION TO CHAPTER 3

Glaciers respond to a number of forcing functions that are active over a wide range of scales from local (e.g., topographic shadowing) to regional or even global. Of these, annual snowfall and summer air temperature are commonly considered to be the most important. If one of these parameters is independently known, glacial records may be useful in reconstructing the other parameter in continental settings where paleoclimate proxy records are scarce. Specifically, the timing and magnitude of local maximum glacial advances have been used to improve the understanding of changes in climate during the past cycle of glaciation (e.g., Gillespie and Molnar, 1995; Porter, 2001; Clark et al. 2009).

The global "Last Glacial Maximum" (LGM) is defined as the period during the latest ~100,000 yr glacial cycle when the global ice volume achieved its maximum. Climate reconstructions based on oxygen-isotope records of marine foraminifera (Hays et al., 1976) placed the timing of the global LGM at ~23–19 ka (Mix et al., 2001). Integrating the high-latitude ice-sheet and mountain-glacier records appeared to strengthen the concept of a synchronous global LGM and also extended its period to ~26–19 ka (Clark et al., 2009).

However, recent evidence from mid-latitude southern hemisphere glacial records (Augustin et al., 2004; Putnam et al., 2013; Rother et al., 2015; Darvill et al., 2016) and continental Asian valley glacier systems (Gillespie et al., 2008; Koppes et al., 2008; Heyman et al., 2011a; Batbaatar and Gillespie, 2016; Gribenski et al., 2016) suggests a more complex behavior than that of synchronized 'global' glaciations, highlighting the often-overlooked importance of regional factors. Such spatial variations in the magnitude of glaciations during a given period were suspected before (Gillespie and Molnar, 1995; Hughes et al., 2013), but with the widespread

introduction of *in-situ* cosmogenic surface exposure dating, new quantitative glacial chronologies (e.g., Hughes et al., 2013; Heyman, 2014) have allowed a reliable temporal comparison of maximum mountain glaciations that might not coincide with the timing of the global LGM.

Glacial records from the arid to humid continental environments (Zomer et al., 2008) of Central Asia (Figure 3.1) have revealed that the spatial patterns of glacier advances and retreats as well as the timing of the maxima differ from place to place on a scale of a few hundred kilometers. We postulate that the concept of synchronous glaciations may break down in arid environments where glacier mass balance is controlled by different suites of factors than in more humid settings (e.g., Cuffey and Paterson, 2010, pp. 169–173). For example, in arid–dry subhumid parts of the Kyrgyz Tian Shan (locations are shown in Figure 3.1) the largest glaciers date from Marine Oxygen-Isotope Stage (MIS) 3 or earlier, and MIS 2 glaciers were restricted to cirques (Koppes et al., 2008; Blomdin et al., 2016). On the other hand, in humid southern Siberia, the largest glaciers dated from MIS 3, and the MIS 2 glaciers were only slightly smaller (Gillespie et al., 2008; Batbaatar and Gillespie, 2016). In parts of the northeastern Tibetan plateau, the largest mountain glaciers occurred earlier than ~100 ka (i.e. prior to MIS 4) and no evidence of MIS 2 glaciation has been found (Heyman et al., 2011a). Numerical glacial modeling (Rupper and Roe, 2008; Rupper et al., 2009), albeit of low spatial resolution (1.875°), suggests that this heterogeneous pattern of glacial response is due to the different sensitivity of glaciers to climate forcing in cold, arid regions, where sublimation accounts for more than 50% of the total ice loss. However, this model (Rupper and Roe, 2008; Rupper et al., 2009) has yet to be validated with field observations.

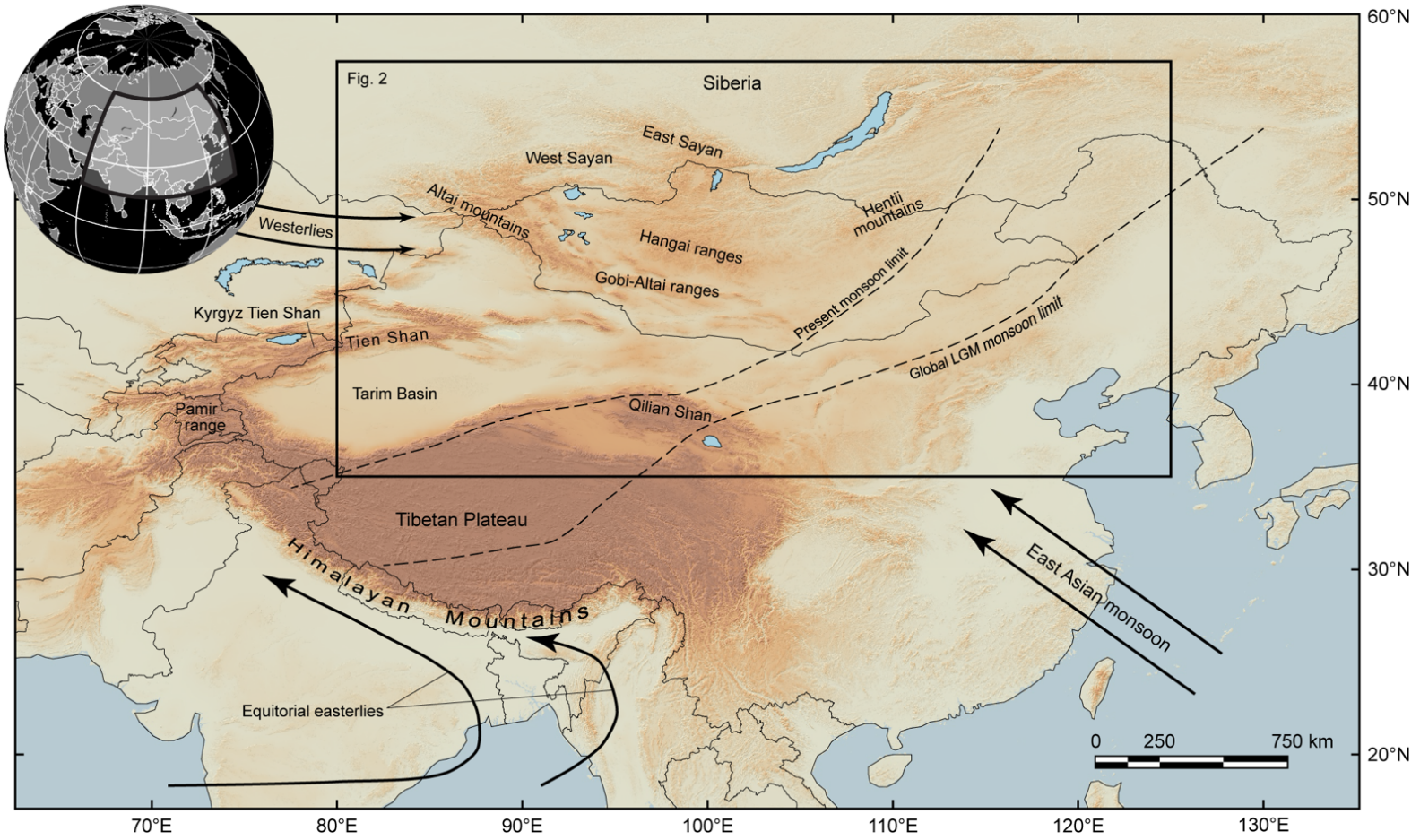

Figure 3.1. Geographic location of the Hangai and Gobi-Altai ranges in East and Central Asia. Dashed lines indicate the modern and global LGM limits of East Asian monsoon (Shi 2002). Solid lines indicate the general direction of major air flows (Benn and Owen 1998). The black rectangle inset refers to the extent of region shown in Figure 3.2.

In this article, we examined the glacial history in five sites in central Mongolia (Figure 3.2), with modern environments grading northward from arid to dry subhumid, and are distributed across a cluster of five cells of the Rupper and Roe model (2008) (Figure 3.3). We selected the sites to be in cold continental climates where melt versus sublimation was predicted to be a significant factor controlling glacier mass balance, and therefore where glaciers and paleoglaciers could be used to test the Rupper/Roe numerical model. According to the Rupper/Roe model, almost all of glacier ice in arid Gichginii is lost via sublimation and in the semiarid Sutai and Ih Bogd ~10–30% of ice is lost via sublimation. In contrast, in dry subhumid Hangai region melting is responsible for more than 40–60% of total ablation (Figure 3.3).

In low-precipitation, sub-freezing sublimation regimes, glaciers are restricted to altitudes close to or above the zero isotherm. As snowfall increases, the glacier will advance below the zero isotherm, but not far because melting is much more efficient at ablation than sublimation. Only when the accumulation rate exceeds ablation will glaciers flow to lower altitudes. This is a mechanism for desynchronizing glacier advances, because of their non-linear response to precipitation differences from place to place: in arid regions glaciers may be restricted to cirques, whereas in more humid regions they may advance or retreat. Likewise, glacier advances in a given valley may respond differently in the face of climate change, for the same reasons.

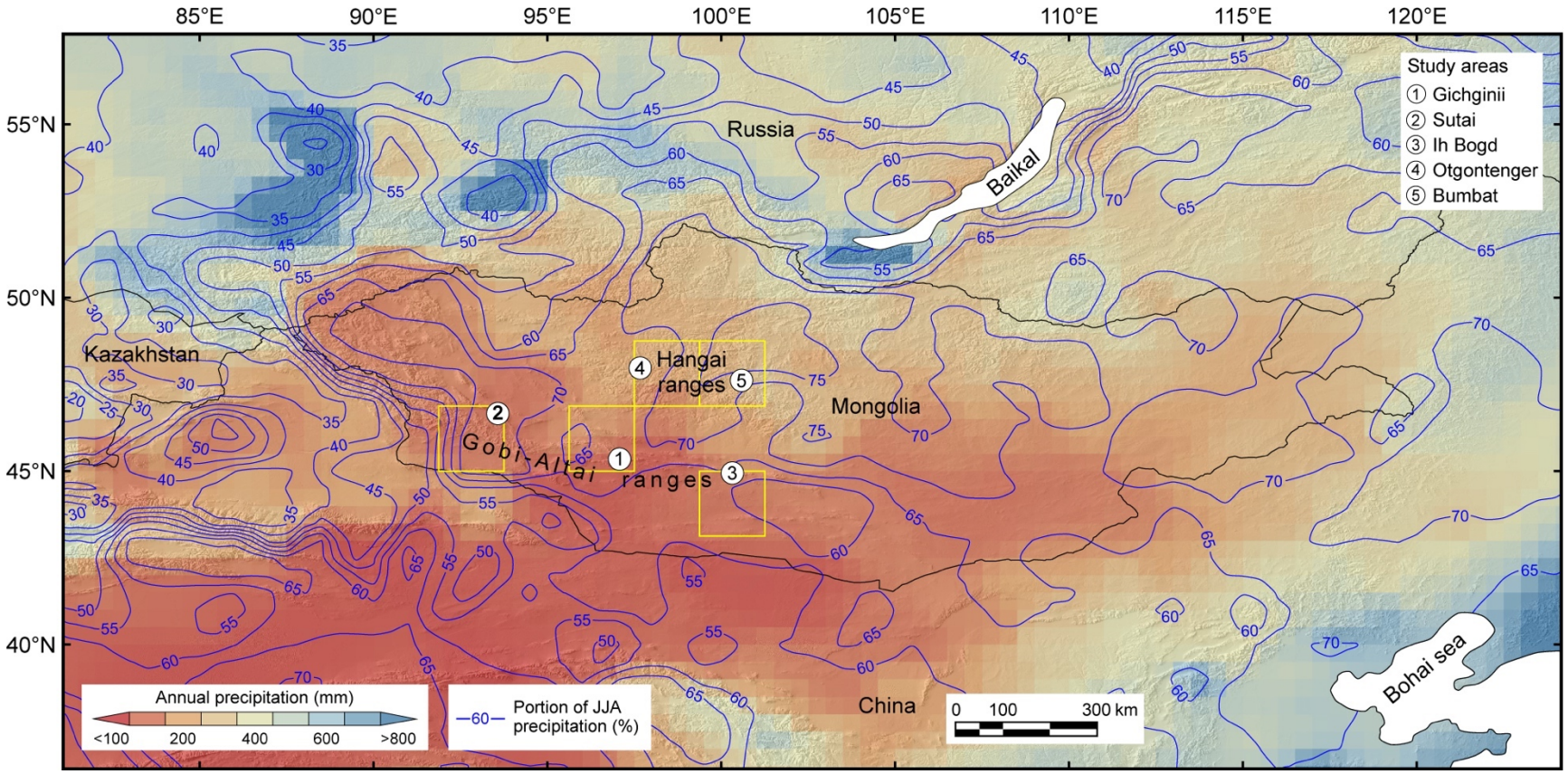

Figure 3.2. Modern annual precipitation and the fraction occurring during summer in Mongolia and adjacent areas. The precipitation data are long-term (1981–2010) monthly means (GPCC V7, at 0.5° × 0.5° resolution; Schneider et al., 2015). The yellow rectangles show the 1.875° cells of the Rupper and Roe (2008) model that were occupied by our field study sites. The shaded relief image in the background is constructed from SRTM V3 data (NASA, 2016).

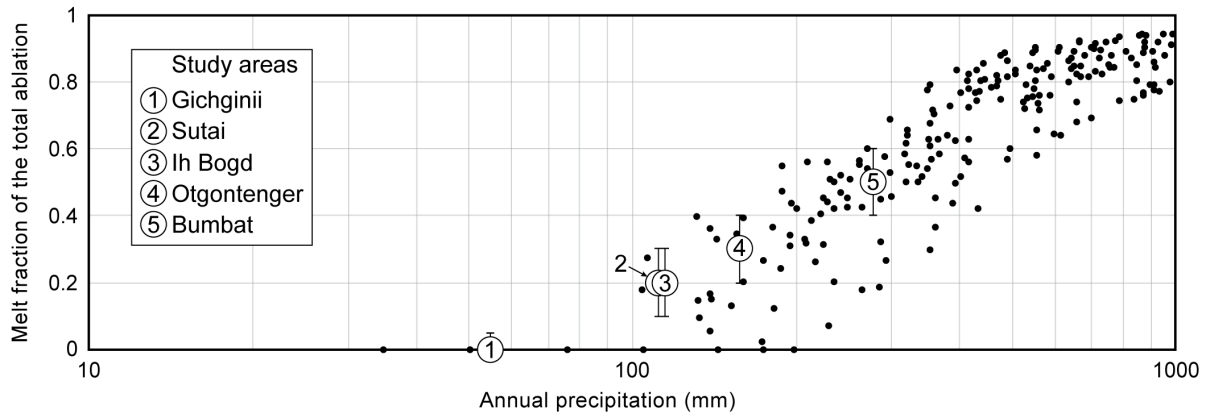

Figure 3.3. Modern annual precipitation and modeled melt fraction of the total ablation at the study sites. The precipitation data were from GPCC V7, at 0.5° × 0.5° resolution (Schneider et al., 2015). The melt fraction was modeled and calculated by Rupper and Roe (2008) to 3000 mm yr^{-1}, but only the 10–1000 mm yr^{-1} range is shown here (note the logarithmic scale). The range of melt fractions calculated in the model for a given annual precipitation similar to the study sites is shown by the whiskers.

Both air temperature (T_a) and precipitation decreased during the global LGM in our study area (e.g., Rupper and Koppes, 2010), and the Rupper/Roe model implies that T_a depression alone cannot drive advance of sublimation-dominated glaciers. We test this model implication in the field by seeking evidence of two modes of glacial asynchrony: 1) asynchrony in the timing of maximum glacier extents between sublimation- and melt-dominated regions; 2) asynchrony in the magnitude of glacier extents within the same sensitivity region due to variability of precipitation changes. However, the Rupper/Roe model covers a vast geographic area with a wide range of climatic conditions. Therefore, until more field mapping and dating can be performed the results discussed in this article should be viewed as a preliminary check of the model.

3.3 METHODS

We sampled 59 glacially deposited boulders and one glacially eroded bedrock knob from five sites in four different mountain ranges (Figure 3.2) encompassing an area of 15,000 km^2. We constructed glacial chronologies in the valleys using ^{10}Be cosmogenic exposure dating (Table 3.1). Nine additional samples from post-glacial strath terraces at Sutai were sampled to determine a minimum age for the glaciers. We also estimated equilibrium-line altitudes (ELAs) for the dated moraines, and using a numerical model (after Rupper and Roe, 2008) examined the climate parameters that influence the glacier ablation. To constrain the local adiabatic lapse rate, we measured summer air temperatures atop the modern ice cap of Sutai. Below, we provide the details of ^{10}Be age analyses, criteria for identifying age outliers, methods to calculate ELAs, and the explanation of the numerical model.

3.3.1 *Cosmic-ray exposure dating*

All samples were chemically prepared for accelerator mass spectrometry (AMS) using methods based on Kohl and Nishiizumi (1992). We ground the rock samples and extracted quartz from the 500–850 μm size fraction. The quartz was further purified by selectively etching in HF. We then added a carrier solution with a very low level of $^{10}Be/^{9}Be$ ($<2\times10^{-15}$) before extracting the Be by column chromatography. Chemical preparation of the samples identified as GN-AG, MOT98-CS, and DHC98 were done at the Cosmogenic Nuclide Laboratory, University of Washington, and the AMS analyses were done at the Center for Accelerator Mass Spectrometry, Lawrence Livermore National Laboratory. The samples identified as GN-JB, HN-JB, SUT-JB, SUT-IM, and OT-AG were chemically prepared at the Cosmogenic Isotope Laboratories, Hebrew University in Jerusalem. The $^{10}Be/^{9}Be$ ratio from numerous full procedural chemistry blanks ranged from 5 $\times10^{-15}$ to 2 $\times10^{-15}$, which was at most 5% of the lowest measured $^{10}Be/^{9}Be$ ratio. AMS analyses

were done at the ANTARES AMS Facility, Australian Nuclear Science and Technology Organization (Fink and Smith, 2007).

The ^{10}Be ages (Table 3.1) were calculated using CRONUS-Earth version 2.2 (Balco et al., 2008). We used the globally calibrated ^{10}Be sea-level high latitude spallation production rate (Heyman, 2014) of 3.99 ± 0.22 atoms g^{-1} yr^{-1} when referenced to the scaling of Lal and Stone (Lal, 1991; Stone, 2000). We assumed 2.65 g cm^{-3} for sample density. All calculations of ^{10}Be ages assumed zero erosion and burial in this study, and we did not account for neutron shielding by snow. An unlikely high erosion rate of 3 mm yr^{-1} would increase an apparent age of 20 ka by ~5% (Chapter 2: Figure 2.25). A 4 month seasonal snowpack of 250 mm depth (e.g., Mitchell and Philip, 2005), a maximum for the modern Gobi-Altai, would increase an apparent age of 20 ka by <2% (Chapter 2). We provide the data for calculation of the ^{10}Be ages in Table 3.2.

Table 3.1. ^{10}Be exposure-ages for samples from the Gobi-Altai and Hangai ranges. Ages are ordered by increasing altitude for each site.

Site	Sample identification	Sample description	Maximum diameter (m)	Boulder height (m)	Exposure age (ka)	1σ uncertainty (ka)	
						Internal[a]	External[b]
Gichginii range Mönh Mösnii valley	*Lateral moraine G2, N 45.4038°, E 97.0704°, 3283–3327 m asl*						
	GN-AG-10B	Quartz vein in schist boulder	0.5	0.3	6.9	0.2	0.4
	GN-AG-11	Quartz vein in schist boulder	0.5	0.4	8.1	0.2	0.5
	GN-JB-004	Quartz vein in schist boulder	0.4	0.2	5.3 *	0.3	0.4
	GN-JB-005	Quartz vein in schist boulder	0.5	0.4	7.5	0.3	0.5
	Lateral moraine G3, N 45.4014°, E 97.0701°, 3340–3361 m asl						
	GN-AG-07	Quartz vein in schist boulder	0.5	0.3	1.6	0.1	0.1
	GN-AG-08	Quartz vein in schist boulder	0.4	0.3	3.2	0.1	0.2
	GN-AG-04	Quartz vein in schist boulder	0.4	0.3	0.8 *	0.03	0.1
	GN-AG-05	Quartz vein in schist boulder	0.3	0.3	2.8	0.1	0.2
	GN-AG-06	Quartz vein in schist boulder	0.4	0.3	2.6	0.1	0.2
	Lateral moraine G4, N 45.4013°, E 97.0697°, 3330–3338 m asl						
	GN-JB-001	Quartz vein in schist boulder	0.4	0.3	0.9	0.1	0.1
	GN-JB-002	Quartz vein in schist boulder	0.5	0.4	1.0	0.1	0.1
	GN-JB-003	Quartz vein in schist boulder	0.6	0.4	1.5	0.3	0.3
	GN-AG-01	Quartz vein in schist boulder	0.5	0.4	1.8	0.1	0.1
	GN-AG-02	Quartz vein in schist boulder	0.5	0.2	1.9	0.1	0.1
	GN-AG-03	Quartz vein in schist boulder	0.5	0.3	1.6	0.05	0.1
Sutai range Northeastern slope	*End moraine NE1, N 46.6418°, E 93.5710°, 3160 m asl*						
	DHC-98-12	Quartz vein in schist boulder	2	1	7.3 *	0.3	0.5
	Left-lateral moraine NE2, N 46.6403°, E 93.5648°, 3240–3270 m asl						
	DHC-98-13	Quartz vein in schist boulder	2.5	0.5	26.2	0.8	1.7
	DHC-98-10	Quartz vein in schist boulder	0.8	0.5	22.9	0.7	1.5
	Left-lateral moraine NE4, N 46.6404°, E 93.5660°, 3250 m asl						
	DHC-98-11	Quartz vein in schist boulder	2	0.8	24.9	1.2	1.8
	Recessional (?) left-lateral moraine, N 46.6398°, E 93.5652°, 3265 m asl						
	DHC-98-15	Quartz vein in schist boulder	2.3	0.6	6.7 *	0.2	0.4
Sutai range Marginal samples	*Marginal moraine between ice caps #1 and 2, N 46.6323°, E 93.5688°, 3620 m asl*						
	MOT98-CS-11a	Quartz vein in schist boulder	0.6	0.3	45.0	1.2	2.8
	MOT98-CS-11b	Quartz vein in schist boulder	0.6	0.3	13.2	0.6	0.9
	MOT98-CS-12	Quartz vein in schist boulder	0.5	0.3	24.8	1.6	2.1
	Erratic at the margins of modern ice cap #3, N 46.6052°, E 93.6192°, 3934 m asl						
	SUT-JB-04A	Vein quartz erratic	0.3	0.2	21.3	0.4	1.2
	Erratic at the margins of modern ice cap #3, N 46.6044°, E 93.6194°, 3926 m asl						
	SUT-JB-04B	Vein quartz erratic	0.25	0.1	41.6	1.0	2.5
Sutai range Southwestern slope	*Glacially eroded bedrock knob, N 46.5999°, E 93.5487°, 3109 m asl*						
	MOT98-CS-22	Porphyroblastic schist bedrock	-	-	22.1	0.8	1.5
	Erratic on the bedrock knob, N 46.5999°, E 93.5487°, 3109 m asl						
	MOT98-CS-23	Quartz vein in schist erratic	2	0.8	72.4 *	2.6	4.8
	Recessional moraine (?), N 46.6094°, E 93.5522°, 3180 m asl						
	MOT98-CS-14	Quartz vein in green schist boulder	0.5	0.1	35.6 *	1.8	2.7
	Boulder outside the crest of moraine SW2, N 46.6101°, E 93.5475°, 3189 m asl						
	MOT98-CS-25	Quartz vein in schist boulder	2	1.5	6.0 *	0.2	0.4
	Right-lateral moraine SW2, N 46.6132°, E 93.5503°, 3240–3270 m asl						
	SUT-JB-02A	Quartz vein in schist boulder	0.5	0.3	15.4	0.4	0.9
	SUT-JB-02B	Quartz vein in schist boulder	0.5	0.3	19.8	0.6	1.3
	SUT-JB-02C	Quartz vein in schist boulder	0.3	0.3	13.9	0.4	0.9
	SUT-JB-02D	Quartz vein in schist boulder	2.5	0.6	15.5	0.5	1.0

Table 3.1 (continued)

Site	Sample identification	Sample description	Maximum diameter (m)	Boulder height (m)	Exposure age (ka)	1σ uncertainty (ka)	
						Internal[a]	External[b]
Ih Bogd range Artsan valley	*Lateral-end moraine IB5, N 44.9564°, E 100.2668°, 3385–3390 m asl*						
	IB-JB-003E	Granitic boulder	1.5	1	16.7	1.2	1.5
	IB-JB-003A	Porphyritic granitic boulder	1	1	7.3 *	0.5	0.6
	IB-JB-003B	Granitic boulder	1.3	1	13.2	1.8	1.9
	IB-JB-003C	Granitic boulder	1	0.5	14.3	0.7	1.1
	IB-JB-003D	Granitic boulder	2	1	13.9	0.9	1.2
	End moraine IB6, N 44.9567°, E 100.2672°, 3402 m asl						
	IB-JB-002	Granitic boulder	2.5	1.5	13.4	0.7	1.0
	Highest lateral-end moraine IB7, N 44.9578°, E100.2675°, 3425 m asl						
	IB-JB-001	Porphyritic granitic boulder	2.5	1	14.4	0.8	1.2
Otgontenger Bogd valley	*End moraine BO1, N 47.6833°, E 97.2067°, 2075 m asl*						
	OT-AG-1	Granitic boulder	1.5	1	22.7	1.2	1.8
	OT-AG-2	Granitic boulder	1.6	1.6	20.2	1.4	1.8
	OT-AG-3	Granitic boulder	2	0.5	23.6	1.3	1.9
Otgontenger Bitüüt valley	*Right-lateral moraine BI2, N 47.5755°, E 97.6677°, 2580 m asl*						
	DHC-98-5	Granitic boulder	1.5	1	31.3	1.0	2.0
	DHC-98-7	Granitic boulder	3	3	82.9 *	2.6	5.3
	DHC-98-8	Granitic boulder	2	0.3	29.9	0.9	1.9
	End moraine, BI8, impounding a lake, N 47.5978°, E 97.6497°, 2725 m asl						
	MOT98-CS-02	Granitic boulder	2	0.5	16.2	0.6	1.1
	End moraine, BI9, impounding a lake, N 47.6035°, E 97.6403°, 2725 m asl						
	DHC-98-3	Granitic boulder	2	1.5	15.0 *	0.5	1.0
	MOT98-CS-04	Granitic boulder	4	1,5	16.5	0.5	1.0
	MOT98-CS-05	Granitic boulder	2	1	16.6	0.5	1.1
Bumbat valley	*Lowest end moraine BU1, N 47.4357°, E 100.3468°, 2130 m asl*						
	HN-JB-01B	Granitic boulder	1.5	0.5	103.7	2.8	6.5
	HN-JB-01C	Granitic boulder	1	0.3	53.6	1.4	3.3
	HN-JB-01A	Granitic boulder	1	0.3	22.5	1.1	1.6
	End moraine BU2, N 47.4158°, E 100.3573°, 2172–2177 m asl						
	HN-JB-02A	Granitic boulder	2	1	22.2 *	0.9	1.5
	HN-JB-02B	Granitic boulder	1.5	0.4	39.5	1.7	2.8
	HN-JB-02C	Granitic boulder	1.5	1	31.8	1.1	2.1
	HN-JB-03A	Granitic boulder	1.5	1	36.5	1.4	2.5
	HN-JB-03B	Granitic boulder	2	1	31.8	1.8	2.5
	HN-JB-03C	Granitic boulder	0.8	0.4	49.9 *	1.8	3.3
Non-glacial deposits at Sutai range, southwestern slope	*Boulders on rock/debris fall, N 46.6068°, E 93.5628°, 3205 m asl*						
	MOT98-CS-20	Quartz vein in schist boulder	0.5	0.5	0.9	0.1	0.1
	MOT98-CS-21	Quartz vein in schist boulder	0.6	0.1	1.6	0.1	0.1
	Schist bedrock strath terrace, N 46.6160°, E 93.5639°, 3273 m asl						
	MOT98-CS-08	Quartz vein in schist boulder	4	0.5	11.9	0.4	0.8
	Boulders on schist strath terrace, N 46.6168°, E 93.5645°, 3290 m asl						
	DHC-98-17	Quartz vein in schist boulder	3	0.5	4.1	0.1	0.3
	DHC-98-18	Quartz vein in schist boulder	0.7	0.2	18.3	0.6	1.2
	MOT98-CS-19	Quartz vein in schist boulder	0.5	0.5	0.9	0.1	0.1
	Boulders on protalus rampart overlying strath terrace, N 46.6176°, E 93.5656°, 3310 m asl						
	SUT-IM-01A	Quartz vein in schist boulder	0.6	0.2	2.6	0.1	0.2
	SUT-IM-01B	Granitic boulder	0.6	0.2	2.9	0.1	0.2
	SUT-IM-01C	Quartz vein in schist boulder	0.5	0.2	2.8	0.1	0.2

a) Internal uncertainty includes uncertainties of measuring sample mass and statistical counting in the $^{10}Be/^{9}Be$ AMS absolute isotopic ratio.
b) External uncertainty includes ^{10}Be production rate uncertainties.

Ages marked with * are outliers (see Methods section) and were not included in ELA calculations.

Table 3.2. ^{10}Be data used for exposure-age calculation

Site	Group	Sample	Location	Altitude (m asl)	Thick-ness (cm)	Production rate (atoms g^{-1} yr^{-1})		Shielding factor	Quartz[c] (g)	Be carrier (mg)	^{10}Be/^{9}Be[d,e] ($\times10^{-15}$)	^{10}Be concentration[e,f] (10^3 atoms g^{-1} SiO_2)	Age[g,h] (ka ± 1σ)
						Spallation[a]	Muons[b]						
Gichginii range (Gobi-Altai)	G2	GN-AG-10B	45.4038/97.0704	3289	1	44.90	0.51	0.99	9.0144	0.2678	157.13 ± 5.06	311.9 ± 10.3	6.9 ± 0.4
		GN-AG-11	45.4038/97.0704	3289	2	44.53	0.51	0.99	10.4866	0.2681	214.35 ± 3.99	366.2 ± 7.6	8.1 ± 0.5
		GN-JB-004	45.4023/97.0702	3327	2	45.54	0.52	0.99	13.8520	0.2121	237.72 ± 10.39	243.2 ± 15.4	5.3 ± 0.4
		GN-JB-005	45.4039/97.0703	3283	2	44.37	0.51	0.99	11.5540	0.2149	269.29 ± 6.69	334.7 ± 12.7	7.5 ± 0.5
	G3	GN-AG-07	45.4014/97.0701	3340	2	45.89	0.52	0.99	9.7160	0.2685	39.26 ± 2.27	72.5 ± 4.2	1.6 ± 0.1
		GN-AG-08	45.4014/97.0701	3340	2	45.89	0.52	0.99	9.2480	0.2682	76.58 ± 1.74	148.4 ± 3.5	3.2 ± 0.2
		GN-AG-04	45.4015/97.0697	3361	2	46.46	0.52	0.99	10.0974	0.2520	22.42 ± 0.74	37.4 ± 1.2	0.8 ± 0.1
		GN-AG-05	45.4015/97.0697	3361	5	45.33	0.51	0.99	10.0976	0.2520	77.31 ± 2.13	128.9 ± 3.6	2.8 ± 0.2
		GN-AG-06	45.4015/97.0697	3361	1	46.84	0.52	0.99	10.0581	0.2516	72.35 ± 1.86	120.9 ± 3.2	2.6 ± 0.2
	G4	GN-JB-001	45.4022/97.0686	3330	2	45.62	0.52	0.99	16.5650	0.2262	45.48 ± 3.44	41.5 ± 4.5	0.9 ± 0.1
		GN-JB-002	45.4024/97.0686	3330	2	45.62	0.52	0.99	10.7350	0.2135	36.03 ± 2.45	47.9 ± 4.7	1.0 ± 0.1
		GN-JB-003	45.4025/97.0689	3336	2	45.78	0.52	0.99	7.4880	0.2135	35.80 ± 4.58	68.2 ± 12.4	1.5 ± 0.3
		GN-AG-01	45.4013/97.0697	3338	1	46.21	0.52	0.99	9.7453	0.2693	46.25 ± 1.28	85.4 ± 2.4	1.8 ± 0.1
		GN-AG-02	45.4013/97.0697	3338	2	45.83	0.52	0.99	11.5492	0.2678	55.77 ± 1.65	86.4 ± 2.6	1.9 ± 0.1
		GN-AG-03	45.4013/97.0697	3338	2	45.83	0.52	0.99	9.4141	0.2686	38.30 ± 1.12	73.0 ± 2.2	1.6 ± 0.1
Sutai range (Gobi-Altai)	NE1	DHC-98-12	46.6418/93.5710	3160	2	41.09	0.49	0.96	39.3700	0.2530	709.99 ± 17.30	304.9 ± 11.4	7.3 ± 0.5
	NE2–4	DHC-98-13	46.6418/93.5659	3240	2	44.03	0.50	0.98	39.8300	0.2520	2744.67 ± 53.94	1160.4 ± 36.2	26.2 ± 1.7
		DHC-98-10	46.6403/93.5648	3270	2	43.92	0.51	0.96	39.9400	0.2500	2421.74 ± 45.69	1012.9 ± 30.6	22.9 ± 1.5
		DHC-98-11	46.6404/93.5661	3250	5	42.78	0.50	0.97	31.7100	0.2540	2003.22 ± 61.99	1072.2 ± 49.3	24.9 ± 1.8
		DHC-98-15	46.6398/93.5652	3265	2	43.78	0.51	0.96	39.1700	0.3030	577.37 ± 13.13	298.4 ± 10.5	6.7 ± 0.4
	Pass between ice caps 1 & 2	MOT98-CS-11a	46.6323/93.5688	3620	1	55.44	0.57	0.98	39.9300	0.2520	5907.10 ± 88.38	2491.1 ± 63.4	45.0 ± 2.8
		MOT98-CS-11b	46.6323/93.5688	3620	1	55.44	0.57	0.98	10.5700	0.2510	465.15 ± 14.23	738.1 ± 33.6	13.2 ± 0.9
		MOT98-CS-12	46.6315/93.5688	3630	2	55.29	0.56	0.98	26.5000	0.2530	2156.31 ± 92.61	1375.6 ± 85.8	24.8 ± 2.1
	Ice cap 3 margin	SUT-JB-04A	46.6052/93.6192	3934	4	66.20	0.61	1	19.7590	0.2460	206.70 ± 6.50	1400.9 ± 26.9	21.3 ± 1.2
		SUT-JB-04B	46.6044/93.6194	3926	3	65.91	0.61	1	19.6910	0.2641	1023.60 ± 16.40	2737.0 ± 64.9	41.6 ± 2.5
	Bedrock & erratic	MOT98-CS-22	46.6012/93.5490	3105	2.5	40.86	0.48	0.99	39.2900	0.2510	2127.87 ± 49.57	908.4 ± 32.6	22.1 ± 1.5
		MOT98-CS-23	46.6012/93.5490	3105	2.5	40.86	0.48	0.99	39.7200	0.2520	6918.88 ± 158.50	2933.2 ± 103.7	72.4 ± 4.8
	SW remnant	MOT98-CS-14	46.6094/93.5522	3180	2.5	42.68	0.49	0.99	9.0000	0.2520	814.53 ± 28.02	1524.0 ± 77.2	35.6 ± 2.7
	SW 2	MOT98-CS-25	46.6101/93.5475	3189	1	43.44	0.50	0.99	40.0500	0.2510	624.02 ± 15.38	261.3 ± 9.8	6.0 ± 0.4
		SUT-JB-02A	46.6126/93.5495	3238	1	44.76	0.51	0.99	20.4500	0.2669	796.90 ± 11.90	695.0 ± 17.7	15.4 ± 0.9
		SUT-JB-02B	46.6132/93.5503	3241	4	43.75	0.50	0.99	18.9490	0.2724	909.40 ± 17.50	873.6 ± 26.8	19.8 ± 1.3
		SUT-JB-02C	46.6132/93.5503	3241	2	44.47	0.50	0.99	20.1050	0.2711	692.40 ± 10.80	623.9 ± 16.3	13.9 ± 0.9
		SUT-JB-02D	46.6147/93.5520	3267	4	44.44	0.50	0.99	20.6780	0.2850	755.50 ± 14.50	695.8 ± 21.3	15.5 ± 1.0
Ih Bogd range (Gobi-Altai)	IB6	IB-JB-003E	44.9563/100.2668	3385	3	46.84	0.53	0.98	7.8410	0.2503	364.34 ± 18.53	777.1 ± 57.0	16.7 ± 1.5
		IB-JB-003A	44.9563/100.2668	3390	3	46.94	0.53	0.98	5.9830	0.4383	69.25 ± 3.24	339.0 ± 22.9	7.3 ± 0.6
		IB-JB-003B	44.9563/100.2668	3390	3	46.94	0.53	0.98	7.3950	0.2489	274.24 ± 25.56	616.7 ± 81.8	13.2 ± 1.9
		IB-JB-003C	44.9563/100.2668	3390	5	46.94	0.53	0.98	6.4350	0.2475	254.66 ± 8.98	654.4 ± 33.9	14.3 ± 1.1
		IB-JB-003D	44.9563/100.2668	3390	5	46.94	0.53	0.98	7.5470	0.2503	288.64 ± 13.29	639.6 ± 42.6	13.9 ± 1.2
	IB5	IB-JB-002	44.9567/100.2672	3402	3	46.14	0.52	0.97	26.643	0.3963	627.71 ± 22.11	623.9 ± 32.3	13.4 ± 1.0
	IB7	IB-JB-001	44.9578/100.2675	3425	5	47.53	0.53	0.97	2.3380	0.2446	95.71 ± 3.82	669.2 ± 38.9	14.4 ± 1.2

Table 3.2 (continued)

Site	Group	Sample	Location	Altitude (m asl)	Thick-ness (cm)	Production rate (atoms g^{-1} yr^{-1})		Shielding factor	Quartz[c] (g)	Be carrier (mg)	$^{10}Be/^{9}Be$[d,e] ($\times10^{-15}$)	^{10}Be concentration[e,f] (10^3 atoms g^{-1} SiO_2)	Age[g,h] (ka ± 1σ)
						Spallation[a]	Muons[b]						
Otgontenger peak (Hangai)	BO1	OT-AG-1	47.6833/97.2067	2075	5	20.74	0.35	0.99	6.7680	0.2121	226.90 ± 8.44	475.2 ± 25.9	22.7 ± 1.8
		OT-AG-2	47.6833/97.2067	2075	5	20.74	0.35	0.99	7.8800	0.2135	234.02 ± 10.86	423.7 ± 28.4	20.2 ± 1.8
		OT-AG-3	47.6833/97.2067	2075	5	20.74	0.35	0.99	7.4390	0.2149	255.90 ± 9.65	494.0 ± 27.3	23.6 ± 1.9
	BI2	DHC-98-5	47.5755/97.6677	2580	3	30.20	0.42	1	39.1400	0.2520	2209.51 ± 41.75	950.6 ± 28.7	31.3 ± 2.0
		DHC-98-7	47.5755/97.6677	2580	3	30.20	0.42	1	8.3200	0.2520	1228.23 ± 23.44	2485.9 ± 75.7	82.9 ± 5.3
		DHC-98-8	47.5755/97.6677	2580	3	30.20	0.42	1	32.9000	0.2530	1767.67 ± 33.29	908.3 ± 27.4	29.9 ± 1.9
	BI8	MOT98-CS-02	47.5978/97.6497	2725	2.5	33.47	0.44	0.98	40.7200	0.2530	1292.31 ± 31.4	536.5 ± 19.9	16.2 ± 1.1
	BI9	DHC-98-3	47.6035/97.6403	2725	2.5	32.72	0.43	0.98	40.0700	0.2550	1164.20 ± 27.15	495.1 ± 17.8	15.0 ± 1.0
		MOT98-CS-04	47.6035/97.6405	2725	2.5	32.72	0.43	0.98	38.6600	0.2520	1253.91 ± 23.7	546.2 ± 16.5	16.5 ± 1.0
		MOT98-CS-05	47.6035/97.6405	2725	2.5	32.72	0.43	0.98	31.3700	0.3030	849.20 ± 16.25	548.1 ± 16.7	16.6 ± 1.1
Bumbat valley (Hangai)	BU1	HN-JB-01B	47.4355/100.3471	2128	2	22.24	0.36	1	7.5740	0.2530	1023.60 ± 16.40	2284.8 ± 61.0	103.7 ± 6.5
		HN-JB-01C	47.4355/100.3471	2128	3	22.06	0.36	1	6.6310	0.2697	436.55 ± 6.90	1186.5 ± 31.4	53.6 ± 3.3
		HN-JB-01A	47.4357/100.3468	2130	3	22.09	0.36	1	6.7270	0.2446	206.70 ± 6.50	502.2 ± 23.4	22.5 ± 1.6
	BU2	HN-JB-02A	47.4158/100.3573	2172	3	22.52	0.37	0.99	4.0770	0.2836	108.53 ± 3.04	504.5 ± 21.2	22.2 ± 1.5
		HN-JB-02B	47.4164/100.3559	2173	4	22.36	0.37	0.99	2.0590	0.2585	106.04 ± 2.93	889.6 ± 37.0	39.5 ± 2.8
		HN-JB-02C	47.4164/100.3559	2173	3	22.54	0.37	0.99	5.5590	0.2836	211.83 ± 4.85	722.1 ± 25.5	31.8 ± 2.1
		HN-JB-03A	47.4180/100.3525	2177	5	22.46	0.37	1	6.8460	0.2738	309.30 ± 7.50	826.6 ± 30.7	36.5 ± 2.5
		HN-JB-03B	47.4180/100.3525	2177	4	22.65	0.37	1	11.5840	0.2780	452.40 ± 17.30	725.5 ± 40.6	31.8 ± 2.5
		HN-JB-03C	47.4180/100.3525	2177	5	22.46	0.37	1	6.5930	0.2794	397.00 ± 9.20	1124.2 ± 40.1	49.9 ± 3.3
Non-glacial deposits at Sutai (Gobi-Altai)		MOT98-CS-20	46.6068/93.5628	3205	3	43.16	0.50	0.99	39.0000	0.2520	95.47 ± 6.61	41.2 ± 4.1	0.9 ± 0.1
		MOT98-CS-21	46.6068/93.5628	3205	3	43.16	0.50	0.99	39.7800	0.2520	164.00 ± 7.18	69.4 ± 4.4	1.6 ± 0.1
		MOT98-CS-08	46.6160/93.5639	3273	2.5	45.16	0.51	0.99	39.3600	0.2520	1263.39 ± 29.04	540.5 ± 19.2	11.9 ± 0.8
		DHC-98-17	46.6168/93.5645	3290	3	44.97	0.51	0.98	34.6500	0.3050	313.60 ± 7.33	184.5 ± 6.6	4.1 ± 0.3
		DHC-98-18	46.6168/93.5645	3290	1	45.72	0.51	0.98	34.3200	0.3030	1426.30 ± 27.03	841.4 ± 25.5	18.3 ± 1.2
		MOT98-CS-19	46.6168/93.5645	3290	3	44.97	0.51	0.98	39.4900	0.2530	98.67 ± 9.12	42.2 ± 5.6	0.9 ± 0.1
		SUT-IM-01A	46.6177/93.5656	3310	4	44.22	0.51	0.96	15.4490	0.2655	101.47 ± 3.01	116.5 ± 4.3	2.6 ± 0.2
		SUT-IM-01B	46.6177/93.5656	3310	3	44.58	0.51	0.96	14.2310	0.2724	101.65 ± 2.92	130.0 ± 4.7	2.9 ± 0.2
		SUT-IM-01C	46.6177/93.5656	3310	2	44.95	0.51	0.96	16.2570	0.2627	116.98 ± 3.83	126.3 ± 5.0	2.8 ± 0.2

[a] Constant (time-invariant) ^{10}Be production rate value of 3.99 ± 0.22 atoms g^{-1} yr^{-1} (Heyman, 2014) scaled by method of Lal (1991) and Stone (2000).

[b] Constant (time-invariant) local production rate based on Heisinger et al. (2002a, 2002b).

[c] Density of 2.65 g cm^{-3} was used based on the quartz vein and granitic composition of the surface samples.

[d] AMS isotope ratios measured at LLNL were normalized to ^{10}Be/Be standards prepared by Nishiizumi et al. (2007) with a nominal value of ^{10}Be/Be = 2.85 × 10^{-12}. Samples measured at ANSTO (see Fink & Smith 2007) were normalized to the NIST 4325-SRM with a ^{10}Be/Be value of 27.9 × 10^{-12} or 07KN-5-2 with a ^{10}Be/Be value of 8.56 × 10^{-12}. All three standard reference materials are internally consistent (see Nishiizumi et al., 2007).

[e] Uncertainties are reported at the 1σ confidence level.

[f] Propagated uncertainties include uncertainty in the blank, carrier concentration (1%), and counting statistics.

[g] Propagated 1σ "external" uncertainty in the model age includes "internal" uncertainties introduced in (f) in addition to a 5.5 % uncertainty in the production rate of ^{10}Be and a 1% uncertainty in the ^{10}Be decay constant. All ^{10}Be concentrations were converted to ages using a ^{10}Be half-life of 1.389 × 10^{6} yr (Chmeleff et al., 2010) using CRONUS-Earth calculator version 2.2 (Balco et al., 2008) to calculate the ages. The ^{10}Be standard is called 07KNSTD in CRONUS-Earth.

[h] We assumed zero erosion of the rock and no burial history. An erosion rate of 3 mm yr^{-1} would increase an age of 30 ka by ~10% (Batbaatar and Gillespie, 2016).

3.3.2 *Outlier identification of ^{10}Be ages*

Our work covered a broad, complex area and the number of dated samples per moraine was smaller than desired in order to characterize a population with a well-determined arithmetic mean and standard deviation. In studies such as this, identification of outliers is important, and commonly problematic. Key assumptions used in cosmic-ray exposure dating of glacial boulders—no inheritance, preservation of sample orientation and constant ^{10}Be production—predict a normal distribution of ages with low standard deviation roughly equal to analytical uncertainty. Large standard deviation of a population scatter is in question if dating for glacial boulders assumes no transportation of boulders after the initial deposition, and field context is helpful to sort through the distribution of ages.

We used series of analyses to identify outliers in the following order: 1) calculate the mean, μ_{group}, and standard deviation, σ_{group}, for n ages grouped according to landform; 2) calculate the reduced chi-squared value, $R\chi^2$, for n ages to test if the scatter in the group cannot be explained by analytical uncertainty alone; 3) for each sample i, calculate the normalized deviation, δ_i, from the mean calculated excluding the age of the tested sample, x_i. Samples for which δ_i>2 were rejected as outliers; 4) test whether in sequence of moraines the ^{10}Be ages were consistent with the relative ages of the moraines inferred geomorphically; 5) recalculate the $R\chi^2$ excluding the outliers; 6) evaluate the identified outliers using Chauvenet's (1960) and Peirce's (Ross, 2003) criterion to confirm that the surviving group samples contained no outliers. After excluding the outliers, we averaged the sample ages for a given landform and compounded standard deviation of the "reduced" group with the "internal" sample measurement uncertainties with the systematic uncertainties in the production and decay rates of ^{10}Be ("external" uncertainties). We report this

1σ total uncertainty as the duration of glacier advances or standstills for the given landform. Below we describe each of the analysis in detail.

Reduced chi-squared test (Table 3.3). It is defined as the chi-square per degree of freedom as below:

$$R\chi^2 = \frac{\chi^2}{n-1} \tag{3.3}$$

where $R\chi^2$ is the reduced chi-square, n is sample number in the group. The χ^2 is calculated as:

$$\chi^2 = \sum_{i=n}^{n} \frac{(x_i - \mu_{group})}{\sigma_i} \tag{3.4}$$

where x_i is the age of sample i, μ_{group} is the mean of the grouped ages, and σ_i is the internal uncertainty of sample i.

Normalized deviation from the mean (Table 3.3). For each sample, the normalized deviation from the mean, δ_i, was calculated as below:

$$\delta_i = \frac{|x_i - \mu_{n-i}|}{\sqrt{({\sigma_{n-i}}^2 + {\sigma_i}^2)}} \tag{3.5}$$

where μ_{n-i} is the mean of the grouped ages excluding the tested sample age x_i, σ_{n-i} is the standard deviation of the grouped ages excluding the tested sample age x_i. The sample was identified as outlier if the $\delta_i > 2$.

Chauvenet's criterion (Table 3.4). In Chauvenet's test it is assumed that the population is normally distributed and characterized by a mean and standard deviation (1σ), and the normalized probability of a data point in the distribution is calculated. If the product of the probability of data

point and the number of samples falls below 0.5, the data point is rejected as an outlier. The normal variance, z, is calculated as below:

$$z = \frac{|x_i - \mu_{group}|}{\sigma_{group}} \quad (3.6)$$

where σ_{group} is the standard deviation of the grouped ages. Next, normal density function was calculated using the NORMDIST(x_i, μ_{group}, σ_{group},TRUE) function of Microsoft Excel, in which the TRUE denotes that the NORMDIST function is calculating the cumulative distribution function from negative infinity to x_i. If the $z > 0.5$ the tail of the normal distribution is calculated as $2(1 - z)$, or if $z < 0.5$ the tail of the normal distribution is calculated as $2z$. Finally, these values were multiplied by the sample number to calculate the Chauvenet's criterion value. The sample age is rejected if the Chauvenet's criterion value < 0.5.

Peirce's criterion (Table 3.5). We used Ross' (2003) tabulated tables of Peirce R values to confirm the identified outliers. In Peirce's test the maximum allowable deviation of the group is calculated by multiplying a tabulated value corresponding to the number of samples and the standard deviation of the group, σ_{group}, and then compared to the actual deviation of a sample age from the mean, $|x_i - \mu_{group}|$. The data point is rejected if the deviation of the sample age from the mean is greater than the maximum allowable deviation, which is dependent on the sample number and standard deviation of the age group, and is unique to the grouped ages. Summary of outlier analyses is given in Table 3.6.

We also used the modified Kolmogorov-Smirnov test formulated by Lilliefors (1967). The Lilliefors formulation is commonly used to test whether the population is from a normal distribution when the mean and variance are unknown. We used the built-in function "lillietest" in Matlab. According to the Matlab documentation, the Lilliefors test statistic is defined as:

$$D^* = \left(x_i - \mu_{group}\right)\left|\hat{F}(x) - G(x)\right| \tag{3.7}$$

where $\hat{F}(x)$ is the empirical cumulative density function, and $G(x)$ is the hypothesized cumulative density function characterized by μ_{group} and σ_{group}.

In all age groups the Lilliefors test returned 0 logical answer at its default 5% significance level, which means that either 1) the population was normally distributed; or 2) the sample number was too low to reject the hypothesis that it wasn't.

Identification of outliers within a population of cosmogenic exposure ages depends largely on the AMS measurement quality of the dataset, the number of samples in the population expected to be coeval and the inherent variability of geologic processes associated with the preservation of the landform. Statistically, increasing the number of samples can define a population better, which can lead to a clearer selection of outliers from a well-defined population. However, if the exposure variability due to geologic processes is sufficiently great, the standard deviation of the population may not decrease simply by doing more analyses. For small sample sets, the consistency between the exposure ages and the sample positions with the sequence of moraines may provide the only criterion with which to identify an outlier.

Table 3.3. Outlier evaluation by "normalized deviation" method

Group	Sample ID	Age, x_i (ka)	1σ internal uncer-tainty in age, σ_i (ka)	CONSIDERING ALL SAMPLES				1σ normalized deviation from the excluded mean, δ_i	Reject if δ_i >2	REVISED AFTER OUTLIER REJECTION			
				μ, mean of the group (ka)	σ_{group}, 1σ st. dev of the group (ka)	$\chi^2 = \sum (X_i - \mu)^2/\sigma_i^2$	$R\chi^2 = \chi^2 / (n-1)$			μ, mean of the group (ka)	1σ st. dev of the group (ka)	$\chi^2 = \sum (X_i - \mu)^2/\sigma_i^2$	$R\chi^2 = \chi^2 / (n-1)$
Moraine G2	GN-JB-004	5.29	0.34	6.9	1.2	77.4	25.8	3.07	Reject	7.5	0.6	21.9	10.9
	GN-AG-10B	6.88	0.23					0.06	Accept				
	GN-JB-005	7.47	0.28					0.48	Accept				
	GN-AG-11	8.15	0.17					1.41	Accept				
Moraine G3	GN-AG-04	0.80	0.03	2.2	1.0	2426.2	606.6	2.47	Reject	2.5	0.7	198.6	66.2
	GN-AG-07	1.56	0.09					0.73	Accept				
	GN-AG-06	2.55	0.07					0.41	Accept				
	GN-AG-05	2.81	0.08					0.74	Accept				
	GN-AG-08	3.20	0.08					1.37	Accept				
Moraine G4	GN-JB-001	0.90	0.10	1.4	0.4	161.3	32.3	1.88	Accept	1.4	0.4	161.3	32.3
	GN-JB-002	1.04	0.10					1.22	Accept				
	GN-JB-003	1.47	0.27					0.05	Accept				
	GN-AG-03	1.58	0.05					0.35	Accept				
	GN-AG-01	1.83	0.05					1.14	Accept				
	GN-AG-02	1.87	0.06					1.30	Accept				
NE Slope, Moraine NE1	DHC-98-12	7.35	0.28	-	-	-	-	-	-				
NE Slope, Moraine NE2-4	DHC-98-15	6.75	0.24	20.2	9.1	3231.2	1077.1	10.69	Reject	24.7	1.7	9.9	5.0
	DHC-98-10	22.93	0.70					0.33	Accept				
	DHC-98-11	24.93	1.15					0.60	Accept				
	DHC-98-13	26.23	0.82					0.80	Accept				
Pass between ice caps #1 & 2	MOT98-CS-11b	13.22	0.60										
	MOT98-CS-12	24.78	0.16										
	MOT98-CS-11a	44.98	1.16										
Margin of ice cap #3	SUT-JB-04A	21.25	0.41										
	SUT-JB-04B	41.57	1.00										
SW Slope, Bedrock & erratic	MOT98-CS-22	22.15	0.80	47.3	35.5	-	-	-	-	-	-	-	-
	MOT98-CS-23	72.41	2.61					-	-				
SW Slope, moraine remnant(?)	MOT98-CS-14	35.61	1.82					-	-				
SW Slope, Moraine SW2	MOT98-CS-25	5.96	0.22	14.1	5.1	1487.6	371.9	3.99	Reject	16.2	2.5	78.9	26.3
	SUT-JB-02C	13.92	0.37					0.05	Accept				
	SUT-JB-02A	15.41	0.39					0.27	Accept				
	SUT-JB-02D	15.54	0.48					0.30	Accept				
	SUT-JB-02B	19.84	0.61					1.55	Accept				

Table 3.3 (continued)

Group	Sample ID	Age, x_i (ka)	1σ internal uncer-tainty in age, σ_i (ka)	CONSIDERING ALL SAMPLES				1σ normalized deviation from the excluded mean, δ_i	Reject if δ_i >2	REVISED AFTER OUTLIER REJECTION			
				μ, mean of the group (ka)	σ_{group}, 1σ st. dev of the group (ka)	$\chi^2 = \sum (X_i - \mu)^2/\sigma_i^2$	$R\chi^2 = \chi^2 / (n-1)$			μ, mean of the group (ka)	1σ st. dev of the group (ka)	$\chi^2 = \sum (X_i - \mu)^2/\sigma_i^2$	$R\chi^2 = \chi^2 / (n-1)$
Moraine IB5-6	IB-JB-003A	7.25	0.49	13.1	3.1	155.8	31.2	4.73	Reject	14.3	1.4	6.0	1.5
	IB-JB-003B	13.22	1.76					0.03	Accept				
	IB-JB-002	13.41	0.70					0.09	Accept				
	IB-JB-003D	13.93	0.93					0.27	Accept				
	IB-JB-003C	14.26	0.74					0.38	Accept				
	IB-JB-003E	16.72	1.23					1.36	Accept				
Moraine IB7	IB-JB-001	14.44	0.84	-	-			-	-				
Bogd valley, Moraine BO1	OT-AG-2	20.18	1.36	22.1	1.7	3.4	1.7	1.94	Accept	22.1	1.7	3.4	1.7
	OT-AG-1	22.65	1.24					0.29	Accept				
	OT-AG-3	23.55	1.31					0.98	Accept				
Bitüüt valley, Moraine BI2	DHC-98-8	29.89	0.91	48.0	30.2	890.2	445.1	0.75	Accept	30.6	1.0	1.2	1.2
	DHC-98-5	31.30	0.95					0.67	Accept				
	DHC-98-7	82.90	2.58					18.91	Reject				
Bitüüt valley, Moraine BI8	MOT98-CS-02	16.25	0.61	-	-								
Bitüüt valley, Moraine BI9	DHC-98-3	14.99	0.54	16.0	0.9	6.0	3.0	2.92	Reject	16.6	0.04	0.01	0.01
	MOT98-CS-04	16.54	0.50					0.60	Accept				
	MOT98-CS-05	16.60	0.51					0.69	Accept				
Moraine BU1	HN-JB-01A	22.50	1.05	60.0	41.0	1529.4	764.7	1.59	Uncertain		-	-	
	HN-JB-01C	53.64	1.44					0.16	Uncertain				
	HN-JB-01B	103.73	2.84					2.96	Uncertain				
Moraine BU2	HN-JB-02A	22.16	0.94	35.3	9.3	281.2	56.2	2.09	Reject	34.9	3.8	20.0	6.7
	HN-JB-02C	31.77	1.13					0.41	Accept				
	HN-JB-03B	31.78	1.79					0.41	Accept				
	HN-JB-03A	36.54	1.37					0.15	Accept				
	HN-JB-02B	39.54	1.66					0.50	Accept				
	HN-JB-03C	49.86	1.80					2.56	Reject				

Groups with a single sample, and groups with non-glacial samples were excluded from the outlier analysis.

Table 3.4. Outlier evaluation by Chauvenet's (1960) criteria

Group	Sample ID	Age, X_i (ka)	1σ internal uncertainty in age (ka)	Before outlier analysis			Norm. Variance	normdist. (-inf < x)	normdist. (-x < x)	normdist. (tail)	Np: Chauvenet's criterion
				Number of samples within the group	μ, mean of the group (ka)	1σ st.dev of the group (ka)	$z = \|X_i - \mu\|/\sigma$	(integral)	(integral)	(integral)	(Reject if <0.5)
Moraine G2	GN-JB-004	5.3	0.3	4	**6.9**	**1.2**	1.4	0.087	0.825	0.175	0.70
	GN-AG-10B	6.9	0.2				0.1	0.478	0.044	0.956	3.82
	GN-JB-005	7.5	0.3				0.4	0.666	0.331	0.669	2.67
	GN-AG-11	8.2	0.2				1.0	0.838	0.675	0.325	1.30
Moraine G3	GN-AG-04	0.8	0.0	5	**2.2**	**1.0**	1.4	0.080	0.841	0.159	0.80
	GN-AG-07	1.6	0.1				0.6	0.263	0.475	0.525	2.63
	GN-AG-06	2.6	0.1				0.4	0.645	0.290	0.710	3.55
	GN-AG-05	2.8	0.1				0.6	0.738	0.476	0.524	2.62
	GN-AG-08	3.2	0.1				1.0	0.849	0.699	0.301	1.51
Moraine G4	GN-JB-001	0.9	0.1	6	**1.4**	**0.4**	1.4	0.086	0.827	0.173	1.04
	GN-JB-002	1.0	0.1				1.0	0.155	0.690	0.310	1.86
	GN-JB-003	1.5	0.3				0.1	0.521	0.043	0.957	5.74
	GN-AG-03	1.6	0.1				0.3	0.628	0.257	0.743	4.46
	GN-AG-01	1.8	0.1				0.9	0.829	0.657	0.343	2.06
	GN-AG-02	1.9	0.1				1.0	0.853	0.706	0.294	1.77
NE Slope, Moraine NE2-4	DHC-98-15	6.8	0.2	4	**20.2**	**9.1**	1.5	0.069	0.862	0.138	0.55
	DHC-98-10	22.9	0.7				0.3	0.618	0.236	0.764	3.06
	DHC-98-11	24.9	1.2				0.5	0.698	0.397	0.603	2.41
	DHC-98-13	26.2	0.8				0.7	0.746	0.493	0.507	2.03
SW Slope, Moraine SW2	MOT98-CS-25	6.0	0.2	5	**14.1**	**5.1**	1.6	0.054	0.893	0.107	0.54
	SUT-JB-02C	13.9	0.4				0.0	0.483	0.034	0.966	4.83
	SUT-JB-02A	15.4	0.4				0.3	0.599	0.199	0.801	4.01
	SUT-JB-02D	15.5	0.5				0.3	0.609	0.218	0.782	3.91
	SUT-JB-02B	19.8	0.6				1.1	0.870	0.739	0.261	1.30

Table 3.4 (continued)

Group	Sample ID	Age, X_i (ka)	1σ internal uncertainty in age (ka)	Before outlier analysis			Norm. Variance	normdist. (-inf < x)	normdist. (-x < x)	normdist. (tail)	Np: Chauvenet's criterion
				Number of samples within the group	$z = \lvert X_i - \mu \rvert / \sigma$	1σ st.dev of the group (ka)	$z = \lvert X_i - \mu \rvert / \sigma$	(integral)	(integral)	(integral)	(Reject if <0.5)
Moraine IB5-6	IB-JB-003A	7.3	0.5	6	**13.1**	**3.1**	1.9	0.031	0.939	0.061	0.37
	IB-JB-003B	13.2	1.8				0.0	0.511	0.022	0.978	5.87
	IB-JB-002	13.4	0.7				0.1	0.535	0.071	0.929	5.58
	IB-JB-003D	13.9	0.9				0.3	0.600	0.200	0.800	4.80
	IB-JB-003C	14.3	0.7				0.4	0.640	0.280	0.720	4.32
	IB-JB-003E	16.7	1.2				1.1	0.873	0.746	0.254	1.52
Bogd valley, Moraine BO1	OT-AG-2	20.2	1.4	3	**22.1**	**1.7**	1.1	0.132	0.735	0.265	0.79
	OT-AG-1	22.7	1.2				0.3	0.618	0.236	0.764	2.29
	OT-AG-3	23.6	1.3				0.8	0.793	0.585	0.415	1.24
Bitüüt valley, Moraine BI2	DHC-98-8	29.9	0.9	3	**48.0**	**30.2**	0.6	0.274	0.452	0.548	1.64
	DHC-98-5	31.3	1.0				0.6	0.290	0.420	0.580	1.74
	DHC-98-7	82.9	2.6				1.2	0.876	0.752	0.248	0.75
Bitüüt valley, Moraine BI9	DHC-98-3	15.0	0.5	3	**16.0**	**0.9**	1.2	0.124	0.752	0.248	0.75
	MOT98-CS-04	16.5	0.5				0.5	0.707	0.414	0.586	1.76
	MOT98-CS-05	16.6	0.5				0.6	0.729	0.458	0.542	1.63
Moraine BU1	HN-JB-01A	22.5	1.1	3	**60.0**	**41.0**	0.9	0.180	0.639	0.361	1.08
	HN-JB-01C	53.6	1.4				0.2	0.439	0.122	0.878	2.63
	HN-JB-01B	103.7	2.8				1.1	0.857	0.715	0.285	0.86
Moraine BU2	HN-JB-02A	22.2	0.9	6	**35.3**	**9.3**	1.4	0.078	0.843	0.157	0.94
	HN-JB-02C	31.8	1.1				0.4	0.353	0.295	0.705	4.23
	HN-JB-03B	31.8	1.8				0.4	0.353	0.294	0.706	4.24
	HN-JB-03A	36.5	1.4				0.1	0.554	0.109	0.891	5.35
	HN-JB-02B	39.5	1.7				0.5	0.677	0.355	0.645	3.87
	HN-JB-03C	49.9	1.8				1.6	0.942	0.885	0.115	0.69

Groups with a single sample, and groups with non-glacial samples were excluded from the outlier analysis.

Table 3.5. Outlier evaluation by Peirce's criteria (Ross, 2003)

Group	Sample ID	Age, X_i (ka)	1σ internal uncer-tainty in age (ka)	Before outlier analysis			$\lvert X_i - \mu \rvert$	Peirce R value (cf. Peirce Criterion Table **)	$(Xi - \mu)_{max}$	Reject if: $\lvert X_i - \mu \rvert > (Xi - \mu)max$	Peirce R value (cf. Peirce Criterion Table **)	$(Xi - \mu)_{max}$	Reject if: $\lvert Xi - \mu \rvert > (Xi - \mu)max$
				Number of samples within the group	μ, mean of the group (ka)	1σ st.dev of the group (ka)							
Moraine G2	GN-JB-004	5.3	0.3	4	6.9	1.2	1.658	1.383 (1 out of 4)	1.688	Accept			
	GN-AG-10B	6.9	0.2				0.067			Accept			
	GN-JB-005	7.5	0.3				0.523			Accept			
	GN-AG-11	8.2	0.2				1.203			Accept			
Moraine G3	GN-AG-04	0.8	0.0	5	2.2	1.0	1.384	1.509 (1 out of 5)	1.483	Accept			
	GN-AG-07	1.6	0.1				0.624			Accept			
	GN-AG-06	2.6	0.1				0.366			Accept			
	GN-AG-05	2.8	0.1				0.626			Accept			
	GN-AG-08	3.2	0.1				1.016			Accept			
Moraine G4	GN-JB-001	0.9	0.1	6	1.4	0.4	0.548	1.610 (1 out of 6)	0.647	Accept			
	GN-JB-002	1.0	0.1				0.408			Accept			
	GN-JB-003	1.5	0.3				0.022			Accept			
	GN-AG-03	1.6	0.1				0.132			Accept			
	GN-AG-01	1.8	0.1				0.382			Accept			
	GN-AG-02	1.9	0.1				0.422			Accept			
NE Slope, Moraine NE2-4	DHC-98-15	6.8	0.2	4	20.2	9.1	13.460	1.383 (1 out of 4)	12.551	Reject	1.078 (2 out of 4)	9.783	
	DHC-98-10	22.9	0.7				2.720			Accept			Accept
	DHC-98-11	24.9	1.2				4.720			Accept			Accept
	DHC-98-13	26.2	0.8				6.020			Accept			Accept
SW Slope, Moraine SW2	MOT98-CS-25	6.0	0.2	5	14.1	5.1	8.174	1.509 (1 out of 5)	7.658	Reject	1.200 (2 out of 5)	6.090	
	SUT-JB-02C	13.9	0.4				0.214			Accept			Accept
	SUT-JB-02A	15.4	0.4				1.276			Accept			Accept
	SUT-JB-02D	15.5	0.5				1.406			Accept			Accept
	SUT-JB-02B	19.8	0.6				5.706			Accept			Accept

Table 3.5 (continued)

Group	Sample ID	Age, X_i (ka)	1σ internal uncer-tainty in age (ka)	Before outlier analysis			$\lvert X_i - \mu \rvert$	Peirce R value (cf. Peirce Criterion Table **)	$(Xi - \mu)_{max}$	Reject if: $\lvert X_i - \mu \rvert > (Xi - \mu)max$	Peirce R value (cf. Peirce Criterion Table **)	$(Xi - \mu)_{max}$	Reject if: $\lvert Xi - \mu \rvert > (Xi - \mu)max$
				Number of samples within the group	μ, mean of the group (ka)	1σ st.dev of the group (ka)							
Moraine IB5-6	IB-JB-003A	7.3	0.5	6	13.1	3.1	5.882	1.610	5.064	Reject	1.299	4.086	
	IB-JB-003B	13.2	1.8				0.088	(1 out of 6)		Accept	(2 out of 6)		Accept
	IB-JB-002	13.4	0.7				0.278			Accept			Accept
	IB-JB-003D	13.9	0.9				0.798			Accept			Accept
	IB-JB-003C	14.3	0.7				1.128			Accept			Accept
	IB-JB-003E	16.7	1.2				3.588			Accept			Accept
Bogd valley, Moraine BO1	OT-AG-2	20.2	1.4	3	22.1	1.7	1.947	1.196	2.087	Accept			
	OT-AG-1	22.7	1.2				0.523	(1 out of 3)		Accept			
	OT-AG-3	23.6	1.3				1.423			Accept			
Bitüüt valley, Moraine BI2	DHC-98-8	29.9	0.9	3	48.0	30.2	18.140	1.196	36.127	Accept			
	DHC-98-5	31.3	1.0				16.730	(1 out of 3)		Accept			
	DHC-98-7	82.9	2.6				34.870			Accept			
Bitüüt valley, Moraine BI9	DHC-98-3	15.0	0.5	3	16.0	0.9	1.053	1.383	1.262	Accept			
	MOT98-CS-04	16.5	0.5				0.497	(1 out of 3)		Accept			
	MOT98-CS-05	16.6	0.5				0.557			Accept			
Moraine BU1	HN-JB-01A	22.5	1.1	3	60.0	41.0	37.457	1.196	49.014	Accept			
	HN-JB-01C	53.6	1.4				6.317	(1 out of 3)		Accept			
	HN-JB-01B	103.7	2.8				43.773			Accept			
Moraine BU2	HN-JB-02A	22.2	0.9	6	35.3	9.3	13.115	1.610	14.913	Accept			
	HN-JB-02C	31.8	1.1				3.505	(1 out of 6)		Accept			
	HN-JB-03B	31.8	1.8				3.495			Accept			
	HN-JB-03A	36.5	1.4				1.265			Accept			
	HN-JB-02B	39.5	1.7				4.265			Accept			
	HN-JB-03C	49.9	1.8				14.585			Accept			

Groups with a single sample, and groups with non-glacial samples were excluded from the outlier analysis.

Table 3.6. Summary of outlier evaluations

Group	Sample ID	Age (ka)	1σ internal uncer-tainty[1] in age (ka)	1σ external uncer-tainty[2] in age (ka)	Outlier evaluation method			Group age including all samples (ka)		Group age after rejecting outliers (ka)		Interpreted 1σ age range for the group
					Normalized deviation	Chauvenet's [3]	Peirce's [4]	Mean	1σ total uncer-tainty [5]	Mean	1σ total uncer-tainty [5]	
Moraine G2	GN-JB-004	5.3	0.34	0.4	Rejected	Accepted	Accepted	7.0	1.3	7.5	0.8	8.3–6.7 ka
	GN-AG-10B	6.9	0.23	0.4	Accepted	Accepted	Accepted					
	GN-JB-005	7.5	0.28	0.5	Accepted	Accepted	Accepted					
	GN-AG-11	8.1	0.17	0.5	Accepted	Accepted	Accepted					
Moraine G3	GN-AG-04	0.8	0.03	0.1	Rejected	Accepted	Accepted	2.2	1.0	2.6	0.7	3.3–1.8 ka
	GN-AG-07	1.6	0.09	0.1	Accepted	Accepted	Accepted					
	GN-AG-06	2.6	0.07	0.2	Accepted	Accepted	Accepted					
	GN-AG-05	2.8	0.08	0.2	Accepted	Accepted	Accepted					
	GN-AG-08	3.2	0.08	0.2	Accepted	Accepted	Accepted					
Moraine G4	GN-JB-001	0.9	0.10	0.1	Accepted	Accepted	Accepted	1.5	0.4	1.5	0.4	1.9–1.0 ka
	GN-JB-002	1.0	0.10	0.1	Accepted	Accepted	Accepted					
	GN-JB-003	1.5	0.27	0.3	Accepted	Accepted	Accepted					
	GN-AG-03	1.6	0.05	0.1	Accepted	Accepted	Accepted					
	GN-AG-01	1.8	0.05	0.1	Accepted	Accepted	Accepted					
	GN-AG-02	1.9	0.06	0.1	Accepted	Accepted	Accepted					
NE Slope, Moraine NE2-4	DHC-98-15	6.7	0.24	0.4	Rejected	Accepted	Rejected	20.2	9.2	24.7	2.4	27.0–22.3 ka
	DHC-98-10	22.9	0.70	1.5	Accepted	Accepted	Accepted					
	DHC-98-11	24.9	1.15	1.8	Accepted	Accepted	Accepted					
	DHC-98-13	26.2	0.82	1.7	Accepted	Accepted	Accepted					
Pass between ice caps #1 & 2	MOT98-CS-11b	13.2	0.60	0.9	Uncertain	No eval.	No eval.	-	-	-	-	> 13 (?)
	MOT98-CS-12	24.8	0.16	2.1	Uncertain	No eval.	No eval.					
	MOT98-CS-11a	45.0	1.16	2.8	Uncertain	No eval.	No eval.					
Margin of ice cap #3	SUT-JB-04A	21.3	0.41	1.2	Uncertain	No eval.	No eval.	-	-	-	-	> 21 (?)
	SUT-JB-04B	41.6	1.00	2.5	Uncertain	No eval.	No eval.					
SW Slope, Bedrock & erratic	MOT98-CS-22	22.1	0.80	1.5	Uncertain	No eval.	No eval.	-	-	-	-	> 22 (?)
	MOT98-CS-23	72.4	2.61	4.8	Rejected	No eval.	No eval.					
	MOT98-CS-25	6.0	0.22	0.4	Rejected	Accepted	Rejected					
SW Slope, Moraine SW2	SUT-JB-02C	13.9	0.37	0.9	Accepted	Accepted	Accepted	14.1	5.1	16.2	2.7	18.9–13.4 ka
	SUT-JB-02A	15.4	0.39	0.9	Accepted	Accepted	Accepted					
	SUT-JB-02D	15.5	0.48	1.0	Accepted	Accepted	Accepted					
	SUT-JB-02B	19.8	0.61	1.3	Accepted	Accepted	Accepted					

Table 3.6 (continued)

Group	Sample ID	Age (ka)	1σ internal uncer-tainty[1] in age (ka)	1σ external uncer-tainty[2] in age (ka)	Outlier evaluation method			Group age including all samples (ka)		Group age after rejecting outliers (ka)		Interpreted 1σ age range for the group
					Normalized deviation	Chauvenet's [3]	Peirce's [4]	Mean	1σ total uncer-tainty [5]	Mean	1σ total uncer-tainty [5]	
Moraine IB5-6	IB-JB-003A	7.3	0.49	0.6	Rejected	Rejected	Rejected	13.1	3.4	14.3	1.9	16.2–12.4 ka
	IB-JB-003B	13.2	1.76	1.9	Accepted	Accepted	Accepted					
	IB-JB-002	13.4	0.70	1.0	Accepted	Accepted	Accepted					
	IB-JB-003D	13.9	0.93	1.2	Accepted	Accepted	Accepted					
	IB-JB-003C	14.3	0.74	1.1	Accepted	Accepted	Accepted					
	IB-JB-003E	16.7	1.23	1.5	Accepted	Accepted	Accepted					
Bogd valley, Moraine BO1	OT-AG-2	20.2	1.36	1.8	Accepted	Accepted	Accepted	22.2	2.5	22.2	2.5	24.7–19.6 ka
	OT-AG-1	22.7	1.24	1.8	Accepted	Accepted	Accepted					
	OT-AG-3	23.6	1.31	1.9	Accepted	Accepted	Accepted					
Bitüüt valley, Moraine BI2	DHC-98-8	29.9	0.91	1.9	Accepted	Accepted	Accepted	48.0	30.4	30.6	2.2	32.8–28.4 ka
	DHC-98-5	31.3	0.95	2.0	Accepted	Accepted	Accepted					
	DHC-98-7	82.9	2.58	5.3	Rejected	Accepted	Accepted					
Bitüüt valley, Moraine BI9	DHC-98-3	15.0	0.54	1.0	Rejected	Accepted	Accepted	16.0	1.4	16.6	1.1	17.6–15.5 ka
	MOT98-CS-04	16.5	0.50	1.0	Accepted	Accepted	Accepted					
	MOT98-CS-05	16.6	0.51	1.1	Accepted	Accepted	Accepted					
Moraine BU1	HN-JB-01A	22.5	1.05	1.6	Uncertain	Accepted	Accepted	59.9	41.1	-	-	>> 22 (?)
	HN-JB-01C	53.6	1.44	3.3	Uncertain	Accepted	Accepted					
	HN-JB-01B	103.7	2.84	6.5	Uncertain	Accepted	Accepted					
Moraine BU2	HN-JB-02A	22.2	0.94	1.5	Rejected	Accepted	Accepted	35.3	9.6	34.9	4.5	39.4–30.4 ka
	HN-JB-02C	31.8	1.13	2.1	Accepted	Accepted	Accepted					
	HN-JB-03B	31.8	1.79	2.5	Accepted	Accepted	Accepted					
	HN-JB-03A	36.5	1.37	2.5	Accepted	Accepted	Accepted					
	HN-JB-02B	39.5	1.66	2.8	Accepted	Accepted	Accepted					
	HN-JB-03C	49.9	1.80	3.3	Rejected	Accepted	Accepted					

1) Propagated "internal" uncertainties include uncertainty in the blank, carrier concentration (1%), and counting statistics.

2) Propagated “external” uncertainty in the model age includes “internal” uncertainties in addition to a 5.5 % uncertainty in the production rate of ^{10}Be and a 1% uncertainty in the ^{10}Be decay constant.

3) Chauvenet (1960).

4) Ross (2003)

5) Total uncertainty compounds the 1σ standard deviation of the group and the average of 1σ external uncertainties of ages in the group

3.3.3 *Equilibrium-Line Altitude (ELA)*

We estimated the ELA for the dated lateral moraines using the Maximum-Elevation of Lateral Moraine (MELM) method (Porter, 2001) where possible. If end moraines could be mapped, we used the Toe–Headwall Altitude Ratio (THAR) method (Porter, 2001) with a threshold value of 0.58, as estimated for northern Mongolia by Gillespie et al. (2008). In this approach the ELA may be found by

$$ELA = A_t + 0.58(A_h - A_t) \quad (3.1)$$

where A_h and A_t are the headwall and toe altitudes, respectively. The headwall altitudes of the modern glaciers on Sutai were measured from the visible bergschrund on Google Earth. We selected the headwall altitudes for paleoglaciers at one third of the altitude difference between the cirque floor and the top of the rock cliff (details are given in Table 3.7), which was a similar ratio for schrund-lines estimated in White Mountains, New Hampshire, USA (Goldthwait, 1970). In some cirques the headwall was defined as the point at which avalanche chutes ended in free air, where once the glacier shielded the rock below from erosion. However, in general there is no objective rule with which to estimate headwall altitude. At each valley, we assumed that the paleoglaciers shared the same headwall altitude, resulting in a THAR ELA that is only sensitive to toe altitude, defined as the minimum altitude of the crest of the terminal moraine. Therefore, the paleo headwall altitudes were higher than all the local ELAs, even on the southwestern slope of Sutai where there is a modern glacier.

The precision of the estimated ELAs depends on the accuracy of the GPS units (10 m) used to measure altitudes, the vertical uncertainty of SRTM data (30 m) used in Google Earth. However, the accuracy as judged by agreement among estimation strategies is significantly lower, around ~100 m (e.g., for the Sierra Nevada in the western USA: Gillespie, 1991). This low accuracy only affects the local ELA itself, and not the difference between ELAs for adjacent valleys.

The selection of a threshold value of THAR (ranges from 0.4–0.6) was the biggest source of inaccuracy in our study. For example, for large paleoglaciers such as at Otgontenger, the large difference between the toe and headwall altitudes (~1,300 m) leads to a large uncertainty (~130 m) in the ELA. Small cirque glaciers (and their ELAs), on the other hand, are constrained to lie in a narrow range of altitudes, and their uncertainties can approach the measurement precision.

The Accumulation-Area Ratio (AAR) method of ELA estimation depends on an accurate reconstruction of the paleoglacier extent, which in turn requires accurate information on the headwall altitude and also the thickness of the glacier in order to delimit the ice areas. We did not use the AAR method, normally considered to be the most accurate, to estimate the ELAs, because of the complexity of the outlines of many of the studied paleoglaciers and because of the strong differences in the long profiles of the glaciated valleys we studied.

The local ELA values for a glacial sequence were normalized against the altitudes of the headwall and the minimum ELA for the sequence to compare the magnitudes of ELA lowering for the dated moraines using equation (3.2):

$$ELA_{norm} = \frac{A_h - ELA_{dated}}{A_h - ELA_{min}} \quad (3.2)$$

where ELA_{norm} is the normalized ELA, A_h is the headwall altitude, ELA_{dated} is the ELA for the dated moraine, and ELA_{min} is the ELA for the lowest end moraine in the valley, whether it was dated or not. Thus, ELA_{min} corresponds to the local LGM advance.

Table 3.7. Equilibrium-line altitude estimations

Site	Moraine group	Location (degrees)	Altitude (m asl)	Mean group age (ka)	1σ total uncertainty of the group age (ka)	Toe altitude (m asl)	Estimated ELA (m asl)	Normalized magnitude of local ELA lowering	ELA method	References
Gichginii range, Mönh Mösnii valley	Headwall	45.40005/97.07027	3440	-	-	-	-	-		
	Moraine G1	45.4031/97.0710	3290–3320	?	?	3290	3320	1.00	MELM	This study
	Moraine G2	45.4039/97.0703	3297–3330	7.5	0.8	3297	3330	0.92	MELM	This study
	Moraine G3	45.4015/97.0697	3310–3360	2.6	0.7	3310	3360	0.67	MELM	This study
	Moraine G4	45.4012/97.0697	3320–3365	1.5	0.4	3320	3365	0.63	MELM	This study
	Moraine G5	45.4018/97.0687	3335–3370	?	?	3335	3370	0.58	MELM	This study
			Minimum ELA corresponding the local LGM (m asl) ==>				3320			
Sutai range, NE slope	Headwall	46.63358/93.55765	3800	-	-	-	-	-		
	Moraine N1	46.6418/93.5710	3110–3220	?	?	3110	3510	1.00	THAR	This study
	Moraine NE2–4	46.6418/93.5659	3240–3315	24.7	2.4	3245	3567	0.80	THAR	This study
	Modern glacier	46.6362/93.5540	3555–3920	0.0	0.0	3555	3697	0.36	THAR	This study
			Minimum ELA corresponding the local LGM (m asl) ==>				3510			
Sutai range, SW slope	Headwall	46.62312/93.59323	4100	-	-	-	-	-		
	Bedrock	46.6012/93.5490	3105	> 22 (?)	-	?	?	?		This study
	Moraine SW2	46.6132/93.5503	3238–3275	16.2	2.7	-	3275	1.00	MELM	This study
	Modern glacier	46.6231/93.5932	3545–4100	0.0	0.0	3545	3867	0.28	THAR	This study
			Minimum ELA corresponding the local LGM (m asl) ==>				3275			
Ih Bogd range, Artsan valley	Headwall	44.95975/100.26923	3500	-	-	-	-	-		
	Moraine IB1	44.9559/100.2639	3325–3365	?	?	3325	3427	1.00	THAR	This study
	Moraine IB5-6	44.9563/100.2668	3380–3430	14.3	1.9	3380	3450	0.69	THAR	This study
			Minimum ELA corresponding the local LGM (m asl) ==>				3427			
Otgontenger, Bogd valley	Headwall	47.60961/97.54489	3400	-	-	-	-	-		
	Shuvuun hill (erratics)	47.6835/97.2098	2140	37.5	2.5	2070	2841	1.00	THAR	Rother et al., 2014
	Moraine BO1	47.6833/97.2067	2070–2150	22.2	2.5	2070	2841	1.00	THAR	This study
	Recessional moraine	47.6883/97.2496	2085–2150	18.4	3.3	2150	2875	0.94	THAR	Rother et al., 2014
	Modern ice cap	47.6080/97.5523	4000–3645	0.0	0.0	-	3800	-0.72	THAR	This study
			Minimum ELA corresponding the local LGM (m asl) ==>				2841			
Otgontenger, Bitüüt valley	Headwall	47.65663/97.59901	3100	-	-	-	-	-		
	Moraine BI1	47.5721/97.6751	2510–2555	?	?	2510	2852	1.00	THAR	This study
	Moraine BI2	47.5755/97.6677	2525–2610	30.6	2.2	2525	2859	0.97	THAR	This study
	Moraine BI9	47.6035/97.6405	2721–2730	16.6	1.1	2721	2941	0.64	THAR	This study
			Minimum ELA corresponding the local LGM (m asl) ==>				2852			
Bumbat valley	Headwall	47.29765/100.46943	3080	-	-	-	-	-		
	Moraine BU1	47.4355/100.3471	2110–2210	>> 22 (?)	-	2110	2673	1.00	THAR	This study
	Moraine BU2	47.4180/100.3525	2135–2220	34.9	4.5	2135	2683	0.97	THAR	This study
			Minimum ELA corresponding the local LGM (m asl) ==>				2673			

3.3.4 *Surface-energy balance model*

We followed the methods of Rupper and Roe (2008) to calculate potential ablation as a function of air temperature (T_a) (see detailed explanation and references for the surface-energy balance model in their original article). Our exercise was not aimed to simulate actual glaciers, but rather to demonstrate the variation of ablation via melting and sublimation due to changes only in T_a, which decreases with increasing altitude via the locally measured summer adiabatic lapse rate (8 °C km^{-1}: Table 3.8). This lapse rate was derived from T_a measured atop the Sutai ice cap at 4,000 m asl and the daily mean T_a data from the town of Tonhil 40 km to the southeast and at 2,200 m asl (NOAA, 2016). Because the T_a at Sutai was measured on an ice surface the derived lapse rate of 8 °C km^{-1} is probably greater than environmental lapse rates derived from measurements on land. We used monthly mean reanalysis climate data for the Gichginii range (Kalnay et al., 1996), scaled so that the summer (JJA average) T_a was zero at 3,000 m asl, a condition equivalent to −6 °C decrease from modern T_a. This constraint on the range of T_a in the model may appear to be arbitrary, but it provides an altitude dependency (i.e., decrease) in T_a that is similar to modeled MIS 2 conditions in the Gobi (Annan and Hargreaves, 2013) and it captures the seasonal and annual variability of T_a in the Gobi. Incoming shortwave radiation was reduced due to an assumed summer ice albedo of 0.6 (e.g., Cuffey and Patterson, 2010, pp. 146) and was taken to be constant at all altitudes. We then calculated incoming longwave radiation from T_a under clear sky. The outgoing longwave radiation was calculated from the ice-surface temperature (T_s), which iteratively solved to balance all the energy fluxes, including turbulent sensible and latent heat fluxes. If T_s was positive, it was reset to zero and the net energy flux was calculated again to estimate melting. Major parameters and variables remained constant at all altitudes for simplicity: wind speed = 2 m s^{-1}, relative humidity = 50%, height at which wind speed and air temperature

measured = 2 m, and scalar roughness lengths = 0.5 mm. Long-term monthly mean of *Ta* and precipitation for the study sites are given in Table 3.9. Regional changes in climate parameters during global LGM and Holocene in the study sites are given in Table 3.10.

Table 3.8. Temperature and relative humidity measurements for the Sutai range. We used an EL-USB-2 sensor from Lascar Electronics to measure T_a and humidity above the surface of ice cap #3. The sensors were placed at 4000 m asl and 1.8 m above the ice surface. Weather data for 2200 m asl are from Tonhil town, 40 km southeast of Sutai (NOAA, 2016). The average of our measured near-surface lapse rate (8 °C km^{-1}) was greater than the annually measured lapse rate in the Italian Alps (~6.0 °C km^{-1}: Rolland 2002) and the modeled maximum lapse rates in the Cascade Mountains, Washington State, USA (6.5–7.5 °C km^{-1}: Minder et al., 2010). The lower lapse rate used in the surface-energy model would increase T_a overall, which lengthened the melting season by 1–2 months and decreased the snowfall by 15–20% in the studied sites. However, the increased T_a in winter and spring makes the ice surface warmer, leading to increased sublimation (e.g., Cuffey and Paterson, 2010).

Date	Relative Humidity (%)		Mean Daily T_a (°C)		Lapse rate (°C km^{-1})
	2200 m asl	4000 m asl	2200 m asl	4000 m asl	
5/24/2013	31	76	10.1	−6.7	9.4
5/25/2013	41	81	8.0	−8.2	9.0
5/26/2013	44	77	4.9	−11.0	8.8
5/27/2013	47	83	1.6	−13.3	8.3
5/28/2013	23	45	7.9	−6.5	8.0
5/29/2013	29	56	11.3	−3.2	8.0
5/30/2013	39	74	8.1	−5.5	7.5
5/31/2013	32	48	7.0	−5.6	7.0
6/1/2013	15	43	11.7	−4.7	9.1
6/2/2013	24	56	12.9	−1.7	8.1
6/3/2013	37	85	14.2	−2.3	9.2
6/4/2013	37	70	14.3	−0.7	8.4
6/5/2013	39	74	13.7	−1.0	8.2
6/6/2013	42	62	10.5	−2.3	7.1
6/7/2013	30	70	9.8	−5.1	8.3
6/8/2013	42	81	6.2	−9.3	8.6
6/9/2013	24	47	10.4	−3.2	7.5
6/10/2013	17	34	15.2	1.7	7.5
6/11/2013	19	51	17.2	0.8	9.1
6/12/2013	32	57	11.2	−3.2	8.0
6/13/2013	51	80	8.8	−4.5	7.4
6/14/2013	66	89	7.8	−5.4	7.3
6/15/2013	48	74	9.7	−4.4	7.8
6/16/2013	44	77	10.7	−3.3	7.8
6/17/2013	31	61	14.5	−1.1	8.7
6/18/2013	26	62	16.0	1.1	8.3
6/19/2013	37	78	16.2	1.0	8.5
6/20/2013	82	100	9.6	−1.2	6.0
6/21/2013	73	100	11.1	−1.2	6.8
6/22/2013	79	100	11.7	−0.7	6.9
Average	**39**	**70**	**10.7**	**−3.7**	**8.0**

Table 3.9. Summary of modern climate at the study sites scaled with a lapse rate of 7.9 °C km^{-1} (average of measured summer T_a in Table 3.8). The table below includes monthly mean air temperature (T_a, °C: Kalnay et al., 1996), total precipitation (P, mm: Schneider et al., 2016), and zonal mean solar insolation (S, W m^{-2}). The lower part of the table shows the seasonal and annual mean T_a where winter is December–February, spring is March–May, summer is June–August, and autumn is September–November. Aridity index and corresponding environmental classification (Zomer et al., 2008) are included. Precipitation as snow or rain was not available.

	Gichginii 3380 m asl		Sutai 3870 m asl		Ih Bogd 3470 m asl		Otgontenger 3800 m asl		Bumbat 3100 m asl		45°N
	T_a	P	T_a	P	T_a	P	T_a	P	T_a	P	S
January	−28.7	1	−33.9	1	−30.2	2	−34.1	1	−28.9	2	149
February	−24.8	1	−30.6	1	−26.3	1	−30.6	2	−25.6	2	225
March	−17.4	2	−24.1	2	−18.7	5	−23.6	4	−18.6	6	313
April	−8.2	2	−15.6	4	−9.2	5	−14.8	5	−9.4	10	403
May	−0.1	3	−8.5	12	−1.1	10	−7.1	11	−1.5	26	464
June	5.8	6	−2.6	24	4.7	14	−1.3	25	4.3	51	485
July	7.8	17	0	31	6.8	33	0.9	48	6.4	78	461
August	5.5	13	−1.7	24	4.4	23	−1.2	34	4.2	64	398
September	−0.9	6	−7.8	10	−2.0	12	−7.4	16	−2.0	20	309
October	−10.1	2	−16.6	4	−11.1	4	−16.1	6	−10.6	11	218
November	−20.3	1	−26.4	1	−21.5	2	−26.2	3	−20.8	5	146
December	−27.3	1	−32.5	1	−28.7	2	−32.6	2	−27.3	3	121
Winter	−26.9	2	−32.3	3	−28.4	6	−32.4	5	−27.3	7	165
Spring	−8.6	7	−16.1	18	−9.7	19	−15.2	20	−9.8	42	393
Summer	6.4	37	−1.4	79	5.3	69	−0.5	107	5.0	194	448
Autumn	−10.4	9	−16.9	16	−11.5	18	−16.6	25	−11.1	36	225
Annual	−9.9	55	−16.7	115	−11.1	112	−16.2	158	−10.8	279	308
Aridity index		0.2		0.5		0.4		0.6		0.6	
Classification		arid		semi-arid		semi-arid		dry sub-humid		dry sub-humid	

Table 3.10. Regional changes in climate parameters during global LGM and early Holocene compared to modern values. The table shows the anomalies in annual and summer mean air temperature (T_a), annual precipitation (P), and zonal mean solar insolation (S) at 45°N for global LGM (Owen et al., 1998; Bintanja and van de Wal, 2008; Braconnot 2007; Annan and Hargreaves, 2013) and for early Holocene (Herzschuh, 2006; Miehe et al., 2007; Bintanja and van de Wal, 2008; Jin et al., 2012) compared to modern means. Summer is the mean for June–August, and winter is the mean for December–February.

	Units	22 ka (global LGM)	8 ka (early Holocene)
Summer ΔT_a	°C	−8	3
Annual ΔT_a	°C	−16	−2
Annual ΔP	mm yr^{-1}	× 0.75	× 2
Summer ΔS	W m^{-2}	−5	26
Winter ΔS	W m^{-2}	2	−10

3.4 RESULTS

The major results reported in this article are the mapping and dating of the local maximum glaciations in the arid to subhumid regions of central Mongolia.

3.4.1 *Glaciations in the Gobi-Altai ranges*

Gichginii range… The Gichginii range (Figures 3.2 and 3.4a) lies in the central part of the Gobi-Altai, and of the five sites we studied it receives the least precipitation (~55 mm yr^{-1}; long-term data (Schneider et al., 2015) for an area 0.5° × 0.5° centered on the site). Here, a ~1.5 km^2 plateau shows cryoplanation surfaces at ~3,580, ~3,550, and ~3520 m asl, and it may have provided the base for a paleo-ice cap (Figure 3.5). Similar to modern ice caps at Sutai and their outlet glaciers, this putative paleo-ice cap on the Gichginii plateau appears to have spilled north into the upper Mönh Mösnii valley. The Gichginii plateau consists of dark schist, but the northern wall of the Mönh Mösnii cirque consists of light tan-weathering gray limestone. The southern side of the cirque is a steep (~30°) headwall of schist bedrock which grades down via modern talus beneath bottomless avalanche chutes into a ~15° northeast-sloping cirque floor. The avalanche chutes terminate about 70 m below the plateau, below which where ice once shielded the lower headwall from erosion and deposition; in nearby unglaciated valleys the avalanche chutes reach the valley floors. At least five diamicton ridges were deposited on the cirque floor as much as 250 m below and ~0.6 km from the plateau. The clearly separated linear–arcuate ridges rise ~30 m above the valley floor and within the deposit have a relief of 3–4 m. At the lower edge of the cirque the ridges sit atop schist bedrock. The long profile of Mönh Mösnii valley is concave-convex-concave, typical of glaciated valleys, and the ridges spill over the bedrock lip of the cirque and down to the concave portion of the valley, a vertical distance of ~50 m below.

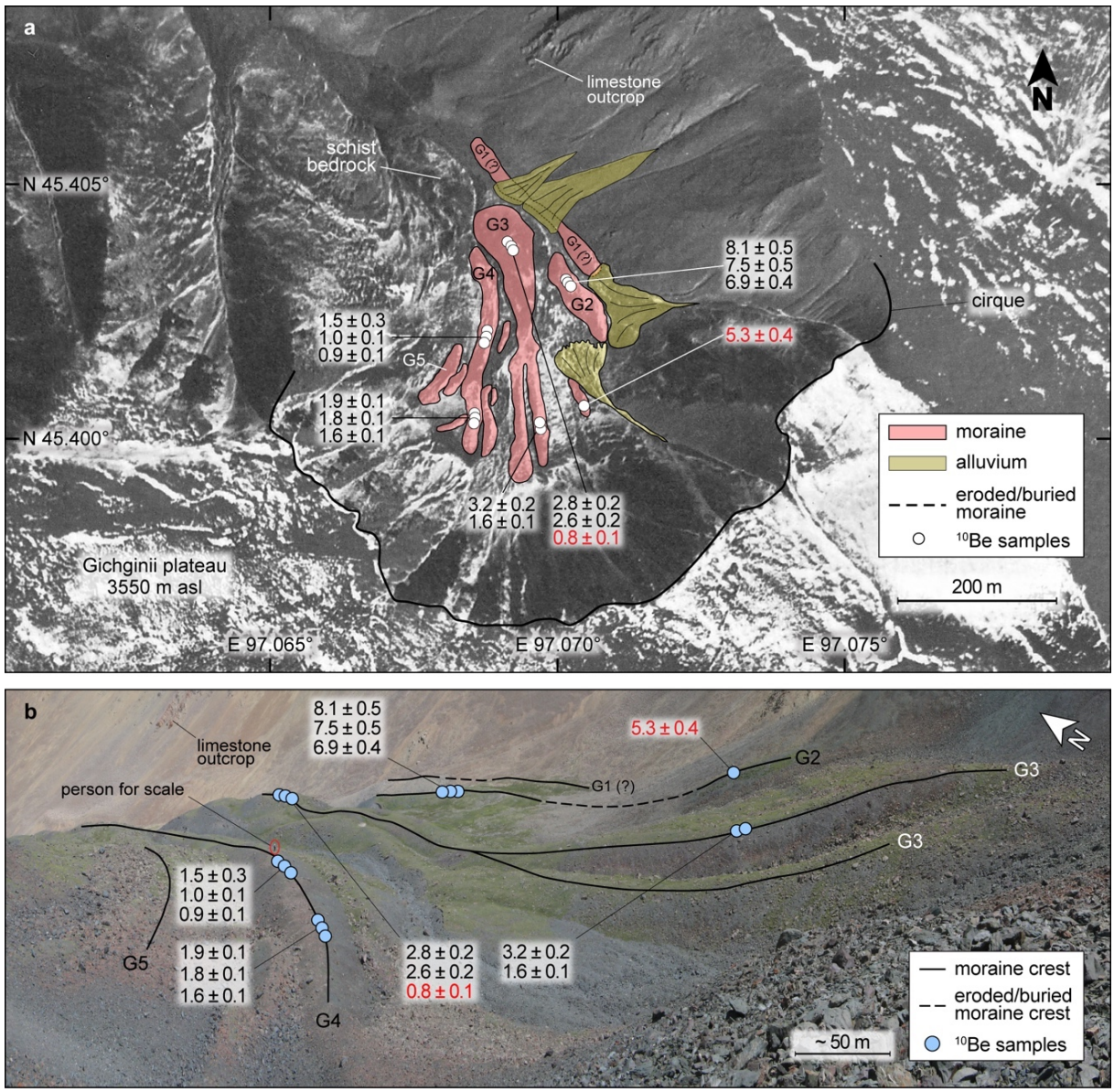

Figure 3.4. Moraines in the Mönh Mösnii valley, Gichginii range, and locations of ^{10}Be ages. a. Aerial photo (National Archives of Mongolia, acquisition winter of 1957) showing sample locations and moraine locations. b. Field photo showing the moraines and ^{10}Be exposure ages. Ice flow was from south to north. ^{10}Be exposure ages are in ka ± 1σ. Rejected ages are shown in red.

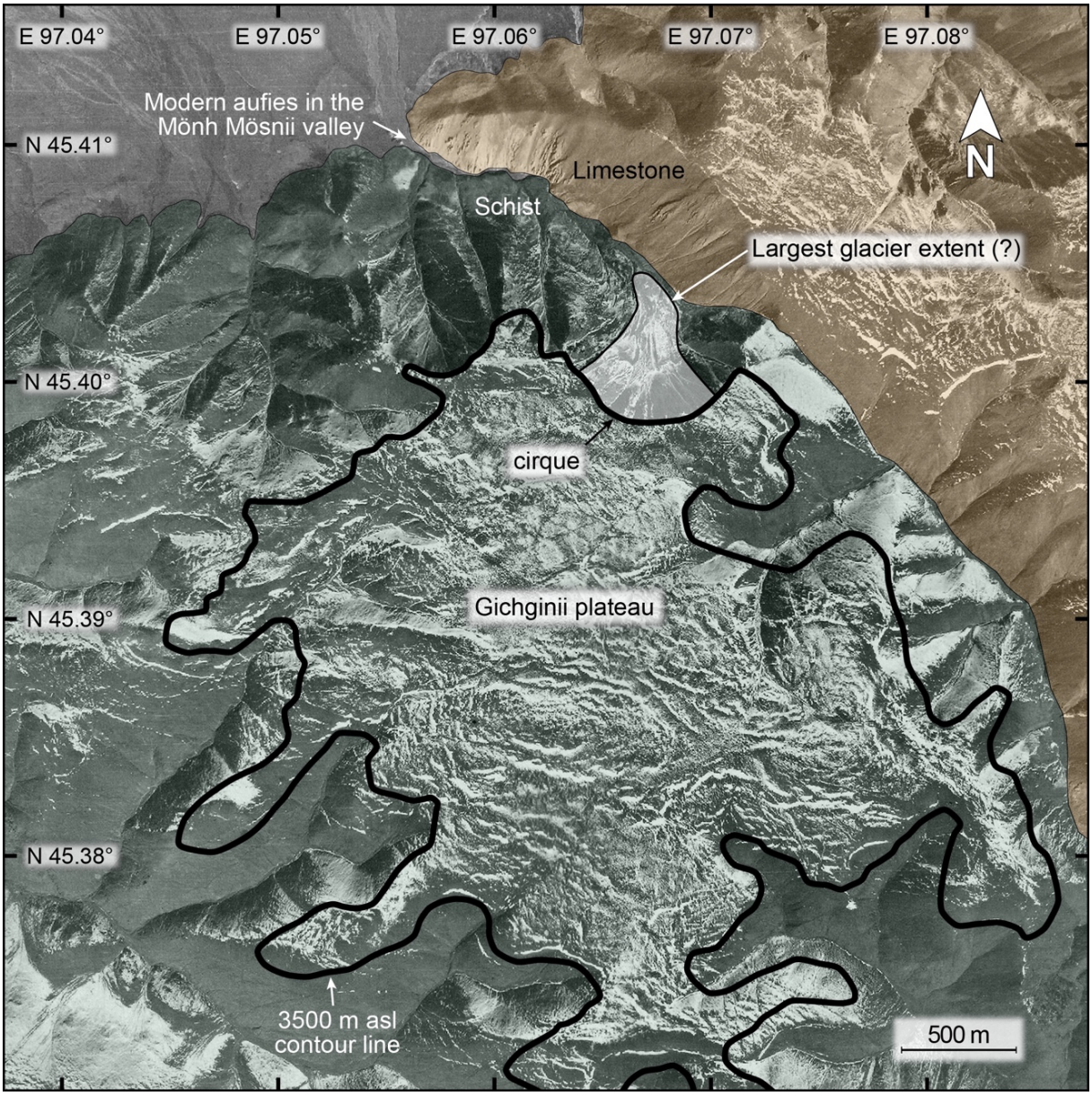

Figure 3.5. Gichginii plateau and maximum glacial extent in the Mönh Mösnii valley. The extent of the largest glacier in the Mönh Mösnii valley is based on the outermost extent of the G2 moraine. A contour line at 3500 m asl roughly delineates the extent of the plateau. The bedrocks in the upper right part of the photo (tan) is limestone, and the bedrocks in the lower left part (gray-green) is schist. Aerial photo was taken in winter of 1957 (National Archives of Mongolia).

The lowest ridge in the cirque, G1, was eroded and remnants were buried by limestone boulders and scree from the northeast, and capped by ~10 cm of loess. Its light color is in sharp contrast with the dark schist of the four inner ridges, with which it is slightly discordant (Figure 3.4b). Although G1 may be an old moraine, it is also possibly a kame terrace impounded against a cirque paleoglacier. No schist boulders (with their included quartz lenses) were found on its surface; thus, there were no opportunities for ^{10}Be dating.

In contrast, moraine ridges G2–G5 (Figure 3.4) consist of sub-angular schist diamict sourced in the south from the Gichginii plateau. G2–G4 are stable and vegetated, and the surface boulders host lichens. Their lack of flow features on or between the ridges argues against an origin as rock glaciers (e.g., D. Trombotto Liaudat, pers. comm., 2017) (see the surface features in Figures 3.6–3.9).

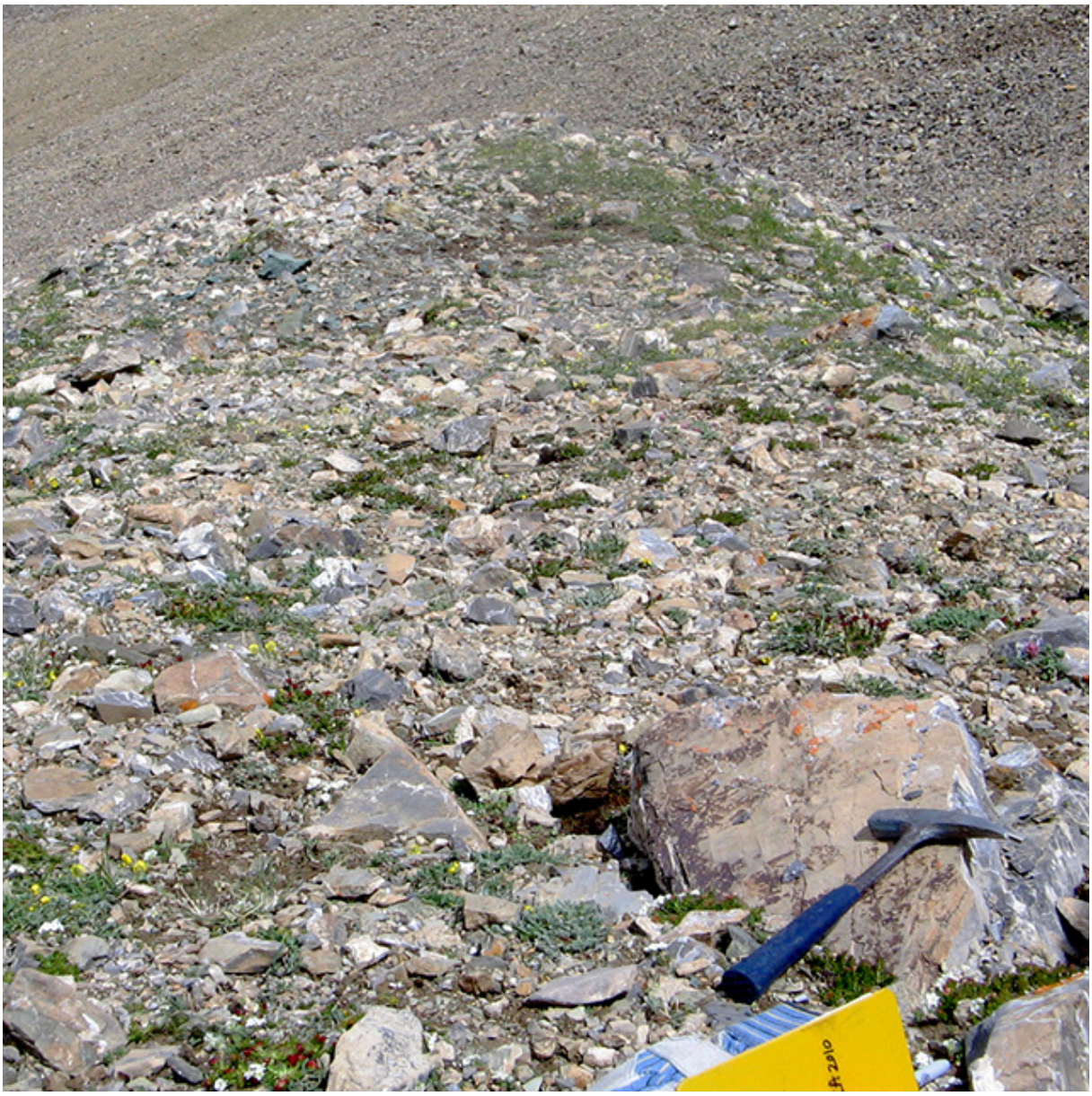

Figure 3.6. The tan-weathering gray limestone boulders on the G1 ridge in the Mönh Mösnii cirque. The white veins (left center) are calcite. The photographer was facing northwest.

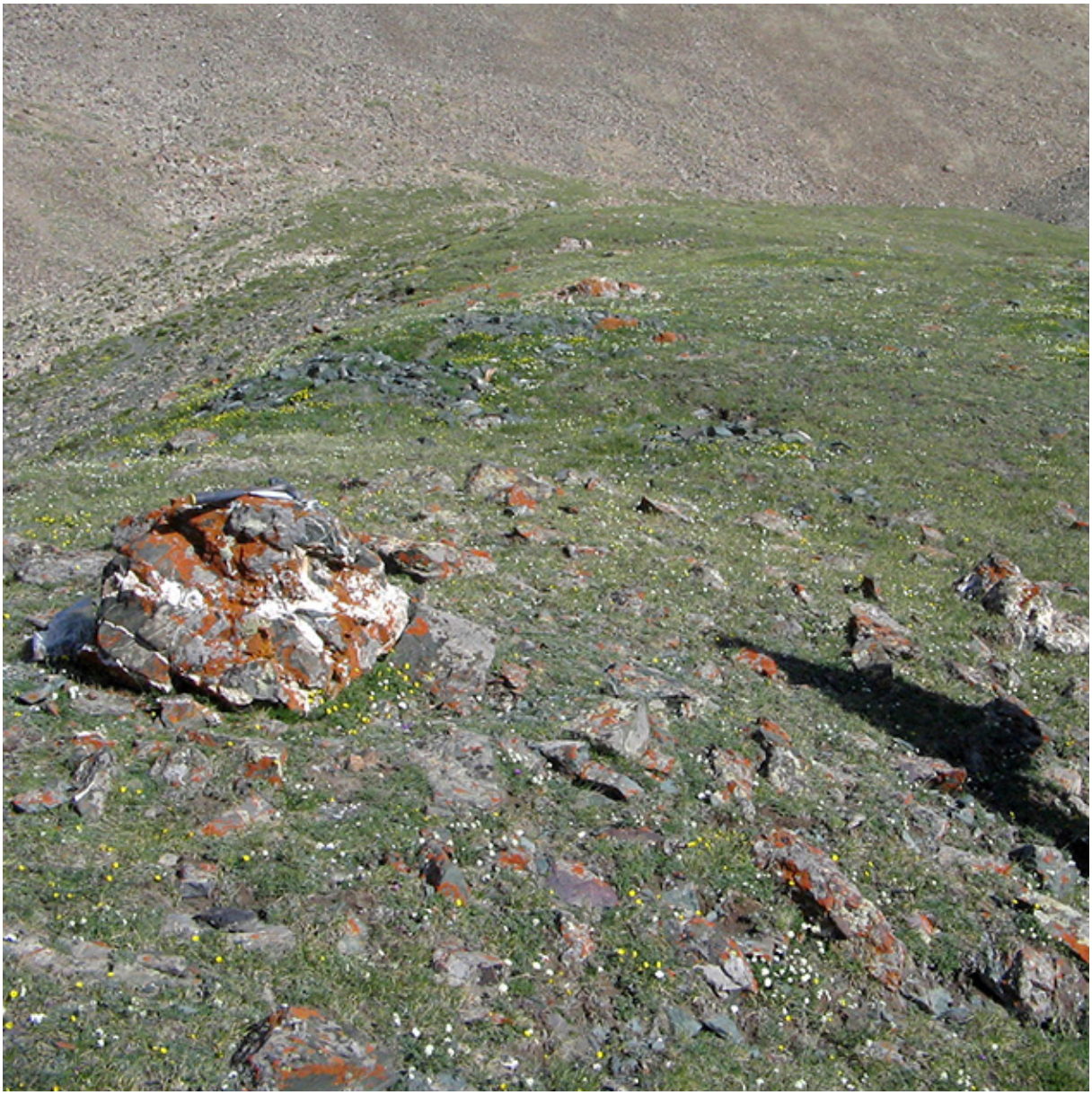

Figure 3.7. Surface of the upper part of the G2 moraine. The quartz vein from the singular boulder (GN-JB-005) was sampled for ^{10}Be analysis. The fractures in the boulder suggests heavy erosion, but the lack of broken pieces surrounding the boulder suggests the boulder could have been a rock fallen on supraglacial till. Note the hammer on top of the boulder for scale. The photographer was facing southeast.

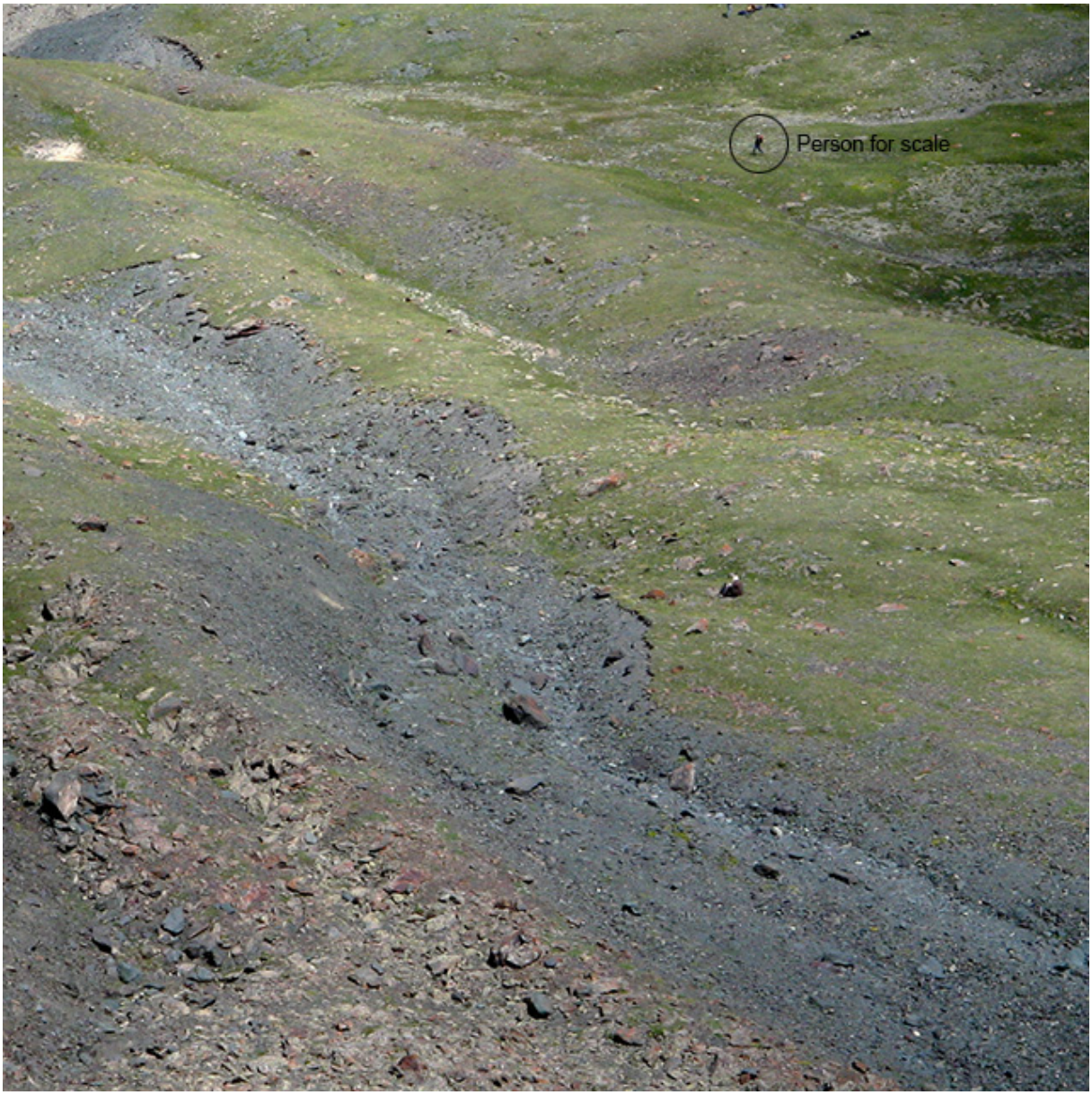

Figure 3.8. Surface features of the upper part of the G3 moraine. The photo was taken from the headwall slope in the south, above the moraine G5. Note people in the photo for scale (top right). G2 moraine is at the top, partly out of the frame. The photographer was facing northeast.

Figure 3.9. Surface features of the lower part of the moraine G4. Beyond the green moraine ridge (G3, top center) the slope of the valley increases. The photographer was facing north.

We sampled every boulder that we could find in the Mönh Mösnii cirque large enough and containing enough quartz lenses to permit the ^{10}Be dating. Four ^{10}Be ages from moraine G2, the oldest dated moraine, were measured and, after excluding one outlier (i.e., n=3), indicate glacial deposition during ~8–7 ka. Approximately 40 m above the G2 moraine, four boulders on the G3 moraine (Figure 3.4) were dated to ~3–2 ka, after excluding one outlier. The youngest moraine we dated, G4, lies at about the same altitude as G3, and six boulders from there gave an age range of ~2–1 ka (Figure 3.10). In the field, G5 appeared to us to be similar to Little Ice Age moraines elsewhere (LIA: after ~0.7 ka, Matthews and Briffa, 2005). The ELAs associated with G1–G5 were 3,320, 3,330, 3,360, 3,365, and 3,370 m asl, respectively. In contrast, the ELAs for the LIA paleoglaciers along the Mongolian–Siberian border (Mönh Saridag peak) 750 km to the NNE were ~3,190 m asl (Batbaatar and Gillespie, 2008) about 180 m lower than G5. The MIS 2 ELA in the northern Mongolia (Darhad basin) was ~2,100 m asl (Gillespie et al., 2008), about 1,220 m lower

than for G1. Thus, the total range of ELAs in northern Mongolia was much greater than in the arid Gichginii range.

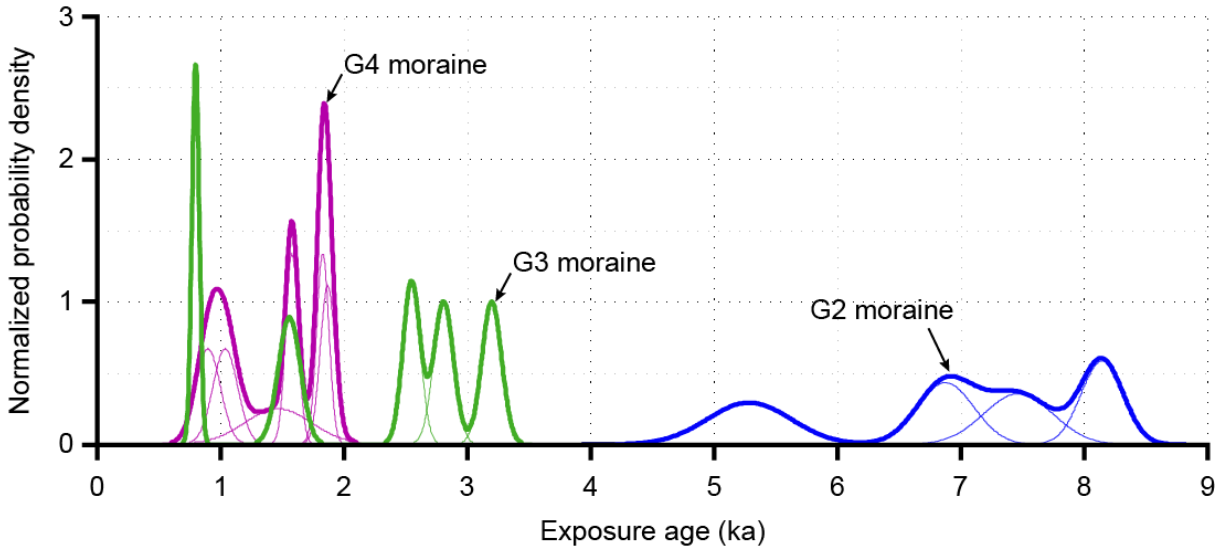

Figure 3.10. Camel plots created using G. Balco's Matlab code for the ^{10}Be ages for the moraines in Gichginii range. The thin lines are probability curves for individual samples (internal uncertainties only), and the thick lines are sum of the individual probability curves. Three of the four ^{10}Be ages from the G2 moraine (blue lines) overlap with each other within 2σ internal uncertainty and constrain the exposure age for this moraine to ~8–7 ka (1σ age range after rejecting outliers). The remaining ^{10}Be age, 5.3 ± 0.3 ka, does not overlap with the older cluster and is regarded as an outlier. Three ^{10}Be ages from the G3 moraine (green lines) overlap within 2σ internal uncertainty around 3.5–2.2 ka (2σ age range of the mean after rejecting outliers). The remaining two ^{10}Be ages do not overlap at all and are regarded as outliers. Four of the six ^{10}Be ages from the G4 moraine (purple lines) formed a mode around 2–1.5 ka. The remaining two ^{10}Be ages at ~0.9 ka overlaps with the youngest age from the older cluster, mainly due to its high (18%) 1σ uncertainty. The younger cluster is only 0.6 ka apart from the older cluster, suggesting the G4 formation ~2–0.8 ka (mean 2σ age range after rejecting outliers). The camel plot for all ^{10}Be ages, including three outliers, show the oldest advance of the Gichginii glaciation at ~9–6 ka, with subsequent glacier re-advances or standstills at ~3.5–2.2 ka and ~2.1–0.8 ka.

The undated G1 feature, which marks the extent of the local LGM in the Gichginii range, lies only ~10 m lower than the crest of the G2 moraine, and therefore the ELAs are nearly the same. Whatever the age of G1, the G1 and G2 paleoglaciers were similar in size and extent. The valley below the cirque is characterized by fluvial, ~10 m deep bedrock inner gorge underlying the talus. The bedrock gorge could have been cut by subglacial streams if the paleoglaciers ever advanced beyond G1. Otherwise, we found no evidence of a glacial advance in the Gichginii range during the global LGM, a cold period of permafrost presence in the Gobi-Altai (Owen et al., 1998). If the Mönh Mösnii valley below the cirque was ever glaciated, it was long enough ago that the moraines have all been removed by erosion.

Sutai range… The Sutai range in the western end of the Gobi-Altai hosts three modern ice caps (referred to as # 1, 2, and 3 in Figure 3.11a). The two largest (#2 and 3) occupy a high plateau southeast of our studied valleys and are narrowly separated today but probably merged during major glaciations. Ice cap #2 feeds at least five well-developed glaciers that descend both the northeastern and southwestern slopes of Sutai. Three boulders from a series of lateral moraines on the northeastern slope, NE2–4 in Figure 3.11b, were dated to ~27–22 ka, after rejecting an outlier of 6.7 ± 0.4 ka. We also rejected a single ^{10}Be age of 7.3 ± 0.5 ka from the lowest end moraine a few hundred meters down valley as it appeared too young for the landform relative to its neighbors.

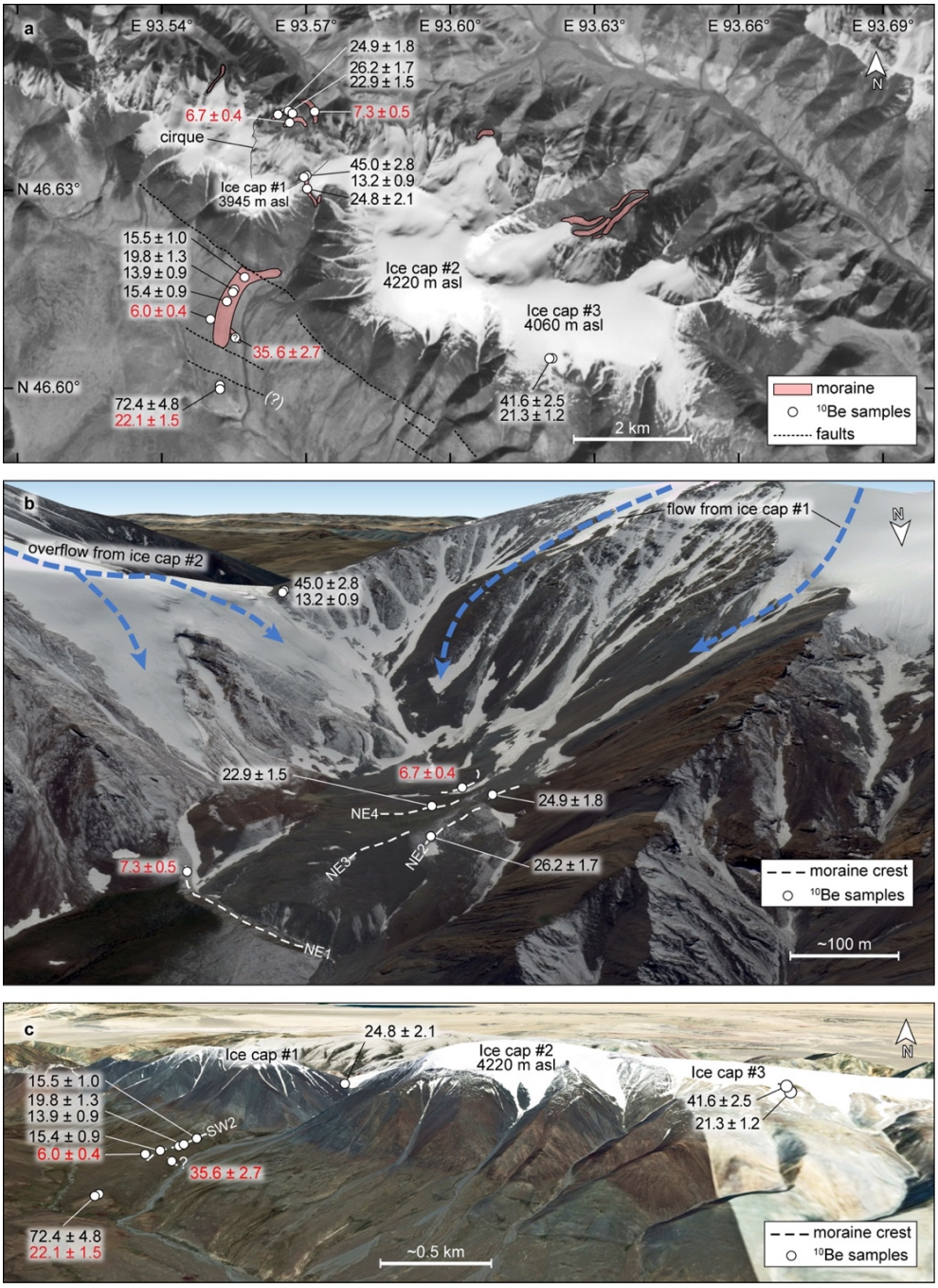

Figure 3.11. Sample locations in Sutai range. a. ASTER image (September 21, 2003; band 3N) showing the southwestern and northeastern slopes of the Sutai range and the ^{10}Be ages for glacial deposits. b. Google Earth perspective view of the moraines in the northeastern slope. c. Google Earth perspective view of the moraines in the southwestern slope. The glaciers in the studied valleys are both fed by ice cap #2. ^{10}Be exposure ages are in ka ± 1σ. Rejected ages are shown in red. Google Earth overlay is the DigitalGlobe and Landsat images acquired in June 2013.

The pass between ice caps #1 and #2 is now occupied by a modern outlet glacier flowing west from ice cap #2. Most of the glacier now flows south and descends down a canyon on the SW side of the ridge, but in the past it also descended to the NE outlet valley (Figure 3.11a and b). About 20 m higher than the glacierized pass is a lateral moraine on the ridge leading to ice cap #1. Deposition there likely resulted from the bedrock ridge diverting both to the northeast and southwest the paleoglacier flowing into the pass. The altitude of this marginal moraine reflects the local depth of the outlet glacier, but not its maximum extent. Given its location, it may even be time-transgressive. We collected three samples from the crest of this moraine: two above the pass itself (~45 ka and ~13 ka) and a third 83 m to the south (~25 ka). The two younger ages could be consistent with the MIS 2 ages from below the pass to the NE. Exactly how this moraine remnant fits into the chronostratigraphic sequence is unclear, however, and with only three ages widely separated in time, an age for the moraine cannot be determined with any confidence.

Near the margins of ice cap #3 on the Sutai plateau, two erratics were sampled from underneath a more extensive paleo-ice cap (Figure 3.11c). The erratics were dated to ~42 and ~21 ka, echoing the disparity of the three ages from the pass. These did not allow us to determine an age relevant to the paleo-ice cap. Viewed collectively, the five samples from the Sutai plateau and the pass began their exposure histories at different times during MIS 2 and 3. More work will be required to unravel their significance.

On the southwestern piedmont of Sutai (Figure 3.11a and c), we dated eight more samples, including six from a right-lateral moraine complex. Four of five boulders from the crest of SW2 right-lateral moraine yielded ages of ~19–13 ka, with the other being rejected as an outlier. Another boulder from what in the field appeared to be a remnant of a recessional moraine was dated to ~36 ka, which clearly was too old for its context. We also sampled an isolated glacially eroded bedrock

knob at 3,105 m asl, ~75 m lower altitude than the preserved moraines and ~0.8 km downslope. The knob has not been heavily weathered or eroded. It was dated to ~22 ka, not inconsistent with the younger SW2 right-lateral moraine. A nearby glacial erratic boulder at the same altitude was dated to ~72 ka, however. It is possible that the erratic simply contained inherited ^{10}Be and is anomalously old; it is also possible that it once sat atop the now-eroded moraine that buried the bedrock knob but was too large to move or erode completely. In this interpretation, the ^{10}Be age of the erratic might be a minimum for the moraine, and the age of the knob may simply reflect exposure since erosion of the moraine. Summary of all the ^{10}Be boulder ages from moraines in Sutai range is given in Figure 3.12.

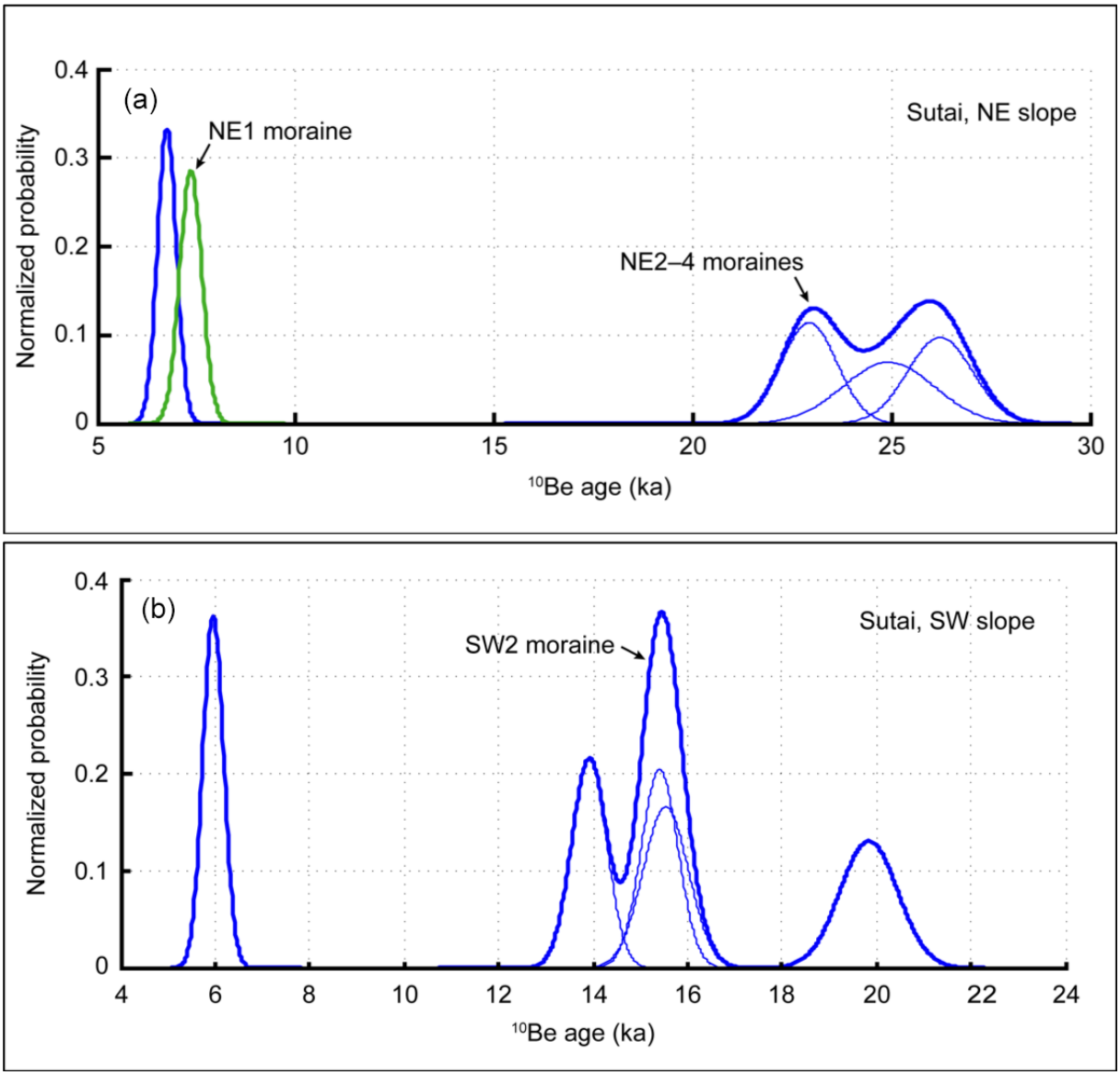

Figure 3.12. Camel plots created using G. Balco's Matlab code for the ^{10}Be ages for the moraines in Sutai range: a) for samples from the NE slope; b) for samples from the SW slope. The thin lines are probability curves for individual samples (internal uncertainties only), and the thick lines are sum of the individual probability curves.

Like the lowest right-lateral moraine, all the left-lateral moraines are missing from the piedmont. We sampled two boulders from what appears to be soliflucting debris where we expected the moraine once was. The debris could have originated as rockfall, possibly triggered by range-front faulting. The two boulders were dated to ~1.6 and 0.9 ka (Figure 3.13a). The evidence of mass wasting from the range front suggests that seismicity in the region in addition to active permafrost processes may have modified the initial exposure position of the boulders there.

Strath terraces formed just above the southwestern piedmont of Sutai after the glaciers receded from their last maximum positions (Figure 3.13a and b). Four boulders on the strath terraces and three more from a protalus rampart burying the terraces yielded wide-ranging ages of ~18–1 ka, and a tight cluster of 3–2.5 ka, respectively.

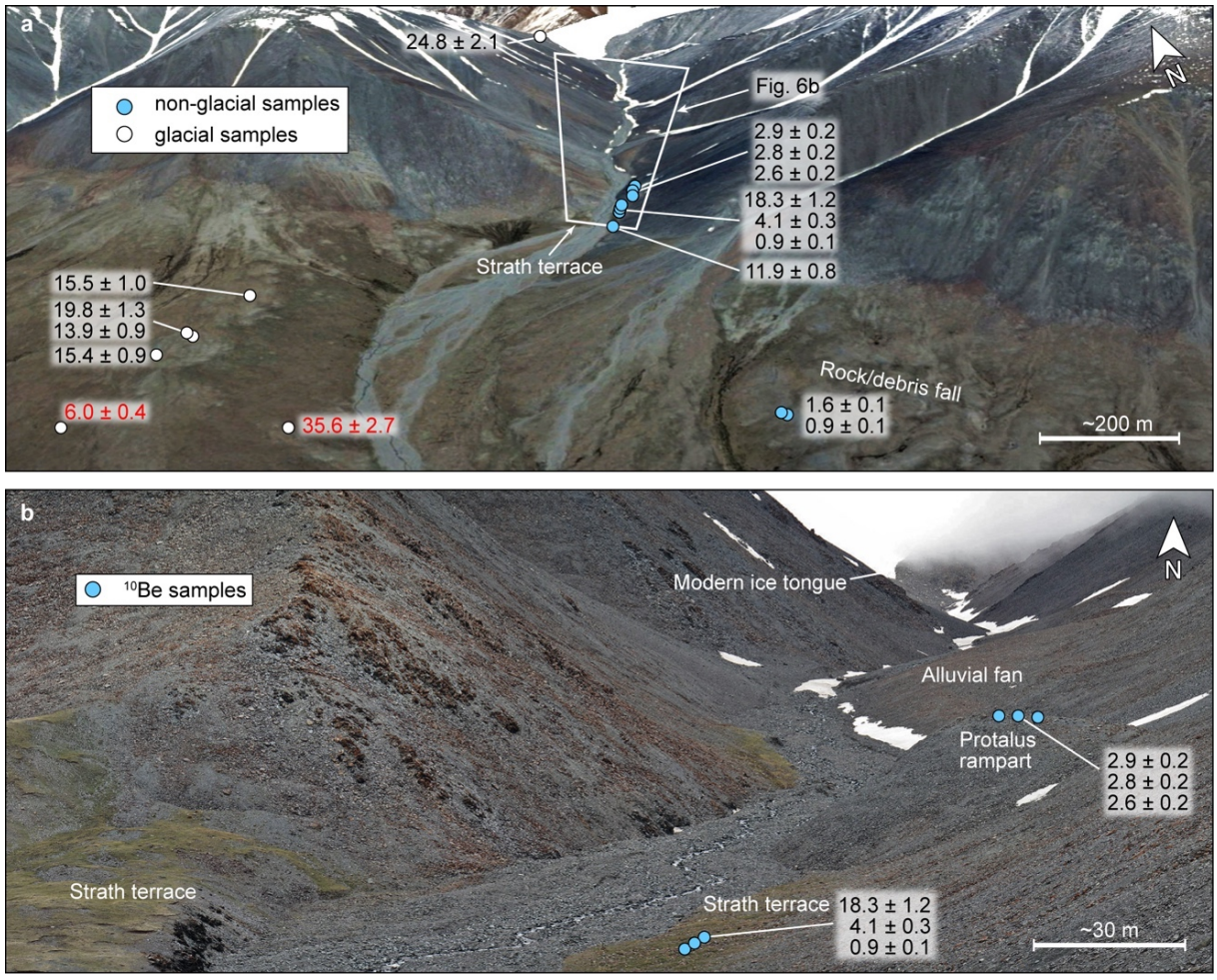

Figure 3.13. Non-glacial samples at Sutai. a. Google Earth perspective view of the southwestern slope and the locations of the glacial (white circles) and non-glacial (blue circles) samples. b. Field photo showing a closer view of the strath terraces on both sides of the stream and protalus rampart and alluvial fan covering the terraces. Numbers refer to ^{10}Be ages, in ka ± 1σ. Rejected age is shown in red. Google Earth overlay is the DigitalGlobe image acquired in June 2013.

Ih Bogd range… Near the easternmost end of the Gobi-Altai, the Ih Bogd range provides evidence of glaciation with well-developed cirques and moraines (Figure 3.14a). The best-preserved evidence on the southern side of Ih Bogd is in Artsan valley, where moraines from at least six advances, labeled as IB1–IB7 in Figure 3.14b, sit ~150–500 m from and 30–130 m below the headwall. A single boulder from the youngest moraine was dated to ~14 ka. Five boulders ~25–35 m down valley, from a series of lateral and end moraines, IB5–6, gave ages that ranged from ~17 to 13 ka. We rejected a ^{10}Be age of 7.3 ± 0.6 ka from the IB5 moraine as an outlier. The altitude of the most distal moraine (IB1, not sampled) was only ~50 m below the IB5 moraine. Summary of all the ^{10}Be boulder ages from Ih Bogd range is given in Figure 3.15.

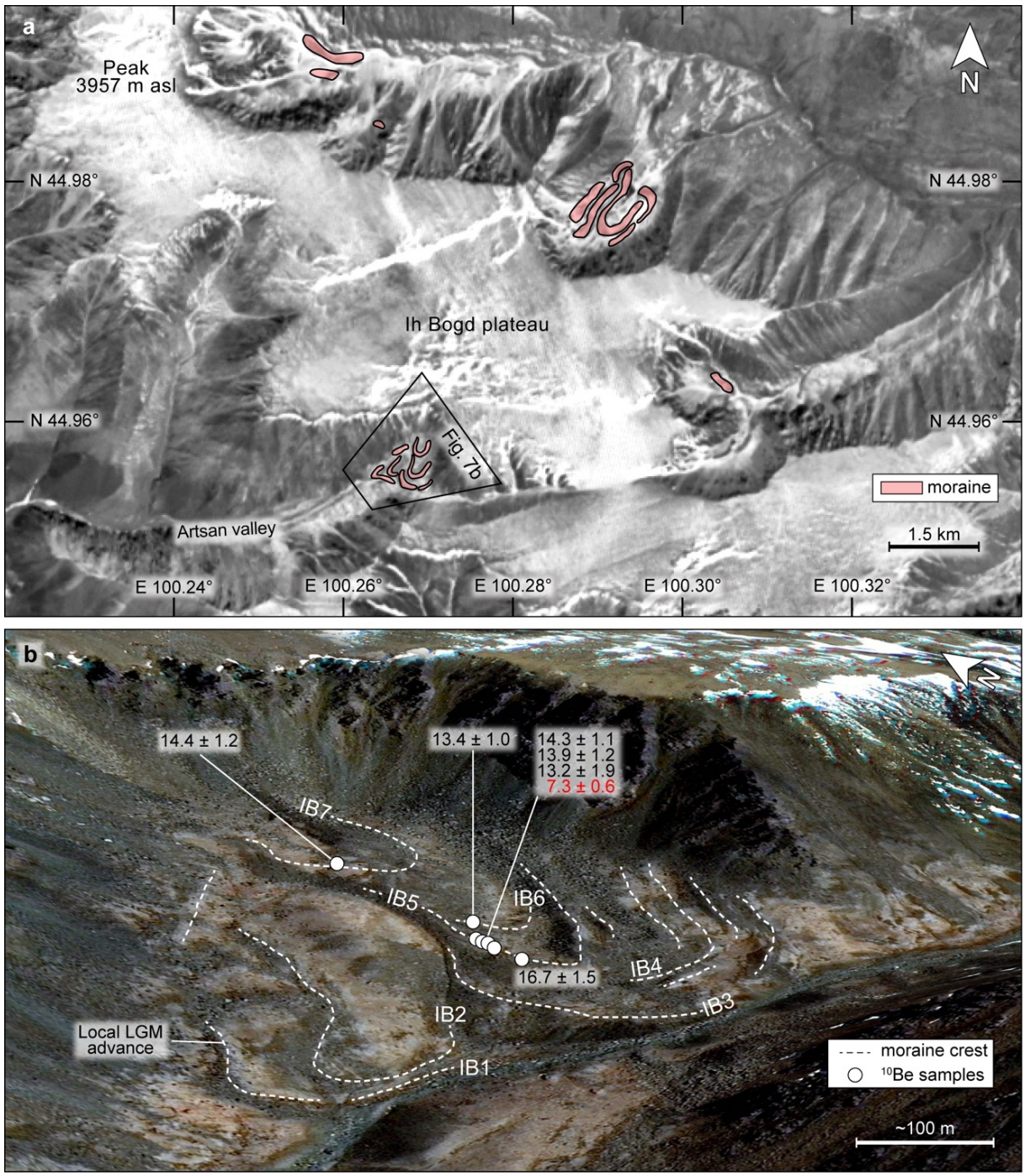

Figure 3.14. Ih Bogd range and the ^{10}Be sample locations. a. ASTER image (acquisition April 14, 2001; band 3N) showing the cirques with glacial deposits. There is no modern ice on the plateau, and snow is covering the white areas on the image. b. Google Earth perspective view (background: DigitalGlobe image acquired in June 2007) showing the dated moraines in the Artsan valley. ^{10}Be exposure ages are in ka ± 1σ. Rejected age is shown in red.

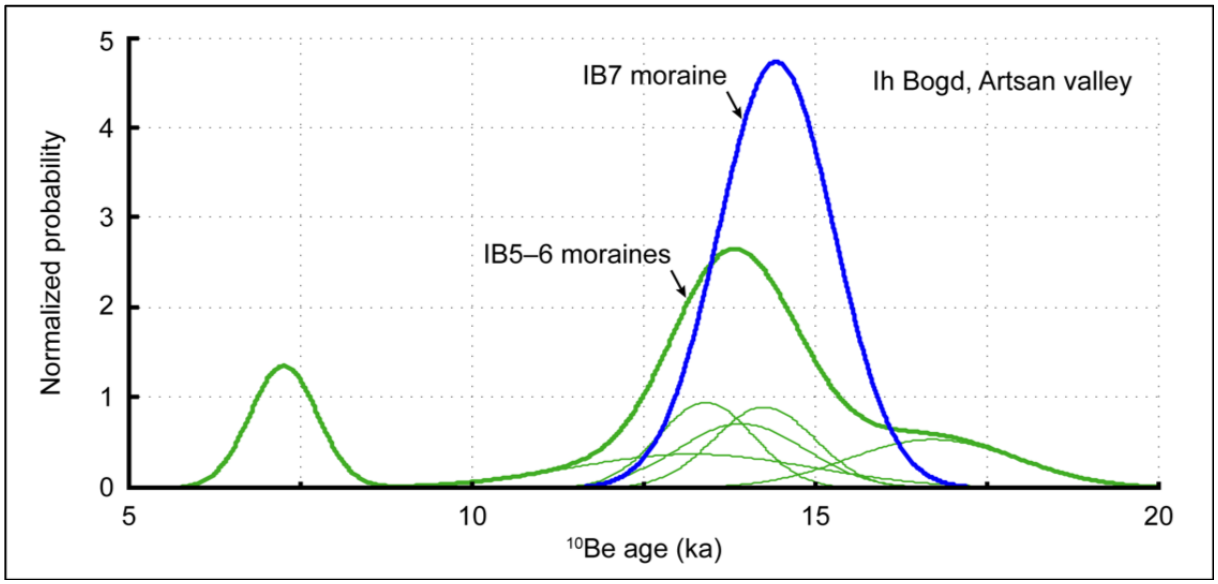

Figure 3.15. Camel plots created using G. Balco's Matlab code for the ^{10}Be ages for the moraines in Ih Bogd range. The thin lines are probability curves for individual samples (internal uncertainties only), and the thick lines are sum of the individual probability curves.

3.4.2 *Glaciations in the Hangai ranges*

In the dry subhumid zone to the north of the three sites in the Gobi-Altai, the Hangai ranges were heavily glaciated before and during the global LGM (Rother et al., 2014), with separate peaks supporting their own ice caps. Otgontenger is the only peak high enough today to preserve a small ice cap. In the Bogd river valley, on the western side of Otgontenger (Figure 16a), Rother et al. (2014) concluded on the basis of ^{10}Be dating, that the outlet glaciers advanced to the local LGM at ~38 ka during MIS 3, but the MIS 2 glaciers were comparable to or slightly smaller. Three glacial boulders we sampled from the lowest terminal moraine in the Bogd valley dated to ~25–20 ka, consistent with the findings of Rother et al. (2014). To extend the glacial history at Otgontenger, we dated glacial boulders in the Bitüüt valley (Figure 16a and b) on the eastern side of Otgontenger. Bitüüt valley is a separate drainage from the Bogd valley, although the outlet glaciers in these valleys probably were sourced from the same ice field. We sampled from three moraines that comprise part of a retreat sequence of at least ten moraines (BI1 to BI9) in Bitüüt valley. Two boulders from one of the oldest Bitüüt end moraines (BI2) were deposited at ~33–28 ka, excluding an outlier at ~83 ka. About ~1.4 km upvalley and an additional ~120 m rise in altitude from the lowest two moraines, three ^{10}Be ages for boulders on the two younger moraines, BI8 and BI9, ranged in age from ~17 to 16 ka (Figure 16b). The boulder age of 15.0 ± 1.0 ka from BI9 was rejected as an outlier. Summary of all the ^{10}Be boulder ages from Otgontenger site is given in Figure 3.17.

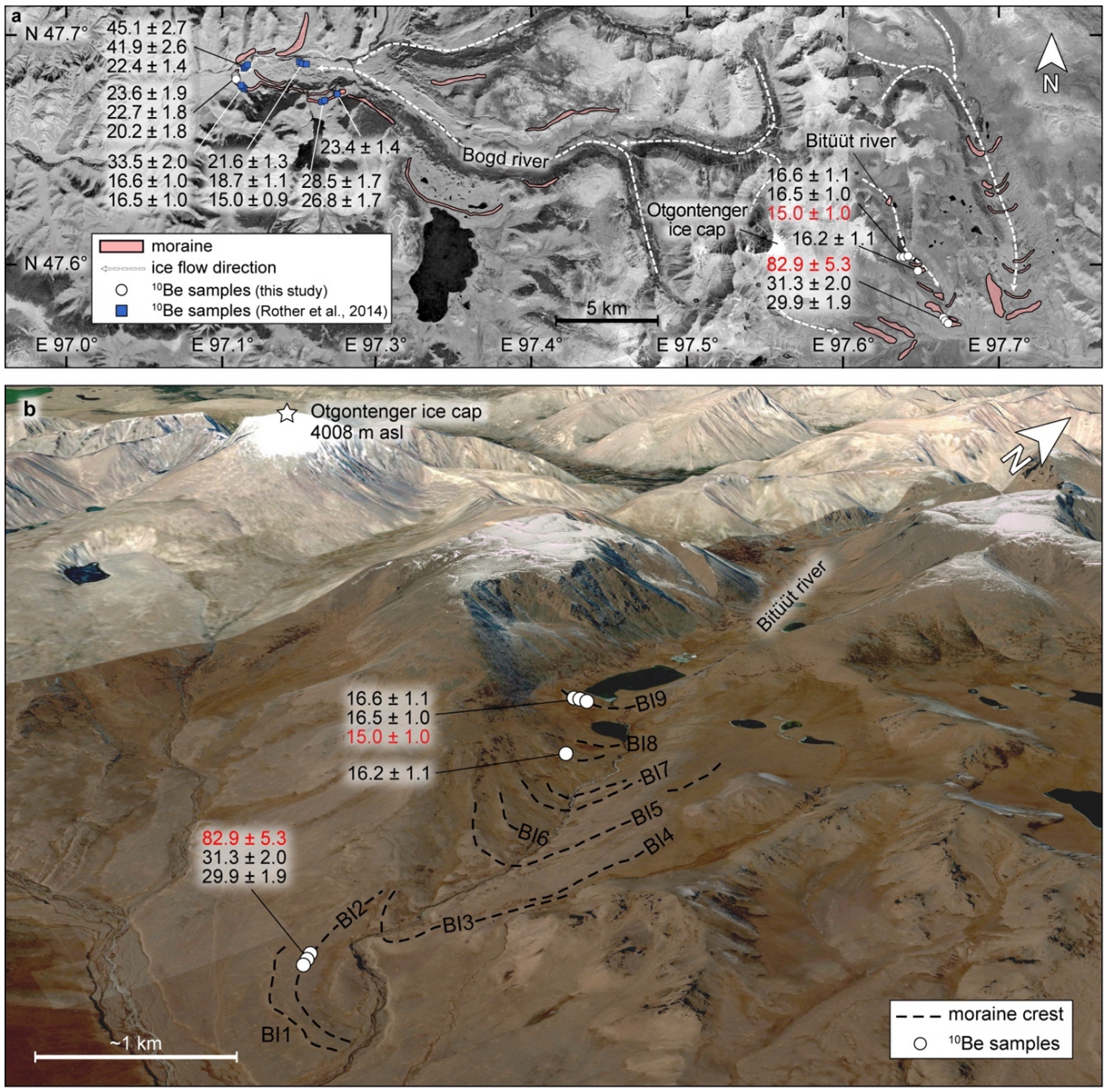

Figure 3.16. Otgontenger site and sample locations. a. map showing prominent moraines and sample locations from this study and Rother et al. (2014). The glaciers from MIS 2 were slightly smaller than from MIS 3, but comparable in size. b. Google Earth perspective view (DigitalGlobe image acquired in October 2011) shows the sets of moraines in the Bitüüt valley east of Otgontenger. ^{10}Be exposure ages are in ka ± 1σ. Rejected ages are shown in red.

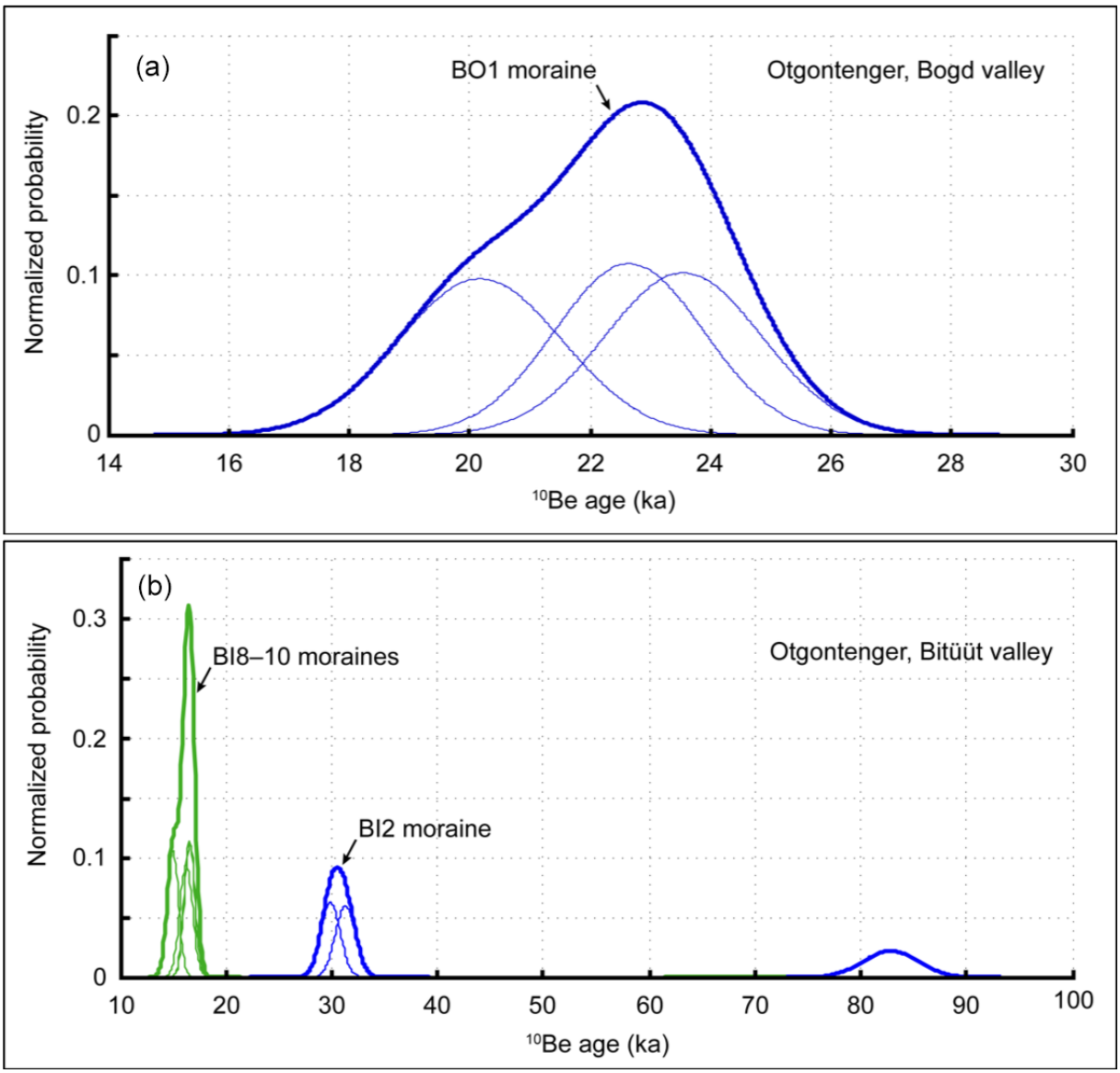

Figure 3.17. Camel plots created using G. Balco's Matlab code for the ^{10}Be ages for the moraines in Otgontenger peak, Hangai range: a) for samples from Bogd valley; b) for samples from Bitüüt valley. The thin lines are probability curves for individual samples (internal uncertainties only), and the thick lines are sum of the individual probability curves.

To complement the chronology of glacial advances in the Hangai ranges, we traveled approximately 200 km east of Otgontenger, and sampled two moraines in another glaciated valley, the Bumbat. Three boulders on the older moraine, BU1 in Figure 3.18a, gave wide-ranging ages of ~104, 54, and 23 ka. Four of six ^{10}Be ages from a younger inner moraine 2.5 km upvalley (BU2 in Figure 3.18) suggest a deposition age of ~39–30 ka. The other two ^{10}Be ages of 49.9 ± 3.3 ka and ~22.2 ± 1.5 ka, were rejected as outliers. Summary of all the ^{10}Be boulder ages from Bumbat valley is given in Figure 3.19. Field photos of some boulders are shown in Figure 3.20.

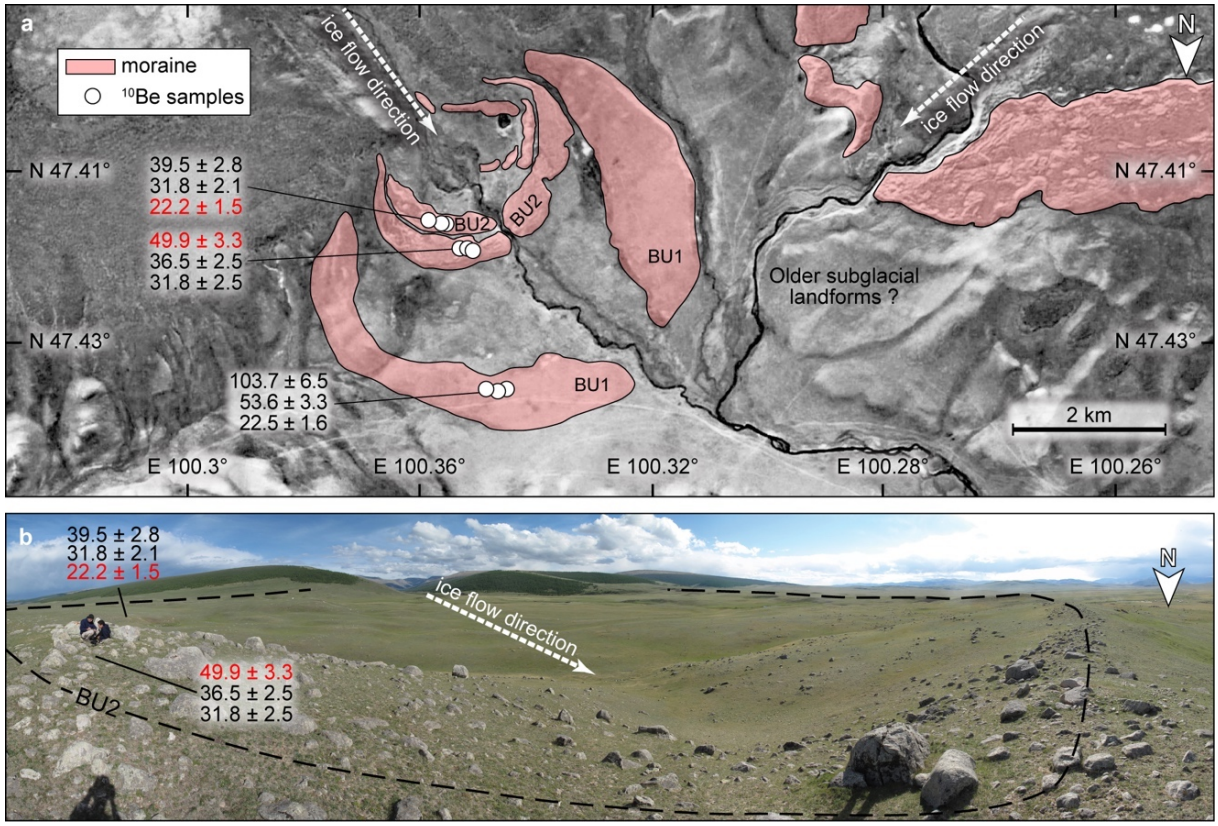

Figure 3.18. The moraines at the Bumbat site, Hangai ranges. a. Map showing the end moraines and locations of the ^{10}Be samples (background is Landsat image from Google Earth). b. Panoramic photo looking southeast showing the surface of the younger end moraine crest (dashed lines). ^{10}Be exposure ages in ka ± 1σ. Rejected ages are shown in red.

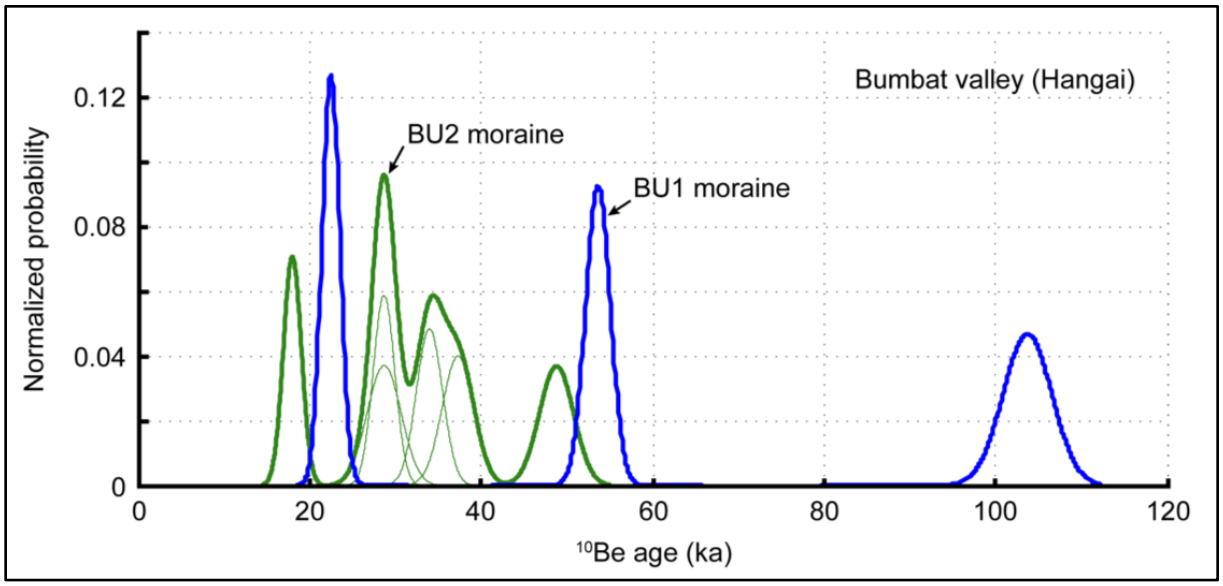

Figure 3.19. Camel plots created using G. Balco's Matlab code for the ^{10}Be ages for the moraines in Bumbat valley in Hangai range. The thin lines are probability curves for individual samples (internal uncertainties only), and the thick lines are sum of the individual probability curves.

Figure 3.20. Field photos of some of the sampled boulders. a, b, c, Samples from the Gichginii range (GN-JB- 001, 003, 005). d, e, f, Samples from the southwestern slope of the Sutai range (SUT-JB- 02D, 04A, and SUT-IM-01B). g, h, i, Samples from the Ih Bogd range (IB-JB- 003E, 003B, 001). j, k, l, Samples from the Bogd river valley in Otgontenger (OT-AG- 1, 2, 3). m, n, o, Samples from the Bumbat valley in the Hangai ranges (HN-JB-01A, 02B, 03A). The hammer, hand-held GPS unit, and a notebook are for scale.

3.4.3 *Mechanisms of ablation in the Gobi-Altai and Hangai ranges*

The reconstruction of paleoclimate from glacial records relies on the empirical relationship between summer T_a and annual precipitation at the ELAs (Ohmura et al., 1992). This approach has recently been extended to arid and semiarid regions in Central Asia (Sakai et al., 2015) (Figure 3.21) using GAMDAM glacier inventory compiled using satellite images and high-resolution climate data (Nuimura et al., 2015). On this annual precipitation vs. summer T_a diagram, we have also plotted the modern climate data (Kalnay et al., 1996; Schneider et al., 2015) at the modern ELA for existing glaciers and at cirque headwalls for currently unglaciated valleys covering the five regions we have studied (black filled symbols in Figure 3.21). Unsurprisingly, the modern glacier at Sutai and the Otgontenger ice cap plot within the limits for glaciation today, but the other three sites are too warm and dry, and plot outside the limits. We then projected the estimated MIS 2 climate (Owen et al., 1998; Braconnot et al., 2007; Bintanja and van de Wal, 2008; Annan and Hargreaves, 2013) to the MIS 2 ELA for the studied paleoglaciers (open symbols, Figure 3.21) onto the diagram. All the estimated MIS 2 data points plotted well within the allowed glaciation zone defined by the modern glacier data, apart from Gichginii site, which appears to be marginal. This suggests that Gichginii may have been too dry to support glaciers during MIS 2, in agreement with the absence of MIS 2 deposits. Had the MIS 2 precipitation at Gichginii marginally higher than the modern value, the Gichginii range would have been glaciated then. For the early Holocene, the modeled summer T_a was 3 °C warmer than today (Jin et al., 2012), which would have been too high to have enabled glaciation per Figure 3.21. However, the existence of Gichginii cirque glaciers requires that snow did survive the summers in the early Holocene; thus, it may be impractical to reconstruct summer T_a for small cirque glaciers in cold, arid conditions using this empirical curve.

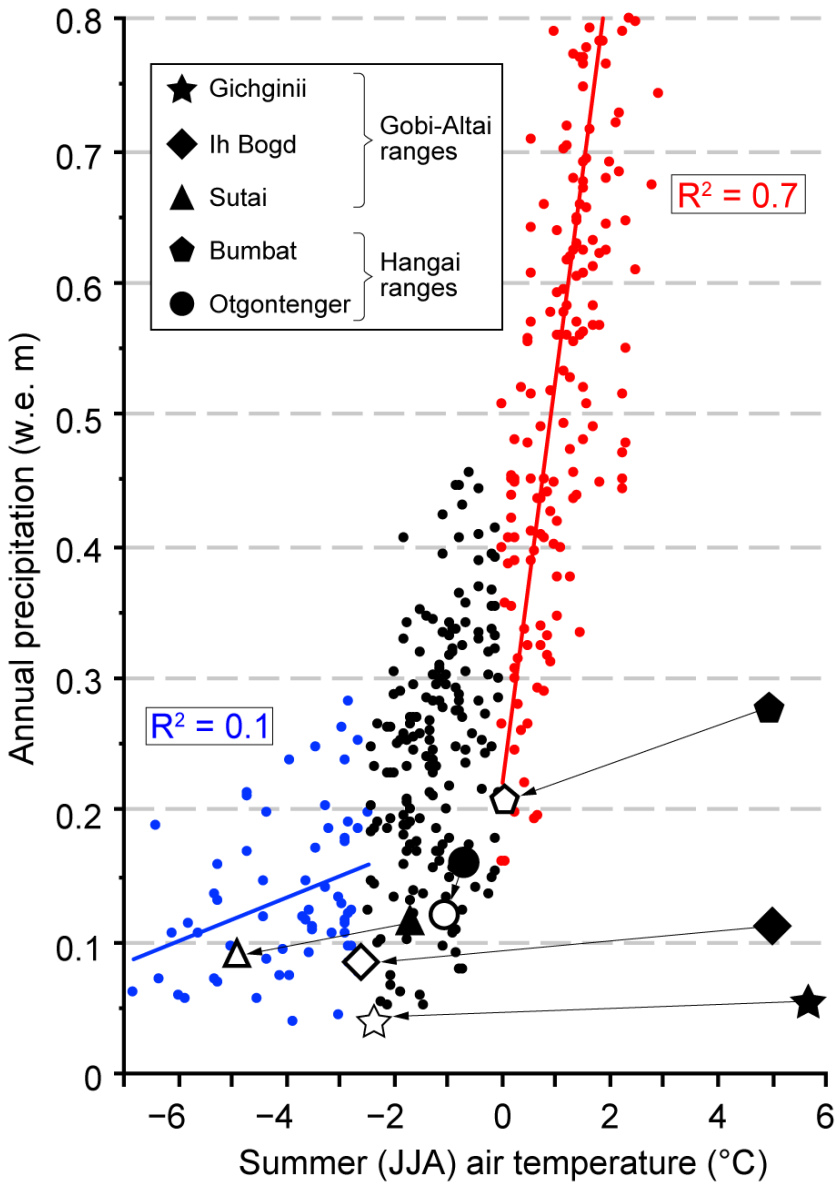

Figure 3.21. The relationship between annual precipitation and summer air temperature at the ELA for modern glaciers in Asia. The data are taken from the GAMDAM glacier inventory (Sakai et al., 2015). Blue dots indicate summer temperatures below −2.5 °C; red dots indicate summer temperatures above zero. At the lowest temperatures ablation is dominated by sublimation (~50–100 mm yr^{-1}) ("precipitation-sensitive regime") and is insensitive to air temperature; in warmer climates ablation depends more on air temperature (300 mm K^{-1}) ("temperature-sensitive regime"). Solid black symbols represent today's climate at the modern ELA for Sutai (3870 m asl) and Otgontenger (3,800 m asl), and headwall altitudes for currently unglaciated valleys (Gichginii 3,440; Ih Bogd: 3,500; Bumbat: 3080 m asl) were used in place of the ELA. Open symbols

represent estimated MIS 2 climate with air temperature = modern − 8 °C (Owen et al., 1998; Bintanja and van de Wal, 2008; Annan and Hargreaves, 2013) and precipitation at 75% of modern (Braconnot et al., 2007) at the MIS 2 ELA (Sutai: 3280; Otgontenger: 2850; Gichginii: 3440; Ih Bogd: 3450; Bumbat: 2690 m asl). Precipitation data are from the GPCC 0.5° v7, long-term (1981–2010) monthly mean (Schneider et al., 2015). Temperature data are from the NCEP/NCAR 2.5° long-term (1981–2010) monthly mean (Kalnay et al., 1996) scaled to the altitude with lapse rate of 8 °C km^{-1}. The region outside the envelope defined by the red/blue data points fall into two categories: above and left, the climate is wetter and/or cooler than at the ELA and would correspond to an altitude within the accumulation zone; below and right of the data points the climate is too dry and/or warm to support glaciers (i.e., within the ablation zone).

We calculated the rates of melting and sublimation at altitudes of 2,000–3,500 m asl to examine the ablation mechanisms of a glacier in cold and arid conditions. Our surface-energy balance model suggests that at lower altitudes (i.e., red zones in Figure 3.21 or 3.22a–d) high T_a provides excess energy available for melting (Figure 3.22b). At higher altitudes and cold climates (i.e., blue zones in Figure 3.21 or 3.22a–d) sublimation dominates ablation where melting cannot occur (Figure 3.22c). For example, at 3,500 m asl, approximately the lowest limit of the Gichginii plateau, direct insolation exceeds net longwave radiation during the summer (Figure 3.22e) but T_a remains low enough that ice cannot melt (Figure 3.22f) and the excessive energy is spent to sublimate it (Figure 3.22g).

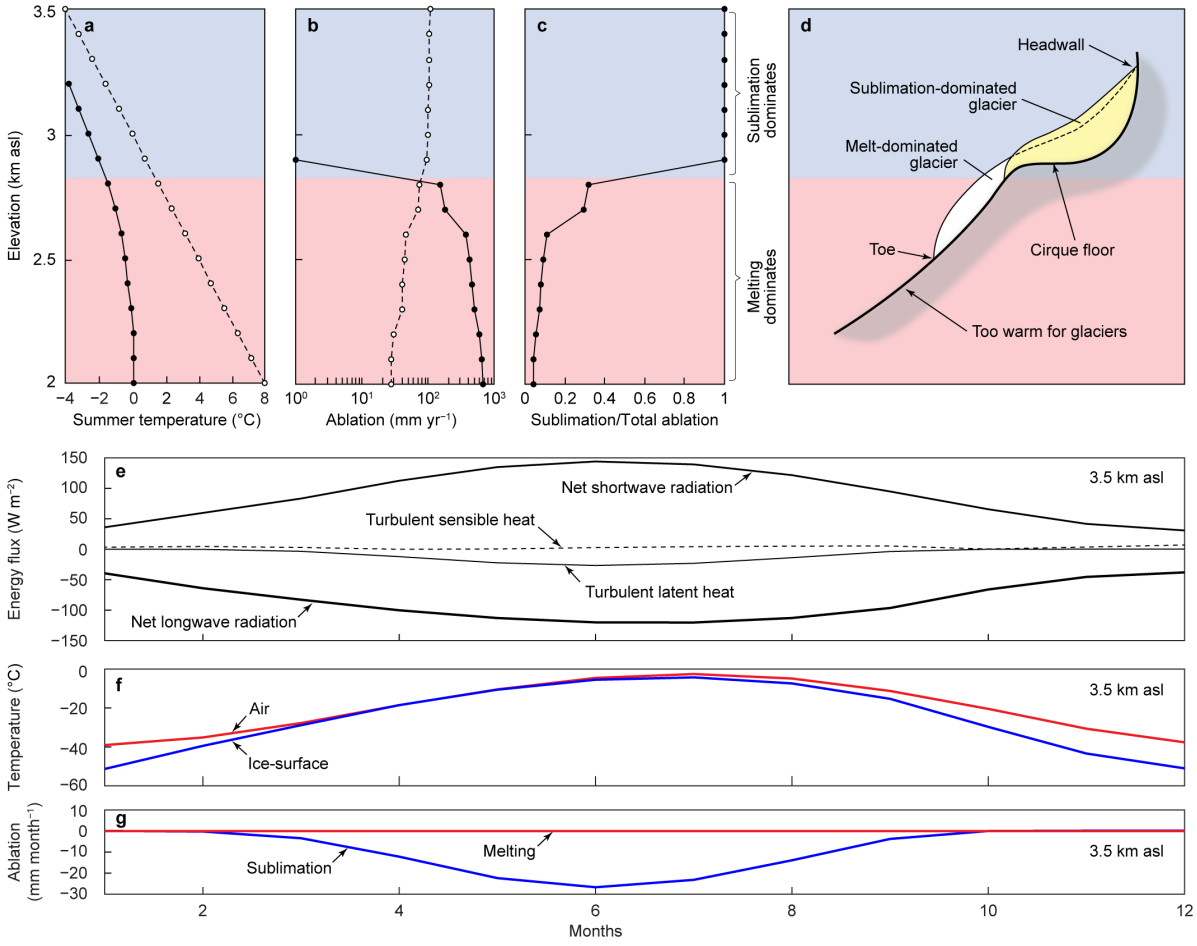

Figure 3.22. Sublimation- and melt-dominated regime for glacier ablation. a. Summer (JJA average) air temperature (open circles) and ice-surface temperature (closed circles). b. Potential annual ablation from sublimation (open circles) and from melting (closed circles). Note the logarithmic scale for horizontal axis. c. Fraction of sublimation to total annual ablation. Sublimation dominates in "blue zone," where at least 50% of ice is lost via sublimation. The transition to the melt-dominated "red zone" is abrupt due to efficient melting. d. Profiles of two hypothetical glaciers under the same conditions except snowfall. The glacier with 110 mm (w.e.) yr^{-1} accumulation is balanced with sublimation before reaching the "red zone" below. An accumulation of 250 mm (w.e.) yr^{-1} will exceed sublimation and the glacier must flow to lower altitudes where melting occurs. e. Monthly mean calculations in the sublimation zone at 3500 m asl of incoming (positive) and outgoing (negative) energy fluxes: f. Monthly mean temperatures of air (top red line) and the ice-surface (bottom blue line); g. Monthly mean ablation due to melting (top red line) and sublimation (bottom blue line).

The normalized ELAs in Figure 3.23a for the Gobi-Altai and Hangai ranges show the timing and the magnitude of the glacial advances compared to the normalized ELA depressions of the local LGMs (100%). At Gichginii, the ELA_{norm} depression indicated by the early Holocene G2 moraine (8–7 ka) (Figure 3.4) was ~90% of the value for the lower undated G1 ridge (Figure 3.23a), assuming the latter was glacially deposited. On the other hand, if G1 was non-glacial then the local LGM occurred during early Holocene, as registered by G2.

Sutai hosts modern glaciers on both SW and NE slopes. The ELA depression of the dated MIS 2 glaciers on the NE slope was ~80% of undated local LGM glacier, and the small modern glacier from the ice cap #1 at Sutai had an ELA_{norm} of ~40% (Figure 3.23a). The glacially eroded bedrock knob (MOT98-CS-22: 22.1 ka) on the SW piedmont of Sutai suggests that the local LGM glacier on the piedmont occurred during MIS 2 (or earlier), but the set of four ^{10}Be ages ranging from ~20 to 14 ka on the right lateral moraine only 130–160 m higher in altitude suggests that extensive paleoglaciers persisted or re-advanced on the piedmont late in MIS 2. The ELA depression of the modern glacier on the SW slope of Sutai was at 28% of the depression during the local LGM.

There are undated local LGM moraines in Ih Bogd range and the ~17–12 ka moraines there were projected in Figure 3.23a to have ELA depression of ~70% the value for the local LGM glacier. The paleoglaciers in all studied valleys in the Hangai ranges, Bogd, Bitüüt and Bumbat, achieved their local LGM extent during MIS 3, not MIS 2 (Figure 3.23a). The modern ELA_{norm} = 0 at Otgontenger, because the top of the modern ice cap of Otgontenger lies more than 500 m above the headwall.

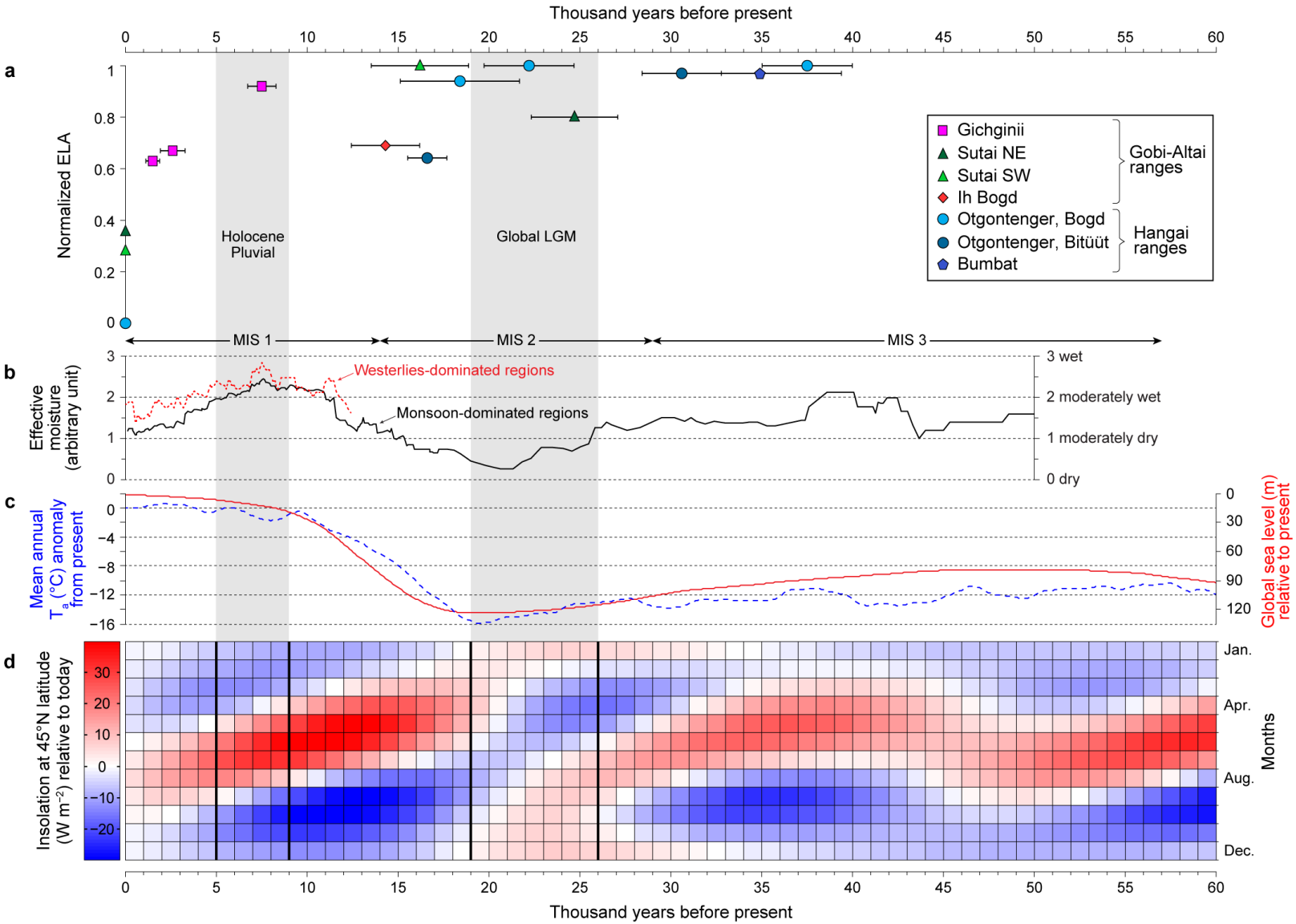
Thousand years before present
a
Normalized ELA
Holocene Pluvial
Global LGM
Gichginii
Sutai NE
Sutai SW
Ih Bogd
Otgontenger, Bogd
Otgontenger, Bitüüt
Bumbat
Gobi-Altai ranges
Hangai ranges
MIS 1
MIS 2
MIS 3
b
Effective moisture (arbitrary unit)
Westerlies-dominated regions
Monsoon-dominated regions
3 wet
2 moderately wet
1 moderately dry
0 dry
c
Mean annual T_a (°C) anomaly from present
Global sea level (m) relative to present
d
Insolation at 45°N latitude (W m^{-2}) relative to today
Jan.
Apr.
Aug.
Dec.
Months
Thousand years before present

Figure 3.23. Timing of local glaciation and the equilibrium-line altitude (ELA) lowering in the studied areas and the changes in regional climate. a. ELA depressions normalized to the ELA during the local LGM (Eqn 1) and the corresponding mean moraine ages with 1σ total uncertainties shown as bracketed line. Dark green triangle for Sutai NE slope and light blue circle for Bogd river valley of Otgontenger are at zero because there are no glaciers today, but the ice caps lie above the headwall. The Otgontenger data include ages from Rother et al. (2014) and this study. b. Average effective moisture (precipitation minus evaporation) reconstructed for regions dominated by westerlies (dashed red line) and monsoon (solid black line) in Central Asia (Herzschuh, 2005). The gray bars correspond to the durations of MIS 2 and the Holocene pluvial period in Mongolia. c. Mean annual surface air temperature for subarctic (40° N–80° N) continents (blue dashed line), and global sea level (red solid line), modeled from the LR-04 marine benthic oxygen-isotope stack (Bintanja and van de Wal, 2008). d. Monthly insolation change from today at 45° N latitude.

3.5 DISCUSSION

3.5.1 *Glacial asynchrony due to differences in climate and the variations of local conditions*

The timing of the local LGM in the Gobi-Altai and Hangai ranges (Figure 3.23a) reveals three modes of glacial behavior and/or timing: 1) in dry subhumid regions—Otgontenger and Bumbat— the MIS 3 glaciers were larger than during MIS 2; 2) in semiarid regions—Sutai and Ih Bogd— MIS 2 glaciers were the largest; and 3) in arid regions—Gichginii— the early Holocene glaciers were as large as the local LGM. Regional changes for the last 60 ka in climate parameters that control the glacier mass balance, such as snowfall (Figure 3.19b), air temperature T_a (Figure 3.23c), and seasonality (Figure 3.23d) explain the glacial asynchrony in all these regions. In particular, greatly reduced regional precipitation can explain the unusual restriction of MIS 2 glaciers to their cirques in some ranges. In normally cold and arid desert ranges, increased precipitation modified by unusual local conditions provided additional accumulation of snow and reduced ablation, which amplified the glacial asynchrony there.

For example, at Sutai any MIS 3 glaciers appear to have been over-run by glaciers during MIS 2. This is consistent with the "synchronous" hypothesis, in which the extent of mountain glaciers and high-latitude ice sheets co-varied closely through time. In contrast, the MIS 3 glaciers in the Hangai ranges extended further down the valley than the glacial advances during MIS 2, the global LGM, observations consistent with earlier studies (Rother et al., 2014). The pattern is consistent with glacial records in the humid Sayan ranges in southern Siberia, where the ELA during MIS 3 was ~75 m lower than during MIS 2 (Gillespie et al., 2008; Batbaatar and Gillespie, 2016). Larger MIS 3 glaciers are not predicted by the "synchronous" hypothesis, since the global ice volume was maximized during the MIS 2 global LGM. Regional precipitation and effective

moisture in Central Asia (Figure 3.23b) were greater during MIS 3 than MIS 2 (Herzschuh, 2005), and this likely contributed to the larger MIS 3 glaciers in the Hangai ranges. After ~28 ka the climate became drier and colder (Figure 3.23b and c). Seasonality, which had been quasi-stable throughout MIS 3, started to change at the beginning of MIS 2: spring and summer insolation decreased (Figure 3.23d), contributing to delayed melting in the spring and reduced ablation in the summer.

The clearest example of asynchronous glacial advances was observed in the Gichginii range, our most arid site in the Gobi-Altai. The lowest ridge, G1 in Figure 3.4, may be a moraine remnant buried by scree and thus may mark the local LGM there, but the ^{10}Be ages from the next oldest moraine, G2 in Figure 3.4, and only ~10 m higher, suggest that a glacial advance of similar ELA occurred during ~8–7 ka. Given the amount of rock excavated in making the Mönh Mösnii cirque compared to the volume of till contained in it today, it is evident that the cirque must have been occupied by Pleistocene glaciers that moved the debris down valley. Thus, the local LGM in the Gichginii range may have occurred during MIS 3 or 2, but even if it is younger, deposits from possible older advances must have been eroded or buried by the Holocene moraines G2–G5 there. This is not surprising because in cycles of glacial advances and retreats, the younger advances commonly overlap and obliterate older ones if the younger one is larger (Gibbons et al., 1984). Obliterative overlap is also a reason why glacial records from MIS 2 are much more abundant and pronounced than older ones from MIS 3 in Central Asia (e.g., Heyman et al., 2011b), and indeed throughout the world.

The early Holocene in Mongolia was a pluvial period with an almost three-fold increase in regional precipitation (Figure 3.23b; Herzschuh, 2005; Miehe et al., 2009), and ~10 °C higher annual T_a than during the global LGM (Figure 3.23c; Bintanja and van de Wal, 2008). During the

early Holocene, insolation increased in summer and decreased in other seasons relative to the global LGM conditions (Figure 3.23d). This may have increased the snow accumulation, especially on the Gichginii paleoglaciers, by two mechanisms: 1) A weakened Siberian high-pressure system during early Holocene (Mayewski et al., 2004) allowed passage of westerly moisture late in spring and early in autumn; 2) Colder springs and autumns preserved more snow. Today, spring and autumn accounts for ~25% of annual precipitation (~55 mm: Figure 3.2) near the Gichginii range and the annual T_a in these transitional seasons is approximately −9 °C at the altitude of the dated moraines (3,340 m asl). Glacial advances of the early Holocene have been documented in similar westerly-dominated regions as well. For example, glaciers in eastern Sayan mountains of southern Siberia advanced at ~10 ka (Batbaatar and Gillespie, 2016). Ice-core records from the Belukha ice cap ~900 km to their southwest reveal that the existing glaciers in the Altai mountains formed ~11–7.5 ka (Aizen et al., 2016). In the semiarid southern Kyrgyz Tian Shan, glaciers of the Aksai basin may have advanced at ~8–5 ka (Koppes et al., 2008). These examples demonstrate that precipitation-driven glacial advances were not unique to the Gichginii paleoglacier during the early Holocene. However, in the Artsan valley of Ih Bogd, no Holocene moraines were found and the youngest glacial advance was ~16–12 ka, following the global LGM. The pattern in the Gobi-Altai is distinctly different from that across the Hangai range and is decidedly different than would be predicted by the "synchronous" hypothesis, in which the largest glaciations occurred at roughly the same time globally. The summary of our interpretation of the moraine ages is given in Table 3.11.

Table 3.11. Average age and total uncertainty for ^{10}Be ages grouped according to landform. The groups are ordered from old to young.

Geographic region	Site	Group	n	Average age* (ka ± 1σ)	Interpreted deposition age** (ka)
Gobi-Altai	Gichginii	G2	3	7.5 ± 0.8	8–7
		G3	4	2.6 ± 0.7	3–2
		G4	6	1.5 ± 0.4	2–1
	Sutai	NE2-4	3	24.7 ± 2.4	27–22
		SW2	4	16.2 ± 2.7	19–13
	Ih Bogd	IB5-6	5	14.3 ± 1.9	16–12
Hangai	Otgontenger	BO1	3	22.2 ± 2.5	25–20
		BI2	2	30.6 ± 2.2	33–28
		BI9	2	16.6 ± 1.1	17–16
	Bumbat	BU1	3	59.9 ± 41.1	>> 22 (?)
		BU2	4	34.9 ± 4.5	39–30

* Outliers are not included in averaging. Lilliefors test (1967) of all the ^{10}Be ages, including the outliers, show that the ages are normally distributed. Thus, the average age and the compounded uncertainty properly characterizes the timing of the moraine formation.

** Exposed boulders are the last ones to be deposited on a moraine when a glacier was advancing or was in standstill. Thus, the ^{10}Be boulder ages predate the retreating of the glacier.

In addition to regional climate conditions, glacial response is modulated by local factors. This is especially true for small cirque glaciers. The Mönh Mösnii cirque in the Gichginii range faces north, and its glaciers were more shadowed than those in the south-facing valleys of Ih Bogd and Sutai. Indeed, the modern north-facing Sutai glaciers are much larger than on the south slopes. Furthermore, accumulation in catchments located downwind from the large high-altitude plateaus common in the Gobi-Altai is augmented by snow blown from them into the cirques by the strong prevailing westerly winds. The Mönh Mösnii valley in the Gichginii range is downwind (east) of a summit plateau (Figure 3.5), three times the area of the cirque (0.5 km^2), increasing the effective

accumulation area. The other valleys we studied likely received less wind drift: cirques in Ih Bogd and Sutai ranges are upwind (west) of a plateau that accumulates much snow. Thus, the additional accumulation of snow on Mönh Mösnii cirque due to local factors likely pushed across the threshold for glaciation, driving the glaciers to lower altitudes than expected from regional climatic conditions alone.

According to the calculation of Rupper and Roe (2008) of melt fractions (Figure 3.3) melt becomes responsible for more than 50% of total ablation when annual precipitation is higher than ~150 mm, which marks the transition from melt-dominated to sublimation-dominated regimes. Precipitation in our five sites bracketed this threshold. At Sutai, Ih Bogd and the Hangai ranges, precipitation is great enough that for glaciers to exist, efficient melting must dominate the total ablation, and the balance of T_a and snowfall controls the glaciation. The peaks of Otgontenger (4,008 m asl) and Sutai (4,220 m asl) have modern ice caps; yet the peak of Ih Bogd (3,957 m asl, only ~140 m lower than the headwall of the modern Sutai glaciers) and with essentially the same climate, does not. The measured summer lapse rate at Sutai (8 °C km^{-1}; Table 3.8) applied to that altitude difference suggests that the Ih Bogd plateau could have a modern ice cap if it were at an altitude like Sutai or Otgontenger. At the Gichginii range, however, precipitation is so low that sublimation alone would be enough to ablate most of the snow and ice even if the summit plateau was higher and colder than Sutai or Otgontenger. Thus, the Gobi-Altai and southern Hangai ranges appear to be very close to the threshold of glaciation today. Evidently, as predicted by numerical models (Rupper and Roe, 2008; Rupper et al., 2009), in the arid environments of the Gobi-Altai insolation and summer T_a are important factors controlling ice mass balance, and minor variations in snowfall as well as T_a can lead to major changes in ELAs.

In considering precipitation-sensitive or sublimation-dominated glaciers, it is important to recognize that melting can also occur, just as some sublimation occurs in temperature-sensitive or melt-dominated systems. Some melting under cold conditions can occur even if $T_a \ll 0°C$. This can occur at the thin edges of snow fields or glaciers, where sunlight can penetrate to a low-albedo substrate, warming it and melting the adjacent ice. It can also occur on glacier surfaces, especially if they are covered with a low-albedo layer of dust that can absorb the sunlight and warm the underlying ice. An example of the former is shown in Figure 3.24, a photograph on the South Col of Chomolungma (Mt. Everest) at 8,000 m asl and with $T_a \approx -28$ °C. It is noteworthy that blowing dust is common in Mongolia, and glaciers there may have been darkened accordingly, perhaps even more than they are today and in our energy modeling, which assumed "clean" ice.

Figure 3.24. Ephemeral running water at the end of a snow field on the South Col of Chomolungma (Mt Everest) at 8000 m asl and air temperature ≈ −28 °C. Photograph by Justin Merle, 20 May 2009.

3.5.2 *Implications for reconstructing paleoclimate from glacier records*

Without an actual measurement of glacier mass balance the ELA must be defined from the altitude of the highest lateral moraine, or from the geometry of the glacier using the THAR and AAR methods. These geometric ELAs are estimated from the altitudes of glacial deposits for paleoglaciers (e.g., Porter, 2001; Heyman, 2014) and using satellite images for modern glaciers (e.g., Kargel et al., 2014), and essentially make a metric with which to reconstruct climate from glacial advances and retreats. However, the physical ELA that is truly derived from physical glacier modeling requires a full account of surface energy and mass balance for individual glaciers. The correlation of geometric and physical ELAs for melt-dominated glaciers is well-defined (Ohmura et al., 1992), and because their ELA is a strong function of T_a (Figure 3.21; Rupper and Roe, 2008) it is practical to reconstruct summer T_a from changes in ELA assuming minimal change in precipitation. However, the physical ELA for a sublimation-dominated glacier is poorly defined because no melting occurs and because the ablation in the higher "accumulation" zone is as strong as it is in the lower "ablation" zone. Moreover, sublimation (thus total ablation) is largely independent of T_a and small changes in precipitation can drive large changes in ELA (Figure 3.25).

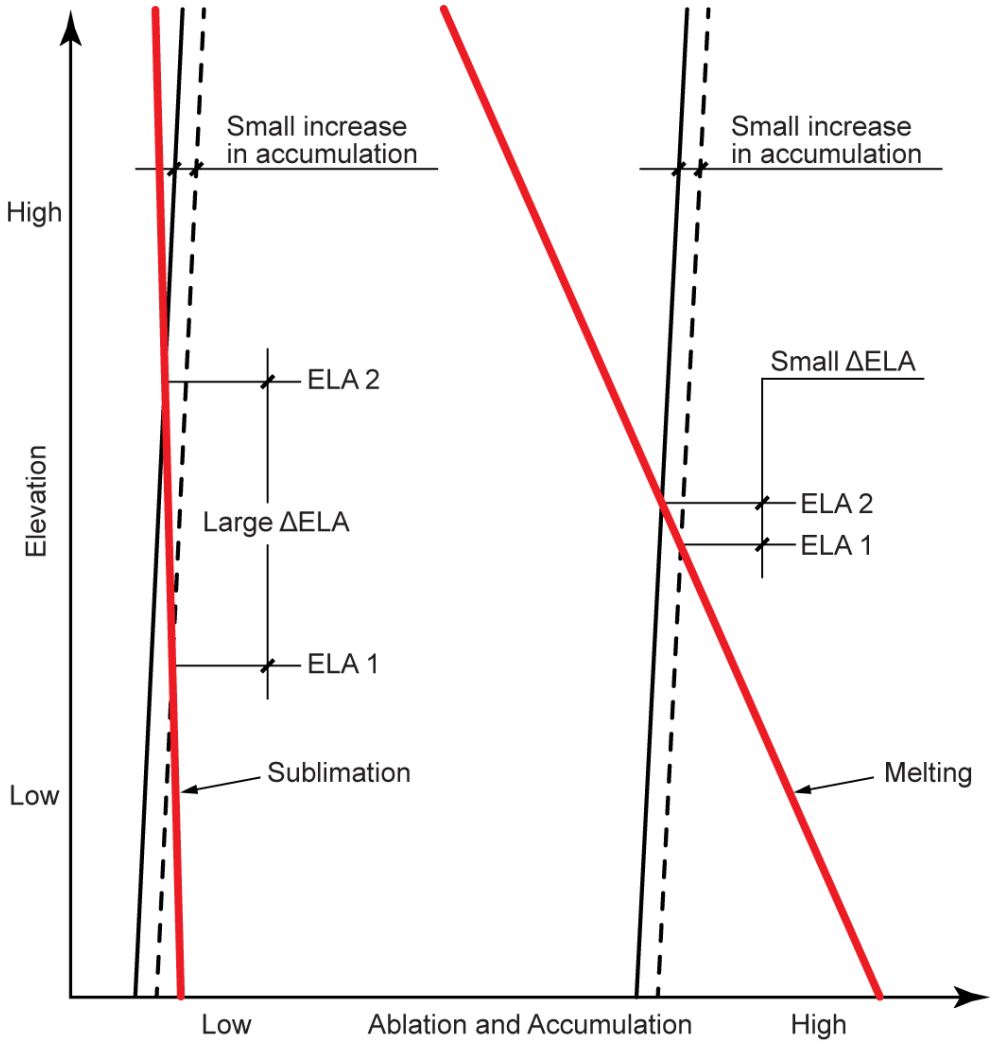

Figure 3.25. Schematic diagram relating ELA depression to change in precipitation. A small increase in precipitation (black line) shifts the amount towards right to the dashed line. In the sublimation-dominated glacier (Left) the ELA is sensitive to precipitation and a small increase in precipitation leads to large ΔELA. However, in melt-dominated glacier (Right) the ELA is insensitive to precipitation and the same increase in precipitation leads to much smaller ΔELA.

In the warming climate caused by human activities (IPCC, 2013) many glaciers are already retreating (Roe et al., 2016). Once limited to their cirques, some will be subject to the same kind of idiosyncratic local factors that we conclude have occurred in the past across the Gobi-Altai, making regional patterns of glacier balance more "noisy" and difficult to interpret in terms of climate. Mountain glaciers now in the "precipitation-sensitive" regime (blue dots of Figure 3.21) may migrate towards the "temperature-sensitive" regime (red dots of Figure 3.21) and in the absence of greatly increased winter snowfall they may retreat catastrophically. Still, other and colder glaciers in the "precipitation-sensitive" regime may simply lengthen as warmer conditions bring increased precipitation without causing them to cross into the "transitional" zone (black dots of Figure 3.21) and/or "temperature-sensitive" regime. Thus, asynchronous behavior should be expected in the future, even under climate-change conditions of simple warming. Our analyses (Figure 3.22) have suggested that under specific conditions some glaciers do not require a cooling climate to advance, and that glacier records can best be understood by identifying the major ablation processes dictating the glacier sensitivity to changes in climate, as predicted by numerical modeling of Rupper and Roe (2008).

3.6 SUMMARY AND CONCLUSIONS

The paleoglaciers in Gichginii range of central Gobi-Altai, advanced at ~8–7 ka, during the early Holocene, with a magnitude similar to their local LGM positions. During the early Holocene, the autumn and spring were warmer than in the global LGM, but the resulting increased ice loss due to melting and sublimation was compensated by increased regional precipitation sufficient to cause a regional pluvial period of high lakes. Additional snow accumulation due to wind drift and shaded cirques also favored Holocene glacier growth. Although the timing of the local LGM at Gichginii was not constrained, for times prior to 10 ka in these cold, extremely arid environments evidently inefficient sublimation could ablate the meager amount of annually accumulated snow and ice, resulted in small glacier advances despite the low temperatures.

In contrast to the temporal pattern of maximum glaciations and arid climate in the Gichginii range, other mountain ranges with higher precipitation in the Gobi-Altai, for example in Artsan valley of Ih Bogd and the southwest slopes of Sutai, remained glaciated until ~16–14 ka, after the global LGM. The largest global LGM advance in the Gobi-Altai was observed on the northeast slopes of Sutai (ELA = 3,640–3,280 m asl; ΔELA = 260–590 m). In Bumbat valley, in the less arid Hangai ranges, the glaciers advanced to their maximum at ~40–30 ka, during MIS 3 and well before the global LGM. Melting dominates ablation in those subhumid areas and increased precipitation during MIS 3 would have driven the glacier advance. However, the Hangai paleoglaciers 20 km west of the Otgontenger ice cap achieved their maximum extent at ~22 ka, during the global LGM. They were similar in size to those of MIS 3 (ELA = 2,840–2,670 m asl; ΔELA ≈ 1,000 m), mainly because over the past 60 ka regional precipitation was at its lowest level during the global LGM even though there was a slightly lower average air temperature in MIS 2 than in MIS 3, which favored glacier growth.

There are three broad implications that can be drawn from our findings: 1) The notion of a near-synchronous northern-hemisphere LGM advances of mountain glaciers is not widely applicable to cold, sub-freezing arid regions; 2) Although less energy-efficient than melt, sublimation becomes more important and can even dominate ablation of glaciers in such regions, where glacier growth there is largely controlled by precipitation and is less sensitive to air temperature; 3) Under modern global climate warming, most glaciers are in retreat, but our results suggest that, although non-intuitively, in some regions, particularly cold deserts, the indirect result of warming could be glacial advance due to increased snowfall. Therefore, changes in glacier growth must be interpreted cautiously to infer climatic past and future conditions.

3.7 REFERENCES IN CHAPTER 3

Aizen, E.M., Aizen, V.B., Takeuchi, N., Mayewski, P.A., Grigholm, B., Joswiak, D.R., Nikitin, S.A., Fujita, K., Nakawo, M., Zapf, A., Schwikowski, M., (2016), Abrupt and moderate climate changes in the mid-latitudes of Asia during the Holocene. Journal of Glaciology. 1–29, doi: 10.1017/jog.2016.34

Annan, J.D., and Hargreaves, J.C., (2013), A new global reconstruction of temperature changes at the Last Glacial Maximum. Climate of the Past 9, 367–376.

Augustin, L., Barbante, C., Barnes, P.R.F., Barnola, J.M., Bigler, M., Castellano, E., Cattani, O., Chappellaz, J., Dahl-Jensen, D., Delmonte, B., Dreyfus, G., Durand, G., Falourd, S., Fischer, H., Flueckiger, J., Hansson, M.E., Huybrechts, P., Jugie, G., Johnsen, S.J., Jouzel, J., Kaufmann, P., Kipfstuhl, J., Lambert, F., Lipenkov, V.Y., Littot, G.C., Longinelli, A., Lorrain, R., Maggi, V., Masson-Delmotte, V., Miller, H., Mulvaney, R., Oerlemans, J., Oerter, H., Orombelli, G., Parrenin, F., Peel, D.A., Petit, J.-R., Raynaud, D., Ritz, C., Ruth, U., Schwander, J., Siegenthaler, U., Souchez, R., Stauffer, B., Steffensen, J.P., Stenni, B., Stocker, T.F., Tabacco, I.E., Udisti, R., van de Wal, R.S.W., van den Broeke, M., Weiss, J., Wilhelms, F., Winther, J.-G., Wolff, E.W., Zucchelli, M., (2004), Eight glacial cycles from an Antarctic ice core. Nature 429, 623–628.

Balco, G., (2011), What is a camel diagram anyway? The bleeding edge of cosmogenic-nuclide geochemistry. https://cosmognosis.wordpress.com/2011/07/25/what-is-a-camel-diagram-anyway/

Balco, G., Stone, J.O., Lifton, N.A., Dunai, T.J., (2008), A complete and easily accessible means of calculating surface exposure ages or erosion rates from ^{10}Be and ^{26}Al measurements. Quaternary Geochronology 3, 174–195.

Batbaatar, J., and Gillespie, A.R., (2016), Outburst floods of the Maly Yenisei. Part II – new age constraints from Darhad basin. International Geology Review 58, 1753–1779.

Benn, D.I., and Owen, L.A., (1998), The role of the Indian summer monsoon and the mid-latitude westerlies in Himalayan glaciation: review and speculative discussion. Journal of the Geological Society 155, 353–363.

Bintanja, R., and van de Wal, R.S.W., (2008), North American ice-sheet dynamics and the onset of 100,000-year glacial cycles. Nature 454, 869–872.

Blomdin, R., Stroeven, A.P., Harbor, J.M., Lifton, N.A., Heyman, J., Gribenski, N., Petrakov, D.A., Caffee, M.W., Ivanov, M.N., Hättestrand, C., Rogozhina, I., (2016), Evaluating the timing of former glacier expansions in the Tian Shan: a key step towards robust spatial correlations. Quaternary Science Reviews 153, 78–96.

Braconnot, P., Otto-Bliesner, B., Harrison, S., Joussaume, S., Peterchmitt, J.Y., Abe-Ouchi, A., Crucifix, M., Driesschaert, E., Fichefet, Th., Hewitt, C.D., Kageyama, M., Kitoh, A., Laîné, A., Loutre, M.F., Marti, O., Merkel, U., Ramstein, G., Valdes, P., Weber, S.L., Yu, Y., Zhao, Y., (2007), Results of PMIP2 coupled simulations of the Mid-Holocene and Last Glacial Maximum – Part 1: experiments and large-scale features. Climate of the Past 3, 261–277.

Chauvenet, W., (1960), Reprint of 1891, fifth ed.. A Manual of Spherical and Practical Astronomy V. II. 1863, pp. 473–566, Dover, N.Y.

Chmeleff, J., von Blanckenburg, F., Kossert, K., Jakob, D., (2010), Determination of the ^{10}Be half-life by multicollector ICP-MS and liquid scintillation counting. Nuclear Instruments and Methods in Physics Research Section B: Beam interactions with Material and Atom 268, 192–199.

Clark, P.U., Dyke, A.S., Shakun, J.D., Carlson, A.E., Clark, J., Wohlfarth, B., Mitrovica, J.X., Hostetler, S.W., McCabe, A.M., (2009), The last glacial maximum. Science 325, 710–713.

Cuffey, K.M., and Paterson, W.S.B., (2010), The Physics of Glaciers, fourth ed. Elsevier, Amsterdam.

Darvill, C.M., Bentley, M.J., Stokes, C.R., Shulmeister, J., (2016), The timing and cause of glacial advances in the southern mid-latitudes during the last glacial cycle based on a synthesis of exposure ages from Patagonia and New Zealand. Quaternary Science Reviews 149, 200–214.

Fink, D., and Smith, A., (2007), An inter-comparison of ^{10}Be and ^{26}Al AMS reference standards and the ^{10}Be half-life. Nuclear Instruments and Methods in Physics Research Section B: Beam interactions with Materials and Atoms 259, 600–609.

Gibbons, A.B., Megeath, J.D., Pierce, K.L., (1984), Probability of moraine survival in a succession of glacial advances. Geology 12, 327–330.

Gillespie, A., and Molnar, P., (1995), Asynchronous maximum advances of mountain and continental glaciers. Reviews of Geophysics 33, 311–364.

Gillespie, A.R., (1991), Testing a new climatic interpretation for the Tahoe glaciation. In I Natural History of Eastern California and High-Altitude Research (Eds. Hall, Jr., C.A., Doyle-Jones, V., Widawski, B.). University of California, Los Angeles, California, Proceedings of the White Mountain Research Station. Symposium 3, 383–398.

Gillespie, A.R., Burke, R.M., Komatsu, G., Bayasgalan, A., (2008), Late Pleistocene glaciers in Darhad Basin, northern Mongolia. Quaternary Research 69, 169–187.

Goldthwait, R.P., (1970), Mountain glaciers of the Residential Range in New Hampshire. Arctic Antarctic and Alpine Research. 2, 85–102.

Gribenski, N., Jansson, K., Lukas, S., Stroeven, A., Harbor, J., Blomdin, R., Ivanov, M., Heyman, J., Petrakov, D., Rudoy, A., Clifton, T., Lifton, N., Caffee, M., (2016), Complex patterns of glacier advances during the Lateglacial in the Chagan-Uzun Valley. Russian Altai. Quaternary Science Reviews 149, 288–305. http://dx.doi.org/10.1016/ j.quascirev.2016.07.032.

Hays, J.D., Imbrie, J., Shackleton, N.J., (1976), Variations in the Earth's orbit: Pacemaker of the ice ages. Science 194, 1121–1132.

Heisinger, B., Lal, D., Jull, A.J.T., Kubik, P., Ivy-Ochs, S., Neumaier, S., Knie, K., Lazarev, V., Nolte, E., (2002a), Production of selected cosmogenic radionuclides by muons: 1. Fast muons. Earth and Planetary Science Letters 200, 345–355.

Heisinger, B., Lal, D., Jull, A.J.T., Kubik, P., Ivy-Ochs, S., Neumaier, S., Knie, K., Lazarev, V., Nolte, E., (2002b), Production of selected cosmogenic radionuclides by muons: 2. Capture of negative muons. Earth and Planetary Science Letters 200, 357–369.

Herzschuh, U., (2006), Palaeo-moisture evolution in monsoonal Central Asia during the last 50,000 years. Quaternary Science Reviews 25, 163–178.

Heyman, J., (2014), Paleoglaciation of the Tibetan Plateau and surrounding mountains based on exposure ages and ELA depression estimates. Quaternary Science Reviews 91, 30–41.

Heyman, J., Stroeven, A., Caffee, M.W., Hättestrand, C., Harbor, J.M., Li, Y., Alexanderson, H., Zhou, L., Hubbard, A., (2011a), Palaeoglaciology of Bayan Har Shan, NE Tibetan Plateau: exposure ages reveal a missing LGM expansion. Quaternary Sci. Rev. 30, 1988–2001.

Heyman, J., Stroeven, A.P., Harbor, J.M., Caffee, M.W., (2011b), Too young or too old: Evaluating cosmogenic exposure dating based on an analysis of compiled boulder exposure ages. Earth and Planetary Science Letters 302, 71–80.

Hughes, P.D., Gibbard, P.L., Ehlers, J., (2013), Timing of glaciation during the last glacial cycle: evaluating the concept of a global 'Last Glacial Maximum' (LGM). Earth-Science Reviews 125, 171–198.

IPCC, (2013), Climate Change 2013: The physical science basis (Eds. Stocker, T.F., Qin, D., Plattner, G.K., Tignor, M.M., Allen, S.K., Boschung, J., Nauels, A., Xia, Y., Bex, V., Midgley, P.M.), Cambridge Univ. Press.

Jin, L., Chen, F., Morrill, C., Otto-Bliesner, B.L., Rosenbloom, N., (2012), Causes of early Holocene desertification in arid central Asia. Climate Dynamics 38, 1577–1591.

Kalnay, E., Kanamitsu, M., Kistler, R., Collins, W., Deaven, D., Derber, J., Gandin, L., Saha, S., White, G., Woollen, J., Zhu, Y., Chelliah, M., Ebisuzaki, W., Higgins, W., Janowiak, J., Mo, K.C., Ropelewski, C., Wang, J., Leetma, A., Reynolds, R., Jenne, R., (1995), The NCEP/ NCAR 40-year re-analysis project. Bulletin of American Meteorological Society 77, 437–471.

Kargel, J.S., Leonard, G.J., Bishop, M.P., Kääb, A., Raup, B.H. (Eds.), (2014), Global Land Ice Measurements from Space, Springer Praxis Books, Springer, Berlin.

Kohl, C.P., and Nishiizumi, K., (1992), Chemical isolation of quartz for measurement of in-situ -produced cosmogenic nuclides. Geochimica et Cosmochimica Acta 56, 3583–3587.

Koppes, M., Gillespie, A.R., Burke, R.M., Thompson, S.C., Stone, J., (2008), Late Quaternary glaciation in the Kyrgyz Tien Shan. Quaternary Science Reviews 27, 846–866.

Lal, D., (1991), Cosmic ray labeling of erosion surfaces: In situ nuclide production rates and erosion models. Earth and Planetary Science Letters 104, 424–439.

Lilliefors, H.W., (1967), On the Kolmogorov-Smirnov test for normality with mean and variance unknown. Journal of the American Statistical Association 62, 399–402.

Lukas, S., Spencer, J.Q.G., Robinson, R.A.J., Benn, D.I., (2007), Problems associated with luminescence dating of Late Quaternary glacial sediments in the NW Scottish Highlands. Quaternary Geochronology 2, 243–248.

Matthews, J.A., and Briffa, K.R., (2005), The 'Little Ice Age': Re-evaluation of an evolving concept. Geografiska Annaler: Series A, Physical Geography 87, 17–36.

Mayewski, P.A., Rohling, E.E., Stager, J.C., Karlen, W., Maasch, K.A., Meeker, L.D., Meyerson, E.A., Gasse, F., van Kreveld, S., Holmgren, K., Lee-Thorp, J., Rosqvist, G., Rack, F., Staubwasser, M., Schneider, R.R., Steig, E.J., (2004), Holocene climate variability. Quaternary Research 62, 243–255.

Miehe, G., Schültz, F., Miehe, S., Opgenoorth, L., Cermak, J., Samiya, R., Jäger, E.J., Wesche, K., (2007), Mountain forest islands and Holocene environmental changes in Central Asia: A case study from the southern Gobi Altay, Mongolia. Palaeogeography Palaeoclimatology, Palaeoecology. 250, 150–166.

Minder, J.R., Mote, P.W., Lundquist, J.D., (2010), Surface temperature lapse rates over complex terrain: Lessons from the Cascade Mountains. Journal of Geophysical Research 115, D14122, doi:10.1029/2009JD013493.

Mitchell, T. D., and Philip, D. J., (2005), An improved method of constructing a database of monthly climate observations and associated high resolution grids: Interntaional Journal of Climatology 25, 693–712.

Mix, A.C., Bard, E., Schneider, R., (2001), Environmental processes of the ice age: land, oceans, glaciers (EPILOG). Quaternary Science Reviews, 627–657.

National Aeronautics and Space Administration, (2015), Shuttle Radar Topography Mission V3 Global 1 arc second dataset (SRTMGL1), accessed July 2016 using Reverb version 10.128.2.

National Oceanic and Atmospheric Administration, (2016), Integrated Surface Database (ISD), Station Tonhil USAF ID 442660. Accessed from http://www.ncdc.noaa.gov/isd in October 2016.

Nishiizumi, K., Imamura, M., Caffee, M., Southon, J., Finkel, R., McAnich, J., (2007), Absolute calibration of ^{10}Be AMS standards. Nuclear Instruments and Methods in Physics Research Section B: Beam interactions with Material and Atom 258, 403–413.

Nuimura, T., Sakai, A., Taniguchi, K., Nagai, H., Lamsal, D., Tsutaki, S., Kozawa, A., Hoshina, Y., Takenaka, S., Omiya, S., Tsunematsu, K., Tshering, P., Fujita, K., (2015), The GAMDAM glacier inventory: a quality-controlled inventory of Asian glaciers. The Cryosphere 9, 849–864. doi:10.5194/tc-9-849-2015.

Ohmura, A., Kasser, P., Funk, M., (1992), Climate at the equilibrium line of glaciers. Journal of. Glaciology 38, 397–411.

Owen, L.A., Richards, B., Rhodes, E.J., Cunningham, W.D., Windley, B.F., Badamgarov, J., Dorjnamjaa, D., (1998), Relic permafrost structures in the Gobi of Mongolia: age and significance. Journal of Quaternary Science 13, 539–547.

Porter, S.C., (2001), Snowline depression in the tropics during the Last Glaciation. Quaternary Science Reviews 2720, 1067–1091.

Putnam, A.E., Schaefer, J.M., Denton, G.H., Barrell, D.J.A., Birkel, S.D., Andersen, B.G., Kaplan, M.R., Finkel, R.C., Schwartz, R., Doughty, A.M., (2013), The Last Glacial Maximum at 44°S documented by a ^{10}Be moraine chronology at Lake Ohau. Quaternary Science Reviews 27Southern Alps of New Zealand. 62, 114–141.

Roe, G.H., Baker, M.B., Herla, F., (2016), Centennial glacier retreat as categorical evidence of regional climate change. Nature Geoscience. DOI: 10.1038/ngeo2863.

Rolland, C., (2002), Spatial and seasonal variations of air temperature lapse rates in Alpine region. Journal of Climate 16, 1032–1046.

Ross, S.M., (2003), Peirce's criterion for the elimination of suspect experimental data. Journal of Engineering Technology 20, 38–41.

Rother, H., Lehmkuhl, F., Fink, D., Nottebaum, V., (2014), Surface exposure dating reveals MIS-3 glacial maximum in the Khangai Mountains of Mongolia. Quaternary Research 82, 297–308.

Rother, H., Shulmeister, J., Fink, D., Alexander, D., Bell, D., (2015), Surface exposure chronology of the Waimakariri glacial sequence in the Southern Alps of New Zealand: implications for MIS-2 ice extent and LGM glacial mass balance. Earth and Planetary Science Letters 429, 69–81.

Rupper, S., and Koppes, M., (2010), Spatial patterns in Central Asia climate and equilibrium line altitudes. IOP Conf. Series: Earth and Environmental Science 9, 012009. doi:10.1088/1755-1315/9/1/012009

Rupper, S., and Roe, G., (2008), Glacier changes and regional climate: A mass and energy balance approach. Journal of Climate 21, 5384–5401.

Rupper, S., Roe, G., Gillespie, A., (2009), Spatial patterns of Holocene glacier advance and retreat in Central Asia. Quaternary Research 72, 337–346.

Sakai, A., Nuimura, T., Fujita, K., Takenaka, S., Nagai, H., Lamsal, D., (2015), Climate regime of Asian glaciers revealed by GAMDAM Glacier Inventory. The Cryosphere 9, 865–880. doi:10.5194/tc-9-865-2015.

Schneider, U., Becker, A., Finger, P., Meyer-Christoffer, A., Rudolf, B., Ziese, M., (2016), GPCC Full Data Reanalysis Version 7.0: Monthly Land-Surface Precipitation from Rain Gauges built on GTS based and Historic Data. Research Data Archive at the National Center for Atmospheric Research, Computational and Information Systems Laboratory. https://doi.org/10.5065/D6000072. Accessed January 2016.

Shi, Y., (2002), Characteristics of late Quaternary monsoonal glaciation on the Tibetan Plateau and in East Asia. Quaternary International 97–98, 79–91.

Stone, J.O., (2000), Air pressure and cosmogenic isotope production. Journal of Geophysical Research 105, 23753–23759.

Zomer, R.J., Trabucco, A., Bossio, D.A., Verchot, L.V., (2008), Climate change mitigation: A spatial analysis of global land suitability for clean development mechanism afforestation and reforestation. Agriculture, Ecosystems & Environment 126, 67–80.

Chapter 4

SPATIAL PATTERN OF GLACIATIONS ACROSS THE CLIMATE-TRANSECT OF CENTRAL ASIA

The motivation for the study presented in this chapter largely builds on the implications laid out in Chapter 3, where I presented evidence for a temporally and spatially heterogenous pattern of glacial advances in Mongolia and I demonstrated the importance of sublimation in driving this heterogenous pattern. The scope of this chapter expands the areal coverage area to include the high mountain ranges of Altai, Tian Shan, Qilian Shan, and Kunlun. In total, I present new data for cosmic-ray exposure dating of 106 samples spread over 16 sites. Of the samples, 105 were analyzed only for ^{10}Be and 52 were analyzed for ^{10}Be and ^{26}Al. I personally collected, prepared, and analyzed 48 of the ^{10}Be samples, and I calculated all the exposure ages. I am responsible for the photo-interpretative maps for the glacial deposits presented in this chapter. I also used a compilation of exposure-age data from the literature to augment the new data presented here and analyze the spatial and temporal pattern of glaciations in Central Asia. I used the two new techniques presented in Chapter 3: the "normalized ELA depression" scheme to compare relative magnitudes of glacial advances across large areas; and the "normalized deviation" method to identify outlier ages in my new dataset, as well as in the data from the literature.

The contents in this chapter were prepared as an article to be published in a long-form journal, such as a GSA Special Paper with multiple co-authors. Therefore, plural personal pronouns were used in the manuscript.

4.1 ABSTRACT

Paleoclimate inference from glacial records depends on a reliable relationship between the size of the glaciers and the climate parameters that modulate them. The glacier length is easy to estimate from satellite images for modern glaciers, and from the moraine locations for paleoglaciers. However, the glacier length can vary depending on the geometry of the bed even for the glaciers in neighboring valleys. The mass balance of glaciers is more reliable, but it is hard to measure both locally and remotely. An equilibrium-line altitude (ELA), a position on the glacier where annual accumulation and ablation is balanced, can be estimated from topographic maps and aerial or satellite photography. The ELA is primarily a function of snowfall, summer air temperature, and solar insolation. However, the sensitivity of the ELA to these climate parameters varies from region to region and inferring paleoclimate conditions is complicated accordingly. A numerical sensitivity model (Rupper and Roe, 2008) predicts that in regions with annual precipitation <~100 mm yr^{-1}, insolation by itself is adequate to sublime most of the annual accumulation of snow and the ELA is more sensitive to changes in precipitation than in more humid environments. Glaciers can exist only at high altitudes with sub-zero temperatures. In regions with higher precipitation, sublimation is not enough to ablate the accumulation of snow in excess of ~100 mm yr^{-1}. Here, glaciers will thicken and flow to lower altitudes where summer temperatures exceed the freezing point and melting becomes a dominant ablation mechanism. Under these conditions the ELA is sensitive both to changes in precipitation and summer air temperature. It was previously determined that glaciers in the mountains of the arid Gobi Desert achieved or matched their all-time lowest late Quaternary ELAs during the early Holocene (~8 ka), a pluvial period of Central Asia, in accordance with the above heuristic and sensitivity models. In mountains in subhumid climates farther north, the extent of the glaciers during the global Last Glacial Maximum (global

LGM) of MIS 2 was greater than during the Holocene, and similar to the extent during the "interglacial" MIS 3 period. This suggests that higher precipitation during MIS 3 caused the glaciers to grow despite the warmer summers, again consistent with the ELA sensitivities calculated from the models. However, our earlier findings were confined to five adjacent 1.875° × 1.875° cells of the Rupper/Roe model in central Mongolia, although the model covered most of Central Asia. We now extend our comparison of the timing and ELA depressions of glaciers across this vast region, from the Qilian Shan in the NE corner of the Tibetan Plateau to the Aksaiqin basin where the Kunlun and Karakoram meet in the NW corner, and north to the Tian Shan, Altai, and Sayan ranges. This was accomplished with our own field studies and new cosmic-ray exposure (^{10}Be and ^{26}Al) dating, together with other mapping and dating compiled from the literature. We find that the timing of the local LGM of the glaciers that are more sensitive to precipitation does not coincide with the global LGM. This finding suggests 1) the sensitivity of glaciers to precipitation needs to be constrained in order to infer paleoclimates; 2) the sensitivity of glaciers may have changed between glacial and interglacial times. In both cases, the inference of paleo temperatures from glacial records must account for the sensitivity of glaciers to precipitation. Thus, glacier retreat or advance alone is inadequate to make climatic inferences in the absence of careful consideration of the climatic setting in which the glaciers are found and the general mass-balance model for alpine glaciers.

4.2 INTRODUCTION TO CHAPTER 4

The mass balance of a mountain glacier, the difference between accumulation of snow and ablation of glacier ice, is the most accurate quantity through which to define its growth. Because accumulation and ablation both respond to local climate conditions, the fluctuation of glacier mass balance is used to infer changes in climate, past and present. The forcing climate factors and the corresponding changes to the glacier mass balance can be measured and/or estimated at any point on a glacier. Such an exercise at the equilibrium-line altitude (ELA) of a glacier, an estimated altitude at which the annual accumulation and ablation are equal, provides the most useful measure connecting the glacier and climate. Stephen Porter (1975) recognized the significance of defining climate conditions at the ELA and provided one of the most comprehensive instructions on estimating the glacier ELA. Porter (2001) further refined ELA-estimation methods, in which he emphasized the importance of surveying ELAs for glaciers in various climate conditions to accurately reconstruct paleoclimate from glacial evidence. In this study, we report results of cosmic-ray exposure dating of glacially deposited boulders in six mountain ranges of Central Asia (Figure 4.1), and the estimation of modern and paleo-ELAs. We chose the study sites to establish spatial and temporal patterns of glaciations in various climate conditions of Central Asia. Such regional mapping of ELA depressions (ΔELAs), the difference between the modern and paleo-ELAs, may reveal two fundamental aspects of inferring paleoclimate from glacial evidence: a) such mapping may identify glaciers with different sensitivities to climate variables where different ΔELAs are estimated under similar climate conditions; b) it may also be used to reconstruct paleoclimate variables in different regions where various ΔELAs are estimated for glaciers with similar sensitivities.

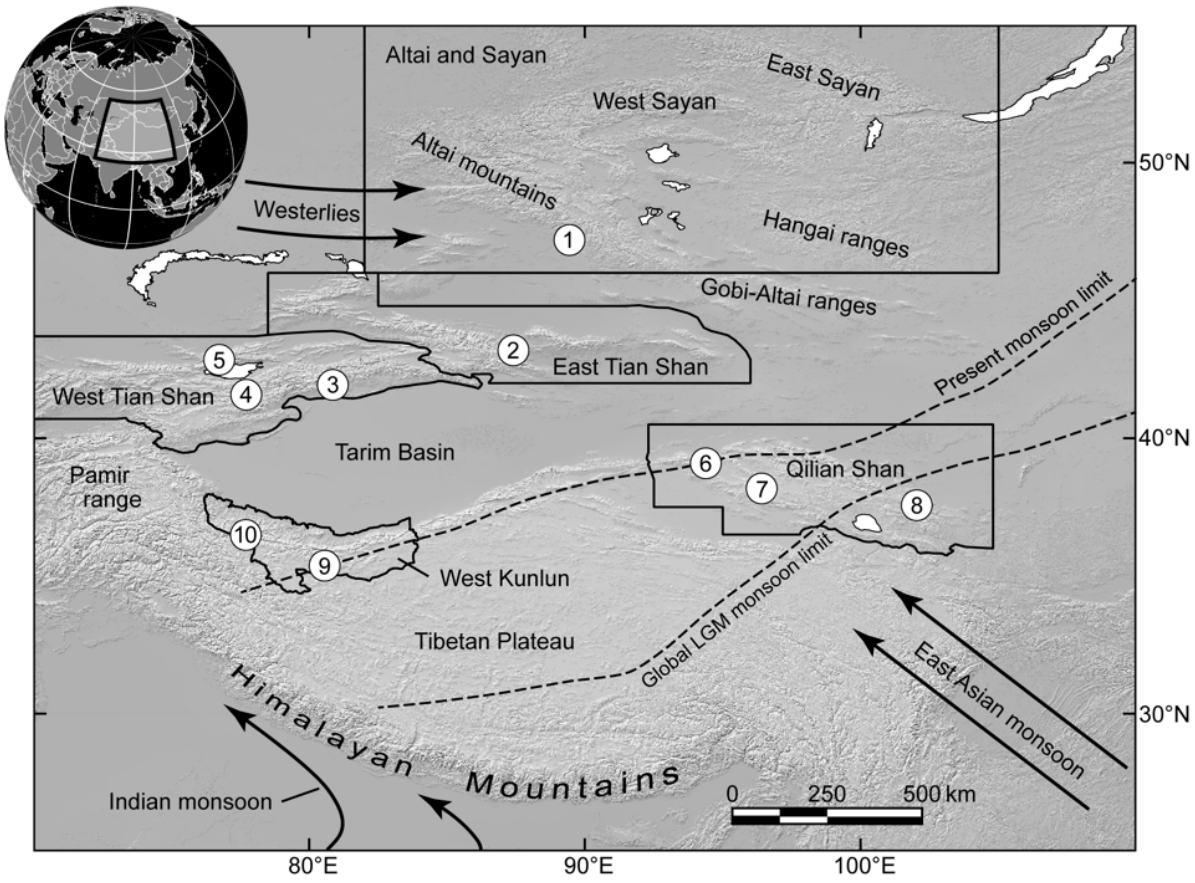

Figure 4.1. Study areas in continental Central Asia: 1) Kax Kurta; 2) Diehanjelegou, Alashanje, and Daxigou; 3) Muzart and Tailan; 4) Suek and Barskoon; 5) Choktal; 6) Altyn Tagh; 7) Dumda; 8) Gangshiqia; 9) Aksaiqin; and 10) Karakax. The delineation and the names of the regions were adopted from the second-order regions defined by the Randolph Glacier Inventory 6.0 (2017). The present and global LGM monsoon limits are from Shi (2002). Thick arrows indicate the general direction of major air flows (Benn and Owen, 1998). The shaded relief image was constructed from SRTM DEM (GTOPO030: U.S. Geological Survey, 2017).

The climate of the Central Asian interior is continental, characterized by low precipitation and cold winters (Peel et al., 2007). The high topography of Central Asia, including the Tibetan plateau, is the main reason for the cold winters. In winter, the Siberian high-pressure system extends south to the Central Asian interior near ~40 °N latitude (Araguas et al., 1998). In summer, more than 60% of the annual precipitation is brought by westerly winds (Sakai et al., 2015). In the

eastern margins of Central Asia, however, monsoons from the Indian and Pacific oceans bring summer moisture to the region (Araguas et al., 1998). In a simplistic scheme, Central Asia can be divided into three zones in terms of the precipitation source: 1) Monsoon-free interior regions; 2) Monsoon-influenced interior regions; 3) The Himalayas, influenced by Indian monsoon (Figure 4.1). We focused our study on the regions of Central Asia where the influence of monsoonal precipitation is minimal because the uncertainty of the monsoon intensity complicates the paleoclimate inference from the glacial evidence. In other words, established a pattern of glacial responses in regions with precipitation mostly sourced from the westerlies.

In order to accurately reconstruct paleoclimate variables from glacial evidence, the sensitivity of glaciers to the climate variables must be established. There are two general models that relate the ELA and climate: a) empirical models of summer air temperature (T_{air}) and annual precipitation (*ppt*) at the ELA (e.g., Ohmura et al., 1992; Sakai et al., 2015); and b) numerical models of ELA that account for various climate variables, including solar insolation (e.g., Mölg and Hardy, 2004; Rupper and Roe, 2008). An empirical curve constructed by Sakai et al. (2015) (Figure 4.2) shows that the relationship between summer T_{air} and annual *ppt* at the ELA is not linear; in warmer climates the ELA responds mostly to T_{air} changes, whereas in cold climates the ELA becomes more sensitive to *ppt* than to T_{air}. The numerical models do not rely on the empirically established sensitivity. They can be used to calculate the heat transferred into and out of the glacier to estimate the ELA and can estimate the relative importance of various climate variables to the glacier mass balance. The numerical sensitivity model of Rupper and Roe (2008) shows that in humid environments energy-efficient melt and subsequent runoff dominates glacier ablation and that changes in glacier mass balance are controlled mostly by fluctuations in T_{air}. However, in cold and arid environments sublimation by itself can ablate most of the accumulation

and the glacier mass balance may be controlled mostly by *ppt* (Figure 4.2). These insights from the empirical and numerical models imply not only that glaciers with different sensitivities can respond differently to the same climate change, but also that the sensitivity of individual glaciers to T_{air} and *ppt* can change as conditions at the ELA fluctuate. The modern annual *ppt* in our study sites range from 65 to 1020 mm (Adler et al., 2003). The glaciers in these low-*ppt* continental climates are predicted to have wide-ranging sensitivities to *ppt* and T_{air} in the empirical and numerical models (e.g., Mölg and Hardy, 2004; Rupper and Roe, 2008; Sakai et al., 2015).

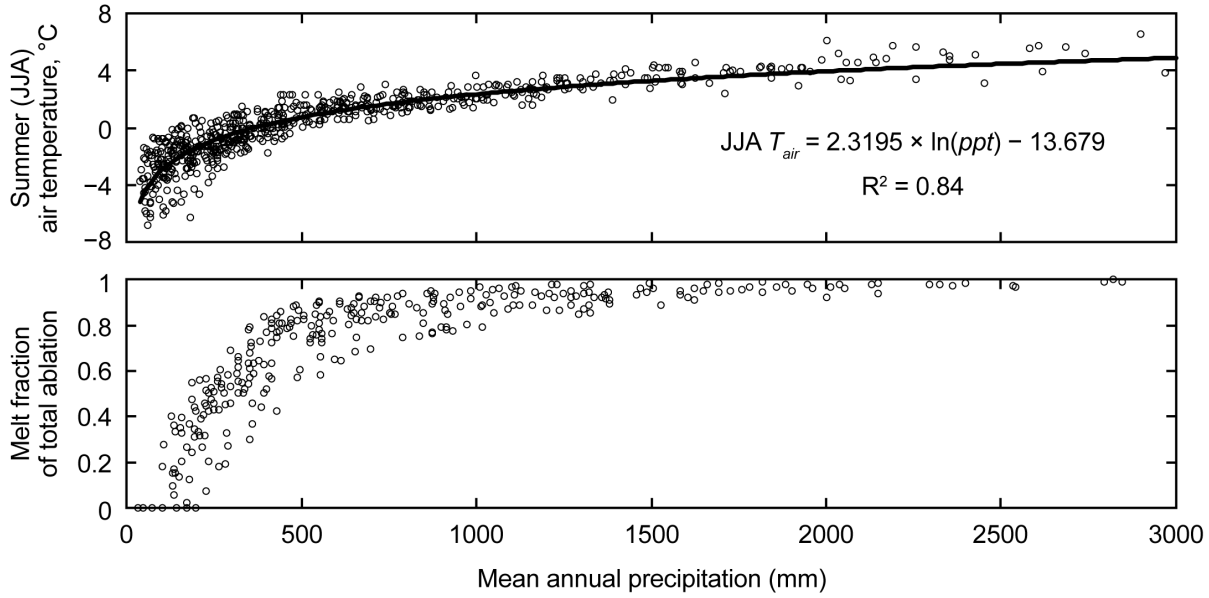

Figure 4.2. Summer air temperature (JJA T_{air}) at the ELA (top panel; from Sakai et al., 2015) and the melt fraction of total ablation (bottom panel; from Rupper and Roe, 2008) for modern Central Asian glaciers in regions with various annual precipitation (*ppt*). The equation and the correlation coefficient (R^2) in the top panel are derived from logarithmic fit (black line) between JJA T_{air} and annual *ppt*. The annual precipitation in the regions considered in this study ranged from 65 to 1020 mm.

4.2.1 *Chronostratigraphic nomenclature and the terms used in this study.*

We used the timing of the Marine Oxygen-Isotope Stages (MIS) constructed by Lisiecki and Raymo (LR04 stack: 2005) as a broad stratigraphic nomenclature. They integrated benthic $\delta^{18}O$ data recovered from 57 globally distributed sites to construct a single record of $\delta^{18}O$ fluctuations through time, and the stages were numbered in sequential order. The duration of the stages and their subdivisions, with an uncertainty of ±4 ka, according to the LR04 stack are as follows: MIS 5: 130–71 ka; MIS 4: 71–57 ka; MIS 3: 57–29 ka; MIS 2: 29–14 ka; and MIS 1: 14–1 ka. The duration of the epochs mentioned in this paper were from the chronostratigraphic units defined by U.S. Geological Survey (2010). We used the term local LGM as the time when the largest glacial advance occurred at a particular site. The term global LGM used in this paper, however, refers to 26.5–19 ka as defined by Clark et al. (2009) based on the timing of the maximum extents of ice sheets and mountain glaciers around the globe. According to Clark et al. (2009) several ice sheets reached their maximum extents at 33–19 ka; the onset of deglaciation of West Antarctic ice sheet that resulted in abrupt sea-level increase occurred 15–14 ka. This timeframe of the global LGM, 33–14 ka, roughly coincides with the duration of MIS 2.

4.2.2 *Concepts and terms to describe sensitivity of ELA to climate variables.*

The relative contributions of melt and sublimation to the total ablation of modern Central Asian glaciers calculated by Rupper and Roe (2008) provide the basis for the following two terms: a) melt-dominated glaciers; and b) sublimation-dominated glaciers. In this study we refer to glaciers as melt-dominated if melt was responsible for more than 50% of total annual ablation. Sublimation-dominated glaciers can occur in hyperarid regions, where as much as 80 mm water equivalent of ice can be lost via sublimation annually (Batbaatar et al., 2018). In other words, the

ratio of sublimation/melt increases with altitude: at higher, colder altitudes a lower percentage of total ablation will be lost via melt. This altitude-dependent ratio of dominant ablation mechanisms is directly related to the ELA sensitivity to changes in T_{air} and *ppt*: if melt cannot occur in sub-zero conditions (and sublimation dominates ablation) only *ppt* can drive accumulation, and hence the ELA. In this study we refer to glaciers as temperature-controlled if more than 50% of the ΔELA can be explained by changes in T_{air}. Likewise, if change in *ppt* is responsible for more than 50% of the ΔELA we refer to these glaciers as precipitation-controlled glaciers.

4.3 METHODS

We sampled 106 boulders found on moraines and lake shorelines at 16 sites in five mountain ranges of Central Asia: Altai, East Tian Shan, West Tian Shan, Qilian Shan, and West Kunlun (Figure 4.1). We measured concentrations of cosmogenic isotopes in the samples, 105 for ^{10}Be and 52 for ^{10}Be and ^{26}Al, to construct the glacial chronology in the study sites. Published boulder ages in the vicinity of the study sites were also considered in order to establish the regional spatial and temporal pattern of glaciations. We used the "normalized deviation" technique outlined by Batbaatar et al. (2018) to identify outlier ages. In order to approximate the glacier mass balance, we estimated the paleo-ELAs based on the dated and undated moraines. For comparison, the modern ELAs were also estimated using the same technique. The modern annual *ppt* and summer T_{air} were calculated using long-term gridded climate datasets. We then used the empirical curve constructed by Sakai et al. (2015), and the melt fractions of total ablation calculated by Rupper and Roe (2008) to infer paleoclimate conditions from the glacial evidence. Below, we describe the details of the modern climate datasets that we used, the cosmic-ray exposure dating, the ELA estimation methods, and the glacier-sensitivity approximation.

4.3.1 *Modern climate at the modern ELAs.*

We characterized the modern long-term values of climate variables based on the following datasets: a) Monthly surface (2 m above ground) T_{air} at the altitude of the gridded cells with 0.5° resolution (based on GTOPO30, U.S. Geological Survey) from Global Historical Climatology Network version 2 and Climate Anomaly Monitoring System (GHCN CAMS: Fan and van den Dool, 2008); b) Annual *ppt* grids with 2.5° resolution from Global Precipitation Climatology Project (GPCP version 2.3: Adler et al., 2003); c) Monthly T_{air} lapse rate grids with 2.5° resolution from reanalysis data produced by the National Center for Environmental Prediction and the National Center for Atmospheric Research (NCEP/NCAR reanalysis version 1: Kalnay et al., 1996). The long-term monthly mean values of climate variables in all of these climate datasets were calculated from data covering 1981–2010. We calculated the summer values of T_{air} and the lapse rate by averaging the June, July, and August values. The modern ELAs were estimated from the glacier altitudes provided in the Randolph Glacier Inventory 6.0 (RGI Consortium, 2017) and from Google Earth. The delineations of the mountain ranges are from Global Terrestrial Network for Glaciers (GTN-G, 2017) and the identification numbers for modern glaciers follow the RGI 6.0 inventory. The local names of the valleys and peaks were based on the interviews with local people and published literature.

4.3.2 *Cosmic-ray exposure dating and outlier evaluations.*

We followed the standard procedures for the exposure dating method: a) crush the sampled rocks to small pieces; b) extract the quartz minerals from the sample by dissolving the other minerals in HF acid; c) extract the Be and Al from the samples using column chromatography; d) measure the isotope ratios, $^{10}Be/^{9}Be$ and $^{26}Al/^{27}Al$, by accelerator mass spectrometry; e) calculate the ^{10}Be and

^{26}Al concentrations accounting for the half-lives of the isotopes and the sample mass. The rock samples were prepared at the cosmogenic nuclide laboratories at the University of Washington, the University of Vermont, and the Hebrew University of Jerusalem. The Be ratios were measured at the ANTERES facility at the Australian Nuclear Science and Technology Organisation (Fink and Smith, 2007) against the standard known as 07KNSTD (Nishiizumi et al., 2007), and the Center for Accelerator Mass Spectroscopy at the Lawrence Livermore National Laboratory (CAMS LLNL) using the standard known as KNSTD with a different nominal value of ^{10}Be/^{9}Be than the 07KNSTD (Nishiizumi et al., 2007). The Al ratios were measured at CAMS LLNL using the standard KNSTD (Nishiizumi, 2004). The exposure ages were calculated using CRONUS-Earth (Balco et al., 2008) version 2.3 with ^{10}Be and ^{26}Al production rates by Borchers et al. (2016). The cosmic-ray shielding factor was calculated in CRONUS-Earth calculator using horizon-angle measurements made in the field. The density of the samples was assumed to be 2.65 g cm^{-3}. We used the exposure ages based on the constant production rate model with a spallation scaling scheme of Lal (1991)/Stone (2000). For samples with measurements of both Be and Al concentrations the difference between ^{10}Be and ^{26}Al ages were not large, averaged at ~12%, of the ^{10}Be ages calculated for the sample. This age difference was similar to the mean external uncertainties of ~11% for ^{10}Be and ~13% for ^{26}Al ages. Therefore, we based our glacial chronology in the study sites based on the ^{10}Be ages to be compatible with the ^{10}Be ages available in the literature. However, we describe in detail in the Results section when ^{10}Be and ^{26}Al ages show significant differences for an individual sample.

We used the literature data compiled by J. Heyman (expage-201803; 2018) to recalculate the exposure ages available in the studied mountain ranges. We followed Batbaatar et al.'s (2018) "normalized deviation" method to identify outliers in the new and recalculated literature ages. This

method compares an individual age and its analytical (internal) uncertainty with the mean of the remaining ages in the group, using equation (4.1):

$$\delta_i = \frac{|x_i - \mu_{n-i}|}{\sqrt{std_{n-i}{}^2 + \sigma_i{}^2}} \quad (4.1)$$

where, δ_i is the normalized deviation for the age being tested, x_i, among n number of samples, μ_{n-i} is the mean of the group excluding x_i, std_{n-i} is the 1σ standard deviation of the group excluding x_i, and σ_i is the 1σ analytical uncertainty of x_i. An outlier is identified if $\delta_i > 2$. After rejecting the outliers, we calculated the mean of the remaining ages and compounded the 1σ standard deviation and 1σ internal uncertainty of the remaining ages to derive 1σ total uncertainty of the age-group. If an age-group had only two samples, we simply calculated the mean of the ages and derived the total uncertainty the same way described above. If the total uncertainty of the group exceeded 50% of the mean, the mean age was deemed unreliable and was excluded from the ELA analysis. We also used Chauvenet's (1969) and Peirce's (Ross, 2003) statistical tests to check the robustness of the normalized deviation method.

We carefully examined boulders in the field to look for any evidence of burial and sampled from the top of the boulders to avoid eroded or exhumed surfaces to the extent possible. The reported ages assume no erosion and burial, but we acknowledge that was not true in some cases where we observed and documented heavy erosion of the boulders. We discuss the limitations in the interpretation of these old ages in the Results section. The younger boulders did not exhibit erosion, and the age uncertainty due to erosion was not large enough to change our interpretation. For example, Batbaatar and Gillespie (2016) estimated that an apparent age of ~20 ka would increase by ~5% due to an unlikely erosion rate of 3 mm yr^{-1}, and ~2% due to shielding by a 4-

month seasonal snowpack of 250 mm depth in the Gobi-Altai range. We report the exposure ages, recognizing that they represent minima for the dated landforms.

The basic assumption in using cosmogenic nuclides for dating glacial boulders is that the accumulation of cosmogenic nuclides starts at a time when the boulder is deposited by a glacier and exposed to the sky. The boulders sampled from the moraine crests, excluding push moraines, are deposited when and where the glacier ablation exceeds accumulation. According to Anderson et al. (2014) many moraines appear to have formed within ~50 years, a period appropriate to be representative of climate calculated from the interannual variables of weather. Therefore, we have assumed that the paleoglaciers were in equilibrium with climate when they formed the moraines, and the boulders we sampled from the moraine crests represent a time when the paleoglacier was in standstill. In other words, our reported mean group ages after rejecting outliers are neither 'advance' nor 'deglaciation' ages. Even without accounting for the age uncertainties due to exposure prior to the deposition and burial history post deposition, typical analytical uncertainties of the exposure ages do not permit us to determine whether the glacier was advancing or receding.

4.3.3 *Equilibrium-line altitude*

By definition, the equilibrium line of glaciers is situated on the glacier surface where annual accumulation and ablation are equal, and the ELA is a direct proxy for annual mass balance. An accurate inference of climate from ELAs then has to be derived from the annual ELAs averaged over the time period of climate statistics (e.g., 30 years). In our study, we define the estimated paleo-ELAs from moraine locations as this 'climate-ELA'. Above, we defined that the exposure ages for the moraines represent the time of glacier standstills, and the paleo-ELAs estimated from

the dated moraines are therefore interpreted as the climate-ELA for glaciers in equilibrium with climate. However, in the absence of annual measurements of glacier mass balance or the glacier itself the mass balance ELA is approximated by geometric ELAs estimated using empirical constraints.

There are many ways to estimate the ELA, of which the Toe-Headwall Altitude Ratio (THAR) and Accumulation-Area Ratio (AAR) methods are the most reliable (e.g., Porter, 1975; Meierding, 1982; Porter, 2001). The AAR approach assumes that the accumulation area covers a certain fraction of the total area of the glacier (~65% for most temperate, debris-free glaciers: Porter, 2001) and to measure this fraction requires accurate estimations of glacier outline. We did not use the AAR method due the lack of constraints on the outlines of dated paleoglaciers. Instead, we used the simpler THAR method to estimate the ELAs using equation (4.2):

$$ELA = A_t + THAR(A_h - A_t) \quad (4.2)$$

where, A_t is toe altitude, A_h is headwall altitude, and *THAR* is a threshold value unique to a glacier. For modern glaciers we used minimum and maximum altitudes provided in the Randolph Glacier Inventory 6.0 (RGI Consortium, 2017) as toe and headwall altitudes. For paleoglaciers the minimum altitude of a moraine was taken to approximate the toe altitude. For paleo-headwall altitudes, however, we estimated from four altitudes above the glaciated valley: a) of bergschrunds visible on Google Earth; b) one third of the altitude difference between the cirque floor and the peak; c) of the point where avalanche chutes end in free air above the cirque floor, assuming that once the glacier shielded the rocks below from erosion; d) of the highest peak in cases where glacial horns do not exist. We assumed that the paleoglaciers in the same valley share the same headwall, which makes the THAR ELAs sensitive only to the toe altitudes.

Our approach follows the methods used by Batbaatar et al. (2018), who noted that the greatest uncertainty in the ELA estimation was the selection of a threshold *THAR* value. For example, in high-relief areas ~2000 m difference between the toe and headwall altitudes would lead to ELA difference of ~200 m depending on the choice of a threshold *THAR* value of 0.5 or 0.6, and the corresponding ΔELA values would differ by ~130 m. However, only ~20% of the local glacial maximum established in this study exhibited >1500 m difference in toe and headwall altitudes. The majority of the paleoglaciers considered in this study were less extensive and the accuracy of their THAR ELAs approach the accuracy of ~100 m, similar to the ELA accuracy estimated for the Sierra Nevada glaciers in the western USA (Gillespie, 1991).

We also used the maximum elevation of lateral moraines (MELM) as minimum estimates for the local ELAs (Porter, 2001) where the dated lateral moraines do not fit morphologically with the end moraines, or where recognizable end moraines simply do not exist. The precision of the MELM ELA must be approximated from the accuracy of the GPS unit (~10 m) and the vertical uncertainty of the terrain data. The RGI 6.0 inventory uses ASTER GDEM (NASA and METI) and Google Earth uses SRTM data for altitude, in which both elevation data have a vertical uncertainty of 30 m.

4.3.4 *Normalized ELA depression*

Modern glaciers in Central Asia are predicted to exhibit large spatial variations of sensitivities (Rupper and Roe, 2008). In the past under a different climate, the ELAs might have exhibited yet another spatial variation. This glacial asynchrony, in both spatial and temporal sense, can be examined by normalizing the local ELAs to the headwall altitude and plotting the values in a

timeseries. We followed Batbaatar et al.'s (2018) approach to calculate the normalized ELA depression, ΔELA_{norm} (dimensionless), using equation (4.3):

$$\Delta ELA_{norm} = \frac{A_h - ELA_{dated}}{A_h - ELA_{min}} \quad (4.3)$$

where, ELA_{dated} is an ELA estimated from a dated moraine, ELA_{min} is the lowest ELA within a valley, estimated from the lowest moraine regardless of whether the moraine was dated or not. Therefore, ELA_{min} represents the spatial magnitude of the local LGM standstill. When ELA_{dated} corresponds to ΔELA_{norm} = 1 the moraine age represents the timing of the local LGM. The ΔELA_{norm} can be a useful basis for visualization to decipher the reasons for the spatial and temporal variations of glacier advances. For example, the ΔELA_{norm} for glaciers with similar sensitivities can be plotted in a timeseries to identify the periods when variation in the magnitude of climate change may have been responsible for spatial asynchrony.

4.3.5 *Sensitivity of modern glaciers in Central Asia*

Glacier ablation can be expressed as a function of altitude because it depends on the heat exchange between the surface of the glacier and atmospheric conditions at various altitudes (Rupper, 2007). T_{air} and insolation are the significant regulators of ablation, and together with *ppt* can be used to define the climatic conditions at the ELA (e.g., Rupper and Roe, 2008). Ohmura et al. (1992) constructed summer T_{air} (proxy for ablation) and annual *ppt* (proxy for accumulation) at the ELA to empirically establish the relationship between these two important climate variables. Rupper and Roe (2008) found that in high-precipitation regions T_{air} was the most effective regulator of glacier mass balance. We therefore focused on two climate variables in this study, T_{air} and *ppt*.

Vargo et al. (2018) used a numerical model to calculate the spatial variation of ablation for modern Andean glaciers. They quantified the ELA sensitivities to T_{air}, *ppt*, and solar insolation, finding that the ELA sensitivity to T_{air}, C_{temp}, was ~180 m °C^{-1} regardless of the local *ppt*. However, the ELA sensitivity to annual *ppt*, C_{ppt}, in hyperarid regions was greater than in more humid regions, and C_{ppt} gradually decreased as the accumulation increased. Such parametrized sensitivity calculations have not been completed for Central Asia. Shea and Immerzeel (2016) compiled ΔELA data from high-altitude regions around the world to derive an empirical equation to estimate C_{temp} in relation to annual *ppt*:

$$C_{temp} = 16.46(ppt - 379.61)^{0.32} \quad (4.4)$$

Equation (4.4) does not permit the calculation of C_{temp} if the *ppt* is below 379 mm because *ppt* in the regions considered by Shea and Immerzeel (2016) ranged from 410 to 3000 mm. This approach was successfully used in the calculations of glacier recessions in the Himalayas and Hindu Kush under various warming climates (Kraaijenbrink et al., 2017) because annual *ppt* there permits the use of equation (4.4). However, annual *ppt* in most of our study sites was below 379 mm. Glaciers in such cold and arid regions are expected to be more sensitive to *ppt* than to T_{air} variations (Rupper and Roe, 2008; Sakai et al., 2015).

We used melt fraction values of Rupper and Roe (2008) to characterize the C_{temp} of modern glaciers in the vicinity of the dated moraines. Most of the studied valleys host modern glaciers in their cirques, but in the absence of a modern glacier we approximated the modern ELA (above the cirque headwall) from the ELA of the nearest glacier with the same aspect as the studied valley. Although the melt fraction of Rupper and Roe (2008) is related to C_{temp} and C_{ppt}, we note that their proportionalities are unknown, and quantified approximations of the sensitivities should not be made from the melt fraction.

4.4 RESULTS

The mountain ranges considered in this study cover approximately 715,000 km^2. We studied one valley in the Altai range, three valleys in the East Tian Shan, five valleys in the West Tian Shan, three separate mountain ranges within the broader Qilian Shan, and three glaciated valleys in the West Kunlun. The exposure age results (Tables 4.1–4.2) are organized by the mountain ranges where the study sites are located. The outlier evaluations for grouped ages with more than three samples are summarized in Table 4.3. The mean ages for the age-groups with two samples are summarized in Table 4.4. For each site we report the new exposure ages along with the modern and paleo-ELA results (Table 4.5). We also describe the modern climate conditions at the modern ELA (Table 4.6). We follow these descriptions with the recalculated exposure ages from literature, with further discussion of our interpretation of the new and literature ages. We provide the paleoclimate inferences based on the reconstruction of the dated paleo-ELAs within each mountain range at the end of the section.

4.4.1 *Altai range, Kax Kurta*

Spanning over 1000 km in an approximately NW–SE direction, the Altai range crosses the borders between Russia, Mongolia, and China (#1 in Figure 4.1). Our study site, Kax Kurta valley, is located in the southeastern part of the range (Figure 4.3). The altitude of the highest peak in the vicinity is ~3220 m asl and hosts a small perennial (?) snowfield in a sheltered part of the SW-facing cirque. The Kax Kurta valley is unglaciated now. We sampled two moraines located in a sequential order within the ~2.7 km wide valley. Two boulders from the highest end moraine in the valley, Kax Kurta-A (Figure 4.3), gave a mean ^{10}Be age of 17.3 ± 1.0 ka corresponding to THAR ELA of 2970 m asl. Approximately 5 km downvalley, an undated, well-preserved end

moraine gave a THAR ELA of ~2840 m asl. Around 1.5 km farther down the valley we collected a single boulder from a left-lateral moraine, Kax Kurta-B, which gave a ^{10}Be age of 21.6 ± 2.5 ka and an ^{26}Al age of 22.5 ± 2.4 ka. However, we cannot confidently constrain the age of this moraine from a single sample. This lateral moraine was probably deposited by the largest paleoglacier in the valley with a THAR ELA of ~2760 m asl. The nearest modern glacier with NW cirque orientation similar to the Kax Kurta cirque can be found ~50 km to the north. This modern glacier had a THAR ELA of ~3570 m asl (*ppt* ~200 mm and summer T_{air} = 4 ± 1.1 °C at the ELA), which was higher than the headwalls of the Kax Kurta paleoglacier. Approximately 260 km to the NW, Gribenski et al. (2018) sampled the three lowest moraines in the Kanas valley and dated them to ~21–18 ka with a THAR ELA of ~2510 m asl.

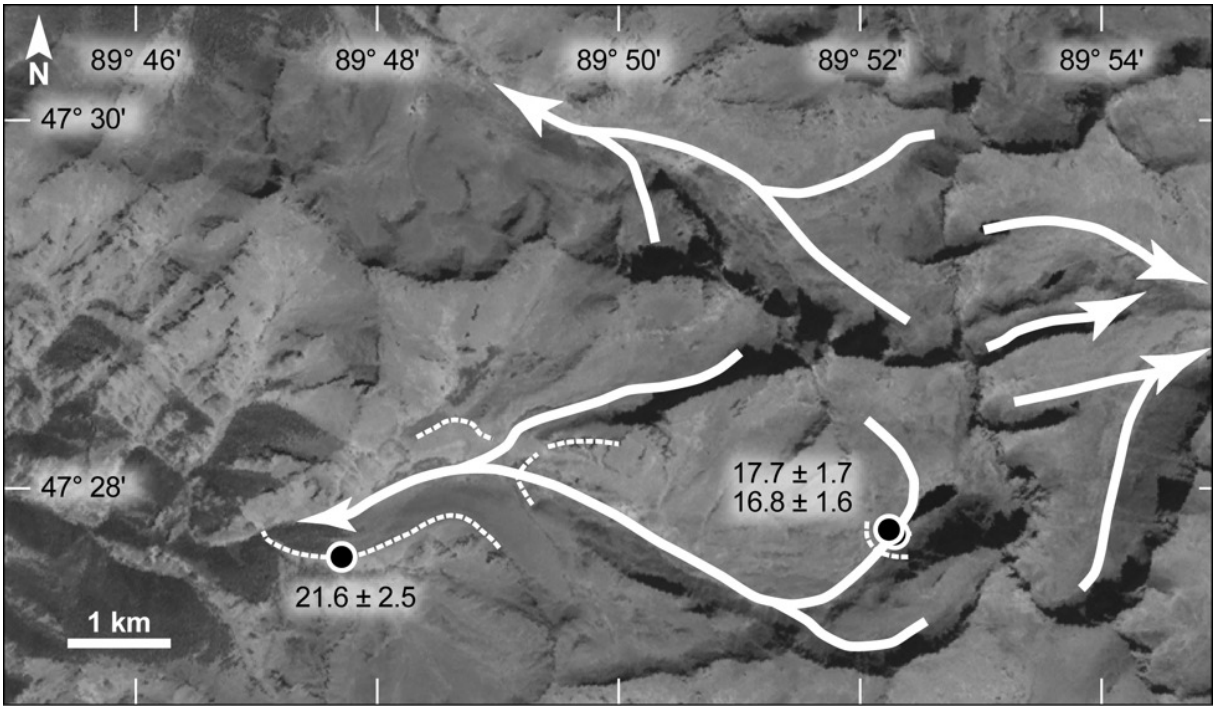

Figure 4.3. ^{10}Be samples in Kax Kurta valley, Altai range. Black circles indicate the locations of ^{10}Be and ^{26}Al samples. White arrows indicate the directions of paleo outlet glaciers. The dashed lines indicate the moraine crests. The background image is from Google Earth, DigitalGlobe (2017).

Another 120 km to the NE, Reuther et al. (2007), Reuther (2007), and Gribenski et al. (2016) dated a series of end and lateral moraines in the Chagan Uzun valley. The left-lateral moraines on the northern walls of the valley were deposited ~26–18 ka, corresponding to a MELM ELA of ~2640–2330 m asl. The boulders on the lower end moraines gave a mean age of 18.8 ± 1.9 ka with THAR ELA of ~2920 m asl. Herget et al. (2017) noted that these lower end moraines do not represent the largest glacial extent in the Chagan Uzun valley and that the lowest moraines in the valley were eroded by megafloods from the Chuya basin.

4.4.2 *East Tian Shan, Diehanjelegou*

The study site, Diehanjelegou valley (Figure 4.4 a–b), is located in the SE corner of the East Tian Shan, which spans ~360 km in the NW–SE direction. We sampled four boulders from a right-lateral moraine on the piedmont at the mouth of the valley, which gave a mean ^{10}Be age of 31.9 ± 9.3 ka. One of the samples in this group, XCS-104, yielded a significantly older ^{26}Al age (43.3 ± 4.5 ka) than the ^{10}Be age (30.0 ± 3.0 ka) implying the sample may have been partially buried at some point. Two boulders from the left-lateral moraine at a similar altitude gave a mean ^{10}Be age of 30 ± 12.2 ka. Both of these moraines correspond to a THAR ELA of ~3620 m asl. The valley contains two cirques now narrowly separated by a ridge, but the dated paleoglacier filled them all, overtopping the ridges. The highest modern glacier in the cirque has THAR ELA of ~3870 m asl (annual *ppt* ~250 m and summer T_{air} = 7.4 ± 0.9 °C at the ELA).

4.4.3 *East Tian Shan, Alashanje*

We sampled two boulders from an outermost right-lateral moraine in the lower part of the Alashanje valley (Figure 4.4c), which gave a mean ^{10}Be age of 67.7 ± 23.2 ka. Li et al. (2014) collected three samples on the upper part of the moraine to derive a mean ^{10}Be age of 76.1 ± 5.9 ka after one outlier was rejected. On the other side of the river, a left-lateral moraine sits at a similar altitude to the lower portion of the right-lateral moraine, and Li et al. (2014) dated it to a mean ^{10}Be age of 46.8 ± 6.5 ka (n=7, one outlier). These two lateral moraines correspond to THAR ELAs of ~3810–3770 m asl. However, the evidence for the maximum paleoglacier extent in this valley, the eroded hummocky till overlying the local fan, can be found further down the valley ~340 m in altitude below the two dated lateral moraines. The glaciated surface was not dated, and the lowest altitude of this hummocky terrain corresponds to a THAR ELA of ~3710 m asl. ~15 km upvalley and ~850 m above the lowest moraine two closely located end moraines were dated to ~29 and 26

ka (Li et al., 2014). The highest of the dated moraines in the valley, ~18 ka (Li et al., 2014), was found only ~210 m below and ~2 km away from the modern glacier tongue. The peaks around this site are ~400 m higher than the peaks around the Diehanjelegou valley, and the higher altitude of the Alashanje site is reflected in the colder summer T_{air} of ~3.4 ± 0.7 °C although they are in close proximity and receive the same annual *ppt* of ~250 m.

4.4.4 *East Tian Shan, Daxigou*

The paleoglaciers in the trunk Daxigou valley were fed by smaller glaciers sourced from 13 separate cirques, mostly oriented northward (Figure 4.4d). The valley itself is oriented W-E, unlike the northward-facing Diehanjelegou and south-facing Alashanje valleys. Despite the large number of tributary valleys contributing glacier ice, the U-shaped Daxigou valley extends for only ~16 km until it becomes a V-shaped valley with no evidence of glaciation. The rough outline of this paleoglacier, the largest in Daxigou, can be traced from the trimlines found especially on the southern side of the valley. The THAR ELA for this paleoglacier was ~3570 m asl, the value for the local LGM. ~4 km upvalley from the inferred end of the local LGM glacier, Li et al. (2011) collected two boulders from a left-lateral moraine, and ^{10}Be-dated them to ~21 and 18 ka. We collected two additional boulders from the same moraine, ^{10}Be-dated to ~23 and 19 ka, and the total of four boulders gave a mean ^{10}Be age of 19.3 ± 1.7 ka (n=4, one outlier). This standstill within the global LGM corresponds to an estimated THAR ELA of ~3670 m asl, ~120 m higher than for the local LGM. ~2 km upvalley we sampled two boulders from a previously studied lateral moraine (Li et al., 2014) and the total of six boulders gave a mean ^{10}Be age of 17.4 ± 1.5 ka. Another moraine nearby was ^{10}Be-dated to 17.7 ± 0.8 ka (n=3, one outlier; Kong et al., 2009). This location was on a broad flat area only ~220 m below the modern glaciers' termini. There, the ^{10}Be age of a boulder we collected from an end moraine was added to four ^{10}Be ages previously reported

by Kong et al. (2009) to give a mean ^{10}Be age of 19.6 ± 3.7 ka (after one outlier was deleted). Only 300 m away, Li et al. (2011) dated another moraine to obtain a mean ^{10}Be age of 17.3 ± 0.7 ka (n=2). These moraines correspond to a THAR ELA of ~3900 m asl, which was only ~100 m below the estimated modern ELA. These ages and the estimated paleo-ELAs suggest that the paleoglacier in Daxigou receded dramatically at the end of the global LGM, from ~80% to ~40% of the local LGM ΔELA_{norm} within about 2000 years. The youngest moraine in the valley, a nearby unbreached end moraine, was located ~100 m below the modern glacier terminus, which was dated to 0.3 ± 0.1 ka (n=8, one outlier; Li et al., 2014; this study). The THAR ELA for the modern glacier, ~4000 m asl, was ~25% of the local LGM ΔELA_{norm} in Daxigou.

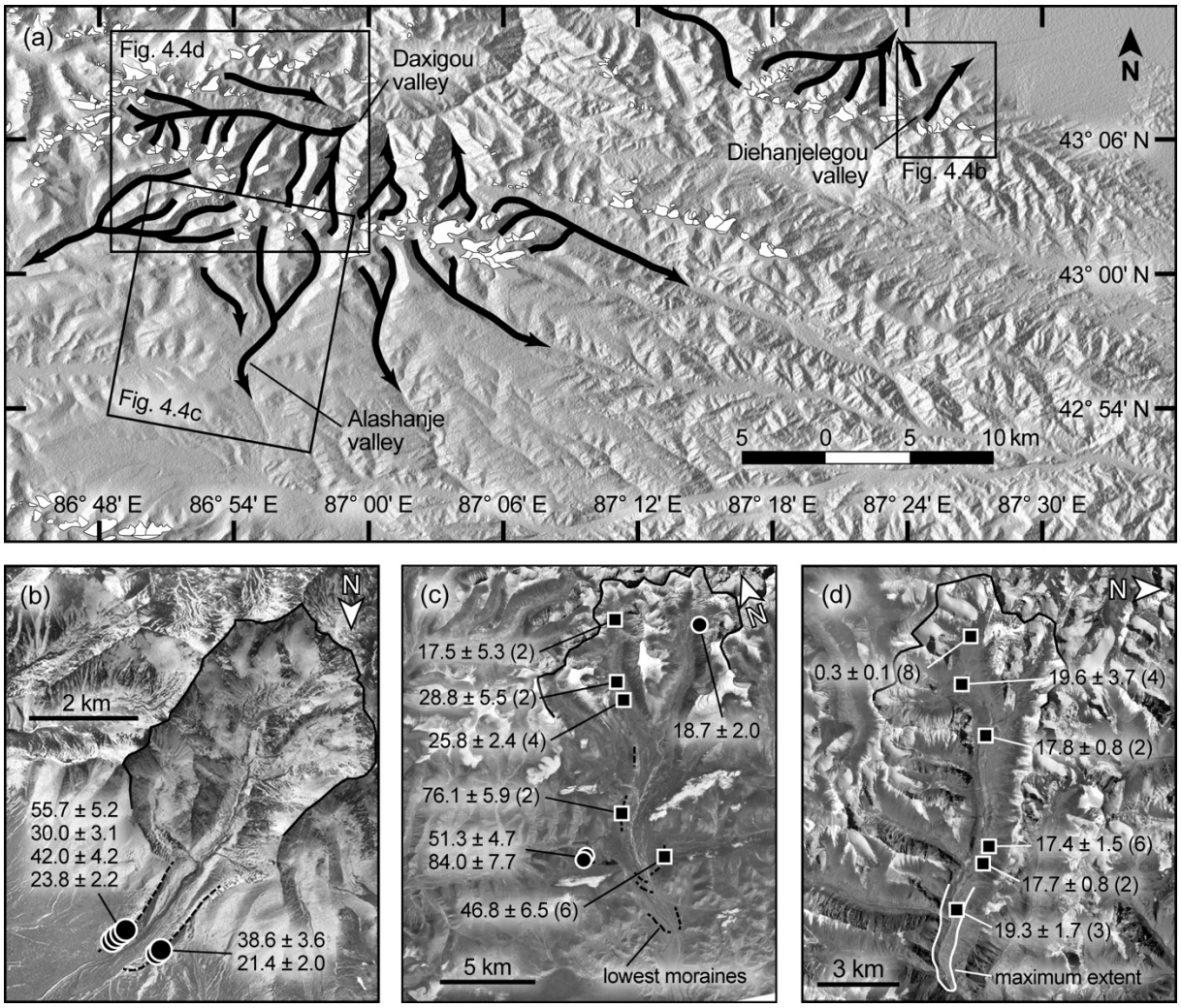

Figure 4.4. Study sites in East Tian Shan (a) showing the major directions of paleo outlet glaciers (black arrows) and the extent of modern glaciers (white polygons). The background shaded relief image was from ASTER GDEM V2 (NASA and METI, 2017); (b) Diehanjelegou valley (background Google Earth image); (c) Alashanje valley (ASTER image, NASA 2017); (d) Daxigou valley (ASTER image, NASA 2017). The circles indicate individual ^{10}Be and ^{26}Al samples. The squares represent mean ^{10}Be ages after rejecting outliers, in ka ± 1σ total uncertainty (number of samples in parentheses), calculated using data reported in this study, Kong et al. (2009), Li et al. (2011), and Li et al. (2014). The dashed lines are moraine crests. The thin black lines delineate the arêtes. See text for details of which individual samples were included in the calculations of the mean ^{10}Be ages. The extent of modern glaciers was from RGI 6.0 (2017).

4.4.5 *West Tian Shan, Muzart.*

The western section of the Tian Shan range extends ~1200 km from the west in Kyrgyzstan to the east in China (Figure 4.1). The large alluvial fan emanating from Muzart valley is overlain by a series of at least 14 end moraines. We sampled two boulders from the outermost moraine, which gave a mean ^{10}Be age of 21.7 ± 5.5 ka (THAR ELA 4490 m asl) (Figure 4.5). Upvalley ~4.5 km the lowest moraine we sampled two more boulders with a mean ^{10}Be age of 16 ± 1.4 ka (THAR ELA ~4520 m asl). The paleoglaciers that deposited the dated piedmont moraines were sourced from today's heavily glaciated cirques with various orientations. Because of this complexity, the absolute THAR ELA values for the two piedmont moraines may not be readily comparable to the THAR ELAs estimated for smaller glaciers with simple geometry. However, the ΔELA_{norm} values within Muzart valley may provide a better comparison of relative glacial extents and their timing in comparison to other glaciers in Central Asia. The modern glaciers were estimated to have THAR ELAs of ~4820 m asl (summer T_{air} of 0.1 ± 0.7 °C; annual *ppt* ~150 mm), which was ~80% of the local LGM ΔELA_{norm}.

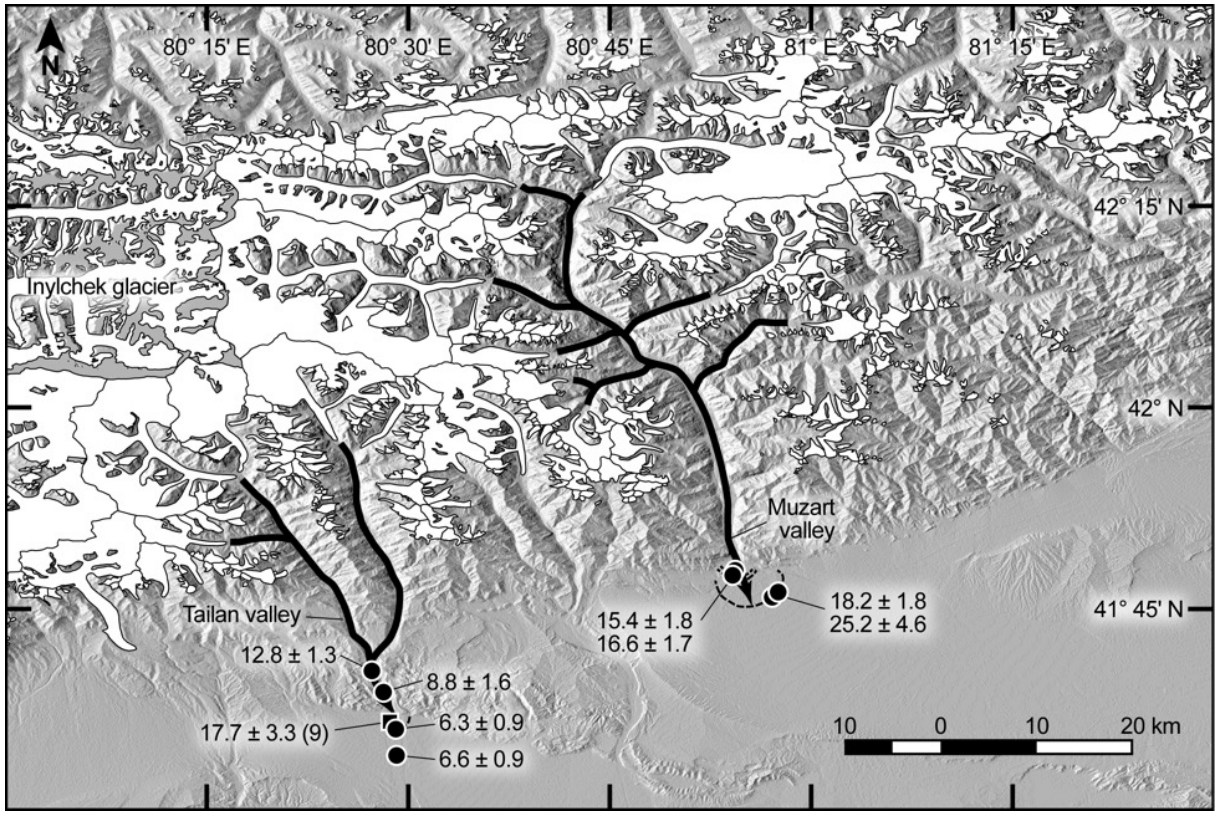

Figure 4.5. Muzart and Tailan sites in West Tian Shan. The white polygons indicate the extent of modern glaciers (RGI 6.0, 2017). The black arrows indicate direction of outlet glaciers from the ice field. The dashed lines indicate moraines crests. Circles indicate the individual ^{10}Be ages, in ka ± 1σ external uncertainty, reported in this study. The square is a mean ^{10}Be age, ka ± 1σ total uncertainty (number of samples in the mean), calculated using data from Hubert-Ferrari et al. (2005). The background shaded relief was constructed using SRTM DEM (U.S. Geological Survey, 2017).

4.4.6 *West Tian Shan, Tailan*

Approximately 40 km to the west of Muzart piedmont, a large alluvial fan emanates from the mouth of Tailan valley (Figure 4.5). A younger fan can be clearly distinguished from the older ones using satellite images. We collected a boulder from the youngest fan, which gave a ^{10}Be age of 6.6 ± 0.9 ka. Close to the mouth of the valley, there are at least seven sets of moraines. Hubert-Ferrari et al. (2005) collected ten glacial boulders that gave a mean ^{10}Be age of 17.7 ± 3.3 ka (after

one outlier was removed), from a moraine that corresponded to THAR ELA of 3970 m asl. Although the dated moraine was not from the lowest paleoglacier, and because the topographic gradient is low (~25 m km^{-1}) there is little difference (~35 m) between the estimated ELAs of the dated and the lowest moraines. The modern ELA was estimated to be ~4560 m asl (~60% of the local LGM ΔELA_{norm}) with summer T_{air} of 5.3 ± 0.7 °C; annual *ppt* ~150 mm.

The difference between the estimated summer T_{air} at the modern ELAs for Muzart and Tailan is ~5 °C, but the difference between their modern ELAs is ~250 m. Accounting for the same lapse rate estimated for these sites the 250 m ELA difference would correspond to a T_{air} difference of only ~2 °C. There are two reasons for this discrepancy: a) the threshold *THAR* value for the modern glacier in the Muzart valley was set slightly high; and/or b) the altitude of the grid cell in the T_{air} data (Fan and van den Dool, 2008) for Tailan was set ~750 m higher than for Muzart. Nevertheless, the 250 m ELA difference for these neighboring glaciers is reasonable within the accuracy of the THAR method despite the complications due to different cirque orientations and the heavy cover of debris.

The Inylchek glacier (Figure 4.5) flows to the west and its cirques share the ~7400–6800 m asl high peaks with the neighboring Muzart and Tailan cirques. Lifton et al. (2014) found remnants of ~150 ka moraines (n=2 ^{10}Be; THAR ELA ~4200 m asl) underlying the ~16 ka moraine (n=2 ^{10}Be; THAR ELA ~4220 m asl). The ELA estimates and the ^{10}Be ages from Muzart, Tailan, and Inylchek suggest that the local LGM in this part of West Tian Shan did not occur during MIS 2, but the global LGM glaciers of MIS 2 were as large as those of the older advances.

4.4.7 *West Tian Shan, Barskoon and Suek*

200 km west of Inylchek glacier the altitude drops rapidly by ~2000 m where north-facing modern glaciers around Barskoon and Suek valleys (Figure 4.6) sit limited to their cirques. We sampled three boulders in the middle of the large moraine complex incised by Suek river, which gave a mean ^{10}Be age of 20.8 ± 1.5 ka. Blomdin et al. (2016) sampled boulders from the outermost margins of the moraine complex that gave a mean ^{10}Be ages of 25.7 ± 7.5 (n=2) and 89.5 ± 7.9 ka (n=5; one outlier rejection). The THAR ELAs for the Suek moraine complex range from 3880 to 3810 m asl. The local LGM during MIS 5 inferred from the Suek moraine complex and similar extent of glaciers during MIS 2 are consistent with the spatial and temporal pattern of glacial extents in the other sites in the West Tian Shan (Figure 4.6).

The paleoglaciers that deposited the Suek moraines were sourced from two separate ice fields, one over Terskey Ala Tau range in the north and the other over Ak-Shyrak range in the south (Figure 4.6). Near Barskoon pass, in Terskey Ala Tau, we sampled four boulders from the left-lateral moraine of a paleoglacier that once contributed to the Suek paleoglaciers. These gave a mean ^{10}Be age of 16.6 ± 1.7 ka (one outlier). From this moraine we estimated a THAR ELA of ~4030 m asl, which was ~40% of the ΔELA_{norm} for local and global LGM ELAs estimated from the Suek moraines themselves. ~3 km upvalley we sampled three boulders from an end moraine located ~500 m from the modern glacier, to obtain a mean ^{10}Be age of ~0.4 ± 0.1 ka. The THAR ELA for this Holocene moraine, 4020 m asl, was only ~30 m lower than the modern THAR ELA (summer T_{air} = 2.4 ± 1.3 °C; annual *ppt* ~250 mm).

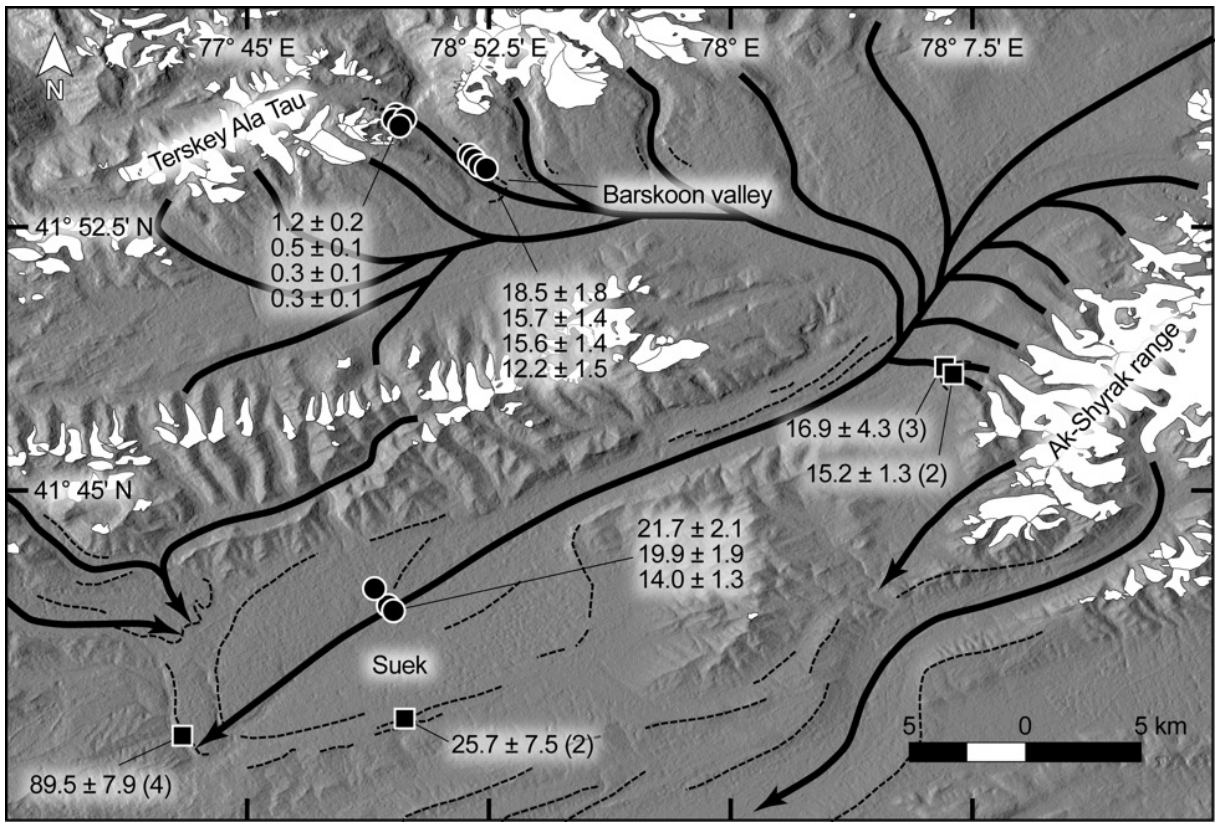

Figure 4.6. Barskoon and Suek study sites in West Tian Shan. The black arrows indicate the flow directions of paleo outlet glaciers sourced from ice fields in Terskey Ala Tau and Ak-Shyrak ranges. The dashed lines indicate moraine crests. The circles indicate the individual ^{10}Be ages, ka ± 1σ external uncertainty, reported in this study. The squares indicate mean ^{10}Be ages, ka ± 1σ total uncertainty (number of samples in the mean), calculated using data from Blomdin et al. (2016). The extent of modern glaciers (white polygons) is from RGI 6.0 (2017). The background shaded relief was constructed using ASTER GDEM V2 (NASA and METI, 2017).

Blomdin et al. (2016) collected boulders from two end moraines sitting close to a modern glacier in Ak-Shyrak range (Figure 4.6), one of the southern sources for the Suek paleoglaciers. The moraines were dated to 16.9 ± 4.3 ka (n=4, one outlier) and 15.2 ± 1.3 ka (n=3, one outlier) corresponding to similar THAR ELAs of ~4100 m asl (~50 lower than the local modern ELA). The timing and the spatial extents of these late global LGM moraines are consistent and suggest that the Suek paleoglaciers receded rather rapidly; within ~9 ka the glaciers retreated from their near-maxima (ELA increase of ~200–150 m, or length reduction of ~60–40 km) to very close proximity of the modern glaciers.

4.4.8 *West Tian Shan, Gulbel*

Terskey Ala Tau range, ~40 km NW of the Barskoon pass, we sampled a set of lateral and end moraines in Korumdy river valley, near Gulbel pass (Figure 4.7). There, paleoglaciers were sourced from four now-separated cirques, and during MIS 3 the paleoglaciers flowed both westward and also eastward over Gulbel pass (Koppes et al., 2008). More recently, the paleoglacier flowed only westward and did not overtop Gulbel pass. We sampled three boulders from the right-lateral moraines west of the Gulbel pass, obtaining mean a mean ^{10}Be age of 21.9 ± 0.7 ka (after one outlier was removed) with a corresponding THAR ELA of ~3890 m asl. Near this sampling site one boulder from the outermost moraine crest was dated to ~97 ka (Koppes et al., 2008). ~9 km upvalley, another right-lateral moraine was ^{10}Be-dated to 17.3 ± 1.1 ka (n=3; THAR ELA ~3790 m asl). ~30 m below the lateral moraine we found a remnant of an end moraine, which was ^{10}Be-dated to 16.8 ± 1.0 ka (n=3; THAR ELA ~3870 m asl). The modern ELA was estimated to be ~4000 m asl (summer T_{air} = −2.2 ± 1.2 °C; annual *ppt* ~320 mm), corresponding to ~40% ΔELA_{norm}.

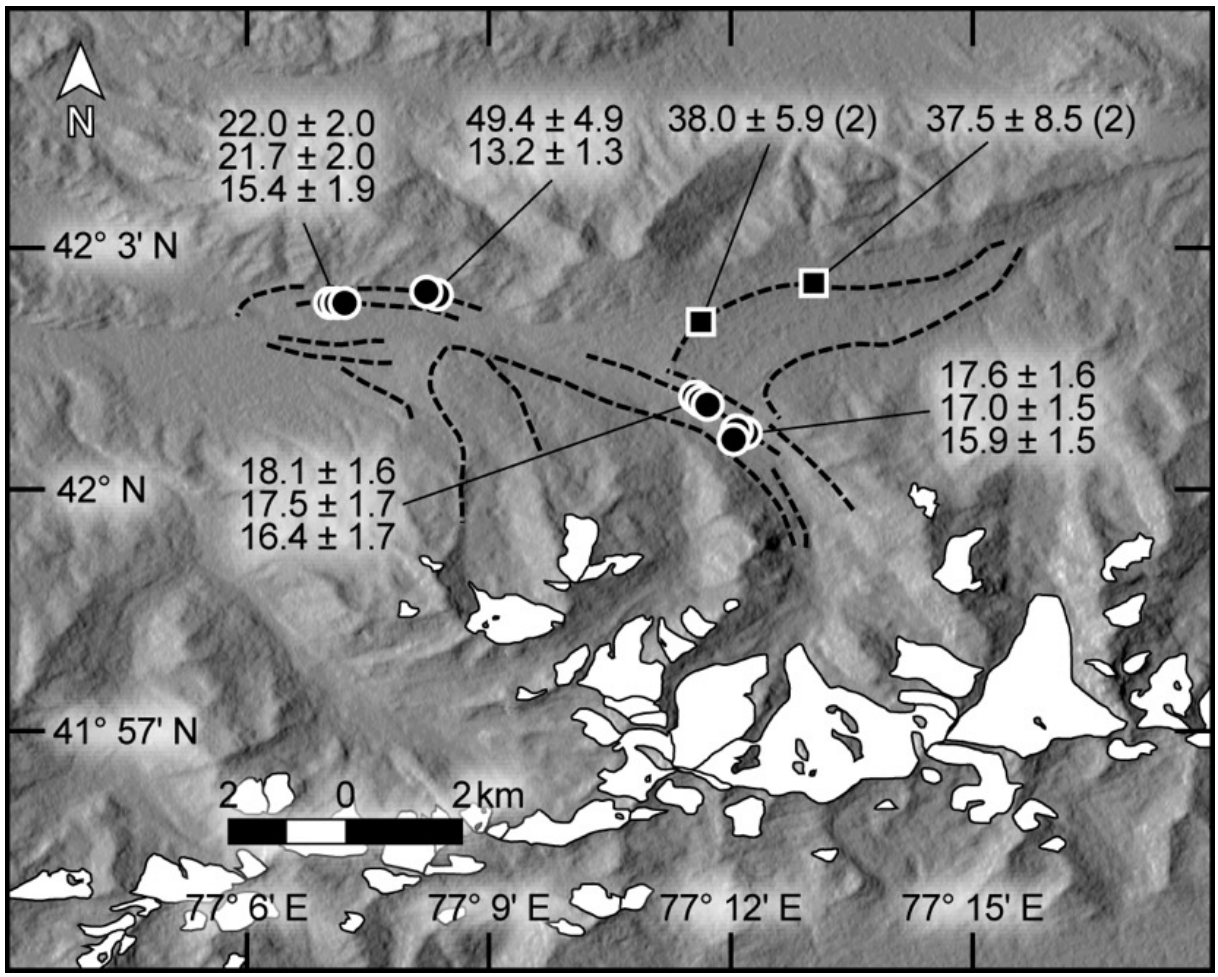

Figure 4.7. Gulbel study site in West Tian Shan. The dashed lines indicate moraine crests. The circles indicate the individual ^{10}Be ages, ka ± 1σ external uncertainty, reported in this study. The squares indicate mean ^{10}Be ages, ka ± 1σ total uncertainty (number of samples in the mean), calculated using data from Koppes et al. (2016). The extent of modern glaciers (white polygons) is from RGI 6.0 (2017). The background shaded relief was constructed using ASTER GDEM V2 (NASA and METI, 2017).

4.4.9 *West Tian Shan, Choktal*

The Zalisky Ala Tau range, at the border between Kyrgyzstan and Kazakstan, marks the northernmost extent of West Tian Shan (Figure 4.8). We sampled from the moraines in Choktal valley that were deposited by paleoglaciers sourced from six now-separated cirques facing south. The lowest moraines in the valley were not dated (THAR ELA ~3680 m asl). ~7 km upvalley, three samples from the left-lateral moraine gave a mean ^{10}Be age of 22.2 ± 1.4 ka (THAR ELA ~3720 m asl, ~90% ΔELA_{norm}). Near one of the modern glaciers there were two end moraines in close proximity, which we ^{10}Be-dated to 15.4 ± 0.6 (n=3; THAR ELA ~4090 m asl) and 0.3 ± 0.1 ka (n=3; THAR ELA ~4110 m asl). The modern ELA was estimated to be ~4180 m asl (summer T_{air} = 7.6 ± 1.0 °C; annual *ppt* ~420 mm). The timing and the rapid recession at the end of the global LGM, and the close proximity of late Holocene moraines to the modern glacier in Choktal appear to be similar to temporal and spatial pattern of glaciation observed in Suek and Barskoon sites.

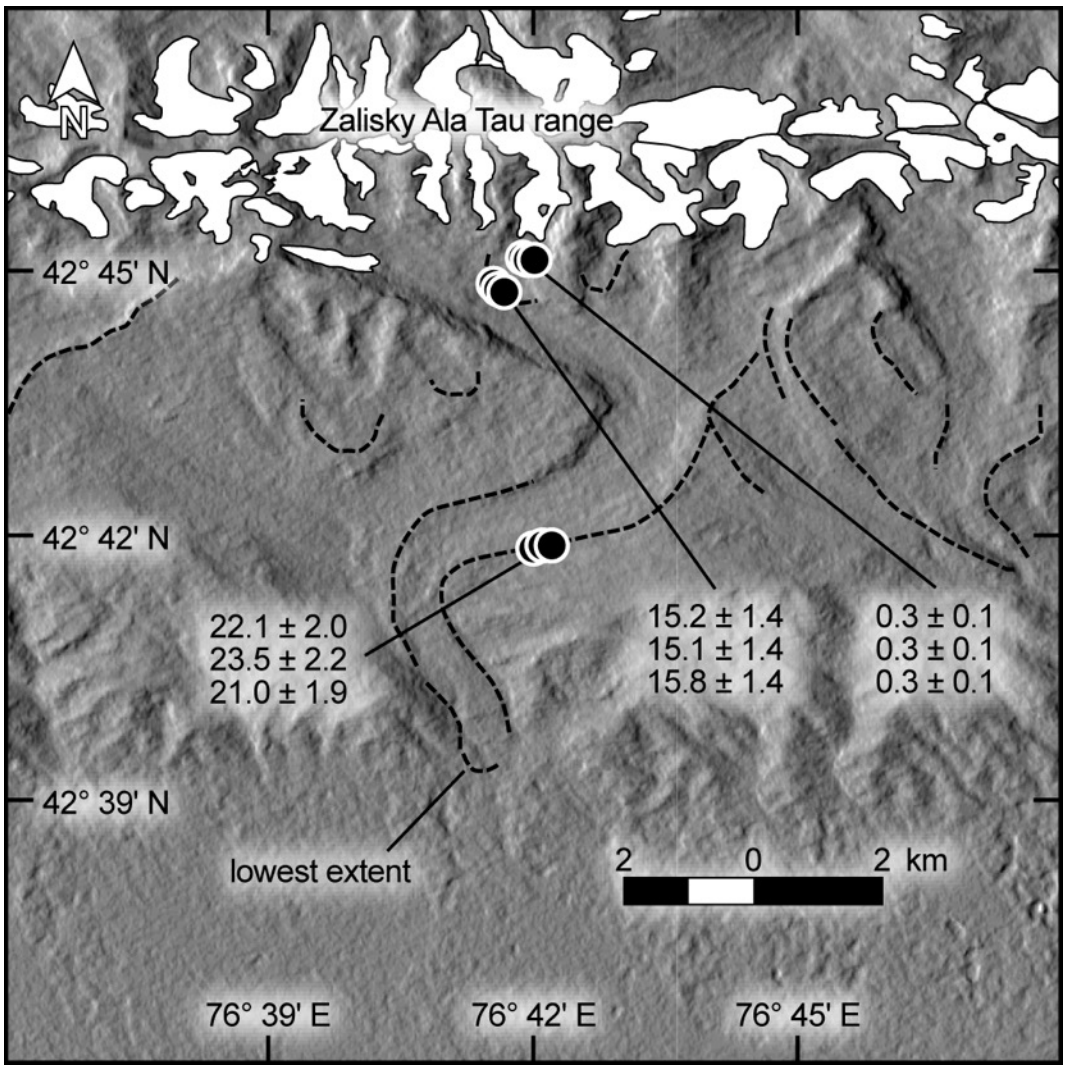

Figure 4.8. Choktal study site in West Tian Shan. The dashed lines indicate moraine crests. The circles indicate the individual ^{10}Be ages, ka ± 1σ external uncertainty, reported in this study. The extent of modern glaciers (white polygons) is from RGI 6.0 (2017). The background shaded relief was constructed using ASTER GDEM V2 (NASA and METI, 2017).

4.4.10 *Qilian Shan, Altyn Tagh*

The glaciated part of the approximately W-E oriented Altyn Tagh range at the northern end of the Qaidam basin consists of two parallel mountain ridges south of the city of Dunhuang. These are ~30 km long and join the ranges of the Qilian Shan in the east. This was the most arid site among the regions considered in this study with ~65 mm annual *ppt*. The southern ridge contained granitoid bedrock that would be appropriate for exposure dating. However, we were allowed to sample only from the northern part of the range where the local schist and serpentinite rocks were too poor in quartz for ^{10}Be analysis.

The modern glacier in our studied valley is located in the north-facing cirque below the highest (5500 m asl) peak of the northern ridge (Figure 4.9). We sampled a right-lateral moraine in close proximity to the modern glacier, but no sample yielded enough quartz to analyze for ^{10}Be. We sampled five schist boulders from an end moraine, only ~40 m below and ~150 away from the modern glacier tongue, of which only one had enough quartz (from stringers) to date, and this yielded a ^{10}Be age of 1.4 ± 0.2 ka (Figure 4.9b). The THAR ELA estimated from this moraine was ~5060 m asl. Approximately 350 m downvalley from the sampled moraine, the flat cirque floor transitions into a ~60 m narrow valley with steep walls. The lowest altitude of the cirque floor may place a limit on the maximum extent of the paleoglacier there. The bottom of this cirque floor yielded THAR ELA of ~5030 m asl. The modern THAR ELA was ~5080 m asl. There was no other evidence of glaciation below the sampled moraine. We visited an adjacent north-facing valley to the west and observed a similar pattern: the end moraine was very close to the modern glacier and we observed no evidence of a larger advance below the cirque. Summer T_{air} at the modern ELA was estimated to be 6.8 ± 1.4 °C at this site.

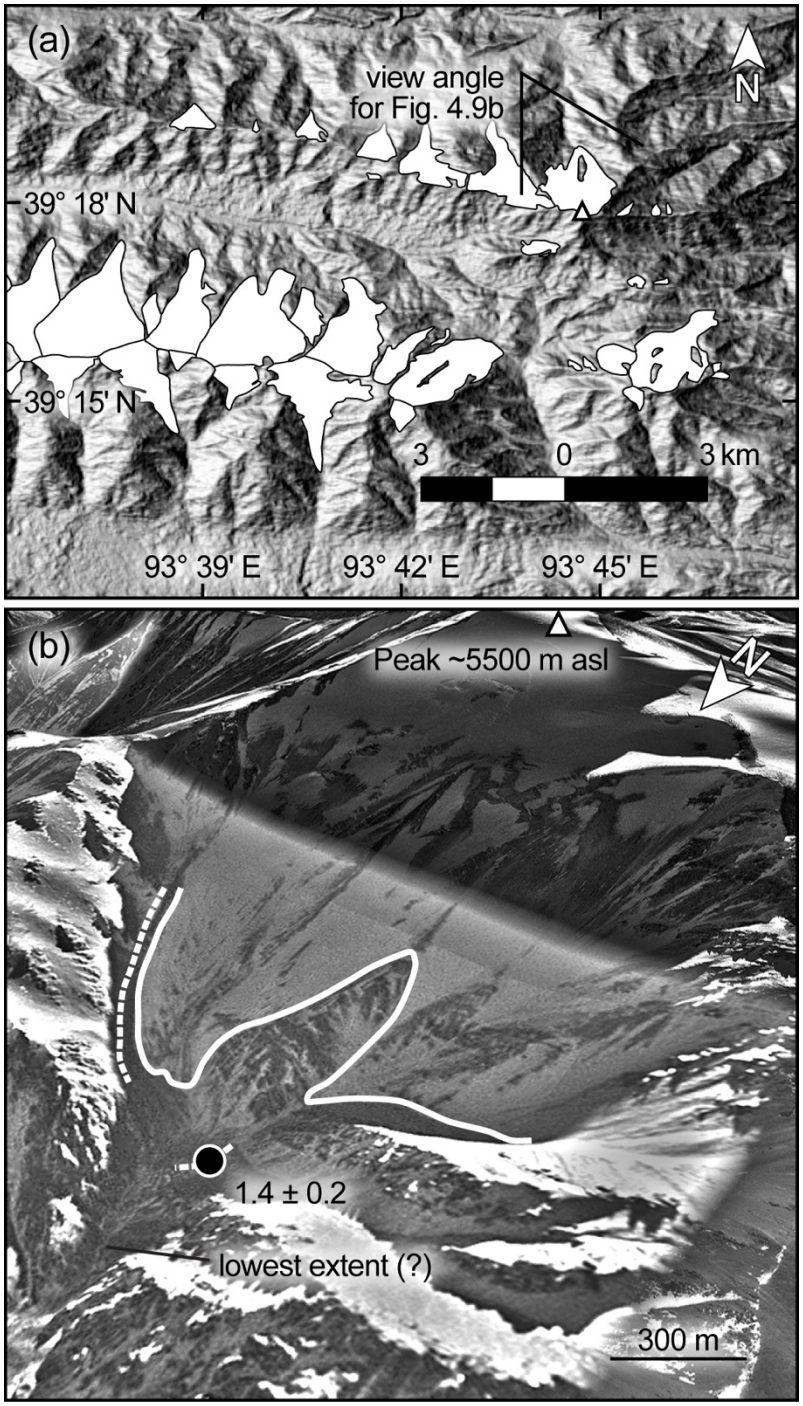

Figure 4.9. Altyn Tagh study site in Qilian Shan, showing (a) modern glaciers (white polygons: RGI 6.0, 2017) around the study site (background shaded relief was constructed using ASTER GDEM V2, NASA and METI, 2017); and (b) Perspective view (Google Earth, DigitalGlobe) of the moraines (dashed lines) and the modern glacier tongue (white line) at the sampling site. The circle indicates the ^{10}Be age, ka ± 1σ external uncertainty, reported in this study.

4.4.11 *Qilian Shan, Dumda[3] (Dunde ice cap, 5325 m asl)*

270 km to the southeast of the Altyn Tagh range, the Dunde ice cap crests an approximately W-E oriented range (Figure 4.10). Thompson et al. (1989) extracted three ice cores from the Dunde ice cap and inferred from $\delta^{18}O$ concentrations that the regional T_{air} was lowest during the global LGM. The modern Dunde ice cap covers only one third of the high plateau on the eastern end of the range, and the paleoglaciers sourced from the ice cap flowed to the north, south, and east forming well-developed wide valleys. We sampled from the heavily-eroded end moraine marking the local LGM extent in the Dumda river valley. Three boulders gave a mean ^{10}Be age of 131.5 ± 9.3 ka after rejecting one outlier identified by the "normalized deviation" method. However, Chauvenet's (1969) and Peirce's (Ross, 2003) criteria did not identify any outliers; without rejecting the outlier the three ^{10}Be boulder ages would give a mean of 140.5 ± 16.8 ka. This local LGM extent corresponds to THAR ELA of ~4760 m asl. ~12 km upvalley from the dated moraine another end moraine can be identified from Google Earth imagery, and this moraine corresponds to a THAR ELA of ~4880 m asl. The modern ELA was estimated to be ~5060 m asl (summer T_{air} = 2.4 ± 1.5 °C; annual *ppt* ~120 mm), corresponding to ~40% ΔELA_{norm}.

[3] The local ethnic Mongol herders called the range "Mösön Uul", which translates from Mongolian to "Icy mountain". The studied river valley is locally called "Dumda" (meaning "middle," spelling per old Mongolian script). Thompson et al. (1989) spelled the ice cap on the range "Dunde," a convention we adopt here.

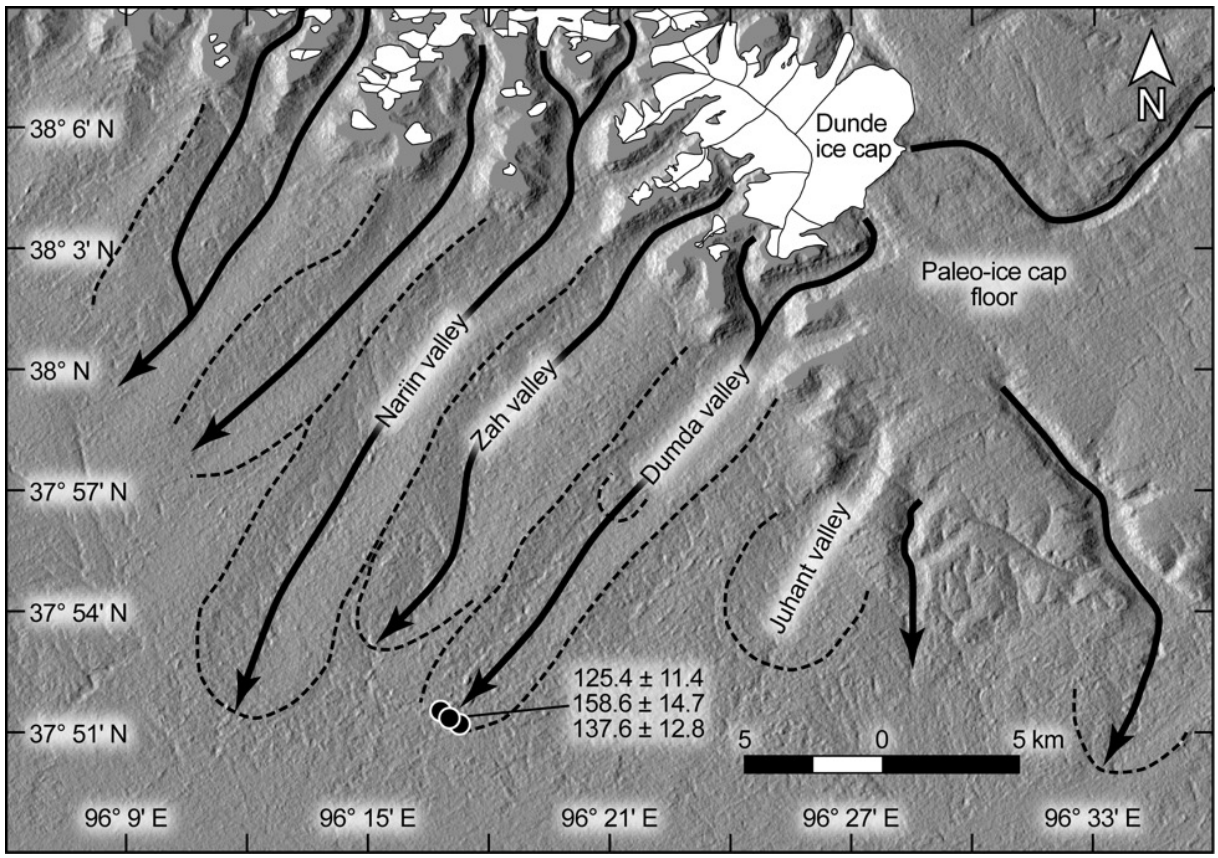

Figure 4.10. Dumda study site near the Dunde ice cap in Qilian Shan. The dashed lines indicate moraine crests. The black arrows indicate the maximum extent of the paleo outlet glaciers sourced from the Dunde ice field. The circles indicate individual ^{10}Be ages, ka ± 1σ external uncertainty, reported in this study. The extent of modern glaciers (white polygons) is from RGI 6.0 (2017). The background shaded relief was constructed using ASTER GDEM V2 (NASA and METI, 2017).

4.4.12 *Qilian Shan, Gangshiqia*

Located 120 km northeast of the Qinghai lake, the Lenglong Ling range marks the eastern end of Qilian Shan. The valley we studied, with a SW-facing cirque below the Gangshiqia peak (Figure 4.11), has a relatively simple and straight geometry and is oriented in the SW-NE direction. The coarse-scale hummocky terrain provides evidence for stagnant ice that was left from the largest paleoglaciers in the valley. Owen et al. (2003) ^{10}Be-dated five boulders from two locations in the hummocky terrain to 13.8 ± 3.4 (n=2) and 13.1 ± 1.3 ka (n=3). We collected a boulder ~10 m above Owen et al.'s (2003) location and ^{10}Be-dated it to 18.0 ± 2.0 ka. Close to the mouth of the valley, there are two right-lateral moraines at altitudes of ~3610 and ~3550 m asl. There, we sampled two boulders from each moraine to obtain mean ^{10}Be ages of 18.2 ± 1.0 (MELM ELA ~3710 m asl) and 14.0 ± 1.5 ka (MELM ELA ~3680 m asl), located in stratigraphic order. ~7 km upvalley from the piedmont the right-lateral moraine was ^{10}Be-dated to 11.7 ± 4.1 ka (n=6, one outlier), corresponding to MELM ELA of ~4320 m asl. The THAR ELA for the modern glacier was ~4770 m asl (summer $T_{air} = -1.9 \pm 1.1$ °C; annual *ppt* ~210 mm) at ~20% ΔELA_{norm}.

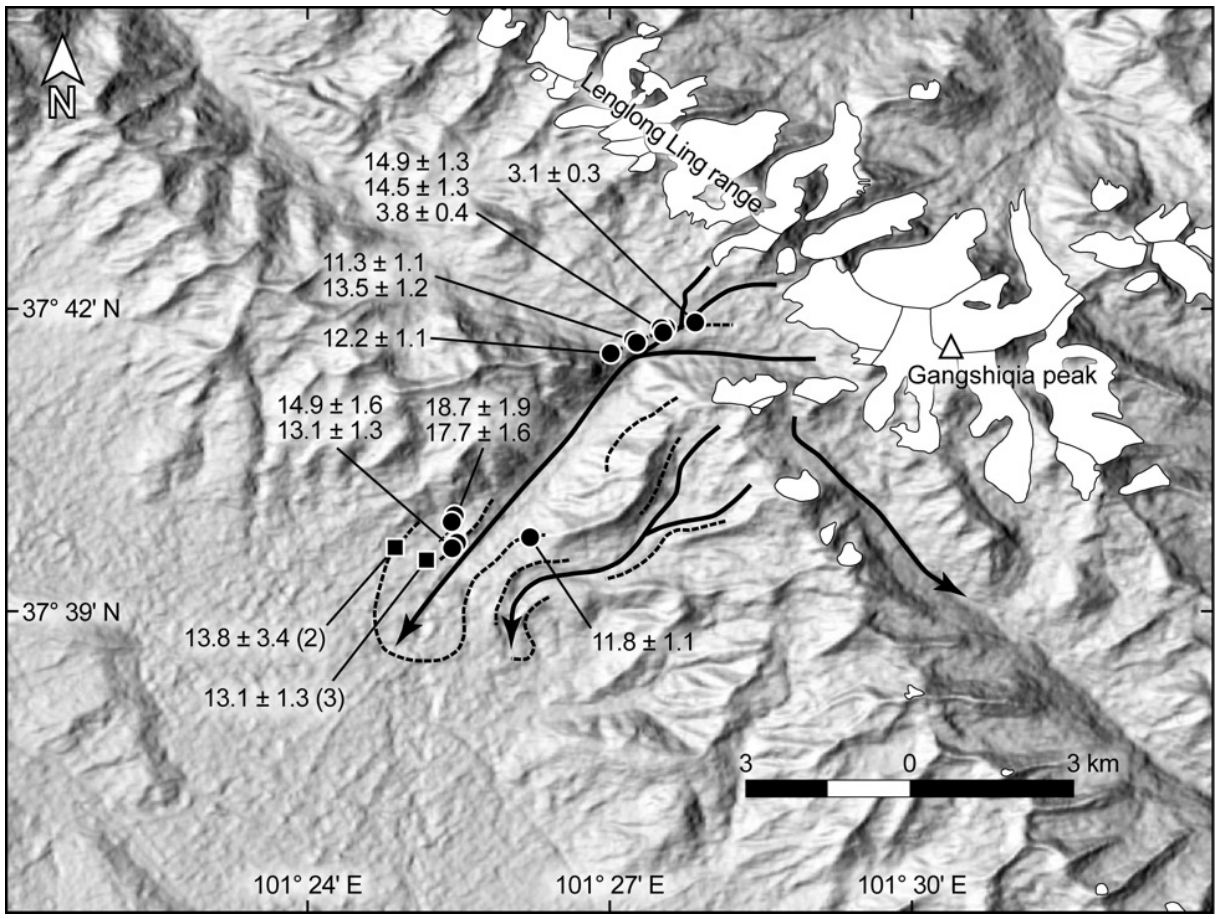

Figure 4.11. Gangshiqia study site in Qilian Shan. The dashed lines indicate moraine crests. The black arrows indicate the flow direction of the paleoglaciers. The circles indicate individual ^{10}Be ages, ka ± 1σ external uncertainty, reported in this study. The squares indicate mean ^{10}Be ages, ka ± 1σ total uncertainty (number of samples in the mean), calculated using data from Owen et al. (2003). The extent of modern glaciers (white polygons) is from RGI 6.0 (2017). The background shaded relief was constructed using ASTER GDEM V2 (NASA and METI, 2017).

4.4.13 *West Kunlun, Aksaiqin*

Located at the southwestern end of the Taklamakan desert, the western Kunlun range stretches ~680 km in NW-SE direction and hosts large ice fields and their outlet glaciers today (Figure 4.12). According to J. Heyman's "expage" compilation of exposure ages in the literature, none of the moraines in the West Kunlun has been dated. The Aksaiqin site was located at the piedmont of Quanshui glacier (N 35.457° and E 80.389°), an outlet glacier cresting at ~6350 m asl. Yasuda (2015) examined the terminus of the outlet glaciers around the study site using a series of Landsat satellite images to show that Quanshui glacier did not advance or retreat during 1972–2013, from which he classified the glacier as a non-surging, climatically controlled "normal" glacier.

The subdued half-circular ridge ~6 km SW from the modern glacier tongue may mark the local LGM extent of Quanshui glacier (THAR ELA ~5900 m asl). Two boulders from a distinct end moraine located ~3 km upvalley from the lowest moraine (?) gave a mean ^{10}Be age of 31.1 ± 12.3 ka. The lowest moraine corresponds to a THAR ELA of 5966 m asl. The glacial lake below the glacier terminus is impounded behind two sets of lateral-end moraines. A single boulder from the outermost end moraine was ^{10}Be-dated to 184.5 ± 17.5 ka. Two boulders collected from the inner lateral-end moraine gave ^{10}Be ages of 15.5 ± 1.4 ka and 42.8 ± 3.8 ka. The large discrepancy between these two ages does not permit us to confidently constrain the age of the innermost moraine, but the ^{10}Be ages suggest that this moraine was formed before the Holocene. The THAR ELA was estimated to be ~5974 m asl for the innermost moraine, which is an indistinguishable value from the ELA for the late Pleistocene moraine. The THAR ELA for the modern glacier was ~6000 m asl (summer T_{air} = −0.5 ± 1.1 °C; annual *ppt* ~120 mm) representing ~80% of the local LGM ELA depression.

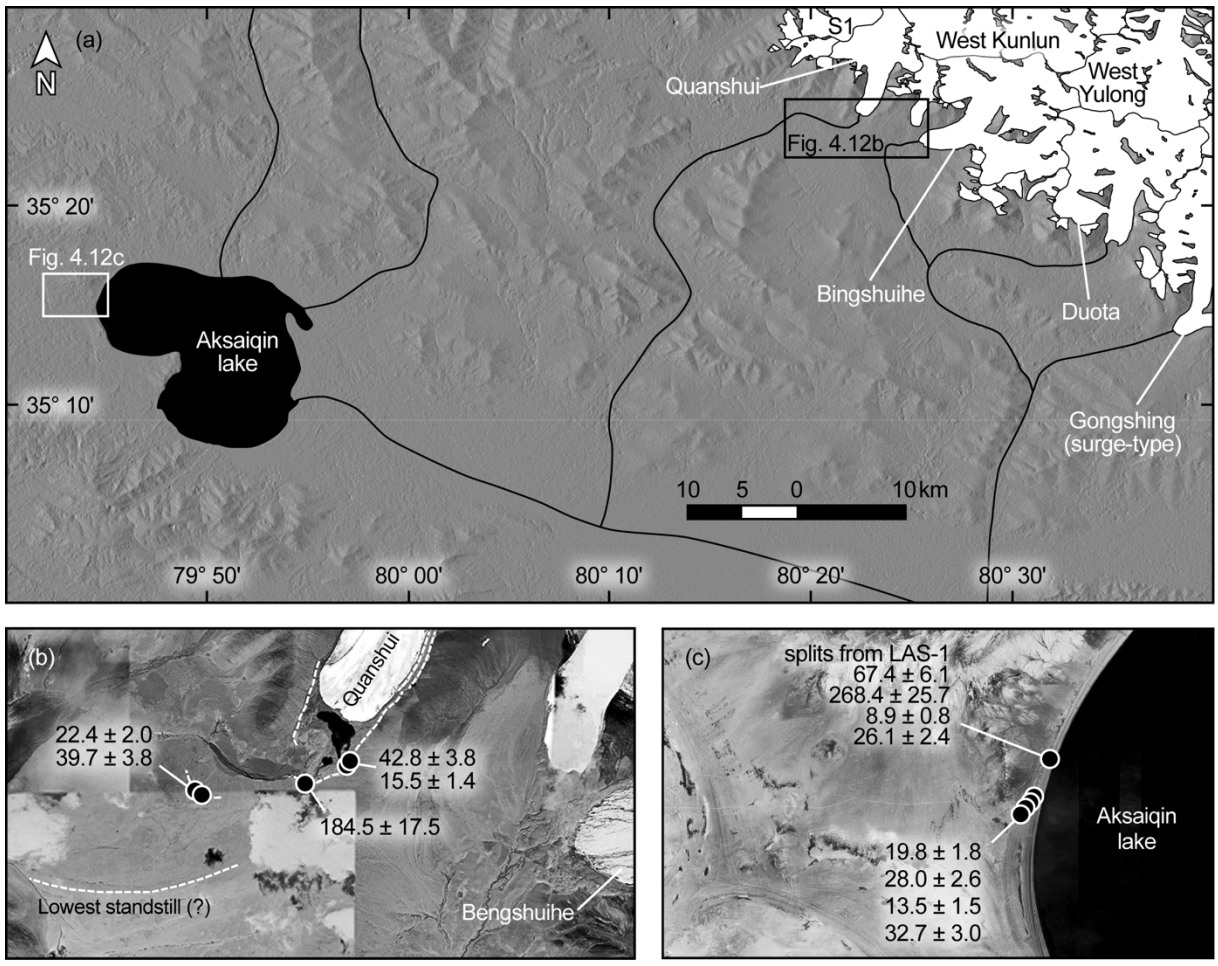

Figure 4.12. Study sites near Askaiqin lake and Quanshui glacier in West Kunlun showing (a) extent of modern glaciers (white polygons; RGI 6.0, 2017); (b) the moraine crests (dashed lines) and the ^{10}Be ages (circles), ka ± 1σ external uncertainty, reported in this study; (c) western end of the Aksaiqin lake and the ^{10}Be ages (circles), ka ± 1σ external uncertainty, reported in this study. The glacier names and the types are from Yasuda (2015). The background shaded relief in (a) was constructed using ASTER GDEM V2 (NASA and METI, 2017). The background in (b) and (c) are Google Earth, DigitalGlobe images.

4.4.14 *West Kunlun, Aksaiqin lake*

Meltwater from the glaciers identified as RGI60-13.53621 and RGI60-13.38107 in the Randolph Glacier Inventory drains to Aksaiqin lake. The lake surface currently stands at 4850 m asl. We collected three boulders from the paleo-shorelines at 9, 13, and 25 m above the current lake-level and ^{10}Be-dated them to 28.0 ± 2.6, 13.5 ± 1.5, and 32.7 ± 3.0 ka, respectively. The ^{10}Be ages suggest that the lake-level has been relatively constant since the global LGM and that the supply of meltwater from the glaciers may not have changed significantly as well. However, the large discrepancy among the ^{10}Be ages shows that more dating will be required to define a shoreline chronology. We analyzed four splits of one sample of shoreline pebbles, LAS-1, to see how the variability on the cm scale compared to the difference among terraces (Table 4.2). The comparison suggests that pebble-to-pebble age differences are as great as the age differences among the amalgamated pebble samples from the adjacent shorelines. The large discrepancy between the ^{10}Be and ^{26}Al ages for these pebbles indicate a complicated partial burying since their deposition.

4.4.15 *West Kunlun, Karakax*

At the end of the NW end of the West Kunlun, a ~60 km long range stretches in an approximately W-E direction. It is heavily glaciated today. The Karakax study site was chosen at the mouths of two glaciated tributary valleys carved by two south-flowing large outlet glaciers emanating from a large ice field (Figure 4.13). The paleoglacier in the eastern valley, termed Karakax-A, is sourced from at least seven cirque areas, and the paleoglacier in the western valley, termed Karakax-B, is sourced from at least four large cirque areas. The sediment-filled floor of Karakax-A was ~350 m below the trimlines, which indicate the minimum thickness of the largest paleoglacier in the valley. The modern glacier in Karakax-B terminates at ~5180 m asl, ~80 m lower than the terminus of the

Karakax-A glacier. The fans in the valley, fed by outwash from the glaciers, extend ~6 km from the glacier termini. The fan was offset along the left-lateral strike-slip Altyn Tagh fault.

We collected three boulders from the surface of the eastern margin of the fan and ^{10}Be-dated them to 90.2 ± 3.6 ka (mean after removing one outlier). The moraine crests deposited by the Karakax-B paleoglacier on the fans are preserved better above the Altyn Tagh fault than close to the valley floor. Two boulders from the right-lateral moraine gave a mean ^{10}Be age of 80.7 ± 8.4 ka; two boulders from the left-lateral moraine gave a similar mean ^{10}Be age of 88.7 ± 12.6 ka. These near-maximum standstills of late MIS 5 are temporally asynchronous with the MIS 3 local LGM standstills of Aksaiqin paleoglaciers. The modern glacier in Karakax-B valley, identified as RGI60-13.40092 in the Randolph Glacier Inventory, has a THAR ELA of ~5720 m asl (summer T_{air} = 0.4 ± 1.0 °C; annual *ppt* ~170 mm). The lack of cobbles and boulders on the surfaces of other nearby fans along the Altyn Tagh Fault was attributed to salt weathering in the upper 30 cm of the soil horizon (Farr and Chadwick, 1996). The existence of large gypsum and other soluble salt crystals and the lack of $CaCO_3$ in the soils away from riparian areas suggests hyperaridity in the region extending back for tens of thousands of years, as suggested by the local glacial chronology.

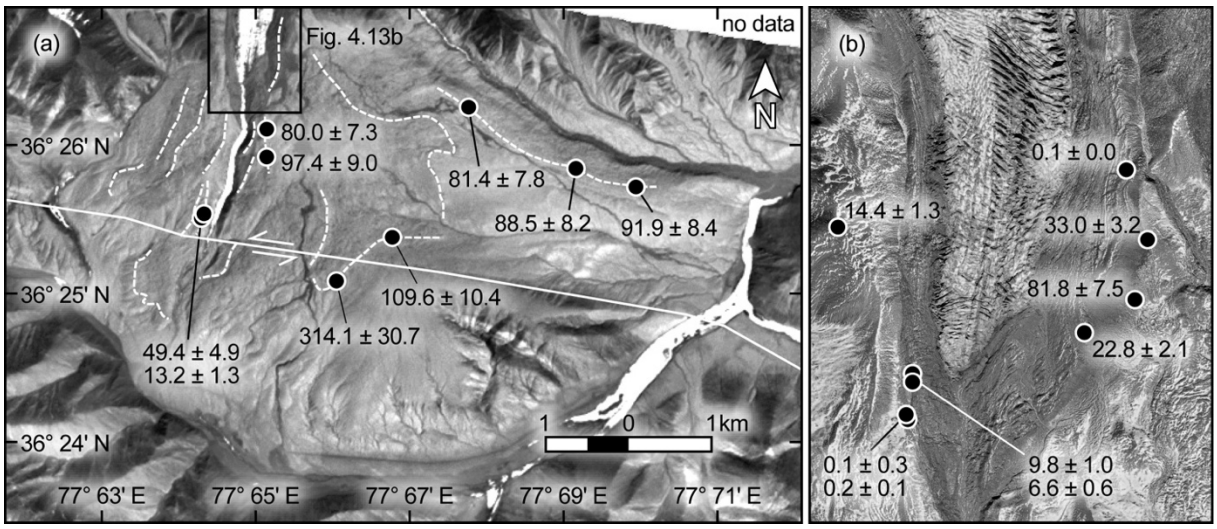

Figure 4.13. Karakax study site in West Kunlun showing (a) the modern glacier tongue, the moraine crests (dashed lines), the ^{10}Be ages (circles), ka ± 1σ external uncertainty, reported in this study, and the Altyn Tagh fault (white line with arrows indicating the slip); (b) the ^{10}Be ages (circles), ka ± 1σ external uncertainty, reported in this study. The background images are (a) ASTER image (NASA, 2017), and (b) Google Earth, DigitalGlobe.

4.4.16 *Modern and paleo-ELA gradients in Central Asia*

We estimated the ELAs (*THAR = 0.6*) for modern glaciers in Central Asia using the toe altitudes provided in the Randolph Glacier Inventory (RGI 6.0, 2017) and the headwall altitudes we measured in Google Earth (Figure 4.14). We also used the paleo-ELAs for MIS 2 paleoglaciers and the modern ELAs (Table 4.5) to map ΔELAs during MIS 2 (Figure 4.15). The results of the ELA analysis and our interpretation are reported below.

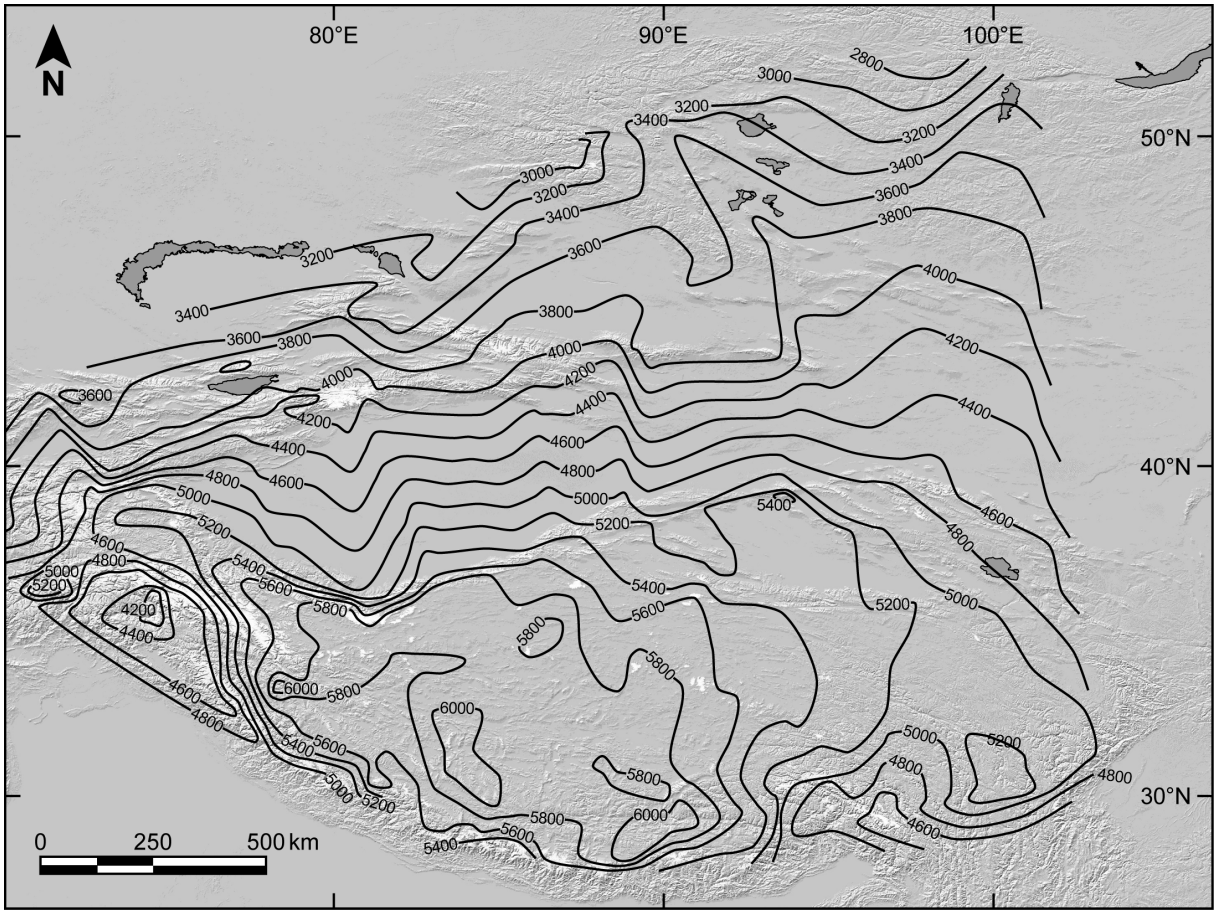

Figure 4.14. Map of modern ELA in Central Asia. The extent of modern glaciers (white polygons) and their toe altitudes were from Randolph Glacier Inventory (RGI 6.0, 2017) and the THAR ELAs were estimated by using the headwall altitudes we measured in Google Earth. The glaciers in more humid regions in the margins of the continent are located at much lower altitudes compared to the glaciers in the interior, where arid climate limits the glaciers to cold temperatures of high altitudes. The shaded relief image in the background was constructed from SRTM DEM (GTOPO030: U.S. Geological Survey, 2017).

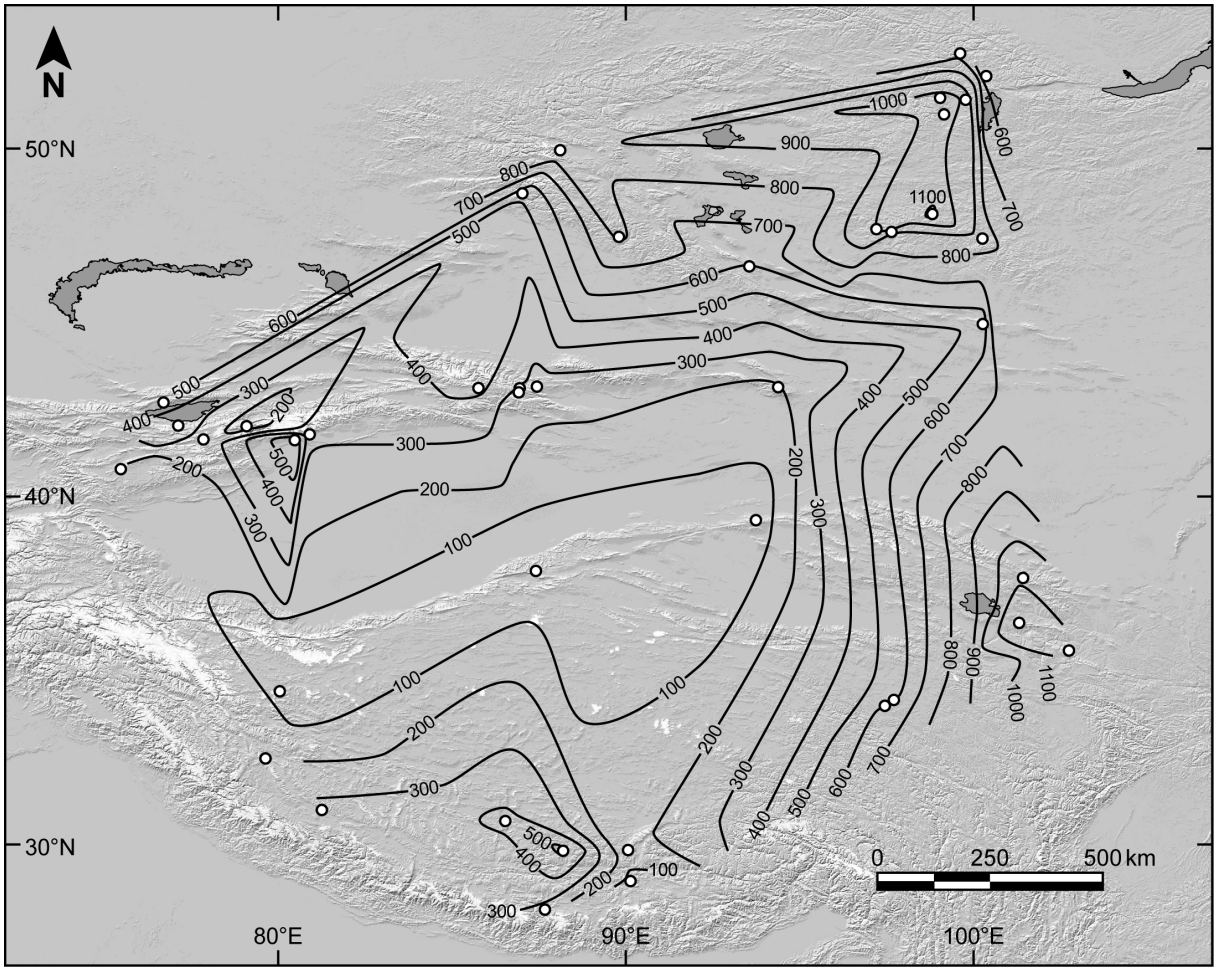

Figure 4.15. Map of MIS 2 maximum ΔELAs in Central Asia, based on the new ^{10}Be ages reported in this study and from the literature. We estimated the paleo THAR ELAs using the altitudes of the dated moraines and the headwall altitudes we measured in Google Earth. The ΔELAs were then derived using the modern ELA data shown in Figure 4.14. The white dots indicate the locations of the dated moraines. The extent of modern glaciers (white polygons) were from Randolph Glacier Inventory (RGI 6.0, 2017). The glaciers in the hyperarid interior of the continent exhibited the smallest ΔELAs. These sublimation-dominated glaciers are already located in high altitudes with much colder climates than in more humid regions, and the large depression of T_{air} during MIS 2 was ineffective in driving the growth of these glaciers. The shaded relief image in the background was constructed from SRTM DEM (GTOPO030: U.S. Geological Survey, 2017).

Perhaps the most global factor driving the variations in climate is solar insolation and its variation across the latitudinal transect. The latitudinal gradients of modern and MIS 2 paleo-ELAs (Figures 4.16a–d) show strong correlations for both the modern ELAs ($R^2 = 0.93$) and for MIS 2 paleo-ELAs ($R^2 = 0.89$). The modern ELAs in interior Central Asian increase by ~125 m per 1° increase in latitude (Figure 4.16a). During MIS 2 the latitudinal gradient the paleo-ELAs slightly increase to ~155 m ELA change per 1° change in latitude (Figure 4.16a). This shift in the latitudinal gradient of paleo-ELAs during MIS 2, however, was largely derived from large ΔELAs for high latitude (45–50° N) glaciers and relatively smaller ΔELAs observed in mid-latitudes, 35–45° N (Figure 4.16b).

The global LGM, its coldest peak defined at ~21 ka by the modeling community, is one of the best-studied periods of the last glacial cycle. Twelve general circulation models (GCMs) with various boundary conditions for global LGM showed decrease in T_{air} everywhere in Central Asia, with higher magnitudes of depression in in high latitudes (Rupper and Koppes, 2010). It is consistent with the latitudinal gradient of the paleo-ELAs (Figure 4.16a) for melt-dominated glaciers, indicating that T_{air} was indeed the controlling factor in their growth. However, many glaciers in the interior of Central Asia exhibited smaller ΔELAs during MIS 2 both in absolute value and magnitude (Figures 4.16b–c).

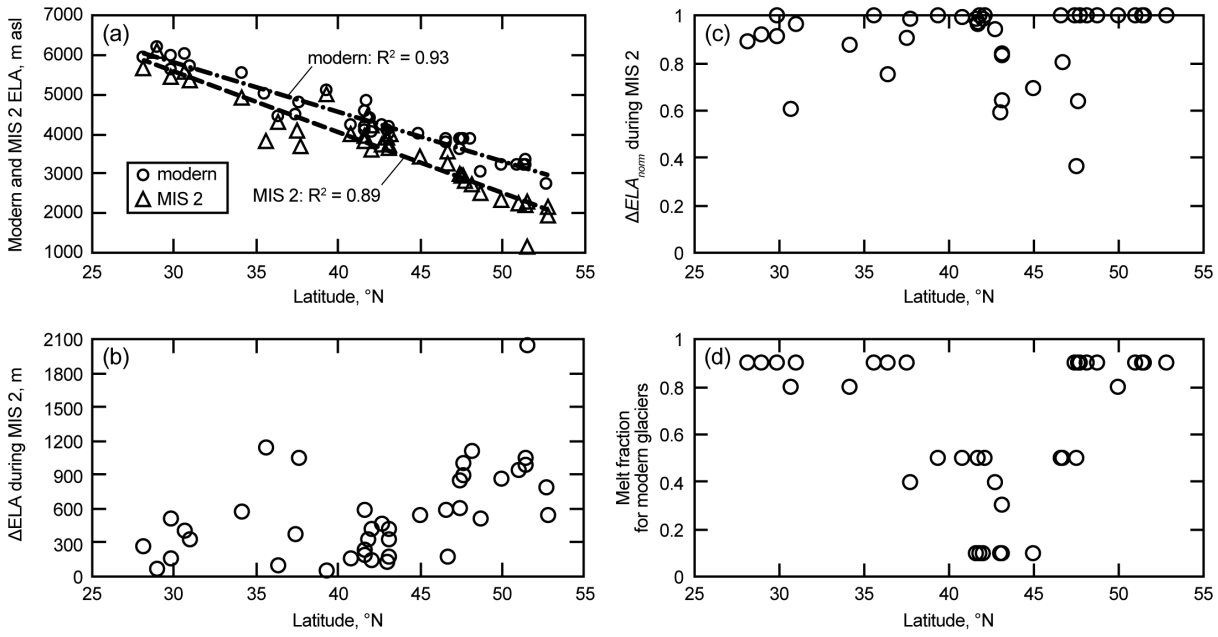

Figure 4.16. Latitudinal gradients of modern and minimum MIS 2 ELAs: a) The paleo-ELA for the lowest dated MIS 2 standstills (triangles) and their corresponding modern ELA (circles); b) ΔELA values for the dated MIS 2 standstills; c) ΔELA_{norm} for the dated MIS 2 standstills; d) Melt fraction for the modern glaciers (from Rupper and Roe, 2008). Modern and paleo-ELAs both show strong latitudinal gradient, implying that the strongest control on glacier advances is insolation. However, the absolute values of ΔELA do not exhibit a latitudinal gradient, suggesting that variable local climate and topographic conditions control the magnitudes of the glacier advances. Ablation is dominated by sublimation in the interior regions of Central Asia (35–45 °N), where many MIS 2 glaciers did not advance to their local maximum.

Annan and Hargreaves (2013) used GCMs to show that the T_{air} over all of Central Asia was uniformly depressed by 4–8 °C with an uncertainty of 2–4 °C during the global LGM. Using the regional atmospheric lapse rates of ~6.5 °C km^{-1} and assuming no changes in *ppt*, which we argue against, the observed MIS 2 ΔELAs (mean 440 ± 338 m, 1σ) would indicate a mean T_{air} depressions of ~2.9 ± 1.9 °C (1σ). However, the map of ΔELAs during MIS 2 (Figure 4.15) reveals a detailed pattern of the response of glaciers to the climate changes of MIS 2. The small ΔELAs observed in the interior of the continent are for sublimation-dominated glaciers (e.g., Figure 4.16d). If the uniform T_{air} depression of 4–8 °C was true, the small ΔELAs indicate that the sublimation-dominated glaciers were not sensitive to changes in T_{air}. In other words, the T_{air} depression of 4–8 °C during the global LGM would have resulted in ~620–1230 m ΔELAs and the T_{air} alone cannot explain the small values of observed ΔELAs.

It is difficult to reliably model changes in *ppt* using GCMs largely due to a variety of potential configurations to simulate the changes in the westerly winds and South Asian monsoon (Rupper and Koppes, 2010). In the melt-dominated regions of Central Asia, the ΔELAs were large (Figure 4.15), ranging from ~500 m in the interior up to average 1500 m in the northern regions. The modeled T_{air} depressions are expected to drive these large ΔELAs during MIS 2 even accounting for decrease in *ppt*, indicating that the glaciers are indeed good proxy for reconstructing T_{air} in melt-dominated regions. However, in the interior of Central Asia the modern glaciers are located in cold, high altitudes (Figure 4.14) and many of them were limited to their cirques during MIS 2 showing small ΔELA_{norm} (Figure 4.16c) and small ΔELAs (Figure 4.15). In these cold, arid regions a significant portion of the ablation is regulated by sublimation (Figure 4.16d). In other words, sublimation can ablate most of the additional accumulation in the prolonged cold seasons of MIS 2, and the glaciers cannot grow even under large depressions of T_{air}. These sublimation-

dominated glaciers can be useful to reconstruct paleo-*ppt* if the T_{air} was constrained from an independent proxy.

The timing of local LGM extents (ΔELA_{norm} >80%; Figure 4.17) constructed from cosmic-ray exposure dating combined with field and photo-interpreted mapping reveals an asynchronous temporal and spatial pattern of glaciations in Central Asia. Many glaciers did not extend to their local maxima during MIS 2, suggesting that they did not respond sensitively to the low insolation and cold T_{air} of the global LGM. Despite the warmer T_{air} during MIS 3–5 than in MIS 2 many glaciers advanced to their local maxima. Relatively low values of melt fractions predicted in the regions where these MIS 3–5 glaciers are located and their subsequent smaller advances during MIS 2 indicate that they may have been precipitation-controlled glaciers. In other words, increased *ppt* during MIS 3 may have provided additional accumulation and driven the glaciers to their local LGM extent, and later during MIS 2 a drier climate limited the accumulation despite the decreased T_{air}. These older glacial maxima were observed in regions with annual *ppt* ranging from ~310–110 mm.

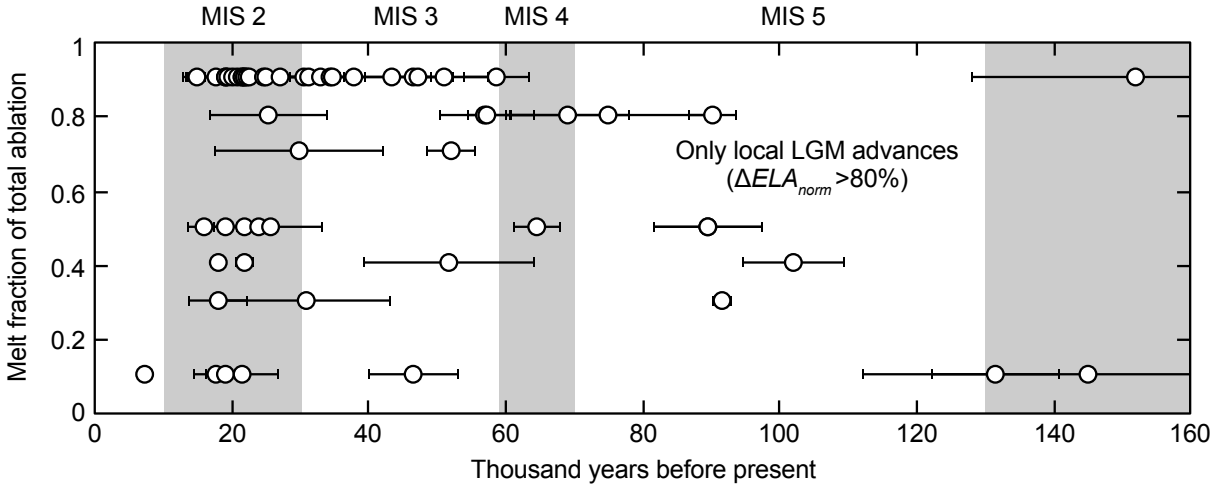

Figure 4.17. The melt fraction of modern glaciers and the timing of the local LGM standstills. Most of the glaciers advanced to their local maxima during MIS 2. However, many glaciers with low melt fractions (i.e., precipitation-controlled) advanced to their local LGM standstills during MIS 3–5, much earlier than the global MIS 2 LGM.

4.5 DISCUSSION

An accurate reconstruction of T_{air} and *ppt* from paleo-ELAs estimated from moraine locations depends on three fundamental assumptions: 1) The modern ELA, measured or estimated, is in equilibrium with the forcing climate factors; 2) The sensitivity of a glacier to forcing climate factors was similar in the past; and 3) The local modern lapse rate was similar in the past. Below, we will discuss the implications of these assumptions for reconstructing paleoclimate from paleo-ELA estimations.

Modern glaciers in Central Asia are losing mass, evident from direct measurements (summarized by Medvedeff and Roe, 2015) and from satellite measurements (summarized by Gardner et al., 2013). Aggregated data of glacier length measurements show that the observed glacier recessions for the last 30 years were more than their natural variability, an indication of changes in climate driving the retreats (Roe et al., 2017). Numerical modeling of changes in glacier area suggest that ~25% of the recent shrinkage of glacier area were due to anthropogenic climate warming (Marzeion et al., 2014). The comparison of natural response time of glacier length change to climate variability showed that the modern glaciers are in "disequilibrium" with the current climate and further glacier retreats are inevitable even if the climate stopped warming today (Christian et al., 2018). These evaluations strongly imply that the estimated modern ELAs are not steady-state ELAs—that climate variables estimated at the modern ELA may not be accurate for paleoclimate reconstructions. However, the ELA change over the last 30 years are in the order of tens of m, and the estimated ΔELAs for MIS 5–2 glaciers are measured in the hundreds of m. We agree with Christian et al. (2018) that the paleoclimate inference from Holocene glaciers require calibration of the estimated ΔELAs, but the large spatial and temporal changes in ELAs for MIS 5–2 glaciers represent large enough signals that their ΔELAs may be good proxies for

reconstructing paleo-T_{air}. On the other hand, the low ΔELAs for MIS 5–2 glaciers were mainly for precipitation-controlled glaciers, they may provide a new opportunity to reconstruct paleo-*ppt*, if the regional T_{air} depression is determined from other independent proxy. Nevertheless, this problem highlights the need to further investigate the sensitivity of glaciers in hyper-arid regions.

The empirical curve between summer T_{air} and annual *ppt* at the modern ELA for the glaciers in Central Asia (Figure 4.2a; Sakai et al., 2015) was derived from glaciers with various local conditions, such as cirque orientation, slope, or rock type of the bed. The numerical sensitivity model of Rupper and Roe (2008; Figure 4.2b) also considered glaciers with various local conditions for calculations of melt fractions. These two diagrams demonstrate that glaciers, regardless of their geometric settings, can change their sensitivity in response to changes in climate forcing. It is not a new insight—glaciers will always tend to equilibrate with the current climate. If a new climate persists long enough the glacier may eventually shift to a new set of T_{air} and *ppt* on the empirical curve of Sakai et al. (2015) or may acquire a new value of melt fraction on the Rupper and Roe's curve (2008). In other words, the sensitivity of an individual glacier to climate forcing did change in the past and will change in the future. For example, the sensitivity analysis of glaciers in the Andes (Vargo et al., 2018) showed that some glaciers in hyperarid regions became less sensitive to *ppt* when *ppt* increased beyond 100% of the modern value (from 220 to 440 mm yr^{-1}). A precipitation-controlled paleoglacier in Gobi-Altai range advanced to its near-maxima during early Holocene, an advance that would not have happened without annual *ppt* increase of at least 150% more than the modern value (from 150 to 230 mm yr^{-1}). There are now a large number of cosmic-ray exposure dates available for Central Asian glaciers located under variety of climate settings and their relative paleo-ELA estimations are useful to identify glaciers that are

most sensitive to a climate variable of interest. Quantifying ELA sensitivities, however, remains the important issue for inferring paleoclimate from glacial evidence.

Temperature records at high altitudes and latitudes are sparse and gridded reanalysis climate datasets tend to show bias towards lower altitudes. In turn, numerical modeling studies of glaciers using these T_{air} rely on atmospheric lapse rates of free air (usually 6–7 °C km^{-1}) to scale T_{air} to approximate the climate conditions at high altitudes. The T_{air} lapse rate used in the paleoclimate reconstruction from glaciers, however, can be a source of major uncertainty. For example, the lapse rate of summer T_{air} measured over maritime Canadian Arctic glaciers (~4 °C km^{-1}) were consistently lower than in free air (Gardner et al., 2009). Batbaatar et al. (2018) measured T_{air} on a glacier surface in Gobi-Altai to determine that the lapse rate there was ~8 °C km^{-1}, higher than a lapse rate of ~6.5 °C km^{-1} calculated from NCEP/NCAR reanalysis data (Kalnay et al., 1996), which we used in this study. Combination of weather station data at low and high altitudes and numerical modeling showed that windward side of the Cascade Range in Washington, USA, exhibited a much lower lapse rates of 5.2–3.9 °C km^{-1} (Justin et al., 2010). Gardner and Sharp (2009) recommended using variable lapse rates glacier mass balance calculations depending on the region. In addition to the various modern values, the lapse rates also varied in the past and there is no easy way to recover that information. One way to address this problem would be account for various lapse rates and compound with the uncertainties of the ΔELA values and the T_{air} used for modern climate. For example, accounting a range lapse rate of 5.5–7.5 °C km^{-1} the mean ΔELA of 440 ± 338 m for the Central Asian glaciers surveyed in this study would indicate a mean T_{air} depression of 2.9 °C with a large uncertainty of 6.4 °C.

The heterogeneous patterns of glacial advances in Central Asia have been noted before. Gillespie and Molnar (1995) emphasized the older and larger glacial advances than the global LGM advances and indicated that the increased precipitation and low temperature were responsible for asynchronous glaciations in different regions. Rupper and Roe (2008) formulated a model to account for the role of sublimation in the ablation of glaciers and highlighted the regions where glaciers may be more sensitive to changes in *ppt* than to T_{air}. Hughes et al. (2013) surveyed local LGM advances throughout the world to show that the glacial maxima in Central Asia occurred well before MIS 2, bringing the terminology of "Last Glacial Maximum" into question. The timing of local LGM advances in Central Asia and their corresponding melt fractions plotted in Figure 4.17 is our demonstration to highlight that 1) glaciers with different sensitivities respond differently to a similar magnitude of climate change; and 2) glaciers with similar sensitivities may vary advance or retreat at different times because local conditions are different. The schematics of such spatially and temporally heterogenous advances and retreats of glaciers in response to changes in T_{air} and *ppt* (Figure 4.18) illustrates that a series of ΔELAs observed in the field can be explained by the changes in the x and y axes. In that sense, the observed heterogeneity in the pattern of glacial advances in Central Asia provides an opportunity to evaluate paleoclimate reconstructions from independent proxies and/or validate numerical sensitivity analyses of glaciers in a continental setting.

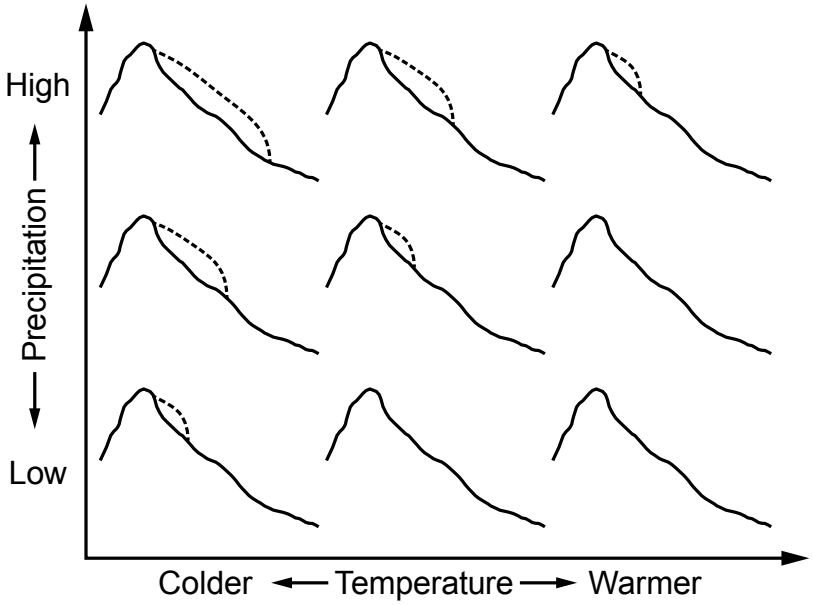

Figure 4.18. Glacier advance and retreat in response to changing climate. The two important climate variables for glacier mass balance, air temperature and precipitation, change in any direction in the schematic diagram. The ΔELA corresponding to changes in climate might differ depending on what direction the change is headed. For example, if the temperature gets colder in tandem with precipitation (from top right to bottom left) the corresponding ΔELA will be similar.

4.6 SUMMARY AND CONCLUSIONS

We used cosmic-ray exposure dating to construct glacial chronology over various climate conditions in Central Asia. The regions considered in this study included Altai, Tian Shan, Qilian Shan and Kunlun ranges, and the gridded reanalysis climate data showed that the summer air temperature ranged from −2.2 to 7.6 °C, and the annual precipitation ranged from 65 to 1020 mm. Altitudes of modern glaciers from Randolph Glacier Inventory were compiled to estimate the equilibrium-line altitudes for the modern glaciers. We used the altitudes of our dated moraines and of the previously dated moraines available in the literature to estimate paleo equilibrium-line altitudes using toe-head altitude ratio and maximum-elevation of lateral moraine methods. The results show that the paleoglaciers in Central Asia exhibited a highly heterogenous spatial and temporal pattern of glacial advances. Today most of the glaciers in Central Asia are retreating due to the current warming climate, except in the Kunlun region. During the global LGM, defined by the largest extents of ice sheets and low sea-level, many paleoglaciers in Central Asia did not advance to their maxima. The paleoglaciers that the maximum extent coincided with the global LGM were located in humid regions, suggesting that they responded mostly to minima in air temperature and solar insolation. During MIS 3 and 5, periods with higher air temperature than in the global LGM, produced many maximum glacial extents. These paleoglaciers were predicted to be more sensitive to changes in precipitation than in temperature, implying that their local LGM extents may be explained by increased precipitation at the time. The detailed map of observed temporal and spatial asynchrony of glaciations in Central Asia provides a framework from which a numerical sensitivity analyses can be validated.

Table 4.1. New data for cosmogenic nuclide analysis reported in Chapter 4.

Site	Sample	Location (° N/° E)	Elev. m asl	Thick-ness (cm)	Shield-ding factor	Quartz (g)	Be carrier (mg)	$^{10}Be/^{9}Be$ ($\times10^{-15}$)	^{10}Be concentration (10^3 atoms/g SiO2)	^{10}Be standard	^{26}Al concentration (10^3 atoms/g SiO2)	^{26}Al standard	Sampling date mm/dd/yy
Aksaiqin glacier	AG1-1	35.39662/80.34292	5450	0.5	1.0	--	--	--	4461.7 ± 177.3	KNSTD	25801.3 ± 1245.9	KNSTD	04/07/95
Aksaiqin glacier	AG1-2	35.39650/80.34284	5450	5	1.0	--	--	--	2432.8 ± 76	KNSTD	17482.2 ± 913.4	KNSTD	04/07/95
Aksaiqin glacier	AG1-3	35.39938/80.37218	5510	0.5	1.0	--	--	--	1801 ± 43.4	KNSTD	9556.4 ± 522.7	KNSTD	04/07/95
Aksaiqin glacier	AG1-4	35.39938/80.37218	5510	1	1.0	--	--	--	4908.5 ± 118.8	KNSTD	24213.1 ± 2076.7	KNSTD	04/07/95
Aksaiqin glacier	AG1-6	35.39727/80.36554	5428	1	1.0	--	--	--	19721.3 ± 585.8	KNSTD	124199.2 ± 6767.3	KNSTD	04/07/95
Barskoon	BS-001A	41.88323/77.70568	3822	2	1.0	11.338	0.2711	10.30 ± 1.50	16.5 ± 3.4	07KNSTD	--	--	06/10/11
Barskoon	BS-002A	41.88323/77.70568	3822	2	1.0	14.826	0.2752	22.20 ± 3.1	27.5 ± 5.5	07KNSTD	--	--	06/10/11
Barskoon	BS-002B	41.88323/77.70568	3822	2	1.0	15.68	0.2697	15.50 ± 2.10	17.8 ± 3.4	07KNSTD	--	--	06/10/11
Barskoon	BS-004A	41.88288/77.70610	3831	3	1.0	14.097	0.2711	51.20 ± 4.60	65.8 ± 8.4	07KNSTD	--	--	06/10/11
Barskoon	BS-007A	41.87017/77.73407	3791	3	1.0	13.667	0.2766	636.20 ± 9.90	860.4 ± 22.5	07KNSTD	--	--	06/10/11
Barskoon	BS-007B	41.87017/77.73407	3791	5	1.0	15.077	0.2599	726.50 ± 10.50	836.8 ± 20.8	07KNSTD	--	--	06/10/11
Barskoon	BS-007C	41.86975/77.73563	3805	2	1.0	16.131	0.2724	908.90 ± 25.30	1025.6 ± 42.9	07KNSTD	--	--	06/10/11
Barskoon	BS-007D	41.86975/77.73563	3805	1	1.0	16.201	0.2655	626.00 ± 40.20	685.5 ± 63	07KNSTD	--	--	06/10/11
Altyn Tagh	CAT-02C	39.31450/93.74186	4401	3	0.92	15.757	0.2446	89.87 ± 5.53	93.2 ± 8.2	07KNSTD	--	--	09/23/11
Dumda	CH-DU-01	37.85994/96.28808	4039	1	1.0	8.98	0.246	3779.00 ± 44.20	6917.6 ± 150.5	07KNSTD	--	--	09/20/11
Dumda	CH-DU-02	37.85203/96.28636	4036	1	1.0	6.872	0.2446	3642.30 ± 53.29	8663 ± 217.1	07KNSTD	--	--	09/20/11
Dumda	CH-DU-03	37.86278/96.28833	4056	1	1.0	7.135	0.2475	3294.90 ± 56.41	7637.4 ± 214.1	07KNSTD	--	--	09/20/11
Choktal	CR-001A	42.70139/76.70089	3197	3	1.0	9.547	0.3016	417.30 ± 7.68	880.9 ± 26.1	07KNSTD	--	--	06/11/11
Choktal	CR-001B	42.70139/76.70089	3197	5	1.0	9.85	0.2738	497.21 ± 10.54	923.5 ± 30.6	07KNSTD	--	--	06/11/11
Choktal	CR-001C	42.70139/76.70089	3197	3	1.0	10.858	0.2794	487.76 ± 8.88	838.7 ± 24.6	07KNSTD	--	--	06/11/11
Choktal	CR-002A	42.74965/76.69540	3574	3	0.98	10.886	0.2655	7.51 ± 1.23	12.2 ± 2.8	07KNSTD	--	--	06/12/11
Choktal	CR-002D	42.75083/76.69513	3588	3	0.97	10.423	0.2655	7.32 ± 1.52	12.5 ± 3.7	07KNSTD	--	--	06/12/11
Choktal	CR-002E	42.75083/76.69513	3588	3	0.97	10.949	0.2711	7.23 ± 1.16	12 ± 2.7	07KNSTD	--	--	06/12/11
Choktal	CR-003A	42.74775/76.69392	3535	10	0.98	10.487	0.246	437.75 ± 8.97	686.2 ± 22.1	07KNSTD	--	--	06/12/11
Choktal	CR-003C	42.74775/76.69392	3535	5	0.98	11.758	0.2572	484.10 ± 9.05	707.6 ± 21.2	07KNSTD	--	--	06/12/11
Choktal	CR-003D	42.74707/76.69433	3534	5	0.98	11.002	0.2863	425.24 ± 8.46	739.4 ± 23.3	07KNSTD	--	--	06/12/11
Daxigou	CS-10	43.11882/86.92159	3181	8	0.97	--	--	--	639.5 ± 29.3	KNSTD	--	--	09/11/92
Alashanje	CS-111a	42.92695/86.87829	3267	2.5	1.0	--	--	--	3874 ± 105.4	KNSTD	24188.3 ± 1139.8	KNSTD	07/01/94
Alashanje	CS-111b	42.92695/86.87829	3267	2.5	1.0	--	--	--	2386.9 ± 73.7	KNSTD	15411.7 ± 794.7	KNSTD	07/01/94
Alashanje	CS-112	43.02119/86.97594	3658	5	0.99	--	--	--	1067.1 ± 72	KNSTD	6991.4 ± 589.8	KNSTD	07/02/94
Daxigou	CS-11b	43.11040/86.94462	3021	8	0.97	--	--	--	873.4 ± 35.7	KNSTD	--	--	09/11/92
Daxigou	CS-12a	43.11040/86.94462	2992	8	0.97	--	--	--	717.8 ± 37.5	KNSTD	4592.8 ± 286.2	KNSTD	09/11/92
Daxigou	CS-5	43.11586/86.82338	3718	5	0.97	--	--	--	20.4 ± 11.2	KNSTD	--	--	09/11/92
Daxigou	CS-6	43.11586/86.82338	3718	5	0.97	--	--	--	86.5 ± 12.8	KNSTD	--	--	09/11/92
Daxigou	CS-7b	43.11556/86.84138	3592	5	0.99	--	--	--	917.3 ± 40.9	KNSTD	5161.4 ± 374.7	KNSTD	09/11/92
Daxigou	CS-8	43.11951/86.92004	3417	1	0.99	--	--	--	957.4 ± 44.6	KNSTD	5415.1 ± 333.4	KNSTD	09/11/92
Tailan	CS-14	41.60214/80.48376	1677	6	1.0	--	--	--	97.7 ± 11.2	KNSTD	463.1 ± 37	KNSTD	09/16/92
Tailan	CS-20	41.65480/80.45959	2053	5	1.0	--	--	--	262.4 ± 16	KNSTD	1391 ± 86.5	KNSTD	09/18/92
Tailan	CS-24	41.63056/80.46984	1879	3	1.0	--	--	--	161.6 ± 25.6	KNSTD	1160 ± 107.5	KNSTD	09/19/92
Tailan	CS-27a	41.54257/80.48545	1565	5	1.0	--	--	--	95.3 ± 10.5	KNSTD	361 ± 41.4	KNSTD	09/20/92

Table 4.1 (continued)

Site	Sample	Location (° N/° E)	Elev. m asl	Thick-ness (cm)	Shiel-ding factor	Quartz (g)	Be carrier (mg)	$^{10}Be/^{9}Be$ ($\times10^{-15}$)	^{10}Be concentration (10^3 atoms/g SiO2)	^{10}Be standard	^{26}Al concentration (10^3 atoms/g SiO2)	^{26}Al standard	Sampling date mm/dd/yy
Muzart	CS-28	41.78571/80.90608	1978	4	1.0	--	--	--	303.1 ± 23.6	KNSTD	2183.2 ± 41.4	KNSTD	09/22/92
Muzart	CS-30	41.79149/80.90501	2011	4	1.0	--	--	--	334.3 ± 19.7	KNSTD	1800.3 ± 133.2	KNSTD	09/22/92
Muzart	CS-32	41.77471/80.95658	1889	4	1.0	--	--	--	336.5 ± 16.5	KNSTD	--	--	09/22/92
Muzart	CS-33	41.77288/80.95874	1874	2	1.0	--	--	--	465.9 ± 75	KNSTD	--	--	09/22/92
Gulbel	GP-001	42.03892/77.12420	2803	3	1.0	13.345	0.2808	338.10 ± 19.80	475.4 ± 39.9	07KNSTD	--	--	06/10/11
Gulbel	GP-002C	42.01070/77.19833	3258	5	0.99	13.487	0.2613	485.22 ± 14.80	628.2 ± 28.5	07KNSTD	--	--	06/10/11
Gulbel	GP-002D	42.01238/77.20202	3208	3	0.99	12.341	0.2808	435.76 ± 8.15	662.5 ± 19.9	07KNSTD	--	--	06/10/11
Gulbel	GP-003A	42.01432/77.19927	3265	3	1.0	12.829	0.2641	519.70 ± 13.20	714.9 ± 27.6	07KNSTD	--	--	06/10/11
Gulbel	GP-003B	42.01432/77.19927	3265	3	1.0	14.079	0.2738	514.90 ± 21.10	669.1 ± 39.9	07KNSTD	--	--	06/10/11
Gulbel	GP-003C	42.01447/77.19822	3252	3	1.0	12.421	0.2766	492.30 ± 7.40	732.6 ± 18.7	07KNSTD	--	--	06/10/11
Gulbel	GP-004A	42.03813/77.14208	3001	3	1.0	12.132	0.2613	321.30 ± 11.90	462.4 ± 25.1	07KNSTD	--	--	06/10/11
Gulbel	GP-004B	42.03813/77.14208	3001	3	1.0	10.725	0.2627	1045.70 ± 32.40	1711.5 ± 78.8	07KNSTD	--	--	06/10/11
Gulbel	GP-005	42.03828/77.12057	2781	1	1.0	12.278	0.2613	479.60 ± 8.50	682 ± 19.6	07KNSTD	--	--	06/10/11
Gulbel	GP-006	42.03822/77.12402	2798	2	1.0	11.82	0.2655	447.60 ± 8.50	671.8 ± 20.4	07KNSTD	--	--	06/10/11
Karakax-A	KG1-10	36.44317/77.65680	5225	2.5	1.0	--	--	--	8477.7 ± 224.7	KNSTD	49003.3 ± 2212.3	KNSTD	04/07/95
Karakax-A	KG1-11	36.44196/77.65471	5223	3	1.0	--	--	--	2389.5 ± 81.4	KNSTD	13079.5 ± 607.6	KNSTD	04/07/95
Karakax-A	KG1-12	36.44740/77.65641	5330	3	1.0	--	--	--	14.6 ± 3.3	KNSTD	66.6 ± 14	KNSTD	04/07/95
Karakax-A	KG1-13	36.44506/77.65725	5270	1.5	1.0	--	--	--	--	KNSTD	21574.9 ± 989.2	KNSTD	04/07/95
Karakax-A	KG1-14	36.41666/77.66410	4900	3	1.0	--	--	--	26433.1 ± 768.2	KNSTD	145706.8 ± 12813.8	KNSTD	04/07/95
Karakax-A	KG1-15	36.42323/77.67547	4940	3	1.0	--	--	--	9881.9 ± 341.4	KNSTD	59997.3 ± 3134.3	KNSTD	04/07/95
Karakax-A	KG1-5	36.44554/77.64460	5357	1.5	1.0	--	--	--	1621.9 ± 54.2	KNSTD	8490.3 ± 375.8	KNSTD	04/07/95
Karakax-A	KG1-6	36.42616/77.64395	4980	1.5	1.0	--	--	--	8070.1 ± 284.5	KNSTD	50278.3 ± 2357.6	KNSTD	04/07/95
Karakax-A	KG1-7	36.42616/77.64395	4980	2	1.0	--	--	--	7013.7 ± 205.2	KNSTD	42906.5 ± 2085	KNSTD	04/07/95
Karakax-A	KG1-8	36.43024/77.65266	5100	1.5	1.0	--	--	--	9584.6 ± 282.2	KNSTD	55679.3 ± 2661.3	KNSTD	04/07/95
Karakax-A	KG1-9	36.43243/77.65229	5115	1	1.0	--	--	--	7992.4 ± 211.6	KNSTD	49391.9 ± 2303.8	KNSTD	04/07/95
Karakax-A	LIA-K-1	36.43898/77.64720	5180	2.5	1.0	--	--	--	6.1 ± 26.3	KNSTD	63.7 ± 78.8	KNSTD	04/07/95
Karakax-A	LIA-K-2	36.44025/77.64728	5185	1.5	1.0	--	--	--	687.6 ± 25.8	KNSTD	3934.4 ± 194.2	KNSTD	04/07/95
Karakax-A	LIA-K-3	36.43989/77.64718	5195	2	1.0	--	--	--	1024.1 ± 46.7	KNSTD	6460 ± 305.8	KNSTD	04/07/95
Karakax-A	LIA-K-4	36.43898/77.64720	5200	2.5	1.0	--	--	--	25.9 ± 4.2	KNSTD	117.2 ± 13.1	KNSTD	04/07/95
Karakax-B	KG2-1	36.43685/77.68216	4900	3.5	1.0	--	--	--	7225.5 ± 273	KNSTD	46252.1 ± 4125.3	KNSTD	04/07/95
Karakax-B	KG2-2	36.42821/77.69914	4700	2	0.99	--	--	--	7158.5 ± 215.3	KNSTD	44230.5 ± 3965.9	KNSTD	04/07/95
Karakax-B	KG2-3	36.42720/77.70940	4585	0.5	1.0	--	--	--	7197.5 ± 199.7	KNSTD	44813.3 ± 2864.3	KNSTD	04/07/95
Aksaiqin lake	LAS-1	35.25530/79.74365	4857	1.5	1.0	--	--	--	1694.7 ± 50.5	KNSTD	9702.3 ± 635.9	KNSTD	08/01/95
Aksaiqin lake	LAS-1_split-a	35.26044/79.74630	4857	1.5	1.0	--	--	--	5700 ± 155.5	KNSTD	28731 ± 1268.7	KNSTD	08/01/95
Aksaiqin lake	LAS-1_split-b	35.26044/79.74630	4857	1.5	1.0	--	--	--	21588.4 ± 566.1	KNSTD	93634.1 ± 4149	KNSTD	08/01/95
Aksaiqin lake	LAS-1_split-c	35.26044/79.74630	4857	1.5	1.0	--	--	--	765.9 ± 28.1	KNSTD	4522.2 ± 200.3	KNSTD	08/01/95
Aksaiqin lake	LAS-1_split-d	35.26044/79.74630	4857	1.5	1.0	--	--	--	2226.6 ± 68.8	KNSTD	12958 ± 619.3	KNSTD	08/01/95
Aksaiqin lake	LAS-2	35.25530/79.74365	4859	1.5	1.0	--	--	--	2389.5 ± 81.4	KNSTD	13079.5 ± 607.6	KNSTD	08/01/95
Aksaiqin lake	LAS-3	35.25530/79.74365	4863	1.5	1.0	--	--	--	1159.9 ± 77.7	KNSTD	8155.7 ± 939.2	KNSTD	08/01/95
Aksaiqin lake	LAS-4	35.25530/79.74365	4875	1.5	1.0	--	--	--	2809.4 ± 86.8	KNSTD	15970.7 ± 734.1	KNSTD	08/01/95

Table 4.1 (continued)

Site	Sample	Location (° N/° E)	Elev. m asl	Thick-ness (cm)	Shiel-ding factor	Quartz (g)	Be carrier (mg)	$^{10}Be/^{9}Be$ ($\times10^{-15}$)	^{10}Be concentration (10^3 atoms/g SiO2)	^{10}Be standard	^{26}Al concentration (10^3 atoms/g SiO2)	^{26}Al standard	Sampling date mm/dd/yy
Gangshiqia	QS-GG-001	37.69356/101.45208	4085	3	1.0	7.89	0.246	313.30 ± 7.59	652.7 ± 24.2	07KNSTD	--	--	09/16/11
Gangshiqia	QS-GG-002	37.69356/101.45208	4085	1	1.0	16.474	0.2446	798.94 ± 15.72	792.7 ± 24.7	07KNSTD	--	--	09/16/11
Gangshiqia	QS-GG-003	37.69417/101.45319	4101	5	1.0	16.251	0.246	821.64 ± 17.08	831.1 ± 27.1	07KNSTD	--	--	09/16/11
Gangshiqia	QS-GG-004	37.69417/101.45319	4101	5	1.0	14.127	0.2446	735.81 ± 12.77	851.3 ± 24.1	07KNSTD	--	--	09/16/11
Gangshiqia	QS-GG-005	37.69417/101.45319	4120	4	1.0	8.378	0.246	114.09 ± 4.86	223.9 ± 13.9	07KNSTD	--	--	09/16/11
Gangshiqia	QS-GG-006	37.69444/101.45417	4120	6	1.0	8.412	0.2446	91.94 ± 3.59	178.6 ± 10.2	07KNSTD	--	--	09/16/11
Gangshiqia	QS-GG-007	37.69111/101.45194	4041	3	1.0	12.568	0.246	525.60 ± 11.93	687.5 ± 24.1	07KNSTD	--	--	09/16/11
Gangshiqia	QS-GG-008	37.66339/101.42669	3615	4	0.99	12.229	0.246	613.17 ± 20.43	824.2 ± 40.5	07KNSTD	--	--	09/17/11
Gangshiqia	QS-GG-009	37.66339/101.42669	3615	3	0.99	9.306	0.246	444.50 ± 9.09	785.2 ± 25.3	07KNSTD	--	--	09/17/11
Gangshiqia	QS-GG-010	37.66050/101.42356	3556	3	1.0	4.026	0.246	158.95 ± 6.44	649 ± 38.3	07KNSTD	--	--	09/17/11
Gangshiqia	QS-GG-011	37.66050/101.42356	3556	3	1.0	9.644	0.246	333.18 ± 11.28	567.9 ± 28.4	07KNSTD	--	--	09/17/11
Gangshiqia	QS-GG-012	37.65486/101.41586	3480	3	1.0	8.096	0.2446	371.43 ± 18.85	749.9 ± 54.9	07KNSTD	--	--	09/17/11
Gangshiqia	QS-GG-013	37.65825/101.43286	3640	2	1.0	11.253	0.2446	373.75 ± 9.50	542.9 ± 21	07KNSTD	--	--	09/17/11
Suek	SO-CS-001	41.70825/77.80538	3432	3	1.0	9.819	0.2349	555.80 ± 12.60	888.5 ± 31.1	07KNSTD	--	--	06/09/11
Suek	SO-CS-002A	41.70142/77.81050	3402	2	1.0	9.416	0.2711	322.30 ± 8.60	620.1 ± 25	07KNSTD	--	--	06/09/11
Suek	SO-CS-002B	41.70142/77.81050	3402	5	1.0	10.307	0.246	585.60 ± 15.30	933.9 ± 37	07KNSTD	--	--	06/09/11
Diehanjelegou	XCS-101	43.15883/87.44098	3080	5	1.0	--	--	--	1590.1 ± 54.2	KNSTD	9823.2 ± 460.1	KNSTD	06/25/94
Diehanjelegou	XCS-102	43.15901/87.44026	3122	5	1.0	--	--	--	907.3 ± 33	KNSTD	5284.9 ± 266.2	KNSTD	06/25/94
Diehanjelegou	XCS-103	43.15751/87.45024	3014	5	1.0	--	--	--	2191.9 ± 71.9	KNSTD	12180.8 ± 571.3	KNSTD	06/27/94
Diehanjelegou	XCS-104	43.15690/87.44908	3025	5	1.0	--	--	--	1195.5 ± 65	KNSTD	10412.5 ± 553.3	KNSTD	06/27/94
Diehanjelegou	XCS-105	43.15690/87.44908	3025	5	1.0	--	--	--	1669.3 ± 82.2	KNSTD	10667.8 ± 564.5	KNSTD	06/27/94
Diehanjelegou	XCS-106	43.15690/87.44908	3025	5	1.0	--	--	--	952.1 ± 30	KNSTD	6062.8 ± 277.8	KNSTD	06/27/94
Kax Kurta	XCS-120a	47.46109/89.87250	2794	5	0.97	--	--	--	625.2 ± 26.6	KNSTD	4447.8 ± 294.8	KNSTD	07/09/94
Kax Kurta	XCS-120b	47.46109/89.87250	2794	5	0.97	--	--	--	660.4 ± 26.1	KNSTD	3770.7 ± 280.1	KNSTD	07/09/94
Kax Kurta	XCS-121	47.46111/89.79944	2486	10	1.0	--	--	--	648 ± 50.9	KNSTD	4114.5 ± 244.5	KNSTD	07/10/94

Table 4.2. New ^{10}Be and ^{26}Al exposure ages reported in Chapter 4.

Site	Sample name	Location (° N/° E)	Elevation (m asl)	^{10}Be age (ka ± ext. 1σ)	^{26}Al age (ka ± ext. 1σ)	Sampling date (mm/dd/yy)
Aksaiqin glacier	AG1-1	35.39662/80.34292	5450	39.7 ± 3.8	37.9 ± 3.8	04/07/95
Aksaiqin glacier	AG1-2	35.39650/80.34284	5450	22.4 ± 2.1	26.5 ± 2.7	04/07/95
Aksaiqin glacier	AG1-3	35.39938/80.37218	5510	15.5 ± 1.4	13.5 ± 1.4	04/07/95
Aksaiqin glacier	AG1-4	35.39938/80.37218	5510	42.8 ± 3.8	34.8 ± 4.3	04/07/95
Aksaiqin glacier	AG1-6	35.39727/80.36554	5428	184.5 ± 17.5	200.1 ± 22.4	04/07/95
Barskoon	BS-001A	41.88323/77.70568	3822	0.3 ± 0.1	--	06/10/11
Barskoon	BS-002A	41.88323/77.70568	3822	0.5 ± 0.1	--	06/10/11
Barskoon	BS-002B	41.88323/77.70568	3822	0.3 ± 0.1	--	06/10/11
Barskoon	BS-004A	41.88288/77.70610	3831	1.2 ± 0.2	--	06/10/11
Barskoon	BS-007A	41.87017/77.73407	3791	15.7 ± 1.4	--	06/10/11
Barskoon	BS-007B	41.87017/77.73407	3791	15.6 ± 1.4	--	06/10/11
Barskoon	BS-007C	41.86975/77.73563	3805	18.5 ± 1.8	--	06/10/11
Barskoon	BS-007D	41.86975/77.73563	3805	12.2 ± 1.5	--	06/10/11
Altyn Tagh	CAT-02C	39.31450/93.74186	4401	1.4 ± 0.2	--	09/23/11
Dumda	CH-DU-01	37.85994/96.28808	4039	125.4 ± 11.4	--	09/20/11
Dumda	CH-DU-02	37.85203/96.28636	4036	158.6 ± 14.7	--	09/20/11
Dumda	CH-DU-03	37.86278/96.28833	4056	137.6 ± 12.8	--	09/20/11
Choktal	CR-001A	42.70139/76.70089	3197	22.1 ± 2.0	--	06/11/11
Choktal	CR-001B	42.70139/76.70089	3197	23.5 ± 2.2	--	06/11/11
Choktal	CR-001C	42.70139/76.70089	3197	21.0 ± 1.9	--	06/11/11
Choktal	CR-002A	42.74965/76.69540	3574	0.3 ± 0.1	--	06/12/11
Choktal	CR-002D	42.75083/76.69513	3588	0.3 ± 0.1	--	06/12/11
Choktal	CR-002E	42.75083/76.69513	3588	0.3 ± 0.1	--	06/12/11
Choktal	CR-003A	42.74775/76.69392	3535	15.2 ± 1.4	--	06/12/11
Choktal	CR-003C	42.74775/76.69392	3535	15.1 ± 1.4	--	06/12/11
Choktal	CR-003D	42.74707/76.69433	3534	15.8 ± 1.4	--	06/12/11
Daxigou	CS-10	43.11882/86.92159	3181	15.4 ± 1.5	--	09/11/92
Alashanje	CS-111a	42.92695/86.87829	3267	84.0 ± 7.7	87.7 ± 8.9	07/01/94
Alashanje	CS-111b	42.92695/86.87829	3267	51.3 ± 4.7	55.0 ± 5.6	07/01/94
Alashanje	CS-112	43.02119/86.97594	3658	18.7 ± 2.1	20.2 ± 2.5	07/02/94
Daxigou	CS-11b	43.11040/86.94462	3021	23.2 ± 2.2	--	09/11/92
Daxigou	CS-12a	43.11040/86.94462	2992	19.4 ± 2	20.4 ± 2.2	09/11/92
Tailan	CS-14	41.60214/80.48376	1677	6.3 ± 0.9	4.9 ± 0.6	09/16/92
Tailan	CS-20	41.65480/80.45959	2053	12.8 ± 1.4	11.1 ± 1.2	09/18/92
Tailan	CS-24	41.63056/80.46984	1879	8.8 ± 1.6	10.3 ± 1.3	09/19/92
Tailan	CS-27a	41.54257/80.48545	1565	6.6 ± 0.9	4.1 ± 0.6	09/20/92
Muzart	CS-28	41.78571/80.90608	1978	15.4 ± 1.8	18.2 ± 1.6	09/22/92
Muzart	CS-30	41.79149/80.90501	2011	16.6 ± 1.7	14.7 ± 1.7	09/22/92
Muzart	CS-32	41.77471/80.95658	1889	18.2 ± 1.8	--	09/22/92
Muzart	CS-33	41.77288/80.95874	1874	25.2 ± 4.6	--	09/22/92
Daxigou	CS-5	43.11586/86.82338	3718	0.4 ± 0.2	--	09/11/92
Daxigou	CS-6	43.11586/86.82338	3718	1.5 ± 0.3	--	09/11/92
Daxigou	CS-7b	43.11556/86.84138	3592	16.7 ± 1.6	15.4 ± 1.7	09/11/92
Daxigou	CS-8	43.11951/86.92004	3417	18.6 ± 1.8	17.3 ± 1.8	09/11/92
Gulbel	GP-001	42.03892/77.12420	2803	15.4 ± 1.9	--	06/10/11
Gulbel	GP-002A	42.01147/77.19960	3254	17.6 ± 1.6	--	06/10/11
Gulbel	GP-002C	42.01070/77.19833	3258	15.9 ± 1.5	--	06/10/11
Gulbel	GP-002D	42.01238/77.20202	3208	17.0 ± 1.5	--	06/10/11
Gulbel	GP-003A	42.01432/77.19927	3265	17.5 ± 1.7	--	06/10/11
Gulbel	GP-003B	42.01432/77.19927	3265	16.4 ± 1.7	--	06/10/11
Gulbel	GP-003C	42.01447/77.19822	3252	18.1 ± 1.6	--	06/10/11
Gulbel	GP-004A	42.03813/77.14208	3001	13.2 ± 1.3	--	06/10/11
Gulbel	GP-004B	42.03813/77.14208	3001	49.4 ± 4.9	--	06/10/11
Gulbel	GP-005	42.03828/77.12057	2781	22.0 ± 2.0	--	06/10/11
Gulbel	GP-006	42.03822/77.12402	2798	21.7 ± 2.0	--	06/10/11

Table 4.2 (continued)

Site	Sample name	Location (° N/° E)	Elevation (m asl)	^{10}Be age (ka ± ext. 1σ)	^{26}Al age (ka ± ext. 1σ)	Sampling date (mm/dd/yy)
Karakax	KG1-10	36.44317/77.65680	5225	81.8 ± 7.5	78.8 ± 7.9	04/07/95
Karakax	KG1-11	36.44196/77.65471	5223	22.8 ± 2.1	20.5 ± 2.0	04/07/95
Karakax	KG1-12	36.44740/77.65641	5330	0.1 ± 0	0.1 ± 0.05	04/07/95
Karakax	KG1-13	36.44506/77.65725	5270	--	33 ± 3.3	04/07/95
Karakax	KG1-14	36.41666/77.66410	4900	314.1 ± 30.7	303.3 ± 43.3	04/07/95
Karakax	KG1-15	36.42323/77.67547	4940	109.6 ± 10.4	111.9 ± 11.8	04/07/95
Karakax	KG1-5	36.44554/77.64460	5357	14.4 ± 1.3	12.4 ± 1.2	04/07/95
Karakax	KG1-6	36.42616/77.64395	4980	86.3 ± 8.2	90 ± 9.2	04/07/95
Karakax	KG1-7	36.42616/77.64395	4980	75.1 ± 6.9	76.6 ± 7.8	04/07/95
Karakax	KG1-8	36.43024/77.65266	5100	97.4 ± 9	94.6 ± 9.7	04/07/95
Karakax	KG1-9	36.43243/77.65229	5115	80.0 ± 7.3	82.5 ± 8.4	04/07/95
Karakax	KG2-1	36.43685/77.68216	4900	81.4 ± 7.8	87.2 ± 11.2	04/07/95
Karakax	KG2-2	36.42821/77.69914	4700	88.5 ± 8.2	91.5 ± 11.9	04/07/95
Karakax	KG2-3	36.42720/77.70940	4585	92.0 ± 8.5	95.9 ± 10.7	04/07/95
Aksaiqin lake	LAS-1	35.25530/79.74365	4857	19.8 ± 1.8	18.6 ± 2	08/01/95
Aksaiqin lake	LAS-1_split-a	35.26044/79.74630	4857	67.4 ± 6.2	56.2 ± 5.6	08/01/95
Aksaiqin lake	LAS-1_split-b	35.26044/79.74630	4857	268.4 ± 25.7	196.0 ± 20.8	08/01/95
Aksaiqin lake	LAS-1_split-c	35.26044/79.74630	4857	8.9 ± 0.8	8.7 ± 0.8	08/01/95
Aksaiqin lake	LAS-1_split-d	35.26044/79.74630	4857	26.1 ± 2.4	25.2 ± 2.5	08/01/95
Aksaiqin lake	LAS-2	35.25530/79.74365	4859	28 ± 2.6	25.2 ± 2.5	08/01/95
Aksaiqin lake	LAS-3	35.25530/79.74365	4863	13.5 ± 1.5	15.6 ± 2.3	08/01/95
Aksaiqin lake	LAS-4	35.25530/79.74365	4875	32.7 ± 3	30.6 ± 3.0	08/01/95
Karakax	LIA-K-1	36.43898/77.64720	5180	0.1 ± 0.3	0.1 ± 0.1	04/07/95
Karakax	LIA-K-2	36.44025/77.64728	5185	6.6 ± 0.6	6.2 ± 0.6	04/07/95
Karakax	LIA-K-3	36.43989/77.64718	5195	9.8 ± 1.0	10.1 ± 1	04/07/95
Karakax	LIA-K-4	36.43898/77.64720	5200	0.3 ± 0.1	0.2 ± 0	04/07/95
Gangshiqia	QS-GG-001	37.6936/101.45208	4085	11.3 ± 1.1	--	09/16/11
Gangshiqia	QS-GG-002	37.6936/101.45208	4085	13.5 ± 1.2	--	09/16/11
Gangshiqia	QS-GG-003	37.6942/101.45319	4101	14.5 ± 1.3	--	09/16/11
Gangshiqia	QS-GG-004	37.6942/101.45319	4101	14.9 ± 1.3	--	09/16/11
Gangshiqia	QS-GG-005	37.6942/101.45319	4120	3.8 ± 0.4	--	09/16/11
Gangshiqia	QS-GG-006	37.6944/101.45417	4120	3.1 ± 0.3	--	09/16/11
Gangshiqia	QS-GG-007	37.6911/101.45194	4041	12.2 ± 1.1	--	09/16/11
Gangshiqia	QS-GG-008	37.6634/101.42669	3615	18.7 ± 1.9	--	09/17/11
Gangshiqia	QS-GG-009	37.6634/101.42669	3615	17.7 ± 1.6	--	09/17/11
Gangshiqia	QS-GG-010	37.6605/101.42356	3556	14.9 ± 1.6	--	09/17/11
Gangshiqia	QS-GG-011	37.6605/101.42356	3556	13.1 ± 1.3	--	09/17/11
Gangshiqia	QS-GG-012	37.6549/101.41586	3480	18.0 ± 2.0	--	09/17/11
Gangshiqia	QS-GG-013	37.6583/101.43286	3640	11.8 ± 1.1	--	09/17/11
Suek	SO-CS-001	41.70825/77.80538	3432	19.9 ± 1.9	--	06/09/11
Suek	SO-CS-002A	41.70142/77.81050	3402	14.0 ± 1.3	--	06/09/11
Suek	SO-CS-002B	41.70142/77.81050	3402	21.7 ± 2.1	--	06/09/11
Diehanjelegou	XCS-101	43.15883/87.44098	3080	38.6 ± 3.6	39.4 ± 3.9	06/25/94
Diehanjelegou	XCS-102	43.15901/87.44026	3122	21.4 ± 2	20.5 ± 2.1	06/25/94
Diehanjelegou	XCS-103	43.15751/87.45024	3014	55.7 ± 5.2	51.2 ± 5.1	06/27/94
Diehanjelegou	XCS-104	43.15690/87.44908	3025	30.0 ± 3.1	43.3 ± 4.5	06/27/94
Diehanjelegou	XCS-105	43.15690/87.44908	3025	42.0 ± 4.2	44.4 ± 4.6	06/27/94
Diehanjelegou	XCS-106	43.15690/87.44908	3025	23.8 ± 2.2	25.0 ± 2.5	06/27/94
Kax Kurta	XCS-120a	47.46109/89.87250	2794	16.8 ± 1.6	19.6 ± 2.1	07/09/94
Kax Kurta	XCS-120b	47.46109/89.87250	2794	17.7 ± 1.7	16.6 ± 1.9	07/09/94
Kax Kurta	XCS-121	47.46111/89.79944	2486	21.6 ± 2.5	22.5 ± 2.4	07/10/94

Table 4.3. Summary of outlier evaluations. Group-ID refers to the identification of grouped samples in "expage" compilation (J. Heyman, 2018). n is the number of samples in the group. Mean refers to mean age for the group, given in ka. 1σ refers to the 1σ standard deviation, given in ka. Red boxed cells indicate the values different from the values before the outlier rejection. 1σ total refers to 1σ total uncertainty calculated after the outlier rejections and is given in ka. The total uncertainty compounds the 1σ standard deviation and 1σ internal uncertainty of the individual ages in the group. Red highlighted cells indicate that the 1σ total uncertainty is more than 50% of the mean.

Site name (Subregion)	Publication	Group-ID	Before outlier rejection			Evaluation methodsand mean and 1σ AFTER outlier rejection						Interpreted age for the group after outlier rejection				
						Normalized deviation		Chauvenet's		Peirce's						
			n	Mean	1σ							n	Mean	1σ total	1σ total (%)	1σ age range (ka)
Ala Bash (W Tian Shan)	Koppes et al. (2008)	Kopp2008-J	3	118.5	42.6	142.1	17.2	118.5	42.6	118.5	42.6	2	142.1	17.8	13%	159.9–124.3
	Koppes et al. (2008)	Kopp2008-K	4	102.9	25.1	102.1	6.9	102.9	25.1	102.9	25.1	2	102.1	7.5	7%	109.6–94.7
Alashanje (E Tian Shan)	Li et al. (2014)	Li2014-A	5	57.2	81.7	21.0	13.4	21.0	13.4	21.0	13.4	4	21.0	13.4	64%	34.4–7.7
	Li et al. (2014)	Li2014-B	3	22.1	8.8	17.5	5.2	22.1	8.8	22.1	8.8	2	17.5	5.3	30%	22.8–12.2
	Li et al. (2014)	Li2014-D	5	29.2	7.8	25.8	2.3	25.8	2.3	25.8	2.3	4	25.8	2.4	9%	28.2–23.4
	Li et al. (2014)	Li2014-E	7	52.6	16.3	46.8	6.4	46.8	6.4	46.8	6.4	6	46.8	6.5	14%	53.3–40.4
	Li et al. (2014)	Li2014-F	3	69.0	13.0	76.1	5.8	69.0	13.0	69.0	13.0	2	76.1	5.9	8%	82.1–70.2
Ama Drime (E Himalaya)	Chevalier et al. (2011)	Chev2011-S	3	29.1	19.6	17.8	2.1	29.1	19.6	29.1	19.6	2	17.8	2.1	12%	19.9–15.7
At Bashi (W Tian Shan)	Zech (2012)	Zec2012-A	4	14.8	3.2	16.4	1.0	14.8	3.2	16.4	1.0	3	16.4	1.2	7%	17.6–15.2
	Zech (2012)	Zec2012-B	5	20.1	2.7	19.1	1.7	20.1	2.7	20.1	2.7	4	19.1	1.8	10%	20.9–17.3
	Zech (2012)	Zec2012-C	3	49.3	26.8	64.8	2.6	49.3	26.8	49.3	26.8	2	64.8	3.5	5%	68.3–61.3
Baikal	Horiuchi et al. (2004)	Hori2004-A	3	15.1	0.8	15.1	0.8	15.1	0.8	15.1	0.8	3	15.1	2.1	14%	17.2–13.0
Barskoon & Suek (W Tian Shan)	This study	Barskoon Suu-A	4	15.5	2.6	16.6	1.6	15.5	2.6	15.5	2.6	3	16.6	1.7	10%	18.3–14.9
	This study	Barskoon Suu-C	3	0.4	0.1	0.4	0.1	0.4	0.1	0.4	0.1	3	0.4	0.1	35%	0.5–0.2
	Blomdin et al. (2016)	Blom-A	5	82.8	16.4	89.5	7.7	82.8	16.4	89.5	7.7	4	89.5	7.9	9%	97.4–81.6
	Blomdin et al. (2016)	Blom-B	3	32.1	12.2	25.7	7.5	32.1	12.2	32.1	12.2	2	25.7	7.5	29%	33.3–18.2
	Blomdin et al. (2016)	Blom-C	4	19.4	6.0	16.9	4.3	19.4	6.0	19.4	6.0	3	16.9	4.3	25%	21.3–12.6
	Blomdin et al. (2016)	Blom-D	3	13.8	2.5	15.2	1.2	13.8	2.5	13.8	2.5	2	15.2	1.3	8%	16.4–13.9
	This study	Suek-A	3	18.5	4.0	20.8	1.2	18.5	4.0	18.5	4.0	2	20.8	1.5	7%	22.3–19.3
Bayan Har Shan (Inner Tibet)	Heyman et al. (2011)	Heym2011-C	3	16.2	4.2	13.9	1.6	16.2	4.2	16.2	4.2	2	13.9	1.7	13%	15.6–12.1
	Heyman et al. (2011)	Heym2011-D	4	62.4	15.4	69.3	8.4	62.4	15.4	62.4	15.4	3	69.3	8.7	13%	78.1–60.6
	Heyman et al. (2011)	Heym2011-G	3	71.3	25.0	57.2	6.8	71.3	25.0	71.3	25.0	2	57.2	6.9	12%	64.1–50.3
	Heyman et al. (2011)	Heym2011-H	3	66.0	48.4	39.9	24.8	66.0	48.4	66.0	48.4	2	39.9	24.8	62%	64.7–15.1
	Heyman et al. (2011)	Heym2011-I	3	56.6	25.5	71.3	0.3	56.6	25.5	56.6	25.5	2	71.3	3.7	5%	75.1–67.6
	Heyman et al. (2011)	Heym2011-J	3	38.9	23.3	52.3	3.6	38.9	23.3	38.9	23.3	2	52.3	3.7	7%	56.0–48.6
	Heyman et al. (2011)	Heym2011-L	3	34.0	18.2	23.5	1.0	34.0	18.2	34.0	18.2	2	23.5	1.3	6%	24.8–22.2
	Heyman et al. (2011)	Heym2011-M	3	108.2	80.9	154.3	18.1	108.2	80.9	108.2	80.9	2	154.3	18.6	12%	172.9–135.8
	Heyman et al. (2011)	Heym2011-N	3	60.3	4.5	57.8	1.9	60.3	4.5	60.3	4.5	2	57.8	2.1	4%	59.9–55.6
	Heyman et al. (2011)	Heym2011-O	3	47.6	23.5	34.3	6.7	47.6	23.5	47.6	23.5	2	34.3	6.7	20%	41.0–27.6
Otgontenger, Bitüüt (Hangai)	Batbaatar et al. (2018)	Batb2018-M	3	47.1	29.6	30.0	1.0	47.1	29.6	47.1	29.6	2	30.0	1.3	4%	31.4–28.7
	Batbaatar et al. (2018)	Batb2018-O	3	15.7	0.9	16.3	0.0	15.7	0.9	15.7	0.9	2	16.3	0.5	3%	16.8–15.8
Borohoro (E Tian Shan)	Li et al. (2016)	Li2016-B	3	2.1	3.2	0.3	0.1	2.1	3.2	2.1	3.2	2	0.3	0.1	45%	0.4–0.2
	Zhang et al. (2016a)	Zhan2016a-D	4	63.7	10.6	58.7	4.4	63.7	10.6	58.7	4.4	3	58.7	4.9	8%	63.7–53.8
	Zhang et al. (2016a)	Zhan2016a-F	4	21.7	7.7	18.3	4.3	21.7	7.7	21.7	7.7	3	18.3	4.3	23%	22.6–14.0

Table 4.3 (continued)

Site name (Subregion)	Publication	Group-ID	Before outlier rejection			Evaluation methods and mean and 1σ AFTER outlier rejection						Interpreted age for the group after outlier rejection				
			n	Mean	1σ	Normalized deviation		Chauvenet's		Peirce's		n	Mean	1σ total	1σ total (%)	1σ age range (ka)
Chagan Uzun (Altai)	Gribenski et al. (2016)	Grib2016-A	3	20.8	3.0	19.1	0.4	20.8	3.0	20.8	3.0	2	19.1	0.6	3%	19.6–18.5
	Gribenski et al. (2016)	Grib2016-C	4	18.3	0.8	18.3	0.8	18.3	0.8	18.3	0.8	4	18.3	0.9	5%	19.2–17.4
	Gribenski et al. (2016)	Grib2016-D	4	19.4	1.2	19.4	1.2	19.4	1.2	19.4	1.2	4	19.4	1.3	7%	20.6–18.1
	Gribenski et al. (2016)	Grib2016-E	5	22.0	7.4	18.8	1.8	18.8	1.8	18.8	1.8	4	18.8	1.9	10%	20.6–16.9
	Reuther (2007)	Reu2007-C	3	15.6	0.3	15.6	0.3	15.6	0.3	15.6	0.3	3	15.6	0.9	6%	16.6–14.7
	Reuther (2007)	Reu2007-E	3	20.9	3.7	20.9	3.7	20.9	3.7	20.9	3.7	3	20.9	5.6	27%	26.4–15.3
Cho Oyu (E Himalaya)	Chevalier et al. (2011)	Chev2011-U	4	34.5	2.5	33.2	0.0	34.5	2.5	33.2	0.0	3	33.2	0.9	3%	34.1–32.4
Choktal (W Tian Shan)	This study	Choktal river-A	3	22.2	1.3	22.2	1.3	22.2	1.3	22.2	1.3	3	22.2	1.4	6%	23.6–20.8
	This study	Choktal river-B	3	15.4	0.4	15.4	0.4	15.4	0.4	15.4	0.4	3	15.4	0.6	4%	16.0–14.8
	This study	Choktal river-C	3	0.3	0.0	0.3	0.0	0.3	0.0	0.3	0.0	3	0.3	0.1	28%	0.3–0.2
Daxigou (E Tian Shan)	Kong et al. (2009a)	Kong2009a-A	5	17.9	4.9	19.6	3.6	17.9	4.9	17.9	4.9	4	19.6	3.7	19%	23.3–15.9
	Kong et al. (2009a)	Kong2009a-B	3	16.9	0.8	16.9	0.8	16.9	0.8	16.9	0.8	3	16.9	1.3	8%	18.2–15.6
	Kong et al. (2009a)	Kong2009a-C	3	19.6	3.3	17.7	0.2	19.6	3.3	19.6	3.3	2	17.7	0.8	5%	18.5–16.9
	Kong et al. (2009a)	Kong2009a-D	5	11.7	4.8	9.9	2.6	11.7	4.8	11.2	0.6	4	9.9	2.8	28%	12.6–7.1
	This study	Li2011-D	4	20.3	2.3	19.3	1.4	20.3	2.3	20.3	2.3	3	19.3	1.7	9%	21.0–17.7
	Li et al. (2011)	Li2011-E	6	17.4	1.4	17.4	1.4	17.4	1.4	17.2	1.4	6	17.4	1.5	8%	18.9–16.0
	This study	Li2014-I	9	0.5	0.4	0.3	0.1	0.5	0.4	0.3	0.1	8	0.3	0.1	32%	0.5–0.2
Diehanjelegou (E Tian Shan)	This study	Diehanjelegou-B	4	37.9	14.1	31.9	9.2	37.9	14.1	37.9	14.1	3	31.9	9.4	29%	41.3–22.6
Dumda (Qilian Shan)	This study	Dumda-A	3	140.6	16.8	131.5	8.7	140.6	16.8	140.6	16.8	2	131.5	9.3	7%	140.8–122.2
Gangshiqia (Qilian Shan)	This study	Qilian Shan-D	7	10.5	5.0	11.7	4.1	10.5	5.0	10.5	5.0	6	11.7	4.1	35%	15.8–7.6
Gichginii (Gobi-Altai)	Batbaatar et al. (2018)	Batb2018-A	4	6.8	1.2	7.4	0.6	6.8	1.2	6.8	1.2	3	7.4	0.7	9%	8.0–6.7
	Batbaatar et al. (2018)	Batb2018-B	5	2.1	1.0	2.5	0.7	2.1	1.0	2.1	1.0	4	2.5	0.7	28%	3.2–1.8
	Batbaatar et al. (2018)	Batb2018-C	6	1.4	0.4	1.4	0.4	1.4	0.4	1.4	0.4	6	1.4	0.4	29%	1.8–1.0
Gulbel (W Tian Shan)	This study	Gulbel pass-A	3	19.7	3.7	21.9	0.3	19.7	3.7	19.7	3.7	2	21.9	0.7	3%	22.6–21.2
	This study	Gulbel pass-C	3	17.3	0.9	17.3	0.9	17.3	0.9	17.3	0.9	3	17.3	1.1	6%	18.5–16.2
	This study	Gulbel pass-D	3	16.8	0.9	16.8	0.9	16.8	0.9	16.8	0.9	3	16.8	1.1	6%	17.8–15.7
Gurla Mandhata (W Himalaya)	Chevalier et al. (2011)	Chev2011-W	4	41.9	16.3	48.4	12.3	41.9	16.3	41.9	16.3	3	48.4	12.4	26%	60.7–36.0
Gyalgar (Hangai)	Batbaatar and Gillespie (2016)	BatGil2016-L	3	64.8	78.4	19.6	3.7	64.8	78.4	64.8	78.4	2	19.6	3.9	20%	23.4–15.7
	Batbaatar and Gillespie (2016)	BatGil2016-N	3	31.5	15.2	22.8	3.3	31.5	15.2	31.5	15.2	2	22.8	3.4	15%	26.2–19.5
Haiyuan (Qilian Shan)	Lasserre et al. (2002)	Lass2002-A	12	9.5	4.2	9.5	4.2	9.5	4.2	9.5	4.2	12	9.5	4.3	45%	13.7–5.2
Högiin (Darhad)	Gillespie et al. (2008)	Gill2008-F	3	164.4	69.5	125.2	21.4	164.4	69.5	164.4	69.5	2	125.2	21.6	17%	146.8–103.7
	Gillespie et al. (2008)	Gill2008-G	3	29.8	14.3	22.4	8.8	29.8	14.3	29.8	14.3	2	22.4	8.8	39%	31.3–13.6
Hoh lake (Hangai)	Smith et al. (2016)	Smit2016-B	3	34.1	17.3	43.6	7.7	34.1	17.3	34.1	17.3	2	43.6	7.8	18%	51.3–35.8
Ih Bogd (Gobi-Altai)	Batbaatar et al. (2018)	Batb2018-K	6	12.9	3.1	14.0	1.4	14.0	1.4	14.0	1.4	5	14.0	1.7	12%	15.8–12.3

Table 4.3 (continued)

Site name (Subregion)	Publication	Group-ID	Before outlier rejection			Evaluation methods and mean and 1σ AFTER outlier rejection						Interpreted age for the group after outlier rejection				
			n	Mean	1σ	Normalized deviation		Chauvenet's		Peirce's		n	Mean	1σ total	1σ total (%)	1σ age range (ka)
Jarai (Darhad)	Gillespie et al. (2008)	Gill2008-D	7	28.0	11.3	25.2	9.4	28.0	11.3	28.0	11.3	6	25.2	9.4	38%	34.6–15.7
	Gillespie et al. (2008)	Gill2008-E	3	23.1	6.1	19.7	2.0	23.1	6.1	23.1	6.1	2	19.7	2.0	10%	21.7–17.7
Jombolok (Sayan)	Arzhannikov et al. (2012)	Arzh2012-B	3	24.9	1.1	24.9	1.1	24.9	1.1	24.9	1.1	3	24.9	1.9	8%	26.8–22.9
	Arzhannikov et al. (2012)	Arzh2012-C	3	32.0	10.2	26.1	0.7	32.0	10.2	32.0	10.2	2	26.1	1.8	7%	27.9–24.3
	Batbaatar and Gillespie (2016)	BatGil2016-E	4	24.1	6.7	20.9	1.6	24.1	6.7	20.9	1.6	3	20.9	2.0	9%	22.8–18.9
Kailas (C Himalaya)	Chevalier et al. (2011)	Chev2011-X	8	17.4	1.9	17.4	1.9	17.4	1.9	17.4	1.9	8	17.4	1.9	11%	19.4–15.5
	Chevalier et al. (2011)	Chev2011-Y	14	44.6	12.9	46.5	11.2	44.6	12.9	44.6	12.9	13	46.5	11.2	24%	57.8–35.3
	Chevalier et al. (2011)	Chev2011-Z	7	68.4	91.2	34.1	8.3	34.1	8.3	34.1	8.3	6	34.1	8.3	24%	42.4–25.7
Kalurong (Inner Tibet)	Liu et al. (2017)	Liu2017-B	4	10.7	9.9	10.7	9.9	10.7	9.9	10.7	9.9	4	10.7	11.3	106%	22.0–-0.6
	Liu et al. (2017)	Liu2017-C	3	17.1	7.9	21.6	0.9	17.1	7.9	17.1	7.9	2	21.6	1.1	5%	22.7–20.5
	Liu et al. (2017)	Liu2017-D	3	13.3	5.9	16.7	1.1	13.3	5.9	13.3	5.9	2	16.7	1.2	7%	17.9–15.5
Kanas (Altai)	Gribenski et al. (2018)	Grib2018-A	3	18.5	0.4	18.5	0.4	18.5	0.4	18.5	0.4	3	18.5	0.6	3%	19.1–18.0
	Gribenski et al. (2018)	Grib2018-B	3	17.8	5.6	21.0	0.1	17.8	5.6	17.8	5.6	2	21.0	0.4	2%	21.5–20.6
	Gribenski et al. (2018)	Grib2018-C	3	105.6	123.0	35.0	18.5	105.6	123.0	105.6	123.0	2	35.0	18.5	53%	53.5–16.4
	Gribenski et al. (2018)	Grib2018-D	3	50.1	29.0	66.8	4.0	50.1	29.0	50.1	29.0	2	66.8	4.1	6%	70.9–62.6
Karakax-A (W Kunlun)	This study	Karakax-A	3	87.3	5.4	90.2	2.5	87.3	5.4	87.3	5.4	2	90.2	3.6	4%	93.8–86.6
	This study	Karakax-B5	4	4.2	4.8	2.3	3.7	4.2	4.8	4.2	4.8	3	2.3	3.7	162%	6.0–-1.4
Karola\ (Inner Tibet)	Liu et al. (2017)	Liu2017-E	4	5.5	7.5	2.0	3.2	5.5	7.5	2.0	3.2	3	2.0	3.2	164%	5.2–-1.3
	Liu et al. (2017)	Liu2017-F	4	0.2	0.1	0.2	0.1	0.2	0.1	0.2	0.1	4	0.2	0.1	29%	0.3–0.2
Koyandy (W Tian Shan)	Blomdin et al. (2016)	Blom-E	5	2.1	2.1	1.3	1.3	2.1	2.1	1.3	1.3	4	1.3	1.3	99%	2.6–0.0
	Blomdin et al. (2016)	Blom-F	5	14.5	3.4	15.7	2.6	14.5	3.4	14.5	3.4	4	15.7	2.6	16%	18.2–13.1
La Ji (Qilian Shan)	Owen et al. (2003c)	Owen2003c-C	4	38.1	25.6	25.4	3.0	38.1	25.6	25.4	3.0	3	25.4	3.1	12%	28.4–22.3
Laolongwan (Qilian Shan)	Owen et al. (2003d)	Owen2003d-A	3	13.2	3.9	11.0	0.4	13.2	3.9	13.2	3.9	2	11.0	0.4	4%	11.4–10.6
	Owen et al. (2003d)	Owen2003d-E	3	19.5	0.5	19.2	0.0	19.5	0.5	19.5	0.5	2	19.2	0.7	4%	19.8–18.5
Mawang Kangri (Inner Tibet)	Amidon et al. (2013)	Amid2013-A	7	61.9	20.7	62.7	8.2	61.9	20.7	62.7	8.2	5	62.7	8.3	13%	71.0–54.4
Menyuan (E Tibet)	Wang et al. (2013)	Wang2013-A	3	28.1	3.0	26.5	1.3	28.1	3.0	28.1	3.0	2	26.5	1.5	6%	28.0–24.9
	Wang et al. (2013)	Wang2013-B	8	57.9	20.3	51.1	7.4	51.1	7.4	51.1	7.4	7	51.1	7.6	15%	58.7–43.5
	Wang et al. (2013)	Wang2013-C	5	26.0	2.9	24.9	1.8	26.0	2.9	26.0	2.9	4	24.9	2.0	8%	26.8–22.9
	Wang et al. (2013)	Wang2013-D	4	19.7	1.0	19.7	1.0	19.7	1.0	19.2	0.2	4	19.7	1.2	6%	20.9–18.5
Mönh-Saridag (Sayan)	Batbaatar and Gillespie (2016)	BatGil2016-B	3	10.1	0.5	10.1	0.5	10.1	0.5	10.1	0.5	3	10.1	0.7	7%	10.8–9.4
	Batbaatar and Gillespie (2016)	BatGil2016-D	3	24.5	4.3	26.9	1.4	24.5	4.3	24.5	4.3	2	26.9	1.6	6%	28.5–25.2
Nyainqentanghla (Inner Tibet)	Chevalier et al. (2011)	Chev2011-C	5	15.5	4.8	13.5	2.1	15.5	4.8	13.5	2.1	4	13.5	2.1	16%	15.6–11.4
	Chevalier et al. (2011)	Chev2011-D	10	35.0	13.1	31.7	8.4	35.0	13.1	31.7	8.4	9	31.7	8.4	26%	40.1–23.3
	Chevalier et al. (2011)	Chev2011-E	10	50.3	14.1	53.5	10.3	50.3	14.1	53.5	10.3	9	53.5	10.4	19%	63.9–43.2
	Dong et al. (2017a)	Dong2017a-A	5	16.1	8.0	19.6	1.2	19.6	1.2	19.6	1.2	4	19.6	1.8	9%	21.4–17.9
	Dong et al. (2017a)	Dong2017a-B	5	20.3	0.9	20.3	0.9	20.3	0.9	20.3	0.9	5	20.3	1.2	6%	21.5–19.1

Table 4.3 (continued)

Site name (Subregion)	Publication	Group-ID	Before outlier rejection			Evaluation methods and mean and 1σ AFTER outlier rejection						Interpreted age for the group after outlier rejection				
			n	Mean	1σ	Normalized deviation		Chauvenet's		Peirce's		n	Mean	1σ total	1σ total (%)	1σ age range (ka)
Otgontenger, Bogd (Hangai)	Batbaatar et al. (2018)	Roth2014b-A	6	21.8	6.2	19.6	3.3	19.6	3.3	19.6	3.3	5	19.6	3.4	17%	22.9–16.2
	Rother et al. (2014b)	Roth2014b-B	3	18.1	3.3	19.8	2.0	18.1	3.3	18.1	3.3	2	19.8	2.1	11%	21.9–17.7
	Rother et al. (2014b)	Roth2014b-C	3	25.7	2.5	27.1	1.2	25.7	2.5	25.7	2.5	2	27.1	1.4	5%	28.5–25.7
	Rother et al. (2014b)	Roth2014b-E	3	35.8	12.1	42.7	2.2	35.8	12.1	35.8	12.1	2	42.7	2.5	6%	45.2–40.3
	Rother et al. (2014b)	Roth2014b-F	3	43.9	13.6	36.7	7.6	43.9	13.6	43.9	13.6	2	36.7	7.7	21%	44.4–28.9
	Rother et al. (2014b)	Roth2014b-G	3	41.5	19.6	31.2	11.4	41.5	19.6	41.5	19.6	2	31.2	11.4	37%	42.6–19.8
Sailag (Sayan)	Batbaatar and Gillespie (2016)	Arzh2012-D	12	25.9	19.1	17.8	3.1	22.0	14.1	17.8	3.1	10	17.8	3.3	18%	21.1–14.6
Samdain Kangsang (Inner Tibet)	Chevalier et al. (2011)	Chev2011-A	7	18.4	1.0	18.4	1.0	18.4	1.0	18.4	1.0	7	18.4	1.1	6%	19.5–17.3
	Chevalier et al. (2011)	Chev2011-B	8	20.5	1.8	20.0	1.4	20.5	1.8	20.0	1.4	7	20.0	1.5	7%	21.5–18.6
Sentsa (Sayan)	Arzhannikov et al. (2012)	Arzh2012-A	4	18.3	1.4	17.6	0.4	18.3	1.4	17.6	0.4	3	17.6	1.7	10%	19.3–15.9
Sutai (Gobi-Altai)	Batbaatar et al. (2018)	Batb2018-E	4	19.8	8.9	24.2	1.6	19.8	8.9	24.2	1.6	3	24.2	1.8	8%	26.0–22.4
	Batbaatar et al. (2018)	Batb2018-F	3	27.1	15.7	18.6	8.0	27.1	15.7	27.1	15.7	2	18.6	8.1	43%	26.7–10.5
	Batbaatar et al. (2018)	Batb2018-J	5	13.9	5.0	15.9	2.5	13.9	5.0	15.9	2.5	4	15.9	2.5	16%	18.4–13.3
Tailan (W Tian Shan)	Hubert-Ferrari et al. (2005)	Hube2005-A	10	16.9	3.9	17.7	3.3	16.9	3.9	16.9	3.9	9	17.7	3.3	19%	21.0–14.3
Takelekete (W Tian Shan)	Zhang et al. (2016a)	Zhan2016a-B	8	55.1	14.6	52.0	12.4	55.1	14.6	55.1	14.6	7	52.0	12.5	24%	64.5–39.5
Tanggula Shan (Inner Tibet)	Owen et al. (2005)	Owen2005-L	4	61.2	7.8	57.5	2.8	61.2	7.8	57.5	2.8	3	57.5	3.1	5%	60.6–54.4
	Owen et al. (2005)	Owen2005-M	5	98.9	48.0	98.9	48.0	98.9	48.0	98.9	48.0	5	98.9	48.1	49%	147.0–50.8
	Owen et al. (2005)	Owen2005-N	5	140.9	86.4	140.9	86.4	140.9	86.4	140.9	86.4	5	140.9	87.1	62%	228.0–53.8
	Colgan et al. (2006)	Schä2002-E	7	75.2	14.9	75.2	14.9	75.2	14.9	75.2	14.9	7	75.2	15.3	20%	90.5–59.9
Tangra Yum Co (Inner Tibet)	Rades et al. (2015)	Rade2015-C	3	15.6	6.8	19.5	1.4	15.6	6.8	15.6	6.8	2	19.5	1.5	8%	21.0–17.9
Tomort (E Tian Shan)	Chen et al. (2015)	Chen2015-B	3	15.5	1.7	14.5	0.1	15.5	1.7	15.5	1.7	2	14.5	0.5	3%	15.0–14.1
W Himalaya	Chevalier et al. (2011)	Chev2011-AB	7	159.5	29.4	152.0	23.8	159.5	29.4	159.5	29.4	6	152.0	24.0	16%	176.1–128.0
	Chevalier et al. (2011)	Chev2011-AC	3	65.2	43.7	89.1	19.5	65.2	43.7	65.2	43.7	2	89.1	19.6	22%	108.7–69.5
	Chevalier et al. (2011)	Chev2011-AD	8	59.1	21.9	59.1	21.9	59.1	21.9	59.1	21.9	8	59.1	22.0	37%	81.1–37.2
Xainza (Inner Tibet)	Chevalier et al. (2011)	Chev2011-J	4	432.6	240.3	320.8	107.5	432.6	240.3	432.6	240.3	3	320.8	107.5	34%	428.3–213.2
	Chevalier et al. (2011)	Chev2011-K	5	46.1	2.9	47.2	1.8	46.1	2.9	46.1	2.9	4	47.2	1.9	4%	49.1–45.3
	Chevalier et al. (2011)	Chev2011-L	7	14.2	1.7	13.7	1.0	13.7	1.0	13.7	1.0	6	13.7	1.0	7%	14.7–12.6
	Chevalier et al. (2011)	Chev2011-G	3	87.2	59.1	53.2	8.1	87.2	59.1	87.2	59.1	2	53.2	8.1	15%	61.3–45.2
	Chevalier et al. (2011)	Chev2011-M	11	38.1	14.2	38.1	14.2	38.1	14.2	38.1	14.2	11	38.1	14.3	37%	52.3–23.8
	Chevalier et al. (2011)	Chev2011-N	9	32.2	2.8	31.5	2.0	31.5	2.0	31.5	2.0	8	31.5	2.1	7%	33.6–29.4
	Chevalier et al. (2011)	Chev2011-O	8	29.1	22.3	21.7	8.5	21.7	8.5	21.7	8.5	7	21.7	8.5	39%	30.2–13.2
	Dong et al. (2017b)	Dong2017b-A	4	0.3	0.1	0.3	0.0	0.3	0.1	0.3	0.0	3	0.3	0.1	32%	0.3–0.2
(Hangai)Bumbat valley	Batbaatar et al. (2018)	Batb2018-P	3	58.9	40.3	37.4	21.6	58.9	40.3	58.9	40.3	2	37.4	21.7	58%	59.1–15.7
	Batbaatar et al. (2018)	Batb2018-Q	6	34.7	9.1	34.3	3.8	34.7	9.1	34.7	9.1	4	34.3	4.0	12%	38.3–30.3
	Smith et al. (2016)	Smit2016-C	3	23.9	2.2	22.8	1.4	23.9	2.2	23.9	2.2	2	22.8	1.6	7%	24.4–21.2
(W Tian Shan) Inylchek	Lifton et al. (2014)	Lift2014-A	5	28.8	9.3	31.8	7.4	28.8	9.3	28.8	9.3	4	31.8	7.5	23%	39.3–24.4
	Lifton et al. (2014)	Lift2014-E	5	43.4	30.1	43.4	30.1	43.4	30.1	43.4	30.1	5	43.4	30.1	69%	73.5–13.2
	Lifton et al. (2014)	Lift2014-I	3	104.0	74.9	145.3	31.8	104.0	74.9	104.0	74.9	2	145.3	33.0	23%	178.3–112.2

Table 4.4. Mean ^{10}Be ages for groups with two samples. The groups of ages from literature are identified as in "expage" compilation (J. Heyman, 2018). The groups reported in this study are identified by the study site. The individual and mean ^{10}Be ages and 1σ internal and total uncertainties are in ka. The 1σ total uncertainty compounds the 1σ standard deviation and 1σ internal uncertainties of the individual ages in the group.

Site name (Subregion)	Publication	Group ID	Sample	^{10}Be age	1σ internal	Group mean	1σ total	1σ total (%)
Kax Kurta (Altai)	This study	Kax Kurta-A	XCS-120a	16.79	0.72	17.3	1.0	5.7%
	This study	Kax Kurta-A	XCS-120b	17.74	0.7			
Chagan Uzun (Altai)	Gribenski et al. (2016)	Grib2016-B	AL13C-33	19.2	0.4	25.4	8.8	34.6%
	Gribenski et al. (2016)	Grib2016-B	AL13C-34	31.7	0.4			
Diehanjelegou (E Tian Shan)	This study	Diehanjelegou-C	XCS-101	38.64	1.33	30.0	12.2	40.7%
	This study	Diehanjelegou-C	XCS-102	21.41	0.78			
Alashanje (E Tian Shan)	This study	Alashanje	CS-111b	51.3	1.6	67.7	23.2	34.3%
	This study	Alashanje	CS-111a	84.0	2.3			
	Li et al. (2014)	Li2014-C	AR-10-007	25.0	1.1	28.8	5.5	19.1%
	Li et al. (2014)	Li2014-C	AR-10-011	32.6	0.8			
Daxigou (E Tian Shan)	Li et al. (2011)	Li2011-A	07-13	17.5	0.8	17.3	0.7	3.8%
	Li et al. (2011)	Li2011-A	07-15	17.2	0.4			
	Li et al. (2011)	Li2011-C	07-23	17.3	0.4	16.5	1.2	7.5%
	Li et al. (2011)	Li2011-C	07-25	15.8	0.7			
Muzart (W Tian Shan)	This study	Muzart-A	CS-32	18.2	0.9	21.7	5.5	25.3%
	This study	Muzart-A	CS-33	25.2	4.1			
	This study	Muzart-B	CS-28	15.4	1.2	16.0	1.4	8.7%
	This study	Muzart-B	CS-30	16.6	1.0			
Inylchek (W Tian Shan)	Lifton et al. (2014)	Lift2014-D	TS12-IN-09	19.0	0.5	16.4	4.6	28.0%
	Lifton et al. (2014)	Lift2014-D	TS12-IN-10	13.7	4.8			
	Lifton et al. (2014)	Lift2014-G	TS12-SD-01	16.3	7.7	14.5	4.9	34.1%
	Lifton et al. (2014)	Lift2014-G	TS12-SD-02	12.6	0.6			
Gulbel (W Tian Shan)	This study	Gulbel pass-B	GP-004A	13.24	0.72	31.3	25.6	81.8%
	This study	Gulbel pass-B	GP-004B	49.44	2.3			
	Koppes et al. (2008)	Kopp2008-A	SCT-020901-2	42.1	1.0	38.0	5.9	15.5%
	Koppes et al. (2008)	Kopp2008-A	SCT-020901-3	33.9	0.9			
	Koppes et al. (2008)	Kopp2008-B	SCT-020901-4	31.5	0.8	37.5	8.5	22.8%
	Koppes et al. (2008)	Kopp2008-B	SCT-020901-5	43.5	1.3			
At Bashi (W Tian Shan)	Koppes et al. (2008)	Kopp2008-E	KTS98-CS-62a	5.0	0.2	4.9	0.2	4.6%
	Koppes et al. (2008)	Kopp2008-E	KTS98-CS-62b	4.7	0.1			
Ala Bash (W Tian Shan)	Koppes et al. (2008)	Kopp2008-I	KTS98-CS-87	65.4	0.8	68.2	4.2	6.1%
	Koppes et al. (2008)	Kopp2008-I	KTS98-CS-88	71.1	1.2			
	Koppes et al. (2008)	Kopp2008-L	KTS98-CS-97	92.6	2.2	72.2	29.0	40.2%
	Koppes et al. (2008)	Kopp2008-L	KTS98-CS-98	51.7	1.2			
Gangshiqia (Qilian Shan)	This study	Qilian Shan-A	QS-GG-008	18.7	0.9	18.2	1.0	5.7%
	This study	Qilian Shan-A	QS-GG-009	17.7	0.6			
	This study	Qilian Shan-B	QS-GG-010	14.9	0.9	14.0	1.5	10.9%
	This study	Qilian Shan-B	QS-GG-011	13.1	0.7			
Laolongwan (Qilian Shan)	Owen et al. (2003c)	Owen2003c-F	LJ13	20.6	0.5	20.1	0.8	3.9%
	Owen et al. (2003c)	Owen2003c-F	LJ14	19.6	0.3			
Mawang Kangri (Inner Tibet)	Amidon et al. (2013)	Amid2013-B	18	91.5	1.4	91.9	1.4	1.6%
	Amidon et al. (2013)	Amid2013-B	19	92.4	1.1			
Aksaiqin (W Kunlun)	This study	Aksaiqin-A	AG1-1	39.7	1.6	31.1	12.3	39.7%
	This study	Aksaiqin-A	AG1-2	22.4	0.7			
	This study	Aksaiqin-B	AG1-3	15.5	0.4	29.2	19.3	66.2%
	This study	Aksaiqin-B	AG1-4	42.8	1.1			

Table 4.4 (continued)

Site name (Subregion)	Publication	Group ID	Sample	^{10}Be age	1σ internal	Group mean	1σ total	1σ total (%)
Karakax-B (W Kunlun)	This study	Karakax-B1	KG1-14	314.14	9.89	211.9	144.8	68.3%
	This study	Karakax-B1	KG1-15	109.63	3.89			
	This study	Karakax-B2	KG1-8	97.37	2.94	88.7	12.6	14.2%
	This study	Karakax-B2	KG1-9	79.96	2.16			
	This study	Karakax-B3	KG1-6	86.32	3.11	80.7	8.4	10.4%
	This study	Karakax-B3	KG1-7	75.12	2.24			
	This study	Karakax-B4	KG1-10	81.78	2.21	57.4	34.6	60.2%
	This study	Karakax-B4	KG1-13	32.98	1.54			
Mönh-Saridag (Sayan)	Batbaatar and Gillespie (2016)	BatGil2016-A	070402-ag-RMS-1	12.1	0.6	12.1	0.5	4.1%
	Batbaatar and Gillespie (2016)	BatGil2016-A	070402-ag-RMS-2	12.1	0.4			
	Batbaatar and Gillespie (2016)	BatGil2016-C	070402-ag-RMS-6	1.5	0.1	1.3	0.2	15.0%
	Batbaatar and Gillespie (2016)	BatGil2016-C	070402-ag-RMS-7	1.2	0.1			
Hoit Aguy (Sayan)	Batbaatar and Gillespie (2016)	BatGil2016-H	080709-HA-JB-02	35.4	1.1	34.4	2.0	5.7%
	Batbaatar and Gillespie (2016)	BatGil2016-H	080709-HA-JB-03	33.4	1.6			
Tengis (Sayan)	Batbaatar and Gillespie (2016)	BatGil2016-I	150707-DB-ag-003A	23.5	0.7	21.9	2.3	10.6%
	Batbaatar and Gillespie (2016)	BatGil2016-I	150707-DB-ag-003C	20.3	0.7			
Gyalgar (Hangai)	Batbaatar and Gillespie (2016)	BatGil2016-K	ZAG-ARG-01A	23.9	0.9	21.9	3.0	13.6%
	Batbaatar and Gillespie (2016)	BatGil2016-K	ZAG-ARG-01B	19.8	0.6			
Sutai (Gobi-Altai)	Batbaatar et al. (2018)	Batb2018-H	MOT98-CS-22	21.7	0.8	46.3	34.9	75.3%
	Batbaatar et al. (2018)	Batb2018-H	MOT98-CS-23	70.9	2.6			
Ama Drime (E Himalaya)	Chevalier et al. (2011)	Chev2011-P	T5C-153	396.9	6.1	257.1	197.7	76.9%
	Chevalier et al. (2011)	Chev2011-P	T5C-154	117.3	2.1			
	Chevalier et al. (2011)	Chev2011-Q	T5C-115	30.8	0.8	21.9	12.6	57.5%
	Chevalier et al. (2011)	Chev2011-Q	T5C-118	13.0	0.4			
	Chevalier et al. (2011)	Chev2011-R	T5C-123	17.8	0.4	19.4	2.2	11.5%
	Chevalier et al. (2011)	Chev2011-R	T5C-125	20.9	0.5			
	Chevalier et al. (2011)	Chev2011-T	T5C-133	29.1	0.7	27.4	2.5	9.1%
	Chevalier et al. (2011)	Chev2011-T	T5C-139	25.7	0.8			
Tengis (Sayan)	Gillespie et al. (2008)	Gill2008-A	arg-Tin-01	20.9	0.6	22.2	1.9	8.6%
	Gillespie et al. (2008)	Gill2008-A	arg-Tin-01b	23.5	0.6			
	Gillespie et al. (2008)	Gill2008-B	rmb-Tin-01a	34.0	1.0	30.8	4.6	15.0%
	Gillespie et al. (2008)	Gill2008-B	rmb-Tin-01c	27.6	0.7			
	Gillespie et al. (2008)	Gill2008-C	arg-Uzg-002	16.7	0.6	23.3	9.4	40.3%
	Gillespie et al. (2008)	Gill2008-C	arg-Uzg-003	30.0	0.9			
Bayan Har Shan (Inner Tibet)	Heyman et al. (2011)	Heym2011-E	TB-06-16	50.6	1.1	57.3	9.8	17.0%
	Heyman et al. (2011)	Heym2011-E	TB-06-17	64.1	2.5			
	Heyman et al. (2011)	Heym2011-F	TB-06-05	41.9	1.9	31.0	15.4	49.6%
	Heyman et al. (2011)	Heym2011-F	TB-06-07	20.2	0.8			
	Heyman et al. (2011)	Heym2011-K	TB-07-68	7.0	0.4	5.1	2.7	54.0%
	Heyman et al. (2011)	Heym2011-K	TB-07-69	3.2	0.3			
Otgontenger, Bogd (Hangai)	Rother et al. (2014b)	Roth2014b-D	MON-E-III-II	18.5	0.6	18.4	0.6	3.1%
	Rother et al. (2014b)	Roth2014b-D	MON-E-III-III	18.2	0.5			

Table 4.5. Modern and paleo ELA estimates for glaciers considered in this study. Moraine group IDs with publication year refer to ID numbers in "expage" compilation (J. Heyman, 2018). Locations are given in decimal °N and °E. Altitude is given in m asl. Group mean ages (ka) were calculated after rejecting outliers by the "normalized deviation method. The 1σ total uncertainty of the mean ^{10}Be ages (ka) compounds the 1σ standard deviation and the 1σ total external uncertainties of the individual ages in the group. Toe altitude is given in m. The estimated ELA is given in m asl. ΔELA is given in m. The negative ΔELA_{norm} values indicate that there was no modern glacier in the studied valley and the modern ELA was estimated from the adjacent mountain range. For the ELA methods, THAR stands for Toe–Headwall Altitude Ratio, and MELM stands for Maximum Elevation of Lateral Moraine. The references for the dating studies are given in the last column.

Site name (Subregion)	Moraine group ID	Location	Altitude	Group mean age	1σ total uncertainty	Toe altitude	ELA	ΔELA	ΔELA_{norm}	ELA method	References
Kax Kurta (Altai)	Headwall	47.46170/89.88491	3090	-	-	-	-		-		
	Kax Kurta-C	47.46111/89.79944	2560–2260	21.6 (?)	2.5	2260	2758	811	1.00	THAR=0.6	This study
	Kax Kurta-B	47.46855/89.81950	2540–2460	?	?	2460	2838	731	0.76	THAR=0.6	This study
	Kax Kurta-A	47.46109/89.87250	2810–2790	17.3	1.0	2790	2970	599	0.36	THAR=0.6	This study
	RGI60-10.02561	47.87945/90.02177	3856	0.0	0.0	3139	3569		-1.44	THAR=0.6	RGI 6.0, 2017; This study
			Minimum ELA corresponding to the local LGM (m asl) ==>				2758				
Kanas (Altai)	Headwall	49.11936/87.21318	3260	-	-	-	-		-		
	Grib2018-B	48.69310/87.01430	1390–1380	21.0	0.4	1380	2508	514	1.00	THAR=0.6	Gribenski et al., 2018
	Grib2018-A	48.71110/87.02310	1390–1380	18.5	0.6	1380	2508	514	1.00	THAR=0.6	Gribenski et al., 2018
	RGI60-10.01460	49.11502/87.21350	3250–2665	0.0	0.0	2665	3022		0.32	THAR=0.6	RGI 6.0, 2017; This study
			Minimum ELA corresponding to the local LGM (m asl) ==>				2508				
Chagan Uzun (Altai)	Headwall	49.78780/87.72796	3620	-	-	-	-		-		
	Grib2016-B	49.96234/88.13419	2235	25.4	8.8	-	2325	871	1.00	MELM	Gribenski et al., 2016
	Grib2016-C	49.94995/88.11057	2214	18.3	0.9	-	2325	871	1.00	MELM	Gribenski et al., 2016
	Grib2016-A	49.95213/88.08892	2399	19.1	0.6	-	2635	561	0.76	MELM	Gribenski et al., 2016
	Grib2016-E	50.01659/88.35239	1990–1860	18.8	1.9	1860	2916	280	0.54	THAR=0.6	Gribenski et al., 2016
	Reu2007-E	50.01300/88.29400	1980–1950	20.9	4.5	1950	2952	244	0.52	THAR=0.6	Reuther et al., 2007
	Grib2016-D	49.97573/88.17863	1990-1970	19.4	1.3	1970	2960	236	0.51	THAR=0.6	Gribenski et al., 2016
	RGI60-10.01836	49.79070/87.76070	3620–2560	0.0	0.0	2560	3196		0.33	THAR=0.6	RGI 6.0, 2017; This study
			Minimum ELA corresponding to the local LGM (m asl) ==>				2325				
Diehanjelegou (E Tian Shan)	Headwall	43.10699/87.41183	4040	-	-	-	-		-		
	Diehanjelegou-C	43.15883/87.44098	3200–2990	30.0	12.2	2990	3620	253	1.00	THAR=0.6	This study
	Diehanjelegou-B	43.15751/87.45024	3170–3000	31.9	9.3	3000	3624	249	0.99	THAR=0.6	This study
	RGI60-13.48197	43.10758/87.40946	4040–3622	0.0	0.0	3622	3873		0.40	THAR=0.6	RGI 6.0, 2017; This study
			Minimum ELA corresponding to the local LGM (m asl) ==>				3620				

Table 4.5 (continued)

Site name (Subregion)	Moraine group ID	Location	Altitude	Group mean age	1σ total uncertainty	Toe altitude	ELA	ΔELA	ΔELA_{norm}	ELA method	References
Daxigou (E Tian Shan)	Headwall	43.10466/86.80319	4150	-	-	-	-		-		
	Daxigou-min	43.11206/86.98956	3170–2710	?	?	2710	3574	424	1.00	THAR=0.6	This study
	Li2011-D	43.11000/86.94500	3030–3005	19.3	1.7	2960	3674	324	0.83	THAR=0.6	Li et al., 2011; This study
	Kong2009-C	43.11630/86.92920	3170–3120	17.7	0.8	3120	3738	260	0.72	THAR=0.6	Kong et al., 2009
	Li2011-E	43.11900/86.92000	3210–3180	17.4	1.5	3180	3762	236	0.67	THAR=0.6	Li et al., 2011; This study
	Kong2009a-A	43.11380/86.84280	3590–3520	19.6	3.7	3520	3898	100	0.44	THAR=0.6	Kong et al., 2009; This study
	Li2014-I	43.11500/86.82500	3920–3665	0.3	0.1	3665	3956	42	0.34	THAR=0.6	Li et al., 2014; This study
	RGI60-13.45335	43.11100/86.81000	4150–3770	0.0	0.0	3770	3998		0.26	THAR=0.6	RGI 6.0, 2017; This study
			Minimum ELA corresponding to the local LGM (m asl) ==>				3574				
Muzart (W Tian Shan)	Headwall	42.11801/80.27217	6230	-	-	-	-		-		
	Muzart-A	41.78571/80.90608	1910–1880	21.7	5.5	1880	4490	325	1.00	THAR=0.6	This study
	Muzart-B	41.77471/80.95658	2055–1950	16.0	1.4	1950	4518	297	0.98	THAR=0.6	This study
	RGI60-13.43483	42.15600/80.33400	6230–2692	0.0	0.0	2692	4815		0.81	THAR=0.6	RGI 6.0, 2017; This study
			Minimum ELA corresponding to the local LGM (m asl) ==>				4490				
Tailan (W Tian Shan)	Headwall	42.02066/80.18038	5470	-	-	-	-		-		
	Tailan-A	41.60856/80.49826	1690–1655	?	?	1655	3944	620	1.00	THAR=0.6	This study
	Hube2005-A	41.61900/80.47600	1745–1720	17.7	3.3	1720	3970	594	0.98	THAR=0.6	Hubert-Ferrari et al., 2005
	RGI60-13.43267	42.00500/80.25100	5470–3206	0.0	0.0	3206	4564		0.59	THAR=0.6	RGI 6.0, 2017; This study
			Minimum ELA corresponding to the local LGM (m asl) ==>				3944				
Inylchek (W Tian Shan)	Headwall	42.06455/80.21891	5330								
	Lift2014-I	41.96749/79.10616	2885–2500	145.3	33.0	2500	4198	160	1.00	THAR=0.6	Lifton et al., 2014
	Lift2014-D	42.02038/79.08981	2800–2700	16.4	4.6	2550	4218	140	0.98	THAR=0.6	Lifton et al., 2014
	Lift2014-A	42.02238/79.07863	2650–2610	31.8	7.4	2600	4238	120	0.96	THAR=0.6	Lifton et al., 2014
	RGI60-13.05000	42.06250/80.19330	5330–2901	0.0	0.0	2901	4358		0.86	THAR=0.6	RGI 6.0, 2017; This study
			Minimum ELA corresponding to the local LGM (m asl) ==>				4198				
Choktal (W Tian Shan)	Headwall	42.77621/76.69341	4470	-	-	-	-		-		
	Choktal-min	42.66645/76.69000	2510–2490	?	?	2490	3678	506	1.00	THAR=0.6	This study
	Choktal river-A	42.70139/76.70089	3180–2600	22.2	1.4	2600	3722	462	0.94	THAR=0.6	This study
	Choktal river-B	42.74965/76.69540	3545–3525	15.4	0.6	3525	4092	92	0.48	THAR=0.6	This study
	Choktal river-C	42.74775/76.69392	3650–3560	0.3	0.1	3560	4106	78	0.46	THAR=0.6	This study
	RGI60-13.10123	42.77544/76.69582	4470–3754	0.0	0.0	3754	4184		0.36	THAR=0.6	RGI 6.0, 2017; This study
			Minimum ELA corresponding to the local LGM (m asl) ==>				3678				
Barskoon-Suek (W Tian Shan)	Headwall	41.87271/77.68842	4180	-	-	-	-		-		
	Blom-A	41.61920/77.72883	3419	89.5	7.9	3250	3808	260	1.00	THAR=0.6	Blomdin et al., 2016
	Blom-B	41.64029/77.85004	3501	25.7	7.5	3290	3824	244	0.96	THAR=0.6	Blomdin et al., 2016
	Suek-A	41.70825/77.80538	3432	20.8	1.5	3432	3881	187	0.80	THAR=0.6	This study
	Barskoon Suu-A	41.87017/77.73407	3390–3770	16.6	1.7	3770	4016	52	0.44	THAR=0.6	This study
	Barskoon Suu-C	41.88323/77.70568	3785–3780	0.4	0.1	3780	4020	48	0.43	THAR=0.6	This study
	RGI60-13.06827	41.87555/77.69468	4180–3900	0.0	0.0	3900	4068		0.30	THAR=0.6	RGI 6.0, 2017; This study
			Minimum ELA corresponding to the local LGM (m asl) ==>				3808				

Table 4.5 (continued)

Site name (Subregion)	Moraine group ID	Location	Altitude	Group mean age	1σ total uncertainty	Toe altitude	ELA	ΔELA	ΔELA_{norm}	ELA method	References
Gulbel (W Tian Shan)	Headwall	41.93756/77.21921	4280	-	-	-	-		-		
	Gulbel pass-A	42.03892/77.12420	2980–2550	21.9	0.7	2550	3588	424	1.00	THAR=0.6	This study
	Kopp2008-A–B	42.03800/77.21900	3330–2875	37.5	8.5	2875	3718	294	0.81	THAR=0.6	Koppes et al., 2008
	Gulbel pass-C	42.01432/77.19927	3310–3240	17.3	1.1	3060	3792	220	0.71	THAR=0.6	This study
	Gulbel pass-D	42.01147/77.19960	3275–3245	16.8	1.0	3245	3866	146	0.60	THAR=0.6	This study
	RGI60-13.09143	41.94801/77.21979	4280–3611	0.0	0.0	3611	4012		0.39	THAR=0.6	RGI 6.0, 2017; This study
			Minimum ELA corresponding to the local LGM (m asl) ==>				3588				
Ala Bash (W Tian Shan)	Headwall	41.98920/76.39711	3890								
	Kopp2008-K	42.09400/76.46100	2165–2125	102.1	7.5	2125	3184	596	1.00	THAR=0.6	Koppes et al., 2008
	Kopp2008-I	42.08000/76.45800	2880–2180	68.2	4.2	2180	3206	574	0.97	THAR=0.6	Koppes et al., 2008
	Kopp2008-J	42.08900/76.46600	2355–2190	142.1	17.8	2190	3210	570	0.96	THAR=0.6	Koppes et al., 2008
	Kopp2008-L	42.06400/76.44300	2880–2660	72.2	29.0	2880	3486	294	0.57	MELM	Koppes et al., 2008
	RGI60-13.09249	41.99266/76.39944	3890–3614	0.0	0.0	3614	3780		0.16	THAR=0.6	RGI 6.0, 2017; This study
			Minimum ELA corresponding to the local LGM (m asl) ==>				3184				
At Bashi (W Tian Shan)	Headwall	41.02972/76.03060	4320								
	At Bashi-min	40.75447/75.53657	3630–3560	?	?	3560	4016	170	1.00	THAR=0.6	This study
	Zec2012-B	40.78740/75.47280	4020–3800	19.1	1.8	-	4020	166	0.99	MELM	Zech et al., 2012
	Zec2012-C	40.76500/75.50250	3685–3625	64.8	3.5	3625	4042	144	0.91	THAR=0.6	Zech et al., 2012
	Zec2012-A	40.78270/75.48760	3845–3855	16.4	1.2	3855	4134	52	0.61	THAR=0.6	Zech et al., 2012
	RGI60-13.10354	40.98173/75.80253	4654–3986	0.0	0.0	3986	4186		0.44	THAR=0.6	RGI 6.0, 2017; This study
			Minimum ELA corresponding to the local LGM (m asl) ==>				4016				
Altyn Tagh (Qilian Shan)	Headwall	39.29904/93.74684	5490	-	-	-	-		-		
	Altyn-Tagh-min	39.32046/93.74070	4310–4260	MIS2 (?)	?	4350	5034	47	1.00	THAR=0.6	This study
	Altyn-Tagh-A	39.31450/93.74186	4450–4408	>1.4 (?)	-	4408	5057	24	0.95	THAR=0.6	This study
	RGI60-13.33340	39.30500/93.74400	5490–4467	0.0	0.0	4467	5081		0.90	THAR=0.6	RGI 6.0, 2017; This study
			Minimum ELA corresponding to the local LGM (m asl) ==>				5034				
Dumda (Qilian Shan)	Headwall	38.09836/96.41447	5245	-	-	-	-		-		
	Dumda-A	37.85994/96.28808	4075–4040	131.5	9.3	4040	4763	296	1.00	THAR=0.6	This study
	Dumda-B	37.94356/96.35546	4430–4340	?	?	4340	4883	176	0.75	THAR=0.6	This study
	RGI60-13.35425	38.06800/96.41900	5245–4780	0.0	0.0	4780	5059		0.39	THAR=0.6	RGI 6.0, 2017; This study
			Minimum ELA corresponding to the local LGM (m asl) ==>				4763				
Gangshiqia (Qilian Shan)	Headwall	37.69763/101.49482	5030	-	-	-	-		-		
	Qilian Shan-B	37.66050/101.42356	3620–3530	14.0	1.5	-	3680	1087	1.00	MELM	This study
	Qilian Shan-A	37.66339/101.42669	3710–3570	18.2	1.0	-	3710	1057	0.98	MELM	This study
	Qilian Shan-D	37.69356/101.45208	4320–4080	11.7	4.1	-	4320	447	0.53	MELM	This study
	RGI60-13.23977	37.70100/101.48600	5030–4372	0.0	0.0	4372	4767		0.19	THAR=0.6	RGI 6.0, 2017; This study
			Minimum ELA corresponding to the local LGM (m asl) ==>				3680				
Laolongwan (Qilian Shan)	Headwall	37.52571/101.78778	4520	-	-	-	-		-		
	Owen2003d-A	37.44100/101.76200	3360–3340	11.0	0.4	3340	4048	425	1.00	THAR=0.6	Owen et al., 2003d
	Owen2003d-E	37.46000/101.76600	3460	19.1	0.7	3460	4096	377	0.90	THAR=0.6	Owen et al., 2003d
	RGI60-13.24015	37.52400/101.78700	4520–4403	?	?	4403	4473		0.10	THAR=0.6	RGI 6.0, 2017; This study
			Minimum ELA corresponding to the local LGM (m asl) ==>				4048				

Table 4.5 (continued)

Site name (Subregion)	Moraine group ID	Location	Altitude	Group mean age	1σ total uncertainty	Toe altitude	ELA	ΔELA	ΔELA_{norm}	ELA method	References
Haiyuan (Qilian Shan)	Headwall	37.50956/101.81563	4580	-	-	-	-		-		
	Qilian Shan-3A	37.53946/101.85044	3790–3590	?	?	-	3790	620	1.00	MELM	This study
	Lass2002-A	37.53300/101.84900	4000–3830	9.5	4.2	-	4000	410	0.73	MELM	Lasserre et al., 2002
	RGI60-13.31354	37.51300/101.81700	4580–4155	0.0	0.0	4155	4410		0.22	THAR=0.6	RGI 6.0, 2017; This study
			Minimum ELA corresponding to the local LGM (m asl) ==>				3790				
La Ji (Qilian Shan)	Headwall	36.30868/101.27483	4730	-	-	-	-		-		
	Qilian Shan-4A	36.35885/101.35535	3770–3710	?	?	3710	4220	1278	1.00	THAR=0.6	This study
	Owen2003c-C	36.37000/101.31200	4000–3920	25.4	3.1	3920	4304	1194	0.79	THAR=0.6	Owen et al., 2003c
	RGI60-13.23909	34.73500/99.542000	6198–4520	0.0	0.0	4520	5600		-2.13	THAR=0.6	RGI 6.0, 2017; This study
			Minimum ELA corresponding to the local LGM (m asl) ==>				4220				
Mawang Kangri (Inner Tibet)	Headwall	34.31438/80.04106	6365	-	-	-	-		-		
	Amid2013-C	34.42557/80.04985	5330–5285	?	?	5285	5933	68	1.00	THAR=0.6	Amidon et al., 2013
	Amid2013-B	34.42230/80.04760	5300–5290	91.9	1.4	5290	5935	66	1.00	THAR=0.6	Amidon et al., 2013
	Amid2013-A	34.41270/80.04640	5340–5320	62.7	8.3	5320	5947	54	0.97	THAR=0.6	Amidon et al., 2013
	RGI60-13.53522	34.33800/80.04600	6365–5454	0.0	0.0	5454	6001		0.84	THAR=0.6	RGI 6.0, 2017; This study
			Minimum ELA corresponding to the local LGM (m asl) ==>				5933				
Aksaiqin (W Kunlun)	Headwall	35.50944/80.40755	6350	-	-	-	-		-		
	Aksaiqin-min (?)	35.37847/80.31855	5270–5230	?	?	5230	5902	96	1.00	THAR=0.6	This study
	Aksaiqin-A	35.39662/80.34292	5400–5390	31.1	12.3	5390	5966	32	0.86	THAR=0.6	This study
	Aksaiqin-B	35.39718/80.36552	5440–5410	> 29 (?)	?	5410	5974	24	0.84	THAR=0.6	This study
	RGI60-13.53668	35.45700/80.38900	6350–5471	0.0	0.0	5471	5998		0.78	THAR=0.6	RGI 6.0, 2017; This study
			Minimum ELA corresponding to the local LGM (m asl) ==>				5902				
Karakax-A (W Kunlun)	Headwall	36.49935/77.63702	6030	-	-	-	-		-		
	Karakax-A	36.43685/77.68216	5030–4840	90.2	3.6	-	5030	696	1.00	MELM	This study
	RGI60-13.40102	36.50000/77.66800	6020–5271	0.0	0.0	5271	5726		0.30	THAR=0.6	RGI 6.0, 2017; This study
			Minimum ELA corresponding to the local LGM (m asl) ==>				5030				
Karakax-B (W Kunlun)	Headwall	36.49193/77.60021	6080	-	-	-	-		-		
	Karakax-B-min	36.41326/77.63702	4740–4700	?	?	4700	5528	190	1.00	THAR=0.6	This study
	Karakax-B2	36.43024/77.65266	5100-5000	88.7	12.6	4990	5644	74	0.79	THAR=0.6	This study
	Karakax-B3	36.42616/77.64395	5130–5080	80.7	8.4	5080	5680	38	0.72	THAR=0.6	This study
	RGI60-13.40092	36.48000/77.63000	6080–5176	0.0	0.0	5176	5718		0.66	THAR=0.6	RGI 6.0, 2017; This study
			Minimum ELA corresponding to the local LGM (m asl) ==>				5528				
Gichginii range (Gob-Altai)	Headwall	45.40005/97.07027	3440	-	-	-	-		-		
	Moraine G1	45.40310/97.07100	3290–3320	?	?	3290	3320	425	1.00	MELM	Batbaatar et al., 2018
	Batb2018-A	45.40390/97.07030	3297–3330	7.5	0.8	3297	3330	415	0.92	MELM	Batbaatar et al., 2018
	Batb2018-B	45.40150/97.06970	3310–3360	2.6	0.7	3310	3360	385	0.67	MELM	Batbaatar et al., 2018
	Batb2018-C	45.40120/97.06970	3320–3365	1.5	0.4	3320	3365	380	0.63	MELM	Batbaatar et al., 2018
	Moraine G5	45.40180/97.06870	3335–3370	?	?	3335	3370	375	0.58	MELM	Batbaatar et al., 2018
	RGI60-10.02900	46.63943/93.54810	3670–3980	0.0	0.0	3670	3745		-2.55	THAR=0.58	RGI 6.0, 2017; This study
			Minimum ELA corresponding to the local LGM (m asl) ==>				3320				
Sutai range, NE (Gobi-Altai)	Headwall	46.63358/93.55765	3800	-	-	-	-		-		
	Moraine N1	46.64180/93.57100	3110–3220	?	?	3110	3510	235	1.00	THAR=0.58	Batbaatar et al., 2018
	Batb2018-E	46.64180/93.56590	3240–3315	24.2	1.8	3245	3567	179	0.80	THAR=0.58	Batbaatar et al., 2018
	RGI60-10.02900	46.63943/93.54810	3670–3980	0.0	0.0	3670	3745		0.19	THAR=0.58	RGI 6.0, 2017; This study
			Minimum ELA corresponding to the local LGM (m asl) ==>				3510				

Table 4.5 (continued)

Site name (Subregion)	Moraine group ID	Location	Altitude	Group mean age	1σ total uncertainty	Toe altitude	ELA	ΔELA	ΔELA_{norm}	ELA method	References
Sutai range, SW (Gobi-Altai)	Headwall	46.62312/93.59323	4100	-	-	-	-		-		
	Bedrock	46.60120/93.54900	3105	> 22 (?)	-	?	?	#VALUE!	?		Batbaatar et al., 2018
	Batb2018-J	46.61320/93.55030	3238–3275	16.2	2.7	-	3275	592	1.00	MELM	Batbaatar et al., 2018
	RGI60-10.02893	46.62310/93.59320	3545–4200	0.0	0.0	3545	3867		0.28	THAR=0.58	RGI 6.0, 2017; This study
			Minimum ELA corresponding to the local LGM (m asl) ==>				3275				
Ih Bogd range (Gobi-Altai)	Headwall	44.95975/100.26923	3500	-	-	-	-				
	Moraine IB1	44.95590/100.26390	3325–3365	?	?	3325	3427	565	1.00	THAR=0.58	Batbaatar et al., 2018
	Batb2018-K	44.95630/100.26680	3380–3430	14.3	1.9	3380	3450	541	0.69	THAR=0.58	Batbaatar et al., 2018
	RGI60-10.02898	46.61224/93.60343	4180–3730	0.0	0.0	3730	3991		-6.68	THAR=0.58	RGI 6.0, 2017; This study
			Minimum ELA corresponding to the local LGM (m asl) ==>				3427				
Otgontenger, Bogd (Hangai)	Headwall	47.60961/97.54489	3400	-	-	-	-				
	Roth2014b-E	47.68350/97.20980	2140	37.5	2.5	2070	2841	998	1.00	THAR=0.58	Rother et al., 2014
	Roth2014b-A	47.68330/97.20670	2070–2150	22.2	2.5	2070	2841	998	1.00	THAR=0.58	Rother et al., 2014; Batbaatar et al., 2018
	Roth2014b-B	47.68830/97.24960	2085–2150	18.4	3.3	2150	2875	964	0.94	THAR=0.58	Rother et al., 2014
	RGI60-10.02907	47.60800/97.55230	3645–3980	0.0	0.0	3645	3839		-0.79	THAR=0.58	RGI 6.0, 2017; This study
			Minimum ELA corresponding to the local LGM (m asl) ==>				2841				
Otgontenger, Bitüüt (Hangai)	Headwall	47.65663/97.59901	3100	-	-	-	-				
	Moraine BI1	47.57210/97.67510	2510–2555	?	?	2510	2852	987	1.00	THAR=0.58	Batbaatar et al., 2018
	Batb2018-M	47.57550/97.66770	2525–2610	30.6	2.2	2525	2859	981	0.97	THAR=0.58	Batbaatar et al., 2018
	Batb2018-O	47.60350/97.64050	2721–2730	16.6	1.1	2721	2941	898	0.64	THAR=0.58	Batbaatar et al., 2018
	RGI60-10.02907	47.60800/97.55230	3645–3980	0.0	0.0	3645	3839		-2.98	THAR=0.58	RGI 6.0, 2017; This study
			Minimum ELA corresponding to the local LGM (m asl) ==>				2852		0		
Bumbat valley (Hangai)	Headwall	47.29765/100.46943	3250	-	-	-	-				
	Moraine BU1	47.43550/100.34710	2110–2210	>> 22 (?)	-	2110	2771	1068	1.00	THAR=0.58	Batbaatar et al., 2018
	Batb2018-Q	47.41800/100.35250	2135–2220	34.9	4.5	2135	2782	1058	0.98	THAR=0.58	Batbaatar et al., 2018
	RGI60-10.02907	47.60800/97.55230	3645–3980	0.0	0.0	3645	3839		-1.23	THAR=0.58	RGI 6.0, 2017; This study
			Minimum ELA corresponding to the local LGM (m asl) ==>				2771				
Baikal	Headwall	51.29832/105.18027	2100	-	-	-	-				
	Hori2004-A	51.50000/104.90000	500	15.1	2.1	450	1428	1760	1.00	THAR=0.58	Horiuchi et al., 2004
	RGI60-10.02911	51.72290/100.60045	3431–2978	0	0	2978	3188		-1.62	THAR=0.58	RGI 6.0, 2017; This study
			Minimum ELA corresponding to the local LGM (m asl) ==>				1134				
Ama Drime (E Himalaya)	Headwall	28.17317/87.59605	6130	-	-	-	-				
	Ama Dime min	28.11033/87.69552	4800	MIS 3 (?)	?	4800	5598	319	1.00	THAR=0.6	This study
	Chev2011-T	28.13100/87.67100	5006	27.4	2.5	4940	5654	263	0.89	THAR=0.6	Chevalier et al., 2011
	Chev2011-S	28.14600/87.65300	5151	17.8	2.1	5040	5694	223	0.82	THAR=0.6	Chevalier et al., 2011
	Chev2011-R	28.15000/87.65100	5223	19.4	2.2	5040	5694	223	0.82	THAR=0.6	Chevalier et al., 2011
	RGI60-15.10593	28.16400/87.59500	6292–5597	0	0	5597	5917		0.40	THAR=0.6	RGI 6.0, 2017; This study
			Minimum ELA corresponding to the local LGM (m asl) ==>				5598				
Bayan Har Shan-1 (Inner Tibet)	Headwall	34.25862/97.62143	5130	-	-	-	-				
	Heym2011-J	33.87692/97.23156	4501	52.3	3.7	4500	4878	650	1.00	THAR=0.6	Heyman et al., 2011
	Heym2011-M	33.96478/97.32528	4560	154.3	18.6	4560	4902	626	0.90	THAR=0.6	Heyman et al., 2011
	Heym2011-C	33.98667/97.44905	4573	13.9	1.7	4573	4907	621	0.88	THAR=0.6	Heyman et al., 2011
	RGI60-13.23950	34.77100/99.46100	6058–4926	0	0	4926	5528		-1.58	THAR=0.6	RGI 6.0, 2017; This study
			Minimum ELA corresponding to the local LGM (m asl) ==>				4878				

Table 4.5 (continued)

Site name (Subregion)	Moraine group ID	Location	Altitude	Group mean age	1σ total uncertainty	Toe altitude	ELA	ΔELA	ΔELA_{norm}	ELA method	References
Bayan Har Shan-2 (Inner Tibet)	Headwall	34.25862/97.62143	5130	-	-	-	-				
	Heym2011-G	34.15697/98.02033	4590	57.2	6.9	4590	4914	602	1.00	THAR=0.6	Heyman et al., 2011
	Heym2011-O	34.16431/98.13153	4646	34.3	6.7	4650	4938	578	0.89	THAR=0.6	Heyman et al., 2011
	Heym2011-L	34.15606/97.70853	4657	23.5	1.3	4660	4942	574	0.87	THAR=0.6	Heyman et al., 2011
	RGI60-13.23886	34.83600/99.46000	6252–4462	0	0	4460	5516		-1.79	THAR=0.6	RGI 6.0, 2017; This study
			Minimum ELA corresponding to the local LGM (m asl) ==>				4914				
Bayan Har Shan-3 (Inner Tibet)	Headwall	34.25862/97.62143	5130	-	-	-	-				
	Heym2011-D	34.60492/98.01506	4248	69.3	8.7	4250	4778	738	1.00	THAR=0.6	Heyman et al., 2011
	Heym2011-E	34.52578/97.98753	4332	57.3	9.8	4330	4810	706	0.91	THAR=0.6	Heyman et al., 2011
	Heym2011-I	34.39153/97.75956	4509	71.3	3.7	4510	4882	634	0.70	THAR=0.6	Heyman et al., 2011
	Heym2011-N	34.33731/97.60611	4546	57.8	2.1	4550	4898	618	0.66	THAR=0.6	Heyman et al., 2011
	RGI60-13.23886	34.83600/99.46000	6252–4462	0	0	4460	5516		-1.10	THAR=0.6	RGI 6.0, 2017; This study
			Minimum ELA corresponding to the local LGM (m asl) ==>				4778				
Borohoro-1 (E Tian Shan)	Headwall	43.73968/84.36614	3910	-	-	-	-				
	Borohoro-1_min	43.81986/84.47217	2320	?	?	2320	3274	470	1.00	THAR=0.6	This study
	Li2016-B	43.73870/84.40320	3477	0.3	0.1	3400	3706	38	0.32	THAR=0.6	Li et al., 2016
	RGI60-13.47247	43.73100/84.39100	3901–3495	0	0	3495	3744		0.26	THAR=0.6	RGI 6.0, 2017; This study
			Minimum ELA corresponding to the local LGM (m asl) ==>				3274				
Borohoro-2 (E Tian Shan)	Headwall	43.25063/84.87091	3690	-	-	-	-				
	Zhan2016a-D	43.17630/84.88080	2871	58.7	4.9	2730	3306	522	1.00	THAR=0.6	Zhang et al., 2016a
	RGI60-13.29827	43.45800/84.78500	4094–3573	0	0	3570	3828		-0.36	THAR=0.6	RGI 6.0, 2017; This study
			Minimum ELA corresponding to the local LGM (m asl) ==>				3306				
Borohoro-3 (E Tian Shan)	Headwall	43.19631/85.76349	4140	-	-	-	-				
	Borohoro-2_min	43.10803/85.62103	2955	?	?	2970	3672	493	1.00	THAR=0.6	This study
	Zhan2016a-F	43.11690/85.75960	3159	18.3	4.3	3160	3748	417	0.84	THAR=0.6	Zhang et al., 2016a
	RGI60-13.44596	43.23100/85.46400	4504–3737	0	0	3737	4165		-0.05	THAR=0.6	RGI 6.0, 2017; This study
			Minimum ELA corresponding to the local LGM (m asl) ==>				3672				
Chuluut (Hangai)	Headwall	47.14022/100.08214	3480	-	-	-	-				
	Smit2016-C	47.41260/100.25660	2274	22.8	1.6	2270	2983	856	1.00	THAR=0.58	Smith et al., 2016
	RGI60-10.02907	47.60800/97.55230	3645–3980	0.0	0.0	3645	3839		-2.98	THAR=0.58	RGI 6.0, 2017; This study
			Minimum ELA corresponding to the local LGM (m asl) ==>				2983				
Cho Oyu (E Himalaya)	Headwall	28.08364/86.65164	6680	-	-	-	-				
	Cho Oyu min	28.40828/86.64946	4660	?	?	4660	5872	194	1.00	THAR=0.58	This study
	Chev2011-U	28.34800/86.62700	4948	33.2	0.9	4900	5968	98	0.88	THAR=0.58	Chevalier et al., 2011
	RGI60-15.10147	28.12100/86.59000	8181–5145	0	0	5145	6066		0.76	THAR=0.58	RGI 6.0, 2017; This study
			Minimum ELA corresponding to the local LGM (m asl) ==>				5872				
Gyalgar (Hangai)	Headwall	48.22352/98.80971	3070	-	-	-	-				
	BatGil2016-L	48.11805/98.81583	2253	19.6	3.9	2250	2726	1114	1.00	THAR=0.58	Batbaatar and Gillespie, 2016
	BatGil2016-N	48.18288/98.80468	2585	22.8	3.4	2430	2801	1038	0.78	THAR=0.58	Batbaatar and Gillespie, 2016
	BatGil2016-K	48.18377/98.78145	2472	21.9	3	2430	2801	1038	0.78	THAR=0.58	Batbaatar and Gillespie, 2016
	RGI60-10.02907	47.60800/97.55230	3645–3980	0.0	0.0	3645	3839		-2.23	THAR=0.58	RGI 6.0, 2017; This study
			Minimum ELA corresponding to the local LGM (m asl) ==>				2726				
Högiin (Darhad)	Headwall	50.9046/98.45774	2650	-	-	-	-				
	Gill2008-F	51.00600/99.12500	1716	125.2	21.6	1680	2243	945	1.00	THAR=0.58	Gillespie et al., 2008
	Gill2008-G	50.98100/99.15200	1679	22.4	8.8	1680	2243	945	1.00	THAR=0.58	Gillespie et al., 2008
	RGI60-10.02911	51.72290/100.60045	3431–2978	0	0	2978	3188		-1.32	THAR=0.58	RGI 6.0, 2017; This study
			Minimum ELA corresponding to the local LGM (m asl) ==>				2243				

Table 4.5 (continued)

Site name (Subregion)	Moraine group ID	Location	Altitude	Group mean age	1σ total uncertainty	Toe altitude	ELA	ΔELA	ΔELA_{norm}	ELA method	References
Höh lake (Hangai)	Headwall	47.54828/98.34070	3470	-	-	-	-				
	Hoh lake min	47.42426/98.57352	2540	?	?	2540	3079	760	1.00	THAR=0.58	This study
	Smit2016-B	47.46310/98.56910	2676	43.6	7.8	2670	3134	705	0.86	THAR=0.58	Smith et al., 2016
	RGI60-10.02907	47.60800/97.55230	3645–3980	0.0	0.0	3645	3839		-0.95	THAR=0.58	RGI 6.0, 2017; This study
			Minimum ELA corresponding to the local LGM (m asl) ==>				3079				
Hoit Aguy (Sayan)	Headwall	51.57306/98.67007	2750	-	-	-	-				
	BatGil2016-H	51.55206/98.71469	2332	34.4	2	2140	2494	694	1.00	THAR=0.58	Batbaatar and Gillespie, 2016
	RGI60-10.02911	51.72290/100.60045	3431–2978	0	0	2978	3188		-1.71	THAR=0.58	RGI 6.0, 2017; This study
			Minimum ELA corresponding to the local LGM (m asl) ==>				2494				
Jarai (Darhad)	Headwall	51.64175/99.91152	2620	-	-	-	-				
	Gill2008-D	51.39957/99.77220	1633	25.2	9.4	1630	2204	984	1.00	THAR=0.58	Gillespie et al., 2008
	Gill2008-E	51.39935/99.79990	1676	19.7	2	1670	2221	967	0.96	THAR=0.58	Gillespie et al., 2008
	RGI60-10.02911	51.72290/100.60045	3431–2978	0	0	2978	3188		-1.37	THAR=0.58	RGI 6.0, 2017; This study
			Minimum ELA corresponding to the local LGM (m asl) ==>				2204				
Jombolok (Sayan)	Headwall	52.68309/98.94914	2650	-	-	-	-				
	Arzh2012-B	52.75221/99.70855	1288	24.9	1.9	1280	2075	657	1.00	THAR=0.58	Arzhannikov et al., 2012
	Arzh2012-C	52.74003/99.63303	1410	26.1	1.8	1280	2075	657	1.00	THAR=0.58	Arzhannikov et al., 2012
	BatGil2016-E	52.73107/99.61505	1410	20.9	2	1280	2075	657	1.00	THAR=0.58	Batbaatar and Gillespie, 2016
	RGI60-10.02962	52.50381/98.81916	3029–2362	0	0	2360	2731		-0.14	THAR=0.58	RGI 6.0, 2017; This study
			Minimum ELA corresponding to the local LGM (m asl) ==>				1947				
Kailas (C Himalaya)	Headwall	31.11871/81.38241	5810	-	-	-	-				
	Chev2011-Y	31.00800/81.24000	4800	46.5	11.2	4650	5346	352	1.00	THAR=0.6	Chevalier et al., 2011
	Chev2011-X	30.99400/81.25600	4793	17.4	1.9	4700	5366	332	0.96	THAR=0.6	Chevalier et al., 2011
	RGI60-14.27874	31.12100/81.38300	6021–5531	0	0	5530	5698		0.24	THAR=0.6	RGI 6.0, 2017; This study
			Minimum ELA corresponding to the local LGM (m asl) ==>				5346				
Kalurong (Inner Tibet)	Headwall	28.94196/90.16749	6830	-	-	-	-				
	Kalurong min	28.95499/90.11634	4820	?	?	4820	6026	132	1.00	THAR=0.6	This study
	Liu2017-C	28.95000/90.13500	4988	21.6	1.1	4988	6093	65	0.92	THAR=0.6	Liu et al., 2017
	Liu2017-D	28.94900/90.13400	5017	16.7	1.2	4988	6093	65	0.92	THAR=0.6	Liu et al., 2017
	RGI60-13.26374	28.94200/90.15400	6846–5153	0	0	5150	6158		0.84	THAR=0.6	RGI 6.0, 2017; This study
			Minimum ELA corresponding to the local LGM (m asl) ==>				6026				
Menyuan (E Tibet)	Headwall	35.52433/102.70265	4520	-	-	-	-				
	Wang2013-A	35.57510/102.74390	3614	26.5	1.5	-	3850	1142	1.00	MELM	Wang et al., 2013
	Wang2013-B	35.56920/102.73950	3719	51.1	7.6	-	3850	1142	1.00	MELM	Wang et al., 2013
	Wang2013-C	35.56910/102.73560	3680	24.9	2	3420	4080	912	0.66	THAR=0.6	Wang et al., 2013
	Wang2013-D	35.58290/102.72710	3304	19.7	1.2	3420	4080	912	0.66	THAR=0.6	Wang et al., 2013
	RGI60-13.23874	33.29300/101.10800	5295-4679	0	0	4679	4992		-0.70	THAR=0.6	RGI 6.0, 2017; This study
			Minimum ELA corresponding to the local LGM (m asl) ==>				3850				
Mönh-Saridag (Sayan)	Headwall	51.72290/100.60045	3340	-	-	-	-				
	Monh-Saridag min	52.08062/100.36462	1600	> MIS 2 (?)	?	1600	2609	579	1.00	THAR=0.58	This study
	BatGil2016-D	51.73867/100.60086	2640	26.9	1.6	2590	3025	163	0.43	THAR=0.58	Batbaatar and Gillespie, 2016
	BatGil2016-A	51.73609/100.59985	2640	12.1	0.5	2630	3042	146	0.41	THAR=0.58	Batbaatar and Gillespie, 2016
	BatGil2016-B	51.73092/100.60073	2800	10.1	0.7	2730	3084	104	0.35	THAR=0.58	Batbaatar and Gillespie, 2016
	BatGil2016-C	51.72860/100.59832	2900	1.3	0.2	2840	3130	58	0.29	THAR=0.58	Batbaatar and Gillespie, 2016
	RGI60-10.02911	51.72290/100.60045	3431–2978	0	0	2978	3188		0.21	THAR=0.58	RGI 6.0, 2017; This study
			Minimum ELA corresponding to the local LGM (m asl) ==>				2609				

Table 4.5 (continued)

Site name (Subregion)	Moraine group ID	Location	Altitude	Group mean age	1σ total uncertainty	Toe altitude	ELA	ΔELA	ΔELA_{norm}	ELA method	References
Nyainqentanghla (Inner Tibet)	Headwall	29.90656/90.03821	5850	-	-	-	-				
	Nyainqentanghla min	29.80792/90.03907	4700	?	?	4700	5390	207	1.00	THAR=0.6	This study
	Dong2017a-A	29.85056/90.06389	4940	19.6	1.8	4850	5450	147	0.87	THAR=0.6	Dong et al., 2017a
	Dong2017a-B	29.84264/90.06400	4840	20.3	1.2	4800	5430	167	0.91	THAR=0.6	Dong et al., 2017a
	RGI60-13.28457	29.91200/90.04000	6693–5217	0	0	5217	5597		0.55	THAR=0.6	RGI 6.0, 2017; This study
						Minimum ELA corresponding to the local LGM (m asl) ==>	5390				
Sailag (Sayan)	Headwall	52.84551/99.68752	2780	-	-	-	-				
	Arzh2012-D	52.77712/99.71842	1355	17.8	3.3	1355	2182	551	1.00	THAR=0.58	Arzhannikov et al., 2012; Batbaatar and Gillespie, 2016
	RGI60-10.02962	52.50381/98.81916	3029–2362	0	0	2360	2731		0.08	THAR=0.58	RGI 6.0, 2017; This study
						Minimum ELA corresponding to the local LGM (m asl) ==>	2182				
Tanggula Shan-1 (Inner Tibet)	Headwall	32.82702/91.98870	5690	-	-	-	-				
	Schä2002-E	32.93200/91.96600	5198	75.2	15.3	5145	5472	52	1.00	THAR=0.6	Schäfer, 2000; Colgan et al., 2006
	RGI60-13.24560	32.83500/91.97200	5775–5275	0	0	5275	5524		0.76	THAR=0.6	RGI 6.0, 2017; This study
						Minimum ELA corresponding to the local LGM (m asl) ==>	5472				
Tanggula Shan-2 (Inner Tibet)	Headwall	32.82305/91.95122	5535	-	-	-	-				
	Owen2005-M	32.82033/91.88920	5050	98.9	48.1	5050	5341	235	1.00	THAR=0.6	Owen et al., 2005
	Owen2005-L	32.82765/91.90705	5100	57.5	3.1	5100	5361	215	0.90	THAR=0.6	Owen et al., 2005
	RGI60-13.49424	32.81300/91.95500	5718–5391	0	0	5390	5576		-0.21	THAR=0.6	RGI 6.0, 2017; This study
						Minimum ELA corresponding to the local LGM (m asl) ==>	5341				
Tangra Yum Co (Inner Tibet)	Headwall	32.82702/91.98870	6210	-	-	-	-				
	Tangra Yum Co min	30.67241/86.53905	5090	?	?	-	5200	811	1.00	MELM	This study
	Rade2015-C	30.67574/86.53188	5160	19.5	1.5	-	5600	411	0.60	MELM	Rades et al., 2015
	RGI60-13.50116	30.66900/86.47700	6344–5713	0	0	5713	6011		0.20	THAR=0.6	RGI 6.0, 2017; This study
						Minimum ELA corresponding to the local LGM (m asl) ==>	5200				
Tengis (Sayan)	Headwall	52.04949/99.08284	2750	-	-	-	-				
	BatGil2016-I	51.45358/99.03870	1630	21.9	2.3	1630	2280	1049	1.00	THAR=0.58	Batbaatar and Gillespie, 2016
	Gill2008-A	51.47922/99.05553	1645	22.2	1.9	1630	2280	1049	1.00	THAR=0.58	Gillespie et al., 2008
	RGI60-10.02915	51.71783/100.60229	3405–3230	0	0	3230	3329		-1.23	THAR=0.58	RGI 6.0, 2017; This study
						Minimum ELA corresponding to the local LGM (m asl) ==>	2280				
Karlik Shan (E Tian Shan)	Headwall	43.09262/94.31996	4530	-	-	-	-				
	Karlik Shan min	43.22553/94.40281	2430	>23 ka (?)	-	2430	3690	483	1.00	THAR=0.6	Chen et al., 2015; This study
	Chen2015-B	43.14300/94.38030	3330	14.5	0.5	3190	3994	179	0.64	THAR=0.6	Chen et al., 2015
	RGI60-13.45052	43.10600/94.32600	4713–3637	0	0	3637	4173		0.43	THAR=0.6	RGI 6.0, 2017; This study
						Minimum ELA corresponding to the local LGM (m asl) ==>	3690				
W Himalaya	Headwall	32.42909/79.57832	5870	-	-	-	-				
	Chev2011-AB	32.48522/79.66877	4310	152	24	4280	5234	567	1.00	THAR=0.6	Chevalier et al., 2011
	Chev2011-AD	32.48655/79.64740	4500	59.1	22	4380	5274	527	0.94	THAR=0.6	Chevalier et al., 2011
	Chev2011-AC	32.48998/79.64917	4440	89.1	19.6	4440	5298	503	0.90	THAR=0.6	Chevalier et al., 2011
	RGI60-14.26038	32.40600/79.65400	6217–5697	0	0	5697	5801		0.11	THAR=0.6	RGI 6.0, 2017; This study
						Minimum ELA corresponding to the local LGM (m asl) ==>	5234				

Table 4.5 (continued)

Site name (Subregion)	Moraine group ID	Location	Altitude	Group mean age	1σ total uncertainty	Toe altitude	ELA	ΔELA	ΔELA_{norm}	ELA method	References
	Headwall	30.61830/88.46012	5900	-	-	-	-				
	Chev2011-J	30.59900/88.52900	4975	320.8	107.5	4875	5490	309	1.00	THAR=0.6	Chevalier et al., 2011
Xainza-1	Chev2011-K	30.59500/88.51900	5000	47.2	1.9	4920	5508	291	0.96	THAR=0.6	Chevalier et al., 2011
(Inner Tibet)	Chev2011-L	30.61100/88.49700	5250	13.7	1	5250	5640	159	0.63	THAR=0.6	Chevalier et al., 2011
	RGI60-13.49524	30.62100/88.46300	5904–5648	0	0	5648	5799		0.25	THAR=0.6	RGI 6.0, 2017; This study
					Minimum ELA corresponding to the local LGM (m asl) ==>		5490				
	Headwall	30.04722/88.44836	5810	-	-	-	-				
Xainza-2	Chev2011-M	30.07900/88.42500	5330	38.1	14.3	5050	5506	223	1.00	THAR=0.6	Chevalier et al., 2011
(Inner Tibet)	RGI60-13.49505	30.08100/88.46600	5826–5584	0	0	5584	5729		0.27	THAR=0.6	RGI 6.0, 2017; This study
					Minimum ELA corresponding to the local LGM (m asl) ==>		5506				
	Headwall	29.87657/88.34573	6000	-	-	-	-				
Xainza-3	Chev2011-N	29.93600/88.34900	5190	31.5	2.1	4965	5586	256	1.00	THAR=0.6	Chevalier et al., 2011
(Inner Tibet)	RGI60-13.28247	29.88200/88.35100	6007–5606	0	0	5606	5842		0.38	THAR=0.6	RGI 6.0, 2017; This study
					Minimum ELA corresponding to the local LGM (m asl) ==>		5586				
	Headwall	29.76492/88.27966	6155	-	-	-	-				
Xainza-4	Chev2011-O	29.82100/88.19400	5370	21.7	8.5	4930 (?)	5440	520	1.00	MELM	Chevalier et al., 2011
(Inner Tibet)	RGI60-13.28213	29.76700/88.27500	6158–5668	0	0	5668	5960		0.27	THAR=0.6	RGI 6.0, 2017; This study
					Minimum ELA corresponding to the local LGM (m asl) ==>		5440				
	Headwall	43.03203/86.94117	4220	-	-	-	-		-		
	Alashanje-min	42.88266/86.92311	3140–2950	?	?	2950	3712	337	1.00	THAR=0.6	This study
	Li2014-E	42.92100/86.92400	3290–3100	46.8	6.5	3100	3772	277	0.88	THAR=0.6	Li et al., 2014; This study
	Alashanje	42.92695/86.87829	3280–3200	67.7	23.2	3200	3812	237	0.80	THAR=0.6	This study
Alashanje	Li2014-F	42.94100/86.89800	3400	76.1	5.9	3230	3824	225	0.78	THAR=0.6	Li et al., 2014; This study
(E Tian Shan)	Li2014-D	42.99300/86.91900	3477	25.8	2.4	3477	3923	126	0.59	THAR=0.6	Li et al., 2014; This study
	Li2014-B	43.02800/86.92300	3515–3490	17.5	5.3	3490	3928	121	0.57	THAR=0.6	Li et al., 2014; This study
	Li2014-C	42.99900/86.91700	3610	28.8	5.5	3610	3976	73	0.48	THAR=0.6	Li et al., 2014; This study
	RGI60-13.48109	43.03500/86.94100	4220–3793	0.0	0.0	3793	4049		0.34	THAR=0.6	RGI 6.0, 2017; This study
					Minimum ELA corresponding to the local LGM (m asl) ==>		3712				
	Headwall	43.07423/83.56789	3765								
Takelekete	Zhan2016a-B	42.99170/83.58550	2910–2860	52.0	12.5	2860	3403	306	1.00	THAR=0.6	Zhang et al., 2016
(W Tian Shan)	RGI60-13.44521	43.07500/83.57100	3765–3624	0.0	0.0	3624	3709		0.16	THAR=0.6	RGI 6.0, 2017; This study
					Minimum ELA corresponding to the local LGM (m asl) ==>		3403				
	Headwall	41.78191/78.16933	4400	-	-	-	-		-		
	Blom-A	41.61920/77.72883	3419	89.5	7.9	3250	3940	214	1.00	THAR=0.6	Blomdin et al., 2016
	Blom-B	41.64029/77.85004	3501	25.7	7.5	3290	3956	198	0.97	THAR=0.6	Blomdin et al., 2016
Suek	Suek-A	41.70825/77.80538	3432	20.8	1.5	3432	4013	141	0.84	THAR=0.6	This study
(W Tian Shan)	Blom-C	41.81677/78.11690	3790–3600	16.9	4.3	3600	4080	74	0.70	THAR=0.6	Blomdin et al., 2016
	Blom-D	41.81433/78.11182	3730–3670	15.2	1.3	3670	4108	46	0.63	THAR=0.6	Blomdin et al., 2016
	RGI60-13.07064	41.79322/78.16376	4400–3785	0.0	0.0	3785	4154		0.53	THAR=0.6	RGI 6.0, 2017; This study
					Minimum ELA corresponding to the local LGM (m asl) ==>		3940				

Table 4.6. Modern and paleo-ELAs for dated moraines, and modern climate conditions at the modern ELA. Modern glaciers ID numbers refer to identification in RGI 6.0 (2017). Mean group ages (ka) were calculated after rejecting outliers. The 1σ total uncertainty of the mean ^{10}Be ages (ka) compounds the 1σ standard deviation and the 1σ total external uncertainties of the individual ages in the group. Locations are given in °N and °E. Modern and paleo-ELAs are in m asl. The ELA depression, ΔELA, is given in m. Summer (JJA) lapse rate is in °C km^{-1} (Kalnay et al., 1996); modern annual precipitation (*ppt*) is given in mm (Adler et al., 2003); JJA air temperature (T_{air}) is in °C (Fan and van den Dool, 2008). Melt fraction is from Rupper and Roe (2008). The references for the dating studies are given in the last column.

Site (Subregion)	Group-ID	Latitude/Longitude	Modern glacier ID	Mean group age ± 1σ total uncertainty	Paleo-ELA	Modern ELA	ΔELA	ΔELA_{norm}	*ppt*	JJA Lapse rate	Modern JJA T_{air} at modern ELA ± uncertainty	Melt Fraction	References
Aksaiqin (W Kunlun)	Aksaiqin-A	35.3966/80.3429	13.53668	31.1±12.3	5966	5998	32	0.86	116	6.7	-1.1±1.1	0.3	This study
	Aksaiqin-B	35.3971/80.3655	13.53668	> 29 (?)	5974	5998	24	0.84	116	6.7	-1.1±1.1	0.3	This study
	Aksaiqin-min	35.3784/80.3185	13.53668	?	5902	5998	96	1.00	116	6.7	-1.1±1.1	0.3	This study
Ala Bash (W Tian Shan)	Kopp2008-I	42.0800/76.4580	13.09249	68.2±4.2	3206	3780	574	0.97	313	6.5	4.9±0.9	0.4	Koppes et al., 2008
	Kopp2008-J	42.0890/76.4660	13.09249	142.1±17.8	3210	3780	570	0.96	313	6.5	4.9±0.9	0.4	Koppes et al., 2008
	Kopp2008-K	42.0940/76.4610	13.09249	102.1±7.5	3184	3780	596	1.00	313	6.5	4.9±0.9	0.4	Koppes et al., 2008
	Kopp2008-L	42.0640/76.4430	13.09249	72.2±29	3486	3780	294	0.57	313	6.5	4.9±0.9	0.4	Koppes et al., 2008
Alashanje (E Tian Shan)	Alashanje	42.9269/86.8782	13.48109	67.7±23.2	3812	4049	237	0.80	248	6.4	3.4±0.7	0.1	This study
	Alashanje-min	42.8826/86.9231	13.48109	?	3712	4049	337	1.00	248	6.4	3.4±0.7	0.1	This study
	Li2014-B	43.0280/86.9230	13.48109	17.5±5.3	3928	4049	121	0.57	248	6.4	4.4±0.7	0.1	Li et al., 2014; This study
	Li2014-C	42.9990/86.9170	13.48109	28.8±5.5	3976	4049	73	0.48	248	6.4	3.4±0.7	0.1	Li et al., 2014; This study
	Li2014-D	42.9930/86.9190	13.48109	25.8±2.4	3923	4049	126	0.59	248	6.4	3.4±0.7	0.1	Li et al., 2014; This study
	Li2014-E	42.9210/86.9240	13.48109	46.8±6.5	3772	4049	277	0.88	248	6.4	3.4±0.7	0.1	Li et al., 2014; This study
	Li2014-F	42.9410/86.8980	13.48109	76.1±5.9	3824	4049	225	0.78	248	6.4	3.4±0.7	0.1	Li et al., 2014; This study
Altyn Tagh (Qilian Shan)	Altyn-Tagh-A	39.3145/93.7418	13.33340	>1.4 (?)	5057	5081	24	0.95	64	6.8	6.9±1.4	0.5	This study
	Altyn-Tagh-min	39.3204/93.7407	13.33340	MIS 2 (?)	5034	5081	47	1.00	64	6.8	6.9±1.4	0.5	This study
Ama Drime (E Himalaya)	Ama Dime-min	28.1103/87.6955	15.10593	MIS 3 (?)	5598	5917	319	1.00	720	6.1	4.2±0.5	0.9	This study
	Chev2011-R	28.1500/87.6510	15.10593	19.4±2.2	5694	5917	223	0.82	720	6.1	4.2±0.5	0.9	Chevalier et al., 2011
	Chev2011-S	28.1460/87.6530	15.10593	17.8±2.1	5694	5917	223	0.82	720	6.1	4.2±0.5	0.9	Chevalier et al., 2011
	Chev2011-T	28.1310/87.6710	15.10593	27.4±2.5	5654	5917	263	0.89	720	6.1	4.2±0.5	0.9	Chevalier et al., 2011
At Bashi (W Tian Shan)	At Bashi-min	40.7544/75.5365	13.10354	?	4016	4186	170	1.00	313	6.7	1.3±1.5	0.5	This study
	Zec2012-A	40.7827/75.4876	13.10354	16.4±1.2	4134	4186	52	0.61	313	6.7	1.2±1.7	0.5	Zech et al., 2012
	Zec2012-B	40.7874/75.4728	13.10354	19.1±1.8	4020	4186	166	0.99	313	6.7	1.2±1.7	0.5	Zech et al., 2012
	Zec2012-C	40.7650/75.5025	13.10354	64.8±3.5	4042	4186	144	0.91	313	6.7	1.3±1.5	0.5	Zech et al., 2012
Baikal	Hori2004-A	51.500/104.9000	10.02911	15.1±2.1	1134	3188	2054	1.00	581	6.1	-4.2±2	0.9	Horiuchi et al., 2004
Barskoon-Suek (W Tian Shan)	Barskoon Suu-A	41.8701/77.7340	13.06827	16.6±1.7	4016	4068	52	0.44	254	6.5	2.3±1.3	0.5	This study
	Barskoon Suu-C	41.8832/77.7056	13.06827	0.4±0.1	4020	4068	48	0.43	254	6.5	2.3±1.3	0.5	This study
	Blom-A	41.6192/77.7288	13.06827	89.5±7.9	3808	4068	260	1.00	254	6.5	2.3±1.3	0.5	Blomdin et al., 2016
	Blom-B	41.6402/77.8500	13.06827	25.7±7.5	3824	4068	244	0.96	254	6.5	2.3±1.3	0.5	Blomdin et al., 2016
	Suek-A	41.7082/77.8053	13.06827	20.8±1.5	3881	4068	187	0.80	254	6.5	2.3±1.3	0.5	This study

Table 4.6 (continued)

Site (Subregion)	Group-ID	Latitude/Longitude	Modern glacier ID	Mean group age ± 1σ total uncertainty	Paleo-ELA	Modern ELA	ΔELA	ΔELA_{norm}	*ppt*	JJA Lapse rate	Modern JJA T_{air} at modern ELA ± uncertainty	Melt Fraction	References
Borohoro-1	Borohoro-1_min	43.8198/84.4721	13.23886	?	3274	3744	470	1.00	263	6.4	5.5±1	0.9	This study
(E Tian Shan)	Li2016-B	43.7387/84.4032	13.23886	0.3±0.1	3706	3744	38	0.32	263	6.3	5.5±1	0.9	Li et al., 2016
Borohoro-2 (E Tian Shan)	Zhan2016a-D	43.1763/84.8808	13.29827	58.7±4.9	3306	3828	522	1.00	263	6.3	2.3±0.9	0.9	Zhang et al., 2016a
Borohoro-3	Borohoro-2_min	43.1080/85.6210	13.44596	?	3672	4165	493	1.00	248	6.3	1.5±0.6	0.3	This study
(E Tian Shan)	Zhan2016a-F	43.1169/85.7596	13.44596	18.3±4.3	3748	4165	417	0.84	248	6.3	1.5±0.6	0.3	Zhang et al., 2016a
Bumbat valley	Batb2018-Q	47.4180/100.3520	10.02907	34.9±4.5	2782	3839	1058	0.98	242	6.5	1.1±1.3	0.9	Batbaatar et al., 2018
(Hangai)	Moraine BU1	47.4355/100.3470	10.02907	>> 22 (?)	2771	3839	1068	1.00	242	6.5	1.1±1.3	0.9	Batbaatar et al., 2018
	Grib2016-A	49.9521/88.0889	10.01836	19.1±0.6	2635	3196	561	0.76	204	6.3	4.4±1.2	0.9	Gribenski et al., 2016
	Grib2016-B	49.9623/88.1341	10.01836	25.4±8.8	2325	3196	871	1.00	204	6.3	4.4±1.2	0.8	Gribenski et al., 2016
Chagan Uzun	Grib2016-C	49.9499/88.1105	10.01836	18.3±0.9	2325	3196	871	1.00	204	6.3	4.4±1.2	0.9	Gribenski et al., 2016
(Altai)	Grib2016-D	49.9757/88.1786	10.01836	19.4±1.3	2960	3196	236	0.51	204	6.3	4.4±1.2	0.8	Gribenski et al., 2016
	Grib2016-E	50.0165/88.3523	10.01836	18.8±1.9	2916	3196	280	0.54	510	6.3	4.4±1.3	0.8	Gribenski et al., 2016
	Reu2007-E	50.0130/88.2940	10.01836	20.9±4.5	2952	3196	244	0.52	510	6.3	4.4±1.3	0.8	Reuther et al., 2007
Cho Oyu	Chev2011-U	28.3480/86.6270	15.10147	33.2±0.9	5968	6066	98	0.88	1001	6.1	6.1±0.9	0.9	Chevalier et al., 2011
(E Himalaya)	Cho Oyu min	28.4082/86.6494	15.10147	?	5872	6066	194	1.00	1001	6.1	6.1±0.9	0.9	This study
	Choktal river-A	42.7013/76.7008	13.10123	22.2±1.4	3722	4184	462	0.94	416	6.5	7.6±1	0.4	This study
Choktal	Choktal river-B	42.7496/76.6954	13.10123	15.4±0.6	4092	4184	92	0.48	416	6.5	7.6±1	0.4	This study
(W Tian Shan)	Choktal river-C	42.7477/76.6939	13.10123	0.3±0.1	4106	4184	78	0.46	416	6.5	7.6±1	0.4	This study
	Choktal-min	42.6664/76.6900	13.10123	?	3678	4184	506	1.00	416	6.5	7.6±1	0.4	This study
Chuluut (Hangai)	Smit2016-C	47.4126/100.256	10.02907	22.8±1.6	2983	3839	856	1.00	242	6.5	1.1±1.3	0.9	Smith et al., 2016
	Daxigou-min	43.1120/86.9895	13.45335	?	3574	3998	424	1.00	248	6.4	4.7±0.7	0.1	This study
	Kong2009-C	43.1163/86.9292	13.45335	17.7±0.8	3738	3998	260	0.72	248	6.4	4.7±0.7	0.1	Kong et al., 2009
Daxigou	Kong2009a-A	43.1138/86.8428	13.45335	19.6±3.7	3898	3998	100	0.44	248	6.4	4.7±0.7	0.1	Kong et al., 2009; This study
(E Tian Shan)	Li2011-D	43.1100/86.9450	13.45335	19.3±1.7	3674	3998	324	0.83	248	6.4	4.7±0.7	0.1	Li et al., 2011; This study
	Li2011-E	43.1190/86.9200	13.45335	17.44±1.5	3762	3998	236	0.67	248	6.4	4.7±0.7	0.1	Li et al., 2011; This study
	Li2014-I	43.1150/86.8250	13.45335	0.3±0.1	3956	3998	42	0.34	248	6.4	4.7±0.7	0.1	Li et al., 2014; This study
Diehanjelegou	Diehanjelegou-B	43.1575/87.4502	13.48197	31.9±9.3	3624	3873	249	0.99	248	6.4	7.4±0.9	0.7	This study
(E Tian Shan)	Diehanjelegou-C	43.1588/87.4409	13.48197	30±12.2	3620	3873	253	1.00	248	6.4	7.4±0.9	0.7	This study
Dumda	Dumda-A	37.8599/96.2880	13.35425	131.5±9.3	4763	5059	296	1.00	115	6.6	2.4±1.5	0.1	This study
(Qilian Shan)	Dumda-B	37.9435/96.3554	13.35425	?	4883	5059	176	0.75	115	6.6	2.4±1.5	0.1	This study
	Qilian Shan-A	37.6633/101.426	13.23977	18.2±1	3710	4767	1057	0.98	210	6.5	-1.9±1.1	0.4	This study
Gangshiqia (Qilian Shan)	Qilian Shan-B	37.6605/101.423	13.23977	14±1.5	3680	4767	1087	1.00	210	6.5	-1.9±1.1	0.4	This study
	Qilian Shan-D	37.6935/101.452	13.23977	11.7±4.1	4320	4767	447	0.53	210	6.5	-1.9±1.1	0.4	This study
	Batb2018-A	45.4039/97.0703	10.02900	7.5±0.8	3330	3745	415	0.92	147	6.3	15.8±1.2	0.1	Batbaatar et al., 2018
	Batb2018-B	45.4015/97.0697	10.02900	2.6±0.7	3360	3745	385	0.67	147	6.3	15.8±1.2	0.1	Batbaatar et al., 2018
Gichginii range (Gob-Altai)	Batb2018-C	45.4012/97.0697	10.02900	1.5±0.4	3365	3745	380	0.63	147	6.3	15.8±1.2	0.1	Batbaatar et al., 2018
	Moraine G1	45.4031/97.0710	10.02900	?	3320	3745	425	1.00	147	6.3	15.8±1.2	0.1	Batbaatar et al., 2018
	Moraine G5	45.4018/97.0687	10.02900	?	3370	3745	375	0.58	147	6.3	15.8±1.2	0.1	Batbaatar et al., 2018
	Gulbel pass-A	42.0389/77.1242	13.09143	21.9±0.7	3588	4012	424	1.00	313	6.5	-2.2±1.2	0.5	This study
Gulbel	Gulbel pass-C	42.0143/77.1992	13.09143	17.3±1.1	3792	4012	220	0.71	313	6.5	-2.2±1.2	0.5	This study
(W Tian Shan)	Gulbel pass-D	42.0114/77.1996	13.09143	16.8±1	3866	4012	146	0.60	313	6.5	-2.2±1.2	0.5	This study
	Kopp2008-A–B	42.0380/77.2190	13.09143	37.5±8.5	3718	4012	294	0.81	313	6.5	-2.2±1.2	0.5	Koppes et al., 2008

Table 4.6 (continued)

Site (Subregion)	Group-ID	Latitude/Longitude	Modern glacier ID	Mean group age ± 1σ total uncertainty	Paleo-ELA	Modern ELA	ΔELA	ΔELA_{norm}	*ppt*	JJA Lapse rate	Modern JJA T_{air} at modern ELA ± uncertainty	Melt Fraction	References
Högiin (Darhad)	Gill2008-F	51.0060/99.1250	10.02911	125.2±21.6	2243	3188	945	1.00	336	6.7	0.8±1.4	0.9	Gillespie et al., 2008
	Gill2008-G	50.9810/99.1520	10.02911	22.4±8.8	2243	3188	945	1.00	336	6.7	0.6±1.2	0.9	Gillespie et al., 2008
Höh lake (Hangai)	Höh lake min	47.4242/98.5735	10.02907	?	3079	3839	760	1.00	152	6.5	1.7±1.3	0.9	This study
	Smit2016-B	47.4631/98.5691	10.02907	43.6±7.8	3134	3839	705	0.86	152	6.5	1.7±1.3	0.9	Smith et al., 2016
Hoit Aguy (Sayan)	BatGil2016-H	51.5520/98.7146	10.02911	34.4±2	2494	3188	694	1.00	336	6.5	1.4±1.4	0.9	Batbaatar and Gillespie, 2016
Ih Bogd range (Gobi-Altai)	Batb2018-K	44.9563/100.266	10.02898	14.3±1.9	3450	3991	541	0.69	110	6.2	4.2±1.1	0.1	Batbaatar et al., 2018
	Moraine IB1	44.9559/100.263	10.02898	?	3427	3991	565	1.00	110	6.2	4.2±1.1	0.1	Batbaatar et al., 2018
Inylchek (W Tian Shan)	Lift2014-A	42.0223/79.0786	13.05000	31.8±7.4	4238	4358	120	0.96	254	6.5	-0.7±1.3	0.1	Lifton et al., 2014
	Lift2014-D	42.0203/79.0898	13.05000	16.4±4.6	4218	4358	140	0.98	254	6.5	-0.7±1.3	0.1	Lifton et al., 2014
	Lift2014-I	41.9674/79.1061	13.05000	145.3±33	4198	4358	160	1.00	254	6.5	2.3±1.2	0.1	Lifton et al., 2014
Jarai (Darhad)	Gill2008-D	51.3995/99.7722	10.02911	25.2±9.4	2204	3188	984	1.00	336	6.4	0.9±1.4	0.9	Gillespie et al., 2008
	Gill2008-E	51.3993/99.7999	10.02911	19.7±2	2221	3188	967	0.96	336	6.4	0.9±1.4	0.9	Gillespie et al., 2008
Jombolok (Sayan)	Arzh2012-B	52.7522/99.7085	10.02962	24.9±1.9	1947	2731	784	1.00	536	6.4	5.5±1.6	0.9	Arzhannikov et al., 2012
	Arzh2012-C	52.7400/99.6330	10.02962	26.1±1.8	1947	2731	784	1.00	536	6.4	5.5±1.6	0.9	Arzhannikov et al., 2012
	BatGil2016-E	52.7310/99.6150	10.02962	20.9±2	1947	2731	784	1.00	536	6.4	5.5±1.6	0.9	Batbaatar and Gillespie, 2016
Kailas (C Himalaya)	Chev2011-X	30.9940/81.2560	14.27874	17.4±1.9	5366	5698	332	0.96	507	6.5	7.3±1.8	0.9	Chevalier et al., 2011
	Chev2011-Y	31.0080/81.2400	14.27874	46.5±11.2	5346	5698	352	1.00	507	6.1	11.9±2	0.9	Chevalier et al., 2011
Kalurong (Inner Tibet)	Kalurong min	28.9549/90.1163	13.26374	?	6026	6158	132	1.00	747	6.7	0.3±0.3	0.9	This study
	Liu2017-C	28.9500/90.1350	13.26374	21.6±1.1	6093	6158	65	0.92	747	6.7	0.3±0.3	0.9	Liu et al., 2017
	Liu2017-D	28.9490/90.1340	13.26374	16.7±1.2	6093	6158	65	0.92	747	6.7	0.3±0.3	0.9	Liu et al., 2017
Kanas (Altai)	Grib2018-A	48.7111/87.0231	10.01460	18.5±0.6	2508	3022	514	1.00	476	6.6	5.5±1.2	0.9	Gribenski et al., 2018
	Grib2018-B	48.6931/87.0143	10.01460	21±0.4	2508	3022	514	1.00	476	6.6	5.5±1.2	0.9	Gribenski et al., 2018
Karakax-A (W Kunlun)	Karakax-A	36.4368/77.6821	13.40102	90.2±3.6	5030	5726	696	1.00	166	6.9	0.3±1	0.8	This study
Karakax-B (W Kunlun)	Karakax-B-min	36.4132/77.6370	13.40092	?	5528	5718	190	1.00	166	6.9	0.4±1	0.8	This study
	Karakax-B2	36.4302/77.6526	13.40092	88.7±12.6	5644	5718	74	0.79	166	6.9	0.4±1	0.8	This study
	Karakax-B3	36.4261/77.6439	13.40092	80.7±8.4	5680	5718	38	0.72	166	6.9	0.4±1	0.8	This study
Karlik Shan (E Tian Shan)	Chen2015-B	43.1430/94.3803	13.45052	14.5±0.5	3994	4173	179	0.64	120	6.5	7.8±0.9	0.1	Chen et al., 2015
	Karlik Shan min	43.2255/94.4028	13.45052	>23 ka (?)	3690	4173	483	1.00	120	6.5	7.8±0.9	0.1	Chen et al., 2015; This study
Kax Kurta (Altai)	Kax Kurta-A	47.4610/89.8725	10.02561	17.3±1	2970	3569	599	0.36	199	6.6	4±1.1	0.5	This study
	Kax Kurta-B	47.4685/89.8195	10.02561	?	2838	3569	731	0.76	199	6.6	4±1.1	0.5	This study
	Kax Kurta-C	47.4611/89.7994	10.02561	21.6 (?)±2.5	2758	3569	811	1.00	199	6.6	4±1.1	0.5	This study
La Ji (Qilian Shan)	Owen2003c-C	36.3700/101.3120	13.31354	25.4±3.1	4304	4410	106	0.75	390	6.5	4.2±1.3	0.9	Owen et al., 2003c
	Qilian Shan-4A	36.3588/101.355	13.31354	?	4220	4410	190	1.00	390	6.5	4.2±1.3	0.9	This study
Laolongwan (Qilian Shan)	Owen2003d-A	37.4410/101.7620	13.24015	11±0.4	4048	4473	425	1.00	390	6.5	2.8±1.1	0.9	Owen et al., 2003d
	Owen2003d-E	37.4600/101.7660	13.24015	19.1±0.7	4096	4473	377	0.90	390	6.5	2.8±1.1	0.9	Owen et al., 2003d
Mawang Kangri (Inner Tibet)	Amid2013-A	34.4127/80.0464	13.53522	62.7±8.3	5947	6001	54	0.97	239	6.7	2.9±1.6	0.3	Amidon et al., 2013
	Amid2013-B	34.4223/80.0476	13.53522	91.9±1.4	5935	6001	66	1.00	239	6.7	2.9±1.6	0.3	Amidon et al., 2013
	Amid2013-C	34.4255/80.0498	13.53522	?	5933	6001	68	1.00	239	6.7	2.9±1.6	0.3	Amidon et al., 2013
Menyuan (E Tibet)	Wang2013-A	35.5751/102.743	13.23874	26.5±1.5	3850	4992	1142	1.00	358	6.5	-2.5±1.3	0.9	Wang et al., 2013
	Wang2013-B	35.5692/102.739	13.23874	51.1±7.6	3850	4992	1142	1.00	358	6.5	-2.5±1.3	0.9	Wang et al., 2013
	Wang2013-C	35.5691/102.735	13.23874	24.9±2	4080	4992	912	0.66	358	6.5	-2.5±1.3	0.9	Wang et al., 2013
	Wang2013-D	35.5829/102.727	13.23874	19.7±1.2	4080	4992	912	0.66	358	6.5	-2.5±1.3	0.9	Wang et al., 2013

Table 4.6 (continued)

Site (Subregion)	Group-ID	Latitude/Longitude	Modern glacier ID	Mean group age ± 1σ total uncertainty	Paleo-ELA	Modern ELA	ΔELA	ΔELA_{norm}	*ppt*	JJA Lapse rate	Modern JJA T_{air} at modern ELA ± uncertainty	Melt Fraction	References
Muzart (W Tian Shan)	Muzart-A	41.7857/80.9060	13.43483	21.7±5.5	4490	4815	325	1.00	153	6.5	0.1±0.7	0.1	This study
	Muzart-B	41.7747/80.9565	13.43483	16±1.4	4518	4815	297	0.98	153	6.5	0.1±0.7	0.1	This study
Nyainqentanghla (Inner Tibet)	Dong2017a-A	29.8505/90.0638	13.28457	19.6±1.8	5450	5597	147	0.87	747	6.7	3.4±0.5	0.9	Dong et al., 2017a
	Dong2017a-B	29.8426/90.0640	13.28457	20.3±1.2	5430	5597	167	0.91	747	6.7	3.4±0.5	0.9	Dong et al., 2017a
	Nyainqentanghla min	29.8079/90.0390	13.28457	?	5390	5597	207	1.00	747	6.7	3.4±0.5	0.9	This study
Otgontenger, Bitüüt (Hangai)	Batb2018-M	47.5755/97.6677	10.02907	30.6±2.2	2859	3839	981	0.97	263	6.5	3.1±1.3	0.9	Batbaatar et al., 2018
	Batb2018-O	47.6035/97.6405	10.02907	16.6±1.1	2941	3839	898	0.64	263	6.5	3.1±1.3	0.9	Batbaatar et al., 2018
	Moraine BI1	47.5721/97.6751	10.02907	?	2852	3839	987	1.00	263	6.5	3.1±1.3	0.9	Batbaatar et al., 2018
Otgontenger, Bogd (Hangai)	Roth2014b-A	47.6833/97.2067	10.02907	22.2±2.5	2841	3839	998	1.00	223	6.5	1.4±1.3	0.9	Rother et al., 2014; Batbaatar et al., 2018
	Roth2014b-B	47.6883/97.2496	10.02907	18.4±3.3	2875	3839	964	0.94	223	6.5	1.4±1.3	0.9	Rother et al., 2014
	Roth2014b-E	47.6835/97.2098	10.02907	37.5±2.5	2841	3839	998	1.00	223	6.5	1.4±1.3	0.9	Rother et al., 2014
Sailag (Sayan)	Arzh2012-D	52.7771/99.7184	10.02962	17.8±3.3	2182	2731	550	1.00	536	6.4	5.5±1.6	0.9	Arzhannikov et al., 2012; Batbaatar and Gillespie, 2016
Suek (W Tian Shan)	Blom-A	41.6192/77.7288	13.07064	89.5±7.9	3940	4154	214	1.00	254	6.5	1.7±1.3	0.5	Blomdin et al., 2016
	Blom-B	41.6402/77.8500	13.07064	25.7±7.5	3956	4154	198	0.97	254	6.5	1.7±1.3	0.5	Blomdin et al., 2016
	Blom-C	41.8167/78.1169	13.07064	16.9±4.3	4080	4154	74	0.70	254	6.5	2±1.3	0.5	Blomdin et al., 2016
	Blom-D	41.8143/78.1118	13.07064	15.2±1.3	4108	4154	46	0.63	254	6.5	2±1.3	0.5	Blomdin et al., 2016
	Suek-A	41.7082/77.8053	13.07064	20.8±1.5	4013	4154	141	0.84	254	6.5	1.7±1.3	0.5	This study
Sutai range, NE (Gobi-Altai)	Batb2018-E	46.6418/93.5659	10.02900	24.2±1.8	3567	3745	179	0.80	122	6.6	4.6±1	0.5	Batbaatar et al., 2018
	Moraine N1	46.6418/93.5710	10.02900	?	3510	3745	235	1.00	122	6.6	4.6±1	0.5	Batbaatar et al., 2018
Sutai range, SW (Gobi-Altai)	Batb2018-J	46.6132/93.5503	10.02893	16.2±2.7	3275	3867	592	1.00	122	6.6	3.8±1	0.5	Batbaatar et al., 2018
Tailan (W Tian Shan)	Hube2005-A	41.6190/80.4760	13.43267	17.7±3.3	3970	4564	594	0.98	153	6.5	5.3±0.8	0.1	Hubert-Ferrari et al., 2005
	Tailan-A	41.6085/80.4982	13.43267	?	3944	4564	620	1.00	153	6.5	5.3±0.8	0.1	This study
Takelekete (W Tian Shan)	Zhan2016a-B	42.9917/83.5855	13.44521	52±12.5	3403	3709	306	1.00	263	6.3	1.4±0.8	0.4	Zhang et al., 2016
Tanggula Shan-1 (Inner Tibet)	Schä2002-E	32.9320/91.9660	13.24560	75.2±15.3	5472	5524	52	1.00	317	6.6	2.3±1.1	0.8	Schäfer, 2000; Colgan et al., 2006
Tanggula Shan-2 (Inner Tibet)	Owen2005-L	32.8276/91.9070	13.49424	57.5±3.1	5361	5576	215	0.90	317	6.6	1.9±1.1	0.8	Owen et al., 2005
	Owen2005-M	32.8203/91.8892	13.49424	98.9±48.1	5341	5576	235	1.00	317	6.6	1.9±1.1	0.8	Owen et al., 2005
Tangra Yum Co (Inner Tibet)	Rade2015-C	30.6757/86.5318	13.50116	19.5±1.5	5600	6011	411	0.60	411	6.7	2.2±0.8	0.8	Rades et al., 2015
	Tangra Yum Co min	30.6724/86.5390	13.50116	?	5200	6011	811	1.00	411	6.7	2.2±0.8	0.8	This study
Tengis (Sayan)	BatGil2016-I	51.4535/99.0387	10.02915	21.9±2.3	2280	3329	1049	1.00	336	6.4	0.3±1.4	0.9	Batbaatar and Gillespie, 2016
	Gill2008-A	51.4792/99.0555	10.02915	22.2±1.9	2280	3329	1049	1.00	336	6.4	0.3±1.4	0.9	Gillespie et al., 2008
W Himalaya	Chev2011-AB	32.4852/79.6687	14.26038	152±24	5234	5801	567	1.00	1021	6.5	1±2	0.9	Chevalier et al., 2011
	Chev2011-AC	32.4899/79.6491	14.26038	89.1±19.6	5298	5801	503	0.90	1021	6.5	1±2	0.9	Chevalier et al., 2011
	Chev2011-AD	32.4865/79.6474	14.26038	59.1±22	5274	5801	527	0.94	1021	6.5	1±2	0.9	Chevalier et al., 2011

Table 4.6 (continued)

Site (Subregion)	Group-ID	Latitude/Longitude	Modern glacier ID	Mean group age ± 1σ total uncertainty	Paleo-ELA	Modern ELA	ΔELA	ΔELAnorm	ppt	JJA Lapse rate	Modern JJA Tair at modern ELA ± uncertainty	Melt Fraction	References
Xainza-1 (Inner Tibet)	Chev2011-J	30.5990/88.5290	13.49524	320.8±107.5	5490	5799	309	1.00	410	6.7	3.2±0.6	0.9	Chevalier et al., 2011
	Chev2011-K	30.5950/88.5190	13.49524	47.2±1.9	5508	5799	291	0.96	410	6.7	3.2±0.6	0.9	Chevalier et al., 2011
	Chev2011-L	30.6110/88.4970	13.49524	13.7±1	5640	5799	159	0.63	410	6.7	3.5±0.7	0.9	Chevalier et al., 2011
Xainza-2 (Inner Tibet)	Chev2011-M	30.0790/88.4250	13.49505	38.1±14.3	5506	5729	223	1.00	410	6.7	5.1±0.5	0.9	Chevalier et al., 2011
Xainza-3 (Inner Tibet)	Chev2011-N	29.9360/88.3490	13.28247	31.5±2.1	5586	5842	256	1.00	720	6.7	5.9±0.4	0.9	Chevalier et al., 2011
Xainza-4 (Inner Tibet)	Chev2011-O	29.8210/88.1940	13.28213	21.7±8.5	5440	5960	520	1.00	720	6.7	5.1±0.4	0.9	Chevalier et al., 2011
Bayan Har Shan-1 (Inner Tibet)	Heym2011-C	33.9866/97.4490	13.23950	13.9±1.7	4907	5528	621	0.88	528	6.4	-2.1±1	0.7	Heyman et al., 2011
	Heym2011-J	33.8769/97.2315	13.23950	52.3±3.7	4878	5528	650	1.00	528	6.4	-2.1±1	0.7	Heyman et al., 2011
	Heym2011-M	33.9647/97.3252	13.23950	154.3±18.6	4902	5528	626	0.90	528	6.4	-2.1±1	0.7	Heyman et al., 2011
	Heym2011-G	34.1569/98.0203	13.23886	57.2±6.9	4914	5516	602	1.00	615	6.4	-2.4±1.2	0.8	Heyman et al., 2011
Bayan Har Shan-2 (Inner Tibet)	Heym2011-L	34.1560/97.7085	13.23886	23.5±1.3	4942	5516	574	0.87	615	6.4	-0.9±1.2	0.8	Heyman et al., 2011
	Heym2011-O	34.1643/98.1315	13.23886	34.3±6.7	4938	5516	578	0.89	615	6.4	-2.4±1.2	0.8	Heyman et al., 2011
Bayan Har Shan-3 (Inner Tibet)	Heym2011-D	34.6049/98.0150	13.23886	69.3±8.7	4778	5516	738	1.00	615	6.4	-2.3±1.3	0.8	Heyman et al., 2011
	Heym2011-E	34.5257/97.9875	13.23886	57.3±9.8	4810	5516	706	0.91	615	6.4	-2.8±1.4	0.8	Heyman et al., 2011
	Heym2011-I	34.3915/97.7595	13.23886	71.3±3.7	4882	5516	634	0.70	615	6.4	-0.9±1.2	0.8	Heyman et al., 2011
	Heym2011-N	34.3373/97.6061	13.23886	57.8±2.1	4898	5516	618	0.66	615	6.4	-0.9±1.2	0.8	Heyman et al., 2011
Gyalgar (Hangai)	BatGil2016-K	48.1837/98.7814	10.02907	21.9±3	2801	3839	1038	0.78	263	6.5	-0.4±1.3	0.9	Batbaatar and Gillespie, 2016
	BatGil2016-L	48.1180/98.8158	10.02907	19.6±3.9	2726	3839	1114	1.00	263	6.5	-0.4±1.3	0.9	Batbaatar and Gillespie, 2016
	BatGil2016-N	48.1828/98.8046	10.02907	22.8±3.4	2801	3839	1038	0.78	263	6.5	-0.4±1.3	0.9	Batbaatar and Gillespie, 2016
Haiyuan (Qilian Shan)	Lass2002-A	37.5330/101.8490	13.31354	9.5±4.2	4000	4410	410	0.73	210	6.5	1.7±1.1	0.4	Lasserre et al., 2002
	Qilian Shan-3A	37.5394/101.8500	13.31354	?	3790	4410	620	1.00	210	6.5	1.7±1.1	0.4	This study
Mönh-Saridag (Sayan)	BatGil2016-A	51.7360/100.599	10.02911	12.1±0.5	3042	3188	146	0.41	419	6.4	3.3±1.4	0.9	Batbaatar and Gillespie, 2016
	BatGil2016-B	51.7309/100.600	10.02911	10.1±0.7	3084	3188	104	0.35	419	6.4	3.3±1.4	0.9	Batbaatar and Gillespie, 2016
	BatGil2016-C	51.7286/100.598	10.02911	1.3±0.2	3130	3188	58	0.29	419	6.4	3.3±1.4	0.9	Batbaatar and Gillespie, 2016
	BatGil2016-D	51.7386/100.600	10.02911	26.9±1.6	3025	3188	163	0.43	419	6.4	3.3±1.4	0.9	Batbaatar and Gillespie, 2016
	Mönh-Saridag min	52.0806/100.364	10.02911	> MIS 2 (?)	2609	3188	579	1.00	419	6.4	0.7±1.3	0.9	This study

4.7 REFERENCES IN CHAPTER 4

Adler, R.F., Huffman, G.J., Chang, A., Ferraro, R., Xie, P., Janowiak, J., Rudolf, B., Schneider, U., Curtis, S., Bolvin, D., Gruber, A., Susskind, J., Arkin, P., (2003), The Version 2 Global Precipitation Climatology Project (GPCP) Monthly Precipitation Analysis (1979-Present). Journal of Hydrometeorology 4, 1147–1167.

Amidon, W.H., Bookhagen, B., Avouac, J-P., Smith, T., Rood, D., (2013), Late Pleistocene glacial advances in the western Tibet interior. Earth and Planetary Science Letters 381, 210–221.

Anderson, L.S., Roe, G.H., Anderson, R.S., (2014), The effects of interannual climate variability on the moraine record. Geology 42 2014, 55–58.

Araguás-Araguás, L., Froehlich, K., Rozanski, K., (1998), Stable isotope composition of precipitation over Southeast Asia. Journal of Geophysical Research 103, 28721–28742.

Arzhannikov, S.G., Braucher, R., Jolivet, M., Arzhannikova, A.V., Vassallo, R., Chauvet, A., Bourlès, D., Chauvet, F., (2012), History of late Pleistocene glaciations in the central Sayan-Tuva Upland (southern Siberia). Quaternary Science Reviews, v. 49, p. 16–32.

Balco, G., Stone, J.O., Lifton, N.A., Dunai, T.J., (2008), A complete and easily accessible means of calculating surface exposure ages or erosion rates from ^{10}Be and ^{26}Al measurements. Quaternary Geochronology 3, 174–195.

Batbaatar, J., and Gillespie, A., (2016), Outburst floods of the Maly Yenisei. Part II – new age constraints from Darhad basin. International Geology Review 58 (14), 1753–1779. http://dx.doi.org/10.1080/00206814.2016.1193452.

Batbaatar, J., Gillespie, A., Fink, D., Matmon, A., Fujioka, T., (2018), Asynchronous glaciations in arid continental climate. Quaternary Science Reviews 182, 1–19.

Benn, D.I., and Owen, L.A., (1998), The role of the Indian summer monsoon and the mid- latitude westerlies in Himalayan glaciation: review and speculative discussion. Journal of the Geological Society 155, 353–363.

Blomdin, R., Stroeven, A.P., Harbor, J.M., Lifton, N.A., Heyman, J., Gribenski, N., Petrakov, D.A., Caffee, M.W., Ivanov, M.N., Hättestrand, C., Rogozhina, I., (2016), Evaluating the timing of former glacier expansions in the Tian Shan: a key step towards robust spatial correlations. Quaternary Science Reviews 153, 78–96.

Borchers, B., Marrero, S., Balco, G., Caffee, M., Goehring, B., Lifton, N., Nishiizumi, K., Phillips, F., Schaefer, J., Stone J., (2016), Geological calibration of spallation production rates in the CRONUS-Earth project. Quaternary Geochronology 31, 188–198. 10.1016/j.quageo.2015.01.009

Chauvenet, W., (1960), 1863 Reprint of 1891. A Manual of Spherical and Practical Astronomy, fifth ed., vol. II, pp. 473–566. Dover, N.Y.

Chen, Y.X., Li, Y.K., Wang, Y.Y., Zhang, M., Cui, Z.J., Yi, C.L., (2015), Late Quaternary glacial history of the Karlik Range, easternmost Tian Shan, derived from ^{10}Be surface exposure and optically stimulated luminescence datings. Quaternary Science Reviews 115, 17–27.

Christian, J.E., Koutnik, M., Roe, G., (2018), Committed retreat: controls on glacier disequilibrium in a warming climate. Journal of Glaciology, 1–14. doi: 10.1017/jog.2018.57.

Colgan, P.M., Munroe, J.S., Zhou, S.Z., (2006), Cosmogenic radionuclide evidence for the limited extent of last glacial maximum glaciers in the Tanggula Shan of the central Tibetan Plateau. Quaternary Research 65, 336–339.

Clark, P.U., Dyke, A.S., Shakun, J.D., Carlson, A.E., Clark, J., Wohlfarth, B., Mitrovica, J.X., Hostetler, S.W., McCabe, A.M., (2009), The last glacial maximum. Science 325, 710–713.

Dong, G.C., Xu, X.K., Zhou, W.J., Fu, Y.C., Zhang, L., Li, M., (2017), Cosmogenic ^{10}Be surface exposure dating and glacier reconstruction for the Last Glacial Maximum in the Quemuqu Valley, western Nyainqentanglha Mountains, south Tibet. Journal of Quaternary Science 32, 639–652.

Fan, Y., and van den Dool, H., (2008), A global monthly land surface air temperature analysis for 1948–present. Journal of Geophysical Research 113, D01103, doi:10.1029/2007JD008470.

Farr, T.G., and Chadwick, O.A., (1996), Geomorphic processes and remote sensing signatures of alluvial fans in the Kun Lun Mountains, China. Journal of Geophysical Research 101, E10, 23091–23100.

Fink, D., and Smith, A., (2007), An inter-comparison of ^{10}Be and ^{26}Al AMS reference standards and the ^{10}Be half-life. Nuclear Instruments and Methods in Physics Research B 259, 600–609.

Gardner, A.S., and Sharp, M., (2009), Sensitivity of net mass-balance estimates to near-surface temperature lapse rates when employing the degree-day method to estimate glacier melt. Annals of Glaciology 50 (50), 80–86.

Gardner, A.S., Moholdt, G., Cogley, J.G., Wouters, B., Arendt, A.A., Wahr, J., Berthier, E., Hock, R., Pfeffer, W.T., Kaser, G., Ligtenberg, S.R.M., Bolch, T., Sharp, M.J., Hagen, J.O., van den Broeke, M.R., Paul, F., (2013), A Reconciled Estimate of Glacier Contributions to Sea-Level Rise: 2003 to 2009. Science 340, 852–857. DOI: 10.1126/science.1234532.

Gillespie, A.R., (1991), Testing a new climatic interpretation for the Tahoe glaciation. In: Hall, Jr., C.A., Doyle-Jones, V., Widawski, B. (Eds), Natural History of Eastern California and High-Altitude Research, Proceedings of the White Mountain Research Station. Symposium 3, 383–398.

Gillespie, A., Molnar, P., (1995), Asynchronous maximum advances of mountain and continental glaciers. Reviews of Geophysics 33, 311–364.

Gillespie, A.R., Burke, R.M., Komatsu, G., Bayasgalan, A., (2008), Late Pleistocene glaciers in Darhad Basin, northern Mongolia. Quaternary Research 69, 169–187.

GTN-G, (2017), GTN-G Glacier Regions. Global Terrestrial Network for Glaciers. DOI: 10.5904/gtng-glacreg-2017-07. Online access: http.//dx.doi.org/10.5904/gtng-glacreg-2017-07.

Google Earth, DigitalGlobe, CNES/Airbus, (2017), Images accessed 2017 using Google Earth Pro v. 7.3.2.5491.

Gribenski, N., Jansson, K.N., Lukas, S., Stroeven, A.P., Harbor, J.M., Blomdin, R., Ivanov, M.N., Heyman, J., Petrakov, D.A., Rudoy R., Clifton, T., Lifton, N.A., Caffee, M.W., (2016), Complex patterns of glacier advances during the late glacial in the Chagan Uzun Valley, Russian Altai. Quaternary Science Reviews 149, 288–305.

Gribenski, N., Jansson, K.N., Preusser, F., Harbor, J.M., Stroeven, A.P., Trauerstein, M., Blomdin, R., Heyman, J., Caffee, M.W., Lifton, N.A., Zhang, W., (2018), Re-evaluation of MIS 3 glaciation using cosmogenic radionuclide and single grain luminescence ages, Kanas Valley, Chinese Altai. Journal of Quaternary Science. DOI: 10.1002/jqs.2998.

Herget, J., Carling, P., Agatova, A., Batbaatar, J., Borodavko, P., Gillespie, A., Nepop R., (2017), Comment on Gribenski, N. et al., Complex patterns of glacier advances during the late glacial in the Chagan Uzun Valley, Russian Altai. Quaternary Science Reviews 149, 288–305. Quaternary Science Reviews 168, 216–219, 10.1016/j.quascirev.2017.04.014.

Heyman, J., Stroeven, A.P., Caffee, M.W., Hättestrand, C., Harbor, J.M., Li, Y.K., Alexanderson, H., Zhou, L.P., Hubbard, A., (2011), Palaeoglaciology of Bayan Har Shan, NE Tibetan Plateau: exposure ages reveal a missing LGM expansion. Quaternary Science Reviews 30, 1988–2001.

Heyman, J., (2014), Paleoglaciation of the Tibetan Plateau and surrounding mountains based on exposure ages and ELA depression estimates. Quaternary Science Reviews 91, 30–41.

Heyman, J., (2018), A global compilation of glacial ^{10}Be and ^{26}Al data (expage-201803). http://expage.github.io.

Horiuchi, K., Matsuzaki, H., Osipov, E., Khlystov, O., Fujii, S., (2004), Cosmogenic ^{10}Be and ^{26}Al dating of erratic boulders in the southern coastal area of Lake Baikal, Siberia. Nuclear Instruments and Methods in Physics Research B 223–224, 633–638.

Hubert-Ferrari, A, Suppe J, Van der Woerd J, Wang X, Lu HF, (2005), Irregular earthquake cycle along the southern Tianshan front, Aksu area, China. Journal of Geophysical Research 110, B06402.

Hughes, P.D., Gibbard, P.L., Ehlers, J., (2013), Timing of glaciation during the last glacial cycle: evaluating the concept of a global 'Last Glacial Maximum' (LGM). Earth-Science Reviews 125, 171–198. http://dx.doi.org/10.1016/j.earscirev.2013.07.003.

Kalnay, E., Kanamitsu, M., Kistler, R., Collins, W., Deaven, D., Derber, J., Gandin, L., Saha, S., White, G., Woollen, J., Zhu, Y., Chelliah, M., Ebisuzaki, W., Higgins, W., Janowiak, J., Mo, K.C., Ropelewski, C., Wang, J., Leetma, A., Reynolds, R., Jenne, R., (1995), The NCEP/NCAR 40-year re-analysis project. Bulletin of American Meteorological Society 77, 437–471.

Kong, P., Fink, D., Na, C.G., Huang, F.X., (2009), Late Quaternary glaciation of the Tianshan, Central Asia, using cosmogenic ^{10}Be surface exposure dating. Quaternary Research 72, 229–233.

Koppes, M., Gillespie, A.R., Burke, R.M., Thompson, S.C., Stone, J., (2008), Late quaternary glaciation in the Kyrgyz Tien Shan. Quaternary Science Reviews 27, 846–866.

Kottek, M., Grieser, J., Beck, C., Rudolph, B., Rubel, F., (2006), World Map of the Köppen-Geiger climate classification updated. Meteorologische Zeitschrift 15 (3), 259–263.

Kraaijenbrink, P.D.A., Bierkens, M.F.P., Lutz, A.F., Immerzeel, W.W., (2017), Impact of a global temperature rise of 1.5 degrees Celsius on Asia's glaciers. Nature 549, 257–260.

Lal, D., (1991), Cosmic ray labeling of erosion surfaces: in situ nuclide production rates and erosion models. Earth Planetary Science Letters 104, 424–439.

Lasserre, C., Gaudemer, Y., Tapponnier, P., Mériaux, A-S., Van der Woerd, J., Yuan, D.Y., Ryerson, F.J., Finkel, R.C., Caffee, M.W., (2002), Fast late Pleistocene slip rate on the Leng Long Ling segment of the Haiyuan fault, Qinghai, China. Journal of Geophysical Research 107, B11 2276.

Li, Y.K., Liu, G.N., Kong, P., Harbor, J., Chen, Y.X., Caffee M., (2011), Cosmogenic nuclide constraints on glacial chronology in the source area of the Urumqi River, Tian Shan, China. Journal of Quaternary Science 26, 297–304.

Li, Y.K., Liu, G.N., Chen, Y.X., Li, Y.N., Harbor, J., Stroeven, A.P., Caffee, M., Zhang, M., Li, C.C., Cui, Z.J., (2014), Timing and extent of Quaternary glaciations in the Tianger Range, eastern Tian Shan, China, investigated using ^{10}Be surface exposure dating. Quaternary Science Reviews 98, 7–23.

Li, Y.N., Li, Y.K., Harbor, J., Liu, G.N., Yi, C.L., Caffee, M.W., (2016), Cosmogenic ^{10}Be constraints on Little Ice Age glacial advances in the eastern Tian Shan, China. Quaternary Science Reviews 138, 105–118.

Lifton, N., Beel, C., Hättestrand, C., Kassab, C., Rogozhina, I., Heermance, R., Oskin, M., Burbank, D., Blomdin, R., Gribenski, N., Caffee, M., Goehring, B.M., Heyman, J., Ivanov, M., Li, Y.N., Li, Y.K., Petrakov, D., Usubaliev, R., Codilean, A.T., Chen, Y.X., Harbor, J., Stroeven, A.P., (2014), Constraints on the late Quaternary glacial history of the Inylchek and Sary-Dzaz valleys from in situ cosmogenic ^{10}Be and ^{26}Al, eastern Kyrgyz Tian Shan. Quaternary Science Reviews 101, 77–90.

Lisiecki, L.E., and Raymo, M.E., (2005), A Pliocene-Pleistocene stack of 57 globally distributed benthic δ^{18}O records. Paleoceanography 20, PA1003. doi:10.1029/ 2004PA001071.

Liu, J.H., Yi, C.L., Li, Y.K., Bi, W.L., Zhang, Q., Hu, G., (2017), Glacial fluctuations around the Karola Pass, eastern Lhagoi Kangri range, since the Last Glacial Maximum. Journal of Quaternary Science 32, 516–527.

Marzeion, B., Cogley, J.G., Richter, K., Parkes, D., (2014), Attribution of global glacier mass loss to anthropogenic and natural causes. Science 345, 919–921.

Medvedeff, W.G., and Roe, G.H., (2017), Trends and variability in the global dataset of glacier mass balance. Climate Dynamics 48, 3085. https://doi.org/10.1007/s00382-016-3253-x

Meierding, T.C., (1982), Late Pleistocene glacial equilibrium-line altitudes in the Colorado Front Range: A comparison of methods. Quaternary Research 18. 289–310.

Minder, J.R., Mote, P.W., Lundquist, J.D., (2010), Surface temperature lapse rates over complex terrain: Lessons from the Cascade Mountains. Journal of Geophysical Research 115, D14122. doi:10.1029/2009JD013493.

Mölg, T., and Hardy, D.R., (2004), Ablation and associated energy balance of a horizontal glacier surface on Kilimanjaro. Journal of Geophysical Research 109, D16104. doi:10.1029/2003JD004338.

National Aeronautics and Space Administration (NASA), (2017), Advanced Spaceborne Thermal Emission and Reflection Radiometer (ASTER) accessed March 2017 via https://earthdata.nasa.gov.

National Aeronautics and Space Administration (NASA), The Ministry of Economy, Trade, and Industry (METI) of Japan, (2017), Advanced Spaceborne Thermal Emission and Reflection Radiometer (ASTER) Global Digital Elevation Model Version 2 (GDEM V2) accessed 2017 via https://earthdata.nasa.gov.

Nishiizumi, K., (2004), Preparation of ^{26}Al AMS standards. Nuclear Instruments and Methods in Physics Research B 223–224, 388–392.

Nishiizumi, K., Imamura, M., Caffee, M.W., Southon, J.R., Finkel, R.C., McAninch, J., (2007), Absolute calibration of ^{10}Be AMS standards. Nuclear Instruments and Methods in Physics Research B 258, 403–413.

Ohmura, A., Kasser, P., Funk, M., (1992), Climate at the equilibrium line of glaciers. Journal of Glaciology 38, 397–411.

Owen, L.A., Ma, H.Z., Derbyshire, E., Spencer, J.Q., Barnard, P.L., Nian, Z.Y., Finkel, R.C., Caffee, M.W., (2003a), The timing and style of late Quaternary glaciation in the La Ji Mountains, NE Tibet: evidence for restricted glaciation during the latter part of the last glacial. Zeitschrift für Geomorphologie Supplementband 130, 263–276.

Owen, L.A., Spencer, J.Q., Ma, H.Z., Barnard, P.L., Derbyshire, E., Finkel, R.C., Caffee, M.W., Nian, Z.Y., (2003b), Timing of Late Quaternary glaciation along the southwestern slopes of the Qilian Shan, Tibet. Boreas 32, 281–291.

Owen, L.A., Finkel, R.C., Barnard, P.L., Ma, H.Z., Asahi, K., Caffee, M.W., Derbyshire, E., (2005), Climatic and topographic controls on the style and timing of late Quaternary glaciation throughout Tibet and the Himalaya defined by ^{10}Be cosmogenic radionuclide surface exposure dating. Quaternary Science Reviews 24, 1391–1411.

Porter, S.C., (1975), Equilibrium-line altitudes of Late Quaternary glaciers in the southern Alps, New Zealand. Quaternary Research 5, 27–47.

Porter, S.C., (2001), Snowline depression in the tropics during the last glaciation. Quaternary Science Reviews 20, 1067–1091.

Rades, E.F., Hetzel, R., Strobl, M., Xu, Q., Ding, L., (2015), Defining rates of landscape evolution in a south Tibetan graben with *in situ*-produced cosmogenic ^{10}Be. Earth Surface Processes and Landforms 40, 1862–1876.

Reuther, A.U., (2007), Surface exposure dating of glacial deposits from the last glacial cycle – evidence from the eastern Alps, the Bavarian Forest, the southern Carpathians and the Altai Mountains. Relief Boden Paläoklima 21, 1–213.

Reuther, A.U., Herget, J., Ivy-Ochs, S., Borodavko, P., Kubik, P.W., Heine, K., (2006), Constraining the timing of the most recent cataclysmic flood event from ice-dammed lakes in the Russian Altai Mountains, Siberia, using cosmogenic in situ ^{10}Be. Geology 34, 913–916. doi: 10.1130/G22755A.

RGI Consortium, (2017), Randolph Glacier Inventory – A Dataset of Global Glacier Outlines: Version 6.0: Technical Report, Global Land Ice Measurements from Space, Colorado, USA. Digital Media. DOI: https://doi.org/10.7265/N5-RGI-60.

Roe, G.H., Baker, M.B., Herla, F., (2017), Centennial glacier retreat as categorical evidence of regional climate change. Nature Geoscience 10, 95–99.

Ross, S.M., (2003), Peirce's criterion for the elimination of suspect experimental data. Journal of Engineering Technology 20, 38–41.

Rother, H., Lehmkuhl, F., Fink, D., Nottebaum, V., (2014), Surface exposure dating reveals MIS-3 glacial maximum in the Khangai Mountains of Mongolia. Quaternary Research 82, 297–308.

Rupper, S., and Roe, G., (2008), Glacier changes and regional climate: a mass and energy balance approach. Journal of Climate 21, 5384–5401.

Rupper, S., (2007), Glacier sensitivity and regional climate: Past and present. PhD Dissertation. University of Washington.

Sakai, A., Nuimura, T., Fujita, K., Takenaka, S., Nagai, H., Lamsal, D., (2015), Climate regime of asian glaciers revealed by GAMDAM glacier inventory. Cryosphere 9, 865–880. https://doi.org/10.5194/tc-9-865-2015.

Schäfer, J.M., (2000), Reconstruction of landscape evolution and continental paleoglaciations using in-situ cosmogenic nuclides: examples from Antarctica and the Tibetan Plateau. PhD thesis, ETH Zürich.

Shea, J.M., and Immerzeel, W.W., (2016), An assessment of basin-scale glaciological and hydrological sensitivities in the Hindu Kush–Himalaya. Annals of Glaciology 57 (71) 308–318. doi: 10.3189/2016AoG71A073

Shi, Y., (2002), Characteristics of late quaternary monsoonal glaciation on the tibetan plateau and in east Asia. Quaternary International 97–98, 79–91.

Smith, S.G., Wegmann, K.W., Ancuta, L.D., Gosse, J.C., Hopkins, C.E., (2016), Paleotopography and erosion rates in the central Hangay Dome, Mongolia: landscape evolution since the mid-Miocene. Journal of Asian Earth Sciences 125, 37–57.

Stone, J.O., (2000), Air pressure and cosmogenic isotope production. Journal of Geophysical Research: Solid Earth 105, 23753–23759.

Thompson, L.G., Mosley-Thompson, E., Davis, M.E., Bolzan, J.F., Dai, J., Yao, T., Gundestrup, N., Wu, X., Klein, L., Xie Z., (1989), Holocene-Late Pleistocene climatic ice core records from Qinghai-Tibetan Plateau. Science 246, 474–477.

U.S. Geological Survey, (2017), Global 30 Arc-Second Elevation (GTOPO30). These data are distributed by the Land Processes Distributed Active Archive Center (LP DAAC), located at USGS/EROS, Sioux Falls, SD. http://lpdaac.usgs.gov.

U.S. Geological Survey Geological Names Committee, (2010), Divisions of geologic time—Major chronostratigraphic and geochronologic units: Fact Sheet 2010–3059. https://pubs.usgs.gov/fs/2010/3059/

Vargo, L.J., Galewsky, J., Rupper, S., Ward, D.J., (2018), Sensitivity of glaciation in the arid subtropical Andes to changes in temperature, precipitation, and solar radiation. Global and Planetary Change 163, 86–96.

Wang, J., Kassab, C., Harbor, J.M., Caffee, M.W., Cui, H., Zhang, G.L., (2013), Cosmogenic nuclide constraints on late Quaternary glacial chronology on the Dalijia Shan, northeastern Tibetan Plateau. Quaternary Research 79, 439–451.

Yasuda, T., (2015), Glacier Surge Dynamics at the West Kunlun Shan inferred from Satellite Remote Sensing, PhD Dissertation, pp. 87. Hokkaido University.

Zech, R., (2012), A late Pleistocene glacial chronology from the Kitschi-Kurumdu Valley, Tien Shan (Kyrgyzstan), based on ^{10}Be surface exposure dating. Quaternary Research 77, 281–288.

Zhang, M., Chen, Y.X., Li, Y.K., Liu, G.N., (2016), Late Quaternary glacial history of the Nalati Range, central Tian Shan, China, investigated using ^{10}Be surface exposure dating. Journal of Quaternary Science 31, 659–670.

Chapter 5

SUMMARY AND CONCLSUSIONS

5.1 SUMMARY AND CONCLUSIONS

The chronology of paleoglaciers in Central Asia has been constructed using cosmic-ray exposure, luminescence, and radiocarbon dating methods. The field areas covered major mountain ranges of Central Asia: East Sayan in southern Siberia, Hangai and Gobi-Altai ranges in Mongolia, the Altai mountains, Tian Shan ranges crossing Kyrgyzstan and China, Qilian Shan and Kunlun ranges in Tibet (Figure 1.2). The locations of the study sites (Figure 1.7) were chosen to sample from the interior regions of the continent where sensitivity of glaciers predicted to vary in proportion to precipitation (Rupper, 2007). At each site, the extents of paleoglaciers were reconstructed using field mapping and photo interpretation of satellite images. The extents of the paleoglaciers allow to reconstruct paleo equilibrium-line altitude (ELA), from which a comparison with the modern values of ELA can be used to infer paleoclimate conditions.

ELA is an altitude on a glacier located at the border between accumulation and ablation zones, making it a measure of glacier mass balance. If the relationship between glacier mass balance and climate conditions was established, then the vertical fluctuations of ELA through time can be used as a paleoclimate proxy. Two general approaches exist to describe climate at the ELA: 1) an empirical curve of summer air temperature and annual precipitation at the ELA (Figure 1.5; Ohmura et al., 1992; Sakai et al., 2015); 2) Physically based numerical models that calculate the sensitivity of ELA to various climate variables (e.g., Figure 1.6; Rupper and Roe, 2008). The empirical curve suggests that in humid regions, the high accumulation of glacier ice has to flow to

lower altitudes where high air temperature causes it to melt. In arid regions the summer air temperature at the ELA is negative, suggesting that the majority of ablation occurs in cold conditions without requiring significant melt. The numerical sensitivity model is consistent with the empirical curve; in humid regions melt is responsible for most of the ablation and a small depression in air temperature can drive a large ELA depression. In arid regions sublimation can dominate the total ablation where melt does not play a significant role, and a small change in precipitation can result in a large ELA depression. Within this framework, I summarize the main conclusions for chapters 2–4 and discuss the implications for paleoclimate reconstruction.

5.1.1 *Paleoglaciers in East Sayan, Altai, and Hangai*

The timing and extents of paleoglaciers in East Sayan and Hangai mountains were constructed in Chapter 2. Darhad basin in northern Mongolia was dammed behind large outlet glaciers from the East Sayan ice field during the Pleistocene. Numerical dating of lacustrine sediments extracted from the basin showed large paleolakes existed during MIS 4–3 and MIS 2, possible only due to impounding by a glacier. A remnant of end moraines from one of the outlet glaciers, the Tengis paleoglacier, was dated to ~22 ka, a peak time of the global LGM. The timing and relative extents of paleoglaciers in the Hangai mountains show a similar pattern: paleoglaciers were as large during MIS 3 as during MIS 2. The boulder ages I reported in Chapter 4 and a review of literature dates for glacial deposits show that the paleoglaciers in Altai mountains extended to their maxima during global LGM. More than 90% of ablation of the glaciers in these mountains was predicted to be due to melt (Rupper and Roe, 2008), suggesting that the paleoglaciers in East Sayan, Altai, and Hangai mountains were indeed responding to minima in insolation and air temperature during MIS 2. However, in Chapter 3, I suggested that the large extents of these paleoglaciers during MIS 3 can be explained by an increase in precipitation despite an increase in air temperature.

5.1.2 *Paleoglaciers in Gobi-Altai*

The chronology of paleoglaciers in three separate ranges in the Mongolian Gobi, Sutai, Gichginii, and Ih Bogd, presents a very interesting test for ELA sensitivities to climate variables. The Sutai range in the east represents a region where glaciers are predicted to have 50% melt fraction (Rupper and Roe, 2008) and the boulder ages I reported in Chapter 3 show that the largest paleoglacier extent there occurred during global LGM. In the west end of the Gobi-Altai a paleoglacier in Ih Bogd (30 % melt fraction) also extended to its maximum during global LGM. However, in the Gichginii range, a region where glaciers are predicted to have <10% melt fraction, I did not find any evidence of global LGM glaciation. Instead, the paleoglaciers there extended to their maximum ~8–7 ka, a time of increased precipitation and air temperature. The Gichginii range receives only ~60 mm of precipitation annually, which is consistent with empirical and numerically established relationship between ELA and climate: in glaciers in arid regions exist in extreme cold conditions and sublimation dominates the ablation process. Paleoclimate inferences from this glacial evidence have to account for the high sensitivity of ELA to precipitation. If the required amount of increase in precipitation is calculated for these sublimation-dominated glaciers a paleo-precipitation can be quantified in arid regions.

5.1.3 *Paleoglaciers in Tian Shan*

The Tian Shan hosts a large number of modern glaciers with a variety of geometries and sensitivities. I reported boulder ages from eight sites to represent glaciers with melt fractions ranging from 10% to 50%. The geometry of the paleoglaciers ranged from simple straight valley glaciers sourced from a few cirques to large complicated outlet glaciers sourced from ice fields. In the east, where glaciers are predicted to have ~10% melt fraction, paleoglaciers in the valleys of Diehanjelegou, Alashanje, and Daxigou extended to their maxima during MIS 4–3. Upvalley, the

moraines in the cirque floor were dated to ~17 ka, suggesting that the glaciers may have retreated due to a decrease in precipitation during the global LGM. To the west, in Kyrgyzstan, the spatial pattern seems to be similar: the largest valley paleoglaciers and outlet glaciers occurred during MIS 4–3, and in some valleys during the peak of the global LGM ~22 ka. One striking similarity between these paleoglaciers can be observed in the Tian Shan: in almost all cases, moraines found in the cirque area, located very close to the modern glaciers, were dated to ~17–15 ka. The glaciers in this region were modeled to have a 50–10% melt fraction, suggesting that a decrease in precipitation may have played a larger role in driving these large ELA depressions than air temperature did. Lacustrine sediments in Issyk-kul may provide constraints on the paleo temperatures, from which ELA sensitivity analysis could be performed to quantify paleo precipitation in the region.

5.1.4 *Paleoglaciers in Qilian Shan*

In the east end of the Qilian Shan, I reported exposure ages for moraines deposited by a paleoglacier sourced from Gangshiqia peak. Of the sites I studied, this is the one region closest to the Pacific Ocean and the glaciers there probably were the most influenced by the monsoon. The glaciers there were predicted to have a 50–90% melt fraction. The paleoglaciers extended to their maxima during the global LGM, probably responding to the minima in insolation and air temperature. ~450 km to the west it becomes more continental near the Mösön Uul, where I sampled the oldest boulders (~130 ka) reported in this dissertation. The boulders in Dumda valley were heavily eroded and the exposure ages are minima. Although the moraine remnant was located ~25 km from the modern Dunde ice cap it represented only ~300 m ELA depression. ~260 km to the northwest Altyn Tagh range marks the western end of Qilian Shan. The spatial pattern of paleoglaciers in Dumda was an opposite of what I found in the Altyn Tagh, where moraines were

located only ~200 m away from the modern glaciers and the cirque floor extends for only ~300 m until it transitions to a V-shaped narrow valley. Despite their large differences in glacial extents, however, these two systems show similarity in that the paleoglaciers during the global LGM were limited to their cirques. The glaciers in these two regions predicted to have melt fractions of ~20–10%, suggesting that the lack of precipitation may explain the limited global LGM extent.

5.1.5 *Paleoglaciers in western Kunlun*

In Chapter 4, I reported boulder ages from two sites in western Kunlun: Aksaiqin (30% melt fraction) in the east and Karakax (80% melt fraction) in the west. In both sites the lowest moraines were found within a few km from the modern glacier tongue. Both paleoglaciers extended to their maxima well before the global LGM, suggesting that air temperatures at the time did not drive any glacier growth. It is a very similar pattern observed in the Altyn Tagh site, where glaciers exhibited no significant advances in response to the changing air temperatures. The modern glaciers in these regions may be an excellent case study to constrain the sensitivity of ELA to climate variables using high-resolution climate data.

5.2 DISCUSSION

5.2.1 *Sensitivity of paleoglaciers in Central Asia*

The heterogeneous spatial and temporal patterns of paleo-ELAs in Central Asia can be classified into the following categories depending on their sensitivity to air temperature and precipitation:

- Temperature-sensitive glaciers: biggest ≥MIS 3, big MIS 2, small MIS 1
- Temperature-controlled glaciers: big (?) ≥MIS 3, biggest MIS 2, small MIS 1
- Precipitation-sensitive glaciers: biggest ≥MIS 3, small MIS 2, small MIS 1
- Precipitation-controlled glaciers: small ≥MIS 2, relatively large MIS 1

The highly variable relative spatial extents of paleoglaciers in Central Asia can be compared using normalized ELA depressions (ΔELA_{norm}) summarized in Figure 5.1. During MIS 5–4 only one paleoglacier with a high melt fraction advanced to its maximum. During MIS 3 some of the high-melt fraction paleoglaciers started advancing and may have been responding to increased precipitation during MIS 3. MIS 2, a loose timeframe of the global LGM, saw a large number of maximum extents. The comparison of ΔELA_{norm} for MIS 2 paleoglaciers with various melt fractions reveals a general pattern of asynchronous glacial advances: high-melt fraction glaciers advanced earlier in MIS 2 and subsequently became smaller, probably responding to the minima in air temperature and insolation with less sensitivity to decreased precipitation. However, medium and low-melt fraction glaciers extended to their maxima at the end of MIS 2, probably responding to increased precipitation then. An extreme example of a precipitation-controlled glacier can be observed in the Gichginii range, Gobi-Altai, with a 92% ΔELA_{norm} at ~7.5 ka.

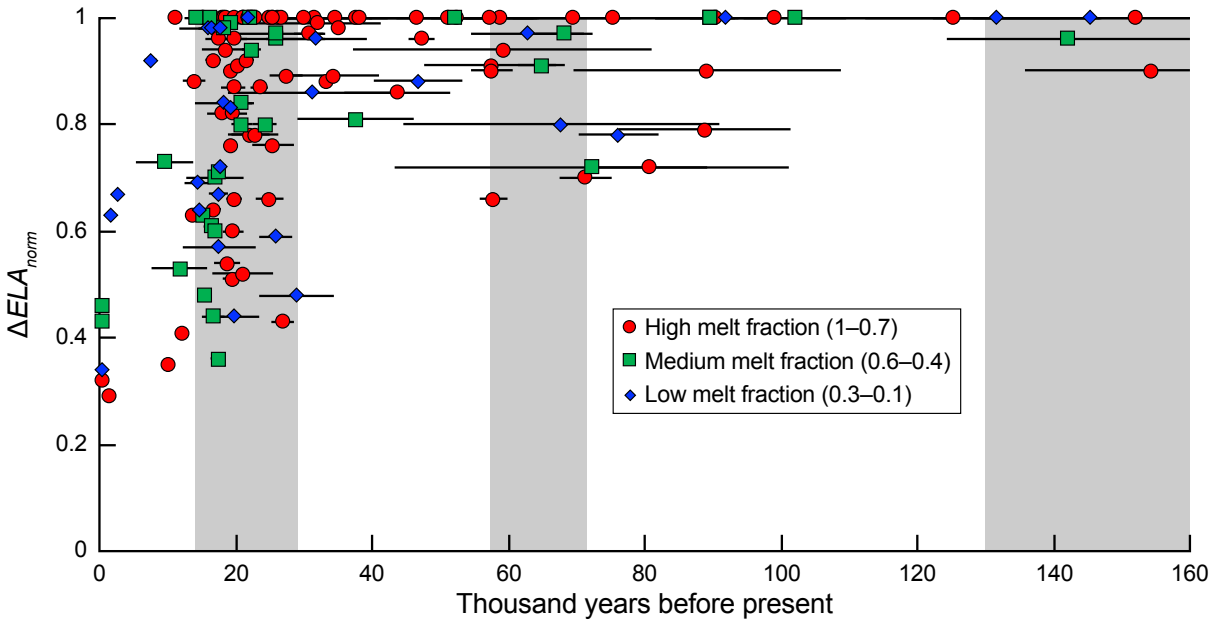

Figure 5.1. Normalized ELA depressions (ΔELA_{norm}) in Central Asia through time. The data points include the ΔELA_{norm} values estimated from ^{10}Be ages reported in chapters 2–4, in addition to ^{10}Be ages reported by Amidon et al. (2013), Blomdin et al. (2016), Gribenski et al. (2016), Gribenski et al. (2017), Hubert-Ferrari et al. (2005), Koppes et al. (2008), Lasserre et al. (2002), Li et al. (2014), Li et al. (2016), Lifton et al. (2014), Owen et al. (2003a; 2003b), Reuther (2007), Rother et al. (2014), Zech (2012), and Zhang et al. (2016). Melt fraction values are from Rupper and Roe (2008). The classification of MIS is from Lisiecki and Raymo (2005).

5.2.2 *Future directions in inferring paleoclimate from paleo-ELA*

An accurate reconstruction of paleoclimate from paleo-ELAs require accurate measurements in three areas: 1) dating; 2) ELA estimation; 3) Sensitivity of ELA. I discuss future research directions for each of these areas in the following paragraphs.

Cosmic-ray exposure dating has allowed, for the first time, a direct dating of glacial boulders. Today more than 2700 ^{10}Be ages for glacial boulders and bedrock are available for Central Asia alone (expage compilation: Heyman, 2018). The chemical preparations of the rock samples and AMS measurements of ^{10}Be/^{9}Be, data reporting of the data (e.g., Dunai and Stuart, 2009), and online exposure-age calculators (e.g., Balco et al., 2008) have been standardized in the last 20 years. Heyman (2014) noted that prior exposure and/or erosion of the boulders and bedrock were the reason for large scatter in the exposure-age data. However, as I showed in Chapter 4, the total uncertainties of grouped ages do not hinder a comparison of paleoglaciations on the 10^3-yr scale. This is a good temporal resolution for a paleoclimate reconstruction from glacial records.

Methods to estimate modern and paleo-ELAs vary (e.g., Porter, 2001). A simple toe-to-head altitude ratio (THAR) method was used to construct the empirical curve of summer air temperature and precipitation at the modern ELAs (Nuimura et al., 2014). Paleo-ELAs for Central Asian glaciers have also been constructed using THAR method (Heyman, 2014). In each study, the ELAs estimated from the simple THAR method allowed accurate comparisons of ELAs for different regions, albeit the ELAs are imprecise. The modern and paleo-ELAs I reported in chapters 2–4 also were also based on THAR method, and may likewise be imprecise. However, the normalized ELA depression technique I developed in Chapter 3 allows a direct comparison of relative magnitudes of paleoglacier extents for given period. In the future, a continental-scale map

of threshold values of THAR and AAR will be useful. The compilation of such a map can be constructed using worldwide glacier inventories (e.g., GLIMS) in combination with numerical modeling of accumulation and ablation areas.

The sensitivity of ELA to climate variables is the most pressing issue in reconstructing paleoclimate from glacial records. The empirical curve relating summer air temperature and annual precipitation at the ELA (e.g., Ohmura et al., 1992; Sakai et al., 2015) and physically based numerical models (e.g., Rupper and Roe) both require accurate and high-resolution climate data. Vargo et al. (2018), for example, resampled the low-resolution NCEP/NCAR reanalysis data (Kalnay et al., 1995) using high-resolution elevation data to derive high-resolution air temperatures in their study sites. Gardner and Sharp (2009) noted that the use of a universal lapse rate might give inaccurate values of air temperatures at high altitudes and recommended using vertically variable lapse rates depending on the region. To that end, I would like to see a continental-scale map of ELA sensitivities. Such a map would be helpful in better constraining the relative roles of air temperature and precipitation in driving the ELA depressions of Central Asian glaciers.

5.3 REFERENCES IN CHAPTER 5

Amidon, W.H., Bookhagen, B., Avouac, J-P., Smith, T., Rood, D., (2013), Late Pleistocene glacial advances in the western Tibet interior. Earth and Planetary Science Letters 381, 210–221.

Balco, G., Stone, J.O., Lifton, N.A., Dunai, T.J., (2008), A complete and easily accessible means of calculating surface exposure ages or erosion rates from ^{10}Be and ^{26}Al measurements: Quaternary Geochronology, v. 3, p. 174–195.

Blomdin, R., Stroeven, A.P., Harbor, J.M., Lifton, N.A., Heyman, J., Gribenski, N., Petrakov, D.A., Caffee, M.W., Ivanov, M.N., Hättestrand, C., Rogozhina, I., (2016), Evaluating the timing of former glacier expansions in the Tian Shan: a key step towards robust spatial correlations. Quaternary Science Reviews 153, 78–96.

Dunai, T.J., and Stuart, F.M., (2009), Reporting of cosmogenic nuclide data for exposure age and erosion rate determinations. Quaternary Geochronology 4, 437–440.

Gardner, A.S., and Sharp, M., (2009), Sensitivity of net mass-balance estimates to near-surface temperature lapse rates when employing the degree-day method to estimate glacier melt. Annals of Glaciology 50 (50), 80–86.

Gribenski, N., Jansson, K.N., Lukas, S., Stroeven, A.P., Harbor, J.M., Blomdin, R., Ivanov, M.N., Heyman, J., Petrakov, D.A., Rudoy R., Clifton, T., Lifton, N.A., Caffee, M.W., (2016), Complex patterns of glacier advances during the late glacial in the Chagan Uzun Valley, Russian Altai. Quaternary Science Reviews 149, 288–305.

Gribenski, N., Jansson, K.N., Preusser, F., Harbor, J.M., Stroeven, A.P., Trauerstein, M., Blomdin, R., Heyman, J., Caffee, M.W., Lifton, N.A., Zhang, W., (2018), Re-evaluation of MIS 3 glaciation using cosmogenic radionuclide and single grain luminescence ages, Kanas Valley, Chinese Altai. Journal of Quaternary Science. DOI: 10.1002/jqs.2998.

Heyman, J., (2014), Paleoglaciation of the Tibetan Plateau and surrounding mountains based on exposure ages and ELA depression estimates: Quaternary Science Reviews, v. 91, p. 30–41.

Heyman, J., (2018), Expage: A global compilation of glacial ^{10}Be and ^{26}Al data (expage-201803). Accessed at http://expage.github.io/index.html.

Hubert-Ferrari, A., Suppe, J., Van der Woerd, J., Wang, X., Lu, H.F., (2005), Irregular earthquake cycle along the southern Tianshan front, Aksu area, China. Journal of Geophysical Research 110, B06402.

Kalnay, E., Kanamitsu, M., Kistler, R., Collins, W., Deaven, D., Derber, J., Gandin, L., Saha, S., White, G., Woollen, J., Zhu, Y., Chelliah, M., Ebisuzaki, W., Higgins, W., Janowiak, J., Mo, K.C., Ropelewski, C., Wang, J., Leetma, A., Reynolds, R., Jenne, R., (1995), The NCEP/NCAR 40-year re-analysis project. Bulletin of the American Meteorological Society 77, 437–471.

Koppes, M., Gillespie, A.R., Burke, R.M., Thompson, S.C., Stone, J., (2008), Late Quaternary glaciation in the Kyrgyz Tien Shan: Quaternary Science Reviews, v. 27, p. 846–866.

Lasserre C, Gaudemer Y, Tapponnier P, Mériaux A-S, Van der Woerd J, Yuan DY, Ryerson FJ, Finkel RC, Caffee MW, (2002), Fast late Pleistocene slip rate on the Leng Long Ling segment of the Haiyuan fault, Qinghai, China. Journal of Geophysical Research 107, B11 2276.

Lifton, N., Beel, C., Hättestrand, C., Kassab, C., Rogozhina, I., Heermance, R., Oskin, M., Burbank, D., Blomdin, R., Gribenski, N., Caffee, M., Goehring, B.M., Heyman, J., Ivanov, M., Li, Y.N., Li, Y.K., Petrakov, D., Usubaliev, R., Codilean, A.T., Chen, Y.X., Harbor, J., Stroeven, A.P., (2014), Constraints on the late Quaternary glacial history of the Inylchek and Sary-Dzaz valleys from in situ cosmogenic ^{10}Be and ^{26}Al, eastern Kyrgyz Tian Shan. Quaternary Science Reviews 101, 77–90.

Lisiecki, L.E., and Raymo, M.E., (2005), A Pliocene-Pleistocene stack of 57 globally distributed benthic δ18O records: Paleoceanography, v. 20, PA1003, doi:10.1029/2004PA001071.

Nuimura, T., Sakai, A., Taniguchi, K., Nagai, H., Lamsal, D., Tsutaki, S., Kozawa, A., Hoshina, Y., Takenaka, S., Omiya, S., Tsunematsu, K., Tshering, P., Fujita, K., (2015), The GAMDAM glacier inventory: A quality-controlled inventory of Asian glaciers. The Cryosphere 9, 849–864. https://doi.org/10.5194/tc-9-849-2015.

Ohmura, A., Kasser, P., Funk, M., (1992), Climate at the equilibrium line of glaciers. Journal of Glaciology 38, 397–411.

Owen, L.A., Ma, H.Z., Derbyshire, E., Spencer, J.Q., Barnard, P.L., Nian, Z.Y., Finkel, R.C., Caffee, M.W., (2003a), The timing and style of late Quaternary glaciation in the La Ji Mountains, NE Tibet: evidence for restricted glaciation during the latter part of the last glacial. Zeitschrift für Geomorphologie Supplementband 130, 263–276.

Owen, L.A., Spencer, J.Q., Ma, H.Z., Barnard, P.L., Derbyshire, E., Finkel, R.C., Caffee, M.W., Nian, Z.Y., (2003b), Timing of Late Quaternary glaciation along the southwestern slopes of the Qilian Shan, Tibet. Boreas 32, 281–291.

Reuther, A.U., (2007), Surface exposure dating of glacial deposits from the last glacial cycle – evidence from the eastern Alps, the Bavarian Forest, the southern Carpathians and the Altai Mountains. Relief Boden Paläoklima 21, 1–213.

Rother, H., Lehmkuhl, F., Fink, D., Nottebaum, V., (2014), Surface exposure dating reveals MIS-3 glacial maximum in the Khangai Mountains of Mongolia. Quaternary Research, v. 82, p. 297–308.

Rupper, S., (2007), Glacier sensitivity and regional climate: Past and present. PhD Dissertation. University of Washington.

Rupper, S., and Roe, G., (2008), Glacier changes and regional climate: A mass and energy balance approach. Journal of Climate, v. 21, p. 5384–5401.

Sakai, A., Nuimura, T., Fujita, K., Takenaka, S., Nagai, H., Lamsal, D., (2015), Climate regime of Asian glaciers revealed by GAMDAM glacier inventory. The Cryosphere, v. 9, p. 868–880.

Vargo, L.J., Galewsky, J., Rupper, S., Ward, D.J., (2018), Sensitivity of glaciation in the arid subtropical Andes to changes in temperature, precipitation, and solar radiation. Global and Planetary Change 163, 86–96.

Zech, R., (2012), A late Pleistocene glacial chronology from the Kitschi-Kurumdu Valley, Tien Shan (Kyrgyzstan), based on ^{10}Be surface exposure dating. Quaternary Research 77, 281–288.

Zhang, M., Chen, Y.X., Li, Y.K., Liu, G.N., (2016), Late Quaternary glacial history of the Nalati Range, central Tian Shan, China, investigated using ^{10}Be surface exposure dating. Journal of Quaternary Science 31, 659–670.

BIBLIOGRAPHY

Adamiec, G., and Aitken, M., (1998), Dose-rate conversion factors: update. Ancient TL, v. 16, no. 2, p. 37–50.

Adler, R.F., Huffman, G.J., Chang, A., Ferraro, R., Xie, P., Janowiak, J., Rudolf, B., Schneider, U., Curtis, S., Bolvin, D., Gruber, A., Susskind, J., Arkin, P., (2003), The Version 2 Global Precipitation Climatology Project (GPCP) Monthly Precipitation Analysis (1979-Present). Journal of Hydrometeorology 4, 1147–1167.

Aizen, E.M., Aizen, V.B., Takeuchi, N., Mayewski, P.A., Grigholm, B., Joswiak, D.R., Nikitin, S.A., Fujita, K., Nakawo, M., Zapf, A., Schwikowski, M., (2016), Abrupt and moderate climate changes in the mid-latitudes of Asia during the Holocene. Journal of Glaciology. 1–29, doi: 10.1017/jog.2016.34

Allen, J.R.L., (1968), Current ripples: their relation to patterns of water and sediment motion. North-Holland Pub. Co., 433 p.

Amidon, W.H., Bookhagen, B., Avouac, J-P., Smith, T., Rood, D., (2013), Late Pleistocene glacial advances in the western Tibet interior. Earth and Planetary Science Letters 381, 210–221.

Anderson, L.S., Roe, G.H., Anderson, R.S., (2014), The effects of interannual climate variability on the moraine record. Geology 42 2014, 55–58.

Andrews, J.T., (1975), Glacial Systems. An Approach to Glaciers and their Environments. North Scituate, MA, Duxbury Press.

Annan, J.D., and Hargreaves, J.C., (2013), A new global reconstruction of temperature changes at the Last Glacial Maximum. Climate of the Past 9, 367–376.

Araguás-Araguás, L., Froehlich, K., Rozanski, K., (1998), Stable isotope composition of precipitation over Southeast Asia. Journal of Geophysical Research 103, 28721–28742.

Arnold, L.J., Bailey, R.M., Tucker, G.E., (2007), Statistical treatment of fluvial dose distributions from southern Colorado arroyo deposits. Quaternary Chronology, v. 2, p. 162–167.

Arzhannikov, S.G., Alexeev, S.V., Glyzin, A.V., Razmakhnina, T.B., Orlova, L.A., (2000), Prirodnaya obstanovka v golotsene zapadnoi chasti Todzhinskoi vpadiny (na primere razreza Merzly Yar) (Natural conditions in the western part of the Todzhinsky basin in the Holocene (by the example of “Merzly Yar” section)). The Problems of Climatic and Environmental Reconstruction in the Holocene and Pleistocene, Novosibirsk, p. 18–29 (in Russian).

Arzhannikov, S.G., Braucher, R., Jolivet, M., Arzhannikova, A.V., Vassallo, R., Chauvet, A., Bourlès, D., Chauvet, F., (2012), History of late Pleistocene glaciations in the central Sayan-Tuva Upland (southern Siberia). Quaternary Science Reviews, v. 49, p. 16-32.

Auclair, M., Lamothe, M., Huot, S., (2003), Measurement of anomalous fading for feldspar IRSL using SAR. Radiation Measurements, v. 37, p. 487–492.

Augustin, L., Barbante, C., Barnes, P.R.F., Barnola, J.M., Bigler, M., Castellano, E., Cattani, O., Chappellaz, J., Dahl-Jensen, D., Delmonte, B., Dreyfus, G., Durand, G., Falourd, S., Fischer, H., Flueckiger, J., Hansson, M.E., Huybrechts, P., Jugie, G., Johnsen, S.J., Jouzel, J., Kaufmann, P., Kipfstuhl, J., Lambert, F., Lipenkov, V.Y., Littot, G.C., Longinelli, A., Lorrain, R., Maggi, V., Masson-Delmotte, V., Miller, H., Mulvaney, R., Oerlemans, J., Oerter, H., Orombelli, G., Parrenin, F., Peel, D.A., Petit, J.-R., Raynaud, D., Ritz, C., Ruth, U., Schwander, J., Siegenthaler, U., Souchez, R., Stauffer, B., Steffensen, J.P., Stenni, B., Stocker, T.F., Tabacco, I.E., Udisti, R., van de Wal, R.S.W., van den Broeke, M., Weiss, J., Wilhelms, F., Winther, J.-G., Wolff, E.W., Zucchelli, M., (2004), Eight glacial cycles from an Antarctic ice core. Nature 429, 623–628.

Bacon, S.N., Bayasgalan, A., Gillespie, A., Raymond, B., (2003), Paleoseismic displacement from landform subjected to periglacial processes: Observations along the Jarai Gol fault near the Tamyn Am Hills, Darhad Depression, northern Mongolia. XVI INQUA Congress, Geological Society of America Abstracts with Programs, p. 103.

Baker, V.R., and Milton, D.J., (1974), Erosion by catastrophic floods on Mars and Earth. Icarus, v. 23, p. 27–41.

Baker, V.R., (1973), Paleohydrology and sedimentology of Lake Missoula flooding in Eastern Washington. Geological Society of America Special Paper, v. 144, p. 1–79.

Baker, V.R., (1982), The channels of Mars. University of Texas Press, Austin, Texas, 198 p.

Baker, V.R., Benito, G., Rudoy, A.N., (1993), Paleohydrology of late Pleistocene superflooding, Altai Mountains, Siberia. Science, v. 259, p. 348–350.

Balco, G., (2011), What is a camel diagram anyway? The bleeding edge of cosmogenic-nuclide geochemistry. https://cosmognosis.wordpress.com/2011/07/25/what-is-a-camel-diagram-anyway/

Balco, G., (2006), Converting Al and Be isotope ratio measurements to nuclide concentrations in quartz: Documentation for CRONUS-Earth Calculator, version 2.2. Online: http://hess.ess.washington.edu/math/docs/al_be_v22/al_be_docs.html.

Balco, G., Briner, J., Finkel, R.C., Rayburn, J.A., Ridge, J.C., Schaefer, J.M., (2009), Regional beryllium-10 production rate calibration for northeastern North America. Quaternary Geochronology, v. 4, p. 93-107.

Balco, G., Stone, J.O., Lifton, N.A., Dunai, T.J., (2008), A complete and easily accessible means of calculating surface exposure ages or erosion rates from ^{10}Be and ^{26}Al measurements. Quaternary Geochronology, v. 3, p. 174–195.

Banerjee, D., Murray, A.S., Bøtter-Jensen, L., Lang, A., (2001), Equivalent dose estimation using a single aliquot of polymineral fine grains. Radiation Measurements, v. 33(1), p. 73–94.

Batbaatar, J., and Gillespie, A.R., (2016), Outburst floods of the Maly Yenisei. Part I – review. International Geology Review. doi:10.1080/00206814.2015.1114908

Batbaatar, J., and Gillespie, A., (2016), Outburst floods of the Maly Yenisei. Part II – new age constraints from Darhad basin. International Geology Review 58 (14), 1753–1779. http://dx.doi.org/10.1080/00206814.2016.1193452.

Batbaatar, J., and Gillespie, A.R., (2012), Equilibrium-line altitudes in cold hyperarid settings. Abstract C43E-06 presented at 2012 Fall Meeting, AGU, San Francisco, Calif., 3–7 Dec.

Batbaatar, J., Feathers, J.K., Gillespie, A.R., (2009), IRSL feldspar dates for paleolake sediments from Darhad Basin, Mongolia. Geological Society of America, Abstracts with Programs, v. 41, no. 7, p. 382.

Batbaatar, J., Gillespie, A.R., Schreiber, B C., (2012), Tectonics and environment at the western end of the Baikal rift: Paleolake sediment record from Darhad Basin, northern Mongolia. Geological Society of America Abstracts with Programs, v. 44, no. 3, p. 56.

Batbaatar, J., Gillespie, A.R., Fedotov, A., Bayasgalan, A., (2008), The 92-m sediment core from paleolake Darhad, Mongolia. Proceedings, 7th International Symposium "Environmental Changes in East Eurasia and Adjacent Areas – High Resolution Environmental Records of Terrestrial Sediments", Ulaanbaatar–Hatgal, Mongolia, August 23-29, p. 66–74.

Batbaatar, J., Gillespie, A., Fink, D., Matmon, A., Fujioka, T., (2018), Asynchronous glaciations in arid continental climate. Quaternary Science Reviews 182, 1–19.

Benito, G., and O'Connor, J.E., (2003), Number and size of last-glacial Missoula floods in the Columbia River valley between the Pasco Basin, Washington, and Portland, Oregon. Geological Society of America Bulletin, v. 115, no. 5, p. 624–638.

Benn, D.I., and Hulton, N.R.J., (2010), An Excel™ spreadsheet program for reconstructing the surface profile of former mountain glaciers and ice caps. Computers and Geosciences 36, 605–610.

Benn, D.I., and Owen, L.A., (1998), The role of the Indian summer monsoon and the mid- latitude westerlies in Himalayan glaciation: review and speculative discussion. Journal of the Geological Society 155, 353–363.

Bezrukova, E.V., Tarasov, P.E., Solovieva, N., Krivonogov, S.K., Riedel, F., (2010), Last glacial-interglacial vegetation and environmental dynamics in southern Siberia: chronology, forcing and feedbacks. Palaeogeography, Palaeoclimatology, Palaeoecology, v. 296, p. 185–198.

Bintanja, R., and van de Wal, R.S.W., (2008), North American ice-sheet dynamics and the onset of 100,000-year glacial cycles. Nature 454, 869–872.

Blomdin, R., Heyman, J., Stroeven, A.P., Hättestrand, C., Harbor, J.M., Gribenski, N., Jansson, K.N., Petrakov, D.A., Ivanov, M.N., Alexander, O., Rudoy, A.N., Walther, M., (2014), Glacial geomorphology of the Altai and Western Sayan Mountains, Central Asia. Journal of Maps, 10.1080/17445647.2014.992177.

Blomdin, R., Stroeven, A.P., Harbor, J.M., Lifton, N.A., Heyman, J., Gribenski, N., Petrakov, D.A., Caffee, M.W., Ivanov, M.N., Hättestrand, C., Rogozhina, I., (2016), Evaluating the timing of former glacier expansions in the Tian Shan: a key step towards robust spatial correlations. Quaternary Science Reviews 153, 78–96.

Borchers, B., Marrero, S., Balco, G., Caffee, M., Goehring, B., Lifton, N., Nishiizumi, K., Phillips, F., Schaefer, J., Stone J., (2016), Geological calibration of spallation production rates in the CRONUS-Earth project. Quaternary Geochronology 31, 188–198. 10.1016/j.quageo.2015.01.009.

Braconnot, P., Otto-Bliesner, B., Harrison, S., Joussaume, S., Peterchmitt, J.Y., Abe-Ouchi, A., Crucifix, M., Driesschaert, E., Fichefet, Th., Hewitt, C.D., Kageyama, M., Kitoh, A., Laîné, A., Loutre, M.F., Marti, O., Merkel, U., Ramstein, G., Valdes, P., Weber, S.L., Yu, Y., Zhao, Y., (2007), Results of PMIP2 coupled simulations of the Mid-Holocene and Last Glacial Maximum – Part 1: experiments and large-scale features. Climate of the Past 3, 261–277.

Bretz, J H., (1923), The Channeled Scablands of the Columbia Plateau. Journal of Geology, v. 31, p. 617–649.

Bretz, J H., (1969), The Lake Missoula floods and the Channeled Scabland. The Journal of Geology, v. 77, no. 5, p. 505–543.

Carling, P.A., Kirkbride, A.D., Parnachov, S., Borodavko, P.S., Berger, G.W., (2002), Late Quaternary catastrophic flooding in the Altai Mountains of south-central Siberia: a synoptic overview and introduction to flood deposit sedimentology, in Martini, I.P., Baker, and V.R., Garzon, G., eds., Flood and Megaflood Processes and Deposits: Recent and Ancient Examples. International Association of Sedimentologists Special Publication, v. 32, Blackwell Science, London, p. 17–35.

Carson, R.J., Gillespie, A.R., Bayasgalan, A., (2003), Late Quaternary geology along the Högiin Gol, northern Mongolia. Proceedings of the Oregon Academy of Science, v. 39, p. 20–21.

Cejudo-Figueiras, C., Morales, E.A., Wetzel, C.E., Blanco, S., Hoffmann, L., Ector, L., (2011), Analysis of the type of Fragilaria construens var. subsalina (Bacillariophyceae) and description of two morphologically related taxa from Europe and the United States. Phycologia, v. 50 (1), p. 67–77.

Channell, J.E.T., Xuan, C., Hodell, D.A., (2009), Stacking paleointensity and oxygen isotope data for the last 1.5 Myr (PISO-1500). Earth and Planetary Sciences Letters, v. 283, p. 14–23.

Charlesworth, J.K., (1957), The Quaternary Era. London, Edward Arnold, 2 vols, 591 pp. and 1700 pp.

Chauvenet, W., (1960), 1863 Reprint of 1891. A Manual of Spherical and Practical Astronomy, fifth ed., vol. II, pp. 473–566. Dover, N.Y.

Chen, Y.X., Li, Y.K., Wang, Y.Y., Zhang, M., Cui, Z.J., Yi, C.L., (2015), Late Quaternary glacial history of the Karlik Range, easternmost Tian Shan, derived from ^{10}Be surface exposure and optically stimulated luminescence datings. Quaternary Science Reviews 115, 17–27.

Chmeleff, J., von Blanckenburg, F., Kossert, K., Jakob, D., (2010), Determination of the ^{10}Be half-life by multicollector ICP-MS and liquid scintillation counting. Nuclear Instruments and Methods in Physics Research Section B: Beam interactions with Material and Atom 268, 192–199.

Christian, J.E., Koutnik, M., Roe, G., (2018), Committed retreat: controls on glacier disequilibrium in a warming climate. Journal of Glaciology, 1–14. doi: 10.1017/jog.2018.57.

Colgan, P.M., Munroe, J.S., Zhou, S.Z., (2006), Cosmogenic radionuclide evidence for the limited extent of last glacial maximum glaciers in the Tanggula Shan of the central Tibetan Plateau. Quaternary Research 65, 336–339.

Clark, P.U., Dyke, A.S., Shakun, J.D., Carlson, A.E., Clark, J., Wohlfarth, B., Mitrovica, J.X., Hostetler, S.W., McCabe, A.M., (2009), The last glacial maximum. Science 325, 710–713.

Clarke, G.K.C., Mathews, W.H., Pack, R.T., (1984), Outburst floods from glacial Lake Missoula. Quaternary Research, v. 22, p. 289–299.

Clauser, C., and Huenges, E., (1995), Thermal conductivity of rocks and minerals, in Ahrens, T.J., ed., Rock physics and phase relations: A handbook of physical constants. Washington DC, American Geophysical Union Reference Shelf, v. 3, p. 105–126.

Cortes, D.D., Martin, A.I., Yun, T.S., Francisca, F.M., Santamarina, J.C., Ruppel, C., (2009), Thermal conductivity of hydrate-bearing sediments. Journal of Geophysical Research, v. 114, B11103, p. 1–10.

Craig, R.G., (1987), Dynamics of a Missoula flood, in Mayer, L., and Nash, D., eds., Catastrophic flooding, Winchester, Allen and Unwin, p. 305–332.

Cuffey, K.M., and Paterson, W.S.B., (2010), The Physics of Glaciers, fourth ed. Elsevier, Amsterdam.

Darvill, C.M., Bentley, M.J., Stokes, C.R., Shulmeister, J., (2016), The timing and cause of glacial advances in the southern mid-latitudes during the last glacial cycle based on a synthesis of exposure ages from Patagonia and New Zealand. Quaternary Science Reviews 149, 200–214.

Desilets, D., and Zreda, M., (2003), Spatial and temporal distribution of secondary cosmic-ray nucleon intensities and applications to in-situ cosmogenic dating. Earth and Planetary Science Letters, v. 206, p. 21–42.

Desilets, D., Zreda, M., Prabu, T., (2006), Extended scaling factors for in situ cosmogenic nuclides: new measurements at low latitude. Earth and Planetary Science Letters, v. 246, p. 265–276.

Ditchburn, R.G. and Whitehead, N.E., (1994), The separation of ^{10}Be from silicates. 3d Workshop of the South Pacific Environmental Radioactivity Association, p. 4-7.

Dong, G.C., Xu, X.K., Zhou, W.J., Fu, Y.C., Zhang, L., Li, M., (2017), Cosmogenic ^{10}Be surface exposure dating and glacier reconstruction for the Last Glacial Maximum in the Quemuqu Valley, western Nyainqentanglha Mountains, south Tibet. Journal of Quaternary Science 32, 639–652.

Dorofeyuk, N.I., and Tarasov, P.E., (1998), Vegetation and levels of the lakes in the north of Mongolia during the last 12500 years, by the data of palynologic and diatom analyses. Stratigraphy and Geological Correlation, v. 6, p. 73–87.

Dunai, T., (2001), Influence of secular variation of the geomagnetic field on production rates of in situ produced cosmogenic nuclides. Earth and Planetary Science Letters, v. 193, p. 197–212.

Dunai, T.J., and Stuart, F.M., (2009), Reporting of cosmogenic nuclide data for exposure age and erosion rate determinations. Quaternary Geochronology 4, 437–440.

Edlund, M.B., Williams, R.M., Soninkhishig, N., (2003), The planktonic diatom diversity of ancient Lake Hovsgol, Mongolia. Phycologia, v. 42, p. 232–260.

Fan, Y., and van den Dool, H., (2008), A global monthly land surface air temperature analysis for 1948–present. Journal of Geophysical Research 113, D01103, doi:10.1029/2007JD008470.

Farr, T.G., and Chadwick, O.A., (1996), Geomorphic processes and remote sensing signatures of alluvial fans in the Kun Lun Mountains, China. Journal of Geophysical Research 101, E10, 23091–23100.

Farr, T.G., Rosen, P.A., Caro, E., Crippen, R., Duren, R., Hensley, S., Kobrick, M., Paller, M., Rodriguez, E., Roth, L., Seal, D., Shaffer, S., Shimada, J., Umland, J., Werner, M., Oskin, M., Burbank, D., Alsdorf, D., (2007), The Shuttle Radar Topography Mission. Reviews of Geophysics, v. 45, RG2004, p. 1–33.

Feathers, J.K., and Pagonis, V., (2015), Dating quartz near saturation – Simulations and application at archaeological sites in South Africa and South Carolina. Quaternary Geochronology, v. 30, p. 416–421.

Feathers, J.K., Casson, M.A., Henck, A.S., Chithambo, M.L., (2012), Application of pulsed OSL to polymineral fine-grained samples. Radiation Measurements, v. 47, p. 201–209.

Fink, D., and Smith, A., (2007), An inter-comparison of ^{10}Be and ^{26}Al AMS reference standards and the ^{10}Be half-life. Nuclear Instruments and Methods in Physics Research B 259, 600–609.

Fisher, T.G., (2003), Chronology of glacial Lake Agassiz meltwater routed to the Gulf of Mexico. Quaternary Research, v. 59 no. 2, p. 271–76.

Frey, H., Machguth, H., Huss, M., Huggel, C., Bajracharya, S., Bolch, T., Kulkarni, A., Linsbauer, A., Salzmann, N., Stoffel, M., (2014), Estimating the volume of glaciers in the Himalayan–Karakoram region using different methods. The Cryosphere 8, 2313–2333, doi: 10.5194/tc-8-2313-2014.

Fridleifsson, I.B., Bertani, R., Huenges, E., Lund, J.W., Rybach, L., (2008), The possible role and contribution of geothermal energy to the mitigation of climate change, in Hohmeyer, O., and Trittin, T., eds., Proceedings of IPCC Scoping meetings on renewable energy sources, Lübeck, Germany, p. 59–80.

Fu, P., Heyman, J., Hättestrand, C., Stroeven, A.P., Harbor, J.M., (2012), Glacial geomorphology of the Shaluli Shan area, southeastern Tibetan plateau. Journal of Maps 8, 48–55. http://dx.doi.org/10.1080/17445647.2012.668762.

Galbraith, R.F., and Roberts, R.G., (2012), Statistical aspects of equivalent dose and error calculation and display in OSL dating: an overview and some recommendations. Quaternary Geochronology, v. 11, p. 1–27.

Gardner, A.S., and Sharp, M., (2009), Sensitivity of net mass-balance estimates to near-surface temperature lapse rates when employing the degree-day method to estimate glacier melt. Annals of Glaciology 50 (50), 80–86.

Gardner, A.S., Moholdt, G., Cogley, J.G., Wouters, B., Arendt, A.A., Wahr, J., Berthier, E., Hock, R., Pfeffer, W.T., Kaser, G., Ligtenberg, S.R.M., Bolch, T., Sharp, M.J., Hagen, J.O., van den Broeke, M.R., Paul, F., (2013), A Reconciled Estimate of Glacier Contributions to Sea-Level Rise: 2003 to 2009. Science 340, 852–857. DOI: 10.1126/science.1234532.

Gibbons, A.B., Megeath, J.D., Pierce, K.L., (1984), Probability of moraine survival in a succession of glacial advances. Geology 12, 327–330.

Gillespie, A.R., (1991), Testing a new climatic interpretation for the Tahoe glaciation, in Hall Jr., C.A., Doyle-Jones, V., and Widawski, B., eds, Natural History of Eastern California and High-Altitude Research, White Mountain Research Station Symposium Volume 3. Los Angeles, CA, University of California, p. 383–398.

Gillespie, A., and Molnar, P., (1995), Asynchronous maximum advances of mountain and continental glaciers. Reviews of Geophysics, 33, 311–364.

Gillespie, A.R., Bayasgalan, A., Kuharic, M.V., (2005), Sediment core from ice-dammed paleolake Darhad, Mongolia. Geological Society of America Abstracts with Programs, v. 37, no. 7, p. 543.

Gillespie, A.R., Burke, R.M., Komatsu, G., Bayasgalan, A., (2008), Late Pleistocene glaciers in Darhad Basin, northern Mongolia. Quaternary Research v. 69, p. 169–187.

Gillespie, A.R., Rupper, S., Roe, G., (2003), Climatic interpretation from mountain glaciations in Central Asia. Geological Society of America Abstracts with Programs, v. 35, p. 414.

GLIMS and NSIDC, (2018), Global Land Ice Measurements from Space glacier database. Compiled and made available by the international GLIMS community and the National Snow and Ice Data Center, Boulder CO, U.S.A. DOI:10.7265/N5V98602.

Goldthwait, R.P., (1970), Mountain glaciers of the Residential Range in New Hampshire. Arctic Antarctic and Alpine Research. 2, 85–102.

Google Earth, DigitalGlobe, CNES/Airbus, (2017), Images accessed 2017 using Google Earth Pro v. 7.3.2.5491.

Gosse, J.C., and Phillips, F.M., (2001), Terrestrial in situ cosmogenic nuclides: theory and application. Quaternary Science Reviews, v. 20, p. 1475–1560.

Gravis, G.F., (1974), Geocryological conditions of Mongolian People's Republic, in Melnikov, P.I., ed., Transactions of the Joint Soviet-Mongolian Scientific-Research Geological Expedition, v. 10, Nauka, Moscow, p. 117–132 (in Russian)

Gravis, G.F., and Lisun, A.M., (1974), Ritmostratigrafiya chetvertichnykh otlozheniy Mongoliy po palinologicheskim dannym i istoriya razvitiya mnogoletnemerzlykh gornykh porod (Rhythmic-stratigraphy of Quaternary sediments in Mongolia according to palynological evidence and evolution history of permafrost), in Melnikov, P.I., ed., Geocryological conditions of Mongolian People's Republic, Transactions of the Joint Soviet-Mongolian Scientific-Research Geological Expedition, v. 10. Moscow, Nauka, p. 148–186. (in Russian)

Gribenski, N., Jansson, K.N., Lukas, S., Stroeven, A.P., Harbor, J.M., Blomdin, R., Ivanov, M.N., Heyman, J., Petrakov, D.A., Rudoy R., Clifton, T., Lifton, N.A., Caffee, M.W., (2016), Complex patterns of glacier advances during the late glacial in the Chagan Uzun Valley, Russian Altai. Quaternary Science Reviews 149, 288–305.

Gribenski, N., Jansson, K.N., Preusser, F., Harbor, J.M., Stroeven, A.P., Trauerstein, M., Blomdin, R., Heyman, J., Caffee, M.W., Lifton, N.A., Zhang, W., (2018), Re-evaluation of MIS 3 glaciation using cosmogenic radionuclide and single grain luminescence ages, Kanas Valley, Chinese Altai. Journal of Quaternary Science. DOI: 10.1002/jqs.2998.

Gross, G., Kerschner, H., Patzelt, G., (1976), Methodische Untersuchungen über die Schneegrenze in alpinen Gletschergebieten. Zeitschrift für Gletscherkunde und Glazialgeologie, v. 12, p. 223–251.

Grosswald, M.G., (1965), Razvitie relyefa Sayano-Tuvinskogo nagorya (Geomorphological development of the Sayan-Tuva upland). Nauka, Moscow, 166 p. (in Russian).

Grosswald, M.G., (1987), Poslednee oledenenie Sayano-Tuvinskogo nagorya: morfologiya, intensivnost pitaniya, podprudnye ozera (The last glaciation of the Sayany-Tuva highland: morphology and the rate of filling of ice-dammed lakes), in Kotikov, V.M., and Grosswald, M.G., eds., Interaction of Glaciations with the Atmosphere and Ocean, Nauka, Moscow, p. 152–170 (in Russian).

Grosswald, M.G., (1999), Evraziiskie gidrosfernye katastrofy i oledenenie Arktiki (Cataclysmic Megafloods in Eurasia and the Polar Ice Sheets). Nauchny Mir, Moscow, 117 p. (in Russian).

Grosswald, M.G., and Rudoy, A.N., (1996), Quaternary glacier-dammed lakes in the mountains of Siberia. Polar Geography, v. 20, p. 180–198.

GTN-G, (2017), GTN-G Glacier Regions. Global Terrestrial Network for Glaciers. DOI: 10.5904/gtng-glacreg-2017-07. Online access: http.//dx.doi.org/10.5904/gtng-glacreg-2017-07.

Guiry, M.D., and Guiry, G.M., (2015), AlgaeBase. World-wide electronic publication, National University of Ireland, Galway: http://www.algaebase.org; searched in September, 2015.

Hallet, B., and Putkonen, J., (1994), Surface dating of dynamic landforms: Young boulders and aging moraines. Science, v. 265, p. 937–940.

Harris, I., Jones, P.D., Osborn, T.J., Lister, D.H., (2014), Updated high-resolution grids of monthly climatic observations – the CRU TS3.10 Dataset. International Journal of Climatology, v. 34, p. 623–642.

Hays, J.D., Imbrie, J., Shackleton, N.J., (1976), Variations in the Earth's orbit: Pacemaker of the ice ages. Science 194, 1121–1132.

Heisinger, B., Lal, D., Jull, A.J.T., Kubik, P., Ivy-Ochs, S., Neumaier, S., Knie, K., Lazarev, V., Nolte, E., (2002a), Production of selected cosmogenic radionuclides by muons: 1. Fast muons. Earth and Planetary Science Letters 200, 345–355.

Heisinger, B., Lal, D., Jull, A.J.T., Kubik, P., Ivy-Ochs, S., Neumaier, S., Knie, K., Lazarev, V., Nolte, E., (2002b), Production of selected cosmogenic radionuclides by muons: 2. Capture of negative muons. Earth and Planetary Science Letters 200, 357–369.

Herget, J., (2005), Reconstruction of Pleistocene Ice-dammed Lake Outburst floods in the Altai Mountains, Siberia. Geological Society of America Special Paper, v. 386, 118 p.

Herget, J., (2012), Ice-dammed lake outburst floods in the Altai Mountains, Siberia – A review with links for further readings. Tomsk State University Journal of Biology, v. 1 no. 17, p. 148–168.

Herget, J., Carling, P., Agatova, A., Batbaatar, J., Borodavko, P., Gillespie, A., Nepop R., (2017), Comment on Gribenski, N. et al., 2016. Complex patterns of glacier advances during the late glacial in the Chagan Uzun Valley, Russian Altai. Quaternary Science Reviews 149, 288–305. Quaternary Science Reviews 168, 216–¯219, 10.1016/j.quascirev.2017.04.014.

Herzschuh, U., (2006), Palaeo-moisture evolution in monsoonal Central Asia during the last 50,000 years. Quaternary Science Reviews 25, 163–178.

Heyman, J., (2014), Paleoglaciation of the Tibetan Plateau and surrounding mountains based on exposure ages and ELA depression estimates. Quaternary Science Reviews, v. 91, p. 30–41.

Heyman, J., (2018), Expage: A global compilation of glacial ^{10}Be and ^{26}Al data (expage-201803). Accessed at http://expage.github.io/index.html.

Heyman, J., Hättestrand, C.H., Stroeven, A.P., (2008), Glacial geomorphology of the Bayan Har sector of the NE Tibetan plateau. Journal of Maps 4, 42–62. http://dx.doi.org/ 10.4113/jom.2008.96.

Heyman, J., Stroeven, A., Caffee, M.W., Hättestrand, C., Harbor, J.M., Li, Y., Alexanderson, H., Zhou, L., Hubbard, A., (2011a), Palaeoglaciology of Bayan Har Shan, NE Tibetan Plateau: exposure ages reveal a missing LGM expansion. Quaternary Sci. Rev. 30, 1988–2001.

Heyman, J., Stroeven, A.P., Harbor, J.M., Caffee, M.W., (2011b), Too young or too old: Evaluating cosmogenic exposure dating based on an analysis of compiled boulder exposure ages. Earth and Planetary Science Letters 302, 71–80.

Horiuchi, K., Matsuzaki, H., Osipov, E., Khlystov, O., Fujii, S., (2004), Cosmogenic ^{10}Be and ^{26}Al dating of erratic boulders in the southern coastal area of Lake Baikal, Siberia. Nuclear Instruments and Methods in Physics Research B 223–224, 633–638.

Hubert-Ferrari, A., Suppe, J., Van der Woerd, J., Wang, X., Lu, H.F., (2005), Irregular earthquake cycle along the southern Tianshan front, Aksu area, China. Journal of Geophysical Research 110, B06402.

Hughes, P.D., Gibbard, P.L., Ehlers, J., (2013), Timing of glaciation during the last glacial cycle: evaluating the concept of a global 'Last Glacial Maximum' (LGM). Earth-Science Reviews 125, 171–198. http://dx.doi.org/10.1016/j.earscirev.2013.07.003.

Hülle, D., Hilgers, A., Radtke, U., Stolz, C., Hempelmann, N., Grunert, J., Felauer, T., Lehmkuhl, F., (2010), OSL dating of sediments from the Gobi Desert, Southern Mongolia. Quaternary Geochronology, v. 5, p. 107–113.

Huntley, D.J., and Lamothe, M., (2001), Ubiquity of anomalous fading in K-feldspars and the measurement and correction for it in optical dating. Canadian Journal of Earth Sciences, v. 38, p. 1093–1106.

IPCC, (2013), Climate Change 2013: The physical science basis (Eds. Stocker, T.F., Qin, D., Plattner, G.K., Tignor, M.M., Allen, S.K., Boschung, J., Nauels, A., Xia, Y., Bex, V., Midgley, P.M.), Cambridge Univ. Press.

Ishikawa, M., and Yamkhin, J., (2015), Formation chronology of Arsain pingo, Darhad basin, northern Mongolia. Permafrost and Periglacial Processes, doi: 10.1002/ppp.1877.

Janz, L., Feathers, J.K., Burr, G.S., (2015), Dating surface assemblages using pottery and eggshell: assessing radiocarbon and luminescence techniques in Northeast Asia. Journal of Archaeological Science, v. 57, p. 119–129.

Jin, L., Chen, F., Morrill, C., Otto-Bliesner, B.L., Rosenbloom, N., (2012), Causes of early Holocene desertification in arid central Asia. Climate Dynamics 38, 1577–1591.

Jóhannesson, T., (2002), The initiation of the 1996 jökulhlaup from Lake Grímsvötn, Vatnajökull, Iceland, in Snorrason, Á., Finnsdóttir, H.P., and Moss, M., eds., The extremes of the extremes—Extraordinary floods. Wallingford, Oxfordshire, England, IAHS Press, International Association of Hydrological Sciences Publication No. 271, p. 57–64.

Kalnay, E., Kanamitsu, M., Kistler, R., Collins, W., Deaven, D., Derber, J., Gandin, L., Saha, S., White, G., Woollen, J., Zhu, Y., Chelliah, M., Ebisuzaki, W., Higgins, W., Janowiak, J., Mo, K.C., Ropelewski, C., Wang, J., Leetma, A., Reynolds, R., Jenne, R., (1995), The NCEP/NCAR 40-year re-analysis project. Bulletin of the American Meteorological Society 77, 437–471.

Kargel, J.S., Leonard, G.J., Bishop, M.P., Kääb, A., Raup, B.H. (Eds.), (2014), Global Land Ice Measurements from Space, Springer Praxis Books, Springer, Berlin.

Kayastha, R.B., Ohata, T., Ageta, Y., (1999), Application of a mass-balance model to a Himalayan glacier. Journal of Glaciology 45, 559–567.

Kohl, C.P., and Nishiizumi, K., (1992), Chemical isolation of quartz for measurement of in-situ - produced cosmogenic nuclides. Geochimica et Cosmochimica Acta 56, 3583–3587.

Komatsu, G., Arzhannikov, S.G., Gillespie, A.R., Burke, R.M., Miyamoto, H., Baker, V.R., (2009), Quaternary paleolake formation and cataclysmic flooding along the upper Yenisei River. Geomorphology, v. 104, p. 143–164.

Komatsu, G., Baker, V.R., Arzhannikov, S.G., Gallagher, R., Arzhannikova, A.V., Murana, A., Oguchi, T., (2016), Late Quaternary catastrophic flooding related to paleodrainage reorganization and paleolake formation in northern Eurasia: A history of alternative hypotheses and indications for future research. International Geology Review, v. (in press).

Komatsu, G., Clute, S.K., Baker, V.R., (1997), Preliminary remote sensing assessment of Pleistocene cataclysmic floods in Central Asia, in Proceedings, Lunar and Planetary Science Conference, 28th, p. 747–748.

Komatsu, G., Arzhannikov, S.G., Arzhannikova, A.V., Ori, G.G., (2007), Origin of glacial-fluvial landforms in the Azas Plateau volcanic field, the Tuva Republic, Russia: Role of ice-magma interaction. Geomorphology, v. 88, p. 352–366.

Kong, P., Fink, D., Na, C.G., Huang, F.X., (2009), Late Quaternary glaciation of the Tianshan, Central Asia, using cosmogenic ^{10}Be surface exposure dating. Quaternary Research 72, 229–233.

Koppes, M., Gillespie, A.R., Burke, R.M., Thompson, S.C., Stone, J., (2008), Late Quaternary glaciation in the Kyrgyz Tien Shan. Quaternary Science Reviews, v. 27, p. 846–866.

Koppes, M.N., and Montgomery, D.R., (2009), The relative efficacy of fluvial and glacial erosion over modern to orogenic timescales. Nature Geoscience, 2 (9), 644–647.

Kottek, M., Grieser, J., Beck, C., Rudolph, B., Rubel, F., (2006), World Map of the Köppen-Geiger climate classification updated. Meteorologische Zeitschrift 15 (3), 259–263.

Kraaijenbrink, P.D.A., Bierkens, M.F.P., Lutz, A.F., Immerzeel, W.W., (2017), Impact of a global temperature rise of 1.5 degrees Celsius on Asia's glaciers. Nature, 549 (7671), 257. doi: 10.1038/nature23878.

Krivonogov, S.K., Kazansky, A.Y., Oyunchimeg, Ts., Narantsetseg, Ts., Tomurhuu, D., Dolgorsuren, Kh., (2008), New in studies of the Darhad basin, Mongolia. Proceedings, 7th International Symposium “Environmental Changes in East Eurasia and Adjacent Areas – High Resolution Environmental Records of Terrestrial Sediments”, Ulaanbaatar–Hatgal, Mongolia, August 23-29, p. 66–74.

Krivonogov, S.K., Sheinkman, V.S., Mistryukov, A.A., (2005), Ice damming of the Darhad paleolake (northern Mongolia) during the Late Pleistocene. Quaternary International, v. 136, p. 83–94.

Krivonogov, S.K., Yi, S., Kashiwaya, K., Kim, J.C., Narantsetseg, T., Oyunchimeg, T., Safonova, I.Y., Kazansky, A.Y., Sitnikova, T., Kim, J.Y., Hasebe, N., (2012), Solved and unsolved problems of sedimentation, glaciation and paleolakes of the Darhad Basin, Northern Mongolia. Quaternary Science Reviews, v. 56, p. 142–163.

Lal, D., (1991), Cosmic ray labeling of erosion surfaces: in situ nuclide production rates and erosion models. Earth and Planetary Science Letters, v. 104, p. 424–439.

Lasserre, C., Gaudemer, Y., Tapponnier, P., Mériaux, A-S., van der Woerd, J., Yuan, D.Y., Ryerson, F.J., Finkel, R.C., Caffee, M.W., (2002), Fast late Pleistocene slip rate on the Leng Long Ling segment of the Haiyuan fault, Qinghai, China. Journal of Geophysical Research 107, B11 2276.

Lehmkuhl F., Hilgers, A., Fries, S., Hülle, D., Schlütz, F., Shumilovskikh, L., Felauer, T., Protze, J., (2011), Holocene geomorphological processes and soil development as indicators for environmental change around Karakorum, Upper Orkhon Valley (Central Mongolia). Catena, v. 87, p. 31–44.

Li, Y.K., Liu, G.N., Chen, Y.X., Li, Y.N., Harbor, J., Stroeven, A.P., Caffee, M., Zhang, M., Li, C.C., Cui, Z.J., (2014), Timing and extent of Quaternary glaciations in the Tianger Range, eastern Tian Shan, China, investigated using ^{10}Be surface exposure dating. Quaternary Science Reviews 98, 7–23.

Li, Y.K., Liu, G.N., Kong, P., Harbor, J., Chen, Y.X., Caffee M., (2011), Cosmogenic nuclide constraints on glacial chronology in the source area of the Urumqi River, Tian Shan, China. Journal of Quaternary Science 26, 297–304.

Li, Y.N., Li, Y.K., Harbor, J., Liu, G.N., Yi, C.L., Caffee, M.W., (2016), Cosmogenic ^{10}Be constraints on Little Ice Age glacial advances in the eastern Tian Shan, China. Quaternary Science Reviews 138, 105–118.

Lifton, N., Beel, C., Hättestrand, C., Kassab, C., Rogozhina, I., Heermance, R., Oskin, M., Burbank, D., Blomdin, R., Gribenski, N., Caffee, M., Goehring, B.M., Heyman, J., Ivanov, M., Li, Y.N., Li, Y.K., Petrakov, D., Usubaliev, R., Codilean, A.T., Chen, Y.X., Harbor, J., Stroeven, A.P., (2014), Constraints on the late Quaternary glacial history of the Inylchek and Sary-Dzaz valleys from in situ cosmogenic ^{10}Be and ^{26}Al, eastern Kyrgyz Tian Shan. Quaternary Science Reviews 101, 77–90.

Lifton, N.A., Bieber, J.W., Clem, J.M., Duldig, M.L., Evenson, P., Humble, J.E., Pyle, R., (2005), Addressing solar modulation and long-term uncertainties in scaling in situ cosmogenic nuclide production rates. Earth and Planetary Science Letters, v. 239, p. 140–161.

Lilliefors, H.W., (1967), On the Kolmogorov-Smirnov test for normality with mean and variance unknown. Journal of the American Statistical Association 62, 399–402.

Lisiecki, L.E., and Raymo, M.E., (2005), A Pliocene-Pleistocene stack of 57 globally distributed benthic δ18O records. Paleoceanography, v. 20, PA1003, doi:10.1029/2004PA001071.

Litasov, Yu., Hasenaka, T., Litasov, K., Yarmolyuk, V., Sugorakova, A., Lebedev, V., Sasaki, M., Taniguchi, H., (2001a), Petrologic characteristics of Cenozoic alkaline basalts from the Azas Plateau, northeast Tuva (Russia). Northeast Asian Studies 6, Center for Northeast Asian studies, Tohoku University, p. 201–226.

Litasov, K., Ito, Y., Litasov, Yu. Kitakaze, A., Taniguchi, H., (2001b), Lithosphere structure and thermal regime of the upper mantle along Baikal rift axis: Evidences from deep-seated xenoliths. Northeast Asian Studies, v. 6, p. 227–252.

Liu, J.H., Yi, C.L., Li, Y.K., Bi, W.L., Zhang, Q., Hu, G., (2017), Glacial fluctuations around the Karola Pass, eastern Lhagoi Kangri range, since the Last Glacial Maximum. Journal of Quaternary Science 32, 516–527.

Lukas, S., Spencer, J.Q.G., Robinson, R.A.J., Benn, D.I., (2007), Problems associated with luminescence dating of Late Quaternary glacial sediments in the NW Scottish Highlands. Quaternary Geochronology 2, 243–248.

Lüthgens, C., Krbetschek, M., Böse, M., Fuchs, M.C., (2010), Optically simulated luminescence dating of fluvioglacial (sandur) sediments from north-eastern Germany. Quaternary Geochronology, v. 5, p. 237–243.

Lyell, C., (1830–3), Principles of Geology, being an attempt to explain the former changes of the Earth's surface, by reference to causes now in operation, vols. 1–3. John Murray, London.

Malde, H.E., (1968), The catastrophic late Pleistocene Bonneville flood in the Snake River Plain, Idaho, in U.S. Geological Survey Professional Paper, v. 596. United States Government Printing Office, Washington, 52 p.

Mangerud, J., Jakobsson, M., Alexanderson, H., Astakhov, V., Clarke, G., Henriksen, M., Hjort, C., Krinner, G., Lunkka, J.P., Möller, P., Murray, A., Nikolskaya, O., Saarnisto, M., Svendsen, J.I., (2004), Ice-dammed lakes and rerouting of the drainage of Northern Eurasia during the last glaciation. Quaternary Science Reviews, v. 23, p. 1313–1332.

Manley, G., (1959), The late-glacial climate of north-west England. Liverpool and Manchester Geological Journal, v. 2, p. 188–215.

Margold, M., Jansson, K. N., Stroeven, A. P., Jansen, J.D., (2011), Glacial Lake Vitim, a 3000-km^3 outburst flood from Siberia to the Arctic Ocean. Quaternary Research, v. 76, p. 393–396.

Marzeion, B., Cogley, J.G., Richter, K., Parkes, D., (2017), Attribution of global glacier mass loss to anthropogenic and natural causes. Science 345, 919–921.

Matthews, J.A., and Briffa, K.R., (2005), The 'Little Ice Age': Re-evaluation of an evolving concept. Geografiska Annaler. Series A, Physical Geography 87, 17–36.

Mayewski, P.A., Rohling, E.E., Stager, J.C., Karlen, W., Maasch, K.A., Meeker, L.D., Meyerson, E.A., Gasse, F., van Kreveld, S., Holmgren, K., Lee-Thorp, J., Rosqvist, G., Rack, F., Staubwasser, M., Schneider, R.R., Steig, E.J., (2004), Holocene climate variability. Quaternary Research 62, 243–255.

Medvedeff, W.G., and Roe, G.H., (2017), Trends and variability in the global dataset of glacier mass balance. Climate Dynamics 48, 3085. https://doi.org/10.1007/s00382-016-3253-x

Meier, M.F., and Post, A.S., (1962), Recent variations in mass net budgets of glaciers in western North America. International Association of Hydrological Sciences Publication, v. 58, p. 63–77.

Meierding, T.C., (1982), Late Pleistocene glacial equilibrium-line in the Colorado Front Range: a comparison of methods. Quaternary Research, v. 18, 289–310.

Merle, J.R., (2001), Quaternary geology of the Tengis-Shishid Gol region, Khovsgol, Mongolia [Senior thesis]. Whitman College, 56 p.

Miehe, G., Schültz, F., Miehe, S., Opgenoorth, L., Cermak, J., Samiya, R., Jäger, E.J., Wesche, K., (2007), Mountain forest islands and Holocene environmental changes in Central Asia: A case study from the southern Gobi Altay, Mongolia. Palaeogeography Palaeoclimatology, Palaeoecology. 250, 150–166.

Minder, J.R., Mote, P.W., Lundquist, J.D., (2010), Surface temperature lapse rates over complex terrain: Lessons from the Cascade Mountains. Journal of Geophysical Research 115, D14122, doi:10.1029/2009JD013493.

Mitchell, T. D., and Philip, D. J., (2005), An improved method of constructing a database of monthly climate observations and associated high resolution grids. International Journal of Climatology, v. 25, p. 693–712.

Mix, A.C., Bard, E., Schneider, R., (2001), Environmental processes of the ice age: land, oceans, glaciers (EPILOG). Quaternary Science Reviews, 627–657.

Mölg, T., and Hardy, D.R., (2004), Ablation and associated energy balance of a horizontal glacier surface on Kilimanjaro. Journal of Geophysical Research 109, D16104, doi:10.1029/2003JD004338.

Molnar, P., and Tapponnier, P., (1975), Cenozoic tectonics of Asia: Effects of a continental collision. Science 189, 419–26.

Montgomery, D. R., (2013), The Rocks Don't Lie: A Geologist Investigates Noah's Flood. W. W. Norton & Company, 320 p.

Montgomery, D. R., Hallet, B., Yuping, L., Finnegan, N., Anders, A., Gillespie, A., Greenberg, H. M., (2004), Evidence for Holocene megafloods down the Tsangpo River gorge, southeastern Tibet. Quaternary Research, v. 62, p. 201-207.

Morén, B., Heyman, J., Stroeven, A.P., (2011), Glacial geomorphology of the central Tibetan plateau. Journal of Maps 7, 115–125. http://dx.doi.org/10.4113/jom.2011.1161.

Narantsetseg, Ts., Krivonogov, S.K., Oyunchimeg, Ts., Uugantsetseg, B., Burr, G.S., Tomurhuu, D., Dolgorsuren, Kh., (2013), Late Glacial to Middle Holocene climate and environmental changes as recorded in Lake Dood sediments, Darhad Basin, northern Mongolia. Quaternary International, v. 311, p. 12–24.

National Aeronautics and Space Administration LP DAAC, (2018), ASTER Level 1B Registered Radiance at the Sensor, Version 3. NASA EOSDIS Land Processes DAAC, USGS Earth Resources Observation and Science (EROS) Center, Sioux Falls, South Dakota (https://lpdaac.usgs.gov), accessed 2009–2018 at https://lpdaac.usgs.gov/dataset_discovery/aster/aster_products_table/ast_l1b.

National Aeronautics and Space Administration, (2015), Shuttle Radar Topography Mission V3 Global 1 arc second dataset (SRTMGL1), accessed July 2016 using Reverb version 10.128.2.

National Aeronautics and Space Administration, (2017), Advanced Spaceborne Thermal Emission and Reflection Radiometer (ASTER) accessed March 2017 via https://earthdata.nasa.gov.

National Aeronautics and Space Administration (NASA), and The Ministry of Economy, Trade, and Industry (METI) of Japan, (2017), Advanced Spaceborne Thermal Emission and Reflection Radiometer (ASTER) Global Digital Elevation Model Version 2 (GDEM V2) accessed 2017 via https://earthdata.nasa.gov.

National Oceanic and Atmospheric Administration, (2016), Integrated Surface Database (ISD), Station Tonhil USAF ID 442660. Accessed from http://www.ncdc.noaa.gov/isd in October 2016.

Nichols, K.K., Bierman, P.R., Foniri, W.R., Gillespie, A.R., Caffee, M., Finkel, R., (2006), Dates and rates of arid region geomorphic processes. GSA Today, v. 16, no. 8, p. 4–11. doi: 10.1130/GSAT01608.1.

Nishiizumi, K., (2004), Preparation of ^{26}Al AMS standards. Nuclear Instruments and Methods in Physics Research B 223–224, 388–392.

Nishiizumi, K., Imamura, M., Caffee, M., Southon, J., Finkel, R., McAnich, J., (2007), Absolute calibration of ^{10}Be AMS standards. Nuclear Instruments and Methods in Physics Research Section B: Beam interactions with Material and Atom 258, 403–413.

Normark, W.R., and Reid, J.A., (2003), Extensive deposits on the Pacific Plate from Late Pleistocene North American glacial lake outbursts. The Journal of Geology, v. 111, p. 617–637.

Nuimura, T., Sakai, A., Taniguchi, K., Nagai, H., Lamsal, D., Tsutaki, S., Kozawa, A., Hoshina, Y., Takenaka, S., Omiya, S., Tsunematsu, K., Tshering, P., Fujita, K., (2015), The GAMDAM glacier inventory: A quality-controlled inventory of Asian glaciers. The Cryosphere 9, 849–864. https://doi.org/10.5194/tc-9-849-2015.

O'Connor, J.E., and Baker, V.R., (1992), Magnitudes and implications of peak discharges from Glacial Lake Missoula. Geological Society of America Bulletin, v. 104, p. 267–279.

O'Connor, J.E., and Costa, J.E., (2004), The world's largest floods – Their causes and magnitudes. U.S. Geological Survey Circular 1254, Reston, VA, U.S. Geological Survey, 13 p.

Ohmura, A., Kasser, P., Funk, M., (1992), Climate at the equilibrium line of glaciers. Journal of Glaciology 38, 397–411.

Olyunin, V.N., (1965), Neotectonics and Glaciation of East Sayan. Nauka, Moscow, 128 p. (in Russian).

Owen, L.A., Richards, B., Rhodes, E.J., Cunningham, W.D., Windley, B.F., Badamgarov, J., Dorjnamjaa, D., (1998), Relic permafrost structures in the Gobi of Mongolia: age and significance. Journal of Quaternary Science 13, 539–547.

Owen, L.A., Ma, H.Z., Derbyshire, E., Spencer, J.Q., Barnard, P.L., Nian, Z.Y., Finkel, R.C., Caffee, M.W., (2003), The timing and style of late Quaternary glaciation in the La Ji Mountains, NE Tibet: evidence for restricted glaciation during the latter part of the last glacial. Zeitschrift für Geomorphologie Supplementband 130, 263–276.

Owen, L.A., Spencer, J.Q., Ma, H.Z., Barnard, P.L., Derbyshire, E., Finkel, R.C., Caffee, M.W., Nian, Z.Y., (2003), Timing of Late Quaternary glaciation along the southwestern slopes of the Qilian Shan, Tibet. Boreas 32, 281–291.

Owen, L.A., Finkel, R.C., Barnard, P.L., Ma, H.Z., Asahi, K., Caffee, M.W., Derbyshire, E., (2005), Climatic and topographic controls on the style and timing of late Quaternary glaciation throughout Tibet and the Himalaya defined by ^{10}Be cosmogenic radionuclide surface exposure dating. Quaternary Science Reviews 24, 1391–1411.

Pardee, J.T., (1942), Unusual currents in Lake Missoula, Montana. Geological Society of America Bulletin, v. 53, p. 1569-1599.

Peck, J.A., Khosbayar, P., King, J., Fowell, S.J., Aurienbyleg, K., Soninkhishig, N., (2001), The Latest Holocene sedimentary environmental magnetic record from Lake Dood, Mongolia. EOS, v. 82, F337.

Peck, J.A., King, J.W., Colman, S.M., Kravchinsky, V.A., (1994), A rock-magnetic record from Lake Baikal, Siberia: Evidence for Late Quaternary climate change. Earth and Planetary Science Letters, v. 122, p. 221–238.

Peretolchin, S.P., (1908), Ledniki hrebta Munku-Sardyk (Glaciers of the Munku-Sardyk ridge). Tomsk, Izvestiya Tomskogo Teknologicheskogo Instituta (Proceedings of the Tomsk Technological Institute), v. 9, no. 1, p. 47. (in Russian).

Porter, S.C, (1975), Equilibrium-line altitudes of late Quaternary glaciers in the Southern Alps, New Zealand. Quaternary Research 5, 27–47.

Porter, S.C., (2001), Snowline depression in the tropics during the last glaciation. Quaternary Science Reviews 20, 1067–1091.

Prescott, J.R., and Hutton, J.T., (1994), Cosmic ray contributions to dose rates for luminescence and ESR dating: Large depths and long-term time variations. Radiation Measurements, v. 23, p. 497–500.

Prokopenko, A.A., Karabanov, E.B., Kuz'min, M.I., Williams, D.F., (2001), The mechanism of early glaciation during the transition from Kazantsevo climatic optimum to Zyrjanka glacial period (Evidence from bottom sediments of Lake Baikal). Geologiya i Geofizika (Russian Geology and Geophysics), v. 42 (1–2), p. 64–75 (55–65).

Prokopenko, A.A., Kuzmin, M.I., Williams, D.F., Gelety, V.F., Kalmychkov, G.V., Gvozdkov, A.N., Solotchin, P.A., (2005), Basin-wide sedimentation changes and deglacial lake-level rise in the Hovsgol basin, NW Mongolia. Quaternary International, v. 136, p. 59–69.

Putkonen, J., and Swanson, T., (2003), Accuracy of cosmogenic ages for moraines. Quaternary Research, v. 59, p. 255–261.

Putnam, A.E., Denton, G.H., Schaefer, J.M., Barrell, D.J.A., Andersen, B.G., Finkel, R.C., Schwartz, R., Doughty, A.M., Kaplan, M.R., Schlüchter, C., (2010), Glacier advance in southern middle-latitudes during the Antarctic Cold Reversal. Nature Geoscience, v. 3, p. 700–704.

Putnam, A.E., Schaefer, J.M., Denton, G.H., Barrell, D.J.A., Birkel, S.D., Andersen, B.G., Kaplan, M.R., Finkel, R.C., Schwartz, R., Doughty, A.M., (2013), The Last Glacial Maximum at 44°S documented by a ^{10}Be moraine chronology at Lake Ohau. Quaternary Science Reviews 27Southern Alps of New Zealand. 62, 114–141.

Rades, E.F., Hetzel, R., Strobl, M., Xu, Q., Ding, L., (2015), Defining rates of landscape evolution in a south Tibetan graben with *in situ*-produced cosmogenic ^{10}Be. Earth Surface Processes and Landforms 40, 1862–1876.

Ramage, J.M., Smith, J.A., Rodbell, D.T., Seltzer, G.O., (2005), Comparing reconstructed Pleistocene equilibrium-line altitudes in the tropical Andes of central Peru. Journal of Quaternary Science, v. 20, p. 777–788.

Raney, R.K., Luscombe, A.P., Langham, E.J., Ahmed, S., (1991), RADARSAT. Proceedings of the IEEE, v. 79, no. 6, p. 839–849.

Reimer, P.J., Bard, E., Bayliss, A., Beck, J.W., Blackwell, P.G., Ramsey, C.B., Buck, C.E., Cheng, H., Edwards, R.L., Friedrich, M., Grootes, P.M., Guilderson, T.P., Haflidason, H., Hajdas, I., Hatté, C., Heaton, T.J., Hoffmann, D.L., Hogg, A.G., Hughen, K.A., Kaiser, K.F., Kromer, B., Manning, S.W., Niu, M., Reimer, R.W., Richards, D.A., Scott, E.M., Southon, J.R., Staff, R.A., Turney, C.S.M., Plicht, J., (2013), IntCal13 and MARINE13 radiocarbon age calibration curves 0–50,000 years cal BP. Radiocarbon, v. 55, no. 4, p.1869–1887.

Reuther, A.U., (2007), Surface exposure dating of glacial deposits from the last glacial cycle – evidence from the eastern Alps, the Bavarian Forest, the southern Carpathians and the Altai Mountains. Relief Boden Paläoklima 21, 1–213.

Reuther, A.U., Herget, J., Ivy-Ochs, S., Borodavko, P., Kubik, P.W., Heine, K., (2006), Constraining the timing of the most recent cataclysmic flood event from ice-dammed lakes in the Russian Altai Mountains, Siberia, using cosmogenic in situ ^{10}Be. Geology, v. 34, no. 11, p. 913–916.

RGI Consortium, (2017), Randolph Glacier Inventory – A Dataset of Global Glacier Outlines: Version 6.0: Technical Report, Global Land Ice Measurements from Space, Colorado, USA. Digital Media. DOI: https://doi.org/10.7265/N5-RGI-60.

Roe, G.H., Baker, M.B., Herla, F., (2017), Centennial glacier retreat as categorical evidence of regional climate change. Nature Geoscience 10, 95–99.

Rolland, C., (2002), Spatial and seasonal variations of air temperature lapse rates in Alpine region. Journal of Climate 16, 1032–1046.

Ross, S.M., (2003), Peirce's criterion for the elimination of suspect experimental data. Journal of Engineering Technology 20, 38–41.

Rother, H., Lehmkuhl, F., Fink, D., Nottebaum, V., (2014), Surface exposure dating reveals MIS-3 glacial maximum in the Khangai Mountains of Mongolia. Quaternary Research, v. 82, p. 297–308.

Rother, H., Shulmeister, J., Fink, D., Alexander, D., Bell, D., (2015), Surface exposure chronology of the Waimakariri glacial sequence in the Southern Alps of New Zealand: implications for MIS-2 ice extent and LGM glacial mass balance. Earth and Planetary Science Letters 429, 69–81.

Round, F.E., and Bukhtiyarova, L., (1996), Four new genera based on Achnanthes (Achnanthidium) together with a re-definition of Achnanthidium. Diatom Research, v. 11, p. 345–361.

Rudoy, A.N., (2002), Glacier-dammed lakes and geological work of glacial superfloods in the Late Pleistocene, Southern Siberia, Altai Mountains. Quaternary International, v. 87, p. 119–140.

Rudoy, A.N., and Baker, V.R., (1993), Sedimentary effects of cataclysmic late Pleistocene glacial outburst flooding, Altai Mountains, Siberia. Sedimentary Geology, v. 85, p. 53–62.

Rupper, S., (2007), Glacier sensitivity and regional climate: Past and present. PhD Dissertation. University of Washington.

Rupper, S., and Koppes, M., (2010), Spatial patterns in Central Asian climate and equilibrium line altitudes. IOP Conference Series: Earth and Environmental Science, v. 9, no. 012009. doi:10.1088/1755-1315/9/1/012009

Rupper, S., and Roe, G., (2008), Glacier changes and regional climate: A mass and energy balance approach. Journal of Climate, v. 21, p. 5384–5401.

Rupper, S., Roe, G., Gillespie, A., (2009), Spatial patterns of Holocene glacier advance and retreat in Central Asia. Quaternary Research, v. 72, p. 337–346.

Ryan, W. B. F., Pitman III, W. C., Major, C. O., Shimkus, K., Moskalenko, V., Jones, G. A., Dimitrov, P., Goriir, N., Saking, M., Yiice, H., (1997), An abrupt drowning of the Black Sea shelf. Marine Geology, v. 138, p. 119–126.

Sakai, A., Nuimura, T., Fujita, K., Takenaka, S., Nagai, H., Lamsal, D., (2015), Climate regime of Asian glaciers revealed by GAMDAM glacier inventory. The Cryosphere, v. 9, p. 868–880.

Schäfer, J.M., (2000), Reconstruction of landscape evolution and continental paleoglaciations using in-situ cosmogenic nuclides: examples from Antarctica and the Tibetan Plateau. PhD thesis, ETH Zürich.

Schneider, U., Becker, A., Finger, P., Meyer-Christoffer, A., Rudolf, B., Ziese, M., (2016), GPCC Full Data Reanalysis Version 7.0: Monthly Land-Surface Precipitation from Rain Gauges built on GTS based and Historic Data. Research Data Archive at the National Center for Atmospheric Research, Computational and Information Systems Laboratory. https://doi.org/10.5065/D6000072. Accessed January 2016.

Selivanov, E.I., (1967), Neogene-Quaternary giant lakes in Transbaikalia and North Mongolia. Reports of the Academy of Sciences of the USSR, v. 177, p. 175–178 (in Russian).

Shang, Y., Yang, Z., Li, L., Liu, D., Liao, Q., Wang, Y., (2003), A super-large landslide in Tibet in 2000: background, occurrence, disaster, and origin. Geomorphology, v. 54, no. 3–4, p. 225-243.

Sharkhuu, A., Sharkhuu, N., Etzelmüller, B., Heggem, E.S.F., Nelson, F.E., Shiklomanov, N.I., Goulden, C.E., Brown, J., (2007), Permafrost monitoring in the Hovsgol mountain region, Mongolia. Journal of Geophysical Research, v. 112, F02S06, doi:10.1029/2006JF000543.

Shchetnikov, A.A., (2001), Struktura reliefa i noveyshaya tektonika Tunkinskogo rifta (Structure of Relief and Neotectonics of the Tunka Rift) [Abstract of PhD Thesis]. Irkutsk, Institute of Earth's Crust, Siberian Branch, Russian Academy of Sciences, 19 p. (in Russian).

Shea, J.M., and Immerzeel, W.W., (2016), An assessment of basin-scale glaciological and hydrological sensitivities in the Hindu Kush–Himalaya. Annals of Glaciology 57 (71) 308–318. doi: 10.3189/2016AoG71A073

Shi, Y., (2002), Characteristics of late Quaternary monsoonal glaciation on the Tibetan Plateau and in East Asia. Quaternary International 97–98, 79–91.

Smith, S.G., Wegmann, K.W., Ancuta, L.D., Gosse, J.C., Hopkins, C.E., (2016), Paleotopography and erosion rates in the central Hangay Dome, Mongolia: landscape evolution since the mid-Miocene. Journal of Asian Earth Sciences 125, 37–57.

Stone, J.O., (2000), Air pressure and cosmogenic isotope production. Journal of Geophysical Research: Solid Earth 105, 23753–23759.

Stroeven, A.P., Hättestrand, C., Heyman, J., Kleman, J., Morén, B.M., (2013), Glacial geomorphology of the Tian Shan. Journal of Maps 9, 505–512. http://dx.doi.org/10.1080/17445647.2013.820879.

Stuiver, M., and Polach, H.A., (1977), Discussion: reporting of ^{14}C data. Radiocarbon, v. 19, p. 355.

Stuiver, M., and Reimer, P.J., (1993), Extended ^{14}C database and revised CALIB radiocarbon calibration program. Radiocarbon, v. 35, p. 215–230.

Tachikawa, T., Kaku, M., Iwasaki, A., Gesch, D., Oimoen, M., Zhang, Zh., Danielson, J., Krieger, T., Curtis, B., Haase, J., Abrams, M., Crippen, R., Carabajal, C., (2011), ASTER Global Digital Elevation Model Version 2 – Summary of Validation Results. Online: http://asterweb.jpl.nasa.gov/gdem.asp.

Teller, J.T., Leverington, D.W., Mann, J.D., (2002), Freshwater outbursts to the oceans from glacial Lake Agassiz and their role in climate change during the last deglaciation. Quaternary Science Reviews, v. 21, p. 879–887.

Thomas, P.J., Murray, A.S., Sandgren, P., (2003), Age limit and age underestimation using different OSL signals from lacustrine quartz and polymineral fine grains. Quaternary Science Reviews, v. 22, p. 1139–1143.

Thompson, L.G., Mosley-Thompson, E., Davis, M.E., Bolzan, J.F., Dai, J., Yao, T., Gundestrup, N., Wu, X., Klein, L., Xie Z., (1989), Holocene-Late Pleistocene climatic ice core records from Qinghai-Tibetan Plateau. Science 246, 474–477.

Torsnes, I., Rye, N., Nesje, A., (1993), Modern and Little Ice Age equilibrium-line altitudes on outlet valley glaciers from Jostedalsbreen, western Norway: an evaluation of different approaches to their calculation. Arctic and Alpine Research, v. 25, p. 106–116.

U.S. Geological Survey Geological Names Committee, (2010), Divisions of geologic time—Major chronostratigraphic and geochronologic units: Fact Sheet 2010–3059, (https://pubs.usgs.gov/fs/2010/3059/).

U.S. Geological Survey, (2012), Landsat – A global land-imaging mission: U.S. Geological Survey Fact Sheet 2012, 3072, p. 3.

U.S. Geological Survey, (2017), Global 30 Arc-Second Elevation (GTOPO30). These data are distributed by the Land Processes Distributed Active Archive Center (LP DAAC), located at USGS/EROS, Sioux Falls, SD. http://lpdaac.usgs.gov.

U.S. Geological Survey, (2018), Landsat-7 image courtesy of the U.S. Geological Survey, accessed 2009–2018 at https://earthexplorer.usgs.gov.

U.S. Geological Survey Geological Names Committee, (2010), Divisions of geologic time—Major chronostratigraphic and geochronologic units: Fact Sheet 2010–3059. https://pubs.usgs.gov/fs/2010/3059/

Ufland, A.K., Ilyin, A.V., Spirkin, A.I., (1969), Vpadiny baikal'skogo tipa severnoi Mongolii (Baikal-type basins of northern Mongolia). Bulletin of the Moscow Society of Naturalists (MOIP), Geology series, Moscow, Moscow University Publ., v. 44, no. 6, p. 5–22. (in Russian).

Ufland, A.K., Ilyin, A.V., Spirkin, A.I., Shilova, G.N., (1971), Osnovniye cherty stratigrafii i usloviya formirovanya Kainozoiskikh obrazovanii Prikosogolya (MNR) (Main features of stratigraphy and formation of Cenozoic deposits in Prekosogol) (MPR). Bulletin of the Moscow Society of Naturalists (MOIP), Geology Series, Moscow, Moscow University Publ., v. 46, p. 54–69. (in Russian).

Vargo, L.J., Galewsky, J., Rupper, S., Ward, D.J., (2018), Sensitivity of glaciation in the arid subtropical Andes to changes in temperature, precipitation, and solar radiation. Global and Planetary Change 163, 86–96.

Vasil'chuk, Yu.K., Alekseev, S.V., Arzhannikov, S.G., Alekseeva, L.P., Budantseva, N.A., Chizhova, Ju.N., Arzhannikova, A.V., Vasil'chuk, A.C., Kozyreva, E.A., Rybchenko, A.A., Svetlakov, A.A., (2015), Oxygen and hydrogen isotope compositions of lithalsa frozen core: A case study from the Sentsa River valley, East Sayan. Kriosfera Zemli (Earth's Cryosphere), v. 19, no. 2, p. 46–58. http://www.izdatgeo.ru/pdf/earth_cryo/2015-2/46_eng.pdf

Verosub, K.L., and Roberts, A.P., (1995), Environmental magnetism: Past, present, and future. Journal of Geophysical Research, v. 100, no. B2, p. 2175–2192.

Waitt, R.B., Jr., (1980), About 40 last-glacial Lake Missoula jökulhlaups through southern Washington. Journal of Geology, v. 88, p. 653–679.

Wallinga, J., Murray, A.S., Duller, G.A.T., Törnqvist, T.E., (2001), Testing optically simulated luminescence dating of sand-sized quartz and feldspar from fluvial deposits. Earth and Planetary Science Letters, v. 193, p. 617–630.

Wang, J., Kassab, C., Harbor, J.M., Caffee, M.W., Cui, H., Zhang, G.L., (2013), Cosmogenic nuclide constraints on late Quaternary glacial chronology on the Dalijia Shan, northeastern Tibetan Plateau. Quaternary Research 79, 439–451.

Wegmann, K.W., Amgaa, Ts., Frankel, K.L., Dewett, A.P., Bayasgalan, A., (2011), Geologic, geomorphic, and environmental change at the northern termination of the Lake Hövsgöl rift, Mongolia. Proceedings of the Twenty-Fourth Annual Keck Research Symposium in Geology, Union College, Schenectady, NY, April, 2011, p. 220–229.

Wiedmer, M., Montgomery, D. R., Gillespie, A. R., Greenberg, H., (2010), Late Quaternary megafloods from Glacial Lake Atna, Southcentral Alaska, U.S.A.. Quaternary Research, v. 73, p. 413–424. doi: 10.1016/j.yqres.2010.02.005.

Wintle, A.G., and Murray, A.S., (2006), A review of quartz optically stimulated luminescence characteristics and their relevance in single- aliquot regeneration dating protocols. Radiation Measurements, v. 41, p. 369–391.

Wortmann, M., Krysanova, V., Kundzewicz, Z. W., Su, B., Li, X., (2014), Assessing the influence of the Merzbacher Lake outburst floods on discharge using the hydrological model SWIM in the Aksu headwaters, Kyrgyzstan/NW China. Hydrological Processes, v. 28, p. 6337–6350.

Yamskikh, A.F., and Yamskikh, A.A., (1999), Dynamics of the Todza ice-dammed lake (upper Yenisei River, southern Siberia) during the late Pleistocene and Holocene. Science Reports of Tohoku University, 7th Series (Geography) 49, (Special Issue on GLOCOPH 98), p. 143–159.

Yamskikh, A.F., Yamskikh, G.Y., Vasiliev, S.A., Ermolova, N.M., (2001), Paleoecology of the Maina group of multiplayer Paleolithic sites in the Yenisei River valley (at the boundary between West Sayan Mountains and Minusa Depression). Field Guidebook for the Global Continental Paleohydrology Meeting, Krasnoyarsk-Khakassia Tuva Region, Russia, pp. 146–156.

Yang, D., Ye, B., Kane, D.L., (2004), Streamflow changes over Siberian Yenisei River Basin. Journal of Hydrology, v. 296, p. 59–80.

Yasuda, T., (2015), Glacier Surge Dynamics at the West Kunlun Shan inferred from Satellite Remote Sensing, PhD Dissertation, pp. 87. Hokkaido University.

Young, N.E., Schaefer, J.M., Briner J.P., Goehring, B.M., (2013), A Be-10 production rate calibration for the Arctic. Journal of Quaternary Science, v. 28, p. 515–526.

Zech, R., (2012), A late Pleistocene glacial chronology from the Kitschi-Kurumdu Valley, Tien Shan (Kyrgyzstan), based on ^{10}Be surface exposure dating. Quaternary Research 77, 281–288.

Zhang, M., Chen, Y.X., Li, Y.K., Liu, G.N., (2016), Late Quaternary glacial history of the Nalati Range, central Tian Shan, China, investigated using ^{10}Be surface exposure dating. Journal of Quaternary Science 31, 659–670.

Zomer, R.J., Trabucco, A., Bossio, D.A., Verchot, L.V., (2008), Climate change mitigation: A spatial analysis of global land suitability for clean development mechanism afforestation and reforestation. Agriculture, Ecosystems & Environment 126, 67–80.

VITA

Jigjidsurengiin Batbaatar (Жигжидсүрэнгийн Батбаатар) was born in 1982 in Ulaanbaatar, Mongolia. He received the bachelor's and master's degree in geology from Mongolian University of Science and Technology, the School of Geology. In 2003 he started teaching hydrogeology and engineering geology in his alma mater. In 2008 he moved to Seattle to attend a graduate school at the University of Washington. His research focuses on glacial chronology and geomorphology. He lives with his wife and his two children. In addition to Earth sciences, Batbaatar enjoys watching films and playing basketball.